Lawrence Berkeley National Laboratory
Recent Work

Title
PROCEEDINGS OF THE 1975 EEP SUMMER STUDY, JULY 28 -AUG. 20, 1975

Permalink
https://escholarship.org/uc/item/463219d5

Author
Lawrence Berkeley National Laboratory

Publication Date
1975-12-01

eScholarship.org Powered by the California Digital Library
University of California

PEP 1975 SUMMER STUDY

RECEIVED
LAWRENCE
BERKELEY LABORATORY
APR 29 1976
LIBRARY AND
DOCUMENTS SECTION

For Reference

Not to be taken from this room

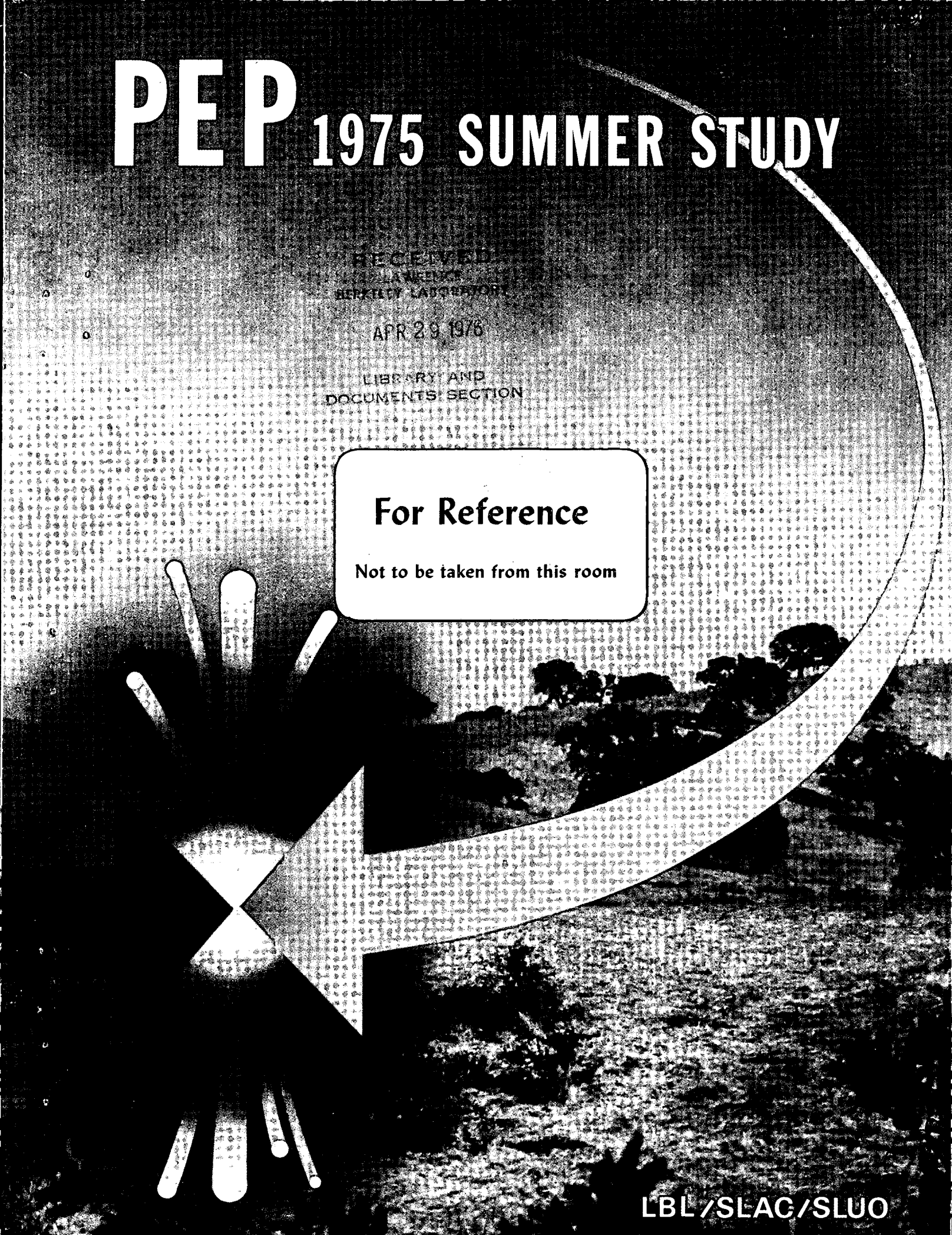

LBL/SLAC/SLUO

DISCLAIMER

This document was prepared as an account of work sponsored by the United States Government. While this document is believed to contain correct information, neither the United States Government nor any agency thereof, nor the Regents of the University of California, nor any of their employees, makes any warranty, express or implied, or assumes any legal responsibility for the accuracy, completeness, or usefulness of any information, apparatus, product, or process disclosed, or represents that its use would not infringe privately owned rights. Reference herein to any specific commercial product, process, or service by its trade name, trademark, manufacturer, or otherwise, does not necessarily constitute or imply its endorsement, recommendation, or favoring by the United States Government or any agency thereof, or the Regents of the University of California. The views and opinions of authors expressed herein do not necessarily state or reflect those of the United States Government or any agency thereof or the Regents of the University of California.

LBL-4800
UC-34d, TID 4500, R63
SLAC-190
PEP-178

PROCEEDINGS

of the

1975 PEP Summer Study

July 28—August 20, 1975

Sponsored by

Lawrence Berkeley Laboratory

Stanford Linear Accelator Center

SLAC/LBL Users Organization

December 1975

Lawrence Berkeley Laboratory

University of California

Berkeley, California

Preface

The reports in these Proceedings are organized in nine sections corresponding to the areas studied by the various working groups. The coordinators and deputy coordinators for each group gathered and edited the individual contributions in their areas of study. The working groups with their coordinators and deputy coordinators are listed in the Introduction.

Following previous Summer Study Proceedings, each report has received a PEP Note number. A complete list of PEP Notes is included in the following introductory pages. Orders for individual PEP Notes or the complete Proceedings may be placed through

Judy Zelver
Building 47, Room 112
Lawrence Berkeley Laboratory
Berkeley, CA 94720

I want to thank the Summer Study participants for their prompt reports, the coordinators and deputy coordinators for their effective editing, Walter Zawojski for the lively cover, and Bob Barton for his patient help in bringing together the many pieces of these Proceedings.

Pier Oddone
Coordinator
1975 PEP Summer Study

0 0 0 0 4 5 0 1 5 4 7

1975 PEP SUMMER STUDY

CONTENTS

List of Participants v

List of PEP Notes vi

Introduction

Introduction 1
K. Strauch

An Experimenter's View of PEP (PEP-179) 4
J. M. Paterson

Comparison of Jet and Phase Space Models at E_{cm} = 30 GeV (PEP-180) 8
G. Hanson and P. Oddone

Polarization Techniques

Report of the Polarization Group (PEP-181) 15
W. Ford, K. Kondo, F. Martin, G. Manning, D. Miller, C. Prescott

Measurement of Weak Interaction Contributions to $e^+e^- \to \mu^+\mu^-$ Using Longitudinal Polarization of the e^+ and e^- Beams (PEP-182) 19
G. Manning

A Beam Pipe for Polarization Experiments (PEP-183) 23
F. Martin

A System for Obtaining Longitudinal Beam Polarization at PEP with Vertical Dipoles Located Outside of the Interaction Region (PEP-184) 26
A. Garren, J. Kadyk

Weak Interactions

Summary of the Weak Interactions Group (PEP-185) 31
A. Benvenuti, W. Ford, D. Hitlin, K. Kondo, G. Manning, R. Morse, T. Rhoades, A. Sessoms, L. Stevenson, K. Strauch, A. Zallo

Iron Ball Mark II (PEP-186) 36
W. T. Ford

EM-Weak Interference in $e^+e^- \to \mu^+\mu^-$ Scattering (PEP-187) 39
R. Morse

Weak-Electromagnetic Interference Effects in $e^+e^- \to$ Hadrons (PEP-188) 43
D. Hitlin, A. Sessoms

General User Magnet

A General Users Magnet Design (PEP-189) 46
F. Lobkowicz, U. Becker, K. Berkelman, M. A. Green, E. Groves, K. Halbach, J. Kadyk, N. Mistry, A. Sessoms, M. Strovink

Use of Discrete Coils in Axial Field Spectrometers (PEP-190) 76
J. D. Taylor, W. A. Wenzel

Neutral Detectors

The Study of Neutral Particles (PEP-191) 84
W. Bartel, F. Bulos, A. Eisner, G. Hanson, D. Hitlin, U. Koetz, R. Kotthaus, D. Lüke, M. Marshak, T. Mast, J. Matthews, C. Peck, K. Strauch, D. Yount

The Crystal Ball at PEP (PEP-192) 88
W. Bartel, F. Bulos, D. Lüke, C. Peck, K. Strauch

A Liquid Argon Neutrals Detector (LAND) for PEP (PEP-193) 94
A. Eisner, G. Hanson, D. Hitlin, U. Koetz, M. Marshak, T. Mast, J. Matthews, C. Peck, D. Yount

Resolving Overlapping Gammas in a Modular Neutrals Detector (PEP-194) 105
F. Bulos

General Detector for Charged and Neutral Particles

Report of the General Purpose Detector Group (PEP-195) 108
A. Barbaro-Galtieri, W. Bartel, F. Bulos, R. Cool, G. Hanson,
U. Koetz, R. Kotthaus, S. Loken, D. Lüke, A. Rothenberg

Considerations for a General Flexible Detector (PEP-196). 116
F. Bulos

The Streamer Chamber as a General Detector (PEP-197) 118
G. Barbiellini, R. Kotthaus, S. Poucher, A. Seidl, F. Villa,
D. Yount

A Time Projection Chamber--1975 (PEP-198) 126
D. Nygren

Comparison of Time Projection and Drift Chamber Detectors (PEP-199) 134
J. A. J. Matthews, A. Rothenberg

Mark II Magnetic Detector for SPEAR (PEP-200) 138
R. R. Larsen

High Monentum Hadrons with Particle Identification

Detection of High Momentum Particles with Identification of the
Final State (PEP-201) 139
U. Becker, R. Cashmore, E. Groves, L. Keller, S. Loken,
C. Morehouse, S. Poucher, M. Strovink

Use of Microchannel Electron Multipliers in High Energy Physics (PEP-202) 157
P. Lecomte, V. Perez-Mendez

Photon-Photon Physics

Photon-Photon Physics (PEP-203) 159
G. Barbiellini, A. Benvenuti, K. Berkelman, A. Courau,
F. Foster, K. -W. Lai, F. Lobkowicz, J. Matthews, N. Mistry,
T. Rhoades

New Particle Searches

Report of the New Particle Group (PEP-204) 176
A. Carroll, B. Cox, A. Eisner, K. W. Lai, F. Lobkowicz, M. Marshak,
J. Marx, J. Matthews, N. Mistry, C. Morehouse, J. Poucher,
R. Rothenberg, A. Seidl, D. Yount

Experimental Areas

Report of the Experimental Areas Group (PEP-205) 215
A. Carroll, B. Case, D. Coyne, F. Foster, F. Lobkowicz, F. Martin,
C. Morehouse, P. Oddone, C. Prescott, L. Keller, G. Manning

0 0 0 0 4 5 0 1 5 4 8

1975 PEP Summer Study

List of Participants

Guido Barbiellini
Lab Nazionali di Frascati

Wulfrin Bartel
DESY

Ulrich F. Becker
MIT

Alberto Benvenuti
Univ. of Wisconsin

Carl Berkelman
Cornell Univ.

Charles D. Buchanan
UCLA

Fatin Bulos
SLAC

Alan S. Carroll
Brookhaven National Lab

Robert Cashmore
Oxford Univ.

David Cline*
Univ. of Wisconsin

Rodney L. Cool
The Rockefeller Univ.

André Courau
LAL Orsay

Bradley Cox
Fermilab

Donald Coyne
Princeton Univ.

Alan M. Eisner
UC Santa Barbara

William T. Ford
Univ. of Pennsylvania

Frank Foster
Univ. of Lancaster

Lina Galtieri
LBL

Eric Groves
LBL

Gail Hanson
SLAC

David Hitlin
SLAC

Barrie E. Hughes
Stanford Univ.

John Kadyk
LBL

Lewis Keller
SLAC

Ulrich Koetz
DESY

Kunitaka Kondo
Tsububa Univ.

Rainer Kotthaus
Max-Planck-Inst.

Kwan-Wu Lai
Brookhaven National Lab

Alan Litke
LBL

Frederick Lobkowicz
Univ. of Rochester

Stewart Loken
LBL

Dieter Lüke
SLAC

Geofrey Manning
Rutherford HEL

Marvin L. Marshak
Univ. of Minnesota

Fred Martin
SLAC

Jay Marx
Yale Univ.

Terry Mast
LBL

John A. J. Matthews
Michigan State Univ.

Donald H. Miller
Northwestern Univ.

Nariman B. Mistry
Cornell Univ.

Charles Morehouse
SLAC

Robert Morse
Univ. of Colorado

Jerry Nelson
LBL

Dave Nygren
LBL

Pier Oddone*
LBL

Charles W. Peck
Cal Tech

Martin Perl
SLAC

John S. Poucher
Vanderbilt Univ.

Charles Prescott
SLAC

Terry G. Rhoades
MIT

Burton Richter*
SLAC

Allan Rothenberg
The Rockefeller Univ.

Andrew Seidl
Univ. of Michigan

Allen Sessoms
Harvard Univ.

Lynn Stevenson
LBL

Karl Strauch*
Harvard Univ.

Mark Strovink
LBL

Francesco Villa
SLAC

Klaus Winter
CERN

David E. Yount
Univ. of Hawaii

Adriano Zallo
Lab Nazionali di Frascati

---

*PEP Summer Study Steering Committee Member

LIST OF PEP NOTES AND REPORTS

NUMBER	AUTHOR	TITLE	DATE
PEP-1 (SLAC-967)	D. Mohl, et. al.	A High Energy Proton-Electron-Positron Colliding Beam System	
PEP-2	Dieter Mohl, Andrew Sessler	A Model for a High Energy Proton-Electron-Positron Colliding Beam System; Spear Plus a Proton Ring	9/15/71
PEP-3	M. Stevenson	Inelastic Electron-Proton Scattering with SPEAR Plus a Proton Ring	10/13/71
PEP-4	(Brookhaven)	ISABELLE	
PEP-5	S. Berman, S. Drell J. Rees, B. Richter	Feasibility Study for a 15 GeV Electron-Positron Storage Ring	
PEP-6	Michel Davier, Al Odian	Electromagnetic Backgrounds and Photon Tagging	11/6/71
PEP-7 (SPEAR - 132)	P.L. Morton, J.R. Rees	How Much Free Space Can We Provide For Experimental Apparatus?	11/71
PEP-8	Dieter Mohl, Andrew Sessler	On the Use of Isabelle in a PEP System and Other Related Topics	11/15/71
PEP-9	Stanley Flatte	Proposed NAL Photoproduction Experiments and some Comparisons with PEP Capabilities	12/6/71
PEP-10	Stanley Flatte	A Question of Duty Cycle	
PEP-11	Fred Gilman	Angular Distributions for Hadrons Produced in PEP Electroproduction Experiments	
PEP-12	Gerson Goldhaber	PEP Kinematics--Deep Inelastic Scattering--Two Exclusive Reactions as Examples	12/1/71
PEP-13	John Kadyk, John Rees	Brookhaven HEDG Meeting of December 10, 1971	12/14/71
PEP-14	A. Odian	Check on the Equivalent Radiation for PEP	
PEP-15	Stanley Brodsky	Radiative Processes in Electron-Proton Collisions at PEP	

0 0 0 0 4 5 0 1 5 4 9

NUMBER	AUTHOR	TITLE	DATE
PEP-16	M.L. Stevenson	The Kinematics and Possible Dynamics of Inelastic Lepton Scattering in PEP (15 GeV electrons on 70 GeV Protons)	2/10/72
PEP-17	Gerson Goldhaber	PEP Kinematics--Additional Remarks on the Reaction of the Type ep → e'ρN*	
PEP-18	Dieter Mohl, Andrew Sessler	PEP Parameters	4/13/72
PEP-19	H. Wiedemann	Limitations of the Transition Energy in Large e - p Colliding Beam Facilities	3/31/72
PEP-20	Lloyd Smith	On the Calculation of Luminosity for Electron-Proton Colliding Beam	4/27/72
PEP-21	M. A. Allen, J. R. Rees	High Voltage RF Systems for the PEP Rings	5/72
PEP-22 (ERAN-192)	A. Sessler	The Self-Destructive Behavior of Stored Electron Beams: The Disease Patterns, Symptons, and Cures	5/12/72
PEP-23	Al Garren	PEP Model One - A Machine Design Example	6/16/72
PEP-24 (CRISP 72-27)	M. L. Stevenson	Conceptual Design of a Hybrid Detector for Electron Physics at ISABELLE and PEP: Solonoid + Quantameter + Hadrometer (calorimeter)	6/15/72
PEP-25	M.A. Allen	Further Consideration of the RF System for PEP	
PEP-26 (SPEAR-147)	J.E. Augustin	Multiple Coulomb Scattering and Gas Bremsstrahlung at SPEAR	
PEP-27	H. Wiedemann	A Correction to Formulas Computing the Touschek Lifetime in Storage Rings.	1/73
PEP-28	A. Sessler	Strongly Turbulent Collective Motion and the Anomalous Size of Stored Particle Beams	4/26/73
PEP-29	R.O. Bangerter	Variable Proton Momentum at PEP	3/20/73
PEP-30 (LBL-1395)	E. Hartwig, V.K. Neil, R.K. Cooper	Noise in Proton Accelerators	3/73
PEP-31 (LBL-1714)	R. Bangerter, A. Garren, et. al.	PEP Lattice Design	3/73

NUMBER	AUTHOR	TITLE	DATE
PEP-32	A. Garren, T. Elioff	Use of the Electron Ring for Protons in the PEP System	4/17/73
PEP-33	Allen, Avery, Elioff, et. al.	Proton-Electron-Positron Design Study (LBL-1746 and SLAC-1220)	3/73
PEP-34 (Rev.)	A. Garren	PEP Model Five: An Update of PEP Parameters	7/17/73
PEP-35	L. Stevenson	Kinematics and Possible Dynamics of $e + \rightarrow \lambda\ e' +$ Hadrons	
PEP-36	T. Elioff	Notes of PEP "Bull Session" of March 1 - 2, 1973	7/6/73
PEP-37 (SPEAR-163)	P. B. Wilson	Beam Loading in High Energy Storage Rings	7/19/73

PEP Notes 38 - 72 are in the 1973
PEP Summer Study Report dated August 1973.

PEP-38	A. Garren	PEP Model Six	
PEP-39	H. Wiedemann	Scaling of FODO-CELL Parameters	
PEP-40	M. Month, A. Ruggiero	Closed Orbit Beam-Beam Effect for Crossing Beams	
PEP-41	D. Mohl	Space-charge Effects at Transition Energy: An Attempt to Scale from the CPS to PEP-6 and Other Machines	
PEP-42	E. Keil	The Excitation of Non-linear Resonances by a Displaced Elliptical Beam	
PEP-43	G. Rees	Bunch Lengthening and Widening Effects Due to the Combination of RF Noise and the Presence of Inductive Wall Elements	
PEP-44	A. Ruggiero	Beam-Beam Limit in SPEAR as a Single Resonance Effect	
PEP-45	F. Sacherer	Bunch Lengthening	
PEP-46	H. Wiedemann	Proton Beam Enlargement by Gas Scattering	
PEP-47	R. Helm	Synchrotron Radiation Integrals from PEP-6	

0 0 0 0 4 5 0 1 5 5 0

NUMBER	AUTHOR	TITLE	DATE
PEP-48	H. Wiedemann	Enlargement of the Electron Beam Cross Section in a Storage Ring due to an Oscillating Synchrotron Radiation Damping Time Constant	
PEP-49	A. Ruggiero	Transverse Bunch-Bunch Instability in PEP (Resistive Wall)	
PEP-50	M. King	Some Comments on Working Points and Resonance Effects in PEP Lattices	
PEP-51	G. Rees	Aspects of PEP as Compared to EPIC	
PEP-52	A. Ruggiero, L. Smith	Calculation of Resonance Effects Due to a Localized Gaussian Charge Distribution	
PEP-53	H. Hereward	Equilibrium Energy Distribution in a non-linear Potential Well in the Presence of Quantum Fluctuation	
PEP-54	A. Ruggiero	Head-Tail Effect in PEP	
PEP-55	M. Melvin, A. Ruggiero	Interaction of a Coasting Beam and a Bunched Beam with Frequency Slip	
PEP-56	H. Hereward	Some Possible Causes of Bunch Shape Distortion in SPEAR	
PEP-57	H. Hereward	Possibility of Observing Turbulence in SPEAR	
PEP-58	H. Wiedemann	e - p Luminosity for Different Energies in PEP	
PEP-59	E. Keil	Diffusion-like Blow-up in Asynchronous Bunched Beam Collisions	
PEP-60	R. H. Helm	A Negative Momentum-Compaction Lattice	
PEP-61 (SPEAR-165)	M.J. Lee, W.W. Lee, et. al.	Magnet Insertion Code (MAGIC)	
PEP-62	R. Chasman, A. Garren, et. al.	PEP with Crossing Angle	
PEP-63	J. Augustin	Longitudinal Beam-Beam Effect in Head-on Collisions	

NUMBER	AUTHOR	TITLE	DATE
PEP-64	J. LeDuff	Behavior of a Stochastic Non-Linear System Excited by an External Harmonic Force.	
PEP-65	J. LeDuff	Diffusion on a Single Non-Linear Resonance in the Case of e-p Collisions	
PEP-66	T. Elioff, H. Hereward, et. al.	Storage Ring Experiments	
PEP-67	H. Hereward	Influence of the Touschek Effect on Life-time Measurement in SPEAR	
PEP-68	D. Mohl, P. Morton	The Use of Rf-Knockout to Measure Synchrotron Oscillation Frequencies and Energy	
PEP-69	J. Rees, B. Richter	Preliminary Design of a 15 GeV Electron-Positron Variable-Tune Storage Ring	
PEP-70	M.A. Green	Superconducting Dipoles and Quadrupoles for the PEP Accelerating Storage Proton Ring	
PEP-71	J. R. LeDuff	Properties of Bunch Lengthening Effect Observed on Existing e^+e^- Storage Rings	
PEP-72	A. Renieri	Incoherent Beam-Beam Effect: A Computer Simulation	
PEP-73			
PEP-74			
PEP-75	R. F. Schwitters	Comments on Obtaining Longitudinally Polarized Beams	10/73
PEP-76	J. B. McCaslin, R.H. Thomas	Neutron Shielding for PEP	11/13/73
PEP-77	A. Garren, J. Kadyk	Detection of Proton Beam Jet in 15 x 200 GeV PEP	1/21/74
PEP-78 (SPEAR-169)	R. Helm, M. J. Lee	Double Thin-Lens Approximation for Preliminary PEPSI8 Lattice Design	12/73
PEP-79	B. Richter	PEP Parameters	1/74
PEP-80	J. Rees, A.V. Lisin	Tentative PEP Stage I Beam Stay - Clear Requirements and Beam Line Space Allocation	1/74

0 0 0 0 4 5 0 1 5 5 1

NUMBER	AUTHOR	TITLE	DATE
PEP-81	P.J. Channell	Transverse Diffusion of Proton Beams Due to Noise	2/14/74
PEP-82	R. H. Thomas	Proton Losses from PEP	2/21/74
PEP-83	T.M. Jenkins, R. H. Thomas	Muon Shielding for PEP	2/21/74
PEP-84	G. E. Fischer	PEP Inflection	3/1/74
PEP-85	G.A. Loew, et. al.	A Few Thoughts Regarding Beam Cavity Mode Excitation in PEP	5/16/74
PEP-86 (LBL-3032)	L. Smith	Proton-Electron-Positron - PEP	5/17/74
PEP-87 (SPEAR-175)	R. Schwitters, B. Richters	A Method for Producing Longitudinal Beam Polarization at PEP	6/74
PEP-88	J. Jurow, N. Dean	Synchrotron Radiation Absorbing Surfaces	7/25/74
PEP-89	M. Allen	Higher Order Modes in SPEAR II Cavities	7/74
PEP-90	M. Sands	Energy Loss to Parasitic Modes of the Accelerating Cavities	
PEP-91	L. J. Laslett	Concerning the Density Distribution and Associated Fields	7/30/74
PEP-92	M. Sands	Parasitic Cavity Losses in SPEAR-2	
PEP-93	L. J. Laslett	Examples of Weak-Beam/Strong-Beam Computations Performed by use of the Program "WEAK8", with Graphic Output	8/5/74
PEP-94	L.J. Laslett	An Example of the Use of Program "WEAK9"	8/6/74
PEP-95	M. Sands	A Bench Measurement of the Energy Loss of a Stored Beam to a Cavity	8/8/74
PEP-96	J. Rees	The PEP Electron-Positron Ring - PEP Stage I	8/12/74
PEP-97	M.Allen P. Wilson	RF Systems for High Energy e^-e^+ Storage Rings	8/14/74
PEP-98	R. Helm M. Lee	Preliminary Design Considerations for the Stage I PEP Lattice	8/14/74
PEP-99	R. Helm, M. Lee, J. Paterson	Beam Enlargement by Mismatching the Energy-Dispersion Function	8/14/74
PEP-100	P. Wilson	Beam Loading in High-Energy Storage Rings	8/20/74

NUMBER	AUTHOR	TITLE	DATE
PEP-101	P. Wilson	Stored Current Capability of the PEP R.F. System	9/10/74
PEP-102	W. Wenzel	Comparison of Two Configurations for Intersection Regions	9/23/74
PEP-103	M. Allen J.M. Paterson P. Wilson	Measurement of Higher Order Mode Losses in SPEAR II by Shift in Synchrotron Phase and Increase in Net Cavity Power	9/19/74
PEP-104	P. Channell	Alternative Theories of the Non-Linear Negative Mass Instability	10/29/74
PEP-105	A.W. Chao P.L. Morton	Physical Picture of the Electro-magnetic Fields Between Two Infinite Conducting Plates Produced by a Point Charge Moving at the Speed of Light	2/3/75
PEP-106	J.M. Jenkins J.B. McCaslin R. H. Thomas	Shielding Required for Radiation Produced by the 15 GeV Stored Electrons	1/20/75
PEP-107	W. Wenzel	PEP Experimental Areas-Winter of '75	2/12/75
PEP-108	LBL-SLAC Joint Study Group	The PEP Electron-Positron Ring: An Update	2/25/75 (from SLAC)
PEP-109 (Health Physics)	W.R. Nelson G.J. Warren R.L. Ford	The Radiation Dose to the Coil Linings and the Production of Nitric Acid and Ozone from PEP Synchrotron Radiation	3/6/75
PEP-110	A.W. Chao M.J. Lee P.L. Morton	Higher Order Multipole Magnet Tolerances	3/7/75
PEP-111	M.J. Lee P.L. Morton J.R. Rees B. Richter	Control of Closed Orbit Deviation Due to Synchrotron Radiation	3/7/75
PEP-112	K. Bane P. Wilson		3/25/75
PEP-113	R.T. Avery J.M. Peterson K.L. Brown	The PEP Injection System	3/27/75
PEP-114	D. Bostic, et al.	Vacuum System for the Stanford-LBL Storage Ring (PEP)	3/27/75
PEP-115	M. Allen J.M. Paterson J.R. Rees P.B. Wilson	Beam Energy Loss to Parasitic Modes in SPEAR II	3/27/75
PEP-116	F. Martin	Background Estimates for PEP	3/28/75
PEP-117	H. Weidemann	Implication of Shorter Cells in PEP	3/28/75
PEP-118	A.W. Chao	Parasitic Loss of a Gaussian Bunch in a Closed Cavity	4/24/75
PEP-119	A.W. Chao P.L. Morton	Differential Energy Loss for a Particle in a Square Pulse of Charge Traveling Between Infinite Conducting Plates	4/75

0 0 0 0 4 5 0 1 5 5 2

NUMBER	AUTHOR	TITLE	DATE
PEP-120	J.L. Pelligrini	Deflection of Relativistic Beams by Means of a Traveling Wave Electrode	5/30/75
PEP-121	E. Keil	The Behavior of Betatron Oscillation in the Vicinity of Half Integral Structure Resonances.	5/30/75
PEP-122 (SPEAR-185)	Roger McConnell	Beam Induced Transit Time Signals at SPEAR	6/6/75
PEP-123	P.B. Wilson		6/9/75
PEP-124	T. Jackson	High Performance Magnet Power Supply Optimization	6/10/75
PEP-125	J. Paterson J. Rees H. Wiedemann	Beam Size Control in PEP	7/21/75
PEP-126	D. Keil	Bunch Lengthening and Bucket Distortion Due to Cavities	5/75
PEP-127	R. Avery	Injection Transfer Line Coordinates	7/31/75
PEP-128	R. Avery	PEP Ring Coordinates - Configuration E	8/11/75
PEP-129	A.W. Chao	On the Horizontal Shape of An Electron Bunch	8/13/75
PEP-130 SPEAR-188	A.W. Chao Martin Lee	Stationary Solution of the Fokker/Planck Equation for Linearly Coupled Motion in an Electron Storage Ring	8/28/75
PEP-131	A. Chao M. Lee	Changing Particle Distribution for Linearly Coupled Motion in an Electron Storage Ring	9/8/75
PEP-132	A. Chao M. Lee P. Morton	Evaluation of the Field Quality of the Prototype PEP Cell Quadrupole Magnet	9/9/75
PEP-133	F. Hall D. Robbins	PEP Cooling Water Systems and Underground Piped Utilities Design Criteria Report	10/7/75
PEP-137		1974 PEP Summer Study (PEP-138-177)	Aug. 1974
PEP-138	K. Strauch	Introductory Remarks	"
PEP-139	J. Rees	The PEP Electron-Positron Ring	"
PEP-140	B. Richter	Event Rates to be Expected at PEP	"
PEP-141	G. Abrams et.al.	Report of the Study Group for the Measurement of the Total Cross Section for $e^+e^- \rightarrow$ Hadrons	"
PEP-142	H. Lynch, R. Schwitters	Non-Magnetic Detector for Measuring σ_T and Charged Multiplicities in e^+e^- Annihilation	"
PEP-143	G. Feldman, D. Hitlin	Precise Measurement of the Total Cross Section	"
PEP-144	D. Nygren	The Time-Projection Chamber - A New 4π Detector for Charged Particles	"

NUMBER	AUTHOR	TITLE	DATE
PEP-145	B. Shen	Contribution of the Two-Photon Annihilation Process in the Measurement of σ_T at PEP	"
PEP-146	G. Buschhorn et.al.	Detection of High-Momentum Hadrons	"
PEP-147	G. Barbiellini	Heavy Hadrons - Group Report	"
PEP-148	A. Barbaro-Galtieri, et.al.	Large-Solid-Angle Detector for Charged and Neutral Particles	"
PEP-149	J. Perez-y-Jorba	The Detection of Low-Energy Charged Particles Identification Up to 3.5 GeV/c	"
PEP-150	P. Spillantini	Study of a Multi-Hadron Facility for PEP Based on Toroidal Field Magnets	"
PEP-151	G. Buschhorn, et.al.	A Streamer Chamber Detector for PEP	"
PEP-152	P. Yamin	Comments on the Simultaneous Measurement of Charged and Neutral Components of Multihadron Events	"
PEP-153	T. Mast, J. Nelson	Some Design Considerations for a Large Solid Angle Charged Plus Neutrals Detector for e^+e^- Storage Rings	"
PEP-154	E. Bloom et.al.	Report on Neutral Particle Detectors and Q.E.D.	"
PEP-155	E. Bloom et.al.	Properties of Some Photon Detectors	Aug. 1974
PEP-156	A. Odian	Liquid Argon Gamma Ray Detector - Variations of the Willis Chamber	"
PEP-157	D. Buchholz, et.al.	Report of the Weak Interactions/EM Final States Group	"
PEP-158	D. Cline, L. Resvanis	Tests of μ-e Universality for Weak Neutral Currents at PEP	"
PEP-159	V. Camerini, et.al.	A Compact Magnetic Detector for μ^+-μ^- Asymmetry Measurements and Longitudinal Polarization Utilization at PEP	"
PEP-160	S. Yellin	A Suggested Detector	"
PEP-161	K. Strauch	Study of the Reaction $e^+e^- \rightarrow \mu^+\mu^-$ with an Iron Solenoid Spectrometer	"
PEP-162	W. Wenzel	Solenoid Spectrometers for $e^+e^- \rightarrow \mu^+\mu^-$ and Other Final States	"
PEP-163	P. Limon, et.al.	Direct Measurement fo Muon Polarization in $e^+e^- \rightarrow \mu^+\mu^-$	"
PEP-164	D. Hitlin, et.al.	Strange Particle Experiments at PEP	"
PEP-165	J. Klems	Parity Violating Momentum Correlations as a Means of Observing Weak Interactions in $e^+e^- \rightarrow$ Hadrons	"
PEP-166	D. Buchholz, et.al.	Polarization Group Coordinators' Summary	"

0 0 0 0 4 5 0 1 5 5 3

NUMBER	AUTHOR	TITLE	DATE
PEP-167	R. Schwitters	Control of Direction of Beam Polarization	"
PEP-168	W. Wenzel	Notes on Longitudinal Beam Polarization	"
PEP-169	W. Toner	Resonance Method to Produce a Polarization Asymmetry in Electron-Positron Storage Rings	"
PEP-170	U. Camerini	Two Methods to Measure the $e^{\pm}$ Polarization at PEP	"
PEP-171	C. Prescott	A Pulsed Polarization Monitor for PEP	"
PEP-172	W. Toner	A First Look at a Polarimeter for EPIC or PEP	"
PEP-173	D. Buchholz, et.al.	An Alternate Way of Measuring Beam Polarization at an e^+e^- Colliding Beam Facility	Aug. 1974
PEP-174	D. Berley, et.al.	New Particle Searches at PEP	"
PEP-175	G. Barbiellini, et.al.	Colliding γ Beams: Two-Photon Processes and Tagging	"
PEP-176	H. Lynch, et.al.	Background Sources at PEP	"
PEP-177	D. Berley, et.al.	Report of the Experimental Areas Group	"

0 0 0 0 4 5 0 1 5 5 4

INTRODUCTION

K. Strauch

The 1975 PEP Summer Study took place in an atmosphere of great excitement and great expectation. The basic discovery of the J/ψ particle on the AGS and on SPEAR has led to the revelation of a whole new "charmed" spectroscopy involving decays with single photon or multi-particle emission. Jet structure has been observed in hadron production above $\sqrt{s}$ = 7 GeV with the "jet axis" remembering the e^- and e^+ beam polarizations. The 1974 Summer Study had considered the possibility of narrow resonances, of single photon emission and of polarization effects in hadron production; but who would have dared to predict that all of these would be observed within one year? The physics of e^+e^- annihilation has indeed proven rich beyond all expectation.

The design of PEP has been refined since last summer. The high energy capability has been improved. The time for polarization of lower energy beams has been reduced by the use of wigglers. The lessons learned from SPEAR with respect to backgrounds from high energy synchrotron radiation, have been applied to the design of the lattice near the interaction region. Most of the suggestions of the 1974 Summer Study have been incorporated into the plans for the experimental areas.

PEP has received a very strong endorsement from the 1975 HEPAP Subpanel on New Facilities, and there are good reasons for optimism that full funding will occur in FY-1976.

The 1975 Study had the following tasks:

1. Discuss the potential PEP physics program, particularly taking into account the newly discovered phenomena and the use of polarized beams.

2. Prepare designs for experimental apparatus to carry out the physics program. An important question concerned the feasibility and desirability of building a General Users Magnet (GUM) with a basic central detector to which each user group would add necessary equipment for a complete experiment. Special attention was also to be given to the application of new existing, or potentially existing technology.

3. Review the design of the experimental areas, designs which are largely based on the concepts developed during the previous year's study. Assuming full funding of PEP in FY'76, a call for proposals for "long lead time" facilities and experiments is tentatively planned for June 1976 with submissions scheduled for December 1976. These not too distant dates helped to bring an atmosphere of happy reality to the 1975 Summer Study.

The Steering Committee consisted of B. Barish (Caltech); D. Cline (Wisconsin); M. Goldberger (Princeton); H. Lubatti (Washington); P. Oddone (LBL); B. Richter (SLAC); K. Strauch (Harvard), Chairman. The organization of the 1974 Study had proven to be satisfactory; the modifications made for 1975 were due only to the more limited time available before the start of the 1975 Lepton-Photon Symposium.

The first day (July 28) was devoted to reviews of the PEP design and of the work of the 1974 Summer Study and to the organization of working groups. The next three days (July 29-31) coincided with the Topical Conference of the 1975 SLAC Summer Institute on Particle Physics which provided a good opportunity to find out the latest news in e^+e^- physics which had not yet appeared in the N.Y. Times. The main work of the Summer Study was carried out between August 1-18. August 19-20 were devoted to summary talks and discussions of the work of the various groups; all delegates to the Lepton-Photon Symposium were invited for these two days, and a large number attended. The program for these two days is appended.

The Steering Committee had the difficult task of selecting 25 physicists from outside the LBL-SLAC community from the 60 who had responded to the letter announcing the Study sent in February to all members of the APS Division of Particles and Fields, and 20 physicists within the LBL-SLAC community. These were joined by 11 colleagues from England, France, Germany, Italy, and Japan.

The following groups were formed at the start of the Study, each with a Coordinator and a Deputy Coordinator:

1. Production and use of polarized beams (D. Miller, F. Martin)
2. Weak interaction experiments (W. Ford, D. Hitlin)
3. General purpose magnetic detector (R. Cool, G. Hanson)
4. Multi-User Magnet (F. Lobkowitz, J. Kadyk)
5. High momentum particle detector and particle identification (U. Becker, M. Strovink)
6. Neutral particle detector (C. Peck, T. Mast)
7. Searches for new particles (J. Marx, C. Morehouse)
8. Two-photon physics (K. Berkelman, N. Mistry)
9. Experimental areas (G. Manning, L. Keller)

This particular group structure proved satisfactory and survived until the end; there was some specialization within groups as is indicated in the papers reporting the work of each group. Participants joined one or more of the groups.

Participants had to work hard and efficiently to make good use of the somewhat limited time available to accomplish the goals of the Summer Study. It is not possible to summarize all of the work which is reported in these Proceedings. I found the following of particular interest. It appears quite feasible to study interference effects between the weak and QED interactions with one beam longitudinally polarized, the other un-

polarized, at least in the reaction $e^+e^- \rightarrow \mu^+\mu^-$; promising solutions were discussed for the problems of space limitation and synchrotron radiation which are present in the polarization scheme of Richter and Schwitters described in the 1974 Proceedings. All final large magnetic detector designs use a solenoidal field produced by a superconductor; differences arise mainly from the use of lumped or continuous coils. A General Users Magnet appears quite feasible and practical; its desirability will, to a large extent, depend on the interests of the user community. With one exception, the specifications of the solenoidal field and volume were similar, suggesting that perhaps two such devices would serve most of the presently envisioned experiments needing large magnetic volumes. (The one exception is a design requiring the use of many micro-channel phototubes which is not yet an economically viable reality.) Photon detection over a wide energy range remains a problem. NaI has most of the desired characteristics, but is too expensive to surround a magnetic field; argon calorimeters are bulky and have problems with low energy response. Every interaction region needs a tagging system, either to study two-photon events, or to at least estimate the two-photon background.

Every general magnetic detector design tries to achieve 4π solid angle coverage, reliable identification and accurate momentum determination of both charged and neutral particles. The discoveries of the last twelve months reemphasize the importance of these goals. Since no one detector has yet been designed which incorporates optimum solutions for each goal, designs differ mainly in their emphasis on different desirable properties.

At PEP energies, hadronic events are expected to involve about twice as many individual particles as at SPEAR. These particles will probably be emitted in two back-to-back jets. Such jets would produce difficult problems in individual track reconstruction and in the use of big Cerenkov counters. To alleviate the problem of track reconstruction, two-promising central detectors surrounding the interaction region were discussed: the Streamer Chamber and the Time Projection Chamber. However, because of limitations in time, only a start was made on the evaluation of the performance of the various detector designs for events with jet structure. Further analysis is needed.

The PEP design group under John Rees and Tom Elioff worked closely and effectively with the Summer Study. The participation of colleagues from the CERN, DESY, Frascati, KEK, Orsay and Rutherford laboratories was most helpful and much appreciated. We thank the management of these laboratories for making this participation possible.

For the second year in a row, LBL played host to the PEP Summer Study. The LBL staff, under the direction of Andy Sessler and Bob Birge, worked most effectively to provide all necessary support and assistance. All participants are greatly indebted to Pier Oddone who more than any other individual was responsible for the fine organization and smooth working of the Study. Margit Birge and helpers cheerfully satisfied all reasonable and unreasonable secretarial requests. Jean Lynch was everybody's friend and helper in her multiple roles as effective housing agent for families, understanding sorority mother for lonely bachelors, cook of delicious barbecues and snacks, elegant and charming hostess of a splendid dinner dance at the San Francisco St. Francis Yacht Club. The hospitality of our Berkeley colleagues was in the best western tradition and greatly appreciated by all visitors and their families.

We thank ERDA whose support made the Summer Study possible. There are many similarities between a Wine Tasting and a Summer Study. Participants are exposed to many bouquets and flavors with the expectation that one or two will prove attractive enough to be worth long and continuous enjoyment. Realization of such long term activity requires, of course, interest in participation and availability of supplies. I believe that the 1975 PEP Summer Study further encouraged the U.S. High Energy Physics community to participate in the PEP program. And, I very much hope that our work helped some to bring closer the realization of this most exciting new tool for probing into the fundamental properties of nature.

0 0 0 0 4 5 0 1 5 5 5

Appendix

Summary Review Sessions of Work of the
1975 PEP Summer Study

Tuesday August 19

Welcome and Introduction	9:30 A.M.
An Experimenter's View of PEP J. M. Paterson	9:45 - 10:30
Polarized Beams at PEP D. Miller	10:30 - 11:15
Coffee Break	11:15 - 11:30
Weak Interaction Effects in QED Reactions and Hadron Production W. Ford	11:30 - 12:45
Lunch (LBL Cafeteria)	
General Purpose Detector R. Cool	2:00 - 3:00 P.M.
Multi-User Detection System F. Lobkowicz	3:00 - 4:00
Coffee Break	4:00 - 4:15
High Momentum Detectors and Particle Identification U. Becker	4:15 - 5:15
Wine and Cheese Reception (LBL Cafeteria)	6:00

Wednesday, August 20:

Streamer Chamber Detector D. Yount	9:30 - 10:00 A.M.
Time Projection Detector D. Nygren	10:00 - 10:30
Neutral Detectors C. Peck	10:30 - 11:15
Coffee Break	11:15 - 11:30
Search for New Particles J. Marx	11:30 - 1:30 P.M.
Lunch (LBL Cafeteria)	12:30 - 1:30 P.M.
Two-Photon Physics K. Berkelman	1:30 - 2:30
Experimental Areas Report G. Manning	2:30 - 3:30
Concluding Remarks	3:30 - 3:45

AN EXPERIMENTER'S VIEW OF PEP

J. M. Paterson

Stanford Linear Accelerator Center

Abstract

Since the 1974 Summer Study, the PEP design has been greatly refined in ways that have very much expanded its physics capability. In this report, I shall briefly discuss the effects of the changes on the luminosity vs. energy function, beam polarization and backgrounds. Experimental facilities are discussed elsewhere in these Proceedings.

INTRODUCTION

During the past twelve months, there have been two very important changes in the basic PEP magnet lattice. The first of these is the change from a 48-cell magnet structure through the curved sections of the ring to a structure with twice as many quadrupole focusing elements evenly distributed; i.e., a 96-cell structure. This structure change does many things to improve PEP, but from the experimenter's point-of-view, the most significant is the expansion of the energy range to higher energies. It also leaves open the possibility of further extension to still higher energies in future improvement programs.

At the same time this design change was made, six short straight sections of 5-metre length were incorporated into the lattice. They are in the centre of each of the curved sextants. The idea was to leave space for the as-yet-unknown beam control devices which may be desirable in the future. Shortly thereafter, three of the six straight sections were occupied by "wiggler" magnets. These magnets are used to control the beam size at energies less than 15 GeV by increasing the synchrotron radiation emitted by the particles. As the wiggler magnets are independent of the main bending magnet system and only locally perturb the orbit, the synchrotron radiation power emitted by the beam can be controlled at any fixed energy, giving smooth control of beam size, energy spread and damping times. A more complete discussion of this system can be found in reports SPEAR-186/PEP-125. Beam size control is necessary to optimize the luminosity at energies less than 15 GeV where one is no longer rf-power limited. This control was previously accomplished by the use of different lattice arrangements at different energies. The new technique is more flexible and has several advantages, including shorter injection times and shorter polarization build-up times at these lower energies.

The updated PEP design, which includes the above changes, is being published essentially simultaneously with this report (viz., PEP Conceptual Design Report, LBL-4288/SLAC-189, October 1975). The reader is referred to this report for the details of what I am about to discuss.

LUMINOSITY VS. ENERGY

Figure 1 shows the luminosity versus energy function for the present PEP design. In the region below 15 GeV, the $\mathscr{L}$uminosity $\propto E^2$ and the stored current $I \propto E$, rising from 3×10^{11} particles/bunch at 5 GeV to 10^{12} particles/bunch at 15 GeV. It should be noted that since last year's Summer Study, SPEAR II has come into being with the same rf frequency as PEP and therefore the same short bunch length. Already in SPEAR II, currents of 3×10^{11} particles/bunch have been stored at the much lower energy of 1.5 GeV. This has greatly reinforced our confidence in the projected PEP performance. In this energy region, the wiggler magnets will be used to maintain a beam size independent of energy, a necessary feature in obtaining this performance.

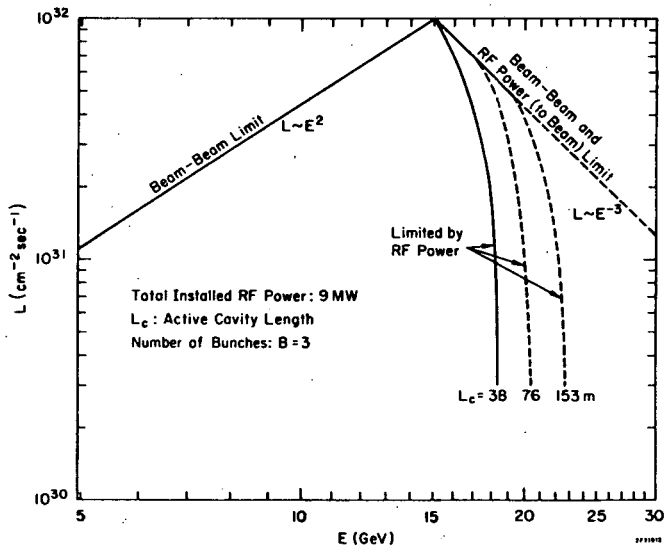

Fig. 1 -- Luminosity versus energy.

As before, the luminosity peaks at $10^{32}cm^{-2}sec^{-1}$ at 15 GeV, where the power lost to synchrotron radiation and to higher-order-mode losses in the vacuum system is balanced by the planned 9-MW rf accelerating system. Above this point, the current that can be stored falls very rapidly, and with a fixed magnet lattice, the luminosity would fall as E^{-10}. It is here that the increased flexibility of the 96-cell lattice becomes important. By using the variable-tune method of beam size control to decrease the beam size as the energy increases (in a fixed lattice the beam size increases as E), the rapid fall in the luminosity function can be ameliorated to a $\mathscr{L} \propto E^{-3}$ dependence. Figure 1 shows

0 0 0 0 4 5 0 1 5 5 6

three different cases where, keeping the rf power a constant, the length of the accelerating structure is increased. The first curve corresponds to the present PEP design and now has a luminosity of $10^{31}\,cm^{-2}\,sec^{-1}$ at 18 GeV. The other curves indicate possible future expansion of the energy range by increasing the length of the accelerating structure without modifications to the lattice. These steps toward a PEP II, although outside the scope of the PEP budget, are inexpensive enough to be undertaken as accelerator improvements.

BEAM POLARIZATION

During last year's study, there was considerable interest in the potential use of the predicted transverse polarization that builds up in a circulating electron beam that is emitting synchrotron radiation. However, there was still some uncertainty as to how fragile the beam polarization would be in routine operation. The very strong non-linear fields associated with operating these high-energy rings with large beam-beam effects could increase the number of depolarizing resonances to the point where they would make the storage ring so sensitive that effective polarization might be impossible to maintain. Experience with SPEAR II in the last year has done much to remove these worries, as a high degree of beam polarization was achieved in routine operation. With a polarization build-up time of 20 mins, the beams were 85% polarized within an hour and were insensitive to operating configurations. A beam depolarizer, which utilises an oscillating transverse field, is presently under construction and will be installed and tested in SPEAR during the coming year. This accumulation of experience on polarization in SPEAR will be very useful in planning for PEP.

Figure 2 shows the polarization build-up time in PEP. The dashed curve corresponds to operation without wiggler magnets and $\tau_{pol} \propto E^{-5}$. When one utilises wigglers to achieve the $\mathscr{L} \propto E^2$ performance, one has the added benefit of a reduction in τ_{pol} at the lower energies as shown in Fig. 2. If the physics required the use of beam polarization at even lower energies, this can be achieved by extending this procedure. Using the presently-designed wiggler magnets at full strength, i.e., 20 kG, would give too large a beam size for the available aperture. However, using the variable tune technique to reduce the beam size as previously described for operation above 15 GeV, one could achieve the performance shown in Fig. 3. This is another example of the improved flexibility and future potential of the present PEP design.

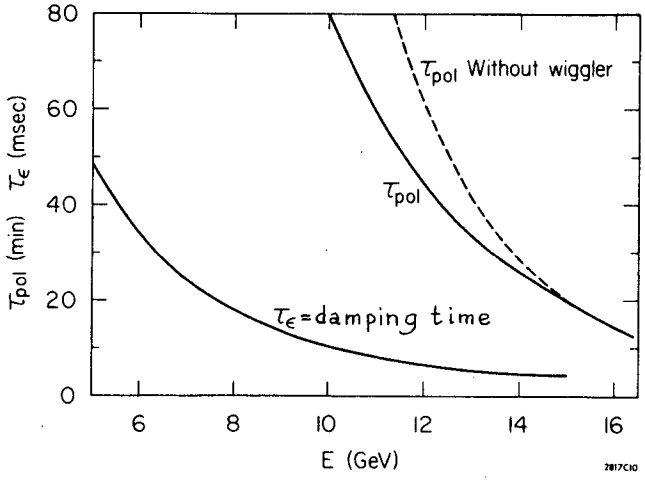

Fig. 2 -- Polarization build-up time versus energy for the case where the lattice configuration is constant.

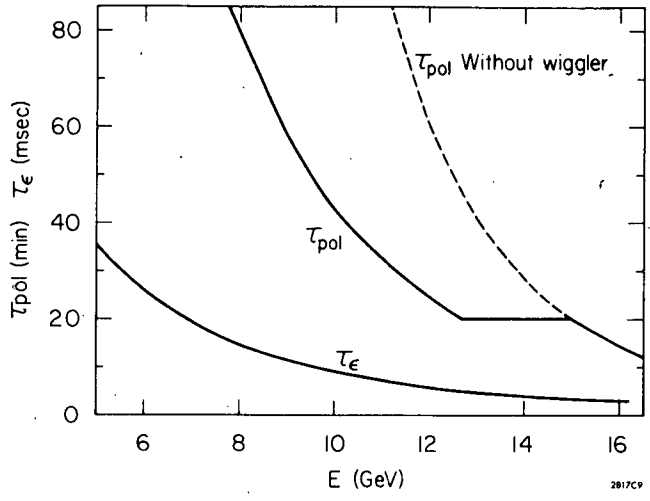

Fig. 3 -- Polarization build-up time versus energy for the case where the wiggler magnets are at full strength and the lattice is varied to maintain a constant beam cross section.

BACKGROUNDS

Estimates of particle loss rates in the neighborhood of the interaction regions were presented in last year's study. They indicated that at the highest currents there is an approximately 50% probability of a particle striking the vacuum chamber close to, or in, the interaction region for each bunch passage. Since then, a more complete Monte-Carlo and tracking calculation has confirmed these estimates (PEP-116). These calculations show that particles which have undergone bremsstrahlung in the curved sextants have only a very small probability of reaching the interaction region and that the source of background events is the bremsstrahlung (both the photons and the electrons) occurring in the 50 metres on either side of the interaction point. This is valid also in SPEAR and has been checked experimentally. It is obvious that a great effort will be made to keep the pressure in this region as low as possible. However, one can also attempt to prevent these particles from targetting on the interaction region beam pipe by including aperture stops in the system. This has been studied for PEP, and Fig. 4 shows a possible set of thick, high-Z collimators which should significantly reduce the number of particles which can contribute to experimental backgrounds.

Figure 4 also shows two new important features. They are: the addition of low-field magnets at the end of the sextants and the movable thin high-Z mask at the end of the interaction region. These devices are necessary to take care of a problem which has become serious in SPEAR and would be even

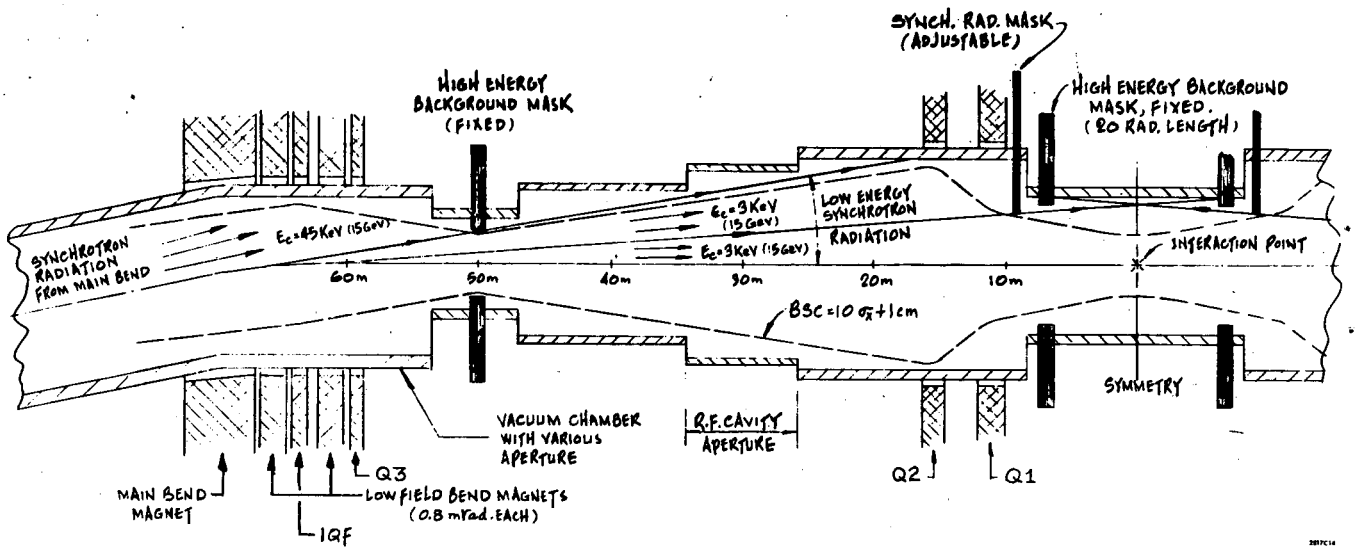

Fig. 4 -- Layout of insertion region straight section showing locations of background collimators, synchrotron radiation masks and low-field magnets.

more serious in PEP. The problem is that as the beam energy increases, the synchrotron radiation power increases as E^4 and the critical photon energy as E^3. This means that the number of hard x-rays or soft γ-rays increases rapidly and masking becomes very difficult. In SPEAR at the higher energies, these hard x-rays scattering from the edge of the tantalum masks which masked the interaction region pipe penetrated the vacuum chamber and literally saturated the counters and chambers in the vicinity. To remove this problem, it was necessary to reduce the flux and photon energy of the radiation impinging on this last mask. This was done in SPEAR, and is planned in PEP, by lowering the bending field at the end of the sextants. These magnets and their synchrotron radiation pattern are shown in Fig. 4. The photon flux through the interaction region with and without the low-field magnets is shown in Fig. 5. These curves are self-explanatory and clearly show that in designing the interaction region vacuum chambers and experimental apparatus, one must take care to avoid the unmasked region close to the beam.

Another important background problem lies in beam-gas interactions within the experimental apparatus. For some experiments, these interactions can simulate the events of interest and require background subtractions. As the gas pressure distribution within the apparatus is difficult to monitor and is a function of the operating conditions of the storage ring, one cannot easily condense the accumulation of data on beam gas background in any quantitative way. With the luminosity region being short (10-15 cm), one can, however, cleanly separate beam gas events from those from e^+-e^- annihilation by studying the distribution of events along the beam axis and extrapolating through the luminous region. This, of course, implies that the apparatus has an acceptance over, say, ±50 cm, which is well understood and has adequate spatial resolution in the beam direction.

When an experimental apparatus becomes large and vacuum pumping of the vacuum chamber is only from the pumps in the neighboring quadrupoles, the pressure in the interaction region could be higher than desired. In designing experiments, consideration should be given to including some pumping capacity within the 20 metres where the experiment is sensitive to the typical e-p scattering events of beam gas interaction.

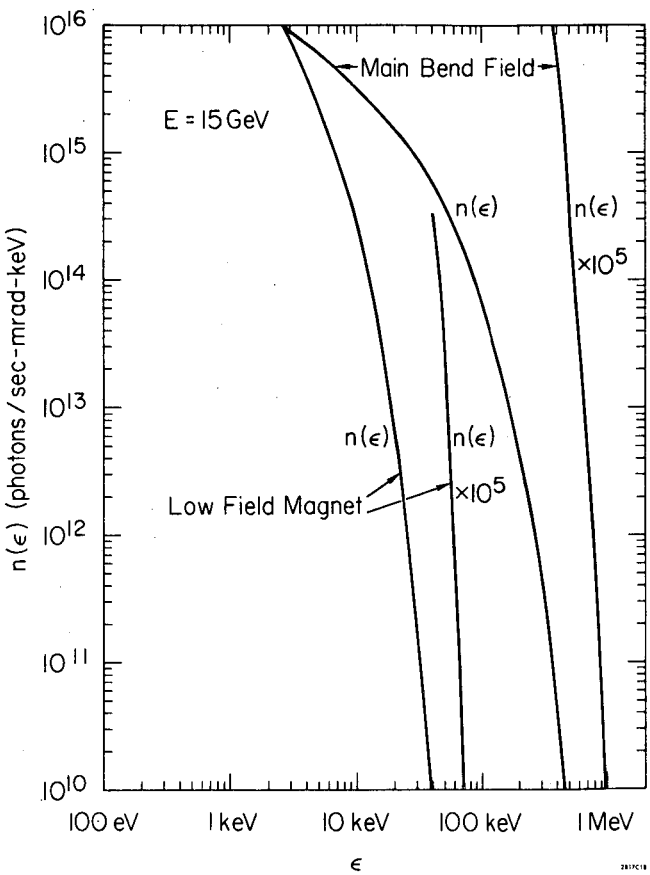

Fig. 5 -- Synchrotron radiation flux versus photon energy for radiation from the main bend magnets and from the low-field magnets.

0 0 0 0 4 5 0 1 5 5 7

CONCLUSIONS

The PEP design has matured during the last year and its physics capability has improved both in overall scope and in detailed execution. The continuing experience with SPEAR is of great assistance in refining the design of both the ring and the experiments. Certainly the "new" physics of the last year has only increased our anticipation of the excitement of PEP.

COMPARISON OF JET AND PHASE-SPACE MODELS AT E_{cm} = 30 GeV

G. Hanson and P. Oddone

I. INTRODUCTION

Data from the SLAC-LBL Magnetic Detector at SPEAR has been compared to a phase-space model and to a jet model.[1,2] Below a center-of-mass energy (E_{cm}) of 4 GeV the data does not distinguish between the two models. Above an E_{cm} of 4 GeV, in particular for the high statistics runs at E_{cm} = 6.2 GeV and E_{cm} = 7.4 GeV, the data agrees with the jet model and disagrees with the phase-space model. Figures 1 and 2 show some preliminary comparisons between the data and the models presented during the SLAC Topical Conference held at the end of July. Figure 1 shows the momentum distribution of charged tracks. The phase-space model shows a much steeper momentum distribution than the data, while the jet model is in agreement with the data except at the highest momentum points where the disagreement may be due to resolution effects not yet taken into account.

Figure 2 compares the sphericity distribution for the data and the two models. The sphericity is obtained by finding the axis such that the sum of the squares of the transverse momentum relative to the axis is minimized. Then the sphericity is defined as

$$S = \frac{3\left(\sum_i P_{\perp_i}^2\right)_{min}}{2\sum_i P_i^2},$$

where P_i and $P_{\perp_i}$ are the momentum and transverse momentum of the i^{th} particle respectively. The jet model fits the data quite well, while the phase-space model does not.

The success of the jet model at SPEAR energies provides the motivation for obtaining its predictions at the highest PEP energy. In the

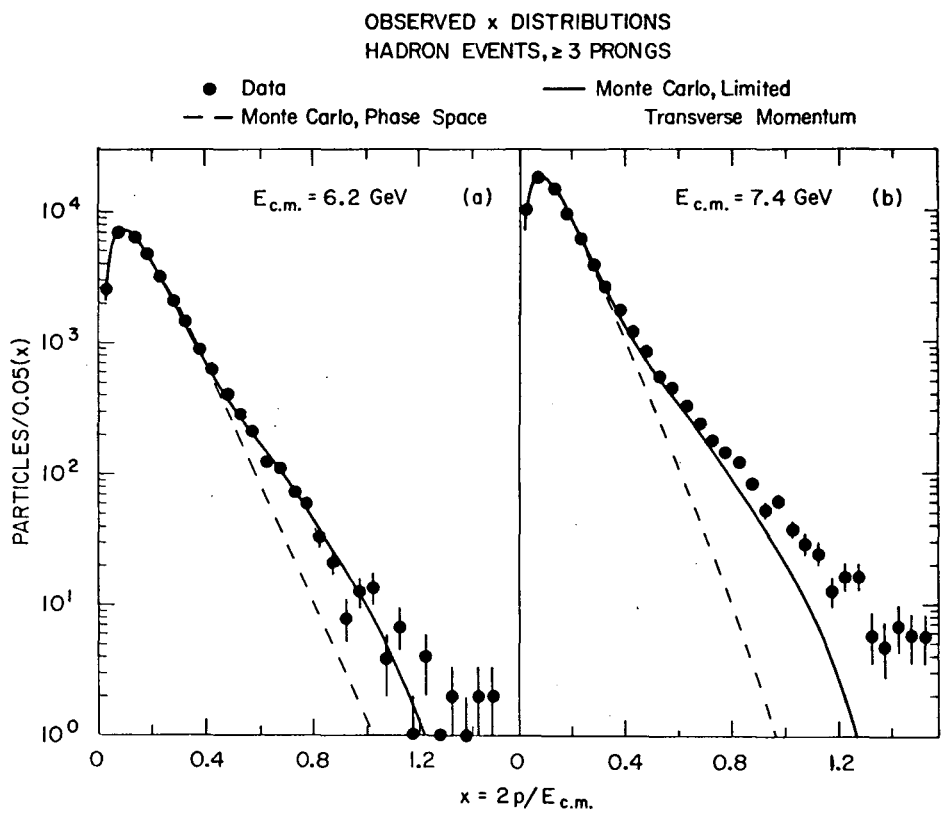

Fig. 1. Momentum distribution for charged tracks for the SLAC/LBL Magnetic Detector data at E_{cm} = 6.2 GeV and E_{cm} = 7.4 GeV.

0 0 0 0 4 5 0 1 5 5 8

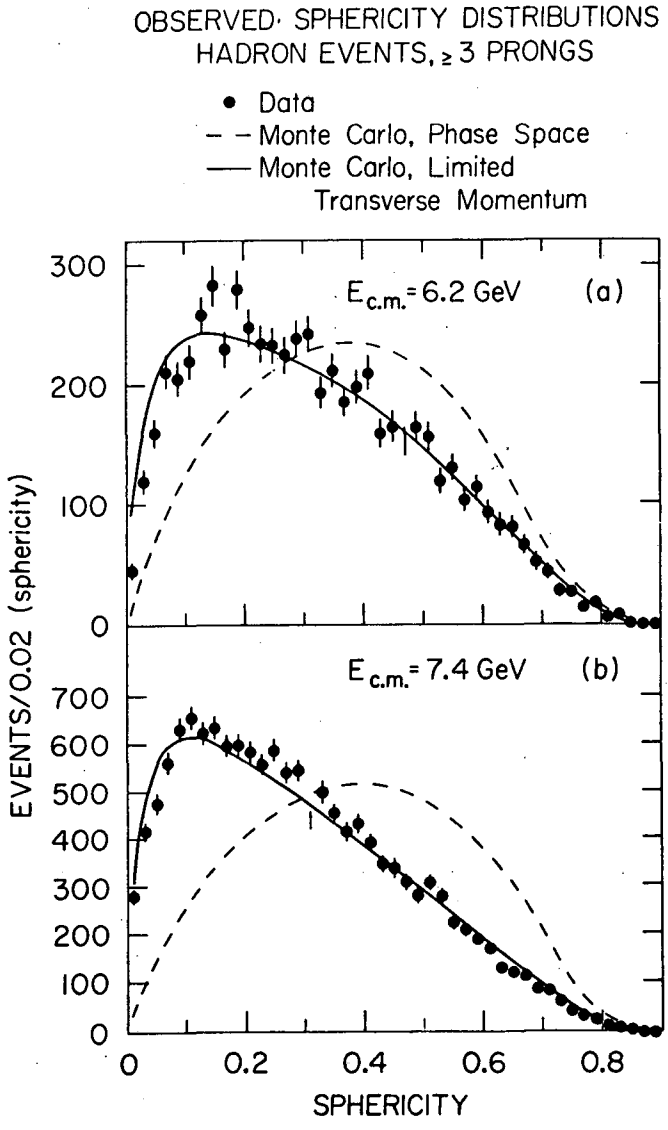

Fig. 2. Sphericity distribution for events from the SLAC/LBL Magnetic Detector at E_{cm} = 6.2 GeV and E_{cm} = 7.4 GeV.

sections that follow we compare the distributions predicted by the jet model to those predicted by the phase-space model at E_{cm} = 30 GeV, and show some distributions which may be helpful in the design of detectors.

II. PHASE-SPACE AND JET MODELS

In the phase-space model, pions (charged and neutral) are produced with momentum and angular distributions according to Lorentz invariant phase space. The total multiplicity is given by a Poisson distribution whose mean can be specified. The fraction of pions which are neutral can also be specified, and the decays $\pi^0 \to \gamma\gamma$ are included.

The jet model has all the features of the phase-space model. Jets are simulated by modifying phase space, according to a matrix element squared (M^2)

$$M^2 = e^{-(\sum_i P_{\perp i}^2)/2r^2},$$

where the summation is over all pions, $P_{\perp i}$ is the transverse momentum of the i^{th} particle relative to a given axis and r is a parameter that can be varied to give the desired mean $P_\perp$. The jet axis can be given any desired angular distribution. For production through a single virtual photon, the general form for the angular distribution for unpolarized beams is

$$\frac{d\sigma}{d\Omega} \propto 1 + a \cdot \cos^2\theta$$

with $-1 \leq a \leq 1$.

For the distributions shown below, we have taken an average multiplicity of 15.3 with a

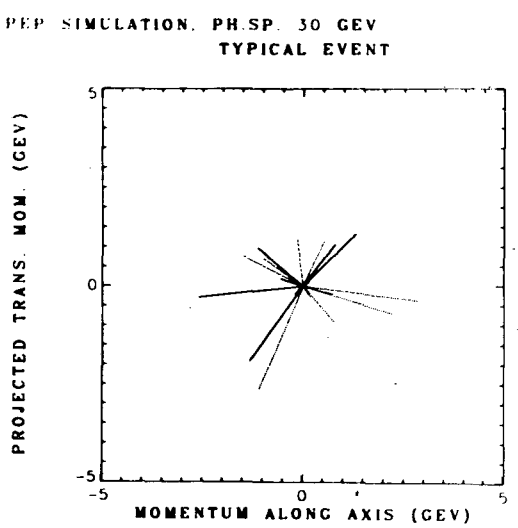

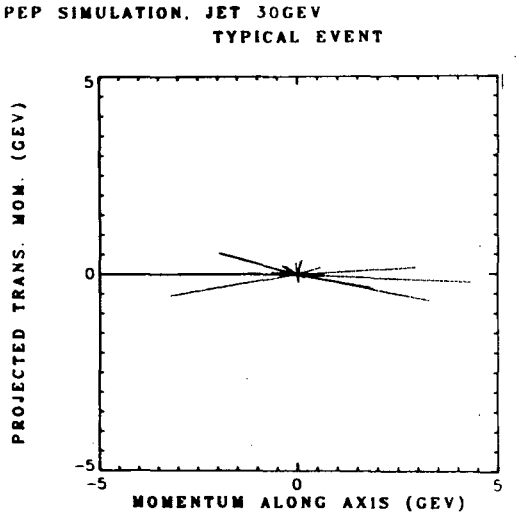

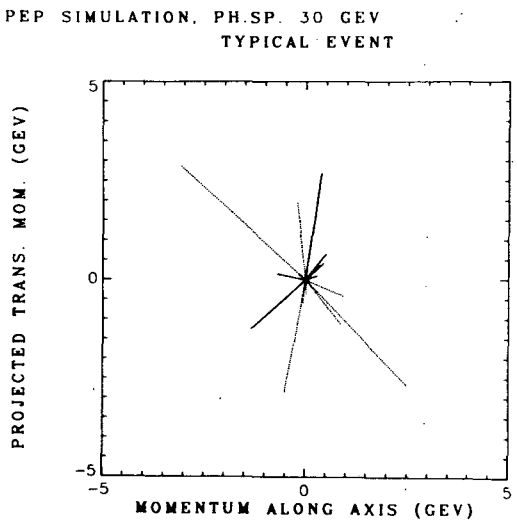

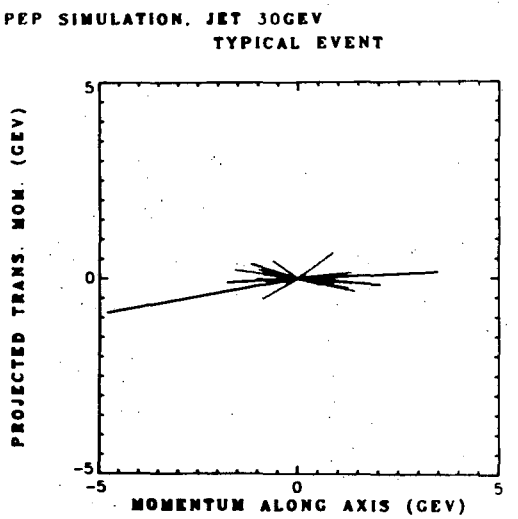

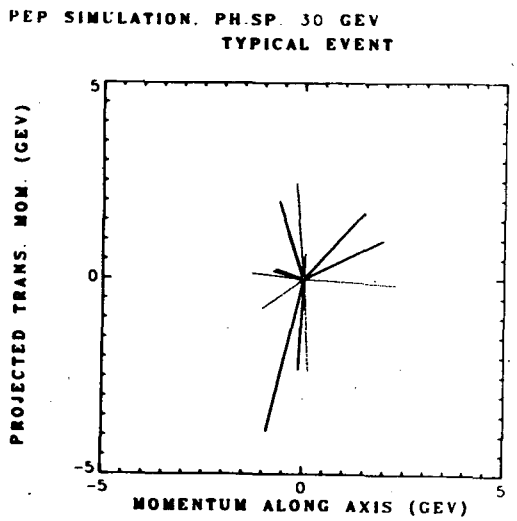

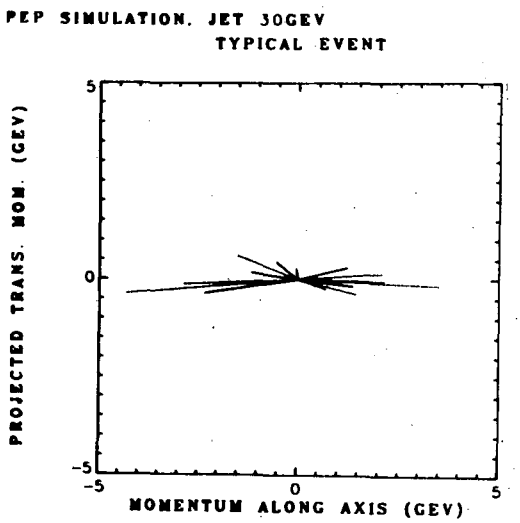

Fig. 3. Some randomly chosen events at E_{cm} = 30 GeV. On the right hand side are the events generated by the jet model, and on the left hand side by the phase-space model. Solid lines are charge pions, and dotted lines are neutral pions.

0 0 0 0 4 5 0 1 5 5 9

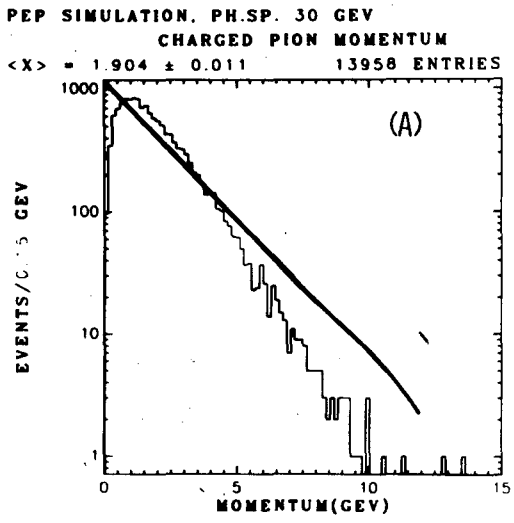

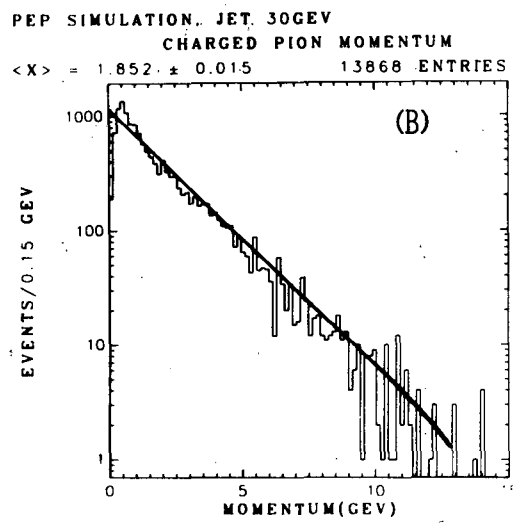

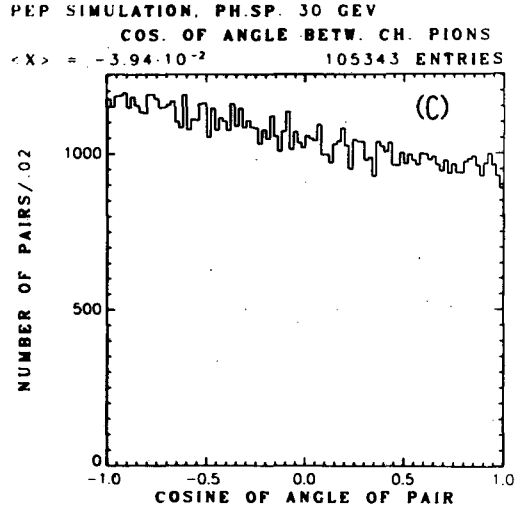

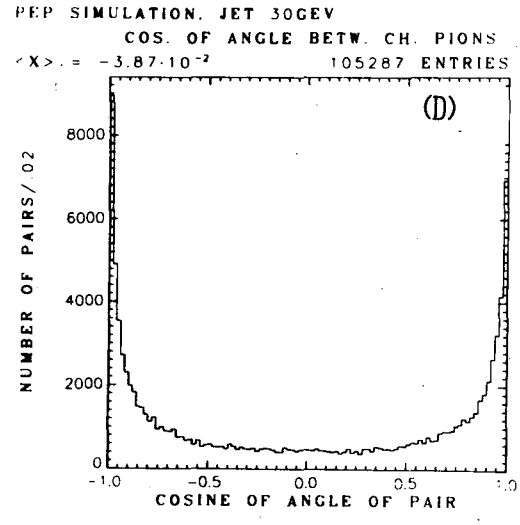

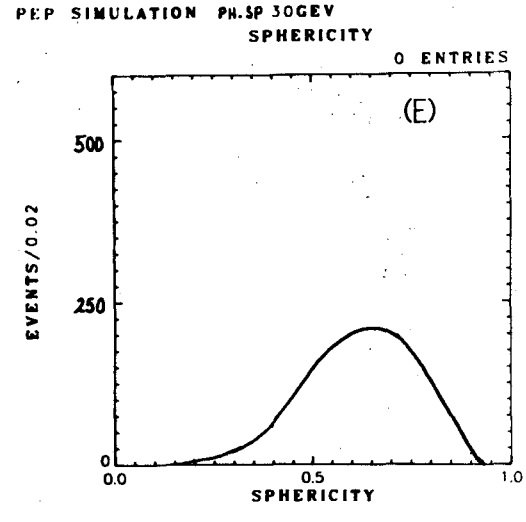

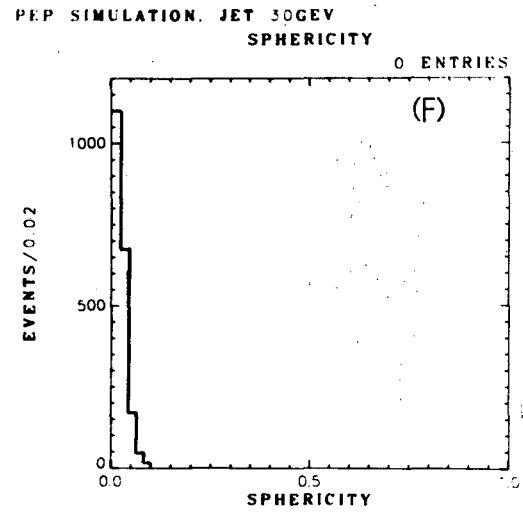

Fig. 4. Distributions for charged tracks generated by the phase-space model and by the jet model. Solid line in Figs. 4(a) and 4(b) are from the scaling form suggested by Richter.[3] The distributions are all based on 2000 events.

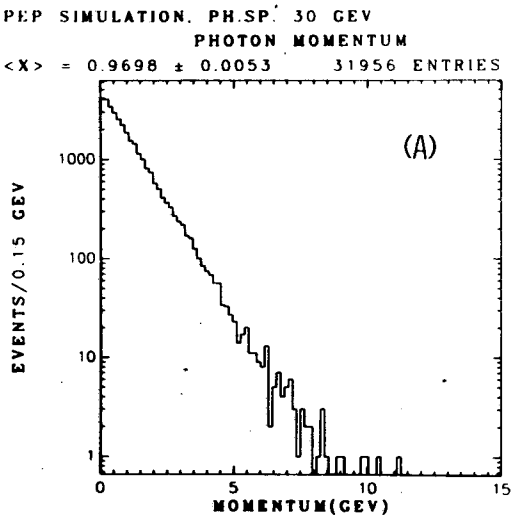

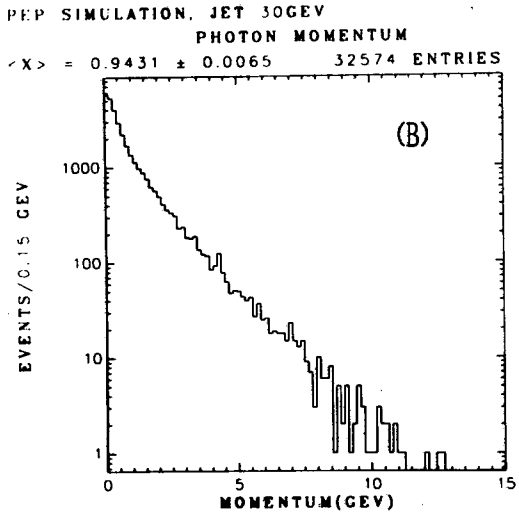

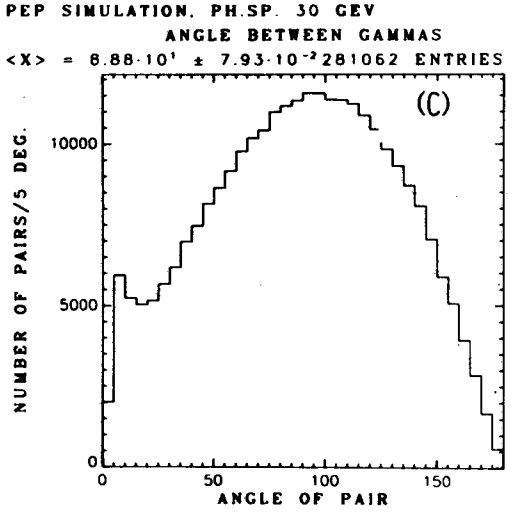

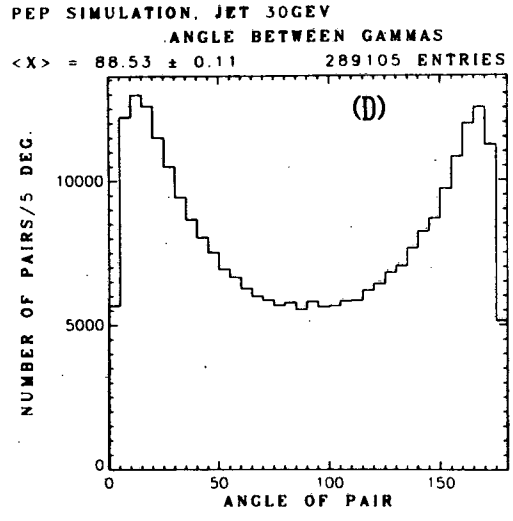

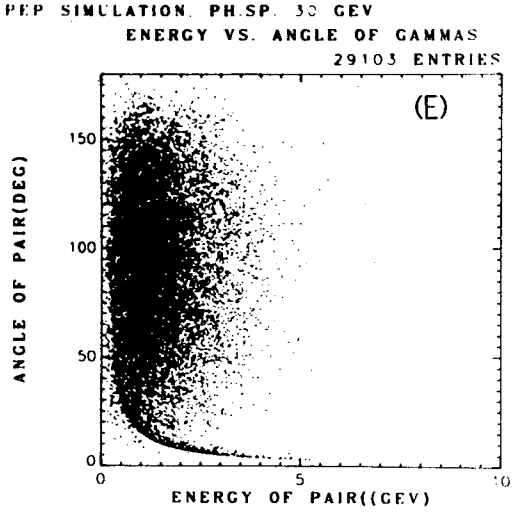

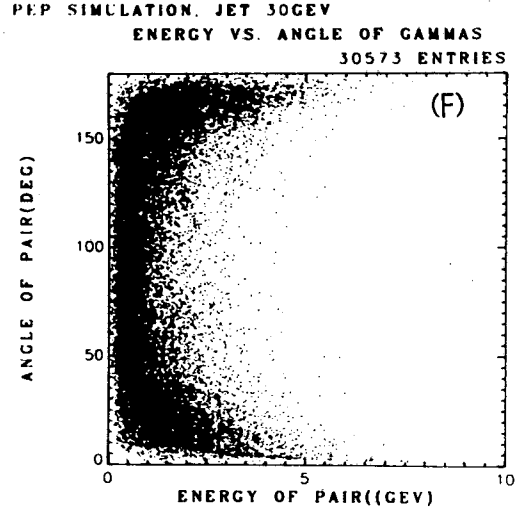

Fig. 5. Distributions for photons generated by the phase-space model and by the jet model. All distributions are based on 2000 events, except the plots 5(e) and 5(f), which are based on 200 events.

0 0 0 0 4 5 0 1 5 6 0

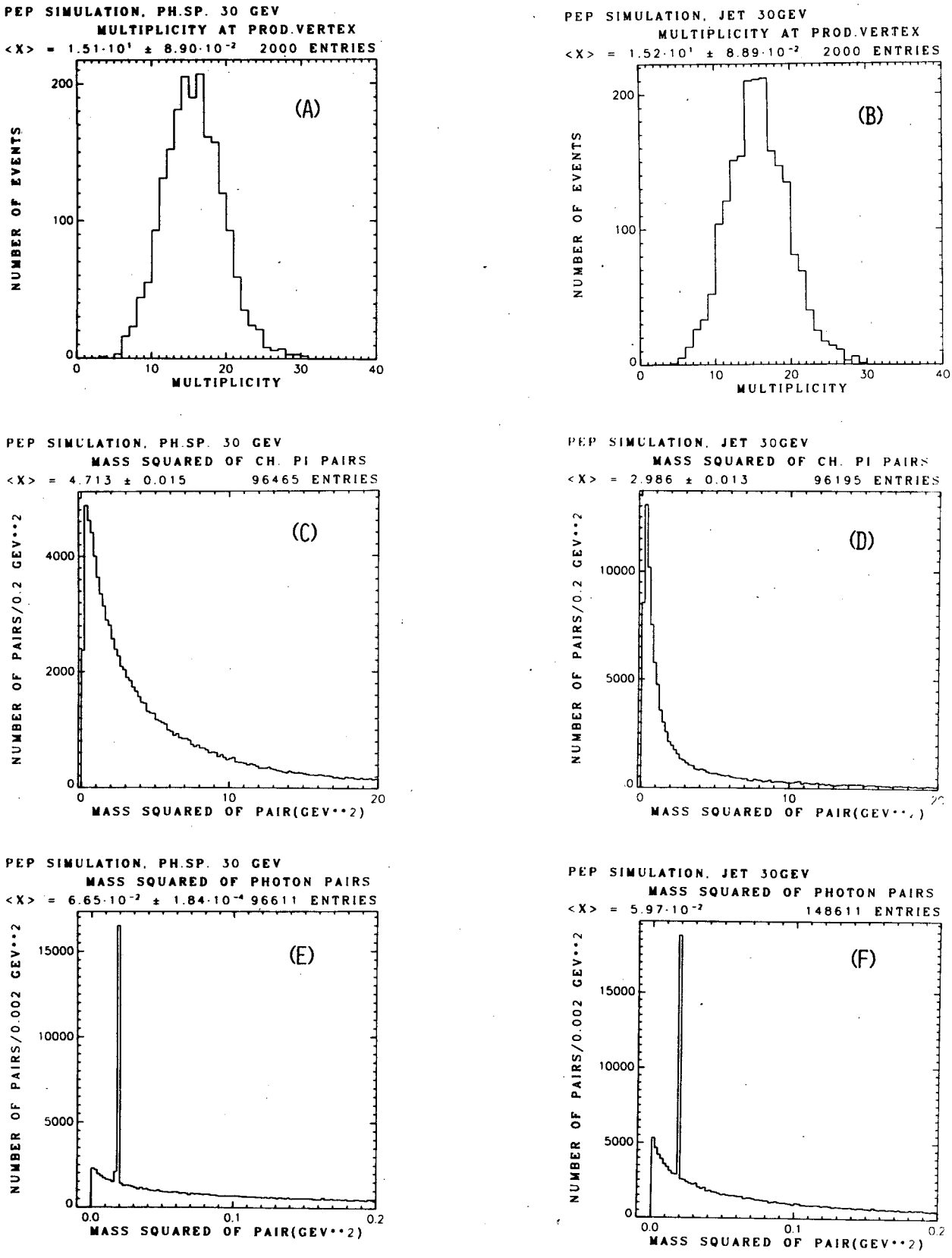

Fig. 6. Distributions useful for estimating backgrounds to two body mass distributions for the phase-space and jet models. The distributions are based on 2000 events.

fraction of π^0 of .54. The average transverse momentum relative to the jet axis is 310 MeV, and the jet axis has been taken along a fixed direction, as the distributions shown do not depend on the angular distribution of the jet axis.

III. COMPARISONS AT E_{cm} = 30 GeV

Figure 3 shows the transverse and longitudinal momentum with respect to the jet axis for some typical events. On the left hand side of Figure 3 appear the events generated by the phase-space model and on the right hand side events generated by the jet model. At E_{cm} = 30 GeV, the difference between the two models is dramatic. At the lower SPEAR energies, statistical distributions with a large number of events were needed to distinguish the two models. At E_{cm} = 30 GeV a couple of events will suffice.

Figures 4(a) and 4(b) show the momentum distribution of charged particles compared to the scaling form discussed by Richter in the 1974 Summer Study.[3] The phase-space model is much steeper than the jet model and is in disagreement with the scaling form. It is interesting to note that the extrapolated multiplicity and the limited transverse momentum, which are the inputs to the jet model, automatically lead to the scaling distribution.

Figures 4(c) and 4(d) show the distribution of angles between two charged particles (pairs). The distribution for the phase-space model is essentially flat, while the jet model shows sharp peaks for angles near 0° and 180°.

Figures 4(e) and 4(f) show the sphericity distribution for charged particles. There is almost no overlap between the two models. The small size of $P_{\perp i}$ compared to the average P_i leads to a sphericity peaked towards small values for the jet model.

Figure 5 shows some distributions for photons derived from the decay of π^0's. The momentum distributions shown in Figs. 5(a) and 5(b) reflect the original π^0 momentum distributions. The angle between photons shown in Figs. 5(c) and 5(d) shows the same pronounced peaking for the jet model as is shown by the distribution for charged pions. At small angles a peak due to photons belonging to the same π^0 appear in the phase-space model. In the jet model, the peak is overwhelmed by the number of small angle pairs. Figures 5(e) and 5(f) show a plot of the momentum of the pairs vs. the angle of the pairs for 200 events.

Figure 6 shows some distributions of interest for calculations of backgrounds to two body mass distributions. Figures 6(a) and 6(b) show the multiplicity distribution for the models. Figures 6(c) and 6(d) show the effective mass of pairs of charged pions, and Figures 6(e) and 6(f) show the effective mass of pairs of photons. For charged particles the jet model increases the number of events for small masses ($M^2 \leq 1.7$ GeV^2) and large masses ($M^2 \geq 40$ GeV^2) compared to the phase-space model.

If the present simple jet model predicts the actual behavior of particles at E_{cm} = 30 GeV, then detectors which try to study events in an exclusive way will need large segmentation, due to the increased density of particles near the axis of the jets. On the other hand, jets will be so easily distinguished that it will be extremely interesting to observe if there exists a separate class of non-jet events.

REFERENCES

1. G. Hanson, SLAC Summer Institute Topical Conference, July 1975.
2. G. Hanson, et al., submitted to Physical Review Letters; SLAC Pub.-1655, LBL-4287.
3. B. Richter, PEP-140, 1974 PEP Summer Study.

0 0 0 0 4 5 0 1 5 6 1

REPORT OF THE POLARIZATION GROUP

W. Ford, K. Kondo, F. Martin, G. Manning, D. Miller, C. Prescott

The physics of intersecting storage rings has been thoroughly discussed by V. N. Baier in his elegant review.[1] The mechanism of radiative polarization and its dependence on machine characteristics is considered in detail. He reviews a number of effects which might be useful in measurement of single-beam polarization; in addition, he shows that angular correlations for secondaries produced in e^+e^- interactions can provide a direct measure of the effective two-beam polarization.

The practical utilization of techniques for measurement of single-beam polarizations at PEP energies was considered in the 1974 Summer Study. It was concluded that the measurement of the asymmetry in the backward scattering of circularly polarized laser photons could provide a satisfactory fast monitor of single-beam polarization. The critical requirements on detector alignment and beam stability were discussed in detail. Several detectors were suggested which might provide satisfactory signal-to-noise in the inevitable background of synchrotron radiation.

During the past year the angular correlations expected for transversely polarized beams have been observed in a series of elegant experiments involving both leptonic and hadronic final states.[2] In SPEAR II polarizations as large as 0.75 are routinely achieved. The observed angular correlations provide a direct measure of average two-beam polarization over time intervals which permit statistically significant samples of data. The $\mu^+\mu^-$ final state, whose properties are calculable from QED, provides a calibration for the two-beam polarization deduced from the more copious hadronic final states.

The achievement of longitudinal polarization is especially important in the exploration of weak-interaction contributions to the e^+e^- annihilation process. We reiterate that any system of magnets operating on both the e^+ and e^- beams can produce only the $\leftarrow\rightarrow$ and $\rightarrow\leftarrow$ states of longitudinal polarization. These are of interest in the study of interactions which do not proceed through the one-photon intermediate state. W. Toner[3] has considered the resonant depolarization of either or both beams using weak solenoidal fields. With either beam depolarized states with net helicity $\lambda = 0$ and $\lambda = 1$ are obtained.

The only practical scheme for achieving longitudinal polarization suggested thus far is that of Richter and Schwitters.[4] A symmetric configuration of magnets is used to rotate transverse polarization to longitudinal immediately before the interaction region and rotate it back to its original state immediately after. Application of the scheme involves severe technical problems since the large magnetic fields required in the insertion result in high local intensities of synchrotron radiation.

We have studied the use of longitudinal polarization in the reaction $e^+e^- \rightarrow \mu^+\mu^-$ as a practical example with high theoretical interest. G. Manning considered modifications of the magnetic insertion which could reduce synchrotron radiation by two or more. In addition, a specific design is suggested which incorporates the optimized magnetic configuration. In this case it is assumed that no particle detection is necessary near the interaction vertex and the synchrotron radiation is 'dumped' up- and downstream. W. Ford and F. Martin have separately considered vacuum chambers in which the synchrotron radiation is absorbed locally so that shielded regions are provided for detectors near the interaction vertex. The report of Ford appears in the Section on Weak Interactions; the reports of Manning and of Martin appear here.

During the Summer Study there was discussion of schemes for rotating the polarization outside of the experimental areas. One such scheme was worked out after the Summer Study by Al Garren and John Kadyk. Their report is included in this section. Most of the synchrotron radiation in their design could be dumped outside the experimental areas, greatly simplifying the design of experiments.

K. Kondo studied the intense local ionization of residual gas in the interaction region due to synchrotron radiation at the insertion. He points out that appropriate electrode structure could result in effective pumping and better vacuum in the interaction region.

It is important at ISR's that potential experimenters have some familiarity with machine operation. To this end we summarize some general considerations in the production and measurement of beam polarization.

I. MECHANISM OF SYNCHROTRON RADIATION

In the classical approximation[5] 7/8 the total synchrotron radiation is polarized in the plane of rotation (σ); 1/8 is polarized along the guide field (π).

Sokolov and Ternov[6] were first to study the effect of spin orientation on radiated intensity using exact solutions of the Dirac equation in a uniform magnetic field. They showed

a) for longitudinal electron polarization the radiated intensity is independent of whether the spin is with or against the direction of motion

b) for polarization along the guide field a small component of the radiated intensity depends on initial and final spin orientations. In particular

$$W_\sigma^{\uparrow\uparrow} = W^{c1}\{\frac{7}{8} - \xi(\frac{25}{12}\sqrt{3} - \zeta) + \text{---}\}$$

$$W_\sigma^{\uparrow\downarrow} = W^{c1}\{\xi^2\ \frac{1}{18}\}$$

$$W_\pi^{\uparrow\uparrow} = W^{c1}\{\frac{1}{8} - \xi\frac{5\sqrt{3}}{24} + \xi^2\ \frac{25}{18} + \text{----}\}$$

$$W_\pi^{\uparrow\downarrow} = W^{c1}\ \xi^2\ \frac{23}{18}\{1 + \zeta\frac{105\sqrt{3}}{184}\}$$

where $W^{c1} = \frac{2\,e^2 c\gamma^4}{3\,R^2}$; $\xi = \frac{3\lambda\gamma^2}{2\,R}$; $\lambda = \frac{\hbar}{mc}$;

and $\gamma = \frac{E}{mc^2}$.

The initial electron spin is along (against) the field for $\zeta = 1(-1)$. The arrows indicate relative spin orientations in initial and final states.

Only the spin-flip term $W_\pi^{\uparrow\downarrow}$ contains a component of radiated intensity dependent on initial spin orientation. At PEP design energies ($R = 170$m, $\gamma = 29{,}354$) the parameter $\xi = 2.936(10^{-6})$ so that

$$W_\pi^{\uparrow\downarrow} = 8.62(10^{-12})\ (1.28)\ \{1 \pm 0.9884\}\ W^{c1}.$$

The total synchrotron radiation at PEP will be $2.6(10^6)$ W/beam. For initially unpolarized beams only 28.6 μW of the radiated intensity for either beam is associated with spin-flip leading to transverse polarization. Within this incredibly small component of the synchrotron radiation transitions leading to alignment along (against) the field for $e^+(e^-)$ are more probable by a factor 171.4 and the beam gradually becomes polarized.

The polarization buildup time τ_p will be inversely proportional to the number of transitions per unit time. With the critical energy $u_c = (3/2)\ (\hbar c\gamma^3/R)$ as a measure of typical photon energy

$$\tau_p^{-1} \propto \frac{W^{c1}\,\xi^2}{u_c} \propto \frac{\gamma^4}{R^2}\ \frac{\gamma^4}{R^2}\ (\frac{\gamma^3}{R})^{-1} \propto \frac{\gamma^5}{R^3}$$

The detailed calculation by Sokolov and Ternov gives

$$\tau_p^{-1} = \frac{5\sqrt{3}}{8}(\alpha\lambda^2 c)\ \frac{\gamma^5}{R^3}.$$

For times $t \gg \tau_p$ the polarization approaches a maximum value of 92.4%.

II. MACHINE CONSIDERATIONS

Since the transverse polarization is 'driven' by only an infinitesimal fraction of the total synchrotron radiation, it is important to determine whether normal machine characteristics might prevent the polarization from reaching its theoretical limit. To do this Baier and collaborators[1] developed a formalism within which the effects of field variations on spin motion could be studied in detail. In this work the radiation damping terms produce the spin alignment.

Since damping terms are small it is convenient to study the spin motion separately. The starting point is the equation of Bargmann, Michel, and Telegdi.[7]

$$\frac{d\underline{s}}{dt} = \frac{e}{mc\gamma}\ \underline{s}\ \times\ [\,(1 + a\gamma)\ \underline{B} - a(\gamma - 1)\underline{B}_\parallel\,].$$

Here $\underline{s}$ is the rest-frame polarization and $a = (g-2)/2$. Let $\underline{B}_0$ be the guide field on the closed equilibrium orbit. The spin precession can be split into three parts

$$\underline{\Omega}_L = \frac{e}{mc\gamma}\ \underline{B}_0$$

$$\underline{\Omega}_0 = \frac{e}{mc\gamma}\ (a\gamma\underline{B}_0) = a\gamma\ \underline{\Omega}_L$$

and $$\underline{\omega} = \frac{e}{mc\gamma}[\,(1 + a\gamma)\ (\underline{B} - \underline{B}_0) + a(\gamma - 1)\underline{B}_\parallel\,]$$

where $\underline{\Omega}_L$ is the precession of the momentum vector $\underline{p}$ in the guide field; $\underline{\Omega}_0$ is the precession of the rest-frame polarization with respect to a coordinate frame fixed to $\underline{p}$; and $\underline{\omega}$ is the perturbation.

With $\hat{z}$ along the direction of motion, $\hat{x}$ radially outward, and $\hat{y}$ along $\underline{B}_0$ (for e^+) to lowest order

$$\underline{\omega} = \frac{e}{mc\gamma}\{[(1 + a\gamma)B_r\,\hat{x} - a(\gamma - 1) \times B_0\,\frac{dy}{dz}\,\hat{z}] + \frac{g}{2}\,B_z\,\hat{z}\}.$$

The first two terms represent normal synchrotron motion; B_r rotates transverse polarization into longitudinal and with vertical betatron oscillations the component of $\underline{B}_0$ parallel to the instantaneous motion rotates transverse polarization into radial. To lowest order the radial betatron oscillations no not depolarize. The third term represents an insert such as a solenoid magnet, etc.

Schwitters[8] has developed a general method for solving equations of spin motion and applied it in a study of depolarization effects in several specific storage ring configurations. He concludes there is no net depolarization due to betatron motion providing the spin-precession frequency is sufficiently far from interger multiples of the horizontal and vertical betatron tunes.

Away from the depolarizing resonances quantum fluctuations in the synchrotron radiation still lead to a stochastic depolarization. Detailed calculations show that for normal storage ring parameters the stochastic depolarization time is long compared to polarization buildup time.[1,8]

0 0 0 0 4 5 0 1 5 6 2

A solenoid couples horizontal and vertical oscillations. Consider a plane-parallel beam entering a region of solenoidal field B_z. The longitudinal flux within an area $\pi\rho^2$ becomes radial flux B_ρ outside the solenoid. Integrating over a Gaussian cylinder starting outside the solenoid and extending to its center gives

$$2\pi\rho \int B_\rho dz = \pi\rho^2 B_z$$

or

$$\int B_\rho dz = \rho B_z/2 .$$

This radial field (due to the return flux) induces an azimuthal component of momentum p_ϕ so that particles initially parallel to the axis now undergo helical motion in the solenoid with radius $\rho/2$ (i.e. the diameter of the helical trajectory for each particle is just equal to its original distance from the solenoid axis). At the exit of the solenoid a flat beam is rotated through an angle

$$\theta = \frac{e}{2pc} \int B_z \, dz .$$

The opposite radial flux at the exit reduces the remaining p_ϕ to zero and the beam particles are again parallel.

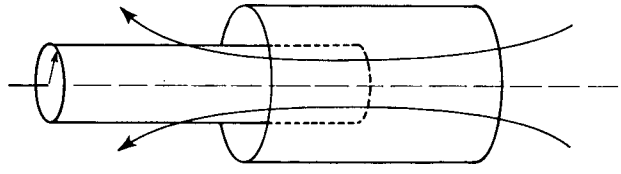

Fig. 1. Longitudinal flux inside solenoid generates radial component outside.

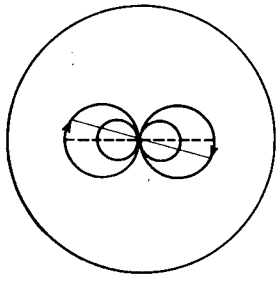

XBL 7511-9611

Fig. 2. End view showing rotation of plane parallel beam because of helical motion induced by radial fringe field at entrance to solenoid.

This coupling of vertical and horizontal betatron oscillations is adequately reduced with the addition of compensating coils at each end of the solenoidal insert so that net $\int B_z dz = 0$. It is easy to see that the compensated solenoid also results in zero net rotation of the polarization to lowest order.

III. DETECTION OF POLARIZATION

A. Single-Beam Polarization

Baier has discussed a variety of effects sensitive to beam polarization; in principle, any of these could be used in its measurement.

1. Touschek Scattering. Scattering will occur between pairs of particles in a bunch due to relative motion. Some fraction of large-angle scatterings will result in loss of particles to the bunch. Since scattering at large angles is damped for electrons with identical polarization (scattering at $\pi/2$ goes to zero in the non-relativistic limit) the beam lifetime will depend upon the degree of polarization.

This effect was used in the first measurement of radiative polarization in the VEPP-2 storage ring.[1] In this case (beam energy 700 MeV) the relative contribution of polarization-dependent terms to beam lifetime was 6%. Since the relative contribution decreases with increasing beam energy the Touschek scattering is not useful as an indicator of beam polarization at PEP energies.

2. Compton Scattering. The cross section for scattering of circularly polarized photons on polarized electrons may be written

$$d\sigma = d\sigma_0 + d\sigma_1 \, \xi_2 \, |\zeta_1| \, \sin\phi$$

where ξ_2 is the degree of circular polarization and ζ_1 is the polarization of the electron; ϕ is the angle between the plane perpendicular to ζ_1 and the plane of scattering. Baier has emphasized that when final state polarizations are unmeasured this is the only correlation allowed by P and T conservation.

3. Scattering off Polarized Electrons. Scattering from atomic beams with polarized electrons would yield large asymmetries for measurement of single-beam polarizations. At present the intensities of atomic beams are not sufficient for adequate counting rates.

B. Polarization in Beam-Beam Interactions

Baier has provided detailed calculations for a number of relevant two (and quasi-two) body final states. Jackson has emphasized, however, that in many cases the angular correlations expected at PEP energies depend only on parity and angular momentum conservation for reactions proceeding through a single intermediate photon.[9]

Polarized beams imply well-defined relative phases for initial helicity states. With both beams transversely polarized

$$(\,|+\rangle + i\,|-\rangle)_{e^+}(\,|+\rangle + i\,|-\rangle)_{e^-} \rightarrow$$

$$|{++}\rangle - |{--}\rangle + i\,(\,|{+-}\rangle + |{-+}\rangle).$$

To order γ^{-1} only the $|+-\rangle$ and $|-+\rangle$ (i.e. $\lambda = \pm 1$) states couple to the virtual intermedi-

ate photon γ_V. The polarization of the photon then

$$i\,(-\underline{e}_x + i\,\underline{e}_y) + i\,(\underline{e}_x + i\,\underline{e}_y) \propto \underline{e}_y$$

along the direction of the guide field.

Consider the reactions involving two pseudoscalar mesons

$$e^+e^- \to \pi^+\pi^-,\ K^+K^-,\ K_LK_S,\ \text{etc.}$$

The only vector in the final state is the relative momentum; the amplitude is then $\underline{e} \cdot \underline{p}$ and

$$\frac{d\sigma}{d\Omega} \propto \cos^2\theta'$$

where θ' is the angle with respect to the field direction. With respect to p_0

$$\frac{d\sigma}{d\Omega} \propto \sin^2\theta \sin^2\phi.$$

For complete transverse polarization production perpendicular to the guide field goes to zero.

Jackson has used the helicity formalism to generalize to more complicated final states. The rotation operators R may be used to form states of definite J for an arbitrary system of particles with fixed internal configuration. The amplitude is then

$$f_{\lambda,\lambda_i}(R,\varkappa,W) \propto \Sigma\,(J+\tfrac{1}{2})\ D^{J*}_{\nu\mu}(R)\langle n;\mu,\varkappa,\lambda|\ S^J(W)\,|\lambda_i\rangle$$

where R represents a rotation of the 'body axes', $\lambda_i(\lambda)$ are initial (final) helicities, $\nu(\mu)$ is the net initial (final) helicity along the initial (final) z-direction; n in the number of particles and $\varkappa$ the remaining quantum numbers.

For a single intermediate photon only terms with $J = 1$, $\nu = \pm 1$ contribute. With parity conservation and full transverse polarization Jackson shows that

$$\frac{d\sigma}{d\Omega} = \frac{1}{2}\ \sigma_T\,(1 + \cos^2\theta + \sin^2\theta\cos 2\phi) + \frac{1}{2}\ \sigma_S \sin^2\theta\,(1 - \cos^2\phi)$$
$$= \sigma_T - (\sigma_T - \sigma_S)\sin^2\theta \sin^2\phi.$$

Final states with net helicity $\mu = 0$ contribute to σ_S; states with $\mu = \pm 1$ contribute to σ_T. It is easy to show that $\sigma_S = 0$ for a large class of final states. Consider

$$e^+e^- \to A + B\ .$$

For states with $\lambda_A = \lambda_B = 0$, the parity operator gives[10]

$$P\,|\,J,M;\ \lambda_A{=}0,\lambda_B{=}0\,\rangle = \eta_A\eta_B(-1)^{J-s_A-s_B}|J,M;\ \lambda_A{=}0,\lambda_B{=}0\,\rangle\ .$$

Consequently, any state for which

$$\eta_A\eta_B(-1)^{J-s_A-s_B} = +1$$

cannot couple to the intermediate photon. This is true, for example, when $A = \pi$ and B is <u>any</u> natural parity resonance. In this case <u>only</u> states with $\mu = \pm 1$ are allowed and $\sigma_S = 0$.

When no conservation law intervenes, $\sigma_S = 0$ or $\sigma_T = 0$ may be a consequence of well-established dynamics. For example, in the $\mu^+\mu^-$ final state QED predicts that $\sigma_S \to 0$ as γ^{-2}. In general, however, the angular correlations provide important new dynamical information.

REFERENCES

1. V. N. Baier, Sov. Phys. Uspekhi 14 (1972)695. This comprehensive review article contains references to much earlier work.
2. Proceedings of the 1975 International Photon-Lepton Conference, Stanford University, to be published.
3. W. Toner, 1974 PEP Summer Study, p. 396.
4. B. Richter and R. Schwitters, 1974 PEP Summer Study, p. 384.
5. See for example, J. D. Jackson, Classical Electrodynamics, Second Edition, John Wiley and Sons, Inc., Chapter 14.
6. A. A. Sokolov and I. M. Ternov, Sov. Phys. Doklady 8 (1964)1203.
7. V. Bargmann, L. Michel, V. Telegdi, Phys. Rev. Letters 2 (1959) 435.
8. R. F. Schwitters, Nuclear Inst. and Methods 118 (1974) 331.
9. J. D. Jackson, LBL Theory Group Note.
10. M. Jacob and G. C. Wick, Ann. Phys. (N.Y.) 7 (1959).

0 0 0 0 4 5 0 1 5 6 3

MEASUREMENT OF WEAK INTERACTION CONTRIBUTIONS TO $e^+e^- \to \mu^+\mu^-$ USING LONGITUDINAL POLARIZATION OF THE e^+ AND e^- BEAMS

G. Manning

I. DIFFERENTIAL CROSS SECTION FOR $e^+e^- \to \mu^+\mu^-$ FOR POLARIZED BEAMS

The cross section for $e^+e^- \to \mu^+\mu^-$, assuming one photon exchange and weak neutral current contributions, is given by:[1]

$$\frac{4s}{\alpha^2}\frac{d\sigma}{d\Omega} = (1+a_1)(1+\cos^2\theta)(1+P_z^+P_z^-) \quad (1)$$
$$- (1+a_2)\sin^2\theta\, P_T^+P_T^-\cos 2\phi$$
$$+ a_3\, 2\cos\theta\,(1+P_z^+P_z^-) + a_4(1+\cos^2\theta)(P_z^+ + P_z^-)$$
$$+ a_5\, 2\cos\theta\,(P_z^+ + P_z^-) - a_6\sin^2\theta\, P_T^+P_T^-\sin 2\phi.$$

(θ, ϕ) is the angle of the μ^- with respect to the e^- direction; P_T^- is the electron beam polarization and is defined to be up; P_T^+ is the positron beam polarization and is down; P_z^- and P_z^+ are defined to be positive in the electron beam direction.

(Note the Schwitters-Richter method[2] of producing longitudinal polarization gives $P_z^+ + P_z^- = 0$. If one beam is depolarized $P_z^+ + P_z^- = \pm 0.92$.)

If only one photon exchange contributes: $a_1 - a_6$ are zero.

$$a_1 = a_2 = DRe(g_v^{e*} g_v^{\mu}) \quad (2)$$
$$a_3 = DRe(g_A^{e*} g_A^{\mu})$$
$$a_4 = DRe(g_v^{\mu} g_A^{e*})$$
$$a_5 = DRe(g_v^{e*} g_A^{\mu})$$
$$a_6 = D\,Im(g_v^{\mu} g_A^{e*})$$
$$D \simeq \frac{s}{2\pi\alpha(s-M_z^2)}$$
$$\simeq -\frac{s}{2\pi\alpha M_z^2} \text{ for } M_z^2 >> s\ .$$

If time reversal is not violated all the g's are real and $a_6 = 0$. If μ-e universality is assumed, $g_A^e = g_A^{\mu}$ and $g_v^e = g_v^{\mu}$.

Table I gives the values of $a_1 - a_6$ for V-A theory and the Weinberg-Salam theory for $s = 900\ GeV^2$, where $C = -sG/4\sqrt{2}\,\pi\alpha$.

TABLE I

	V - A	Weinberg - Salam	
			$\sin^2\theta_w = \frac{1}{3}$
$a_1 = a_2$	$2C = -0.16$	$C(4\sin^2\theta_w - 1)^2$	-0.01
a_3	-0.16	C	-0.08
a_4	-0.16	$C(4\sin^2\theta_w - 1)$	-0.03
a_5	-0.16	$C(4\sin^2\theta_w - 1)$	-0.03
a_6	0	0	0

II. ASYMMETRIES THAT CAN BE MEASURED

A. Charge Asymmetry or Forward-Backward Asymmetry

Define

$$A_{ch} = \frac{d\sigma(\theta) - d\sigma(-\theta)}{d\sigma(\theta) + d\sigma(-\theta)}$$
$$= \frac{[(1+P_z^+P_z^-)a_3 + (P_z^+ + P_z^-)a_5]\,2\cos\theta}{[(1+P_z^+P_z^-)(1+a_1) + (P_z^+ + P_z^-)a_4]\,(1+\cos^2\theta)}$$
$$- P_T^+P_T^-[(1+a_2)\cos 2\phi + a_6\sin 2\phi]\sin^2\theta \quad (3)$$

For $P_T^+ = P_T^- = 0$, no T violation, and μ-e universality, Eq. (3) simplifies to the following:

$$A_{ch} = \left[\frac{(1+P_z^+P_z^-)g_A^2 D + (P_z^+ + P_z^-)g_v g_A D}{(1+P_z^+P_z^-)(1+g_v^2 D) + (P_z^+ + P_z^-)g_v g_A D}\right]\left(\frac{2\cos\theta}{1+\cos^2\theta}\right)$$
$$\simeq \left[g_A^2 D + \frac{P_z^+ + P_z^-}{1+P_z^+P_z^-}\, g_v g_A D\right]\left(\frac{2\cos\theta}{1+\cos^2\theta}\right)$$

The last approximate expression is written to show the dependence upon P_z. The following points can be made:

a. Use of longitudinal polarized beams allows measurement of $g_v g_A$ as well as g_A^2.

b. $P_z^+ + P_z^- = 0$ provides no useful information for weak interactions with V or A. It could be of use in looking for S, P, or T terms.

c. One beam unpolarized and the other beam polarized gives almost as big an effect as when both beams are longitudinally polarized to yield $P_z^+ + P_z^- = 2 \times 0.92$, so there is no need to struggle to get the difficult polarization state.

d. In expression (3) transverse polarization terms only appear as $P_T^+ P_T^-$, whereas longitudinal polarization terms appear as $P_z^+ + P_z^-$. Hence, one can use spin rotations of say 60° rather than 90° to obtain measurable asymmetries, thus greatly reducing the synchrotron radiation problems. If one beam is unpolarized the $P_T^+ P_T^- = 0$. Even if this is not true transverse polarization effects are small and can be measured since they alone produce a ϕ dependence.

B. Asymmetry for Longitudinal Polarization Reversal

Define

$$A_L = \frac{d\sigma(P_z^+, P_z^-) - d\sigma(-P_z^+, -P_z^-)}{d\sigma(P_z^+, P_z^-) + d\sigma(-P_z^+, -P_z^-)}$$

$$A_L = \frac{\left[a_4(1+\cos^2\theta) + a_5\, 2\cos\theta\right]\left[P_z^+ + P_z^-\right]}{\left[(1+P_z^+P_z^-)(1+a_1)(1+\cos^2\theta)+a_3 2\cos\theta\right] - P_T^+P_T^-\sin^2\theta\left[(1+a_2)\cos 2\phi + a_6 \sin 2\phi\right]} \qquad (4)$$

For $P_T^+ = P_T^- = 0$, no T violations, and μ-e universality, the above formula reduces to:

$$A_L = \left[\frac{Dg_a g_v (1+\cos\theta)^2}{(1+Dg_v^2)(1+\cos^2\theta)+Dg_A^2\, 2\cos\theta}\right]\left[\frac{P_z^+ + P_z^-}{1 + P_z^+P_z^-}\right]$$

$$A_L \simeq Dg_A g_v \frac{(1+\cos\theta)^2}{1+\cos^2\theta}\left[\frac{P_z^+ + P_z^-}{1 + P_z^+P_z^-}\right]$$

The following points can be made:

a. One can measure $g_A g_v$.

b. One needs to work at small forward and backward angles in θ.

c. The comments made in II. A. b, c, and d apply here.

C. Values of A_{ch} and A_L for V-A Theory and Weinberg-Salam Theory for Various Values of $P_z^+ + P_z^-$

Table II gives values of A_{ch} and A_L for five combinations of $P_z^+ + P_z^-$ for V-A and Weinberg-Salam theories. P_T^+ and P_T^- are assumed zero.

TABLE II

Case	Values of P_z		V - A		WS with $\sin^2\theta_w = 1/3$	
	P_z^+	P_z^-	A_{ch}	A_L	A_{ch}	A_L
1	.92	.92	0.47 C_1	0.998 C_2	0.11 C_1	0.998 C_3
2	.92	0	0.44 C_1	0.92 C_2	0.11 C_1	0.92 C_3
3	0	0	0.19 C_1	0	0.08 C_1	0
4	.92	-.92	0.19 C_1	0	0.08 C_1	0
5	-.92	0	0.01 C_1	-0.92 C_2	0.05 C_1	-0.92 C_3

$$C_1 = \frac{-2\cos\theta}{1+\cos^2\theta} \qquad C_2 = \frac{-0.16(1+\cos\theta)^2}{0.84(1+\cos^2\theta) - 0.32\cos\theta}$$

$$C_3 = \frac{-0.03(1+\cos\theta)^2}{0.99(1+\cos^2\theta) - .16\cos\theta}$$

III. PRODUCTION OF LONGITUDINAL POLARIZATION

A system for production of longitudinal polarization was described by Schwitters and Richter.[2] Figure 1 shows the general system. Schwitters and Richter had a solution with $B_1 = B_2$ and $L_1 = L_2$. This system does not result in the minimum production of synchrotron radiation. Given an overall system length (L), a gap (G) between magnets and field free region (R) about the interaction point, the requirement of minimum synchrotron power, together with the requirements that the spin is rotated through 90° and that the beam pass

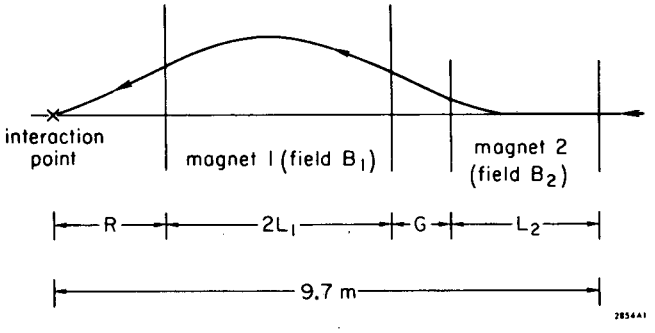

Fig. 1--Magnet system to produce longitudinal polarization. The system is symmetric about the interaction point.

through the interaction point, defines the 4 parameters, L_1, L_2, B_1, and B_2. Figures 2 and 3 show how these parameters vary for different values of L_2. It will be seen that minimum synchrotron power is when $L_2 = 2L_1$; this was pointed out by Wenzel.[3] Some solutions with $L_2 = 2L_1$ are tabulated in Table III. It can be seen that the power increases rapidly with the required central field free space. It can also be seen that the power changes very slowly as the gap between the magnets is

0 0 0 0 4 5 0 1 5 6 4

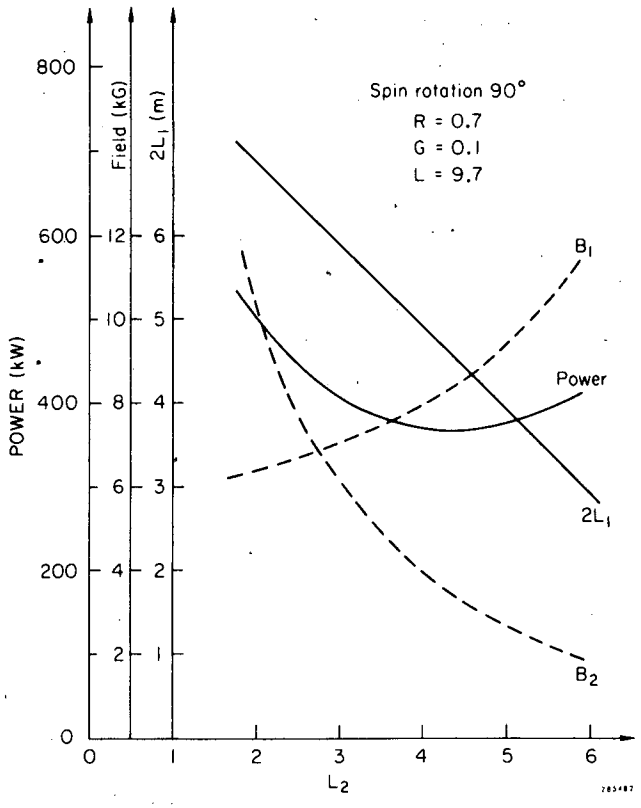

Fig. 2--Plots of total synchrotron power, magnetic fields, and magnet lengths to achieve 90° spin rotation for a field free region at the interaction point of ± 0.7 m with a gap between the magnets of 0.1 m and an overall interaction length of ± 9.7 m.

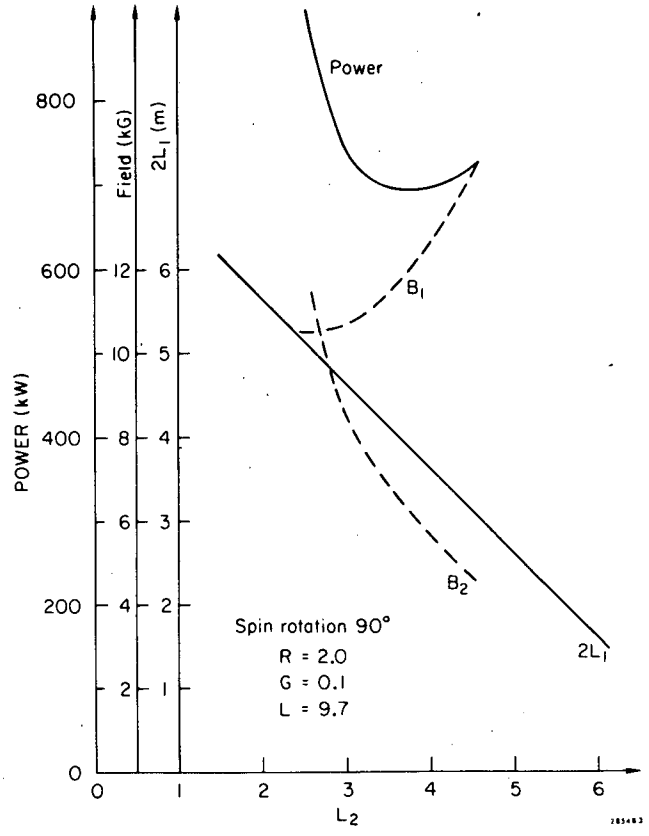

Fig. 3--Plots of total synchrotron power, magnetic fields, and magnet lengths to achieve 90° spin rotation for a field free region at the interaction point of ± 2.0 m with a gap between the magnets of 0.1 m and an overall interaction length of ± 9.7 m.

TABLE III

Particular cases for $L_2 = 2L_1$ (i.e., minimum synchrotron power for 90° spin rotation). Power field values and critical energy are given for 15 GeV for 90° and 60° spin rotation.

			90° Spin Rotation					60° Spin Rotation		
r_1	G	$L_2=2L_1$	B_1	B_2	Power	Ec_1	Ec_2	Power	Ec_1	Ec_2
m	m	m	kG	kG	kW	keV	keV	kW	keV	keV
0	0.1	4.8	7.14	2.35	271	106	35	120	71	23
0.7	0.1	4.45	8.49	3.32	370	126	49	164	84	33
1.0	0.1	4.30	9.18	3.83	425	136	57	189	91	38
2.0	0.1	3.8	12.11	6.05	790	180	90	351	120	60
3.0	0.1	3.3	16.50	9.53	1198	245	142	532	163	95
0.7	0.4	4.3	8.59	3.24	362	128	48	161	85	32
0.7	0.6	4.2	8.67	3.19	358	129	47	159	86	31
0.7	1.0	4.0	8.86	3.11	352	132	46	156	88	31
0.7	1.4	3.8	9.08	3.03	348	135	45	155	90	30
0.7	2.0	3.5	9.50	2.93	346	141	44	154	94	29
0.7	3.0	3.0	10.48	2.81	353	156	42	157	104	28

increased. The critical energy in magnet 1 increases as G is increased. A value of $R_1 = 0.7$ m and G = 1.0m is chosen for a detector described below. The table also includes values for a spin rotation of 60° – this reduces the asymmetries by only 17% but it reduces the power by 56% and the critical energies by 33%.

IV. A COMBINED DETECTOR AND LONGITUDINAL POLARIZER

Figs. 4 and 5 show a detector for $e^+e^- \rightarrow \mu^+\mu^-$ with the polarizing fields built into the detector. The detector is an iron shell with a 5.4 m outer diameter and a 1.4 m inner diameter. The ball has a vertical slice cut through its center of width of about 20 cm. Coils are provided to produce a field with approximately circular symmetry about a vertical axis of the sphere. In the

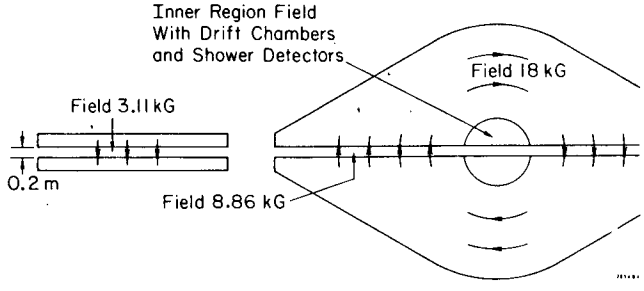

Fig. 4--Sketch of detector for $e^+e^- \rightarrow \mu^+\mu^-$ with longitudinal polarizer built in. The analyzing field of 18 kG in the iron is spread out in the median plane to give a field of 8.86 kG over a distance of 4.0 m. Separate magnets of 4 m length provide a field of 3.11 kG.

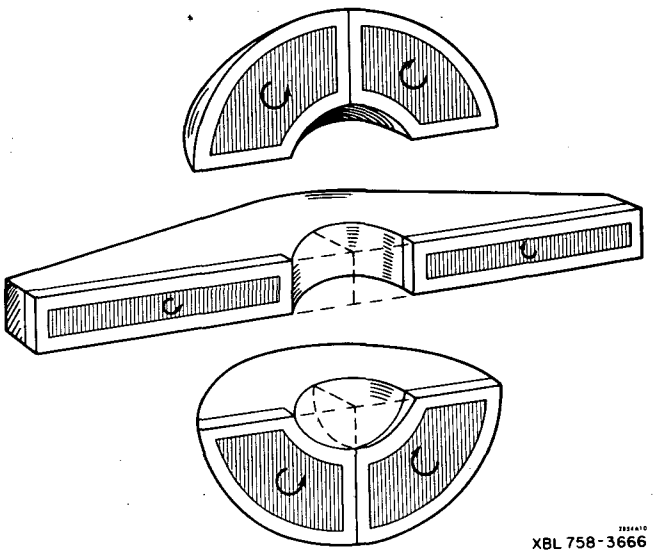

Fig. 5--Schematic view of half of central magnet system showing a possible coil system.

median plane the iron is extended along the beam direction to make a total length of 9.4 m. The field is made to be 8.86 kG over the length of 4.0 m and -8.86 kG over the opposite 4.0 m. The field in the 2m thick iron ball is about 18 kG. Separate coils are used for the median plane section, the section above the plane, and the section below, so that the major part of the muon analyzing field can be kept at 18 kG, independent of the polarizing fields. Separate magnets of length L_2=4.0m are powered to have fields of ± 3.11 kG.

The slot left through the detector allows the synchrotron radiation to be kept in vacuum until it reaches a suitably shielded dump. A brute force solution would be to position these dumps well downstream of the detector. This would require a vacuum chamber of about 3 m vertical height and 20 cm width. It would have substantial side walls. Other solutions are also possible.

The momentum resolution for muons would be ±15% approximately independent of momentum. The iron is about 12 absorption lengths. The solid angle is about $0.95 \times 4\pi$.

$e^+e^- \to \mu^+\mu^-$ can be adequately detected with detectors outside the iron ball. It would be desirable to fill the 1.4 m diameter core with chambers and shower detectors to attempt to detect $e^+e^- \to e^+e^-$ as an independent normalization check. The practicality of this will depend upon how effectively the synchrotron radiation can be dumped.

The weight of the detector would be $\simeq$ 630 tons. The magnet power requirement would be a small fraction of a megawatt.

V. CONCLUSIONS

1. $P_z^{\pm} = \pm 0.92$ with $P_z^{\mp} = 0$ is almost as useful as $P_z^{+} + P_z^{-} = \pm 1.84$ and it is not worthwhile struggling to get the difficult polarization state.
2. It is not necessary to use 90^o spin rotation; 60^o rotation reduces synchrotron power by 56% and leaves the asymmetries 87% of full effect. The transverse polarization effects are proportional to $P_T^+ P_T^-$ and hence are small -- or zero when one P_T is zero. The effects can be checked as they are only ϕ dependent terms.
3. A detector for $e^+e^- \to \mu^+\mu^-$ can be designed that includes the polarization rotation magnets within it. For 90^o spin rotation the synchrotron power is $\simeq$ 350 kW and $\simeq$156 kW for 60^o rotation. It seems possible to leave room for the synchrotron radiation to be kept in vacuum until it is dumped clear of the apparatus.
4. Experiments can be made to measure g_V and g_A to about 10% if the contribution of the weak interaction is at the level predicted by V-A theory. If the Weinberg-Salam model is correct with $\sin^2\theta_W = 1/3$ it should be possible to measure θ_W to an accuracy of 10^o.

REFERENCES

1. Notes by S. Berman at PEP Summer Study, 1974.
2. R. Schwitters and B. Richter, SPEAR-175; PEP Note 87; or 1974 PEP Summer Study (PEP-137), p. 384.
3. W. A. Wenzel, 1974 PEP Summer Study (PEP-137), p. 388.

0 0 0 0 4 5 0 1 5 6 5

A BEAM PIPE FOR POLARIZATION EXPERIMENTS*

F. Martin

A vacuum chamber for the Richter/Schwitters-type polarizer is shown in Fig. 1. Its complicated shape is designed to absorb "all" of the synchrotron radiation coming from the polarizing magnetic fields and cover the energy range from 5 to 15 GeV/c. The basic problems center around the following conditions:

1. the dissipation of the heat produced from absorbing the radiation;
2. the high-energy densities of the radiation;
3. leakage of the radiation from Compton scattering in the high-energy tail;
4. access to the interaction region for the physics.

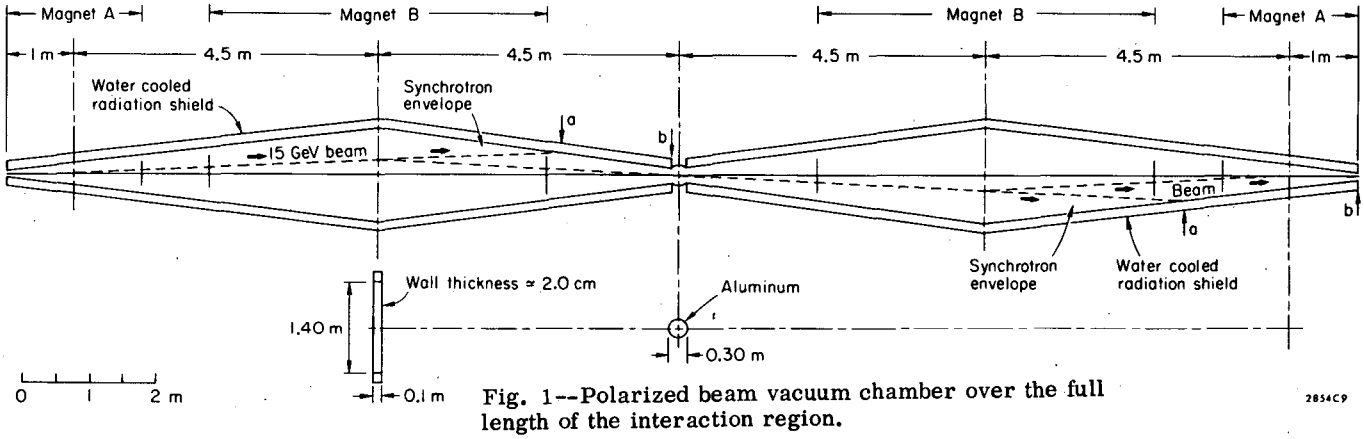

Fig. 1--Polarized beam vacuum chamber over the full length of the interaction region.

The polarizer occupies the full 20 meters with a two-meter clear area across the interaction point. The parameters are tabulated in the table below.

This system has not been optimized to minimize energy power but shows what may be a typical worst case.

The shape of the beam pipe follows the trajectory of the 5-GeV beam. The symmetry allows for reversing the direction of polarization in both beams but one might argue that that is an unnecessary complication.

Magnet	Length	Field (kG)	5 GeV Beam				15 GeV Beam			
			Max. Deflection	Max. Angle	Critical Energy	Power	Max. Deflection	Max. Angle	Critical Energy	Power
A	2 m	11.52			20 keV	8.3 kW			177 keV	75 kW
B	5 m	9.22	66 cm	0.138 rad.	16 keV	13.3kW	22 cm	0.046 rad.	142 keV	120 kW
						21.6kW				195 kW

ENERGY DENSITY

The vacuum chamber is designed to absorb all of the radiation close to the interaction region and inside the experimental apparatus. At 15 GeV, 93% of the radiation falls on the region a-b in the forward direction. The other 7% passes through the interaction region and is lost at the other end of the vacuum pipe and on down the storage ring. Around the interaction point is a 30-cm sphere which sees no direct radiation.

The radiation is spread out over a length of 175 cm, which is equivalent to 1.11 kW/cm. Since the radiation is strongly collimated along the beam direction, the energy densities may run as much as five or six kW per cm^2. Consequently, the type and thickness of the initial impact surface will require some attention. For now it is assumed that a thin sheet of water-cooled stainless steel will be adequate.

* Work supported by U. S. Energy Research and Development Administration.

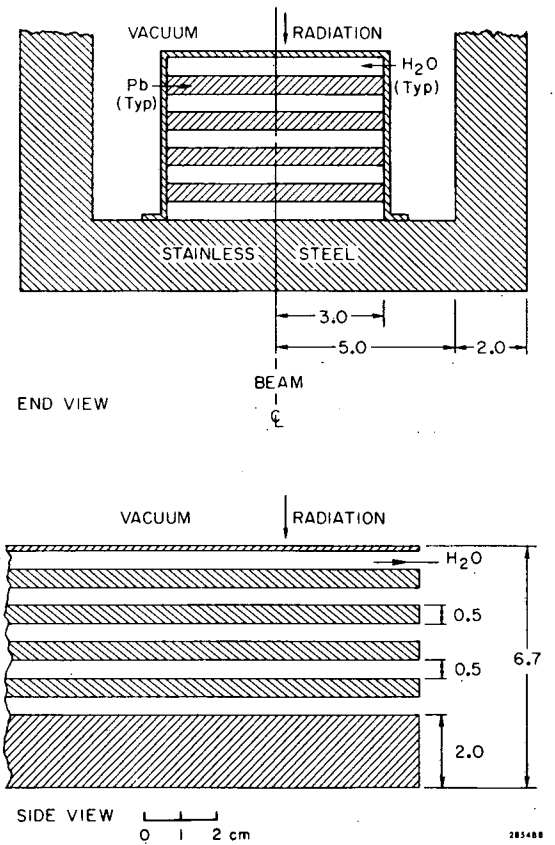

Fig. 2--Water-cooled radiation absorber inside the vacuum chamber, 41.73 g/cm^2 thick.

COOLING

As is shown in Fig. 2, it is proposed to dissipate the heat with circulating water. The total heat in section a-b is roughly 195 kW; then the volume of water to remove this heat (assuming 100% collection efficiency) is:

$$d^2v/dt/\Delta T = \text{power}/c = 195\ \text{kW}/4.184$$
$$= 47 \times 10^3\ \text{cm}^3/\text{sec}/^\circ\text{C}$$

where c is the specific heat of water (4.184 J/cm^3) and ΔT is the temperature rise.

RADIATION ABSORBER

The 1974 PEP Summer Study contained a section on backgrounds (PEP-176). Included in that section is an estimate on the transmission of synchrotron radiation through lead. For a critical energy of 175 keV, an attenuation of 10^5 requires 120 g/cm^2 of lead. In this configuration, the radiation strikes the surface at a grazing angle of 0.15 radians; therefore, the required thickness is only

$$120/11.35 \times 0.15 = 1.56\ \text{cm}\ .$$

In the second figure, a scheme is shown for a water-and-lead absorber inside the vacuum tank. The "thin" outer wall is needed in order to minimize the energy deposition on the outer surface of the absorber. As shown, the total material, including the outer wall, amounts to 41.73 g/cm^2, and, with an incident angle of 0.15, this is equivalent to 278 g/cm^2.

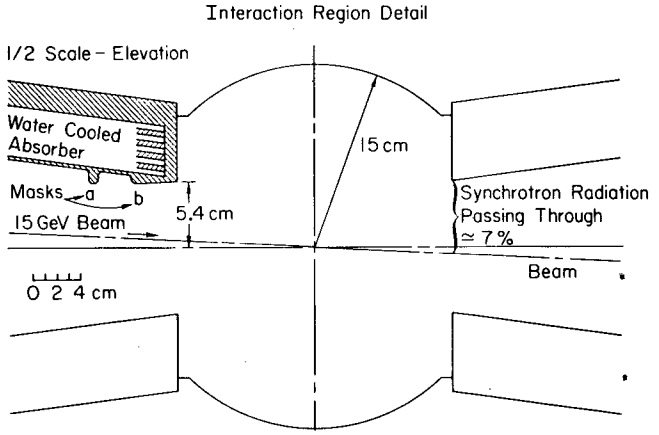

Fig. 3--Elevation view of the vacuum chamber showing the thin window around the interaction region.

The principal weakness of this system with respect to radiation absorption is the Compton scattering from the edges of the beam pipe near the interaction point. In an attempt to break up this secondary scattering, two small masks have been placed at a and b, as shown in Fig. 3. An upper estimate of the amount of secondary scattering can be made. Assume the radiation that strikes in a 2 cm zone back from the end of the shield is the main source of radiation. Then the radiation intercepted by the mask is about 2.3% of 1.95 kW. The amount of solid angle covered by this scattering surface is about 25° out of 360°, or 3.5% of 4π. Therefore, the geometric attenuation reduces the power leaking out to about 0.16 kW per beam. This quantity is further attenuated by the mask and vacuum window. Note also that radiation scattered through relatively large angles is trapped inside the beam pipe.

SIZE OF THE CHAMBER

The vacuum chamber is constructed of stainless steel both to provide rigidity and to withstand the impact of the radiation. The thick walls, as indicated in the figures, are needed to withstand the atmospheric pressure. Two crude estimates on the thickness are computed assuming a drum head 1.40 m in diameter and a 1 cm wide beam 140 cm long with fixed ends. In the former case, the thickness is 1.25 cm and in the latter, 1.77 cm, for a maximum deflection of 0.1 cm. For our purposes, a 2 cm thick wall is proposed. The total weight of the beam pipe and shield is five metric tons.

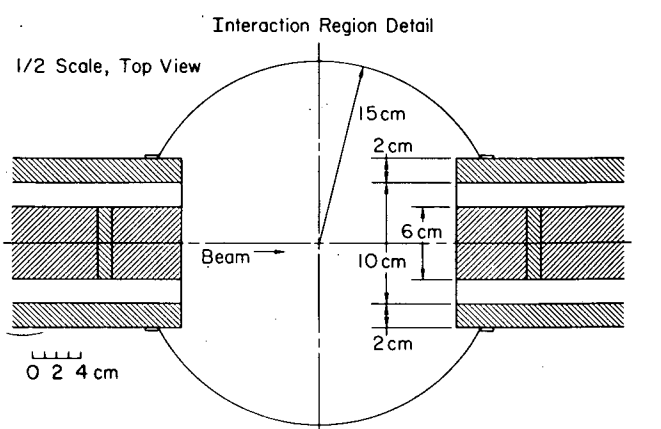

Fig. 4--Plan view of the vacuum chamber with the thin window around the interaction region.

0 0 0 0 4 5 0 1 5 6 6

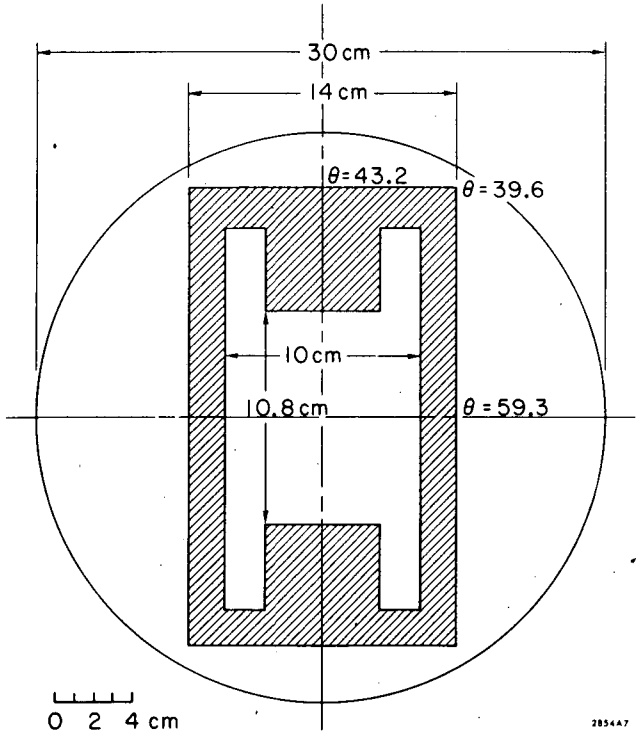

Fig. 5

INTERACTION REGION VISIBILITY

Figs. 4 and 5 are views of the beam pipe at the interaction region. The three angles shown in Fig. 5 are the half-polar angles for particles coming from e^+e^- interactions.

Fig. 5--Vertical cross section through the interaction region, showing the outer thin window. The angles, θ, are the clearance angles for particles produced in the interaction.

A SYSTEM FOR OBTAINING LONGITUDINAL BEAM POLARIZATION AT PEP WITH VERTICAL DIPOLES LOCATED OUTSIDE OF THE INTERACTION REGION

A. Garren and J. Kadyk

I. INTRODUCTION

Recent experiments at SPEAR[1] demonstrate that circulating e^+ and e^- beams become highly polarized along the field direction, to a degree consistent with the theoretical maximum, 92.4%.[2,3] This property of the beams allows use of new and powerful techniques with which to study the weak and electromagnetic interactions. Particularly interesting applications of the spin polarization become possible if the spins are rotated to the longitudinal direction at the interaction point.[4]

To maintain full polarization it is necessary to keep the particles' spin vertical in the circular arcs of the machine, rotate it to the longitudinal direction at the interaction point and then rotate it back to the original vertical direction in the following arc. This can be done by utilizing the g-2 precession of the electrons in vertical bending magnets, or in a combination of solenoidal and horizontal bending magnets.[5,6] In our opinion, the most feasible method proposed to date for use at PEP is that of Schwitters and Richter.[7] This method, shown in Fig. 1, uses

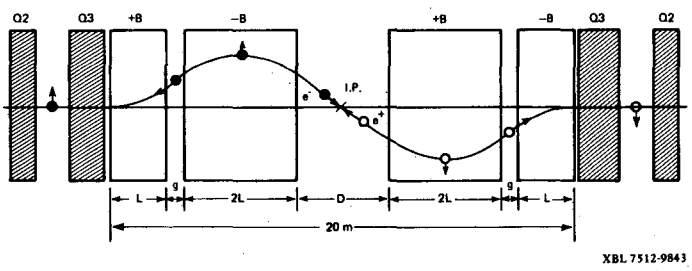

Fig. 1. The Schwitters-Richter Scheme for Producing Longitudinal Beam Polarization (PEP-87). The diagram shows the four vertical bending magnets (unshaded rectangles) inside the 20 m interaction region. They are used to produce longitudinal polarization at the interaction point, IP, as indicated. Spin directions are indicated at various points along the trajectory.

four vertical bending magnets in the interaction region (IR). The spin rotates relative to the momentum by 90° for every 2.305 Tesla-meters of net bending, independent of beam energy. The four magnets have virtually no effect on the beam throughout the ring. The principal change is to introduce vertical dispersion in the IR, except at the interaction point (IP), where it vanishes. However, the magnets fill most of the IR, leaving only a small space (about 3m) for the experimental apparatus, and the fields are high (0.82 T compared to 0.3 T for the horizontal bending magnets). Consequently, a great deal of synchrotron radiation is emitted (~600 kW) locally within the IR, just the region where background should be minimized to assure efficient detector performance.

It is thus important to search for ways to rotate the electron spins that leave more space for the experimental detectors and reduce synchrotron radiation in their vicinity. Wenzel was the first to consider this question. In a previous note he discusses two schemes, each using two dipoles, one or both of which were placed beyond the IR.[8] The focussing doublets at either end of the IR bend both the central orbit and the dispersion to cross the median plane at the IP. The quadrupoles must have very large apertures (about one meter) and be considerably longer than the present low-β quadrupoles. Moreover, their chromatic aberrations result in substantial loss of luminosity.

In this note we propose a spin rotation system (SRS) in which the central orbit is bent by vertical dipoles located outside of the interaction region, and follows the path shown in Fig. 2. The spin is rotated as before by the (g-2) precession in these magnets. Some important features of the system are the following:

1) There is no reduction in luminosity resulting from adding the SRS. 2) Somewhat less (about 30% less) synchrotron power is radiated than in the Schwitters-Richter scheme. 3) Low-field vertical bending magnets and masks are included in the SRS in order to shield the detector from the synchrotron radiation, at least in part. 4) Selection of either the SRS mode or the conventional operating mode is achieved simply by choice of alternative settings of magnet currents. 5) The IR is left completely unencumbered for disposition of the experimental apparatus.

II. DESCRIPTION OF THE SYSTEM

A side view of the spin rotation system (SRS) is shown in Fig. 2, where the standard PEP lattice magnets are shown as open rectangles, and those of the SRS by shaded/black rectangles for vertical dipoles/quadrupoles. Figure 2 shows only half of the system to the left of the IP, the right half being produced by inversion through the IP.

The beam coming from the left enters the SRS at the vertical dipole BV1, the lattice before this element being unmodified. There the beam is deflected upwards 58 mrad, and the following elements are centered on the vertically displaced central orbit. Vertical dipole BV2 deflects the beam back to the horizontal direction. BV3 and the two low field magnets, BVL, bend the beam downwards by 46 mrad to cross the median plane at the IP. These five dipoles, having a net $\int Bdl$ of 2.305 Tm, rotate the polarization of the beams from the vertical direction in the circular arcs to the longitudinal direction at the IP. The corresponding dipoles on the opposite side of

0 0 0 0 4 5 0 1 5 6 7

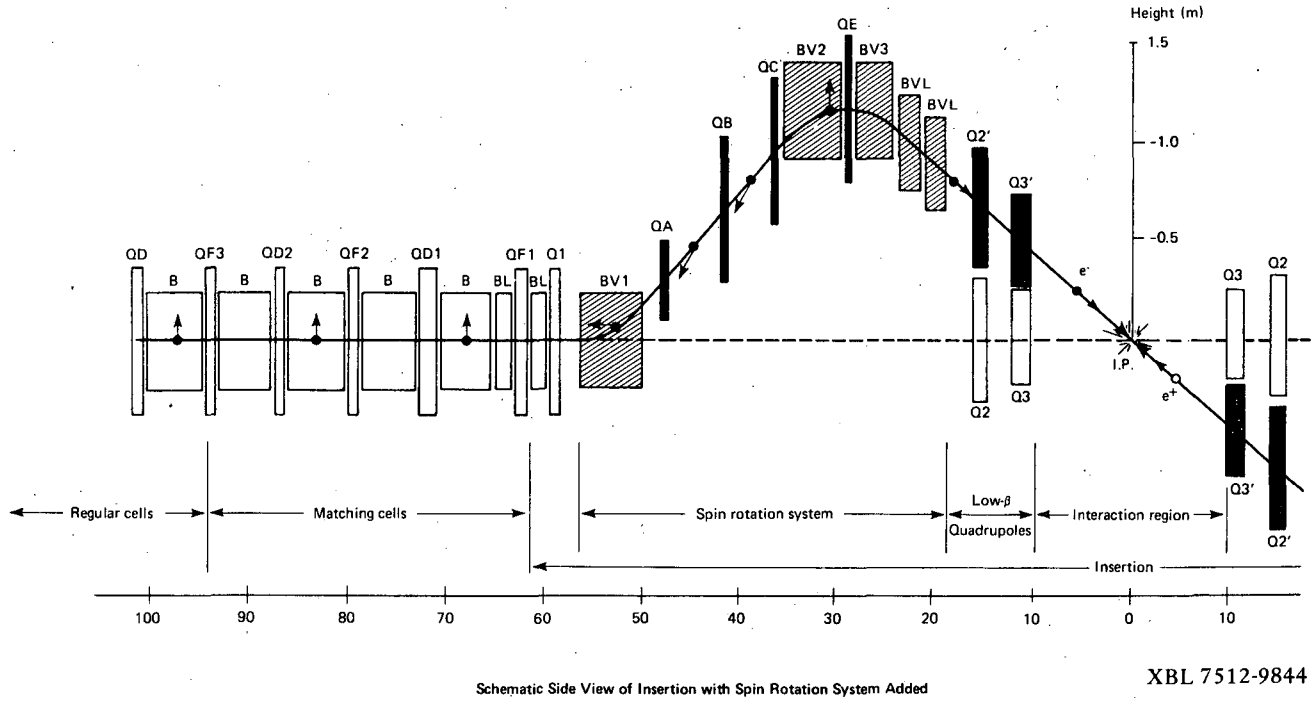

Fig. 2. Schematic Side View of Insertion with Spin Rotation System. magnets of the basic PEP lattice are shown as open rectangles; these are not to be replaced or moved. The new elements, belonging to the spin rotation system, are shown as black (quadrupoles) or shaded (vertical bending magnets). Small arrows indicate spin polarization directions at several points along the beam trajectory.

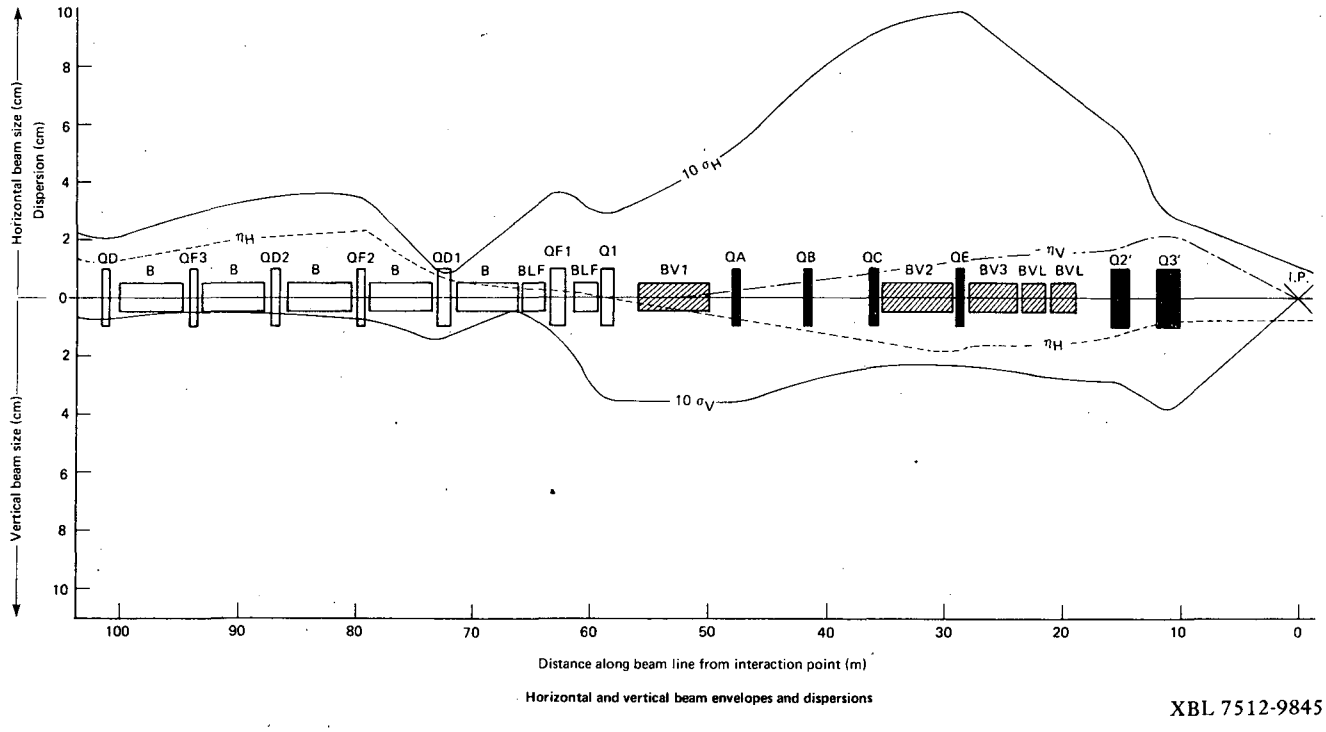

Fig. 3. Horizontal and Vertical Beam Envelopes and Dispersions. Beam envelopes are plotted for the horizontal (upper solid line) and vertical (lower solid line) planes, corresponding to 10σ (10 times the expected rms width). Also shown are the dispersed rays, horizontal and vertical, corresponding to energy spread $\Delta E/E = 1\%$, the $10\sigma_E$ value for 15 GeV beam energy. The envelope width as shown includes the dispersion, combined quadratically with the betatron beam width.

the IP rotate the spin back to the original vertical direction. The vertical low-field magnets, BVL, each deflect the beam 1.6 mrad downwards. Together with appropriate masks, they are intended to shield the detector system from the radiation emitted in BV3. This is similar to the use of the horizontal low-field magnets BL to shield the IR from radiation emitted in the main lattice bending magnets.

The four quadrupoles, QA, QB, QC, QE, lie between the vertical dipoles, and the doublet, Q2', Q3', is placed above the corresponding doublet Q2, Q3 of the standard configuration. These six new quadrupoles are all centered on the displaced beam line.

III. Beam Optics

A. Requirements on Vertical Dispersion

In order to maintain full polarization, the spins must be vertical in the circular arcs of the storage ring. In order to maintain this condition, the particle spins must precess through equal and opposite angles on the two sides of the IP. Since the precession angle is proportional to the rotation of the momentum vector, it follows that in order to keep the spins vertical in the arcs, the dispersion function, $\eta_V(s)$, must be an odd function of s about the IP. If, in addition, $\eta_V(s)$ is identically zero throughout the rest of the ring, systematic spin oscillations outside of the SRS will be eliminated. The vertical dispersion $\eta_V(s)$ has these properties in the method of Schwitters and Richter, shown in Fig. 1, due to the absence of quadrupole lenses in their system. In fact, $\eta_V(s)$ in that case is identical, but reversed in sign, from the vertical displacement of the central orbit.

Unfortunately, this automatic matching of the vertical dispersion does not occur in the system presented here, because of the action of the lenses Q2' and Q3'. In the absence of the elements QA, QB, QC and QE, a nearly parallel beam would be focussed at the IP, vertically. However, the dispersed (off-momentum) rays would be parallel when entering BV3, and therefore not parallel after leaving BV3 and entering Q2'. Thus, the dispersed rays would not be focussed at the IP.

The four new lenses, QA-QE, are added to focus the dispersed ray as well as the beam envelope at the IP. In addition, the strengths of the other quadrupoles between the normal lattice (left of QD) and the IP are altered from the values of the standard configuration.

B. Beam Matching and IP Conditions

The linear beam properties are determined by the betatron functions and the dispersion. In order to obtain the full design luminosity, and minimize the effects of the SRS on the operation of the ring, the betatron functions and dispersion at QD and at the IP were constrained to be the same as in the standard configuration (both horizontally and vertically). Only the slope of the vertical dispersion, $\eta_V' = d\eta_V/ds$, was allowed to be different (non-zero), but this is expected to have a negligible effect. Therefore to the left of QD, in the normal lattice, the beam envelope will also be constrained to be everywhere unchanged from that of the standard configuration. The betatron-function and dispersion values are given in Table I.

Table I. Required Values of the Betatron Function at the Interaction Point And at the Center of QD, the First Normal Cell Quadrupole.

	QD Center		IP	
	Horizontal	Vertical	Horizontal	Vertical
β (m)	12.18	34.12	3.80	0.20
α	0.040	-0.052	0	0
η (m)	1.238	0	-0.74	0
$d\eta/ds$	0.0025	0	0	arbitrary

The matching problem was solved by allowing the strengths of the 12 quadrupoles, QF3 through Q3' inclusive, to be varied. The number of variables may seem unnecessarily large for the seven constraints involved, but this many variables were needed to resolve the conflicting requirements of beam and dispersion focussing discussed above. Even so, the problem is not trivial, and two fitting programs were employed to solve it.[9,10] The resulting quadrupole strengths and other parameters of the system are given in Table II. Beam envelopes and dispersion functions corresponding to ten times the runs widths σ are shown in Fig. 3.

Table II. Magnet Parameters of the Spin Rotation System (See Figs. 2 and 3).

For quads, positive gradient corresponds to horizontal (H) focussing. For vertical (V) bends, positive field bends upwards.

Name	Function	Length (m)	Strength (T or T/m)	Distance, IP to Magnet Mid-Point
QD	Quad	0.64	-7.610	101.303
B	H Bend	5.40	0.3023	97.463
QF3	Quad	0.64	2.567	93.853
B	H Bend	5.40	0.3023	90.563
QD2	Quad	0.64	2.201	86.953
B	H Bend	5.40	0.3023	83.113
QF2	Quad	0.64	10.469	79.503
B	H Bend	5.40	0.3023	76.213
QD1	Quad	1.28	-11.170	72.603
B	H Bend	5.40	0.3023	68.763
BL	H Bend (low field)	2.00	0.0201	64.853
QF1	Quad	1.15	7.018	62.773
BL	H Bend (low field)	2.00	0.0201	60.408
Q1	Quad	1.00	-7.518	58.543
BV1	V Bend	6.00	0.4841	53.000
QA	Quad	0.50	-4.049	47.750
QB	Quad	0.50	2.117	41.750
QC	Quad	0.50	1.845	36.250
BV2	V Bend	6.00	-0.4841	32.500
QD	Quad	0.50	3.995	28.750
BV3	V Bend	4.00	-0.5562	26.000
BVL	V Bend (low field)	2.00	0.0200	22.500
BVL	V Bend (low field)	2.00	0.0200	20.000
Q2	Low-β Quad	1.50	2.390	15.200
Q3	Low-β Quad	2.00	-4.078	11.000
IP	Interaction Point			0.

0 0 0 0 4 5 0 1 5 6 8

IV. LOGISTICS OF INSTALLATION AND OPERATION

A. Operating Modes

Since the technique of spin rotation has never been used in a storage ring, it is inevitable that full operation will only occur after a period of testing and development. Therefore, it is desirable to have operation of the SRS be optional, and to be able to switch over easily to the conventional (non-SRS) operation. A rather natural way to accomplish this is to install two sets of low-β quadrupole doublets, Q2'-Q3', along the vertically displaced beam line as part of the SRS, and Q2-Q3 along the conventional beam line as part of the standard configuration. This will require also two separate beam pipes, which will diverge at BV1 (at 58 mrad) and merge again at the IP (at 46 mrad). With this arrangement, the entire set of new magnets can be turned on or off to permit operation either in the spin rotation mode or in the conventional way.

As presently designed, quadrupoles Q2, Q3 are somewhat too high to give sufficient clearance for the new set Q2', Q3' to be directly above, as shown in Fig. 2. Therefore these elements may have to be staggered with Q2, Q3 or designed with smaller vertical dimensions.

B. Use of the SRS at Different Energies

The design presented here is intended to produce longitudinal polarization at 15 GeV. Since the condition for 90° of spin rotation, 2.305 T-m of vertical bending, is independent of energy, a full polarization capability requires that the system be movable, with the height of the BV2-BV3 line varying inversely with energy, the net $\int Bdl$ being fixed. Although occasional changes in beam line of this nature may be feasible, it is obviously not desirable to make frequent changes. A possible compromise is to change $\int Bdl$ proportionally with beam energy, E, so that the beam optics remains invariant. Then the spin rotation is not precisely 90°, and the net longitudinal polarization will be $\approx 0.924 \sin(\pi E/2E_o)$, where E_o is the design energy for 90° rotation. Since polarization is never complete anyway, one might tolerate values as low as ≈ 0.75 (as long as it is known), allowing E to deviate by ±40% from E_o. For example, this would allow beams to be operated through the SRS over the energy range from about E = 8 to 18 GeV without a beam line alteration.

IV. PRACTICAL CONSIDERATIONS

Although we see no fundamental problems associated with use of the SRS, some important considerations come to mind that will need to be examined in detail.

A. Periodicity

The insertion containing the SRS has a different structure from the others. Since it is only perfectly matched to the rest of the ring for the central momentum, the ring has one-fold periodicity and linear stop-bands exist at half-integral intervals of the tunes ν_x, ν_y for the off-momentum orbits. These may be corrected with suitable adjustments in the sextupole correction system. These, however, must be so designed that third and higher order resonances are not excited.

A one-fold periodicity is also introduced by energy loss in the vertical dipoles. This effect could be removed with compensating rf cavities located in the SRS, between BV2 and BV3.

B. Chromaticity

Not only will the ring have one-fold periodicity, but the chromaticities are increased by large gradients and beta function values in some quadrupoles of the polarization insertion. The maximum beta value is increased from 500 m in the standard configuration to 800m. Again, the consequence of these increases are probably managable.

C. Apertures

Beam sizes are rather large in some magnets of the SRS. Care will be needed in the design, fabrication, and testing of these elements to be sure they meet the somewhat tighter tolerance requirements.

D. Synchrotron Radiation

The new low-field magnets introduced in the present design should permit the shielding of the IR from synchroton radiation emitted from the vertical bending magnets BV1-BV3. However, a detailed study of this question will need to be made to determine where the shielding masks should be placed, and how effective such shielding will be.

V. CONCLUSIONS

This is a "first look" at this particular configuration, not an optimized design. It is intended rather as a demonstration of the feasibility of a system in which the large spin rotation magnets are located outside the IR. The system can, in principle, be turned on or off to allow conventional operation of PEP or operation with the SRS. Operation over a wide energy range also appears possible without moving magnets, with only a relatively small loss in longitudinal polarization. The IR is left unencumbered by the SRS, and the sources of synchrotron radiation are moved out of the IR. However, a careful study is necessary to determine the best design for reducing or eliminating this background radiation.

REFERENCES

1. Azimuthal Asymmetry in Inclusive Hadron Production by e^+e^- Annihilation, R. F. Schwitters, et al., SLAC Publication-1629 (to be published, Phys. Rev. Letters, Nov. 17, 1975). J. G. Learned et al., (submitted for publication)
2. R. F. Schwitters, Nucl. Instruments and Methods, 117, 331 (1974).
3. J. D. Jackson, On Understanding Spin-Flip Synchrotron Radiation and the Transverse Polarization of Electrons in Storage Rings, LBL-4232 (Aug. 1975), submitted to Rev. Mod. Phys.

4. PEP-178, 1975 PEP Summer Study Proceedings. Report of the Weak Interactions/EM Final States Group, PEP-157, 1974 PEP Summer Study Proceedings, p. 283.
5. R. F. Schwitters, Comments on Obtaining Longitudinally Polarized Beams in e^+e^- Storage Rings, PEP Note 75.
6. N. Christ, F. J. M. Farley, and H. G. Hereward, On the Feasibility of Colliding Beam Experiments with Longitudinally Polarized Electrons. Columbia University report CO-2271-16
7. R. F. Schwitters and B. Richter, A Method for Producing Longitudinal Beam Polarization at PEP, SPEAR-175, PEP-87.
8. W. A. Wenzel, Note on Longitudinal Beam Polarization, PEP-168.
9. TRANSPORT, an Ion Optic Program, LBL version, Arthur C. Paul, LBL-2697.
10. MAGIC, A Computer Code for Design Studies of Insertions and Storage Rings, A. S. King, M. J. Lee, W. W. Lee, SLAC-183.

0 0 0 0 4 5 0 1 5 6 9

SUMMARY OF THE WEAK INTERACTIONS GROUP

A. Benevenuti, W. Ford, D. Hitlin, D. Kondo, G. Manning
R. Morse, T. Rhoades, A. Sessoms, L. Stevenson, K. Strauch, A. Zallo

We have studied ways to isolate effects due to a weak neutral current in e^+e^- collisions at PEP energies. We consider below, and in the subgroup reports that follow, the reactions $e^+e^- \to \mu^+\mu^-$, $e^+e^- \to e^+e^-$, and $e^+e^- \to$ hadrons. There is, of course, a substantial overlap between our work and that of the polarization study group, and of the 1974 PEP Summer Study. Our principal conclusions are: (1) with longitudinally polarized $e^+(e^-)$ beams a program of measurements to determine cleanly the weak interaction coupling constants g_A^e, g_A^μ, g_V^e, g_V^μ is feasible; (2) subject to model-dependent interpretation, the single-hadron inclusive processes provide the possibility of observing S,P,T type weak couplings, and an alternative to longitudinally polarized e^+e^- beams for the observation of parity-violating V, A couplings.

I. ISOLATING WEAK EFFECTS

A. $e^+e^- \to \mu^+\mu^-$

In his summer study report G. Manning has recorded the expression for the cross section for $e^+e^- \to \mu^+\mu^-$ with arbitrary polarization of the electrons:

$$\frac{d\sigma}{d\Omega} = \frac{\alpha^2}{4s}\left\{\left[(1+a_1)(1+P_z^+P_z^-)+a_4\,(P_z^++P_z^-)\right]\,(1+\cos^2\theta)\right.$$
$$-\left[(1+a_2)\cos 2\phi - a_6 \sin 2\phi\right]P_T^+P_T^-\sin^2\theta$$
$$\left.+\left[a_3\,(1+P_z^+P_z^-)+a_5\,(P_z^++P_z^-)\right]\,2\cos\theta\right\}$$

with $a_1 = a_2 = D(s)\ \mathrm{Re}\ g_V^{e*}g_V^\mu$

$a_3 = D(s)\ \mathrm{Re}\ g_A^{e*}g_A^\mu$

$a_4 = D(s)\ \mathrm{Re}\ g_A^{e*}g_V^\mu$

$a_5 = D(s)\ \mathrm{Re}\ g_V^{e*}g_A^\mu$

$a_6 = D(s)\ \mathrm{Im}\ g_A^{e*}g_V^\mu$

$$D(s) = \frac{s}{s-M_Z^2}\,\frac{1}{2\pi\alpha} \to \frac{-s}{2\pi\alpha\, M_Z^2} \quad \text{for } s \ll M_Z^2.$$

(See Manning's report for coordinate definitions, and for numerical values of a_i's.).

If the beams are unpolarized, the forward-backward (charge) asymmetry becomes

$$A_\theta \equiv \frac{d\sigma(\theta)-d\sigma(\pi-\theta)}{d\sigma(\theta)+d\sigma(\pi-\theta)}$$
$$= \frac{a_3}{1+a_1}\,\frac{2\cos\theta}{1+\cos^2\theta}$$
$$\simeq a_3\,\frac{2z}{1+z^2} \qquad (z = \cos\theta)$$
$$= D(s)\ \mathrm{Re}\ g_A^{e*}g_A^\mu\,\frac{2z}{1+z^2} \quad . \qquad (1)$$

If the beam polarization is rotated through some angle toward the beam direction, by the method of Schwitters and Richter[1], we get $P_{z_1} = -P_{z_2}$ (and a reduction of P_T) so that all terms in the cross section formula are suppressed. The interesting situation occurs when one of the beams is depolarized[2]. Then $P_z^+ + P_z^- = \pm P_z$ depending on which beam is depolarized, and $1 - P_z^+P_z^- = P_{T_1}P_{T_2} = 0$. For this case the charge asymmetry is

$$A_\theta(P_z) = \frac{a_3 + P_z a_5}{1+a_1+P_z a_4}\,\frac{2z}{1+z^2}\ .$$
$$\simeq (a_3 + P_z\, a_5)(2z/1+z^2).$$

If we record data for both P_z and $-P_z$, the comparison of asymmetries gives

$$\Delta_L(A_\theta) \equiv \frac{1}{2}\,(A_\theta(P_z) - A_\theta(-P_z))$$
$$= P_z\, a_5 \frac{2z}{1+z^2}\ .$$
$$= D(s)\ \mathrm{Re}\ g_V^{e*}\, g_A^\mu\, P_z\,\frac{2z}{1+z^2}\ . \qquad (2)$$

We can also consider a measurement of the change in counting rate, rather than the asymmetry, as P_z is reversed:

$$A_L(\theta) \equiv \frac{d\sigma(\theta,P_z) - d\sigma(\theta,-P_z)}{d\sigma(\theta,P_z) + d\sigma(\theta,-P_z)}$$
$$= \frac{a_4(1+z^2) + a_5\,2z}{(1+a_1)(1+z^2) + a_3\,2z}\,P_z$$
$$\simeq \left(a_4 + a_5 2z/(1+z^2)\right)\ P_z$$

Folding the angular distribution about 90° gives

$$A_{LSym}(\theta) \equiv \frac{1}{2}\,(A_L(\theta) + A_L(\pi-\theta))$$

$$\simeq a_4\, P_z$$

$$= D(s)\ \mathrm{Re}\ g_A^{e*}\, g_V^{\mu}\, P_z. \qquad (3)$$

A test of time-reversal invariance is made by isolating the $a_6 \sin 2\phi$ term:

$$A_\phi(\theta,P_T) \equiv \frac{d\sigma(\theta,\phi)+d\sigma(\pi-\theta,\phi)-\left[d\sigma(\theta,-\phi)+d\sigma(\pi-\theta,-\phi)\right]}{d\sigma(\theta,\phi)+d\sigma(\pi-\theta,\phi)+d\sigma(\theta,-\phi)+d\sigma(\pi-\theta,-\phi)}$$

$$= \frac{a_6\, P_T^2\,(1-z^2)\,\sin 2\phi}{(1+a_1)(1+z^2)-(1+a_2)\,P_T^2(1-z^2)\cos 2\phi}$$

$$\simeq D(s)\ \mathrm{Im}\ g_A^{e*} g_V^{\mu} P_T^2\, \frac{(1-z^2)\,\sin 2\phi}{1+z^2-P_T^2(1-z^2)\,\cos 2\phi}. \qquad (4)$$

A harder experiment is the rate as a function of s:

$$R(s,\theta) \equiv \frac{1}{2}\left[\frac{d\sigma}{d\Omega}\,(\theta) + \frac{d\sigma}{d\Omega}\,(\pi-\theta)\right]$$

$$= \frac{\alpha^2}{4s}\,(1+a_1)(1+z^2)$$

$$= \frac{\alpha^2}{4s}\,(1+D(s)\ \mathrm{Re}\ g_V^{e*} g_V^{\mu})\,(1+z^2)$$

$$R(s) = \frac{4\pi}{3}\,\frac{\alpha^2}{s}\,(1 + D(s)\ \mathrm{Re}\ g_V^{e*} g_V^{\mu}). \qquad (5)$$

The information provided by this measurement is redundant with (1)-(3) provided g_A is not $\ll g_V$ for both μ's and e's.

The experimental requirements and estimates of the magnitudes of the effects for measurements (1) to (5) are summarized in Table I. Numerical differences between the model predictions for the magnitudes differ slightly from those in Manning's report because of the neglect of small (∿16%) terms in the denominators in the derivation of equations (1)-(4). Note that the analyzing power of the asymmetries, • given by the average value of $2z/(1+z^2)$ weighted by the angular distribution $1+\cos^2\theta$, is 3/4, a rather large value. The counting rate for $ee\to\mu\mu$ under the standard assumption[3] is ∿200 per day, or 1.2×10^4• for a two-month run. This is sufficient for measurements of ∿1% precision (for results of an analysis of the statistical errors, see Ref. 4).

A background for the asymmetry and rate measurements is the contribution from order α^3 QED diagrams. This subject is discussed in the report by R. Morse in this summer study. It is found that the asymmetry is very nearly independent of s and of φ (even for $P_T \neq 0$), and depends upon the energy resolution $\frac{\Delta E}{E}$. The weak and QED contributions to A_θ (=δ_A in Morse's notation) are shown in Fig. 1. The large variation of A_θ with φ in the transversely polarized case allows its separation from A_θ^{QED} independent of a quantitative calculation of A_θ^{QED}. For example, if we form the difference $\Delta_\phi(A_\theta)$ between asymmetries in the regions $\cos 2\phi > 0$ and $\cos 2\phi < 0$, we find

TABLE I

Quant. Measured	Parameters Det'd	Polarization	Normal-ization	Magnitude of Effect Meas. at 15 GeV, $\lvert\bar{P}\rvert$ = .924	
				"V-A"	Weinberg ($\sin^2\theta_W$=1/3)
$A_\theta(0)$	$a_3 \sim \mathrm{Re}\ g_A^{e*} g_A^{\mu}$	None*	θ, π-θ	$-.16\,\frac{2Z}{1+Z^2}$ av = -.12	$-.08\,\frac{2Z}{1+Z^2}$ av = -.06
$\Delta_\phi(A_\theta)$	$a_3 \sim \mathrm{Re}\ g_A^{e*} g_A^{\mu}$	Transverse	θ, π-θ	$-.16\,\frac{2.2(1-Z^2)Z}{(1+Z^2)-.29(1-Z^2)^2}$ av = -.06	$-.08\,\frac{2.2(1-Z^2)Z}{(1+Z^2)^2-.29(1-Z^2)^2}$ av = -.03
$\Delta_L(A_\theta)$	$a_5 \sim \mathrm{Re}\ g_V^{e*} g_A^{\mu}$	Long.(1 Beam)	θ, π-θ	$-.15\,\frac{2Z}{1+Z^2}$ † av = -.11	$-.025\,\frac{2Z}{1+Z^2}$ † av = -.02
$A_{Lsym}(\theta)$	$a_4 \sim \mathrm{Re}\ g_A^{e*} g_V^{\mu}$	Long.(1 Beam)	Bunch-pair	-.15	-.025
Rate (s)	$a_1 \sim \mathrm{Re}\ g_V^{e*} g_V^{\mu}$	None	S	-.16	-.01
A_ϕ	$a_6 \sim \mathrm{Im}\ g_A^{e*} g_V^{\mu}$	Transverse	φ, -φ	0	0
$A_{L}(e^+e^-\to e^+e^-)$	$a_3^e \sim \mathrm{Re}\ g_V^{e*}\, g_A^e$	Long. (1 Beam)	Bunch-pair	$-.15\,\frac{2(1-Z^2)(1+Z)^2}{(3+Z^2)^2}$ av = -.04	$-.025\,\frac{2(1-Z^2)(1+Z)^2}{(3+Z^2)^2}$ av = -.006

All but the last row are for $e^+e^-\to\mu^+\mu^-$

$Z = \cos\theta$

* Analyzing power increases slightly with transverse polarization

† Asym. with $P_z^{\pm} = +.924$ is twice this size

0 0 0 0 4 5 0 1 5 7 0

$$\Delta_\phi(A_\theta) = a_3 \frac{4\left[\frac{2P_T^2}{\pi}(1-z^2)\right]z}{(1+z^2)^2-\left[\frac{2P_T^2}{\pi}(1-z^2)\right]^2}. \qquad (6)$$

This quantity is also plotted in Fig. 1(b). Its analyzing power is a factor of two or three smaller than that of A_θ, so the use of a calculation of A_θ^{QED}, will increase the statistical significance of the measurement. In any case the transverse polarization is clearly useful for this experiment.

Note that QED does not contribute to the parity-violating effects observed by inverting the longitudinal polarization.

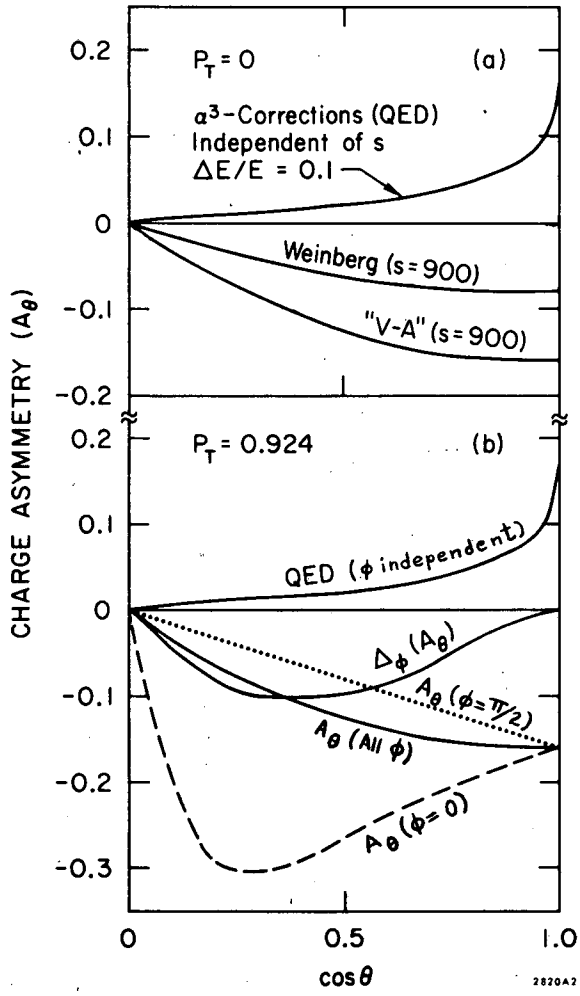

Fig. 1

B. $e^+e^- \to e^+e^-$

From a talk at this summer study by R. Budny we have the expression for the Bhabha cross section:

$$\frac{d\sigma}{d\Omega} = \frac{\alpha^2}{4s}\frac{1}{2}\Big\{(1-P_z^+P_z^-)4B_1+(1+P_z^+P_z^-)(1-z)^2B_2+(1+z)^2B_3$$
$$- P_T^+P_T^-\sin^2\theta\,(B_4\cos 2\phi+B_5\sin 2\phi)$$
$$+ (P_z^++P_z^-)(1+z^2)\,B_6\Big\},$$

with $B_1 = \frac{4}{1-z}\left(\frac{1}{1-z}-\frac{1}{2}(a_1-a_2)\right)$

$B_2 = 1 + a_1 - a_2$

$B_3 = (1+z)^2/(1-z)^2 - 2((1+z)/(1-z))(a_1+a_2)$

$B_4 = 2\left(a_1+a_2-(1+z)/(1-z)\right)\left(1+\frac{1}{2}(a_1-a_2)\right)$

$B_5 = 0$

$B_6 = -2a_3\,(1+z)/(1-z).$

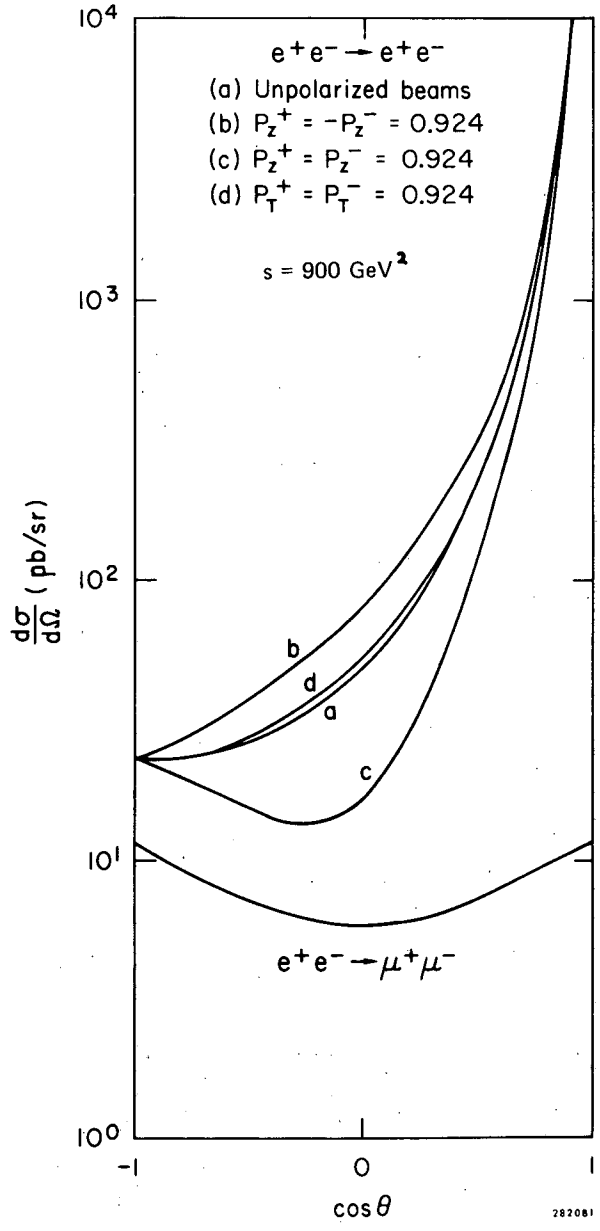

Fig. 2

Here time-reversal invariance has been assumed (hence $B_5=0$). The a_i's are defined analogously to those for $ee \to \mu\mu$:

$$a_1 = D(s)\,g_V^{e2};\ a_2 = D(s)\,g_A^{e2};\ a_3 = D(s)\,g_V^e g_A^e,$$

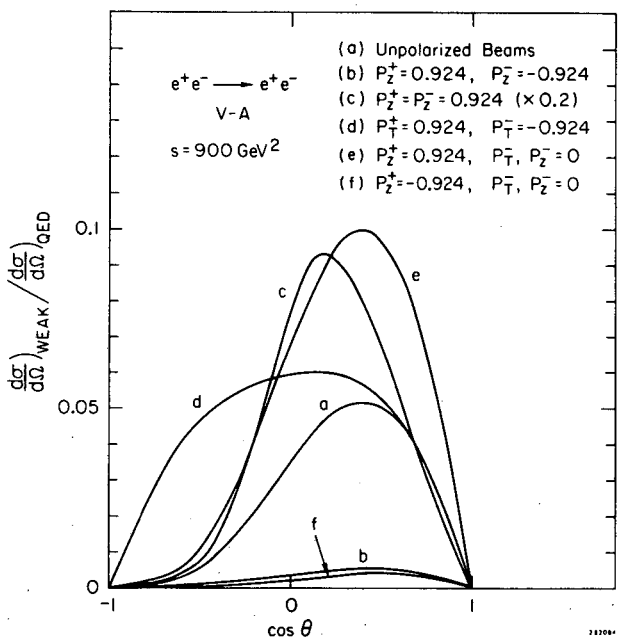

Fig. 3 (a)

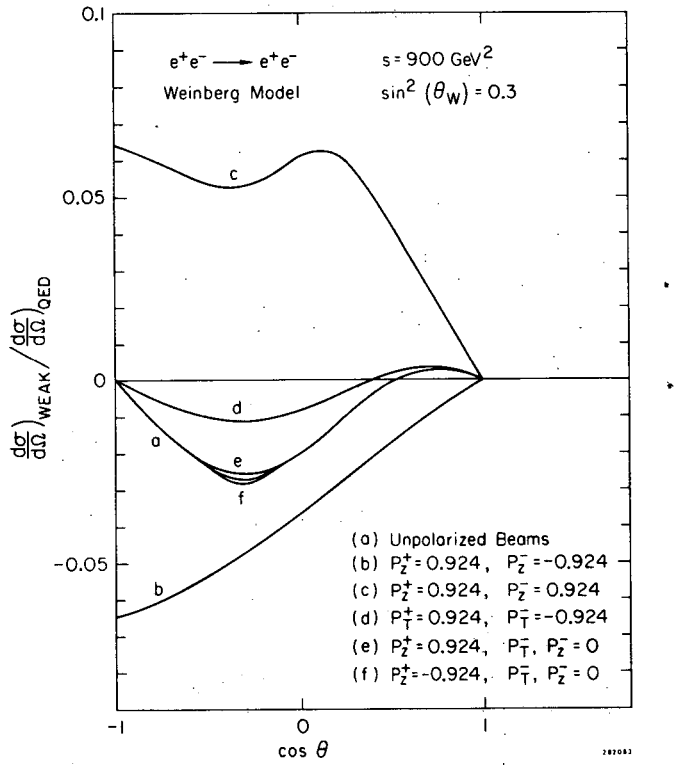

Fig. 3 (b)

where D(s) was defined in section A. The pure QED part of the cross section is plotted in Fig. 2 for various beam polarization conditions. Fig. 3 gives the weak contributions relative to the QED. Although effects of ∿10% in the angular distribution are predicted for some cases, these would be hard to observe against the rapidly falling dominant distribution.

One measurement is feasible with the Bhabhas. The change in rate, integrated over the angular acceptance of the detector, as the polarization $P_z^+ + P_z^-$ (P_z^+ or P_z^-=0) is reversed (curve e - curve f in Fig. 3):

$$A_L^{ee}(\theta) = a_3^{ee} P_z 2 \frac{(1-z^2)(1+z)^2}{(3+z^2)^2} . \qquad (7)$$

The analyzing power is given by the integral of the angular factor weighted by the angular distribution; we estimate $\sqrt{\frac{1}{4}}$ for $|\cos\theta| < .65$. This is a factor of three smaller than the analogous measurement with $\mu^+\mu^-$. The event rate is, however, larger by a factor of ∿3. This experiment has also been listed in Table I.

Collecting the data from the program of experiments listed in Table I we show in Table II the information regarding the coupling constants that can be extracted. Essentially it amounts to a complete description of the leptonic weak neutral currents, within the context of V- and A- type couplings.

Table II.

Beam Polarization	
Transverse(zero)	Longitudinal
$a_3 \sim g_A^e g_A^\mu$	$\frac{a_5}{a_3} = \frac{g_V^e}{g_A^e}$
$(a_1 \sim g_V^e g_V^\mu)$	$\frac{a_4}{a_3} = \frac{g_V^\mu}{g_A^\mu}$
$a_6 \sim \mathrm{Im}\, g_A^{e*} g_V^\mu$	$\frac{a_3^{ee}}{a_3} = \frac{g_A^e}{g_A^\mu}$

C. Inclusive Hadronic Processes

The report in this summer study by D. Hitlin and A. Sessoms discusses prospects for isolating weak effects in single hadron inclusive experiments. Particularly striking is the observation that S, P, and T type weak couplings give rise to terms linear in P_T, in contrast with V, A types which show only correlations with $P_T^+ P_T^-$. Simple tests are therefore possible with a general hadron detector and the natural beam polarization.

Also considered and found feasible by Hitlin and Sessoms is an experiment to measure Λ^0 polarizations, in lieu of longitudinal beam polarizations, to isolate parity-violation.

II. DETECTORS

The summer study reports by W. Ford and G. Manning discuss arrangements for studying ee→μμ and ee with longitudinally polarized beams. Both detectors are of the "iron ball" type. In the first a free space of 4 meters is provided between the polarization rotating magnets to allow flexibility to interchange detectors. An iron ball detector which fits into this region is described in some detail. The scheme of Manning optimizes the synchrotron radiation by providing only a short (1.4 meter) free space for the central detectors. The polarization rotation magnets are extensions of the iron ball, which then can be made thicker to improve punch-through rejection and momentum resolution.

0 0 0 0 4 5 0 1 5 7 1

The cost is the loss of ability to vary the detector configuration, or to run the analyzing field independently of the polarization rotator (eg., to use transversely polarized beams). Detailed studies of the backgrounds due to the synchrotron radiation are needed to decide which approach should be adopted.

REFERENCES

1. R. Schwitters and B. Richter, PEP-87 ('74PEPSS).
2. W. Toner, PEP-169 ('74 PEPSS).
3. B. Richter, PEP-140 ('74 PEPSS).
4. P. Wanderer, et al., PEP-157 ('74 PEPSS), Fig. 4.

IRON BALL, MARK II

W. T. Ford

The detector described here is intended to record events of the reactions $e^+e^- \to \mu^+\mu^-$ and e^+e^- in sufficient detail to permit extraction of the leptonic weak neutral current parameters $g_V^{e,\mu}$ and $g_A^{e,\mu}$ by the method outlined in Refs. 1 and 2. For some of the measurements the e^+ or e^- beam is longitudinally polarized.

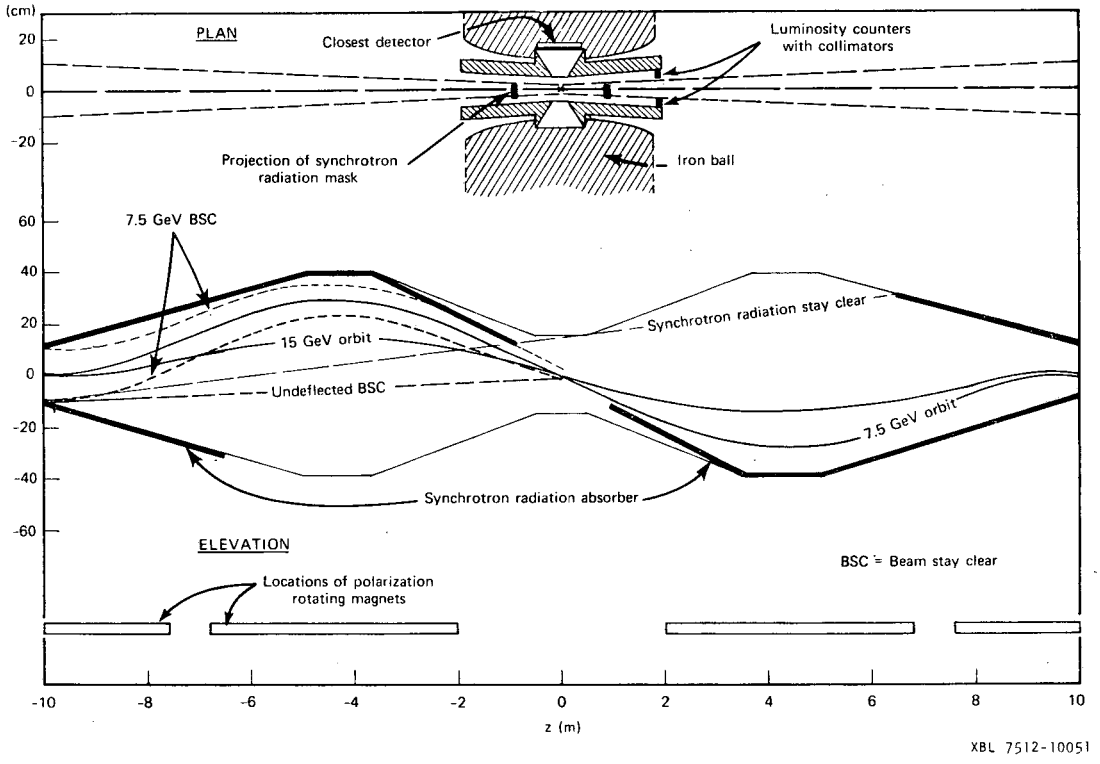

Fig. 1. Plan and elevation views of the experimental area showing the particle trajectories, the location of the polarization rotation magnets and the location of the detector.

The muon-electron detector is shown in Fig. 2. A toroidal magnet provides both particle identification and momentum analysis for the muons (the magnetic field of 16 - 18 kG is contained entirely within the iron). The cylindrical central cavity contains tracking chambers for muons and electrons, and lead scintillator shower counters to identify the electrons over that part of the solid angle that is free of shielding. The tracking devices may be either drift or wire spark chambers, but must provide reasonably good resolution in the polar angle, since the bending of the magnet is in the θ direction. Trigger scintillators (not shown in the figures) are also to be provided.

Surrounding the magnet are 8 "orange-peal" wire spark chambers, each of two gaps and covering the region $\Delta\phi = 45°$, $15° \lesssim \theta \lesssim 165°$. These chambers are made of honeycomb aluminum skin panels fabricated over a curved form and tapered toward the poles. The wires are pre-wound onto mylar sheets which in turn are glued to the panels. The wire orientation is across the narrow dimensions of chamber, along constant-z contours (z being the beam axis), to provide good resolution in θ. Half the wire planes are rotated by 15° to give small-angle stereo determination of the azimuth. Outside the spark chambers are liquid scintillation counters for triggering and time-of-flight measurements.

The acceptance for muons extends over 2π in azimuth and to 15° minimum polar angle, $\simeq$ 97% of 4π. The electron acceptance extends over 2π in azimuth and $50° < \theta < 130°$, or $\frac{1}{3} \times 4\pi$. The momentum resolution (for muons) is $\Delta p/p \approx .21$, limited by multiple scattering.

The background of muon misindentification due to hadron punch-through or decay is $\ll 1\%$ per muon for muons above 10 GeV. For lower energies (which are of interest for searching for anomalous

0 0 0 0 4 5 0 1 5 7 2

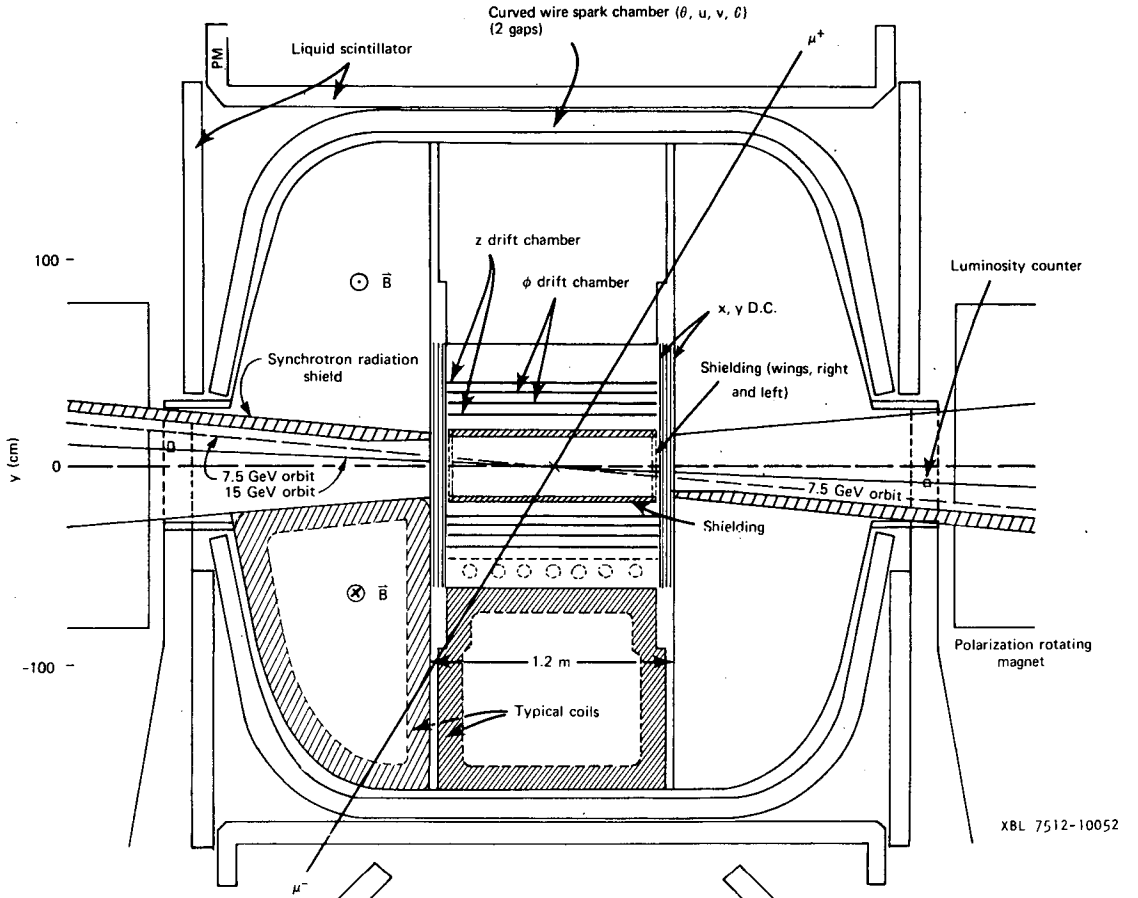

a

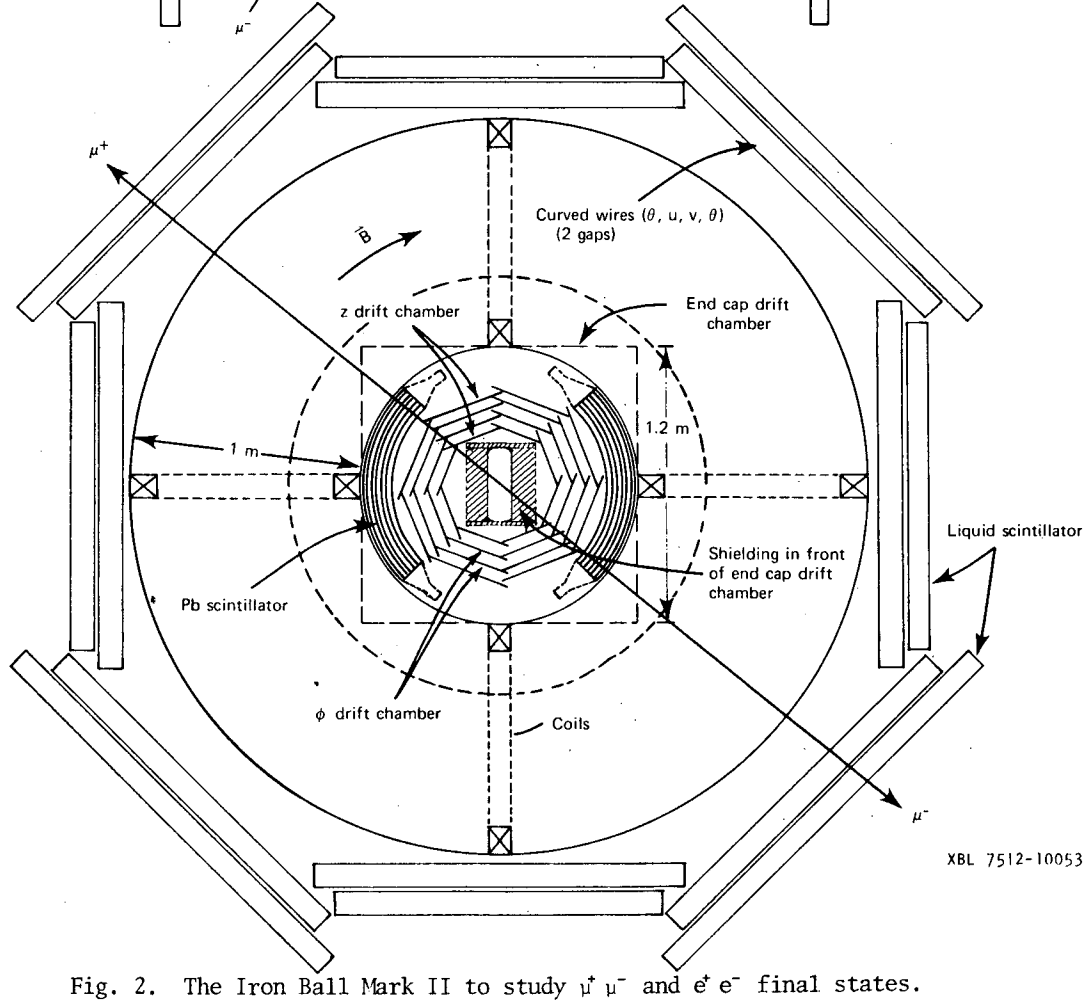

b

Fig. 2. The Iron Ball Mark II to study $\mu^+\mu^-$ and e^+e^- final states.

lepton production), the background is estimated as follows:

p	punch-thru/hadron event	decay/hadron event
1.5 GeV	0.03	0.02
7.5 GeV	0.002	10^{-4}

It should be pointed out that no reliable estimates of the background levels induced by the synchrotron radiation have been made for this configuration. It is possible the only safe procedure would be to extend the vacuum pipe (and bending magnets) vertically to the maximum envelope of the synchrotron radiation, allowing it to pass untouched through the interaction region to a dump at each end. The vacuum chamber than becomes ~ 3 m high, or 1.5 m high if we forego running at less than 15 GeV with full 90° rotation of the polarization. The apparatus would have a gap in the entire vertical plane.

REFERENCES

1. Weak Interactions Study Group summary in this volume.
2. G. Manning, "Measurement of Weak Interaction Contributions to $e^+e^- \to \mu^+\mu^-$ Using Longitudinal Polarization of the e^+ and e^- Beams", report in this volume.
3. R. Schwitters & B. Richter, PPE-87 ('74 SS p. 384).
4. G. Barbiellini, NIM 123, 125 (1975).

0 0 0 0 4 5 0 1 5 7 3

EM-WEAK INTERFERENCE IN $e^+e^- \to \mu^+\mu^-$ SCATTERING

R. Morse

The basic one photon cross-section for e^+e^- annihilation is

$$\frac{4s}{\alpha^2}\frac{d\sigma^o}{d\Omega} = (1 + \cos^2\theta) - P_T^+P_T^- \sin^2\theta \cos 2\phi$$

$$= f^o(\theta,\phi)$$

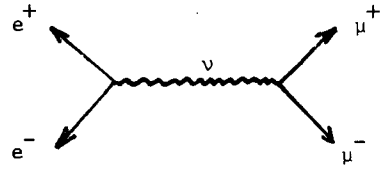

If we allow for the weak neutral current process

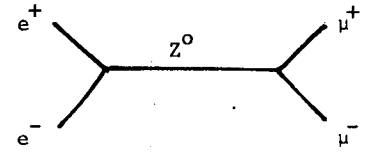

then to first order in Weak-EM interference we have

$$\frac{4s}{\alpha^2}\frac{d\sigma}{d\Omega} = (1 + a_1 s)\, f^o + 2\, a_3\, s \cos\theta = (1 + \delta^W)\, f^o$$

where $\delta^W = a_1 s + \frac{1}{f^o}(2a_3\, s \cos\theta)$,

where the coefficients a_1 and a_3 are given in Table 1. The higher order (α^3) electromagnetic corrections also interfere with the basic one photon process. The effect can be absorbed into $\delta^{EM}(\theta,\phi)$ defined as a modification of the basic single-photon rate.

$$\frac{4s}{\alpha^2}\frac{d\sigma}{d\Omega} = (1 + \delta^{EM})\, f_o$$

so that the entire process is written as (to order α^3)

$$\frac{4s}{\alpha^2}\frac{d\sigma}{d\Omega} = (1 + \delta^W + \delta^{EM})\, f_o = (1 + \delta^T)\, f_o = f^T$$

Table I[3]

$e^+e^- \to \mu^+\mu^-$

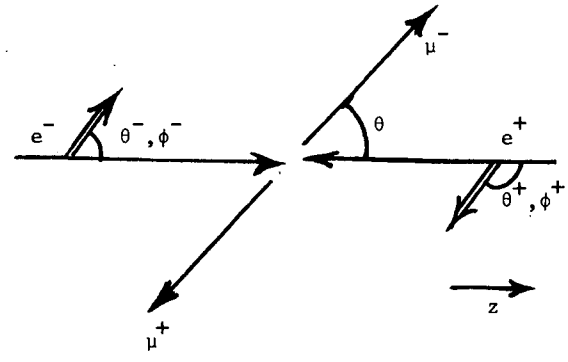

(Natural polarization: $\phi^+=0, \phi^-=\pi, \theta^+=\theta^-=\frac{\pi}{2}$)
With restriction that polarization lie in x-z plane,

$$\frac{d\sigma}{d\Omega} = \frac{\alpha^2}{4s}\{\left[(1+a_1(s))(1+P_z^+P_z^-)+a_4(s)(P_z^++P_z^-)\right](1+\cos^2\theta)$$

$$- \left[(1+a_2(s))\cos 2\phi - a_6(s)\sin 2\phi\right] P_T^+P_T^-\sin^2\theta$$

$$+ \left[a_3(s)(1+P_z^+P_z^-)+a_5(s)(P_z^++P_z^-)\right] 2\cos\theta\}$$

$a_1 = D(s)\ \mathrm{Re}\ g_V^{e*}g_V^{\mu}$

$a_2 = D(s)\ \mathrm{Re}\ g_V^{e*}g_V^{\mu}$

$a_3 = D(s)\ \mathrm{Re}\ g_A^{e*}g_A^{\mu}$

$a_4 = D(s)\ \mathrm{Re}\ g_A^{e*}g_V^{\mu}$

$a_5 = D(s)\ \mathrm{Re}\ g_V^{e*}g_A^{\mu}$

$a_6 = D(s)\ \mathrm{Im}\ g_A^{e*}g_V^{\mu}$

$$D(s) = \sum_z \frac{s}{s-M_Z^2}\frac{g_z^2}{2\pi\alpha} \to -\frac{s}{2\pi\alpha M_Z^2}$$

i) Rates and Asymmetries

(a) The rate is proportional to R where

$$R = \int_\Omega (1 + \delta^T)\, f^o\, d\cos\theta d\phi$$

Note that f^o is symmetric about $\theta = \pi/2$ so that we can write

$$R = 2\int d\cos\theta \left(1 + \delta_s^T(\theta)\right) f^o\, d\phi \text{ where}$$

$\delta_s^T(\theta) = \frac{1}{2}\{\delta^T(\theta) + \delta^T(\pi-\theta)\}$.

We show later that $\delta_s^T(\theta)$ has no ϕ dependence so that the modified rate is simply

$$R = 4\pi \int_0^{\pi/2} d\cos\theta \left(1 + \delta_s^T(\theta)\right)\left(1 + \cos^2\theta\right)$$

the modification of the basic rates is determined entirely by $\delta_s(\theta)$

(b) The asymmetry $A(\theta,\phi)$ is given by the usual formula

$$A(\theta,\phi) = \frac{f^T(\theta,\phi) - f^T(\pi-\theta,\phi)}{f^T(\theta,\phi) + f^T(\pi-\theta,\phi)} = \frac{\delta_A^T(\theta,\phi)}{1 + \delta_s^T(\theta,\phi)}$$

where $\delta_A^T(\theta,\phi) = \frac{1}{2}\{\delta^T(\theta,\phi) - \delta^T(\pi-\theta,\phi)\}$

Note that the asymmetry depends on the rate.

ii) Calculation of the Weak Interference

$$\delta_s^W = a_1 s$$

$$\delta_A^W = \frac{2a_3 s}{f_o} \cos\theta$$

Recall that $f_o = 1 + \cos^2\theta - |P_+P_-|\sin^2\theta \cos 2\phi$ so that at $\phi \cong 45^o$ there are no polarization effects, and at $\phi = 0^o$ the effect is maximal

Here $a_1 = \frac{g_V^2}{2\pi\alpha(S-M_Z^2)} \cong -\frac{g_V^2}{2\pi\alpha M_Z^2}$

and $a_3 = \frac{-g_A^2}{2\pi\alpha M_Z^2}$ assuming $s \ll M_Z^2$ (see Table 1)

We exhibit the δ_s^W, and δ_A^W, behavior on angle in Fig. 1 for an s=900 GeV^2, and a transverse polarization of $P_T^+ = P_T^- = 0.924$ using a V-A Interaction (Weinberg-Salam cuts the effect in half).

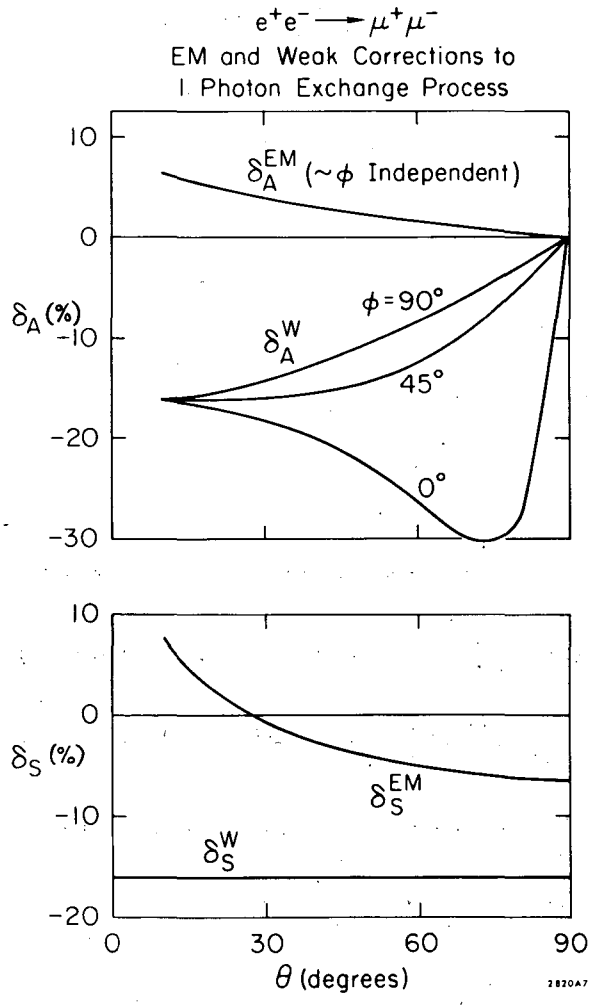

Fig. 1.

The asymmetry due to the WEAK interference is

$$A^W(\theta,\phi) = \frac{\delta_A^W}{1+\delta_s^W} = \frac{2a_3 s}{(1+a_1 s)} \frac{1}{f^o} \cos\theta$$

and is shown in Fig. 2 for s = 900 GeV^2 and 100 GeV^2, for $P_T^+ = P_T^- = 0.924$ and the V-A interaction. The effect of polarization on the ϕ-distributions is quite striking. However, since most experiments in this region are event limited we look at the ϕ-integrated asymmetry

$$\bar{A}^W(\theta) = \frac{1}{2\pi}\int_o^{2\pi} A^W(\theta,\phi)\, d\phi$$

It is also shown in Fig. 2.

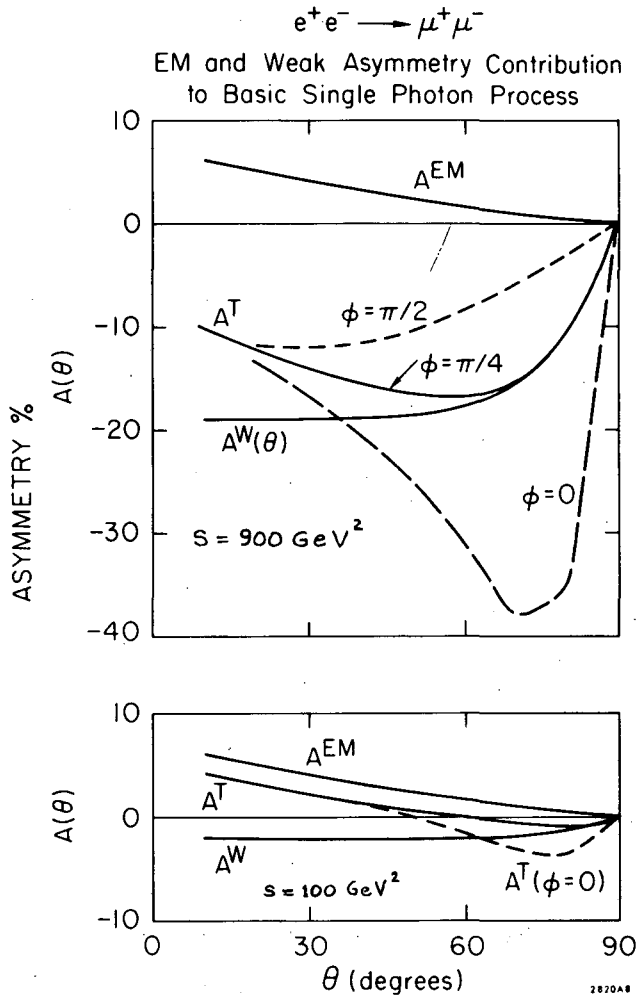

Fig. 2.

iii) Calculation of the higher order (α^3) EM Interference

Brown et al.[1] have shown that - for transverse polarization - that

$$\delta^{EM}_{(\theta,\phi)} = g_1(\theta) + \frac{1}{f^o(\theta,\phi)}\{g_2(\theta)+g_3(\theta)|P_T^+P_T^-|\cos 2\phi\}$$

0 0 0 0 4 5 0 1 5 7 4

$g_2(\theta)$ and $g_3(\theta)$ are anti-symmetric with respect to $\theta \to (\pi-\theta)$ so they do not contribute to the rate. Further there is no net polarization contribution to the rate because of the cos 2ϕ term.

Working with the $\delta_s^{EM}(\theta)$, and $\delta_A^{EM}(\theta,\phi)$ defined as before we note that:

(a) δ_s^{EM} depends on E, ΔE,θ, and

(b) δ_A^{EM} depends on $\Delta E/E$, θ,ϕ -(note, independent of energy).

Unlike δ_A^W, δ_A^{EM} has only a weak dependence on ϕ because

(a) δ_A^{EM} is dominated by $(-\frac{8\alpha}{\pi}\, \ell n \tan\frac{1}{2}\theta \ell n \frac{E}{\Delta E})$ in $g_1(\theta)$

(b) the ϕ dependence of f^o compensates the ϕ dependence in the $g_2(\theta) + g_3(\theta)\ |P_T+P_T^-|$ cos 2ϕ term

Thus only the $\phi = 45^o$ values of δ_A^{EM} are shown in Fig. 1 for E=15 GeV and $\Delta E/E$ =10% (corresponds to s=900 GeV^2)

As before the asymmetry given by

$$A^{EM}_{(\theta,\phi)} = \frac{\delta_A^{EM}(\theta,\phi)}{1+\delta_s^{EM}(\theta)} \approx \bar{A}^{EM}_{(\theta)} = \frac{1}{2\pi}\int_0^{2\pi} A^{EM}_{(\theta,\phi)}\, d\phi$$

is almost $\bar{A}^{EM}_{(\theta)}$ due to the weak ϕ-dependence mentioned above.

The EM corrections are very sensitive to $\Delta E/E$ values, δ_A^{EM} being much more well behaved

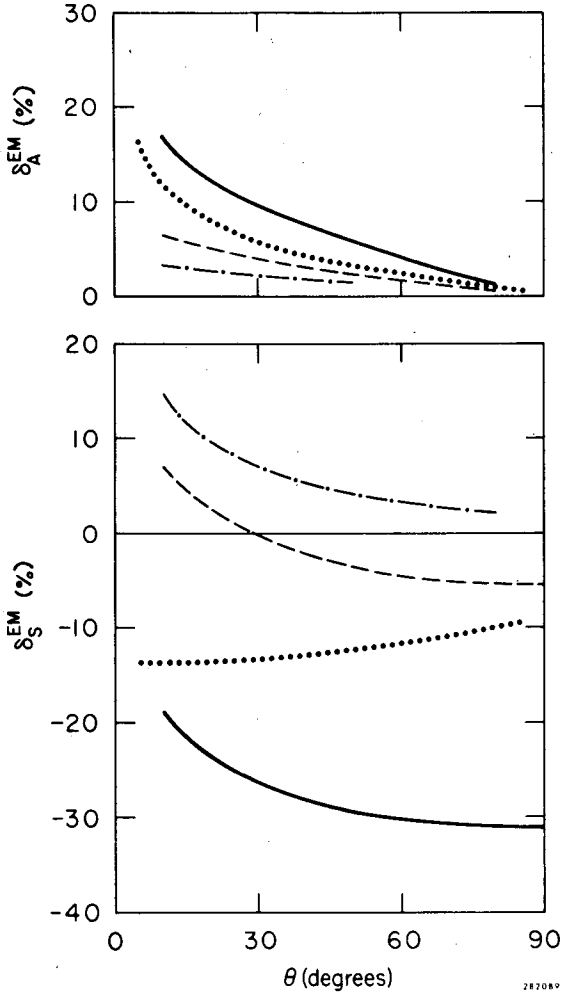

Fig. 3.

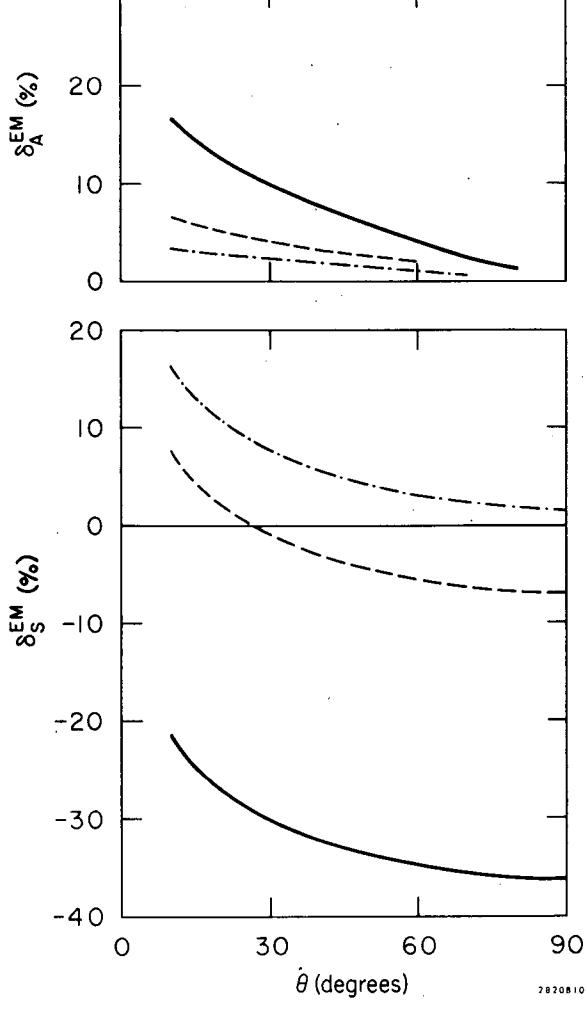

Fig. 4.

than δ_s^{EM}. It may be that the Brown et al. formalism has been pushed into the "hard-photon" region for $\Delta E/E$=10-20%. In Fig. 3 and 4 we present δ_A^{EM} and δ_s^{EM} for the values of s and $\Delta E/E$ shown. We also compare with "hard-photon" calculation of Berends et al.[2] The agreement is not good - though δ_A^{EM} is better than δ_s^{EM}. The behavior remains the same at E=15 GeV. It seems to indicate that a $\Delta E/E$=10% is a tolerable level.

iv) Conclusion

The grand asymmetry $A^T(\theta,\phi)=\left(\frac{\delta_A^W + \delta_A^{EM}}{1+\delta_s^W+\delta_s^{EM}}\right)$ and

the ϕ-integrated asymmetry is shown in Fig. 2 for the values shown. Since the α^3 EM corrections are nearly ϕ-independent one can define $A_\phi(\theta)$ which is(nearly) independent of the α^3 EM correction (to the degree that they are ϕ-independent).

$$A_\phi(\theta) = 4\int_0^{\pi/4} A^T(\theta,\phi)\,d\phi - 4\int_\pi^{\pi/2} A^T(\theta,\phi)\,d\phi$$

$$A_\phi(\theta) \approx \frac{2\pi a_3 s\ \eta(\theta)}{1+\delta_s^W+\delta_s^{EM}} \approx 2\pi a_3\ s\ \eta(\theta)$$

given that the higher order symmetric effects are small. $\eta(\theta)$ which equals $A_\phi(\theta)/2\pi a_3 s$ is shown in Fig. 5. The technique has the strength that the EM corrections need not be well known - it is also statistically weak in that differences are used. This requires lots of data - it may be extravagant.

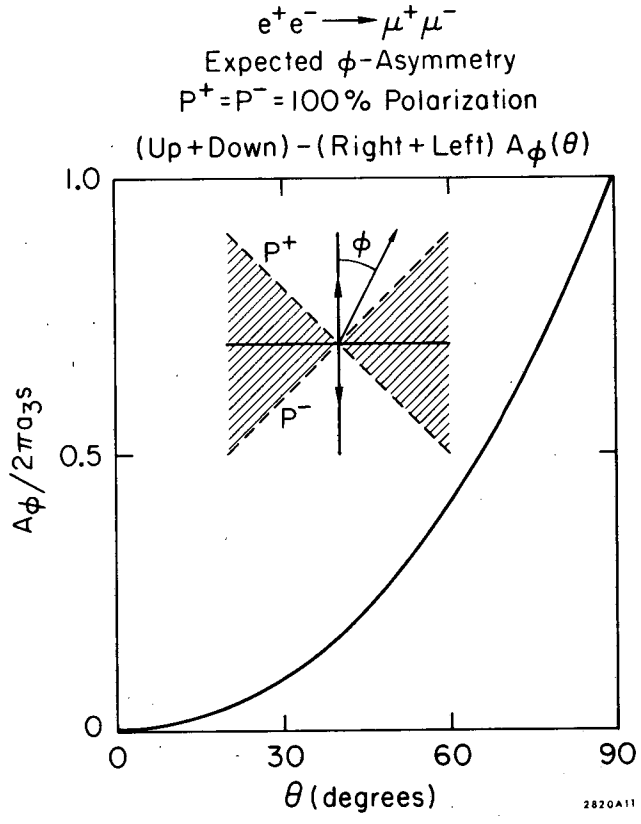

Fig. 5.

References

1. Brown et al., Phys.Lett. 43B, 403 (1973)
2. Berends et al., Nuclear Physics B63, 381 (1973)
3. S. Berman, Lecture given at 1974 PEP Summer Study (unpublished).

0 0 0 0 4 5 0 1 5 7 5

WEAK-ELECTROMAGNETIC INTERFERENCE EFFECTS IN e^+e^- → HADRONS

D. Hitlin - A. Sessoms

Abstract

A program is described which can ascertain the complete space-time structure of neutral weak currents by studying correlations of inclusive hadron distributions, and polarization, with beam polarization.

- - - - - - - - - - - - - - - - - -

The possibility of observing weak-electromagnetic interference effects is one of the most exciting experimental prospects of PEP. The simplest approach to the measurement of such effects is in the pure QED reaction $e^+e^- \to \mu^+\mu^-$. Weinberg-Salam type models of the weak interaction make predictions for the magnitude of such effects, as does "standard" V-A theory. Since neglecting muon form factors and derivative couplings appears justified, it is concluded that a "model independent" analysis of the data from such an experiment can be made. In order to isolate weak effects, however, it is necessary either to measure the polarization of the outgoing 15 Gev muons, or to produce longitudinal polarization in at least one electron beam. Both of these are at best difficult tasks. It is the purpose of this note to point out that it may be practical to see unambiguous effects of weak-electromagnetic interference in such processes as $e^+e^- \to$ hadron + X, and, in fact, to ascertain the complete space-time structure of the weak interaction without the necessity of producing a longitudinally polarized electron beam.

An advantage of this approach is that it does not require the construction of a special detector. Studies of the type we suggest can be carried out quite well in any general purpose PEP detector that has reasonable photon detection capability.

The processes studied are no longer purely leptonic and so questions as to the model dependence of the results arise. In this context, it is worth noting that most of our knowledge of neutral current interactions with neutrinos is based on semileptonic processes, and that within the context of the parton model, or its equivalent, a great deal has been learned.

We suggest investigations of the correlations between inclusive hadron momenta, and helicities, with beam polarization as a means of determining whether the neutral weak current in e^+e^- annihilation is S,P,V,A or T in character. This is possible because, in the limit $m_e/m_Z \to 0$, S, P and T interference terms are all linearly dependent on the transverse polarization of the beams, while V and A terms are either independent of transverse polarization or quadratically dependent on it. Since S, P and T couple to e^+e^- of the same helicity there can be no interference terms dependent solely on the longitudinal polarization. Thus a term involving the longitudinal polarization, either of the beams or the outgoing hadron, signifies the existence of a V or A term.

Dass and Ross[1] have investigated possible interference terms in $e^+e^- \to h(\vec{p}) + X$, where $\vec{p}$ is the hadron momentum. The effective Lagrangian for the neutral weak coupling of the electron field, Ψ, to hadrons, has the form

$$\mathscr{L}_{eff} = \bar{\Psi}\,\Psi\,J_1 + \bar{\Psi}\,\gamma_5\Psi\,J_2 + \Psi\,\gamma_\lambda\,\Psi\,J_3^\lambda + \bar{\Psi}\,\gamma_\lambda\gamma_5\Psi\,J_4^\lambda + \bar{\Psi}\,\sigma_{\lambda\nu}\,\Psi\,J_5^{\lambda\nu}.$$

The interference terms, and their properties under Parity, P, and charge conjugation, C, are shown in Table 1, which is adapted from Dass and Ross.

Table 1

Kinematic structure of the weak electromagnetic interference terms for the process $e^+e^- \to hX$ for the currents $J_1,\ldots,J_5$. The symbols p, p_+,p_-,s_+,s_- are the hadron momentum, the momentum of the e^+ and e^- beams, and the transverse polarization of the e^+ and e^- beams respectively; $2K=p_- - p_+$. The last two columns give the behavior under parity inversion (P) and for charge conjugation (C); odd and even are denoted - and + respectively. The column for C refers to the case h=$\bar{h}$ or to σ_+; for σ_-, the behavior is opposite to that for σ_+.

Hadronic Current	Kinematic Structure in c.m. Frame	P	C
J_1	$p\cdot(h_+s_- - h_-s_+)$	+	-
	$p\cdot(K\times(s_+ + s_-)$	+	+
J_2	$p\cdot(s_+ - s_-)$	-	-
	$p\cdot(K\times(h_-s_+ + h_+s_-))$	-	-
J_3	$1 - h_-h_+$	+	+
	$(h_- - h_+)p\cdot K$	-	+
	$(1-h_-h_+ + s_-s_+)(p\cdot pK\cdot K - p\cdot Kp\cdot K) - 2p\cdot s_-\,p\cdot s_+$	+	+
J_4	$h_- - h_+$	-	-
	$(h_- - h_+)(p\cdot pK\cdot K - p\cdot Kp\cdot K)$	-	-
	$(1-h_-h_+)p\cdot K$	+	-
	$p\cdot s_+\,p\cdot(K\times s_-) + p\cdot s_-\,p\cdot(K\times s_+)$	-	-
J_5	$p\cdot Kp\cdot(h_+s_- - h_-s_+)$	+	+
	$p\cdot KP\cdot(K\times(s_+ + s_-))$	+	+
	$p\cdot Kp\cdot(s_+ - s_-)$	-	+
	$p\cdot Kp\cdot(K\times(h_-s_+ + h_+s_-))$	-	+
	$p\cdot(h_+s_- + h_-s_+)$	+	+
	$p\cdot(K\times(s_+ - s_-))$	+	+
	$p\cdot(s_+ + s_-)$	-	+
	$p\cdot(K\times(h_-s_+ - h_+s_-))$	-	+

What are the expected sizes of the effects? McDonald[3] has estimated that, in the Weinberg model, asymmetries and hadron polarizations will be as large as 7% x $(4 \sin^2\theta_W - 1)$ or approximately 4% for $\sin^2\theta_W = 0.4$. The results of Gatto and Preparata[4] are similar. If the neutral current couplings are as large as the charged current couplings the characteristic effects could be twice as large. These results are similar in magnitude to the asymmetries and polarizations for $e^+e^- \to \mu^+\mu^-$, as one might guess if pointlike, spin ½ partons are coupled to the photon and the weak current.

We can now ask whether there is any evidence that the subsequent dressing of the partons into hadrons carries any information about the vertex. An indication that the hadrons do remember the beam polarization comes from SPEAR data on transverse polarization effects.[5] Data for $\mu^+\mu^-$ final states and inclusive hadron are shown in figure 1. The observed azimuthal asymmetry is plotted against $x = 2p/\sqrt{s}$. For the muon pairs, of course, there is only one value of azimuthal asymmetry. For the hadrons above x=0.3 the distribution shows a 20% asymmetry, consistent with the value for muons. Below x=0.3 the distribution is much less asymmetric. The hadrons with $x \geq 0.3$ thus display the polarization information inherent at the vertex. We conclude that it is reasonable to search for weak effects in inclusive hadron spectra for hadrons with $x \geq 0.3$.

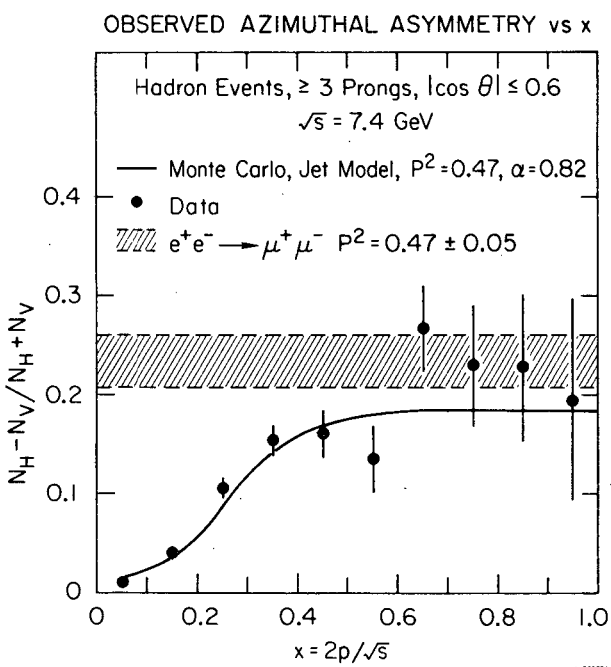

Fig. 1 Observed azimuthal asymmetry vs. x at s=55 GeV^2 at SPEAR II for hadron events, with ≥ 3 prongs, $|\cos\theta| \leq 0.6$.

Inclusive hadron spectra provide a large number of events for these correlation studies. In what follows we will assume a luminosity $\langle\mathscr{L}\rangle = 2.5\times10^{31}$ cm^{-2}sec^{-1} at 15 GeV and a running time of 60 days. This is an integrated luminosity of 1.3×10^{38} cm^{-2}. If R remains constant at 6, then at s = 900,

$$\int s\,\frac{d\sigma}{dx}\,dx = s\langle n_{ch}\rangle\,\sigma_{tot} = 3780 \text{ nb GeV}^2$$

If $\langle n_{ch}\rangle$ grows as ℓns from its present value, which is an extrapolation from SPEAR data, then we will have $\langle n_{ch}\rangle = 7.5$. The total number of charged hadrons produced in our two month run will then be 5.5×10^5. Using Richter's parametrization[6] of $s\frac{d\sigma}{dx}$, we find that 10.7% of the hadrons will have $x \geq 0.3$. The data sample then consists of 5.9×10^4 high x hadrons. With an effective solid angle of .75, we are left with 4.4×10^4 π's. The statistical error on this sample is .5%, so that there are clearly enough statistics to measure correlations of the expected magnitude accurately.

Most calculations of weak-electromagnetic interference effects in e^+e^- annihilation have assumed a V-A structure for the neutral weak coupling. S,P and T couplings should, however, be excluded experimentally before they are excluded theoretically. Let us briefly consider experimental approaches to this end. As we have mentioned, Table 1 shows that STP effects are linear in the transverse polarization of either beam, while V,A effects are either independent of, or quadratic in, the transverse beam polarization.

A correlation which disappears with depolarization of one beam is thus indicative of an SPT effect. With 44,000 inclusive hadrons of $x \geq 0.3$ in our 60 day run, it is a simple matter to take the data in several combinations of transverse and unpolarized beams. The transverse polarization dependence can be isolated either by taking advantage of the polarization buildup time in the ring or by depolarizing one beam. In either case the degree of polarization is easily monitored, as Hanson has shown, by the φ distribution of the $\mu^+\mu^-$ or inclusive hadron events.

Since statistics are large, several conditions can be used, each with sufficient data to see the expected effect at the 3σ level. As a corollary, if no effect is seen, extremely good limits on STP coupling can be derived. These limits should be substantially better than those achievable in muonless neutrino interactions in the forseeable future. As opposed to the V, A case, should a correlation linear in the transverse polarization be seen, it is not possible to confuse the effect with interference with a second order electromagnetic process since those contributions linearly dependent on transverse polarization are suppressed by $\frac{\alpha}{s}\frac{m_e}{E}/G_F \sim 10^{-4}$ relative to weak-first order electromagnetic terms at PEP energies.

If this correlation is seen, we have then to separate SP couplings from T. This is possible on the basis of angular distributions and their behavior when the e^- or the e^+ beam is transversely polarized. For example, at $\theta=\pi/2$ the first four terms in J_5, which are proportional to $\vec{p}\cdot\vec{K}$, vanish. The remaining terms are identical to the SP correlations, except that they do not change sign when the e^+ instead of the e^- beam is transversely polarized, while the J_1, J_2 terms do change sign. It should be noted that the setting of limits on SP or T neutral current coupling does not require either longitudinal polarization of the e^+e^- beams or measurement of final state helicity, since it is not necessary to establish parity violation.

For V,A couplings, on the other hand, the isolation of an unambiguous weak-electromagnetic interference effect does require evidence of parity (or CP!) violation. Charge conjugation non-invariance does not suffice; unless one appeals to the s dependence of the correlation as opposed to the ℓn s

0 0 0 0 4 5 0 1 5 7 6

dependence expected for two photon effects. All but one of the VA correlations which violate parity involve longitudinal beam polarization. The term that does not, requires both beams to be transversely polarized (the normal situation).

It appears to be quite difficult to design a hadronic final state detector which can withstand the hundreds of kw of synchrotron radiation produced in the Richter-Schwitters[7] method of producing longitudinal polarization. One then has the option, as in $e^+e^- \to \mu^+\mu^-$, of measuring the helicity of particles in the final state. In this context it should be noted that if the beams are transversely polarized, (non zero) longitudinal polarization of either a final state muon or hadron can be induced either by the parity conserving weak interaction terms or 1γ-2γ interference. One can be sure that the observation of final state helicity implies parity violation when the observation is made in the plane of the ring however, and this ϕ variation is likely to be of importance in isolating the effect unless one can continuously depolarize the e^+e^- beams.

The difficulties of measuring the polarization of 15 GeV muons are well known and will not be dealt with here. The question is then whether one can measure the helicity of outgoing baryons in inclusive e^+e^- processes. The obvious choice for such a measurement is $e^+e^- \to \Lambda\ (\bar{\Lambda})+X$. This was discussed at last year's Summer Study,[8] so we will only briefly touch upon it here. First, let us estimate the number of Λ's one expects to have at high x at $s=900\ \text{GeV}^2$ in another way.

Using "correspondence arguments", Bjorken and Kogut[9] have made predictions for the inclusive $\bar{p}$ distribution as a function of x in the scaling limit. This spectrum is shown in Figure 2. The fraction of $\bar{p}$'s with $x \geq 0.3$ is 25%. We can assume that Λ's will have a similar inclusive distribution. The current SPEAR data[10] shows a $\bar{p}$/all negative ratio of $\sim$5% at momentum assigned/GeV, this fraction being independent of s and therefore of x for $0.25 \leq x \leq 0.4$. Although there is some evidence that the $\bar{p}$ fraction is even larger at higher x, we will assume that the $\bar{p}$ fraction at high x is 5% and since Λ's are less copiously produced that the $\Lambda+\bar{\Lambda}$ fraction is 5%. Then if $\langle n_{ch} \rangle = 7.5$ at s=900, there should be a high x Λ or $\bar{\Lambda}$ fraction of 0.19/event. Then in our 60 day run with a 75% solid angle, we expect 10.4K high x Λ or $\bar{\Lambda}$. This is essentially the same number as for $\mu^+\mu^-$ events. If we assume that the average helicity of Λ and μ is the same, e.g., 5%, then the observed decay asymmetry is $\alpha_{eff} \times 0.05 = 0.65 \times 0.05 = 0.033$ for Λ's and $\alpha_{eff} \times 0.05 = 0.33 \times 0.05 = 0.017$ for μ's. The 10K events therefore produce less than a 2σ effect for μ's and more than a 3σ effect for Λ's. There are, of course, backgrounds for the Λ decay, such as two photon production $e^+e^- \to e^+e^-+\Lambda+X$, but this also exists for muons, and must be handled in the same way, by a measurement of the total energy of the final state hadrons or muons. Other backgrounds, such as polarized Λ's from Σ^+ or Ξ decay or unpolarized Λ's from $\Sigma^0 \to \Lambda\gamma$ decay, have been previously discussed.[8]

In conclusion, we have shown that it is possible to ascertain the full space-time structure of neutral weak currents by studying inclusive hadron production, and to separate weak-electromagnetic interference from pure electromagnetic effects without the need for longitudinal beam polarization. These correlations can be found in a general detector, provided that control of the transverse beam polarization is exercised.

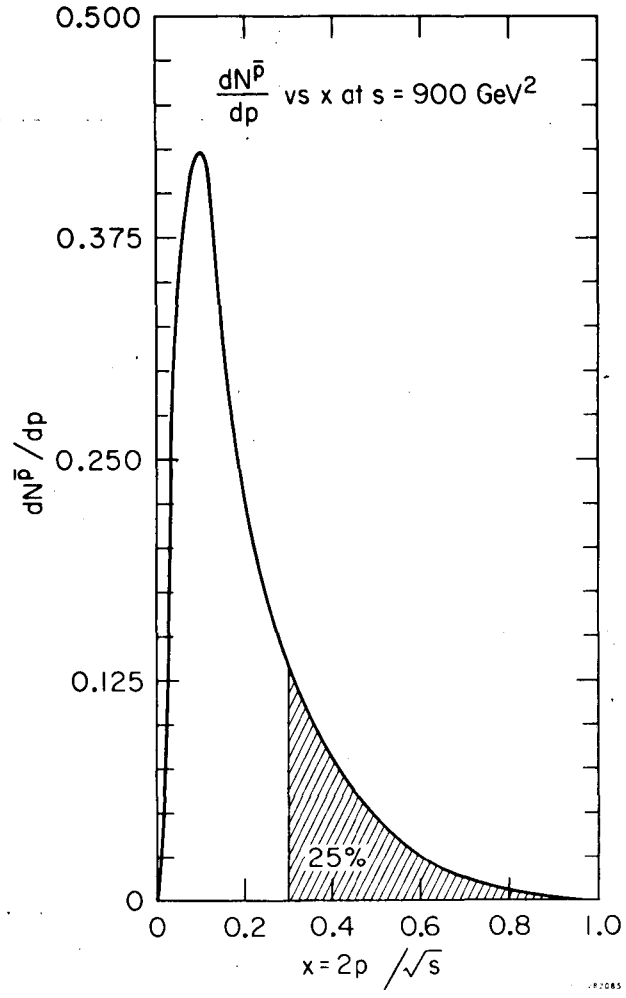

Fig. 2 x distribution of inclusive $\bar{p}$'s at s=900 GeV^2, from Bjorken and Kogut.[9]

REFERENCES

1. G.V. Dass and G.C. Ross, Phys Lett 57B, 173 (1975).
2. ibid. Note the sign change in the second term from that in the published table.
3. A. McDonald, Nucl.Phys. B 75, 343 (1974).
4. R. Gatto and G. Preparata, I.N.F.N. Internal Note 435, 12 Feb. 1973.
5. G. Hanson, Proceedings of the 1975 SLAC Topical Conference on Electromagnetic Structure of Hadrons.
6. B. Richter, PEP-140, 1974 PEP Summer Study.
7. B. Richter and R. Schwitters, PEP-87, 1974 PEP Summer Study.
8. D. Hitlin, J. Marx and P.Yamin, PEP-164, 1974 PEP Summer Study.
9. J.D. Bjorken and J. Kogut, Phys.Rev., D8, 1341 (1973).
10. C. Morehouse, Proceedings of the 1975 SLAC Topical Conference on Electromagnetic Structure of Hadrons.

A GENERAL USERS MAGNET DESIGN

F. Lobkowicz, U. Becker, K. Berkelman,
M. A. Green, E. Groves, K. Halbach, J. Kadyk,
N. Mistry, A. Sessoms, M. Strovink

I. INTRODUCTION

Experience from both SPEAR and DORIS has shown that in order to be best able to do physics at PEP, as complete information as possible should be obtained for each event. There is a fundamental difference between proton storage rings such as the CERN ISR and ee storage rings such as PEP, which necessitate a different approach for any detectors used. At hadronic machines, the interaction rates are large (10^5-10^6/sec), and thus the complete analysis of every event is clearly impossible. Thus, great care has to be taken in the choice of an appropriate trigger to avoid being swamped by unwanted interaction events. On the other hand, inclusive or semi-inclusive data may contain as much physical information as some exclusive channels which make up only a small fraction of the total cross section. Since large statistical samples are in principle available, backgrounds can be investigated by modifying the initial trigger requirements.

At PEP the expected interaction rates of $\lesssim 1$ event/minute are sufficiently small that, were it possible to design a perfect detector able to completely identify all reaction products of every event, only one such detector would have to be built. The necessity for having several intersection regions at PEP, each with its own different experimental setup, is based on the fact that such a perfect detector cannot be built. The mass identification of fast particles via their Cerenkov radiation interferes with the requirement of detecting neutral products such as photons. Pions and kaons decay in flight while their momentum is being measured, thus, creating identification difficulties between hadrons and muons. Therefore, the emphasis for any PEP detector, once a reasonable annihilation trigger has been established, lies in identifying unambiguously the reaction of interest from all the data obtained.

We feel that it is necessary to remind the reader of these rather obvious facts, in order to enable him to appreciate the framework within which we have undertaken to study the possibility of designing a general user magnet (GUM) suitable for a reasonably large set of different experiments.

Basically one can distinguish three types of detectors suitable for PEP. (1) General detectors which try to achieve a reasonable compromise between all detection requirements. They typically require a solid angle of nearly 4π, some particle identification, and both neutral and charge detection. With such detectors, one can study all possible reactions, but may have difficulties identifying specific reactions which form only a small part of the total cross section -- exactly because being a compromise solution they may be unable to uniquely identify reaction products. A prime example of such a detector would be Mark I, presently used at SPEAR, or its improved version Mark II.[1] (2) Highly specialized detectors which can identify uniquely one particular reaction and analyze it completely. As example, we might mention here the iron ball[2] and its various proposed modifications for investigating $e^+e^- \to 2\mu$ or the crystal ball[3] for studying the reaction $e^+e^- \to (n\gamma)$. Such detectors are designed to be ideally suited for one particular reaction, but not easily modified for other reactions.
(3) Semi-specialized detectors which lie in between the two previous categories. Such a detector would have the ability to identify with high reliability some of the reaction products, but still be versatile enough to obtain most of the information contained in the residual reaction products. As examples, let us mention here the study of the reaction $e^+e^- \to e^+e^-$ + hadrons (2γ processes),[4] the investigation of events where at least one particle has a high momentum,[5] or the study of the new particles.[6]

A general user magnet (GUM) has no place in the first two types of detectors. Thus the question which we set out to investigate is whether it is possible to design a magnet system versatile enough so as to be suitable for most, if not all semi-specialized detectors, as required by different experiments. Such detectors will have many features of a general detector. In a way each GUM configuration could be considered a general detector where the compromises have been shifted very far in optimizing its features for one particular reaction.

II. PHYSICS FOR SEMI-SPECIALIZED DETECTORS

Given the extremely fast pace with which physics is currently progressing at electron-positron colliding rings, it is difficult to predict which of the outstanding questions will have been answered by the time PEP starts doing physics, and how many new questions will have appeared by then. Nevertheless, it is useful to consider which particular experiments would require a versatile and easily adaptable magnet system.

A. Search for New Particles[6]

With the discovery of ψ, ψ' and their decays into new narrow states, it seems likely that soon a host of new charmed particles will be found. One can assume that by 1980, when PEP will start its operations, one has begun to study their decay modes. In a quark-model estimate, the inclusive charmed particle cross section should be 5-20% of the total cross section, comparable to $\sigma(e^+e^- \to \mu^+\mu^-)$. Unless the leptonic decay modes are abnormally low, and if the charmed particles are produced in two jets, the best signature for a charmed particle would be a high energy lepton coming from the decay of its opposite charm

0 0 0 0 4 5 0 1 5 7 7

partner. Thus, a detector is required which has a π/e rejection of $\lesssim 10^{-3}$ and/or π/μ rejection of the same order of magnitude, but is also capable of measuring momenta and, if possible, masses of the hadrons from the decay of the charmed particle.

B. 2γ Processes[4]

The reaction $e^+e^- \to e^+e^-$ + hadrons, corresponding to the diagram:

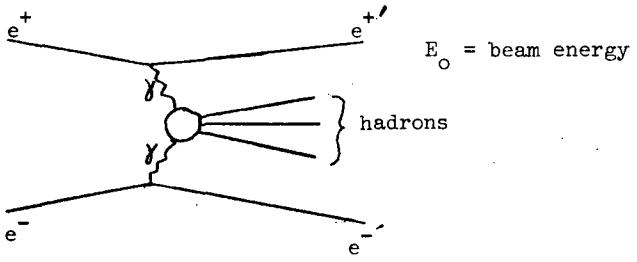

yields the only available information on the process $\gamma + \gamma \to$ hadrons. As long as the scattered electron of energy E' leaves under a small angle θ, the $(\text{mass})^2$ of the photon

$$q^2 \simeq E_o E' \theta^2$$

is quite small and one thus has a colliding photon facility. On the other hand, since the virtual photon angular distribution falls off only $\propto 1/\theta^2$, q^2 values up to 10 $(\text{GeV}/c)^2$ are available with reasonable counting rates.

The two virtual photons in the interaction have typically very different momenta, therefore the c.m. system of the produced hadrons also is moving with large velocities. Any detector capable of detecting 2γ processes has to positively identify the two electrons, and measure their energies. In addition, it has to have the capability of analyzing the product hadrons. Since the hadrons are frequently produced very forward, good momentum resolution at small polar angles is particularly important.

C. High Momentum Hadron Events[5]

One of the weaknesses of all presently contemplated general detectors is their lack of mass identification for medium to high momentum hadrons; this is usually given up in order to enable the detection of the photons coming from π^0, η^0, η', etc., decay. In addition to detecting and identifying high momentum hadrons, it is also desirable to be able to study associated particle multiplicities, momentum distributions, jet structures, etc. Thus, it is insufficient to only measure the high momentum hadron itself; it is necessary to be able, insofar as possible, to reconstruct the whole event.

We have given here only a few typical examples for use of a semi-specialized detector which would require a magnetic field. Many other examples could be given. They all have in common the characteristic that one particular feature serves to uniquely identify the reaction of interest with high reliability. Once this feature has been identified, one wants to obtain as much additional information about the event as physical or financial considerations allow. We stress again that there is no need for a highly restrictive trigger. Indeed, any trigger which rejects most of the beam-gas interactions, cosmic rays and small angle Bhabha events is sufficient. The apparatus has to be designed only to allow the selection of the desired interactions from the raw data.

III. MUM OR GUM

Once it has been decided that a versatile magnet facility should be built for PEP, and before it can be designed in detail, it is necessary to discuss how such a facility would be primarily used. There are basically two possible extreme modes of operation, with a continuous range in between.

(a) In a true multi-user magnet (MUM), the basic facility would be gradually upgraded by individual experimenters who would add their own equipment. Each new experiment would be added to the previously existing setup, until a whole set of experiments is being performed at once on the same facility.

(b) A general user magnet (GUM) would consist of a magnet with a flexible detector inside. This would be modified by each experimental user for his own particular use, without being constrained by any special equipment or modification used in a previous experiment. Thus, only one experiment could be performed at any time, except if two experiments complement each other so that neither has to compromise its performance.

There would be an obvious advantage if the same facility could be used by many experiments at once. Given the low interaction rates expected at PEP, one cannot afford to throw away any events. A possible MUM setup could be arranged by several experiments, dividing among themselves the available solid angle on the periphery, while all would be using the same central detector. Nevertheless, when discussing particular experiments, it is quickly discovered that the requirements of one experiment can only be satisfied by compromising on the other. A facility run in the extreme MUM mode would quickly develop into a general detector in which the necessary compromises are more dictated by historical accidents (sequence of experiments installed) instead of by physics. To cite an example, an experiment designed to identify high-momentum particles requires large Cerenkov counters near the interaction region. Another experiment, e.g., one detecting both charged and neutral particles, would want to install γ-detectors just outside the magnet. If part of the solid angle is covered by Cerenkov counters and part by shower counters, it is very likely that neither of the two experiments will be an unqualified success.

Thus, we have concentrated our design consideration on a GUM. We try for flexibility in the sense that the basic setup could be easily modified for a particular experiment. We do not attempt to design a basic detector which would be suitable for many experiments at the same time. It should be realized, however, that implicit in the GUM idea is the problem that experiments planned for the same GUM will perform sequentially and not simultaneously. This implies that the special physics which forms the basis of the apparatus design may be partially explored by some general

detector group in advance of the GUM group.

It is assumed that those features of the GUM system which would be utilized by all the user groups would be set up and maintained by a set of GUM support people. The systems which would require this support include the operation of the superconducting magnet, the operation and maintainance of the central drift chamber array, and finally the software required for the online computer system, the trackfinding and momentum reconstruction in the central detector, and general bookkeeping. While we do not anticipate that these support functions need require a large number of people, a minimum support effort, such as instituted in many high energy physics laboratories, has proven to be essential for efficient operation of large facilities.

IV. REQUIREMENTS FOR GUM

In specifying the design criteria of a magnet, we have considered typical experiments such as described in Sec. II. Our requirement on any magnet parameter is given by the most stringent reasonable demand of any of the experiments considered. While it is impossible to predict exactly all demands, we have tried to anticipate any other future use of the system.

A. Solid Angle

As for any detectors to be used at PEP, it is imperative that GUM cover as much of the solid angle as possible. Any coil structure should either be sufficiently thin so as not to degrade charged particle or photon momentum resolution or identification, due to interactions in the coil, or the coil should cover a sufficiently small solid angle so as not to seriously jeopardize the physics goals. Any steel necessary for magnetic flux return should be either far away or small enough so as not to cover more than about 10% of 4π.

A particular requirement is posed by any 2γ experiment which is interested in large q^2 events. Since $q^2 = E_o E' \theta^2$, and typically the scattered electron energy E' is of the order 1/2 of the beam energy E_o, one requires for E_o = 15 GeV an opening angle

$$\theta_{max} \sim \frac{\sqrt{(q^2_{max})\ \text{GeV}^2}}{10}$$

which for q^2_{max} = 9 GeV corresponds to θ_{max} = 300 mrad $\approx 20°$. One wants the magnet to be completely open for $0 < \theta < \theta_{max}$ to permit an external tagging setup.

B. Momentum Resolution

Scaling up from SPEAR energies, at 15 GeV an average charged multiplicity of $\langle n_{ch} \rangle \simeq 7.5$ is expected, and assuming that the charged energy is one-half of the total energy, the average momentum of a particle would be about 2 GeV/c. However, on the average, about one particle/event will have a momentum $p \gtrsim 5$ GeV.[5] If these particle momenta are to be measured to 5% or better, a reasonable requirement, it is necessary to have an intrinsic momentum resolution at high momenta of

$$\frac{\Delta p}{p^2} \lesssim 1\%\ \text{GeV}^{-1}.$$

A more stringent requirement is given if the goal is to investigate the very high momentum region ($x = E/E_o > 0.9$). Typically for an integrated luminosity $\int \mathcal{L} dt = 10^{38}\ \text{cm}^{-2}$, and assuming $R \approx 6$, one obtains for a typical experiment

$$n = 360 \text{ events}, \quad x > 0.8$$

or about 1% of the total annihilation events. If it is important to measure the momentum of these events to better than 5%, then:

$$\frac{\Delta p}{p^2} \lesssim 0.3\%\ \text{GeV}^{-1}.$$

This resolution cannot be achieved in our design without providing position measurements outside the magnetic field, to better determine the direction at the magnet exit.

At low momenta, the resolution is limited by multiple scattering. The magnet should be sufficiently strong, and any coil material interposed sufficiently thin, to keep the momentum resolution $\Delta p/p$ due to this effect below 1%, even in the presence of the unavoidable minimum material (beam tube walls, chambers) of a few percent of a radiation length.

In order to clarify any further discussion, we write down the resolution achievable in a magnetic field, given the rms position resolution, Δx perpendicular to the magnetic field, Δz in the magnetic field direction, and an evenly distributed amount of x/x_o of a radiation length:[7]

$$\frac{\Delta p}{p^2} = \frac{27\ \Delta x \sin\theta}{BS^2} \quad \text{due to } \Delta x \qquad (1)$$

$$\frac{\Delta p}{p} = \frac{0.1\ \sqrt{x/x_o}}{\beta\ \sqrt{\sin\theta}\ BS} \quad \text{due to multiple scattering} \qquad (2)$$

$$\frac{\Delta p}{p} = \sin\theta \cos\theta \frac{\Delta z}{R} = \cos^2\theta \frac{\Delta z}{z} \quad \text{due to } \Delta z \qquad (3)$$

where S is the distance traversed perpendicular to the magnetic field $\vec{B}$, $R = z \tan\theta$ and θ is the angle between the particle momentum and the direction of the magnetic field $\vec{B}$. $\vec{B}$ is measured in tesla and all distances in meters. If, after the particle has left the magnetic field, the outgoing direction is measured over another distance S, then Eq. (1) should be replaced by[8]

$$\frac{\Delta p}{p^2} \approx \frac{12\ \Delta x \sin\theta}{BS^2} \qquad (1')$$

We accept a different positional resolution Δz along the magnetic field, because drift chambers measure position accurately only in one direction. Whether one uses a delay-line readout, a small-angle stereo arrangement, or induced pulse readout on strips, Δz is always much bigger than Δx. Actually, the error Δz usually yields a

0 0 0 0 4 5 0 1 5 7 8

negligible contribution to $\Delta p/p$. It is important, however, to the accuracy of $p_z = p \cos\theta$:

$$\frac{\Delta p_z}{p} = \sqrt{\left(\frac{\Delta p}{p}\right)^2 + \left(\frac{\Delta z}{R}\sin^3\theta\right)^2} \quad .$$

Thus, for $\theta \simeq 90°$ at low momenta where multiple scattering dominates $\Delta p/p$, the error $(\Delta z/R)$ should be $\lesssim 1\%$ if it is not to be a dominant contribution. Figure 1 shows the effect of Δz on the two-particle mass resolution at a mass of 3.1 GeV.

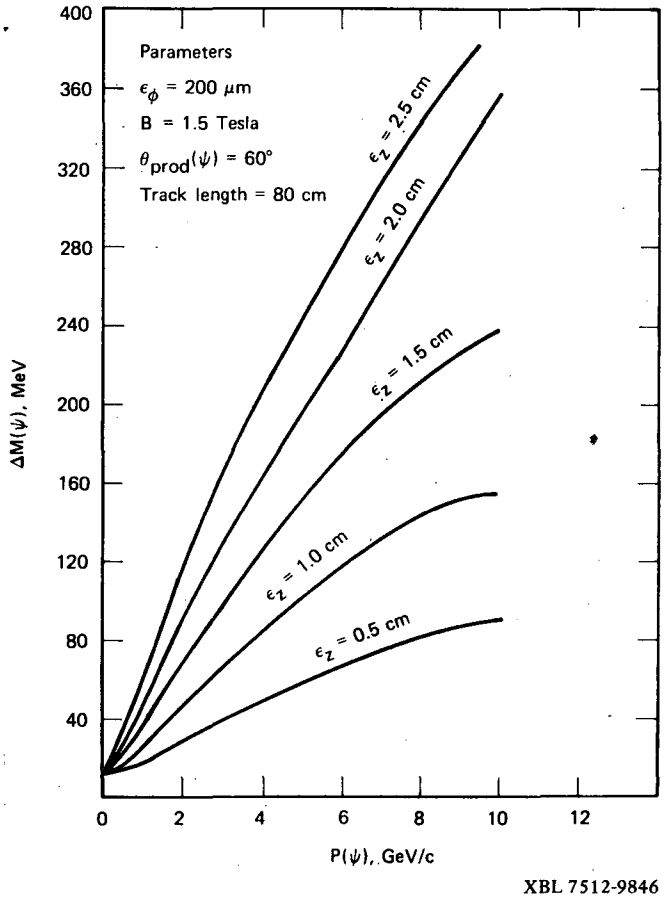

Fig. 1. Mass resolution for the $\psi(3.1)$, from measurement of $\psi(3.1) \to \mu^+\mu^-$ vs. momentum of ψ, for various z resolutions, Δz.

C. Size and Magnetic Field

As can be seen from Eqs. (1) and (2), the required momentum resolution yields lower limits on both BS^2 and BS. S is the minimum distance at which external detectors of appreciable mass, such as γ detectors, calorimeters or Cerenkov counters can be installed. The size and cost of equipment increases roughly proportional to the area which has to be covered; thus, keeping the covered solid angle fixed, the cost increases $\propto S^2$. Clearly it is advantageous to keep the magnet as small as possible, requiring the maximum possible B. However, to prevent saturation in the steel yoke, necessary for flux return in most geometries, the magnetic field should be kept to $B \lesssim 15$ kG. In addition, if superconducting coils are used, the peak magnetic field limits the maximum current density in the coil. This yields a limit on magnetic field of 15-30 kG, depending on the configuration used. If high current density superconductors are used, the size and cost of the coil also increases rapidly with the total stored magnetic energy.*

The most stringent requirement on momentum resolution is Eq. (1'), which for $\Delta p/p^2 \lesssim 0.3\%$ GeV^{-1}, assuming $\Delta x = 0.2$ mm yields

$$BS^2 \gtrsim 0.8 \text{ t-m}^2 = 8 \text{ kG-m}^2.$$

If in addition one wants to limit $\Delta p/p \lesssim 1.5\%$ due to multiple scattering, one obtains for $x/x_o \approx 0.03$ ($\beta \simeq 1$, $\theta = 90°$)

$$BS \gtrsim 1.1 \text{ t-m} = 11 \text{ kG-m} \ .$$

Clearly a minimum magnetic field length of the order of 60-80 cm is required of any system providing the necessary momentum resolution. To this has to be added the beam pipe, coil thickness, etc. Therefore, the magnetic detector will have a minimum diameter of about 2 m.

V. THE MAGNET

In this section we discuss various options of magnet configuration, coil manufacture and yoke design. One particular option, a lumped superconducting solenoid magnet, is investigated in detail.

A. Magnetic Field Configuration

There are in principle three basic magnetic field configurations possible (Figs. 2-5): (1) A purely transverse field, (2) A toroidal field, and (3) A solenoidal field. Of course, various split-field type combinations can be built up from these. In a purely transverse field, either the beam pipe has to be shielded from the field, or special provisions are necessary to reduce the synchrotron radiation background. In either case, material of thickness of the order of one radiation length has to be introduced around the beam pipe. The resulting interactions of hadrons, electrons and photons would be intolerable to most experiments. Toroidal magnetic fields have been successfully used at storage rings before (DASP, ADONE). Other configurations have been proposed (Octopus, Orange) but not as yet built. Most of these designs have the advantage of good (< 1% GeV^{-1}) momentum resolution, but suffer from various defects:

(1) In split coil designs, whether they have iron yokes (DASP, Orange) or use superconducting coils (Octopus), less than 2/3 of the total solid angle is accessible for momentum measurement. In addition, large forces occur between the coils of the only proposed superconducting solution.

(2) In a continuous coil design (PEP-150) any charged particle has to traverse the inner coil material before its momentum can be

*See Appendix A.

(a)

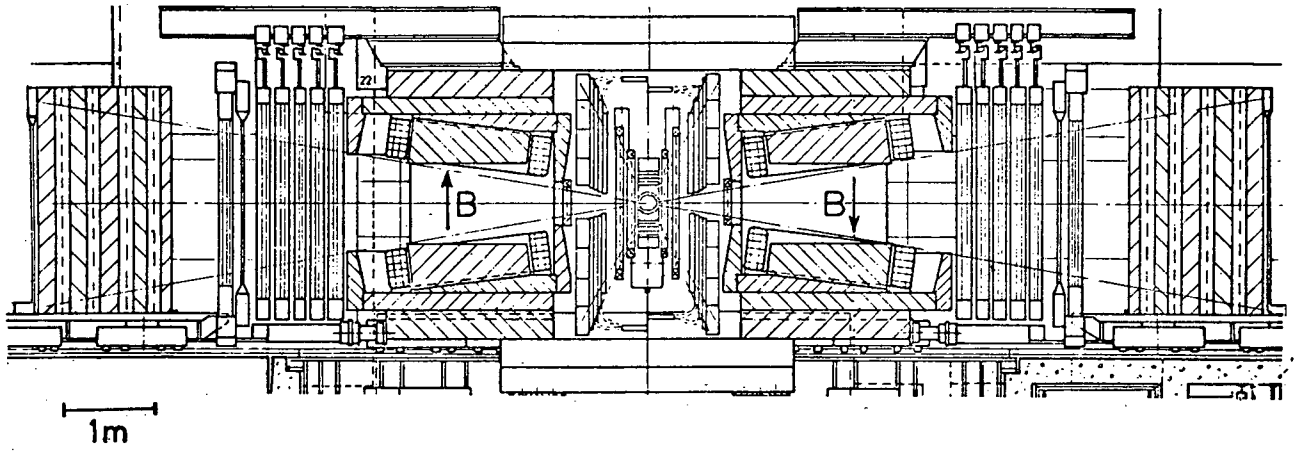

(b)

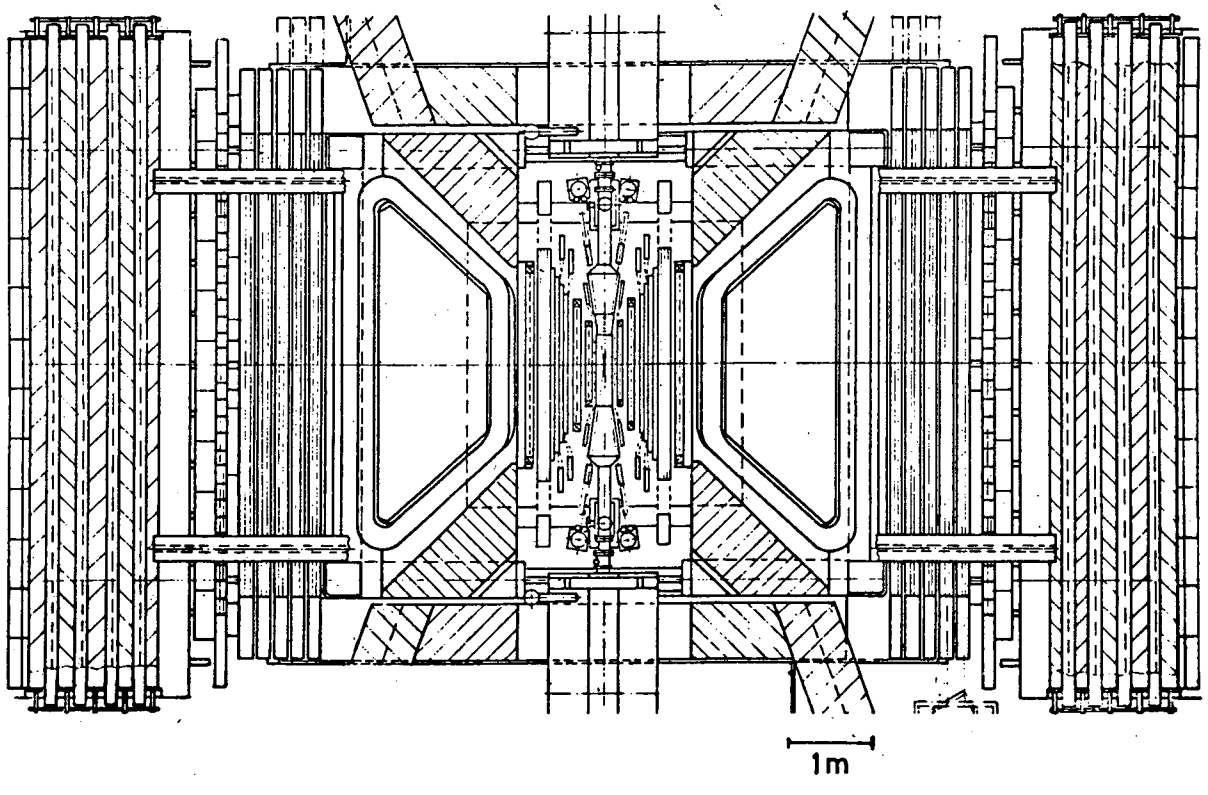

Fig. 2. The DASP Double-Arm Spectrometer, as used at DESY.

0 0 0 0 4 5 0 1 5 7 9

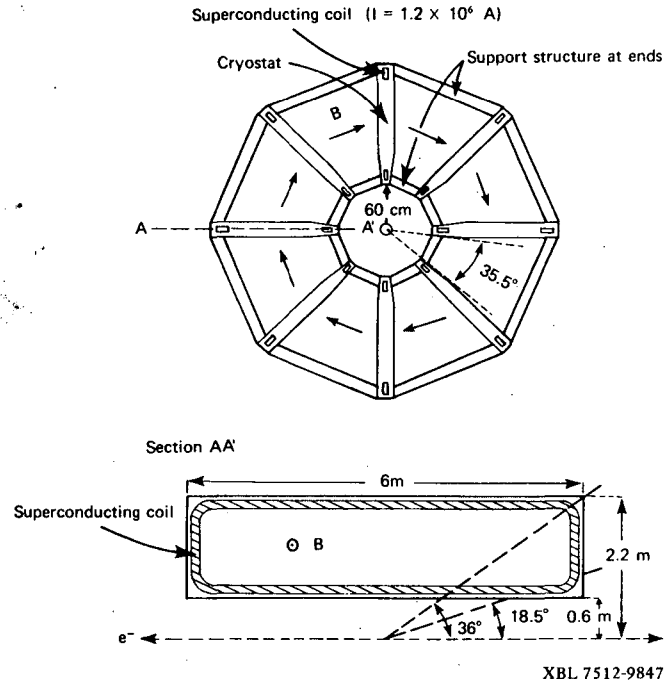

Fig. 3. The proposed Toroidal Field Superconducting Detector Magnet, "Octopus."

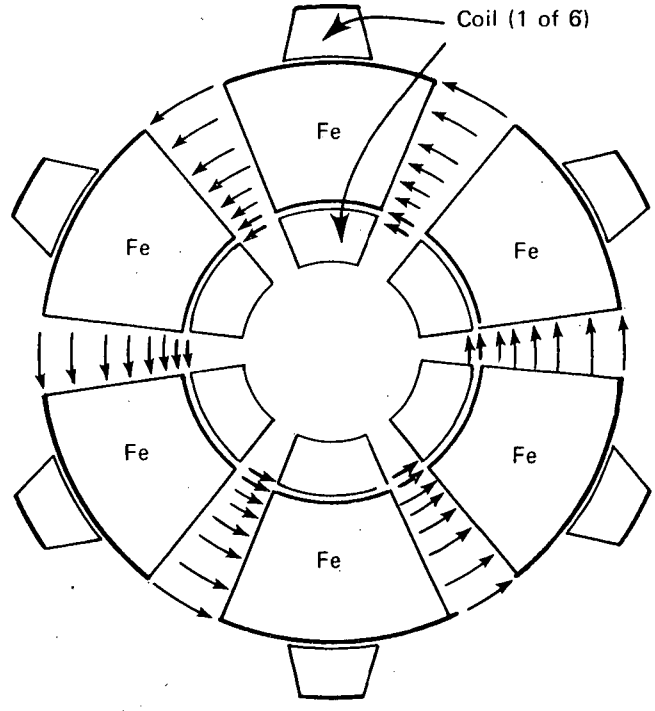

Fig. 4. Proposed detector, "ORANGE."

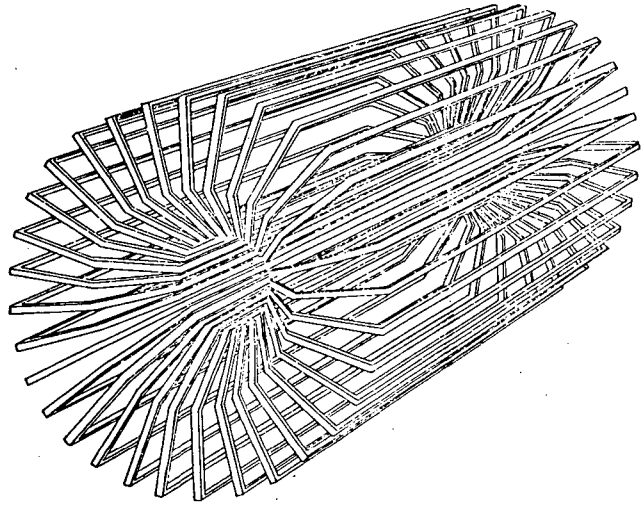

Fig. 5. Proposed continuous coil design for toroidal field (from PEP-150).

measured. This would be tolerable if the superconducting filaments could be imbedded in aluminum. With the usual copper matrix, the required thickness of ~1 radiation length would be too large. Since up to the present there are no commercially available superconducting wires using an aluminum matrix, a major technological advance would be required. Here, also, there are severe mechanical problems associated with the large forces, which could affect superconductor performance.

(3) Any toroidal symmetry of the magnetic field necessitates very accurate tracking in the polar angle θ. The most precise tracking devices in use today are drift chambers or streamer chambers. It would be very difficult to adapt a streamer chamber to such a field configuration, while drift chambers for precise measurement of θ are much more expensive to build than their counterparts that measure ϕ. Also, more material has to be introduced into the measurement region, since the wires cannot be supported from the end.

For these reasons we have chosen a solenoidal field for further consideration. This field configuration has the only disadvantage that compensating coils of opposite polarity have to be introduced into the same straight section. We assume that it will be possible to install these compensating coils sufficiently far away so as not to conflict with the experimental setup. Figure 6 shows the Mark I detector at SPEAR as an example of the solenoidal field detector.

B. The Coil

A solenoid coil interposes material between the inner magnetic region and outer region where external detectors would be added. Consider a solenoid of radius $R \approx 1$ m, magnetic field $B \approx 1.5$ T, and length $L \approx 4$ m. The linear current density in the coil is then

$$j = B/\mu_o = 1.2 \times 10^6 \text{ A/m} .$$

If one wants to limit the power consumption to less than 2 MW a conventional copper coil would be 30 cm = 21 radiation length thick. Even using aluminum, one cannot build such a coil of less than 3 radiation length thickness. On the other hand, recent advances of high current density superconducting materials enable one to build large cryogenic solenoids with moderate (10-20 kG) fields and small (< 1 radiation length) thickness. We have therefore narrowed our design study down to a superconducting design of the following size:

Field	B = 15 kG
Radius	R = 1 m
Length	L = 4 m

The inside of the solenoid would be filled with a tracking detector. If we are conservative and assume a resolution $\Delta x = r\Delta\phi = 0.2$ mm and further allow that 20 cm of the total radius is lost because of the beam pipe and trigger counters, one obtains from Eq. (1)

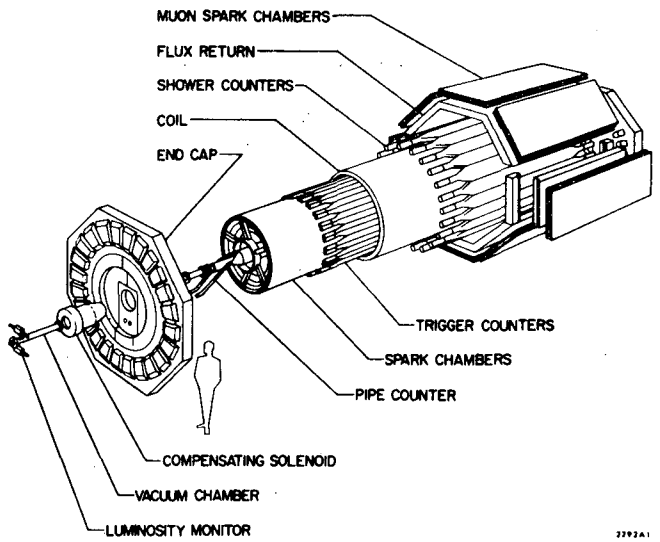

a) Telescoped view.

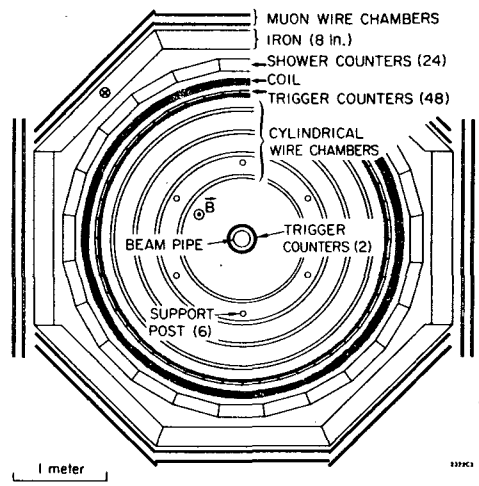

b) End view.

XBL 7511-8979

Fig. 6. Mark I detector at SPEAR.

$$\frac{\Delta p}{p^2} = 0.56 \sin\theta \ (\% \ \text{GeV}^{-1})$$

for $|\cos\theta| < 0.894$ or $26.6° < \theta < 153.4°$. Beyond this angular range, the intrinsic resolution worsens rapidly, because less track length is available in the radial direction. Figure 7 shows the ideal momentum resolution of such a solenoid, ignoring multiple scattering and the uncertainty in z. In calculating the values given in the figure, we have assumed that 15 cm is lost on the inside near the beam pipe, and the outermost measured point is at 95 cm radius. The actual resolution at high momenta will be somewhat worse. If drift chambers are used, the resolution worsens in discrete steps, because with decreasing

0 0 0 0 4 5 0 1 5 8 0

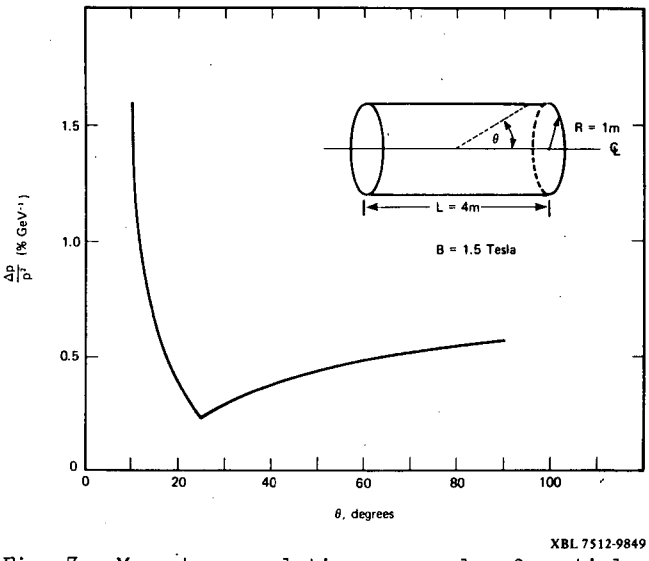

Fig. 7. Momentum resolution vs. angle of particle for detector under study (see text).

angle fewer chambers are available. Furthermore, Eq. (1) assumes that the track is measured over many points to a corridor of width Δx.* If only a few points are available, the resolution will be worse. If a continuous device such as a streamer chamber is used, systematic distortions could also worsen the resolution. To account for these effects we derate the resolution by 20%† and claim an intrinsic resolution at high momenta of $\Delta p/p^2 = 0.7\%\ \text{GeV}^{-1}$, scaling it for other angles as shown in Fig. 7.

The resolution at small angles θ is particularly important for a 2γ experiment, where the c.m. motion of the produced hadrons is appreciable. Furthermore, $\gamma\gamma$ scattering is likely to be largely diffractive (via VDM); thus, many of the hadrons will be produced with $\theta < 30°$. Since the proposed magnet (compare next section) will have an opening core of 19.3°, particles emerging at smaller angles can be measured by external tagging magnets.

Our resolution, while good enough for most experiments, misses the requirement for measuring the very high momentum ($x > 0.9$) particles. Thus drift chambers have to be added outside of the coil to measure their momenta. Using Eq. (1'), one has at $\theta = 90°$:

$$\frac{\Delta p}{p} = 3.75\% \quad \text{at 15 GeV.}$$

This resolution is significantly worsened if appreciable coil material is in the path. If the coil has x/x_0 radiation length, one has to add quadratically at $\theta = 90°$:

$$\left(\frac{\Delta p}{p}\right)_{sc} \approx \frac{5 \times 10^{-2}}{BS} \sqrt{x/x_0} = 4.2\% \sqrt{x/x_0}$$

The multiple scattering error will increase as $1/\sqrt{\sin\theta}$ at smaller angles, while the magnetic field resolution improves proportionally to $\sin\theta$. Thus, for $\sqrt{x/x_0} \sim 0.5$ the multiple scattering error dominates the resolution already at 45°.

As described in more detail in Appendix A, it seems possible to build a continuous superconducting solenoid of 1 m inner radius, having an overall coil + vacuum thickness of 10-12 cm and a total material thickness of 0.45 radiation length. Such a coil thickness is perfectly acceptable for measuring photon energies using a detector outside the coil (e.g., lead glass or liquid argon). As is shown in Fig. 8, pratically all photons of $E_\gamma > 150$ MeV can be detected outside such a coil

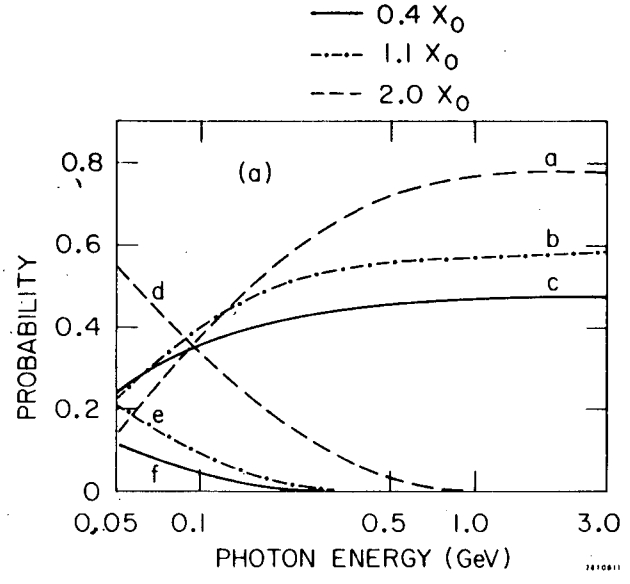

Fig. 8. Probability for photons to convert in a continuous coil vs. photon energy, with (a,b, c) or without (d,e,f) electrons (at least one $\geq$ 2 MeV) coming out of coil, for three coil thicknesses (radiation lengths) (from Lina Galtieri).

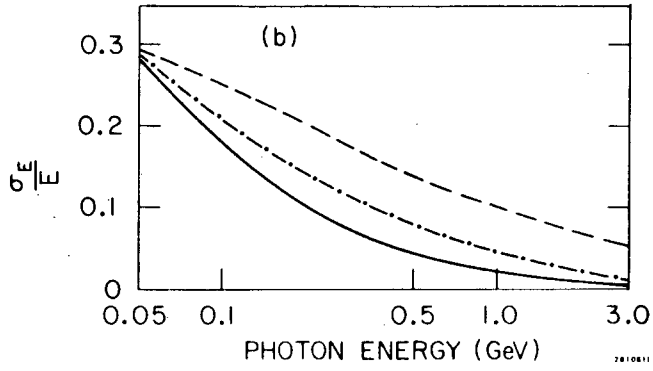

Fig. 9. Rms error in photon energy contributed by energy loss of electron pairs from known γ conversions (from Lina Galtieri).

*"Corridor" means here the path of finite width within which the particle trajectory lies. As used here, the width is dominated by systematic uncertainties, e.g., surveying errors.

†If only three equally spaced drift chambers are used, the resolution given by Eq. (1) is worsened by a factor $\sqrt{3/2} = 1.22$.

and given an energy resolution for the γ-detector of $\sigma = 8\% \sqrt{E}$ even the fluctuations in energy loss give a negligible contribution above this energy.*

It is also possible to build a lumped coil consisting of six individual superconducting coils in a common cryostat.† As detailed in Appendix A, each individual coil would have a cross section of 9 x 13 cm and present a thick (~2.7 radiation length) material for any particle going through it. However, the material between the coils could be kept very thin: if no special measures are taken, the vacuum vessel walls would represent 0.05 radiation length of aluminum. One could, at some additional expense, provide thin windows between the coils, thus reducing the material to $\lesssim$ 0.02 radiation length.

The individual coils are separated and supported by eight struts which totally cover an azimuthal angle of $\Delta\phi/2\pi \approx 0.1$. They constitute ~ 1.5 radiation length of material and thus reduce the solid angle used for big external drift chambers for momentum determination of very high momentum particles.

We have studied the question whether the magnetic field inhomogeneity of a lumped coil system would make momentum reconstruction difficult. Figure 10 shows a magnetic field map for the lumped and continuous coils. One can use as a figure a merit two integrals of the magnetic field along a straight line leaving the interaction point at an angle θ. (See Fig. 11) The first integral

$$I_1 = \int |\vec{u} \times \vec{B}| \, ds = \int B_\perp \, ds = \langle BS \rangle$$

gives the bending due to the magnetic field in the φ-direction for a particle at an angle θ. The second integral

$$I_2 = \int B_\perp \, s \, ds = \int |\vec{u} \times \vec{B}| \, s \, ds = \frac{\langle BS^2 \rangle}{2}$$

is a measure of the distance the particle has been bent away from the plane formed by the beam axis and its direction when leaving the target. Note that the "effective length" of the magnet is given by

$$L_{eff} = I_2/I_1$$

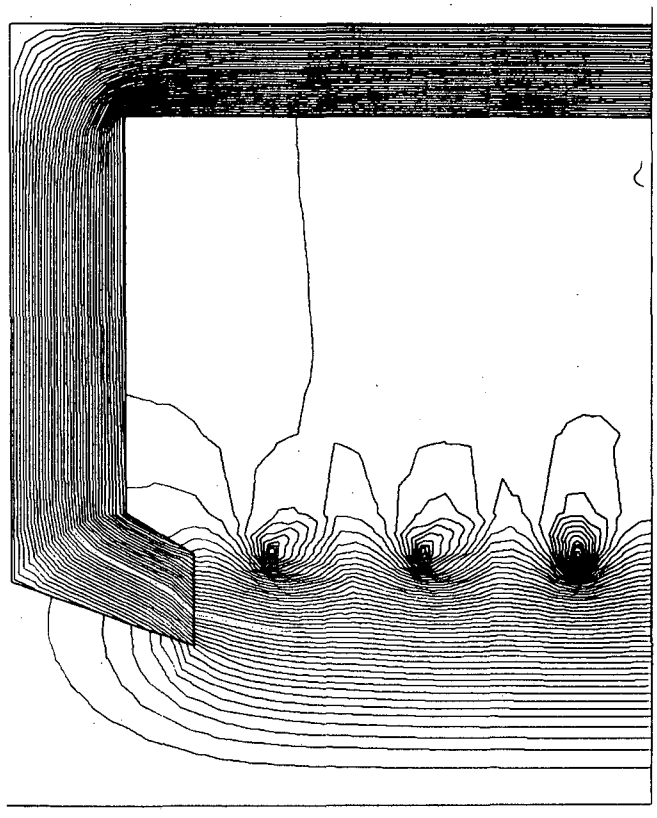

XBL 7511-8980

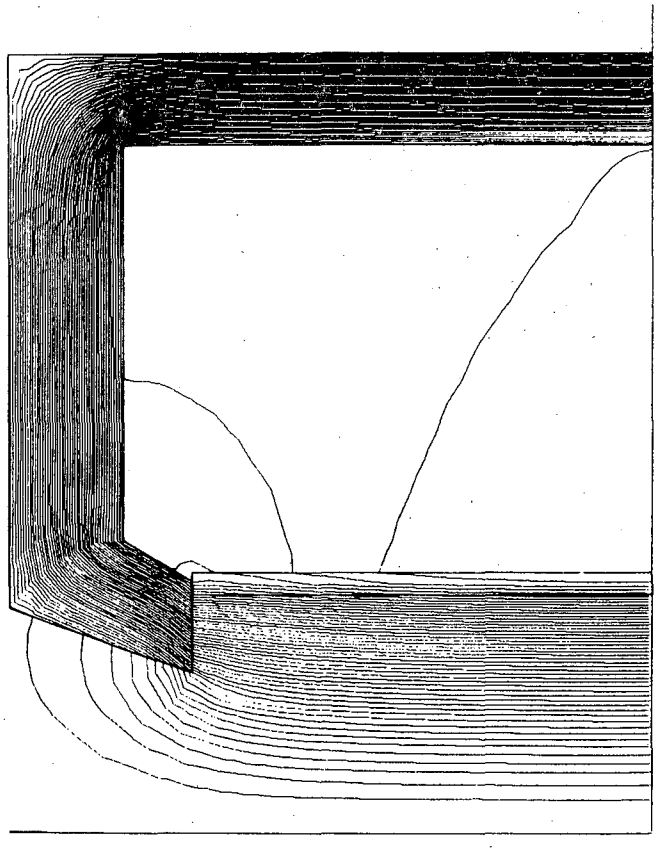

XBL 7511-8981

Fig. 10. Magnetic Field map giving rA_ϕ for (a) lumped coil, and (b) continuous coil solenoidal magnets.

* As described in PEP-204, even the π/e rejection does not appreciably suffer if the particles traverse less than one radiation length of material.

† There has been no study made by this group of the optimum number of lumped coils.

In Fig. 11 we show the two integrals as functions of θ. The integrals go out either to a radius R = 0.95 m or to a distance along the axis z_{max} = 1.90 m, whichever is less. Figure 12 shows the ratio of these integrals between the real magnet and an ideal solenoid of equal size which has everywhere inside a constant magnetic field in the z direction. The falloff of ratios for θ < 25° is due to the large opening in the return yoke

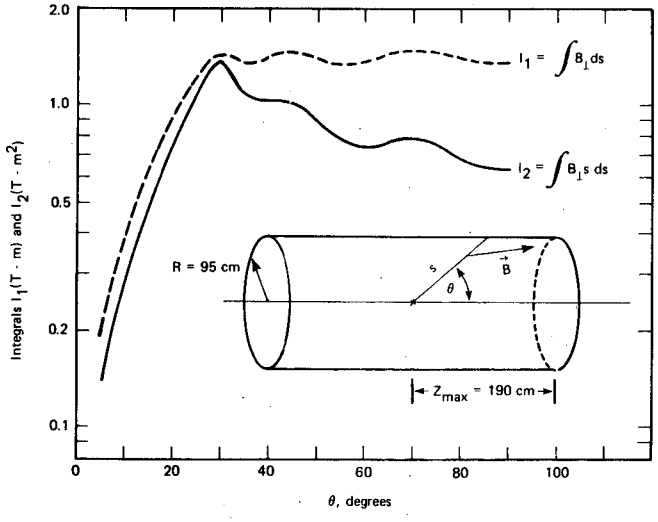

Fig. 11. Integral $I_1 = \int B_\perp ds$ and $I_2 = \int B_\perp sds$, giving respectively the net bending and displacement of the particle trajectory in φ direction, vs. particle direction, θ.

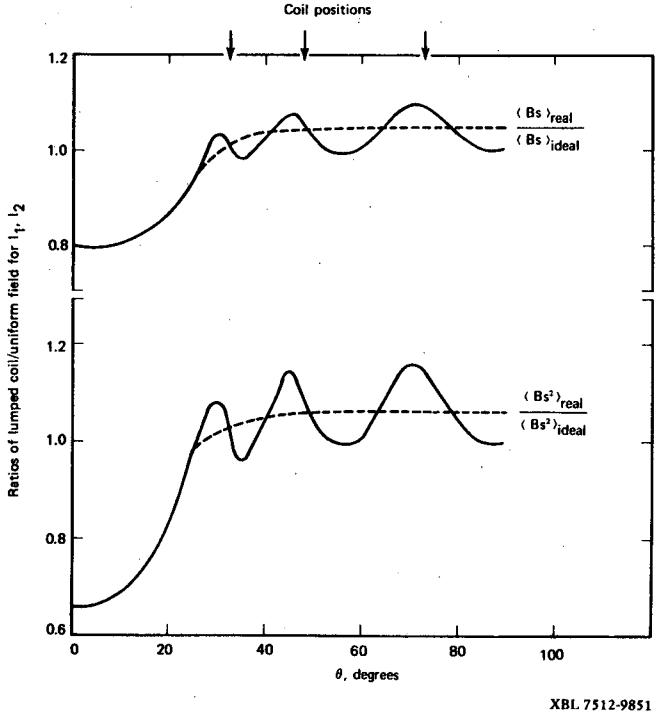

Fig. 12. Ratio of integral I_1 or I_2 for the lumped coil ("Real") to that for a uniform field solenoid ("Ideal"). The dashed line shows the same integrals for a continuous solenoid of same length and radius.

(cf. Figure 7) and is the same for a lumped or a continuous coil. Lumping the coils produces the three wiggles in Fig. 12 (solid line), which are absent in the continuous coil (dashed lines).

Outside the coil the field falls off rapidly (cf. Fig. 13 & discussion in Appendix B, Sec. 4.1). Forty cm beyond the outer vacuum vessel, the field is less than 100 G everywhere except near the return yoke. It is difficult at present to decide whether to choose a lumped or a continuous coil if a single GUM is to be built. The lumped coil requires less sophistication in the art of fabricating superconducting magnets; however, if the presently planned tests at LBL are successful, it may well turn out that a continuous coil is cheaper than a lumped coil. If a continuous superconducting coil, e.g., the Mark II detector, is chosen for a general detector, then there should be at least one GUM of the lumped type to maximally complement the physics which can be done with both facilities. If only one GUM is to be built and developments at SPEAR show that the ultimate in resolution at very high momenta, or in E_γ, is not required, a continuous coil should be represented. One should note that as far as the inner detector and the steel yoke are concerned, the two coil systems are practically interchangeable.

C. Performance of Exterior Devices

Aside from the measurements obtained from the inner chambers, certain other general measure-

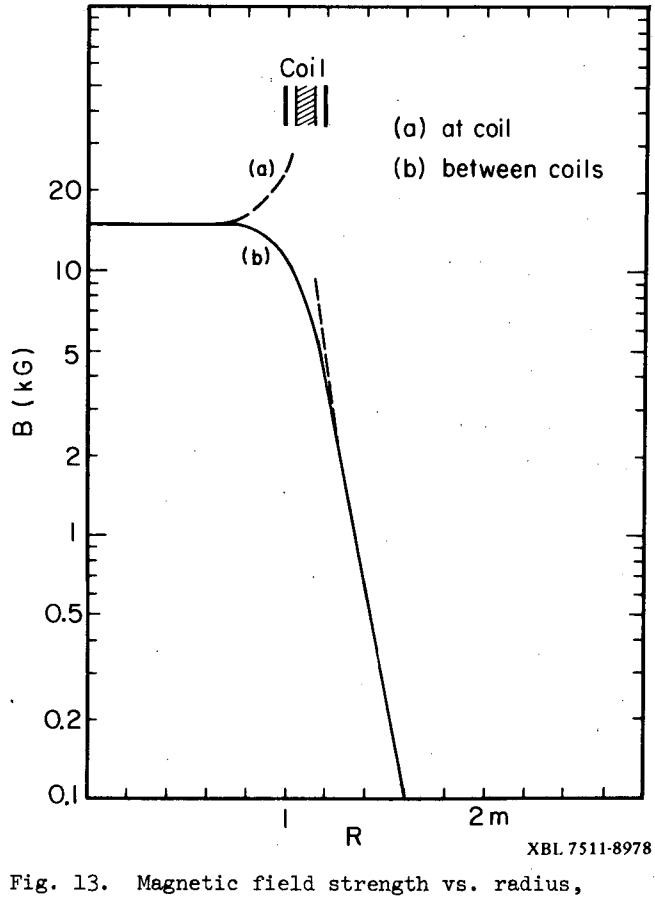

Fig. 13. Magnetic field strength vs. radius, showing field decrease outside the coils.

ment capabilities will be needed by most experiments. Among these are: (a) charged particle identification (up to large x), (b) γ-ray measurement (direction and energy), (c) particle (charged and neutral) correlations. Charged particle identification will generally be accomplished using a set of Cerenkov counters, plus the use of time-of-flight for low momentum particles. Gamma-ray measurement will require a neutral detection scheme, which must lie outside the coil if inner chambers are used for charged particle tracking. Particle correlations will require the neutral detector of (b) and tracking chambers, plus sufficient solid angle and resolution to achieve the desired correlation measurements. It is quite likely that experimenters will want all three options, but at present (a) and (b) tend to be mutually exclusive, for practical reasons.

The presence of coil material and limitations of solid angle and space for measuring devices may significantly compromise these goals. The lumped coil and the continuous coil designs pose different problems. The relative advantages of the two coil designs depend upon the choice of the detection system located external to the coils. The measurement difficulties encountered with either design result from interactions in the coil, causing a loss of energy resolution, or from failure of the particles to reach the external detection system. For example, interactions of γ's in the continuous coil solenoid will cause measurement of γ's to deteriorate, especially at low and moderate energies, while charged particle interactions in the coil will result in loss of some particles before the identification system. The lumped coil design leaves a large part of the available solid angle virtually free of material (~ 0.02 radiation lengths), but is essentially opaque to particles in the small part obstructed by coils and struts. (We assume in both cases that the γ and Cerenkov counters lie outside the coil, since the interior region is fully occupied by tracking chambers.) Table I exhibits some of these effects in detail. The assumptions made in Table I should be carefully noted. The relative importance of these effects will probably require a Monte Carlo analysis for each apparatus design. It should be noted, however, that within the limits of the uncertaintities in the magnet design, the loss of charged particles due to absorption in the lumped coils is roughly equal to the loss to the identification system, due to interaction in a continuous coil.

In addition to the effects noted in the Table, a loss of particle identification will also occur when a converting γ and a charged particle enter the same cell of the Cerenkov counter system. Figure 14 gives estimates for the probability of this occurance vs. the number of cells for a continuous coil. (We have assumed that $\langle n_{ch} \rangle \approx \langle n_{\gamma} \rangle \approx 7.5$) Our estimate for this probability may be somewhat low due to the lateral spread of showers resulting from γ or electron interactions. Low energy electrons in the shower can be produced at large angles (even 45°). Thus, it may be very important to keep Cerenkov counters close to the continuous coil or use a lumped coil design to minimize such conversions. Even in the absence of the coil, there will be such an effect, however, due to the finite wall thickness needed

Table I. Performance of Devices Exterior to Coil

Parameters considered fixed are:
Coil Radius: 1 m
Coil Length: 4 m
Coil Material: Nb-Ti
[a]Current Density: High (i.e., 4-9x10^4 a/cm^2)

	Lumped Coil		Continuous Coil	
	[b]Weighted	Unweighted	[b]Weighted	Unweighted
Coil Thickness:				
t(cm)	~13	13	4.5	3.5
t(g/cm^2)	~29	29	18.2	14.1
X_0 (r.l.)	~2.5	2.5	0.64	0.5
Labs. (absorption lengths)	~0.7	0.7	0.18	0.14
Solid Angle Fraction, $\Omega/4\pi$ (covered by coil)	-	[c]~0.68	-	~0.89
[d]Gamma-Ray Resolution, $\frac{\sigma_\gamma}{E_\gamma}$				
E_γ = 100 MeV	0.25	0.25	0.33	0.32
300 MeV	0.15	0.15	0.18	0.18
1000 MeV	0.08	0.08	0.09	0.09
[e]Gamma Conversion Probability With $e^\pm$ Leaving Coil, (E_e>2 MeV) E_γ = 100 MeV	.017	.012	0.37	0.36
E_γ = 300 MeV	.022	.015	0.48	0.46
E_γ = 1000MeV	.023	.015	0.52	0.48
Without $e^\pm$ Leaving Coil, (E_e<2 MeV) E_γ = 100 MeV	0	0	0.07	0.06
E_γ = 300 MeV	0	0	0	0
E_γ = 1000MeV	0	0	0	0
[e]Fraction of Hadrons Interacting in Coil: Inelastic	.007	.005	0.18	0.14
Total = Elastic + Inelastic	.010	.007	0.26	0.20
No. of Delta Rays per Charged Particle (T_δ>1 MeV)	<<1%	<<1%	~1%	~1%
Fraction of Produced Hadrons Reaching External Detectors Without Interaction	0.68	0.68	0.66	0.71

[a]See Appendix A

[b]Weighted by the $(1+\cos^2\theta)$ hadron distribution and for slant distance through coil.

[c]Solid angle unobstructed by coils, struts, etc.

[d]Assuming the (measured) resolution $.08/\sqrt{E_\gamma}$ from a Pb-liquid argon layered shower detector. It is expected that much better resolutions may ultimately be achieved from pure liquid argon detectors, but this has not yet been tested. If proven, the lumped coil (but not continuous coil) resolutions might improve by nearly an order of magnitude. (PEP-193)

[e]Interactions in continuous coil may be detected, improving resolution. Figures given for lumped coil are for interactions in thin windows between coils. Geometric lengths have been assumed in calculating hadron interaction probabilities. These values will have been underestimated somewhat for $\bar{p}$, or other particles having large intrinsic cross sections.

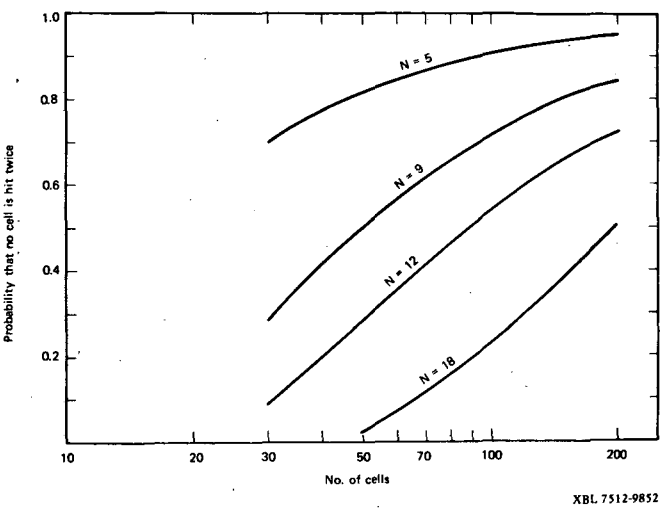

Fig. 14. Probability that no γ shower occurs in the same cell as a charged particle vs. number of cells, for various charge multiplicities N: $N = (N_+ + N_-) = N_\gamma$. A coil thickness of 0.5 radiation lengths has been assumed as γ converter.

0 0 0 0 4 5 0 1 5 8 2

for pressurized Cerenkov counters,* so that the thickness of a continuous coil should be judged on a scale of the subsequent Cerenkov counter wall thickness when considering this problem.

It should be noted that the probability of an event containing two charged hadrons in the same Cerenkov cell is comparable to the problem of confusing γ showers and charged particles. Curves describing this effect are shown in Fig. 15. These curves may overestimate the difficulty as the momentum measurements on the particles made in the inner detector may serve to resolve the confusion.

D. The Steel Yoke

The steel yoke was designed with the following considerations in mind (describing one half):

(i) An opening cone of 20° half-angle should be provided to enable a 2γ experiment to measure externally the electron momenta as well as the momenta of any hadrons emitted in the forward cones.

(ii) The field inhomogeneities should be sufficiently small so as not to impair the momentum resolution for $20° < \theta < 30°$.

(iii) As little outside interference as possible with the experimental setup for $30° < \theta < 90°$ is essential.

(iv) Minimize any steel saturation to maintain field uniformity as much as possible in the central region.

(v) The same yoke should be usable for either a continuous or a lumped coil.

Clearly some of these requirements, in particular (i), (ii) and (iv), work against each other, and thus some reasonable compromise must be reached.

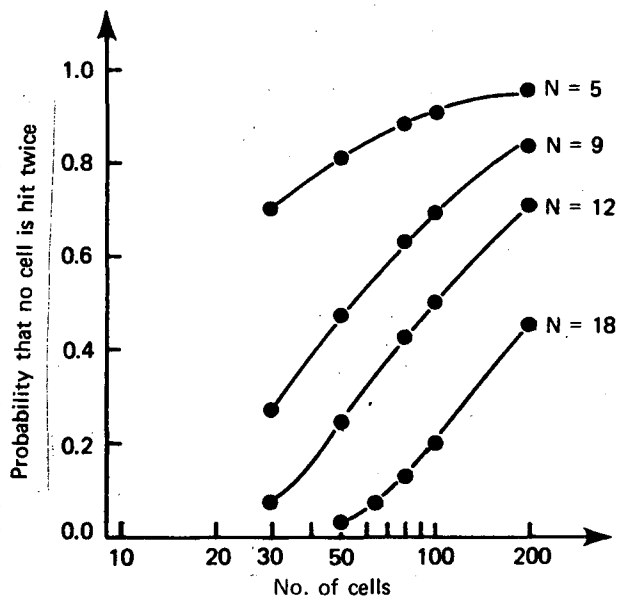

Fig. 15. Probability that no cell has two charged particles vs. number of cells, for various total multiplicities, N.

A side cross section of the yoke is shown in Fig. 16a, while Fig. 16b shows an endview of the same yoke.

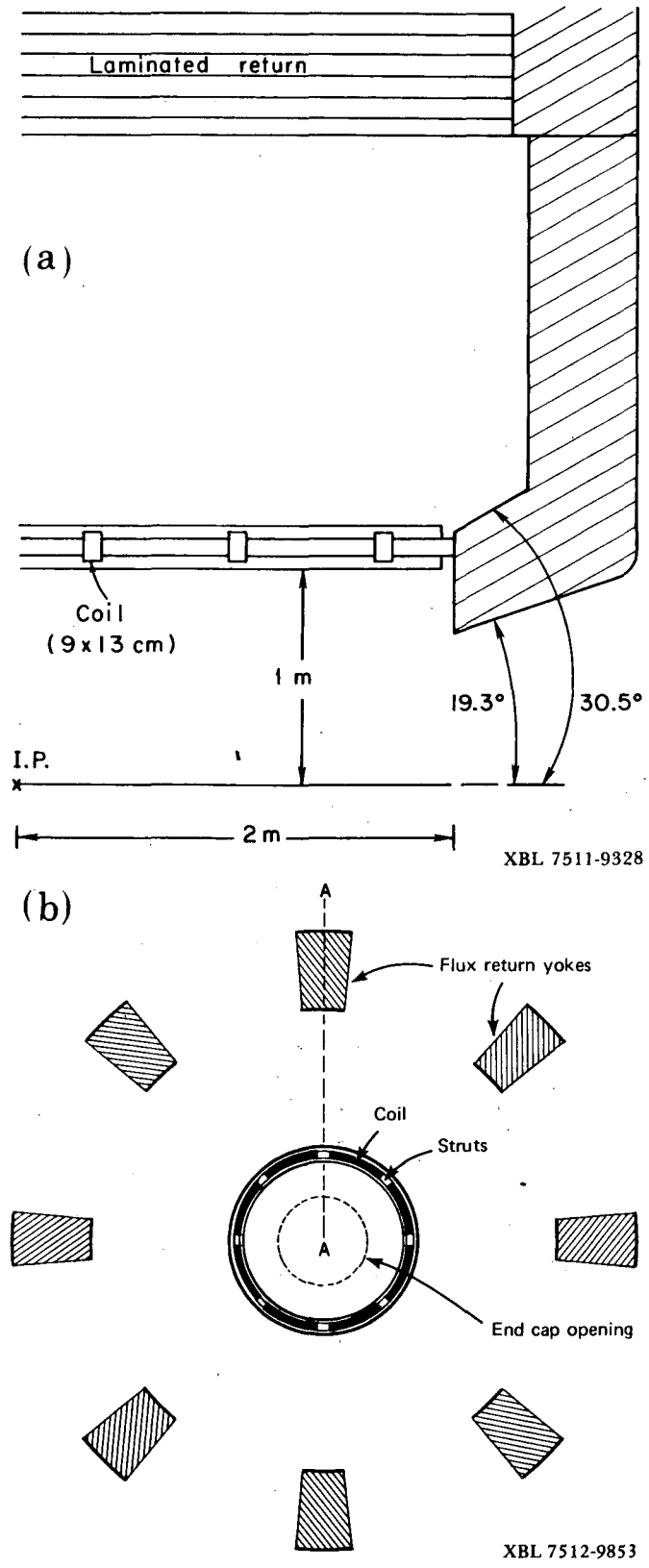

Fig. 16. (a) Lumped coil magnet: longitudinal cross section.
(b) Lumped coil magnet: transverse cross section.

* ~0.15 r.l., for example, in high momentum hadron report.

The yoke is recessed just beyond the coil to provide more space for equipment outside the coil. The large opening of 70 cm radius does not introduce a significant degradation of magnetic field in the region of interest. In Fig. 17 we show the radial dependence of $\vec{B}$ at 10 cm away from the yoke. In the region of interest 70 cm < r < 95 cm, corresponding to 20.2° < θ < 26.6°, the axial field is near its maximum value. The radial field is mainly affected by the saturation in the steel yoke, which saturates most around r = 70 cm (tip A) and r = 110 cm (coil radius, beginning of recess B in return yoke). If it proves to be necessary to reduce B_r at large radii, one could achieve this by moving the beginning of the recess B to larger radii.

The yoke has octagonal symmetry, with 8 veins for flux return. The return veins start at a radius of 3 m, leaving 1.8 m free space outside the coil. The veins cover an azimuthal angle φ = 1.77 radians, leaving slightly more than 0.7 of the solid angle free for additional Cerenkov counters. A peak magnetic field inside the iron of 19 kG is reached at the inner edge of the end pole pieces; everywhere else the field is limited to less than 18 kG. If greater field homogeneity near the end region is required for some particular experiments, it is easy to insert a steel endcap down to smaller radii. Of course, this would also reduce the maximum angle available for tagging. Nevertheless, one could imagine an experiment with reasonably homogeneous field down to θ ≈ 15°, while still permitting a parasitic tagging experiment to operate in the region: 15 mrad < θ < 150 mrad.

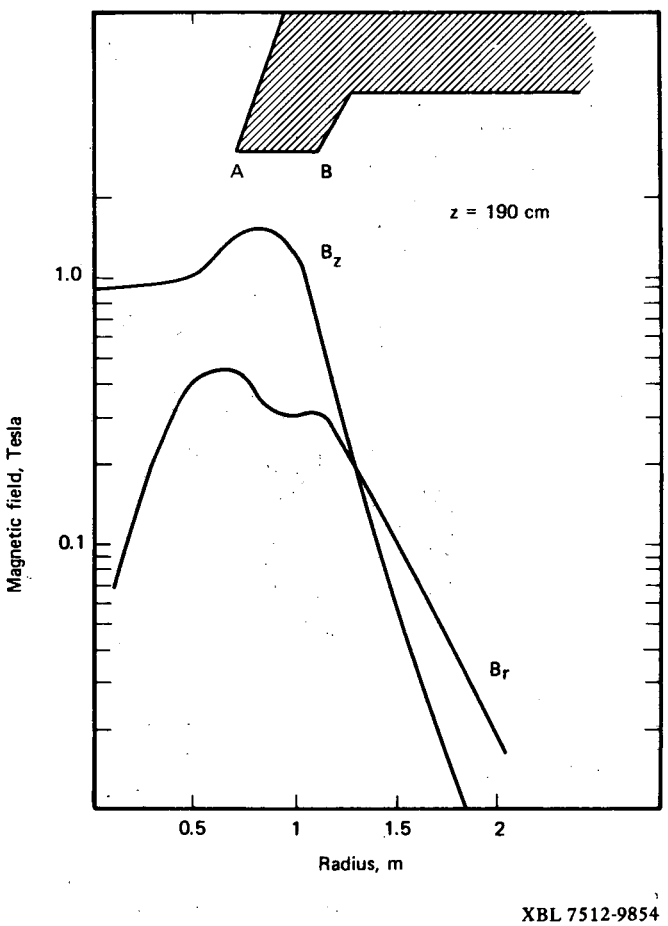

Fig. 17. Strengths of B_z and B_r components of magnetic field near poletip (z = 190 cm).

E. The Compensating Solenoids[9]

Whether a lumped or a continuous coil design is chosen for GUM, compensating coils have to be provided to satisfy the condition

$$\int B_z dz = 0 \ . \qquad \text{(V-1)}$$

This condition is necessary to preserve the decoupling of the vertical and horizontal oscillations. However, any solenoid is also a focussing device, and thus will contribute a tune shift Δν:

$$\Delta\nu = \frac{1}{16\pi}\int \frac{B^2\beta}{p^2}\, dz \qquad \text{(V-2)}$$

where B is the field in the compensator, p is the beam momentum, and β is the betatron function in the straight section. For the main detector, the tune shift is small, because the betatron function has a minimum at the interaction point. However, in order to permit electron tagging for 2γ processes down to small angles, one wants to put the compensating coils at the extreme ends of the interaction region. There the betatron function is approximately

$$\beta = \frac{z^2}{(0.2m)} \qquad \text{(V-3)}$$

and Eq. (V-2) limits the maximum field allowed. If a tune shift is allowed of Δν ≲ 0.02 per compensating coil, then one has the condition:

$$0.32\pi \gtrsim \frac{B^2 L_c \bar{\beta}}{p^2} = \frac{B^2 L_c (z_{max} - L_c/2)^2}{p^2\ (0.2m)} \qquad \text{(V-4)}$$

where L_c is the length of each compensator, and $z_{max} \approx$ 10 m is the distance to the nearest quadrupole at the end of the straight section. The beam momentum p is to be measured in tesla-meters: 15 GeV/c = 50 T-m. Since BL_c for each compensating coil has to be the same as one half of $\int B_z dz$ of the detector magnet or 3.0 T-m, we have at 15 GeV/c the conditon:

$$\frac{(z_{max} - L_c/2)^2}{L_c} \gtrsim 0.32\pi \left(\frac{p}{BL_c}\right)^2 \times (0.2m) \approx 56\ \text{m}.$$

This implies $L_c \gtrsim 1.5$ m. However, barely satisfying Eq. (V-4) would imply that the field in GUM would have to be scaled with the beam energy:

$$B_{max}(\text{kG}) \approx E_o\ (\text{GeV}).$$

Thus one will tend to choose a larger length. Another condition is given by the fact that any

imperfect alignment of the magnets introduces transverse magnetic fields. If the misalignment errors are ~ 0.5 mm, then one has to require

$$\left(\frac{B\ell}{p}\right)^2 \ \bar{\beta} \lesssim 1.4 \text{ m} . \qquad \text{(V-5)}$$

Since $(B\ell/p)^2 = 0.0036$ this implies that:

$$\bar{\beta} \lesssim 390 \text{ m}$$

which because of Eq. (V-3) implies that the compensating magnet center should not be further from the I.P. than

$$\bar{z} = \sqrt{0.2 \times 390} = 8.8 \text{ m} .$$

Since Eq. (V-5) again necessitates scaling B with the beam energy, a reasonable compromise would be a set of 3 m long magnets, with magnetic field of 10 kG. However, both the main GUM as well as the compensating coils should have provision for fine positional adjustment, so that condition (V-5) can be relaxed. One could then use the full magnetic field down to a beam energy of about 10 GeV.

VI. THE INNER DETECTOR

We propose that an initial detector consisting of several layers of wire chambers be installed in GUM. This detector would be sufficiently versatile -- assuming the necessary software for track recognition is part of the GUM package -- to enable initial use of the magnet for experiments. Later on, when special demands are to be met, or the technology has advanced sufficiently, other user-supplied inner detectors could be installed.

A. Initial Inner Detector

A sample design for the inner drift chambers is shown in Figs. 18-21. We propose six sets of two chambers with delay line readout. Such a system is easier to subdivide in ϕ than the small-angle stereo system planned, e.g., for Mark II. In addition, the simultaneous readout of a single point (ϕ,z) instead of two correlated angles ϕ in the small angle stereo system, makes pattern recognition easier. The chambers are cylinders which are divided into quadrants and supported by four vanes attached to the coil support struts. This allows any quadrant of any chamber to be removed and replaced with other equipment without affecting the remaining chambers. The lengths of the chambers are, in meters, 1.20, 2.20, 3.20, 3.80, 3.80, and 3.80. The average radii are, in centimeters, 18, 36, 54, 72, 82, and 92 respectively. This arrangement gives unambiguous six point tracks in the range $26° \lesssim \theta \lesssim 154°$ and unambiguous 4 or 5 point tracks in the range $19.2° \lesssim \theta \lesssim 26°$ and $154° \lesssim \theta \lesssim 160.8°$. It allows a 19.2° front-back cone to be free of material. This greatly aids in the study of two photon processes, as discussed earlier in this report. Figure 20 shows in detail the chamber construction.

A cross section for a typical chamber is shown in Figs. 18 and 19. The material of the chambers is approximately 5×10^{-3} radiation

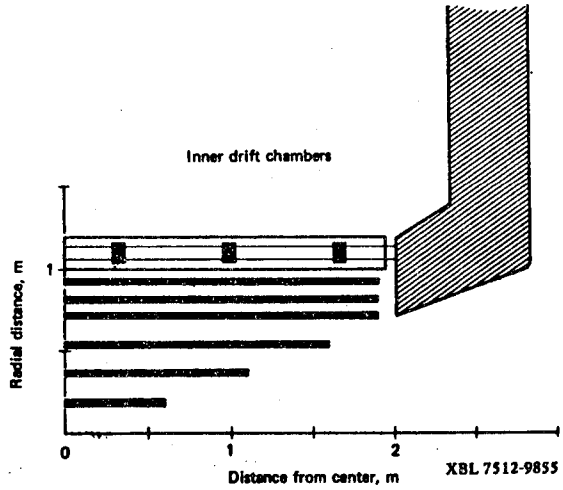

Fig. 18. Drift chambers in GUM: longitudinal cross section.

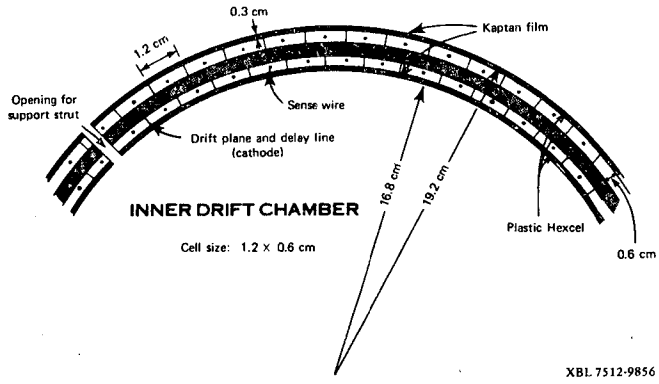

Fig. 19. Drift chambers in GUM; transverse cross section.

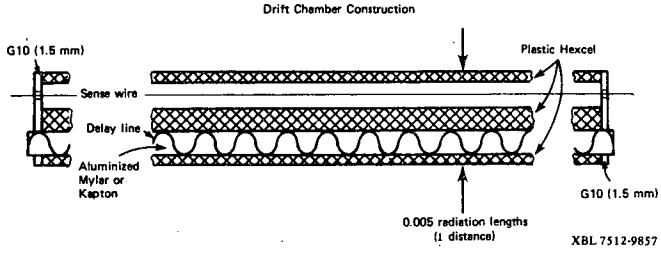

Fig. 20. Drift chambers: construction detail.

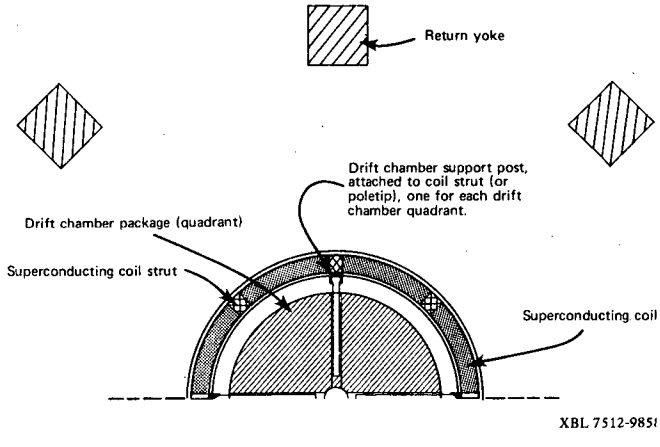

Fig. 21. Drift chambers: support scheme.

lengths (r.l.) thick. The G-10 end plates are 4×10^{-3} r.l. thick. The chambers are made of plastic hexcel material and aluminized mylar. There are three sections of hexcel/mylar laminate, one of which separates the two layers of chamber. The two halves of a chamber are shifted relative to one another by one half cell size to solve the left-right ambiguity. They are separated by 6 mm to allow the local tangent angle of a track to be measured. This greatly aids in pattern recognition.

The delay line is at negative high voltage, while the sense wire is at positive high voltage. The cell size is 1.2 cm with a full width of 6 mm. This configuration allows the chambers to operate in a 16 kG magnetic field without use of field shaping wires which would add significantly to the amount of material in the chambers.

A possible support scheme is shown in Fig. 21. The support vanes are in the shadow of the coil and return yoke, and so do not occupy any of the solid angle available for detectors.

The resolution in the azimuthal direction will be 200 microns or better. The resolution along the chamber, Δz, per delay line readout is given approximately by:

$$\Delta z \cong (\text{resolution for finding center of pulse, nsec}) \times (\text{propagation time of delay line, nsec/cm}).$$

The timing resolution for finding the pulse center is generally the dominant factor in determining Δz. The rise time of a signal, from a sense wire, on a delay line of reasonable length, e.g., 100 nsec $\leqslant \Delta t \leqslant$ 600 nsec, is approximately:

$$\text{rise time} \simeq 6\% \times \text{total propagation time of the line.}$$

The resolution for finding the center of such a pulse is approximately:

$$\Delta t \simeq 4\% \times 2 \times \text{rise time.}$$

For short line, say 100 nsec, with a propagation time of 1.5 nsec/cm, Δz = 3 mm. For longer lines, i.e., 0.5 nsec/cm, we again obtain the same resolution: Δz = 1.8 cm. The obvious improvements are to make less dispersive line, i.e., decrease the rise times, or measure z more often. The former has proven to be technically intractible. The latter solution is straightforward, but expensive. In the proposed chambers each delay line is read out from each end, and there are two delay lines looking at each sense wire. We therefore get four independent measurements of z, and the error is reduced by a factor of two per half chamber.

The number of sense wires in the proposed system is 3160. Each sense wire has an associated delay line readout at each end. The total number of channels to instrument is then 9480.

The disadvantage of our system is the relatively large error in Δz. This error is particularly troublesome if one wants to reconstruct the invariant mass of several hadrons. Figure 1 shows the mass resolution of a typical case $\psi(3.1\ \text{GeV}) \to 2\mu$ (or 2π) in function of the ψ momentum. The resolution is dominated by Δz. It should be noted, however, that the z coordinate of each track is measured independently by each chamber, thereby reducing substantially the net error, Δz, from that due to z resolution of individual chambers.

B. Special Inner Detectors

The inner tracking detector, consisting of drift chambers, is deliberately made in modular form to facilitate removal in part or in toto. As has been mentioned previously, this permits part of the solid angle to be covered by other experimental requirements (e.g., absorber close in, to obtain a clean signal for muon production over half the sensitive region). It also permits the entire set of drift chambers to be removed (perhaps without removing the beam pipe), and the installation a totally different inner detector. Examples of such detectors might be (a) a streamer chamber,[10] or (b) a time-projection chamber.[11] Their compatibility with a General Users Magnet will be discussed briefly as examples of potential versatility of inner detection schemes.

(i) Streamer Chamber.[10] An installed streamer chamber system would appear somewhat as indicated in Fig. 22. Here the design is from a recent study, which uses a set of solid-state imaging chips to readout the visual track information in a filmless manner. Access for the Blumlein feed lines (which are small except near the chamber), and CCD readout is through 20° end cones or between coils. The chips are inside the magnet, since they are not magnetic field sensitive, and the optical images of the stramer chamber tracks are focussed on the chips by means of a set of lenses. The non-uniformity of field is not a problem for the chamber operation or track reconstruction (the space-averaged non-uniformity is $\lesssim 1\%$). Due to the absence of field-sensitive equipment, there are no difficulties which can be

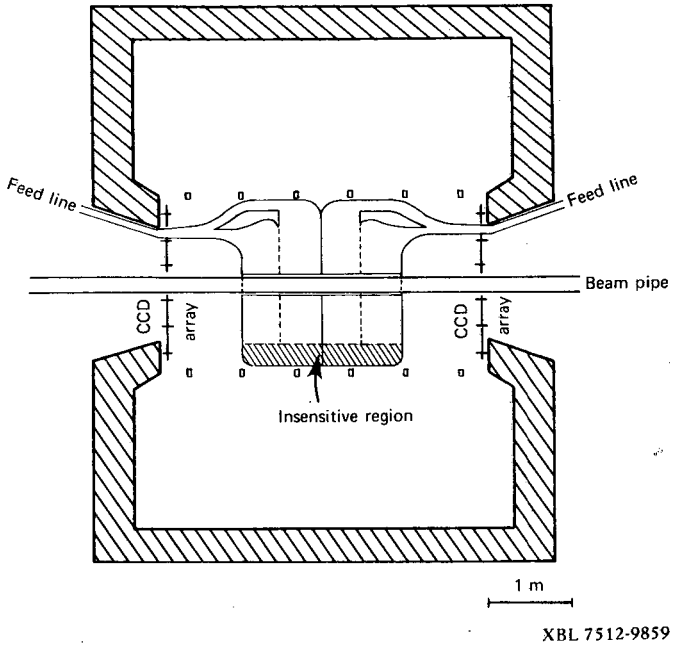

Fig. 22. Example of streamer chamber as central detector in GUM.

0 0 0 0 4 5 0 1 5 8 4

seen due to possible leakage of stray field. In the event of a conventional film readout system instead of the newer solid-state scheme, the GUM offers a natural photographic "port" through one or both of the open end cones.

The spatial resolution in a streamer chamber is expected to be superior to that of a drift chamber.* This might enable one to use only part of the magnet and still have sufficient energy resolution without any external tracking device. Thus, it would be ideally suited for a high p experiment. Also, the problem of unambiguously identifying K_S and Λ decays would be simplified.

(ii) Time Projection Chamber.[11] The time projection chamber (TPC) of D. Nygren offers the potential of both high resolution and direct readout of space points, in a large volume detector. In addition, it can, in principle, provide ionization information to aid in particle identification. As an example, a TPC might be installed in the General Users Magnet, occupying the central one-meter diameter and two-meter length inside a system of coils having just twice these respective dimensions.

Uniformity of field is important for optimum performance of the TPC. This is because a non-alignment of $\vec{B}$ and $\vec{E}$ field directions leads to a deviation of the drifting electrons from the $\vec{E}$ direction, leading to a possible distortion of the track position as read out assuming $\vec{B}$ and $\vec{E}$ are parallel. This is not, however, equivalent to a resolution loss, at least not for small non-uniformities, where such deviations might well be corrected out by mapping in the more inhomogeneous regions. Even without mapping, a non-alignment of fields of about 0.5% corresponds to the intrinsic resolution of the device. This is to be compared with a value of about 0.4% for the maximum non-uniformity (at maximum radius, r = 0.5 m) in the present GUM design, and << 0.5% for the average space point. Thus, with some mapping at large radii (or improvement in magnet design), this magnet should prove quite adequate for operation of the TPC, even with the ends open, so that electron tagging may be done (e.g., in recording the 2γ events).

VII. SOME POSSIBLE CONFIGURATIONS FOR EXPERIMENTS

We have, in close consultation and collaboation with many members of other groups at the PEP 1975 Summer Study, studied some particular applications of GUM.

A. GUM Used in New Particle Detection[6]

The GUM is well suited for use in a large solid-angle detector system for the study of new particles such as charmed hadrons or heavy leptons. These particles are expected to decay into normal leptons (μ or e) with reasonable branching ratios, and a prompt high-energy lepton (say p > 5 GeV/c) may be considered a distinctive signal. For the study of the properties of such new particles, a suitable system would be similar to the "central detector" proposed for the 2γ experiment.[4] An example of such a scheme is shown in Fig. 23. The rejection of charged pions is of the order 10^{-3} $\sigma_{\mu\mu}$ in this system. Contamination due to π^0-Dalitz pairs and conversion of π^0-decay photons in the beam pipe can be reduced below this limit by use of chambers and dE/dx scinitillator near the beam pipe. The "lumped" solenoid coil of the GUM reduces the probability of contamination due to charge exchange of $\pi^\pm$ immediately before the shower counters. The signature for directly produced muons is not optimal in the "normal" configuration of drift chambers, where almost 2 m of flight path is available for pion and kaon decays into muons. The hadron rejection ratio is estimated to be ~ 8 x 10^{-2} $\sigma_{\mu\mu}$ for muons of momentum above 3 GeV/c. However, the flexibility in rearranging the inner detector of the magnet allows a configuration more suitable for direct-muon identification. Thus, a massive absorber of uranium or hevimet, etc., may be placed surrounding the beam pipe at the interaction point over one hemisphere, leaving the other hemisphere open to a track chamber system suitable for observing hadronic or direct-electron final states. Alternatively, smaller segments of the azimuth may be blocked by dense absorber, leaving free regions in between, for observation of correlated μ-e or μ-hadronic states. Details may be found in Ref. 6. Finally, the GUM is particularly suited for the study of new states produced in 2γ reactions, since the

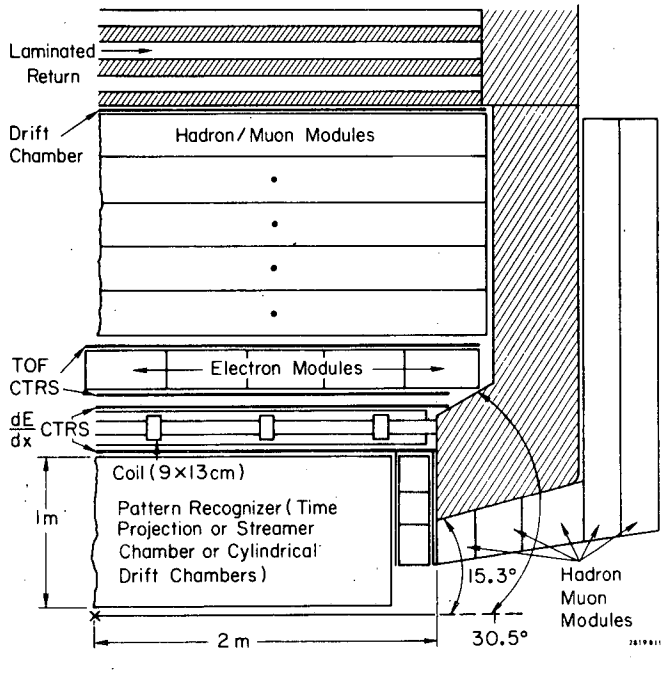

Fig. 23. Side view of charmed particle detector in GUM (see also PEP-204).

*Estimates of the ultimate resolution for streamer chambers vary, but a resolution transverse to the streamer direction of perhaps ~100 μ seems possible. In addition, there is generally much more information per track, due to the "continuous" nature of measurements, so that the momentum resolution may ultimately be considerably better than can be obtained from drift chambers of equivalent space-point resolution. (See Ref. 10)

end-caps of the solenoid are free for tagging up to about 20°.[4]

B. Two-Photon Studies[4]

The PEP study group on two-photon processes has made a design for an experiment using the GUM and supplementing it with transverse field spectrometers covering the 4°-20° regions at each end of the solenoid. Either the lumped-coil or continuous-coil version of GUM could be used equally well. The design is shown in Fig. 24. The outside region is covered by an aerogel Cerenkov counter, followed by a Pb-liquid argon shower counter and a set of muon chambers. The tagging apparatus consists of a very small-angle NaI array, while electrons with scattering angles 50 mrad < θ < 300 mrad are analyzed by a dipole magnet on each end. This setup maximally uses the good momentum resolution achievable in the range 20° < θ < 30°.

C. High-Momentum Detection[5]

The high-momentum group at this Summer Study has designed a detector using the GUM as basic detector. The emphasis of this group is on complete reconstruction and identification of secondaries accompanying a particle of high momentum. A cross sectional sketch of a possible design is shown in Fig. 25. Since the goal is to identify as well as precisely measure all the charged particles in the event, a large part of the volume outside the coil is occupied by three layers of Cerenkov counters, operating in different velocity ranges. Just outside the coil, there are 96 cells of Cerenkov counter C_3 operating with 4.1 atmospheres [isobutane]. This is followed by 160 one-atmosphere CO_2 counters (C_1) at a somewhat larger radius, and finally by 112 one-atmosphere isobutane counters (C_2) at the outside radius. These latter counters are sandwiched between laminated iron return

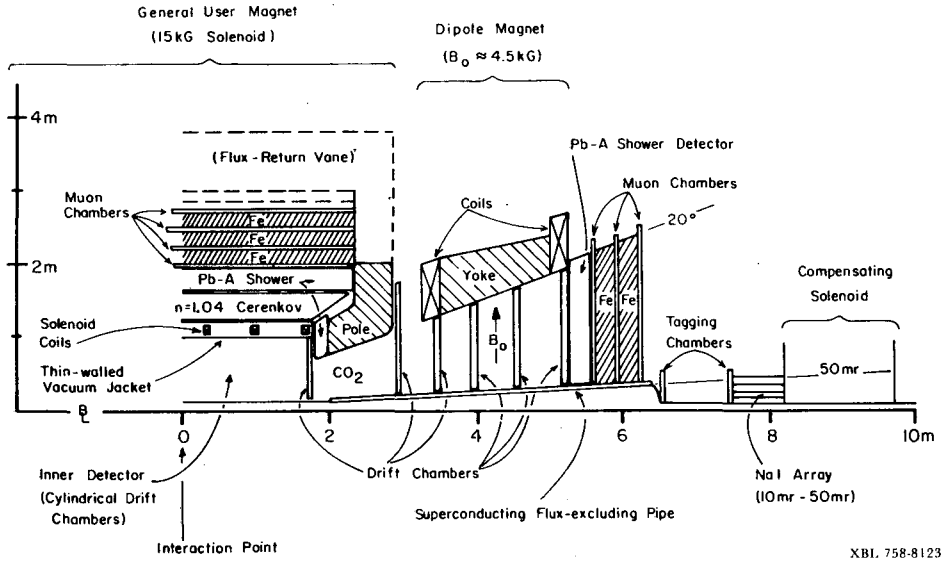

Fig. 24. Two-photon experimental setup in GUM (see also Fig. 15 of PEP-203).

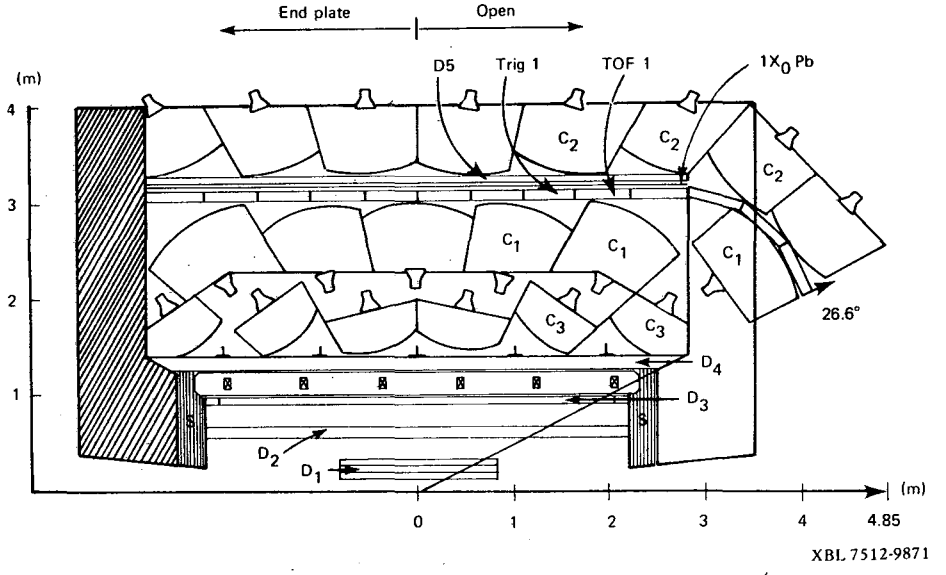

Fig. 25. Side view of high-momentum hadron experiment in GUM (see also PEP-201).

0 0 0 0 4 5 0 1 5 8 5

yokes, which are also part of the γ measuring system. Together, C_3 and C_1 resolve pions from K's and p's (or $\bar{p}$'s) over 0.82(4π) sr solid angle in the momentum range 1.3-15 GeV. Along with C_3, full π/K/p separation is achieved above 1.3 GeV/c over 0.56(4π) sr. Time-of-flight measurements are obtained over a 3 m flight path by scintillation counters adjacent to C_3.

Gamma rays are measured using (1) drift chambers behind 1 r.l. of lead to determine the γ direction, and (2) shower counters (0.26 × 4π sr) consisting of alternate layers of iron and proportional tubes in the laminated flux return. Charged particle measurements are made by the inner set of drift chambers.

In this design, charged particles can be identified and precisely measured over a quite large fraction of the total solid angle. Gamma rays also can be detected and measured, though over a smaller solid angle. The potential for identification of charged particles and gamma-ray measurement exploits the thin windows between the lumped coils, and in other respects, the geometry and size are very similar to the principal GUM design considered previously.

VIII. ALTERNATE DESIGN POSSIBILITIES - LARGE VOLUME LOW $\bar{B}$ GENERAL USER MAGNET[5]

The 6 m diameter 3 kG magnet proposed by this year's high momentum and particle identification group might also be viewed as a candidate for the general user magnet. Compared to the magnets which are the main focus of this report, the large volume device would have the following advantages:

(1) Out to 3 m radius, no appreciable amount of material need separate the user's detector from the beam pipe. Within this radius, the detectors may assume any shape.

(2) Very precise (typically 2-5%) momentum measurement is possible over the full momentum range if the multiple scattering material can be kept small over an appreciable fraction of the trajectory.

(3) The large extent of the magnetic field permits precise momentum measurement outside relatively massive detectors placed close to the beam pipe. Examples other than Cerenkov detectors are: (i) muons may be measured outside a small "lead ball" which suppresses kaon decay and other background, with a momentum resolution ~ 5 × greater than achievable with the usual configurations of magnetized iron; (ii) many concentric shells of thin radiator could be used with drift chambers for electron-pair spectrometry of soft photons. This could be the most economically feasible means of achieving high resolution, both in energy and direction of γ-rays with energies < 100 MeV.

(4) A 3 m flight path may permit velocity measurement by relativistic dE/dx rise. This could be combined with trajectory measurement by means of large-volume drift chambers, time projection detectors, etc. The ambient magnetic field may be helpful in limiting the range of δ-rays which confound the dE/dx measurements.

(5) Addition of specially shaped iron pole faces permit the user to create a particular field shape near the interaction point.

The disadvantages of this magnet as a general user device are obvious:

(i) All phototube assemblies and other detectors must withstand 3 kG. Microchannel-plate photomultipliers available at reasonable cost would relieve this otherwise severe constraint.

(ii) If the high mass and cost of shower counters (e.g., liquid argon) requires their placement with ≈ 1.5 m of the interaction point, the reduction in radius will result in poorer momentum resolution.

(iii) The magnet may be very expensive. If constructed using MINIMAG techniques, it would cost at least twice as much as the lumped solenoid described here. However, there is no need to restrict the superconducting coil thickness to much less than one radiation length or, for that matter, to rule out a conventional coil. Coil forces are proportional to B^2 and therefore very small.

The large volume, low field magnet has attractive features as a general user facility. However, it is less flexible than the magnet system previously discussed. Perhaps this alternative should be considered seriously if microchannel photomultipliers should become available in the near future at a cost comparable to ordinary photomultiplier tubes.

ACKNOWLEDGMENTS

We would like to acknowledge the help of John D. Taylor in helping to prepare and run the program TRIM, on which our field plots are based. We also wish to thank Phillipe Eberhard for a number of relevant and helpful remarks, and Lina Galtieri for use of her result on γ conversions in a solenoid coil. Thanks also to F. Villa and R. Mozley for their advice.

Table II. Comparison of Proposed Magnets and Present Mark II

Coil	Lumped Superconducting	Continuous Superconducting	Continuous Conventional (Mark II)
Radius	1 m	1 m	1.5 m
Length	4 m	4 m	3 m
Magnetic Field	15 kG	15 kG	5.2 kG
Field Strength homogeneity ΔB/B	~10%	~1%[a]	1%
$\left(\frac{\Delta p}{p^2}\right)_{\text{inside}}$	0.67% GeV^{-1}	0.67% GeV^{-1}	0.75% GeV^{-1}
$\left(\frac{\Delta p}{p}\right)_{15\ \text{GeV}}$	3.75%	4.8%	11.2%
Thickness	0.02-0.05 r.l.[b]	0.45 r.l.	0.75 r.l.
	Solid Angle Fraction, (ΔΩ/4π), for:		
$\left(\frac{\Delta p}{(\Delta p)_{90°}}\right) < 1.0$	0.94	0.94	0.92
Cerenkov Counters	0.68	0.89[c]	0.7
Gamma Detection < 0.1 r.l.	0.68	0	0
Gamma Detection < 1 r.l.	0.80	~0.93	~0.93
Overall Size			
Weight:	400 tons	400 tons	(Figures not available)
Length:	6 m	6 m	
Height:	8 m	8 m	
Width:	8 m	8 m	
Cost	$1.5 M	$1.5 M	

[a] With closed end caps.
[b] Thickness of vacuum vessel walls between coils and struts.
[c] With 0.5 r.l. interposed.

REFERENCES

1. SLAC Proposal SP-2 (Mark I Detector). See also PEP-200, this Proceedings.
2. SLAC Proposal SP-7 (IRON BALL).
3. SLAC Proposal SP-24 (CRYSTAL BALL).
4. Group Report on Two-Photon Physics, PEP-203. See also PEP-175, 1974 PEP Summer Study.
5. Group Report on High Momentum Particles and Particle Detection, PEP-201. See also PEP-146, 1974 PEP Summer Study.
6. Group Report on Search for New Particles, PEP-204. See also PEP-174, 1974 PEP Summer Study.
7. PEP-153, T. Mast and J. Nelson, 1974 PEP Summer STudy.
8. The numerical coefficient in this formula represents an average between a setup with only three chambers and one with a very large number of chambers.
9. Private communication, J. M. Patterson and B. Richter.
10. Group Report on Streamer Chamber Detectors PEP-197. See also PEP-151, 1974 PEP Summer Study.
11. Group Report on Time Projection Detector, PEP-198. See also PEP-144, 1974 PEP Summer Study.

APPENDIX A

SUPERCONDUCTING DETECTOR MAGNETS - ALTERNATIVES AND CHOICES

The relative advantages of different magnetic field geometries were discussed Sec. V.A. It was pointed out that the solenoidal coil seems the most attractive from many points of view, and that geometry will be examined in further detail in this note, with special regard to the engineering design considerations.

The questions which are of immediate interest are (1) the size, and (2) whether detectors will be used outside the coil (and certain properties of these detectors). The momentum resolution for charged particles is usually the single most important criterion, and this topic has been discussed in detail in Sec. IV.B. However, this consideration interacts with both (1) and (2), and since a typical experiment is a compromise between various physics objectives and the expense of the detection apparatus, it may be important to consider several kinds of magnets. Therefore, we will discuss the engineering problems associated with three kinds of solenoid magnets: (1) the conventional low current density magnet, (2) the continuous high current density thin coil magnet, and (3) the lumped coil magnet. The conventional solenoid will not permit a significant amount of physics to be performed outside the coil. The continuous thin coiland the lumped coil magnet will permit a considerable amount of interesting physics to be performed outside the coil. Table A-1 compares the three kinds of coils in a magnet with a 0.9 m useful (warm) bore diameter and a useful length of 1.84 m. Longitudinal cross sections of the three kinds of coils are shown in Figs. A-1, A-2, and A-3.

The magnets which are compared in Table A-1 and are shown in Figs. A-1, A-2, and A-3 are

Table A-1. A Comparison of the three kinds of Solenoid Magnets Shown Figs. A-1, A-2, and A-3.

	Thick Conventional	Lumped Coil	Thin Coils
Central Induction (T)	1.5	1.5	1.5
Peak Induction (T) in winding	~1.6	>3.0	1.53
Length Between Poles (m)	1.84	1.84	1.84
Cryostat i.d. (m)	0.90	0.90	0.90
Cryostat o.d. (m)	1.50	1.30	1.10
Current Density (Am^{-2}) in Superconductor	4×10^7	4×10^8	9×10^8
Radiation Thickness at the coils (rad length)	2. - 3.	2. - 3.	0.2 - 0.4
Minimum Radiation Thickness (rad lenghths)	2. - 3.	0.01 - 0.05	0.2 - 0.4
Magnet Cold Mass (kG)	6.9×10^3	5×10^2	2.5×10^2
Percent of Solid Angle Usable for Physics Outside the Coil	0	50 - 55%	80 - 85%

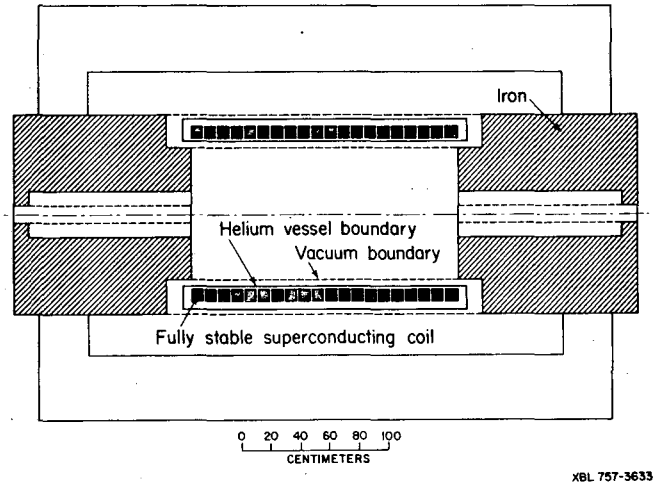

Fig. A-1. The low current density "conventional" superconducting solenoid.

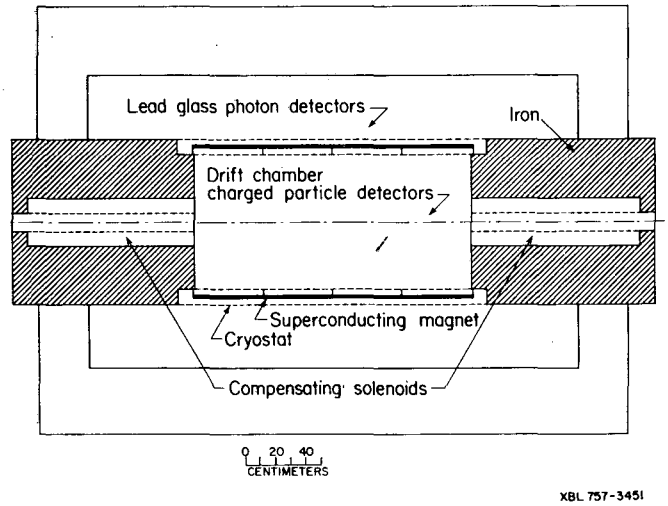

Fig. A-2. The continuous high current density superconducting solenoid.

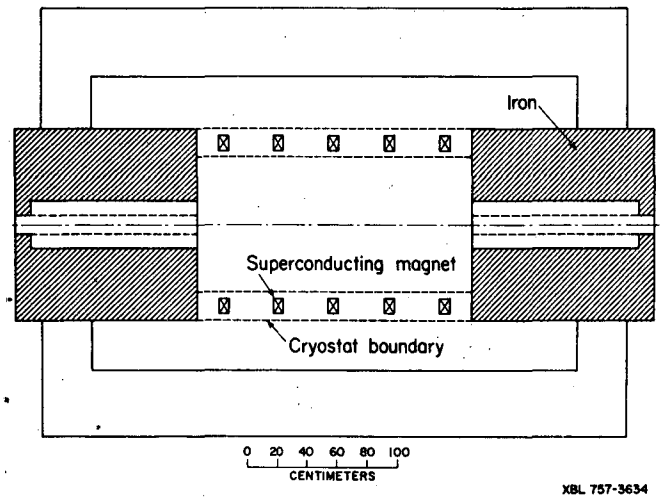

Fig. A-3. The lumped high current density superconducting solenoid.

roughly half the size of those being proposed for PEP. The proposed PEP magnets, which are about 2 meters in diameter and 4 meters long, will have a larger percentage of usable solid angle available for physics than the magnets shown in Table A-1.

It is useful to point out we have more choices available to us than there were just a few years ago. The relative merits of the three choices are discussed in the sections to come.

THE CONVENTIONAL SUPERCONDUCTING SOLENOID MAGNET

The conventional low current density superconducting solenoid has been used in high energy physics for the last eight years. Examples of this kind of magnet includes: the 12-foot bubble chamber at ANL, the 15-foot bubble chamber at Fermi Lab, the Pluto magnet at DESY, the LASS magnet at SLAC, the BEBC, and OMEGA magnets at CERN.

In 1965, Steckly[A-1] showed that if the current in a superconductor could be carried in a copper substrate without heating the superconductor to a temperature above its critical temperature, the superconductor would operate stably. The principle of cryostatic stability is used in nearly all of the large high energy physics detector magnets. This type of magnet will not quench. The current will jump from the superconductor to the copper. Since the magnet will not quench, the solenoid can be made in large sizes (over 6 meters in diameter) with fairly large central inductions (up to 4 T for a large size magnet). The technology is proven and reasonably reliable.

Meaningful physics is nearly impossible outside the magnet coil because, in most cases, its radiation thickness is in excess of two radiation lengths. A cryostatically stable magnet is a low current density magnet. Its thick coils are massive and difficult to cool down from 300° K to 4° K. The cryogenic system used on large conventional solenoids makes them difficult to modularize and test before final assembly. A large conventional superconducting solenoid is expensive to build and requires a large crew to run. However, if large diameters (greater than 2 or 3 meters) and inductions greater than 2 T are required for physics reasons, there probably is no reasonable alternative to the cryostatically stable conventional solenoid magnet.

The major problem which has been encountered in most of the large solenoids built to date has been the cryogenic system. The large bubble chambers are bath cooled. (The superconductor is immersed in a bath of cold helium.) Massive bath cooled solenoids are difficult to cool down under the best of circumstances. The OMEGA magnet represents a positive step forward in large magnet cryogenics. The superconductor, which is hollow like conventional water cooled conductors, carries supercritical helium.[A-2] The cooldown of such a system, if properly designed, will be faster than an equivalent bath cooled magnet. The inventory of helium in contact with the magnet is reduced. However, the primary disadvantage of supercritical helium cooling is the amount of refrigeration required to obtain low enough operating temperatures.

Large conventional bubble chamber solenoids have been major users of superconducting magnet technology. Large magnets of this type will continue to be built. Physics experiments which require some of the particle detection to occur outside of the magnet winding cannot use conventional low current density superconducting magnets. The other alternatives are discussed in the next two sections.

THE THIN HIGH CURRENT DENSITY SOLENOID MAGNET

The thin high current density solenoid magnet has a low radiation thickness over its entire surface. In PEP, the magnet will permit physics to be performed at about 90% of the solid angle outside the coil. The magnetic induction outside the coil will be quite low if the central induction is kept below 1.8 T and if the iron return yoke is properly designed. When the induction outside the coil is low, photomultiplier tubes and other sensitive electronics may be used in that region. The thin solenoid can be easily modularized so that individual magnet sections can be tested separately. The coil mass is low; the cooldown from 300° K to 4° K is relatively easy.

The thin solenoid is not without its disadvantages: The magnet must operate at very high current densities. As a result, large magnetic stresses and high stored energy per unit mass can occur. The magnet will quench if any of the superconductors go normal. A practical upper central induction limit is just over 2.0 T. Large diameter coils, which are stress limited, will have a lower central induction. Small high current density solenoids have been built and operated successfully in experiments. However, large high current density solenoids have not yet been proven.

Engineering studies on the thin solenoid[A-3] show that the concept is technically feasible. Preliminary experimental tests on small magnets have been very encouraging. The remainder of this section will discuss the following: the design characteristics of thin solenoid magnets, the scaling laws for thin magnets, and the LBL test program for thin magnets.

The Design Characteristics for Thin Solenoid Magnets

The thin (low radiation thickness) solenoid should have the following characteristics: 1) It must have uniform radiation thickness (normal to the magnet coil) over the full length of the coil. 2) The cryogenic system should be designed for ease of cool down and simplicity of construction in the thin region of the magnet. 3) The coil should be built in modules which can be tested individually. A thin solenoid which meets the above criteria was designed in conjuction with the MINIMAG experiment.[A-4]

The MINIMAG solenoid was designed so that it could be modularized. The major stress, stored energy, and quench problems were studied. The tubular cooling system permits rapid cooldown and positive cooling consistent with the low radiation thickness requirements of the experiment. The thin solenoid consists of four primary parts: the solenoid bore tube, the superconducting coil, the refrigeration cooling tube, and the cryostat vacuum vessel (See Fig. A-4).

The solenoid bore tube serves as a winding form for the coil, but its most important function is an electrical one. It slows down the quench process (the process of going normal and dumping the magnet stored energy), and it serves as a thermal sink for most of the magnet stored energy during a quench. The superconducting coil is wound with intrinsically stable (twisted fine filamented) superconductor which is operated at 80% of its critical current or less.

The thin solenoid would not have a cryostat in the conventional sense. The inner cryostat vessel is replaced by a coil of aluminum refrigeration tubes which carries flowing two-phase helium. The refrigeration tube forms an integral part of the superconducting magnet. The magnet bore tube, the superconducting windings and refrigeration tube are vacuum impregnated forming a single structure which is suspended inside the vacuum enclosure. The ends of the thin magnet may be thick from a radiation standpoint. Therefore, all of the cryostat support functions, refrigeration feeds and current leads would be in that region.

The superconducting coil is designed to carry all of the magnet stresses put into the system at its peak field. However, we expect

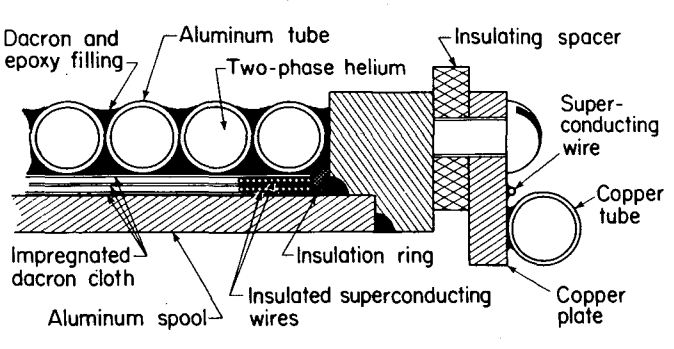

Fig. A-4. Magnified cross section of the thin con-continuous high current density solenoid coil and cooling tube.

that the aluminum bore tube will help support the magnetic stresses in the system, which gives an additional margin of safety.

The thin magnet design proposed for MINIMAG attempted to combine the cryogenic system and superconducting magnet into a single integrated system. It is hoped that one can avoid the kinds of cryogenic problems which have been common on the large bubble chamber magnets. Since the magnet is not cryostatically stable, the liquid helium inventory in contact with the magnet can be reduced. Most of the helium in the system is out of direct contact with the magnet. The tubular cooling system also permits a positive well controlled cooldown process. The cooldown of a "MINIMAG type" thin solenoid should proceed much faster than a comparable low current density magnet.

Scaling Laws for Thin Magnets

Thin coils must operate at lower central inductions as the magnet diameter increases. There are two primary reasons for this; the stored energy per unit coil mass should be less than 25-30 Jg^{-1}. The maximum stress in the conductor (the magnet coil is assumed to carry all of the magnetic stress) should be less than 5×10^8 Nm^{-2} (72,300 psi). Keeping the proceeding limitations in mind one may apply the following scaling law to thin coil constructions:

$$\Gamma = B_o^2 D^{3/2},$$

when: $B_o \leq B_{max}$,

$$E_o \leq E_{max},$$

where:
$$B_o \approx \frac{\mu_o NI}{L},$$

$$E_o \approx \frac{\pi D^2 B_o^2}{8 \mu_o}.$$

We define the proceeding symbols as follows: B_o is the central induction (T); D is the coil diameter (m); L is the coil length between poles (m); E_o is the coil stored energy per unit length ($J\ m^{-1}$); μ_o is the permeability of air ($\mu_o = 4\pi \times 10^{-7}$). Γ is the scaling constant for thin solenoids; B_{max} is the maximum central induction for the magnet; E_{max} is the maximum stored energy per unit length. Γ, B_{max} and E_{max} are functions of the coil radiation thickness. In addition, the maximum practical coil diameter D_{max} is also a function of radiation thickness. Table A-2 presents estimated values of Γ, B_{max}, E_{max} and D_{max} for thin superconducting solenoids of various radiation thicknesses.

The four magnets shown in Table A-2 which have radiation thickness of 0.48, 0.40, 0.32, and 0.25 radiation lengths are assumed to have aluminum bore tubes and cryostats. The "ultra thin solenoid" is assumed to have a magnesium bore tube and cryostat. A radiation thickness of 0.18 radiation lengths is judged to be very close to a lower limit for thin coil technology. A

0 0 0 0 4 5 0 1 5 8 7

magnet which has a radiation thickness of 0.18 radiation lengths will cost 30-50% more than the same magnet when it has a radiation thickness of 0.25 radiation lengths. Table A-3 shows a breakdown of radiation thickness of the magnets shown in Table A-2.

Table A-2. Design Parameter Constants for Various Thin Solenoid Magnets

	Thick	Moderately Thick	Medium	Thin	Ultra[a] Thin
Radiation Thickness (radiation lengths)	0.48	0.40	0.32	0.25	0.18
Scaling Constant Γ	8	6	4	2	2
B_{max} (T)	2.0	2.0	1.6	1.2	1.2
E_{max} (Jm^{-1})	$2x10^6$	$1.5x10^6$	$1x10^6$	$0.5x10^6$	$0.5x10^6$
D_{max} (m)	~3	~3	~2.5	~2	~2

[a]Based on the use of magnesium magnet and cryostat parts.

Table A-3. The Radiation Thickness of Various Components of Low Radiation Thickness Solenoids

	Radiation Thickness (radiation lengths)				
	1 meter diameter solenoid				
Component	Thick	Moderately Thick	Medium	Thin	Ultra[a] Thin
S/C coil	0.20	0.15	0.10	0.05	0.05
Bore tube	0.13	0.10	0.07	0.05	0.03
Cooling tubes	0.04	0.04	0.04	0.04	0.03
Cryostat	0.11	0.11	0.11	0.11	0.07
Total	0.48	0.40	0.32	0.25	0.18
Central Induction (T)	2.00	2.00	1.60	1.20	1.20
	2 meter diameter solenoid				
S/C	0.15	0.11	0.07	0.03	0.03
Bore tube	0.14	0.10	0.06	0.04	0.03
Cooling tubes	0.04	0.04	0.04	0.03	0.02
Cryostat	0.15	0.15	0.15	0.15	0.10
Total	0.48	0.40	0.32	0.25	0.18
Central Induction (T)	1.68	1.46	1.18	0.84	0.84

[a]Based on the use of magnesium magnet and cryostat parts.

Figure A-5 shows a plot of the thin magnet central induction B_o vs. the magnet diameter D for magnet with radiation thickness of 0.48, 0.4, 0.32, 0.25 and 0.18 radiation lengths. Figure A-5 uses the Γ, B_{max}, E_{max}, and D_{max} given in Table A-2. These values are our "best guess" at this time. They are based on limited experimental data. An experimental program now under way at Lawrence Berkeley Laboratory (LBL) will determine much more accurately the values of Γ, B_{max}, E_{max} and D_{max}.

The LBL Experimental Test Program for Thin Magnets

The experimental program is built around the testing of two 1.03 m diameter MINIMAG type prototype coils. These coils have a radiation thickness of 0.24 radiation lengths. The two coils will use different niobium-titanium superconductors. One coil will use 1.8 to 1 copper to superconductor ratio conductor; the other coil will use a 1 to 1 copper to superconductor ratio conductor. Both conductors are 1.0 mm in diameter (the bare diameter before a layer 0.05 mm thick formvar is applied). Both conductors have over 2000 filaments, and they are twisted at the rate of one turn per centimeter. The filament diameter of both conductors is under 15 μm. Both conductors are modern intinsically stable conductors.

The two different conductors are wound on two 6.35 mm (1/4 thick) 1100 series aluminum allow tubes which are 1030 mm in diameter and 500 mm long (including end flanges - See Fig. A-6).

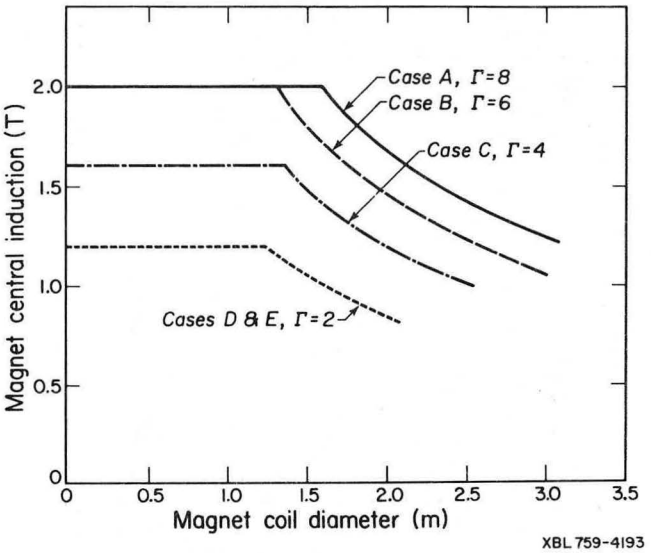

Fig. A-5. Scaling of magnet central induction vs magnet coil diameter:
Case A 0.48 rad. lengths thick
Case B 0.40 rad. lengths thick
Case C 0.32 rad. lengths thick
Case D 0.25 rad. lengths thick
Case E 0.18 rad. lengths thick.

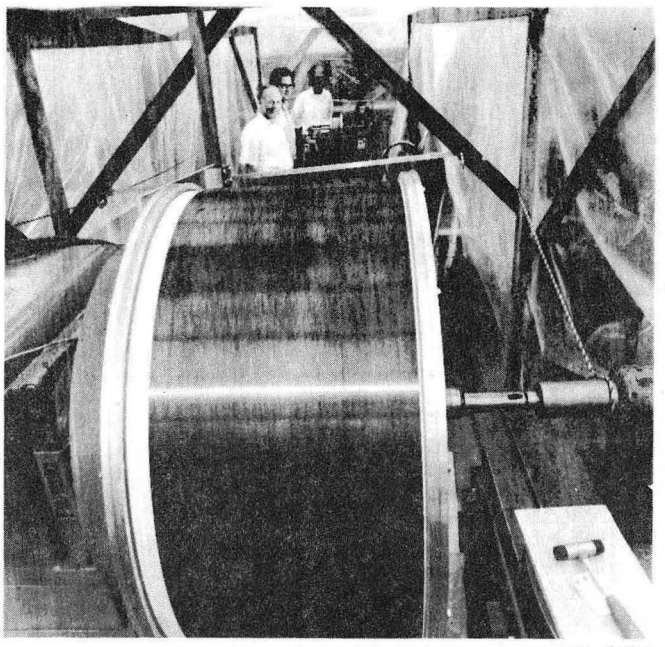

CBB 758-6183

Fig. A-6. The LBL thin continuous coil prototype being wound.

The bore tube is expected to play an important role in controlling the superconducting magnet quench. The superconducting coil has a layer of 12.7 mm o.d. (1/2 inch o.d.) aluminum tube wound around it. This tube will carry two-phase liquid helium as a coolant for the superconducting magnet (See Fig. A-4).

The two superconductors have been tested at high current densities ($> 1.2 \times 10^9$ A m^{-2}) and high magnetic stress ($> 4 \times 10^8$ N m^{-2}) in small oval solenoid tests. The large solenoids will test the conductor under conditions of high current density, high magnetic stress, and high stored energy. We expect to be able to determine experimentally the magnet scaling factors Γ, B_{max} and E_{max}. Thus we expect to prove that high current density superconducting coil technology can be applied to relatively large (1-3 m in diameter) magnets with central inductions from 0.8 to 1.8 T.

THE LUMPED HIGH CURRENT DENSITY SOLENOID MAGNET

The lumped solenoid has a non-uniform radiation thickness over its length. The supports between coils are also thick from a radiation standpoint. The radiation thickness is 0.01 - 0.06 radiation lengths in the thin regions of the magnet; the radiation thickness at the coils and support members will typically exceed two radiation lengths. The regions of very low radiation thickness are useful for certain kinds of physics (i.e., the accurate measurement of the momentum of high momentum charged particles and low energy gamma rays). Like the thin continuous solenoid, the lumped magnet is easily modularized so that individual magnet sections can be tested separately. The coil mass is not as low as the continuous solenoid, but it remains low enough so that the cooldown of the magnet from 300° K to 4° K is relatively easy.

The lumped solenoid must operate at relatively high current densities in the conductor. As a result, the magnet will quench if any of the superconductors goes normal. The quench process must be understood and dealt with. Since the magnet must be designed with the quench process in mind, the central induction of the lumped high current density solenoid should be no higher than 2.0 to 2.5 T. Large diameter lumped coils will be stress limited, so they would be operated at a central induction below 2.0 T.

Numerous small magnets have been operated at the current densities proposed for the lumped solenoid (about 4×10^8 A m^{-2}). Large lumped coil type magnets (~2 m in diameter), which is similar to the lumped solenoid coils, have been built by NASA[A-5] and by the high energy physics laboratory at Stanford University.[A-6] Both magnets have been operated reliably. The lumped coil concept is, in a sense, more proven than the thin continuous solenoid concept.

Preliminary engineering studies on a lumped coil detector indicates the magnet concept is technically feasible. Successful thin coil tests are encouraging for the thick lumped magnets as well. These magnets are not driven to as high a current density as are the thin coils. Successful completion of the large thin coil tests will improve our knowledge of the lumped coil system, and will verify the technical feasibility of the concept and will provide reasonable experimental determination of magnet scaling factors.

The Design Characteristics of Large Lumped Solenoid Magnets

The lumped solenoid will have the following characteristics:

1. The holes of very thin regions of the magnet or magnet cryostat should be as large as possible.
2. The cryogenic system should be designed for ease of cooldown and simplicity of construction.
3. The coil should be easy to test in modules.

Preliminary designs for a proposed CERN experiment[A-7] indicate that the proceeding criteria can be met in a lumped solenoid system.

A lumped solenoid should be easy to modularize. The modules may or may not be identical in physical shape, but they must contain the same number of ampere turns of conductor. The solutions to stress, stored energy and quench problems which are applied in the MINIMAG thin solenoid studies, may be used for the lumped magnet system. The use of the tubular cooling system, which is an important part of the MINIMAG concept and has been successfully employed at SIN,[A-8] can be used to advantage in the lumped coil system.

The lumped solenoid magnet consists of four primary parts: the lumped coil bore tubes, the superconducting windings, the tubular cooling system, and the cryostat vacuum vessels.

The solenoid bore tube serves the same function in the lumped coil solenoid as it does in the thin coil solenoid. In both cases, the coil bore tube controls the magnet quench precess. The lumped coils are not as well coupled inductively to the bore tube as the thin coils (98% coupling is possible in the thin coil system; 90% coupling should be possible in the lumped coil magnet). Like the thin solenoid, the lumped coil solenoid should be wound with intrinsically stable superconductors. The conductor is operated at a lower current density than in the thin continuous coil case. The primary reason for this is that peak induction in the conductor can be twice the central induction of the magnet. (In a thin solenoid, there is less than a 5% difference between the peak and central inductions.) The superconductor in the lumped solenoid would be operated at 75% of its critical current, or less.

Like the thin solenoid, the lumped solenoid should use a tubular cooling system using two phase helium. The refrigeration tubes, the bore tube and superconducting coil form an integrated package. The lumped coils are assembled together with cold force carrying members. The structure, which is mostly holes, is nearly in force equilibrium. The support system which suspends the lumped coil structure to the room temperature outside world is designed to carry gravitational forces and those magnetic forces which are generated by asymetric currents in the system.

Two kinds of cryogenic vacuum vessels can be considered for the lumped solenoid system: the continuous uniform cryostat and the thin window cryostat. The continuous cryostat is less expensive than the thin window cryostat, but its

0 0 0 0 4 5 0 1 5 8 8

radiation thickness is a factor of 3 to 5 greater.

In order to minimize radiation thickness, the continuous cryostat would have to be made of magnesium or magnesium alloy. The thickest part of the cryostat is the outer vacuum can; this thickness is needed to resist buckling due to vacuum loading. Proper mechanical design will result in radiation thicknesses between the coils of 0.05 to 0.07 radiation lengths.

If the physics of the experiment requires less than 0.05 radiation lengths of material in the thin regions of the magnet, the thin window cryostat should be considered. A thin window cryostat can have a radiation thickness as low as 0.01 radiation lengths. It can be built with either aluminum foil or Mylar windows. Both kinds of windows will be quite fragile. Both will require either plastic foam or a screen to protect the windows from damage. A cryostat without windows, in which the cryostat vacuum vessel closely surrounds the coils and struts, has been suggested. The cost of such a cryostat plus maintenance problems associated with such a system rule it out. In addition, there is little physics advantage which can be gained by reducing the minimum radiation thickness from 0.01 radiation lengths to zero.

The thin solenoid tests which will soon be conducted at Berkeley will answer many technical questions which the lumped solenoid poses. The cooling system is essentially the same for the two systems. In some ways, the lumped solenoid design is conservative compared to the continuous thin solenoid design. Therefore, a successful 1 meter diameter thin solenoid test will advance the cause of the lumped solenoid as well.

Scaling Laws for Lumped Magnets

There are two primary criteria which determine the size of the lumped coils in a lumped coil magnet system. They are: stored energy per unit coil mass and magnetic stress. To the first order, the stored energy per unit mass and magnetic stress go together. As a result, the scaling law given here will be based on stored energy per unit coil mass alone. The coil in this case includes the superconductor and the bore tube. Each is treated separately.

The current density in the superconductor (the Nb-Ti alone) is a function of the local temperature, induction and stress. The current density in the overall matrix (copper, other normal metals and superconductors) is a function of the stored energy. The stored energy for a lumped coil magnet with return path and a central induction $B_o \leq 1.8$ T is to the first order:

$$E \approx \frac{\pi D^2 L B_o^2}{8\mu_o}$$

The stored energy per unit superconductor matrix mass is:

$$K_{SC} = \frac{E}{M_{SC}}$$

The stored energy per unit aluminum bore tube mass is:

$$K_{bore} = \frac{E}{M_{bore}}$$

where the symbols are defined as follows: E is the magnet stored energy (J); D is the magnet coil diameter (m) at the center of the windings; L is the magnet length between pole tips (m); B_o is the central induction of the magnet (T); M_{SC} is the total superconductor matrix mass (g), which include the Nb-Ti and all normal metals in the matrix; M_{bore} is the bore tube mass; and μ_o is the permeability of air $\mu_o = 4\pi \times 10^{-7}$.

If the lumped coil magnet is divided into N coil packages, the limits for stored energy per unit mass are:

$$K_{SC} \leq \frac{100}{N} \quad (Jg^{-1})$$

when $4 \leq N \leq 8$

$$K_{SC} \leq 12.5 \quad (Jg^{-1})$$

when $N > 8$

$$K_{SC} \leq 25 \quad (Jg^{-1})$$

when $N < 4$.

In general, the aluminum bore tube should be designed so that $K_{bore} \leq 10\ Jg^{-1}$. Magnetic stress only becomes a problem when K_{SC} is greater than $20\ Jg^{-1}$. The only further restriction on the design is that the superconductor operating current be less than 75% of the superconductor critical current at the peak induction in the coil.

The resulting scaling is as follows: 1) For a given central induction the solid angle lost due to the coils and their support is a constant. 2) The solid angle lost goes as 1/D if one allows B_o to go down as $D^{-\frac{1}{2}}$. Both of the preceeding statements assume that the thickness of the superconducting coil package and its cryostat remain constant as D changes. Scaling probably does not apply when D is greater then 3 meters.

The scaling laws given here for lumped coil systems are approximate. Better scaling laws will result from the series of experiments now going on at LBL.

SUMMARY

Two basic types of detectors can be considered for use on PEP and other intersecting storage ring devices. Both will utilize solenoidal fields with flux paths parallel to the direction of the beams. One type, the conventional superconducting solenoid, permits physics to be performed only inside the coil in the magnetic field. The second type based on high current density technology permits physics to be performed both inside and outside the magnet coil.

Two kinds of high current density magnets can be considered. One is based on a continuous thin coil of uniform radiation thickness; the second is based on lumped coils which have regions of high radiation thickness and regions of near zero radiation thickness. For many experiments the high current density magnets could result in

substantial cost savings in both capital and operating funds. The central induction of such magnets is 2 T or less, and the maximum practical diameter is 2 to 3 meters.

Each of the two types high current density magnets has advantages for some kinds of experiments. If high central inductions and/or large field volumes are required, there is probably no practical alternative at this time to the conventional low current density superconducting solenoid. Since the performance parameters of the high current density magnets are not fully understood, experimental work now under way at LBL will establish the practical limits of operation for magnets using high current density intrinsically stable superconductors.

REFERENCES

A-1. Z. J. J. Stekly and J. L. Zar, "Stable Superconducting Coils", IEET Transactions, NS-12 (3), p. 367 (1965).

A-2. M. Morpurgo, "A Superconducting Solenoid Cooled by Forced Circulation of Supercritical Helium", CERN 69-25 (1969).

A-3. M. A. Green "The Large Superconducting Solenoid for the MINIMAG Experiment", to be published in the Advance in Cryogenic Engineering, LBL-3677, July 1975.

A-4. M. Alston-Garnjost, A. Barbara-Galtieri, O. Dahl, P. Eberhard, R. Kenney, A. Litke, G. Lynch, T. Mast, D. Miller, J. Nelson, S. Parker, M. Pripstein, R. Ross, B. Sadoulet, F. Solmitz, M. Stevenson, and D. Young, "A Proposal to Simultaneously Measure Charged Particles and Gamma Rays over a Large Solid Angle at SPEAR II," Lawrence Berkeley Laboratory Proposal, October 15, 1974.

A-5. W. L. Pope, G. F. Smoot, L. H. Smith, and L. H. Smith, and C. E. Taylor, "Superconducting Magnet and Cryostat for Space Application," in Advances in Cryogenic Engineering, Vol. 20, p. 47.

A-6. "Superconductivity Accelerates Cancer Research," in Cryogenics and Industrial Gases, August 1975, p. 15.

A-7. A Proposal to Study High $P_{\perp}$ Physics with a Large Aperture Hadron Spectrometer at the CERN ISR, British-American-Scandinavian ISR collaboration; CERN/ISRC 75-18, 12 May, 1975, CERN/ISRC 75-21, 25 June, 1975.

A-8. CERN Courier, "Villigen Superconducting Muon Channel Begin Operation,"(A Description of the Swiss Institute for Nuclear Research -- Supercritical Helium-cooled Solenoid) 15 (2): 36 (1975).

0 0 0 0 4 5 0 1 5 8 9

APPENDIX B

DESIGN CONSIDERATIONS FOR A LUMPED SOLENOID*

Klaus Halbach
Lawrence Berkeley Laboratory
University of California
Berkeley, California 94702

1. Introduction

This note is primarily intended to demonstrate which characteristics of a lumped solenoid (with a steel return path that may also be lumped) are important for good performance. This understanding is clearly necessary to make judgments about tradeoffs between qualities of the magnetic field and other desirable attributes of a particular magnet geometry. We also want to show the use of a methodology and some "thinking tools" that can help to obtain the good qualitative understanding of magnetic fields that is necessary for good magnet design, is indispensable for hand calculations, and should be the basis for magnetic field computer runs. While it is clear that it is not possible to say anything basically new along these lines, it seems worthwhile to formulate and state these concepts clearly, since they are not nearly as well known as they ought to be.

To accomplish the stated objective, we first describe the design problem and the general method used to solve it. We then introduce two analog models that often help to get a good qualitative understanding of magnetic fields. In addition, we derive and use a simple formula that can be useful for making quantitative estimates of some properties of magnetic fields. Finally, we apply these methods to the design of the lumped solenoid.

2. The Design Problem and the Methodology Used to Solve It

Fig. B-1 shows a cross-section of the magnet under discussion, with the center line (C_L) representing an axis of cylindrical symmetry. The vertical line at the left represents a symmetry plane. The cross-hatched area indicates the steel that is used to conduct the magnetic flux around the lumped solenoid of radius r_1, the part at the top of the drawing representing either a cylindrical shell or a cross-section through a "vane" in case one chooses to "lump" that part of the steel structure.

The design goal is the production of a reasonably uniform field over a volume that is not too strongly restricted in either the axial or radial direction. Furthermore the magnetic field should be small in a region outside the coils that begins not too far from the coils.

To understand and assess these problems we start with a discussion of the properties of an idealized magnet (infinite permeability μ, $r_2 = \infty$, steel everywhere to the right of the dashed line in Fig. B1) and then investigate one by one the effects of the modifications that have to be applied to the idealized magnet in order to obtain the real magnet.

3. Useful Tools and Concepts for the Discussion of Magnetic Fields

It is often quite easy to obtain a good picture of a magnetic field distribution by applying directly the magnetostatic equations, usually in integrated form ($\oint \vec{H}\cdot d\vec{s} = I$, $\oint \vec{B}\cdot d\vec{a} = 0$). However under some circumstances this procedure does not lead easily to a good qualitative feeling for the fields, particularly when one wants to know the fields close to a coil with steel in the vicinity. If the fields have cylindrical symmetry with no component in the azimuthal direction, or if the fields are of a two dimensional nature, the analog model of current flow in a two dimensional conductive sheet often gives the needed insight much more easily. Although this analog model has been used to physically model 2D magnets (B-1),this use is somewhat complicated in the cylindrical case, and the model is used here only as a conceptual aid. Similar comments apply to a slightly different analog model that we use to visualize magnet fields produced by magnetic charges. In both cases the same labels z, r are used for the Cartesian coordinates on the 2D conductive sheet and for the coordinates of the cylindrically symmetric magnets.

An expansion of 2D dipole fields into exponentials will be done in Sect. 3.3. Even though this may seem to be a rather specialized formula, its derivation is reproduced here not only because it is useful for the magnet under discussion, but is, in the authors opinion, the single most important and useful formula (after the magnetostatic equations) for the understanding and design of magnets.

3.1. The Orthogonal Analog Model (OAM)

Inspection of the magnetostatic equations in cylindrical geometry, and of the equations governing the current flow in a two dimensional conductive medium, shows the following relations: (see rows 1 and 2 of Table 1, and also Fig. B-2.

1) If one makes the resistivity $\rho(r,z)$ of the sheet proportional to $r\cdot\mu(r,z)$ (column 1), and

2) If one injects a current density $j_3(r,z)$ into the top surface of the conductive sheet that is proportional to the exciting current density, $j_\phi(r,z)$, in the magnet (column 2),

Then:

3) Scalar equi-potential lines in the model correspond to surfaces of constant rA (i.e., field

surfaces) in the magnet (column 3), and the vectors $\vec{H}$ and $r\vec{B}$ are obtained by rotating the 2D current density vector $\vec{j}$ and electric field vector $\vec{E}$ in the model by 90° (columns 6 and 7).

The table of equivalents for two dimensional magnetic fields is obtained by removing all factors r from Table B-1.

While this treatment of the permeability μ can be advantageous, it is often more convenient to treat finite permeability effects differently:

First μ is assumed to be infinite in order to obtain an understanding of the fields in the vacuum region. From this one learns how magnetic flux enters the steel, leading in turn to a qualitative understanding of the field lines in the steel, and at the steel-vacuum interface. Whenever a field line in the steel at that interface forms a non-zero angle α with the normal to the interface, a non-zero tangential field component $|\vec{H}_t| = \sin\alpha\ |\vec{B}|/\mu$ exists at that interface. Since that field component is continuous through the interface, it is this component that modifies the field in the vacuum region. Usually, the field produced by this tangential field component H_t is most easily understood if one replaces H_t by a current sheet of strength $I' = |\vec{H}_t|$ on the steel surface. It is easy to see that the current in this sheet points out of (into) the paper plane if the steel lies to the left (right) of the vector $\vec{H}_t$. The fields produced by these current sheets are in turn often most easily obtained by applying again the OAM.

3.2. The Direct Analog Model (DAM)

In discussing magnetic fields produced by magnetic charges (See Sect. 4.3), it is clear that scalar potentials can be used to describe the properties of the fields. In cylindrical geometry, the radial dependencies become clearer if one uses again a two-dimensional conductive sheet model with the appropriate conductivity and current injection. The equivalences between the quantities in the DAM and a cylindrical magnet are given in rows 2 and 3 of Table B-1, with σ representing the conductivity of the sheet, and q the magnetic charge density in the magnet.

3.3. Expansion of 2D-Dipole Fields into Exponentials

Fig. B-3 shows the cross-section of a magnet assumed to be sufficiently long in the direction perpendicular to the paper plane so that the fields can be considered two-dimensional. We assume further that the magnet has mid-plane symmetry and that $\mu = \infty$ in the steel. As a consequence, the fields are perpendicular to the steel surfaces and the midplane.

To find an expression for the fields that is suitable for our purposes and is valid in the region bounded on top and bottom by the flat part of the pole, we first look at, and graphically represent, how H_y depends on y for x = 0 (see Fig. 4): Since div $\vec{H} = \partial H_x/\partial x + \partial H_y/\partial y = 0$, and $H_x \equiv 0$ for $y = 0$ and $y = \pm g/2$, it follows that $\partial H_y/\partial y = 0$ for $y = 0$, $y = \pm g/2$. Mid-plane symmetry requires that H_y is an even function of y, and H_x is an odd function of y, leading qualitatively to functions H_x, H_y as shown in Fig. 4. It follows directly that both H_x and H_y are expandable into Fourier series with period g that should converge quite rapidly since both the functions and at least their first two derivatives with respect to y are continuous. Using the complex representation for these Fourier series, we then form the combination $H^* = H_x - iH_y$ and obtain, by combining the coefficients into a_n:

$$H^* = H_x - i\,H_y = \sum_{-\infty}^{\infty} a_n e^{2\pi n i y/g}. \qquad (1).$$

We have chosen the combination $H_x - iH_y$ because the magnetostatic equations for the vacuum field components H_x and $-H_y$ are the same equations as the Cauchy-Riemann conditions for the real and imaginary part of an analytical function of the complex variable $z = x + iy$. Since we have an explicit expression for the function H^* for the case $x = 0$, we obtain an expression for H^* for $x \neq 0$ by replacing in Eqn. (1) iy by $z = x + iy$. Because $H_x = 0$ in the mid-plane, the coefficients a_n must be purely imaginary. Since the deviations from a uniform field will get smaller as one moves from the left side (x=0) or the right side ($x = x_2$) of the magnet toward its center, the terms with $n < 0$ can contribute significantly only on the left side of the magnet, and those with $n > 0$ only on the right side. It is therefore convenient to rewrite Eqn. (1) in the following way:

$$H^* = i\left(h_0 + \sum_{n=1}^{\infty} h_{-n} e^{-2\pi n z/g} + \sum_{n=1}^{\infty} h_n e^{2\pi n (z-x_2)/g}\right). \qquad (2)$$

The h_n in this formula are real and h_0 represents the central field value.

It is clear from Eqn. (2) that deviations from a uniform field due to the truncation of the poles or by the manner in which the magnet is excited decay very rapidly if the pole edges are shaped in such a way that $h_{-1} = h_1 = 0$. That is, of course, what one does when one shims a pole. A very sophisticated pole contour would also make h_{-2} and h_2 zero, or very small compared to h_0, but trying to cancel higher orders would not be worthwhile. It should also be pointed out that the dependence of H_y on y can be used to measure the low order h_n with relative ease by using appropriately made stacks of measuring coils.

If the excitation of the magnet, or the truncation of the poles, violates mid-plane symmetry, one will also have midplane-antisymmetric fields. For such fields H_y is an odd function of y and H_x an even function of y. A consideration similar to the one made above gives for midplane-antisymmetric fields:

$$H^* = \sum_{n=-\infty}^{\infty} b_n e^{\pi(2n+1)z/g}. \qquad (3)$$

In this formula, the b_n are real, and one can write H^* of course in the same fashion as Eqn. (2). Comparison of Eqn.'s (2) and (3) shows that the most slowly decaying terms in Eqn. (3) decay only half as fast as the slowest terms in Eqn. (2). It should finally be pointed out that Eqn's (2) and (3) can

0 0 0 0 4 5 0 1 5 9 0

be applied to many magnets other than dipoles (e.g., strong focussing dipoles, quadrupoles, etc.) by conformally mapping them into dipoles.

4. Magnet Design Considerations

4.1. Properties of the Ideal Lumped Solenoid

The ideal lumped solenoid is (see Fig. B-1 characterized by $\mu = \infty$; by a steel-vacuum interface along the dashed line on the right side of Fig. 1; and by a cylindrical shell at $r_2 = \infty$ to conduct the flux entering along the dashed line around the solenoid.

For symmetry reasons, the distance between the left boundary of the problem and the center of the adjacent coil is g/2, and we assume the same distance between the dashed line and the center of the coil adjacent to it. This means that we are dealing with a periodic system of fundamental period length g, so that we need to treat only one cell, indicated by the dotted lines. Because of symmetry the magnetic field must be perpendicular to these lines. The line going through the center of the coil is also a line of symmetry, with the field perpendicular to it as well. To get a qualitative feeling for the fields in the cell, we use the OAM (see Sect. 3a). In it the dotted lines represent insulators, the space between them has a resistivity proportional to the distance r from the center line. The current injected over the cross-section of the coil flows in an easily imaginable pattern to the axis of the system, r = 0. While the current density in the OAM is quite non-uniform in the immediate vicinity of the coil, it will obviously smooth out very quickly as one moves toward the axis. A small fraction of the injected current will flow in the vicinity of the symmetry line radially outward, then turn toward the axial direction and, close to the dotted line, flow radially inward. It is quite apparent from this picture that the fields get weak very fast as one moves radially away from the coils. If one were dealing with two-dimensional fields instead of cylindrical fields, the expansion of 2D fields into exponentials (Sect. 3.3) could be directly applied and would yield the result that the dominant term in the description of the field for $r > r_1$, and of the inhomogeneity for $r < r_1$, is proportional to $e^{-2\pi|r-r_1|/g}$. A more detailed 2D model calculation shows that the constant of proportionality for the dominant term equals the average field value H_0 on axis. The fact that we are dealing with cylindrical geometry will obviously modify the details of the decays, but not their basic character. Using again the OAM to see qualitatively the difference between the decay in cylindrical geometry compared to 2D geometry, the fact that the resistivity in the model is proportional to r leads us to conclude that the field outside the coil decays a little faster than indicated above, whereas the field inhomogeneity inside the coil will decay a little slower.

4.2. The Effects Caused by Lumped Return Yokes

If we bring the return flux shell from infinity to a finite value r_2, we bring steel into a region where the pre-existing field is of the order $H_0 e^{-2\pi(r_2-r_1)/g}$. The resulting field modifications in that region will be of the same order, and their effect on the field at location r_1 will be cut down by another factor $e^{-2\pi(r_2-r_1)/g}$. We conclude from this that the effect at $r = r_1$ of moving the steel shell to a finite value r_2 is of order $H_0 e^{-4\pi(r_2-r_1)/g}$, i.e. in most cases negligible, provided $(r_2-r_1)/g > 1/4$.

If we now "lump" the return flux shell in the azimuthal direction into "vanes", the details of the field modification are more complicated. If we assume first that the endplates still extend to $r = \infty$, the periodicity in z is not affected by lumping the steel in the azimuthal direction. We therefore still expect field modifications at $r = r_1$ of the order $H_0 e^{-4\pi(r_2-r_1)/g}$, but there will be some dependence on azimuth. If we then reduce the radius of the endplates to $r = r_2$, there will be some additional field modifications. Although the periodicity in z is destroyed by this process, these additional fields will also be extremely small, since the pre-existing fields at the endplates for $r > r_2$ are very small for a reasonable number (≥ 6) of vanes. While it is not too difficult to pursue this argument in more detail, that treatment would go beyond the scope of this report.

If, for a given distance g between coils, it is necessary to obtain a decay of the fields that is faster than $e^{-2\pi(r-r_1)/g}$ outside the coils, one can accomplish this by putting vanes close to the coil and separating them in the azimuthal direction by a distance D somewhat smaller than g/2. Under these circumstances, eqn. 3 of Sect. 3.3 will approximately describe the decay of fields between vanes, giving there a most slowly decaying term proportional to $e^{-\pi\Delta r/D}$, with Δr representing the distance from the inside edge of the vanes. In this case, the proximity of the coils could cause local saturation problems in the vanes that would have to be studied in more detail than can be done here.

4.3. Effects Caused by Removal of Steel from Region 1

When removing the steel from region 1 (see Figure 1), i.e., the space between the dashed line and the actually desired steel contour, the field to the left of the dashed line will obviously be reduced over some distance. While this field reduction can be partially compensated by a coil close to steel surface α, the use of that coil does not accurately simulate the field modification caused by the removal of the steel. Instead, we use the following procedure: We first put a magnetic surface charge onto the steel-vacuum interface indicated by the dashed line to the left of region 1. If that surface charge equals the local surface magnetic field value B everywhere, removal of the steel does not change any magnetic fields. We therefore obtain the magnetic field modification everywhere by removing those magnetic charges or, equivalently, by adding the same charges with opposite polarity all along the dashed line to the left of region 1. To see the resulting fields, we use the DAM (see Sect. 3.2 and Table 1), with the vacuum region represented by a 2D sheet with conductivity propor-

tional to r, the steel modeled with perfectly conducting electrodes, and the added magnetic charges represented by current injection from the third dimension. Visualizing the resulting current density and electric field in the 2D sheet, it becomes evident that along the dashed line, the axial field component will be very close to 1/2 of the pre-existing value, and that there will be an increase of the fields all along the inside boundary of the endplate. It should be noted that the increase of the conductivity with r in the DAM indicates that the field modification far from the axis is smaller for cylindrical geometry than it would be in 2D geometry. If the hole that is opened up is comparable to the coil radius r_1, the fields outside the coils will clearly increase substantially in the end region.

4.4. Effects Caused by Removal of Steel from Region 2

To obtain a qualitative understanding of the field modifications resulting from removal of steel from region 2, we use the same technique as in section 4.3, and should, in fact, apply it simultaneously in the following way: first place appropriate magnetic charges all along the dashed line, remove the steel, and then place charges with opposite polarity on the dashed line and find the resulting fields with the DAM. Since in region 2 the new steel surface is quite close to the old one, most of the injection current in the DAM will flow to the electrode surface representing the new steel surface. Combining that with the fact that the pre-existing field behaves like $e^{-2\pi\Delta r/g}$, one can conclude that the removal of steel from region 2 has only a small effect on the field distribution.

Breaking the endplate into radial spokes is a more drastic modification. Its effect can be visualized also with the magnetic charge - scalar potential surface representation, and it is qualitatively clear that the effects are small provided one uses a reasonable number of spokes (≥ 6) and does not start the spokes closer to the coil than g/2.

4.5. Effect of Saturation of Steel

By providing sufficient amounts of steel, saturation of the vanes and the outer part of the endplate can be reduced to any desired level. In the region where the magnetic flux enters the steel one cannot add steel at will. Consequently saturation will occur there above a certain level of excitation, and we want to discuss only the field modification caused by saturation of this part of the steel structure. To do so, we use the method outlined in section 3.1.

It is clear that the flux entering the center part of the endplate (surface β) will produce field lines in the region bounded by surfaces α,β,γ, that are in the same general direction as surfaces α and γ. From this follows that the tangential field component at surfaces α and γ will be considerably larger than its value at surface β. Representing these tangential field components by current sheets, and looking at the polarities of the current in the solenoids, the fields, and the current sheets, it is clear that the current sheet at surface α has the same polarity as the solenoidal currents, and the current in the sheets at surfaces β and γ has the opposite polarity. We apply now the OAM to see the resulting fields and find the following: Saturation effects on surface α will increase the field in region 1 and its vicinity, while saturation effects on surfaces β and γ will reduce the field over a region that starts near the left edge of region 1 and has an axial size of the order of the outer radius of surface β.

The fields produced by saturation on surfaces β and γ will also have a considerable range in the radial direction. However, the increase of resistivity with r in the OAM indicates that the radial range of these fields is smaller than it would be in 2D geometry.

To keep the proper perspective, one has to remember that the saturation-produced fields are excited by exceedingly weak current sheets unless one drives the steel extremely hard.

REFERENCE

B-1. A. Asner, P. Bossard, Ch. Iselin, Proc. International Symposium on Magnet Technology, Stanford, 1965.

Table B-1. Equivalences Between Quantities In Cylindrical Magnet and Two Analog Models

		1	2	3	4	5	6	7
1	OAM	ρ	$-j_3$	V	-	-	$\vec{e}_3 x \vec{J}$	$\vec{e}_3 x \vec{E}$
2	Cyl. Magn	$r\mu$	j_ϕ	rA	rq	V	$\vec{H}$	$r\vec{B}$
3	DAM	σ	-	-	$-j_3$	V	$\vec{E}$	$\vec{J}$

DEFINITIONS:

ρ	= resistivity in the 2D sheet
σ	= conductivity in the 2D sheet
j_3	= current density injected into the top of the 2D sheet
$\vec{e}_3$	= unit vector perpendicular to 2D sheet plane
V	= scalar potential in 2D sheet
$\vec{J}$, $\vec{E}$	= current density and electric field in 2D sheet
j_ϕ	= excitation current density in magnet
q	= magnetic charge density in magnet
μ	= permeability of steel
A	= vector potential in magnet
$\vec{H}$,$\vec{B}$	= magnetic fields
r	= distance from axis

0 0 0 0 4 5 0 1 5 9 1

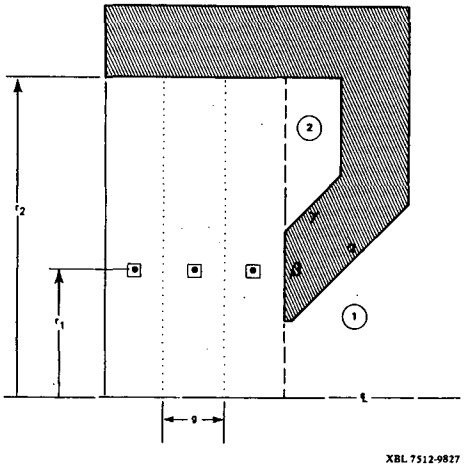

Fig. B-1. Lumped Solenoid Magnet

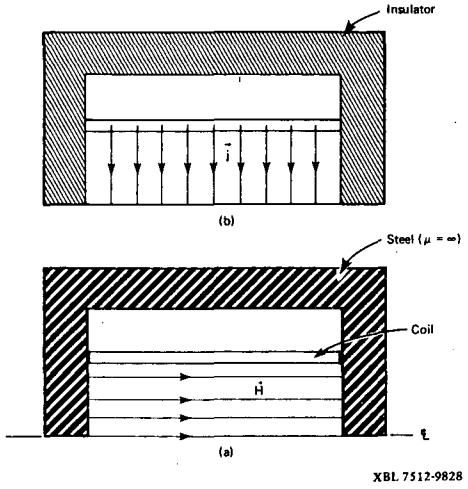

Fig. B-2. Continuous Solenoid in Steel Can
a) $\vec{H}$-Field in Magnet
b) $\vec{j}$-Field in OAM

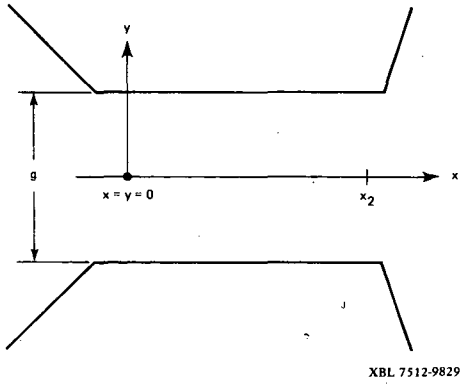

Fig. B-3. Dipole Cross Section

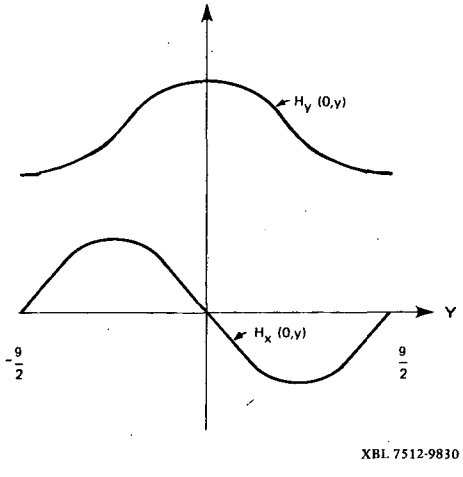

Fig. B-4. Dipole Field Components H_x, H_y vs. y.

USE OF DISCRETE COILS IN AXIAL FIELD SPECTROMETERS

John D. Taylor and W. A. Wenzel

Lawrence Berkeley Laboratory
University of California
Berkeley, California 94720

Abstract

A study of possible configurations for discrete coil axial field superconducting magnets has been carried out, with emphasis on parameters that affect magnetic field strength and uniformity as well as the fraction of open aperture which can be made available for external detectors. It is found that field uniformity is sufficiently good for most purposes if the coil separation is less than the coil radius. The ratio of field strength to fractional loss of open aperture is independent of size for suitably large magnets, but is sensitive to the shape of the coil cross-section.

INTRODUCTION

There are some important advantages in the use of discrete rather than continuous coil units in an axial field spectrometer for a colliding beam facility.[1] Assuming that a large fraction of the aperture can be left clear, i.e., with at most a few percent of a radiation length of material, these advantages are:

1. Secondaries passing through the open aperture are more reliably identified because there is no absorption in the coils. This is most important for charged hadrons.

2. Secondaries passing through the open aperture are more accurately measured by calorimetric methods because there is no absorption in the coils. This is important for hadrons, γ's and e's.

3. Seconardies passing through the open aperture may be more accurately measured in momentum because the resolution obtainable with precision detectors outside the magnet is not limited by coulomb scattering.

4. Backgrounds from interactions in the coils are absent in the open aperture. This circumstance can be used to prepare a cleaner event trigger.

Disadvantages of the open magnet structure are:

1. Because the field is non-uniform, algorithms for the reconstruction of events are more complicated than for the continuous coil.

2. For a given average field the discrete coil solenoid has a larger maximum field than does the continuous solenoid. Therefore, the amount of superconductor needed is larger for the discrete coil solenoid.

3. The support structures for the magnet and cryostat are more complicated than for the continuous solenoid.

This report is a study of the magnetic and aperture characteristics of discrete coil spectrometers. We are not concerned with detector design; rather we will examine particularly the parameters that affect the strength and uniformity of the magnetic field and the amount of open aperture between coils.

GENERAL DESIGN CONSIDERATIONS

General procedures for the design of superconducting coils with materials of the type considered for use here are discussed in a series of reports by M. A. Green.[2] For each coil intrinsically stable superconductor with a relatively high superconductor to copper ratio would be wound on and epoxy-bonded to an aluminum frame. Closed circuit refrigeration would employ two-phase helium in cooling tubes welded to the frame. The conductor would be tightly coupled electro-magnetically to the aluminum, which, in the event of a quench would act as a high conductivity shorted turn to dissipate most of the stored energy of the magnet in a time of some seconds. This process also would distribute widely the thermal energy, causing the quench to spread. Because of these effects, large local voltage buildup in the superconducting coil would be avoided.

Figure 1 shows schematically possible magnet configurations of the type considered. The coils are held together by axial support members with 45-degree symmetry. The thin vacuum windows are supported by a periodic support structure lined up with the coils and the axial coil support members. The cooling tubes are not shown. Two kinds of coil cross-sections, rectangular and elliptical, are considered. For reasons of simplicity and cost we will want to use modular elementary units; but it is obvious that the use of several units of different cross-sections can reduce considerably the loss of aperture. Examples are shown in Fig. 1(b) and (c).

MAGNETIC FIELD

We have studied the field configuration for a half-cell with the geometry shown in Fig. 2. We have used TRIM[3] to find the distribution of the field for nine combinations of dimensions using

$$\frac{R_{fe}}{R} = \begin{matrix} 1.1 \\ 1.2 \\ 1.5 \end{matrix}, \qquad \frac{Z}{R} = \begin{matrix} 0.4 \\ 0.6 \\ 1.0 \end{matrix}. \qquad (1)$$

0 0 0 0 4 5 0 1 5 9 2

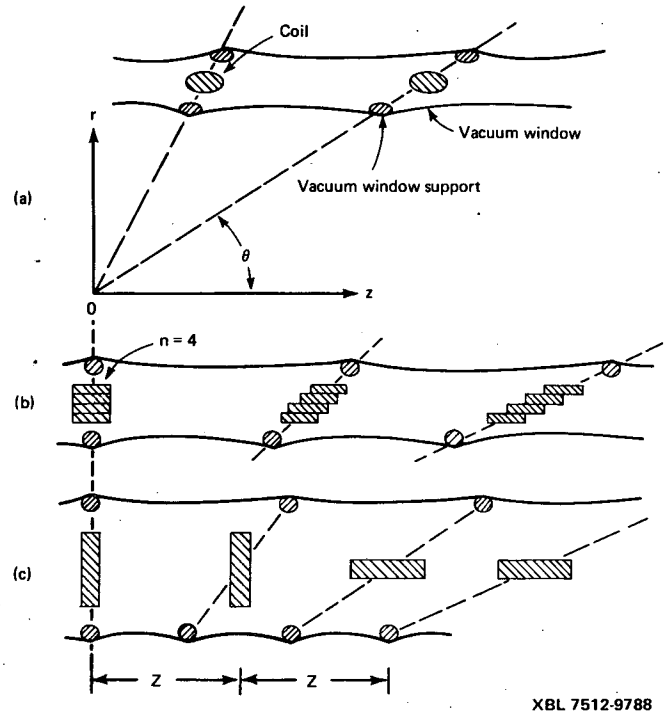

Fig. 1. Schematic of possible coil configurations. a) Single coil module; b) Compound coil structure. n is the number of radially displaced subunits. c) Alternative coils at different polar angles. Z is the separation between coil packages.

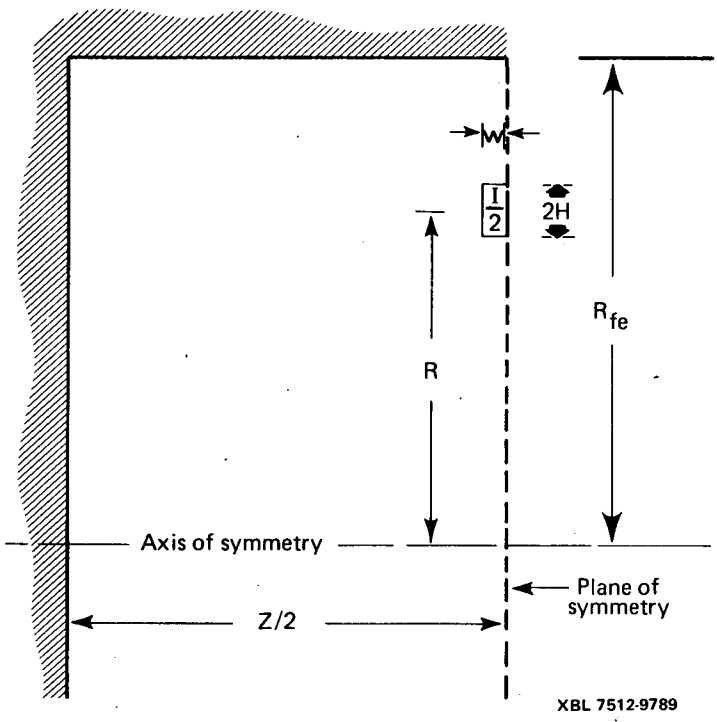

Fig. 2. Dimensions of half-cell studied using TRIM. R and R_{fe} are the radii of coil and iron return yoke, respectively. 2W and 2H are the axial and radial widths of the coils, respectively. S is the coil area. I is the current per coil. The permeability of the iron is taken to be infinite. Z is the distance from the center of the coil to the center of its virtual image in the iron poletip and is the effective coil separation in a multicoil system.

In each case the coil dimensions were

$$\frac{W}{R} = \frac{H}{R} = 0.05 \ .$$

R, R_{fe}, Z, W, and H are defined in Fig. 2. The permeability of the iron was set equal to ∞. For parameters sensitive to the details of coil shape and size we have used approximate analytic expressions.

Field Uniformity

In an axially symmetric field, assumed for the purposes of this study, the important field quantity for measuring particle transverse momentum over radial range r is $B_0 r^2/2 = r\,A_\phi$, where A_ϕ is the vector potential. Figure 3 shows how this quantity can be used to infer the particle transverse momentum in terms of the slope of the trajectory at r and the dispersion at the axis.

In general for axially symmetric fields

$$p_\phi + 0.3\,A_\phi = \text{const.} \qquad (2)$$

where p_ϕ is the momentum in GeV/c and A_ϕ is in T-m. For particles passing through the axis

$$p_\phi + 0.3\,A_\phi = 0. \qquad (3)$$

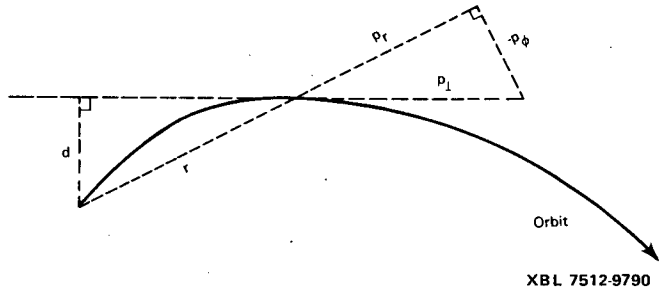

Fig. 3. Projected orbit. In terms of the dispersion d at the axis, the transverse momentum $p_\perp$ is given in terms of the vector potential.

In terms of the transverse momentum it is obvious from Fig. 3 that

$$\frac{d}{r} = -\frac{p_\phi}{p_\perp} \quad \text{or} \quad p_\perp = \frac{0.3\,rA_\phi}{d} \qquad (4)$$

Figure 4 shows the extent of the variation in rA_ϕ with Z at various radii. The effect of the steel return yoke is seen to be small for fields inside the coils, but it is relatively important outside. The non-zero radial width of the cryostat prevents detectors from being located very near the coils, hence the results shown in Fig. 4 should be reasonably independent of coil size and shape.

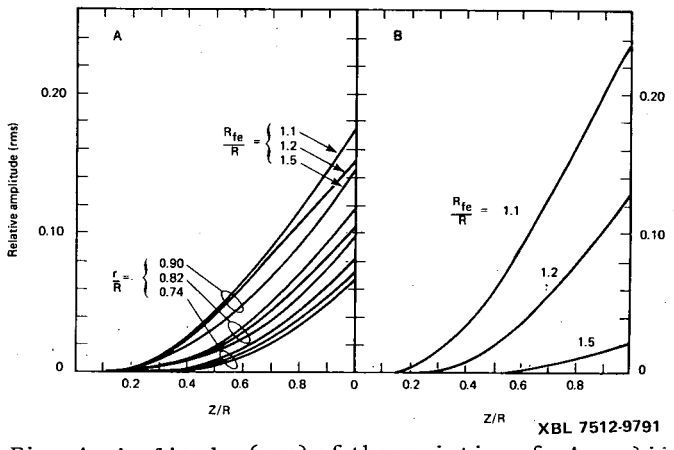

Fig. 4. Amplitude (rms) of the variation of rA_ϕ. a) inside coil and b) at surface of iron return yoke. Plotted data assumes

$$\text{Amplitude (rms)} = \frac{rA_{max} - rA_{min}}{\sqrt{2}(rA_{max} + rA_{min})} .$$

Stored Energy

For a thin continuous solenoid the stored energy per cm length is given by

$$E_0(\text{ergs}) = \frac{B_o^2 R^2}{8} \text{ (emu)} \qquad (5)$$

where the average axial magnetic field B_o is given by

$$B_o = 4\pi \frac{dI}{dz} \text{ (emu)}. \qquad (6)$$

The average axial field in the case of discrete coils is given by

$$B_o = 4\pi \frac{I}{Z} . \qquad (7)$$

The stored energy E for discrete coils of the same radius be written in terms of the ratio

$$\frac{E}{E_0} \equiv e \equiv e_0 + \Delta e \qquad (8)$$

where e_0, which was evaluated using TRIM, depends primarily on the ratio Z/R, and Δe depends on coil size and shape. We have estimated Δe analytically, under the conditions that

$$\left(\frac{W}{Z}\right)^2 \ll 1, \left(\frac{H}{Z}\right)^2 \ll 1, \left(\frac{W}{R}\right)^2 \ll 1, \left(\frac{H}{R}\right)^2 \ll 1,$$

using the field distribution for a circular coil cross-section. This gives

$$\Delta e \approx \frac{Z}{2\pi R} \ln \frac{S_0}{S} \qquad (9)$$

where S is coil area and S_0 is the area used in obtaining e_0 from TRIM. We have neglected the effect of the iron in the small term Δe. Figure 5 shows e_0 and Δe as functions of Z/R and S_0/S.

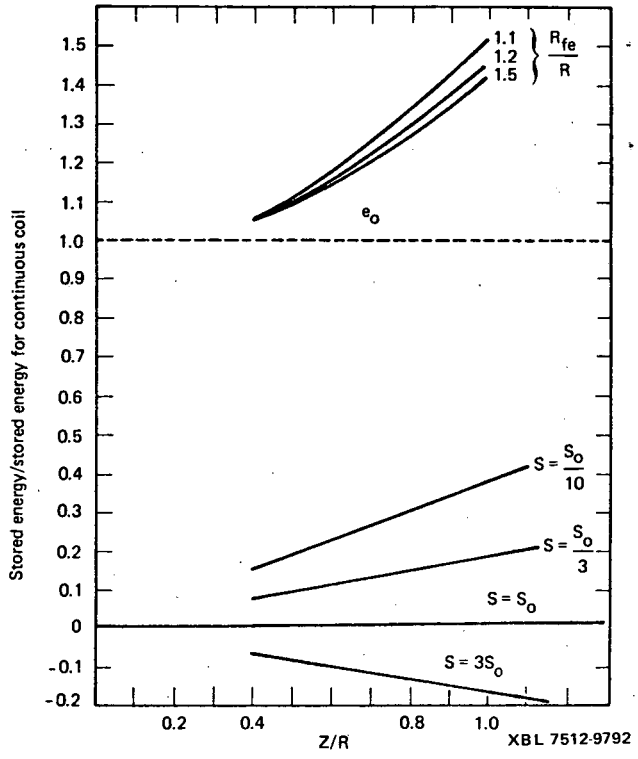

Fig. 5. Stored energy $e = e_0 + \Delta e$. e_0 is the volume integral of the energy density for a rectangular coil of area $S_0 = 0.01R^2$. Δe is the incremental change in stored energy for a coil of area S. $\Delta e = (Z/2\pi R) \ln (S_0/S)$. The curves are accurate only for $Z \gg 2W$.

Maximum field on Coil

The maximum current density in the superconductor is limited by the maximum field on the coil, which for symmetric coils occurs at the inside center surface. The field here, relative to the central field is given by

$$\frac{B_m}{B_0} \equiv m \equiv m_0 + \Delta m \qquad (10)$$

where we neglect the effect of the iron, which is shown in the cases considered by TRIM to be $\lesssim 10$ per cent. Under the conditions

$$\left(\frac{W}{R}\right)^2 \ll 1, \left(\frac{H}{R}\right)^2 \ll 1, \left(\frac{Z}{4R}\right)^2 \ll 1$$

$$m_0 \approx \frac{1}{2} + \frac{1}{\sqrt{4\pi}} \frac{Z}{\sqrt{S}} F + \frac{1}{\pi} \tan^{-1} \sqrt{\frac{4}{\pi}} \frac{\sqrt{S}}{Z}$$

$$\Delta m \approx \frac{Z}{8\pi R} \ln \left(1 + \frac{\pi}{4} \frac{Z^2}{S}\right) \qquad (11)$$

0 0 0 0 4 5 0 1 5 9 3

where F is a form factor for coil shape which depends only on the ratio W/H. See Figs. 6 and 7. For rectangles

$$F = \sqrt{\frac{W}{\pi H}}\left[\frac{2H}{W}\tan^{-1}\frac{W}{2H} + \frac{1}{2}\ell n\left[1 + \left(\frac{2H}{W}\right)^2\right]\right] \cdot (12)$$

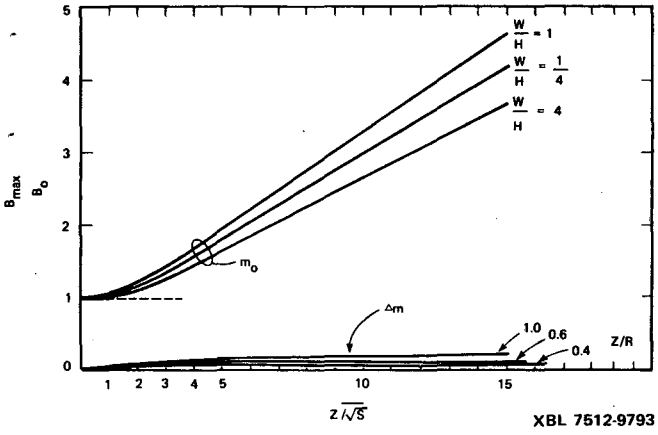

Fig. 6. Maximum field on rectangular coil (inside center) relative to central field for different aspect ratios of coil cross-section. (See Fig. 2). The field ratio $m \equiv m_0 + \Delta m$.

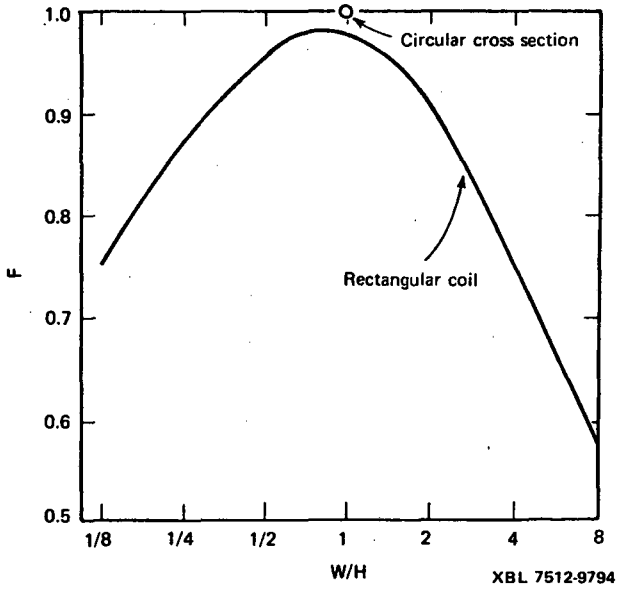

Fig. 7. Form factor for coil.

This is shown in Fig. 7. Obviously, a relatively smaller field on the coil or a higher central field can be obtained if the coil shape is extended either axially or radially.

For ellipses in general we have not calculated F. The W/H dependence will be similar to that for rectangles, however, and may be normalized to the case for circular cross-section (F = 1) shown in Fig. 7.

SUPERCONDUCTOR

For purposes of this study the use of an intrinsically stabilized material like Supercon 252E9, with copper to s/c ratio about 1:1, containing about 3000 strands of superconductor, is assumed. The critical B-i characteristic[2] is shown in Fig. 8. We assume also that the magnet operating point will lie on the dashed line, derived by reducing by a factor of 2 both field and current from the short sample characteristic. This conservative position allows us in what follows to neglect the space lost to insulation and to make the slightly optimistic assumption that the superconducting material is distributed uniformly within the coil area.

In the region of interest the magnet B-i characteristic may be approximated by a straight line, i.e.,

$$B_m = B_c - 3\,i \qquad (13)$$

where $B_c = 5.25\times10^4$G and -3 is the slope in emu. The load line slope is given by

$$\frac{B_m}{i} = \frac{B_m}{B_0}\,\frac{B_0}{i} = \frac{4\pi m S f}{Z} \quad (\text{emu}) \qquad (14)$$

where f is the fraction of the cross-sectional area of the coil occupied by superconductor. 1-f is the fraction of aluminum. Solving (13) and (14) we find for the operating current

$$i = B_c\left(3 + \frac{4\pi m S f}{Z}\right)^{-1} \quad (\text{emu}). \qquad (15)$$

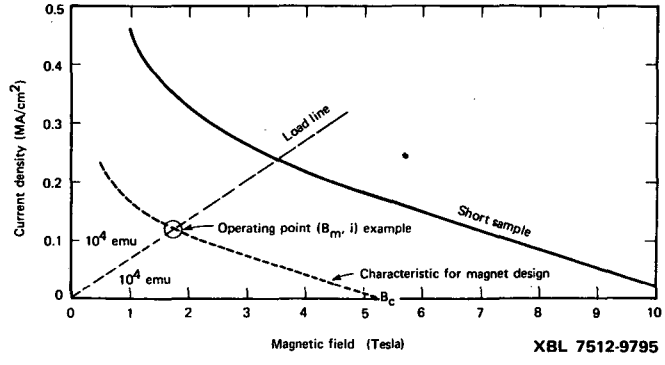

Fig. 8. Current-field characteristics. The solid curve is from Ref. 2 for SUPERCON 252E9. The dashed characteristic is taken to be the locus of operating points for a magnet. The load line is of the form $B_m/i = 4\pi Sf/Z$, for which the parameters are defined in the text.

The central field B_0 is given by

$$\frac{B_c}{B_0} = \frac{Z\,B_c}{4\pi i S f} = \frac{3Z}{4\pi S f} + m \qquad (16)$$

where Z is in cm and S in cm^2.

DECAY TIME CONSTANT

It is essential that immediately following a local quench the decay time of the magnet current be long enough that the energy dissipated in the coil forms has time to raise the coil temperature elsewhere, causing a general quench. The decay time constant is given by

$$\tau = \frac{\text{Inductance}}{\text{Resistance}} = \frac{2E}{\text{Power}} = \frac{e\,E_0\,S(1-f)}{\pi\rho R\,I^2}$$

$$= \frac{2\pi R\,e\,S(1-f)}{\rho Z} \qquad (17)$$

where τ is in ns and resistivity ρ is in ohm-cm. Solving for S

$$S = \frac{\tau\rho\,Z/R}{2\pi(1-f)\,e}. \qquad (18)$$

In practice the resistivity depends sensitively on purity, fabrication and heat treatment.

TEMPERATURE RISE

In a quench essentially all the stored energy goes eventually into heating the superconductor and coil frame. In terms of the (volume) heat capacity and the initial and final tempertures

$$\int_{T_0}^{T_f} C_{eff}\,dT = \frac{\text{Stored energy}}{\text{Coil volume}} = \frac{B_0^2 RZe}{16\pi S}\left(\frac{\text{ergs}}{cm^3}\right) \qquad (19)$$

where B_0 is in Gauss.

C_{eff} obviously depends on f. C_V, shown in Fig. 9, is a composite for aluminum and copper (used for the superconductor), as is the integral, defined by assuming that the temperature dependence of the heat capacity is the same for copper and aluminum so that

$$\text{Energy density} = (1.5 + f)\int_{T_0}^{T} C_V\,dT = \frac{B_0 RZe}{16\pi S}. \qquad (20)$$

LOSS OF APERTURE

In terms of the various dimensions defined in Fig. 2, the fractional aperture loss in θ, defined as the opacity O, is given by

$$O = \frac{\sqrt{S}}{Z} K \qquad (21)$$

where K is a function of the ratio $\frac{W}{H}$ and the polar angle θ.

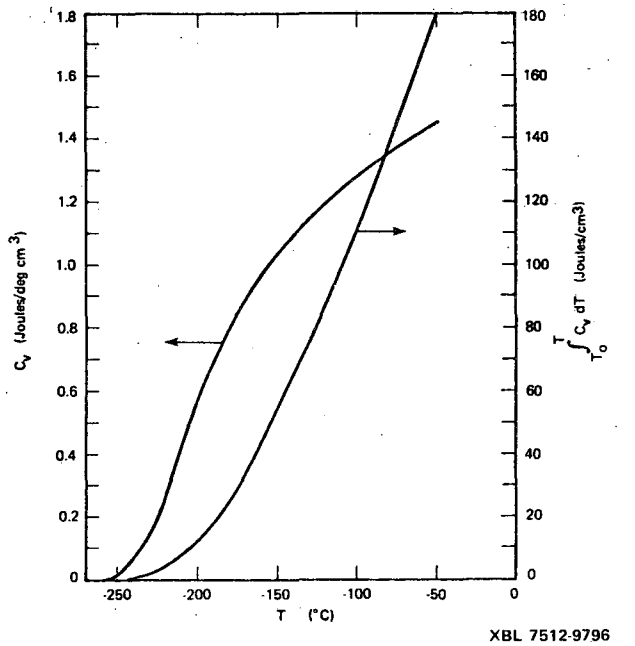

Fig. 9. Heat capacity and final energy density in coil. Effective heat capacity for coil with superconductor fraction f is $C_{eff} \approx (1.5 + f)C_V$. The temperature rise is given in terms of energy density = $(1.5 + f)\int_{T_0}^{T} C_V dT$.

For ellipses, $K = \left[\frac{4}{\pi}\left(\frac{W}{H} + \frac{H}{W}\cot^2\theta\right)\right]^{\frac{1}{2}}$.

For rectangles, $K = \sqrt{\frac{W}{H}} + \sqrt{\frac{H}{n\,W}}\cot\theta$. (22)

n is the number of subunits into which a compound rectangular coil is divided (see Fig. 1(b)). Figure 10 shows K as a function of various angular variables, including solid angle, rapidity

and $L \equiv \cos\theta + \frac{\cos^3\theta}{3}$.

Using only Fig. 10 we would tend to emphasize small values of W/H for large solid angle, and large values of W/H for a detector sensitive to a wide range in L and η. With the compound coil or with two or more different coil shapes (see Fig. 1(c)) optimization over a wider range for cot θ is possible.

CHOICE OF MAGNET PARAMETERS

There are many experimentally sensitive factors that need to be taken into account in the design of the magnet. The important ones considered here are:

1. Field uniformity
2. Field strength or momentum resolution
3. Opacity.

Figure 4 shows that field uniformity depends sensitively and almost exclusively on the ratio Z/R. Uniformity deteriorates rapidly for $Z/R \gtrsim 1$.

0 0 0 0 4 5 0 1 5 9 4

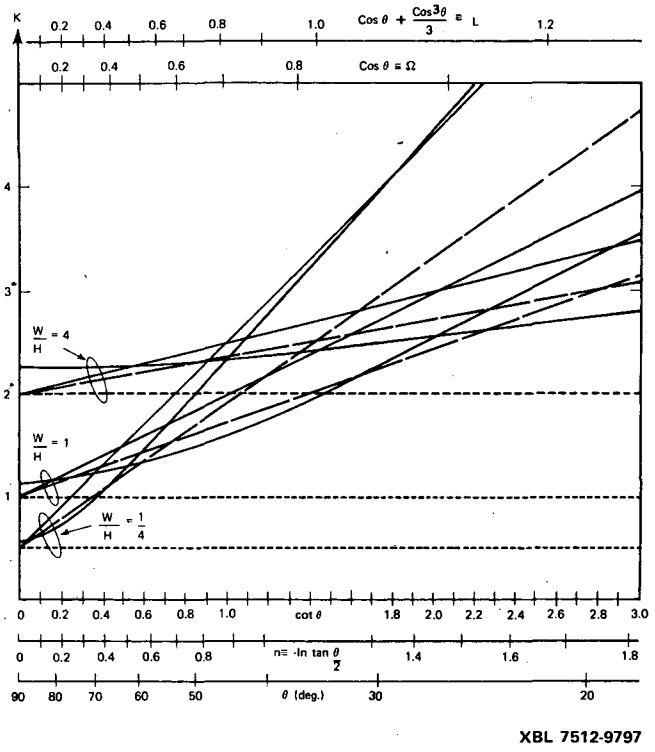

Fig. 10. Form factor K for loss of aperture. For rectangles (straight lines in figure) and ellipses (curved lines) see Eq. 22 in text. n is defined in Fig. 1 for rectangles. Solid lines are for n = 1, dashed lines are for n = 2, and dotted lines are for n = ∞.

From (11), (16), and (21) we see that magnetic field and opacity have similar dependences on Z and S, so that a trade-off between momentum resolution and open aperture is necessary. To study this in more detail we define a figure of merit to be the ratio of the magnetic field to the opacity.

$$(\text{MERIT})^{-1} \equiv \frac{O}{B_0} = \frac{K}{B_c}\sqrt{\frac{S}{Z}}\left(\frac{3Z}{4\pi Sf} + m\right) \qquad (23)$$

Using (11)

$$\frac{O}{B_0} = \frac{K}{\sqrt{4\pi}B_c}\left[F + \sqrt{\frac{\pi S}{Z}} + \frac{3}{f\sqrt{4\pi S}} + \right.$$

$$\left. \frac{1}{Z}\sqrt{\frac{4S}{\pi}}\tan^{-1}\frac{1}{Z}\sqrt{\frac{4S}{\pi}} + \frac{1}{4R}\sqrt{\frac{S}{\pi}}\ln\left(1 + \frac{\pi Z^2}{4S}\right)\right]. \qquad (24)$$

The last two terms are negligible. The second and third terms are optimized (i.e., minimized) for $S = S_m$, where

$$S_m = \frac{3Z}{2\pi f_m} \quad . \qquad (25)$$

Substituting (25) in (24) we obtain in general

$$\frac{O}{B_0} \approx \frac{K}{\sqrt{4\pi}B_c}\left[F + \sqrt{\frac{3}{2Zf}}\left(\sqrt{\frac{S}{S_m}} + \sqrt{\frac{S_m}{S}}\right)\right] \qquad (26)$$

This function is shown in Fig. 11. $\frac{O}{B_0}$ is

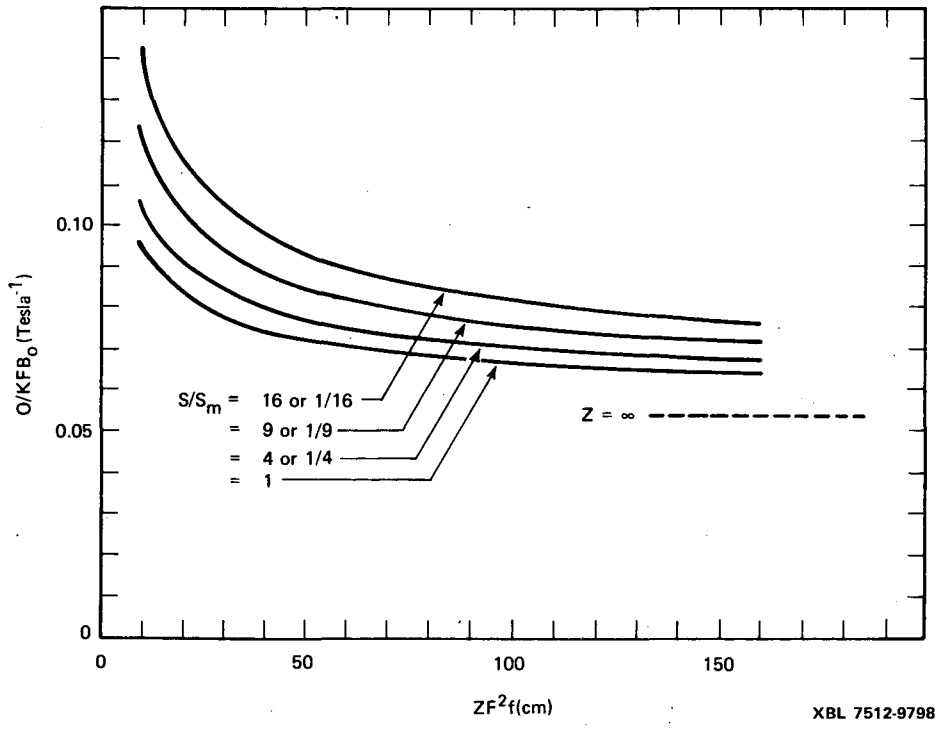

Fig. 11. Ratio of opacity to magnetic field strength vs coil separation. Parameters are defined in the text.

insensitive to the ratio S/S_m and to the size of the magnet for $ZF^2f \gtrsim 50$ cm. The loss of aperture is very sensitive, however, to F and K. For $KF \approx 4/3$ we see that the loss of aperture is about 10% per Tesla of central field.

From (18) and (25) we may determine

$$f_m = (1 + R_t/eR)^{-1} \qquad (27)$$

where we define

$$R_t \equiv \tau\rho/3. \qquad (28)$$

For τ = 3 seconds, $\rho = 10^{-7}$ ohm-cm (1/30 the room temperature value), we find R_t = 100 cm.

For a minimum of the ratio O/B_0, the magnetic field, as determined from (16), (25), (27) and (28) is

$$\frac{B_c}{B_0} = 1 + F\,[Z/6(1 + R_t/eR)]^{\frac{1}{2}}. \qquad (29)$$

Figure 12 shows B_0 for different values of R_t under this minimum condition. These fields are in the interesting range for PEP spectrometers. Taking advantage of the insensitivity of O/B_0 to S/S_m, the area of the coil can be varied to control the design field over a suitable range. Note that the maximum attainable field under the minimum condition decreases with the radius of the magnet approximately as $R^{-\frac{1}{2}}$. In terms of momentum resolution, which, in the absence of coulomb scattering, varies as B_0R^2, the performance, therefore, goes as $R^{3/2}$.

Another constraint is provided by the energy density allowable in the coil. Equation (20) may be rewritten

$$(1.5+f) \qquad \int_{T_0}^{T} C_v dT \equiv W \geq \left(\frac{KB_0}{O}\right)^2 \frac{eR}{16\pi Z} \quad \text{or}$$

$$\frac{B_0}{O} \leq \frac{2.24}{K}\sqrt{\frac{WZ}{eR}} \text{ Tesla} \qquad (30)$$

where W, in Joules/cm^3, is the maximum allowable energy density.

This constraint is similar to that given by (26), except that it provides a (not very sensitive) lower limit on acceptable values of Z/R. Although

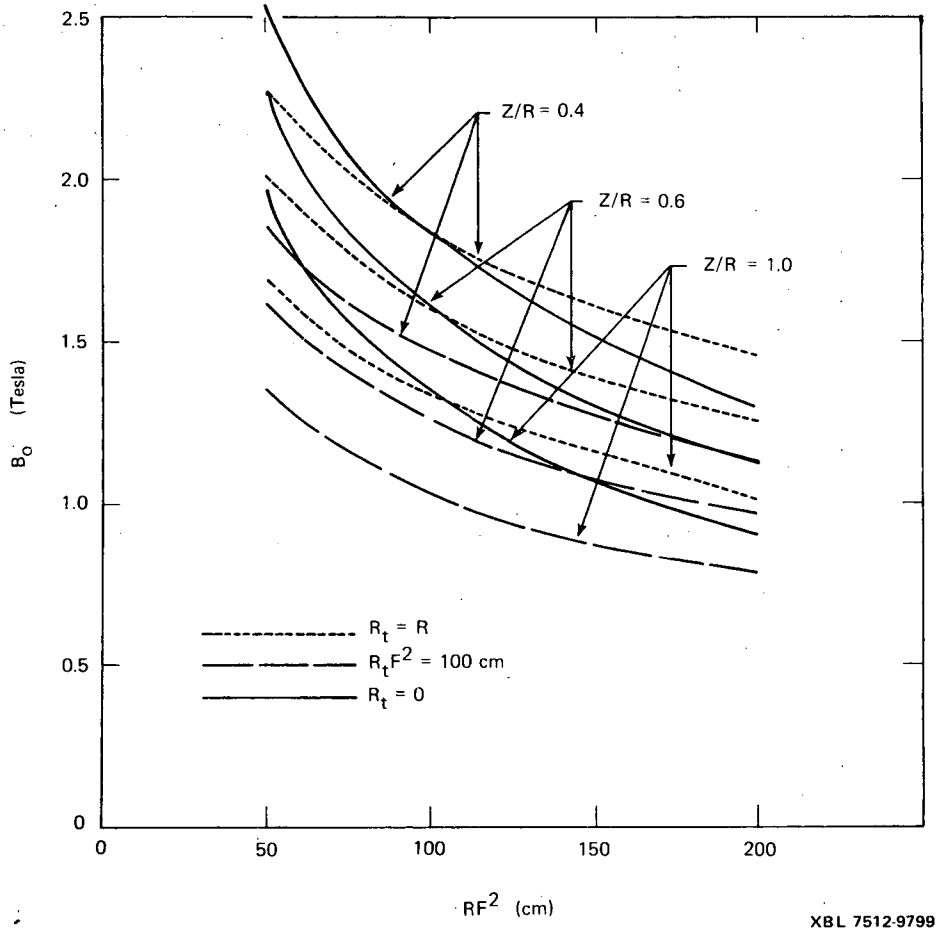

Fig. 12. Magnetic field obtained under conditions that maximize the ratio of field strength to opacity. The parameters are defined in the text.

0 0 0 0 4 5 0 1 5 9 5

for present purposes W is somewhat arbitrary, we note that for W = 200, T = - 100 degrees centigrade. And for Z/R = 0.4, K = 2, this gives

$$\frac{O}{B_0} \approx 0.1 \text{ Tesla}^{-1} \qquad (31)$$

similar to the range established in (26) by the magnetic properties of the superconductor.

In summary, reasonable field uniformity requires that the coil separation not exceed the coil radius. With currently available superconducting material, the ratio of aperture loss to field strength is asymptotically minimized at about 10% per Tesla for coil separations greater than about 50 cm. The conditions on field uniformity and aperture loss per Tesla are, therefore, well satisfied for magnets in the range of interest of PEP spectrometers. The characteristics related to momentum resolution and aperture improve rapidly with magnet size, because (in the absence of coulomb scattering) resolution involves a factor of R^2 times the magnetic field. Coil shape is an important parameter in the optimization of a given magnet configuration.

Assuming that coils with the properties implied here could be built, the total amount of material required would be small. From (25) and (27), for example, we find that, under the minimum condition, the average radial thickness $\bar{t}$ of coil material is given by

$$\bar{t} = S_m/Z = (3/2\pi)\ (1 + R_t/eR)\,. \qquad (32)$$

For $R \gg R_t$, this gives a thickness of about one-half cm or one-third radiation length.

In this report we have ignored many engineering considerations. We have not considered the loss of aperture from the axial coil supports. It appears that this loss will be comparable with that from the coils themselves. The determining factors are primarily structural. Other factors affecting the choice of magnet parameters are detector volume, time of flight, diameter of beam pipe, cost and problems of fabrication. We have considered none of these.

We are indebted for a number of essential discussions to P. H. Eberhard, M. A. Green, and E. S. Groves.

REFERENCES

1. A Proposal to Study High $P_\perp$ Physics with a Large Aperture Hadron Spectrometer at the CERN ISR, British-American-Scandinavian ISR collaboration; CERN/ISRC 75-18, 12 May, 1975, CERN/ISRC 75-21 25 June, 1975.

2. Michael A. Green, Cryogenic Engineering Conference, Kingston, Ontario, Canada, July 22-25, 1975. LBL-3677. Also M. A. Green, Mechanical Engineering Note, Code AB0103, Serial M4833, 28 May, 1975.

3. J. S. Colonias, TRIM: A Magnetostatic Computer Program for the CDC 6600, UCRL-18439, August 29, 1968.

THE STUDY OF NEUTRAL PARTICLES

W. Bartel, F. Bulos, A. Eisner, G. Hanson, D. Hitlin, U. Koetz,
R. Kotthaus, D. Luke, M. Marshak, T. Mast
J. Matthews, C. Peck, K. Strauch, D. Yount

Summary

The range of physics problems for which a detector emphasizing neutrals is most suitable is discussed. The primary goals are the all neutrals cross section, $\sigma_o(e^+e^- \to \text{neutrals})$, the characterization of the neutral energy in multi-hadronic events, the search for monoenergetic photons, and good sensitivity in the difficult region of low energy photons.

Those features of multi-hadronic events which are most relevant to a neutral detector have been calculated using a jet model with parameters extrapolated from SPEAR energies. These distributions are presented and discussed.

I. WHAT TO STUDY

Much less is known about the properties of the neutral particles emitted in high energy reactions than about the properties of the charged particles. The reason is obvious: neutral particles are harder to detect and their properties are more difficult to measure. The neutral energy can appear in the form of photons (decay and single*), neutrons, neutral kaons, and neutrinos. In e^+e^- (and $\gamma\gamma$) reactions, most of the emitted neutral energy is believed to be electromagnetic and primarily from π^o and η^o decays; little is as yet known about the overall importance of the recently discovered single photon emission process. Thus, detectors emphasizing the measurement of photons are needed for the study of the nature of the neutral energy. Neutron and K_L^o detection is desirable for some of the detailed investigations, and may be important at the highest PEP energies.

What is our present knowledge of the neutral energy emitted in $e^+e^- \to$ hadrons, and what questions arise? First, there is essentially nothing known experimentally about the contribution to $\sigma_t(e^+e^- \to \text{hadron})$ of all neutral final states, since present measurements of σ_t rely on a two-charged-particle trigger. The all neutral contribution, σ_o, is believed small because the obvious reactions $e^+e^- \to p\pi^o + q\eta^o$ $(p,q = 1,2\ldots)$ are forbidden by charge conjugation symmetry to first order in the electromagnetic coupling. However, other reactions such as $e^+e^- \to \gamma + p\pi^o + q\eta^o$, $n + \bar{n} + p\pi^o$, etc., are allowed, and remembering that the e^+e^- annihilation process has shown unexpected behavior before, we believe it is important to make direct experimental tests for these possibilities.

A direct approach to the measurement of both σ_t and σ_o is the calorimetric method using a total energy trigger. This was emphasized by Feldman and Hitlin[1] for PEP, and an implementation of it was proposed at SPEAR.[2] Such an apparatus must contain sufficient matter to absorb most of the energy of the final state particles, both charged and neutral, must cover essentially 4π solid angle, and must have high efficiency for detecting the presence of charged particles to isolate the all neutral events. Since all γ detectors (except pair spectrometers) involve a considerable amount of matter, it is natural to incorporate calorimetry and high resolution photon detection in the same apparatus. Considering the importance of the value of σ_t it seems very desirable to measure it by both magnetic and calorimetric methods since they have different biases. Calorimetry is the only practical method we know of for measuring σ_o and this component of σ_t may contain resonances or threshold steps which are hard to observe in σ_t itself.

It has been found[3] at SPEAR that about half of the total energy available when two or more charged particles are detected is emitted as neutral energy. What is the nature and what are the properties of this neutral energy? There are many detailed questions whose answers are expected to be very interesting.

(a) What fraction of the energy is emitted as π^o's, as η^o's, as single γ's, as neutrons, as other neutral particles? How do these fractions vary with energy? Are there resonances or threshold steps?

(b) What are the inclusive spectra of γ's, π^o's, η^o's, and other neutral particles? How do they compare with the charged particles?

(c) Are there other monoenergetic photons in addition to those recently discovered?[4] In cascade decays involving more than one γ, what is their time order of emission?

All of these experimental questions are as important for the 2γ processes as they are for the e^+e^- annihilation.

Depending on the detailed design of the apparatus, other processes can be studied at the same time. In all neutral detectors sensitive to eletromagnetic showers, these would range from the standard QED reactions $(e^+e^- \to e^+e^-, \gamma\gamma, e^+e^- \gamma)$ to a search for heavy electrons $(e^* \to e\gamma)$. The inclusion of a magnet to provide charged particle momentum measurements adds another range of physics involving identification of charged hadrons in the final state, their correlation with the neutrals, and the complete reconstruction of some classes of final states. And, of course, everybody is looking hard for new, unexpected phenomena, and we are excited by the prospects of a detector with sensitivity in an unexplored region.

---

*By single photons are meant photons emitted in transitions between hadronic states.

0 0 0 0 4 5 0 1 5 9 6

II. HOW TO STUDY

It is very much easier to write down the interesting features of the neutral energy than to devise a practical apparatus which has all of the desirable features. In practice, compromises must be made involving performance, complexity, and cost so as to optimize the study of particular areas. The 1974 PEP Summer Study report contains a very useful summary of the properties of photon detectors[5] and of the design considerations involved.[6]

Since everyone expects most of the neutral energy to be electromagnetic, the neutral detection schemes we have considered first concentrate on electromagnetic energy detection, with neutron and K_L^0 detection added on in one case, and magnetic detection in the other. We recognize that a general detector will surely provide some neutrals detection, but we expect practical considerations to limit its energy resolution. Our aim was to provide a more specialized capability complementary to a general detector. Since the 1974 Summer Study there has been a detailed design for SPEAR[2] of an all neutral detector based on NaI (Tℓ) technology ("the Crystal Ball") and made progress has been in the ionization chamber technique using liquid argon. It seemed natural, therefore, to use the crystal ball as one of the starting points, and liquid argon ionization chambers as the other. Since the crystal ball is designed for SPEAR, we concentrated on modification to it to improve its performance in the PEP energy regime. On the other hand, experimental experience with liquid argon ionization chambers is relatively small, and the major thrust of our work was to explore the physics limitations of such devices as low energy photon detectors; we do not consider conventional liquid argon calorimeters, since these are well covered in the literature.[7] We conclude with possible designs resulting from both starting places, but two points must be borne in mind: First, neutral particle detection and calorimetry involves complex physical processes, and so the full evaluation of a particular neutral particle detector requires lengthy Monte Carlo studies of electromagnetic and hadronic showers. These could not be carried out within the time span of the summer study. Secondly, as with most other detectors considered in the summer study, there will be some overlap in physics capability with other detectors. As noted above, any general detector, for example the Mark II version of the SPEAR magnetic detector, contains some photon detection capability, and so our emphasis was on areas not well covered by them.

III. EXPECTED HADRON AND PHOTON DISTRIBUTIONS AT $\sqrt{s}$ = 30 GeV

The performance of a neutral detector is sensitive to the energy and spatial distribution of the particles in multihadronic states. An important experimental discovery[8] in the last year has been the jet structure in the hadronic final state following e^+e^- annihilation. The data shows that in each event, there is an axis about which the transverse momenta are limited, and a phenomenological model consistent with these observations in the SPEAR energy range has been constructed. In this section, we give the results of an extrapolation of this model to $\sqrt{s}$ = 30 GeV, and comparison with the pure phase space isotropic model.

The general features of the two models are similar. Only pions were assumed in the final state. In the phase space model, pions (charged and neutral) are produced with momentum and angular distributions according to Lorentz invariant phase space. The total multiplicity is given by a Poisson distribution whose mean is adjusted to give an average of about 7 charged pions and 7 neutral pions. These numbers are extrapolations in a + b lns of the e^+e^- data for $\sqrt{s}$ = 2.4 to 7.4 GeV. The jet model has the same features as the phase space model, except that an invariant matrix element squared (M^2) is imposed with

$$M^2 = \exp\left(-\frac{1}{2r}\sum_i (P_{\perp i})^2\right),$$

where the summation is over all pions, $P_{\perp i}$ is the transverse momentum of the i^{th} pion relative to a given axis and r is a parameter which was adjusted to give $\langle P_\perp \rangle \approx$ 300 MeV/c. This is in agreement with data up to $\sqrt{s}$ = 7.4 GeV and also with hadronic interactions. The angular distribution of the axis about which $P_\perp$ was computed was chosen to be $(1 + \cos^2\theta)$ which is the case for a pair of spin-1/2 particles.

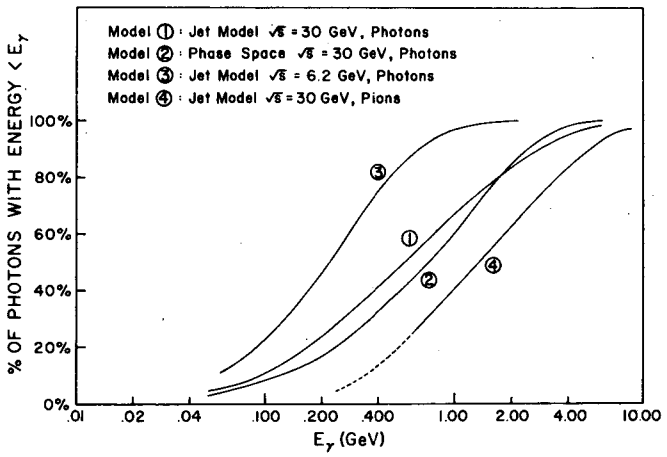

Fig. 1 XBL 759-8200

Of first concern in a neutrals detector is the γ energy spectrum. The integral probability distribution is shown in Fig. 1 for both models at $\sqrt{s}$ = 30 GeV, and for comparison, the jet model results at $\sqrt{s}$ = 6.2 GeV; also shown is the charged pion distribution at $\sqrt{s}$ = 30 GeV. These model calculations indicate that we can expect between 60% and 70% of the photons to be below 1 GeV and about 20% below 200 MeV. An interesting feature of the jet model is that it has relatively more very high and very low energy photons than pure phase space. This is the result of Lorentz transformations along the jet axis, increasing energy for forward decays and decreasing it for backward. This same feature of the distribution is of course seen in the pion distribution (phase space not shown). The corresponding differential distributions are shown in Figs. 2 and 3.

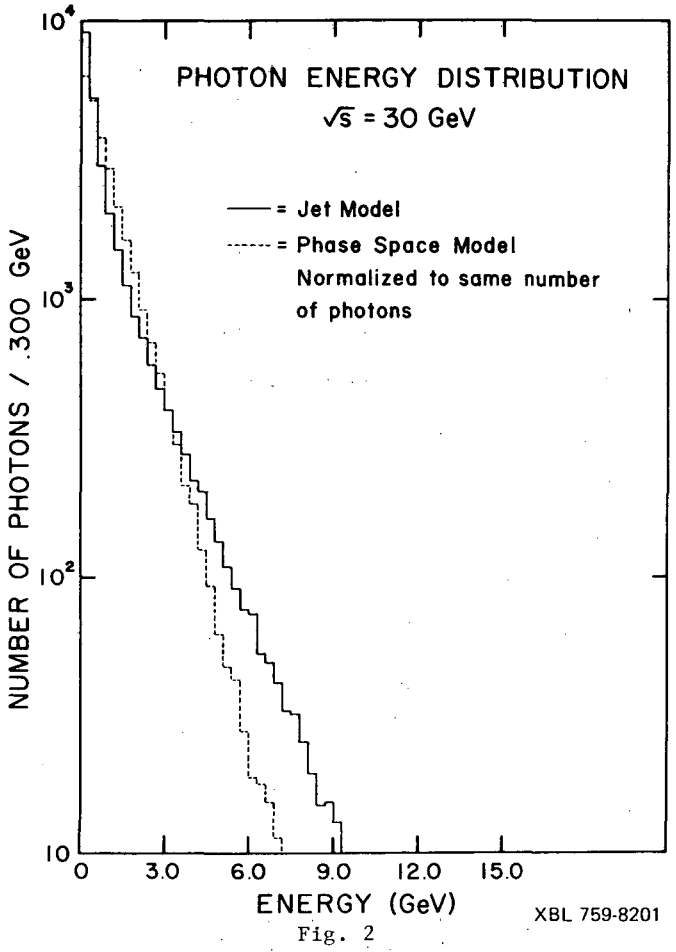

Fig. 2

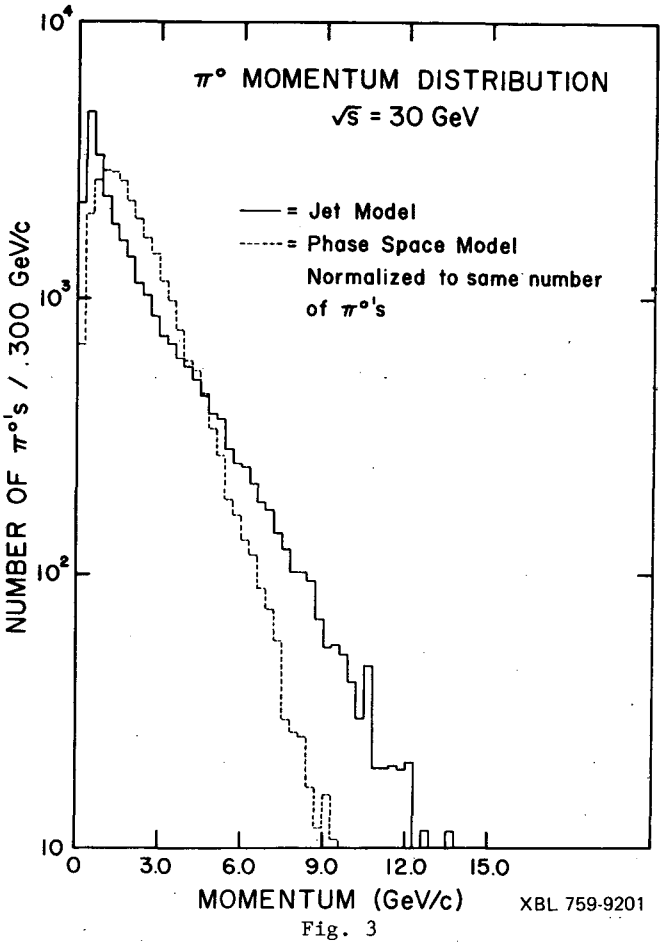

Fig. 3

Because of shower size, each photon distributes its energy over a non-negligible portion of a detector. Thus, the distribution of angles between these γ's is of interest. In Fig. 4, these distributions are shown for both the phase space model and the jet model for $\sqrt{s}$ = 30 GeV. Except

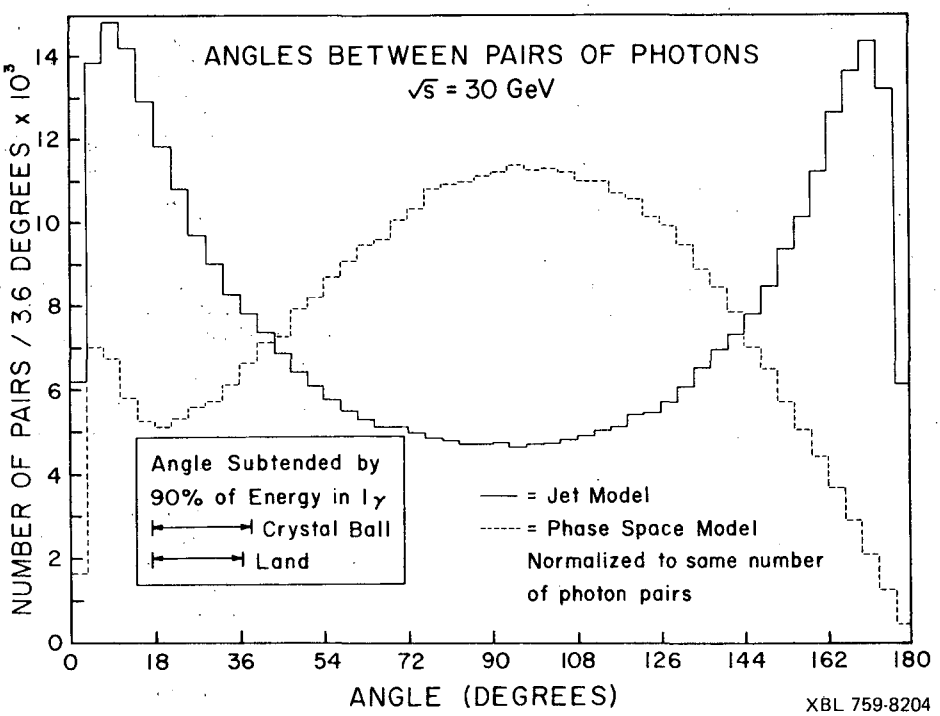

Fig. 4

0 0 0 0 4 5 0 1 5 9 7

for an enhancement at small angles due to high energy π^0's, the phase space model yields a nearly isotropic distribution, as one would expect. The transverse momentum damping about the jet axis, however, manifests itself very strongly in these angular correlations. In fact, the small angle spike from π^0's in the high energy tail is not even visible, being buried under the great multiplicity of small angles between photons in the jet. The figure also shows the angular size of an area which contains about 90% of the energy of a single photon for the two neutrals detectors reported on in the summer study. Clearly, the jet structure is a serious matter in neutrals detectors. About half the pairs in one hemisphere lie within a cone of half-angle 11°, which agrees well with the crude estimate of

$$\frac{\langle P_\perp \rangle}{\sqrt{s}} \times (\text{multiplicity}) = 8^\circ.$$

Thus, if the jet model with transverse momenta limited to about 300 MeV is applicable at PEP, and there is every reason to believe it is, one can expect about 3 or 4 photons in about 1% of 4π. This is approximately the size of a single shower in both the crystal ball and LAND (Liquid Argon Neutrals Detector). A typical event would then contain two such neutral energy blobs diametrically opposed, each blob containing 2, perhaps 3, charged particles in the crystal ball. In the LAND detector which we studied, the magnet would sweep the charged particles aside and disperse them over space, significantly reducing the charged-neutral overlaps.

Of interest in calorimetry are the neutral and charged energy distributions. These energy distributions in the jet model are shown in Fig. 5. Of course, the equal partition of energy between charged and neutral pions just reflects the parameters fed into the model, although the well-known energy crisis supports it.

In conclusion, we note that the expected jet structure at PEP energies will make the energy measurement of single photons in multihadronic states very difficult.

Neither of the neutrals detectors we considered is able to solve this particular experimental problem. On the other hand, if nature does indeed provide us with such a strong focusing effect, the neutrals detectors will provide a simple, direct measurement of their angular distribution and electromagnetic component. Finally, the goals of measuring σ_o and σ_t by calorimetry and of delineating the general features of the neutral energy are not disturbed by this structure of the multihadronic states.

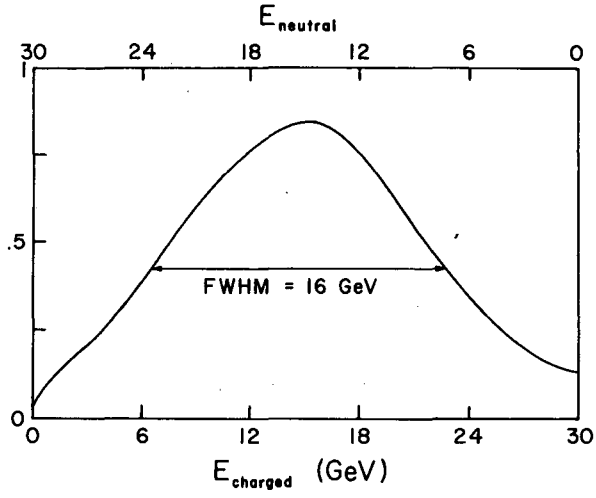

Jet Model-Charged / Neutral Energy Distribution

XBL 759-8203

Fig. 5

REFERENCES

1. G. Feldman and D. Hitlin, PEP Note 143 (1974 PEP Summer Study).
2. Stanford Linear Accelerator Center Proposal SP-24.
3. See R. Schwitters, 1975 Photon-Lepton Conference, for the most recent data.
4. G. Feldman and B. Wiik, 1975 Photon-Lepton Conference.
5. E. Bloom et al., PEP Note 155 (1974 PEP Summer Study Report).
6. T. Mast and J. Nelson, PEP Note 153 (1974 PEP Summer Study Report)
7. W. J. Willis and V. Radeka, Nuc. Instr. and Methods 120, 221 (1974.
8. G. Hanson, 1975 SLAC Summer Institute, and R. Schwitters, 1975 Photon-Lepton Symposium.

THE CRYSTAL BALL AT PEP

W. Bartel, F. Bulos, D. Luke, C. Peck, K. Strauch

Summary

The modifications to the SPEAR version of the Crystal Ball required by the higher energies at PEP are discussed. Since the hadron multiplicity is expected to rise as log s, their average energy must rise. On the other hand, if the hadrons are produced in jets, the low energy part of their spectrum is not heavily depleted. This implies that modifications for high energy particles should not deteriorate low energy performance. An external iron calorimeter for measuring the high energy hadrons, charged and neutral, is considered. To improve the angular resolution on γ's, an active internal converter has been studied, estimates have been made of its expected performance, and difficulties requiring further study have been outlined.

THE CRYSTAL BALL[1]

The Crystal Ball is a neutrals detector designed for SPEAR. Its major component is a spherical shell of NaI(Tℓ), 16 r.l. thick, with inside radius of 25.0 cm, covering about 90% of the sphere. The interior cavity is filled with track chambers to determine the number and directions of charged particles, and the conical beam pipe openings are covered down to about 10° with an array of hexagonal sodium iodide counters, 20 r.l. long. A summary of the relevant parameters of this device is given in Table I and the performance characteristics in the SPEAR energy range are given in ref. 1.

In the SPEAR energy range ($\sqrt{s} \leq 7$ GeV), this apparatus will be able to directly measure the all neutral cross section σ_o by calorimetry and to determine the nature of the neutral energy in general multihadronic events. About 40% of the charged hadrons range out in the NaI so that it is expected to give a calorimetric total energy measurement of about 35% FWHm. Thus, it will yield an independent measurement of σ_t. It is able to detect low energy γ's with good energy resolution, and this property is important for proper selection of a pair of γ's belonging to a π^o in multi-π^o production. And, finally, monoenergetic photons in the hundred MeV range, or even lower, should give strikingly clean peaks in energy spectra, even when they occur in multihadronic events. This is due to the combination of three things. First, NaI has a better energy resolution (a few percent is typical) than any other photon detector used in high energy physics; secondly, the large solid angle coverage for both charged particles and γ's allows clean separation of events by topology, and, finally, many "background" photons from π^o and η decays can be removed by reconstructing the hadron mass.

In the PEP energy regime, however, the average hadron energy is expected to increase, since the multiplicity is expected to rise only as log s. The calculations of the expected spectra are given in the general neutrals report of this Summer Study. The consequences of this trend are that a smaller fraction of the energy carried by charged hadrons will be deposited in the ball proper and that an increasing fraction of the π^o's have energies in the GeV range. This implies that the calorimetric properties of the simple ball become poorer and that the angular resolution on the γ's becomes increasingly more important than energy resolution in reconstructing the π^o mass.

Table I. Properties of Crystal Ball Spherical Shell

Material	NaI(Tℓ)
Signal	≈10^3 photoelectrons/MeV 0.25 μsec decay time constant
Inside/Outside radius	25.0/65.0 cm
Solid Angle Coverage[a]	sphere = 0.90 × 4π sphere = 0.98 × 4π ± end caps
Thickness of shell	40.6 cm 147 gm/cm^2 16 radiation lengths ≈1 hadronic interaction length 195 MeV energy loss, minimum ionizing
Segmentation[b]	shape = triangular prisms solid angle/seg = .0175 sr ± 15% fraction of sphere/seg = .00139 ± 15% half angle of cone with same solid angle = 4.2° = 73 mr = 1.7 cm @ 25.0 cm
Kinetic energy of range particle	245 MeV pions 340 MeV kaons 425 MeV protons
Momentum of range particles	350 MeV/c pions 670 MeV/c Kaons 960 MeV/c protons
Transverse Shower Spread (electromagnetic)	Moliere Radius = 4.4 cm No. segments for ~95% of shower = 6 Fraction of sphere used by 1 γ = ~0.8%

[a] These numbers neglect edge effects of the conical openings and end caps.

[b] Each segment is viewed by a phototube.

0 0 0 0 4 5 0 1 5 9 8

Nevertheless, if e^+e^- → hadrons proceeds via parton pair production, then those π^0's produced backward in the parton's frame give rise to γ's of low energy. Thus we qualitatively obtain the jet model result that as s increases, the dynamic range of photon energies increases; the relative importance of the low energy photons in neutral hadron reconstruction is reduced, but they cannot be ignored. Furthermore, the possibilities of surprises involving low energy photons persuades us that this energy domain must be well covered. The major thrust of our study has therefore been the design of an external iron calorimeter to pick up the energy of high momentum hadrons and an internal active converter to improve the angular resolution on the photons with as little energy resolution degradation as possible.

We find that an iron calorimeter is quite feasible but massive (about 500 tons), even given the relative compactness of the ball. We had hoped that an internal converter could be added without serious degradation of the energy resolution, but we find that this does not seem possible because adequate segmentation cannot be provided.

EXTERNAL CALORIMETER

Let us begin by considering the measurement of σ_t with the unadorned ball at $\sqrt{s}$ = 30 GeV, ignoring any charged hadron energy it detects. First, we note that it is a superb calorimeter for the purely electromagnetic energy in an event and an efficient counter of charged particles. Thus in the absence of beam-gas and 2γ events, no additional apparatus is needed to identify the interesting annihilations, and the observed energy distribution would be expected to have an average of about 15GeV and a FWHM of about 16 GeV.* The purely electromagnetic energy in beam-gas and 2γ events can kinematically range up to 15 and 30 GeV respectively, but the bulk of the electromagnetic distributions would be much lower. Thus, requiring the electromagnetic energy to be above a cutoff of order 7 GeV would eliminate most of the background at a loss of ~20% of the signal. Estimates of beam-gas event rates suggests that they are small enough to be ignorable, but the 2γ background from events in which the electron and positron are lost in the beam pipe are uncomfortably large. The estimated cross section for e^+e^- → e^+e^- + hadron in which both e^+e^- have angles less than 10 mr (assumed minimum angle of tagger) and $E_{hadron} >$ 15 GeV is about 0.05 nb at $\sqrt{s}$ = 30. This is 10% of σ_t (e^+e^- → hadrons) if R = 5. Thus we conclude that the unembellished ball could probably be used to measure σ_t, but the corrections for undetected 1γ events and detected 2γ events would be uncomfortably large. Clearly, before using the simple ball in this mode, much more careful background and signal loss estimates would have to be done than what we have done in this summer study. We now turn to the situation with an external calorimeter.

The design goal of the study was to provide an external calorimeter capable of containing at least 95% of the hadronic shower and covering about the same solid angle as the NaI parts of the system. As noted above, a separation of one photon annihilation from 2γ -reactions where the degraded electrons are not detected can be achieved by measuring the total energy of a reaction over a solid angle close to 4π. The amount of missing energy then allows an identification of 2γ-reactions. Further, information on the direction of the missing momentum, although expected to be poor, may also prove useful. This argument specifically applies to the total cross-section measurement. Another fact is that the ball is essentially a γ detector (It is about 1 hadronic absorption length thick.). Neutrons and K_L^0 are detected only through nuclear interactions, and so an external calorimeter would increase the amount of energy collected from these neutral particles as well as from the charged particles which do not stop in the ball.

Two possible configurations have been considered, one specifically adapted to the crystal ball and the other using the modules designed by the general detector group and described by them.[2] From considerations of interaction lengths per radiation length, ease of handling, and cost, iron was chosen in both.

A calorimeter based upon scintillation counters was considered first. From the work of Engler, et al.[3,4], we deduce the following:

(1) Five absorption lengths are needed. Since the NaI provides one absorption length, the calorimeter requires at least 75 cm of Fe.

(2) To achieve a FWHM resolution of 60% at 2.5 GeV, one must sample every 1 cm of iron. Two cm between plates has been provided for scintillator. The geometry of the calorimeter is shown in Fig. 1 and 2. It consists of 12 major pieces, each longitudinally segmented into 3 parts after 25, 50, and 75 cm of iron. Wire chambers can be installed between these segments to give some position resolution on the hadronic showers and provide μ identification. The capability of this arrangement with regard to the muons is given in Table II.

The weight of this arrangement is estimated to be as follows:

Iron:	Central part	175 tons	
	End caps	370 tons	
Scin:	15% of iron	570 tons	Fe
		80 tons	
		630 tons	Total

Assuming that the light from the scintillators fills 1.5 cm of the 2 cm gaps between plates, the total area of light emitting surface is about $27m^2$ which corresponds to the photocathode area of 2.2 10^5 5" phototube. Thus, sampling only a few percent of this area requires about 1000 5" phototubes. Finally, assuming a cost of $500 per ton of iron, $10 per gallon of mineral oil base liquid scintillator, and $200 per phototube channel, the total cost is about $700K.

The obvious alternative to a scintillation calorimeter is a liquid argon ionization calorimeter, but we did not work out the details.

* See Fig. 5 , "Neutrals Detection at PEP", this volume.

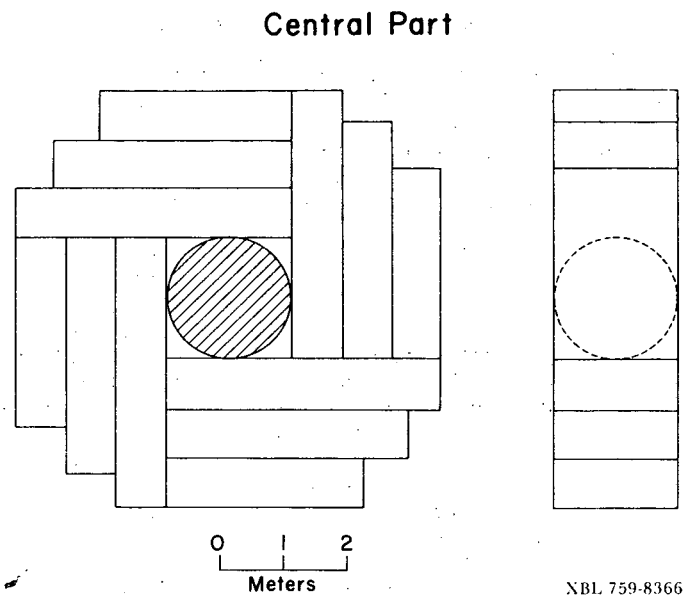

XBL 759-8366

Fig. 1

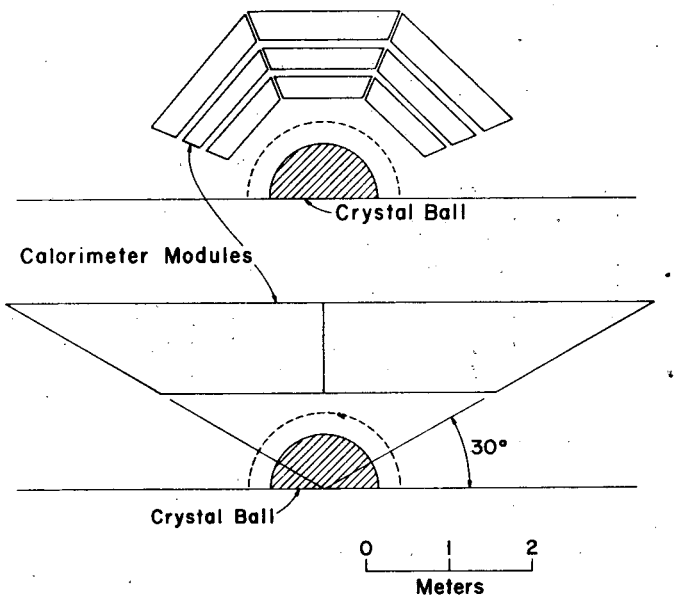

XBL 759-8360

Fig. 3

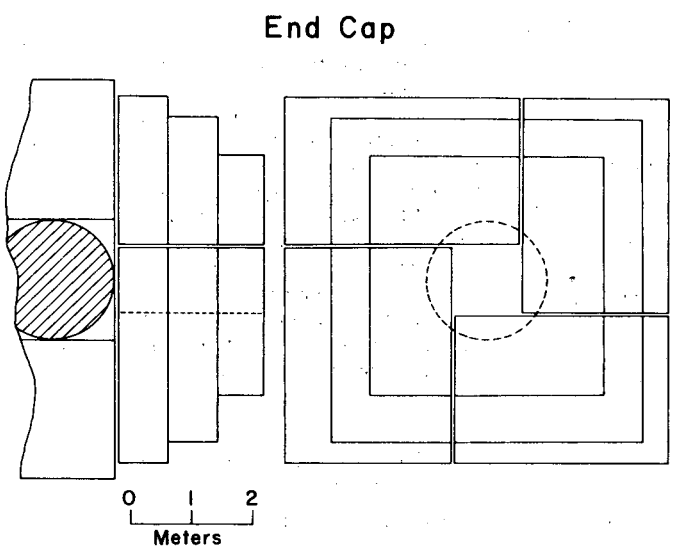

XBL 759-8365

Fig. 2

Table II. Calorimeter Performance.

Wire Plane Number	Min μ mom. to reach plane (MeV/c)	π punch through probability (%)
1	600	8
2	950	2
3	1300	0.4

Another possible arrangement for the calorimeter is based upon the modules considered by the general detector group with the Pb front end part replaced with iron and the last and largest module removed. The geometry is shown in fig. 3. It uses 12 of the "standard" liquid argon ionization chamber modules plus four special end cap modules (not shown). The details of this design are given in the report of the general detector group and will not be repeated here.

INTERNAL CONVERTERS

The angular resolution of the spherical part of the crystal ball is determined by the size of the prism segments. Each of these covers a solid angle equivalent to a cone with half-angle of 4.2°. Thus a photon's direction can be determined to about this angle but not to much better than it. In fact, detailed Monte Carlo studies[5] have shown that for an isolated γ, one can interpolate inside a prism because of the transverse size of a shower and obtain an angular resolution of about 3° at 100 MeV and 2° at 2 GeV. In the ball the uncertainty in reconstructing the mass of a π^0 is dominated by the angular resolution for momenta above about a hundred MeV and in this region,

$$\Delta m = \sqrt{2}\ p\ m\ \Delta\theta$$

where p is the momentum of the particle of mass m and $\Delta\theta$ is the angle uncertainty on one photon. This uncertainty formula assumes that one calculates the invariant mass of a γ-pair with the formula $2E_1E_2(1-\cos\theta)$, where $E_{1,2}$ are the energies of the two photons and θ, the angle between them. However, because of the size of a shower, each photon covers a cone of half angle $\delta\theta$, where $\delta\theta > \Delta\theta$. When $p > m/\delta\theta$, the cones from the two γ's overlap, and other methods than the simple kinematic formula given above must be used to calculate the invariant mass of the pair. Figure 4 shows these relations (including the small effect of the energy resolution in NaI) for representative crystal ball parameters. Although these uncertainty bands are broad compared to the masses of the π^0 and η^0 themselves (which are the usual comparison quantities), it is more relevant to compare them to the width of the

0 0 0 0 4 5 0 1 5 9 9

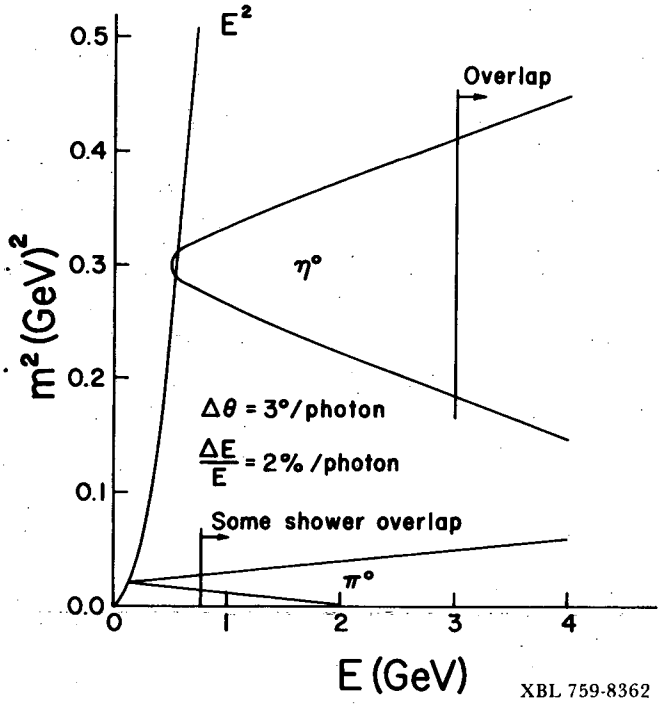

XBL 759-8362

Fig. 4

distribution of invariant mass between pairs of random photons with the same total energy. This distribution ranges from 0 to E^2, where $E=E_1+E_2$, and, for reference, Fig. 4 shows this range. Detailed Monte Carlo studies of the problem of identifying π^0's and η^0's in multi-hadronic events have been done for the SPEAR energy range, and the results are given in Ref. 1.

One approach to improving the angular resolution is to simply increase the number of segments in the sphere and increase its radius R. In addition to improving the angular resolution, this option provides other benefits, viz., reduction in the probability that two unrelated γ's have overlapping showers and finer binning of the transverse spread of a shower. This later is potentially useful in reconstructing the invariant mass of a pair of overlapping γ's by Walker's second moment method or extensions of it.[6] The random overlaps probability as a function of multiplicity for an isotropic γ distribution is shown in fig. 5. The parameter f is the fraction of the sphere used by a single γ and, for the present geometry, its value is 0.83%. As an example, consider increasing the NaI volume a factor of 2 and segmenting the sphere into 1280 prisms; then the outside radius becomes 80 cm, the inside becomes 40 cm, and shower max occurs at about 47 cm. The angular resolution is then reduced to about 2.3° for 100 MeV photons, assuming the same ability to interpolate inside a prism. The fraction of a sphere covered by a shower is reduced to about .46%. The reduction in randoms overlap is also shown in fig. 5. If the jet structure of multihadronic events develops as expected, every event will contain significant overlaps and the statistical calculation based on isotropy is irrelevant. On the basis of this exercise, it did not seem profitable to pursue the matter further. The point is simply that as radius R increases, the angular resolution decreases as 1/R, the required number of segments roughly as R^2, and the volume as R^3.

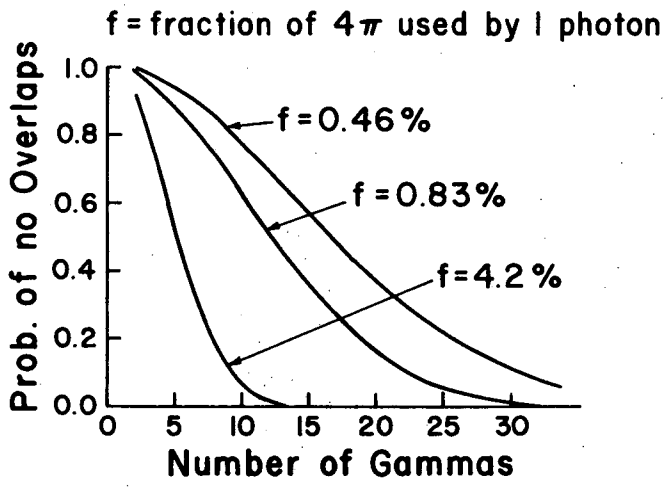

Fig. 5 XBL 759-8364

A more profitable approach is to introduce converters in the cavity of the ball. An elaborate system is not possible because of space limitations, and we settled on the following requirements:

(a) Angular resolution of about 10 mr. This is five times better than the unmodified ball and would hopefully (see below) provide a count of the number of γ's contained in an unresolved energy blob observed in the ball. Since the individual energies of two nearby γ's cannot be disintangled, and the average direction of the total energy has a 50 mr uncertainty, one cannot calculate a mass in the manner assumed earlier, but must resort to statistical fitting to distinguish π's from accidental overlaps.

(b) energy resolution compatible to that of the main detector. This forces one to an NaI active converter to preserve the energy resolution in the 100 to 200 MeV region. Table III shows the resolution of the system if a lead glass active converter with

$$\frac{\Delta E}{E} = .05/\sqrt{E}\ (\text{GeV})$$

were used.

(c) conversion efficiency of about 70%. As shown in Table III, this is achieved with two radiation lengths. Higher efficiency is not possible in the small cavity of the ball. Figure 6 shows the probability that 0, 1, or 2 photons do not materialize in

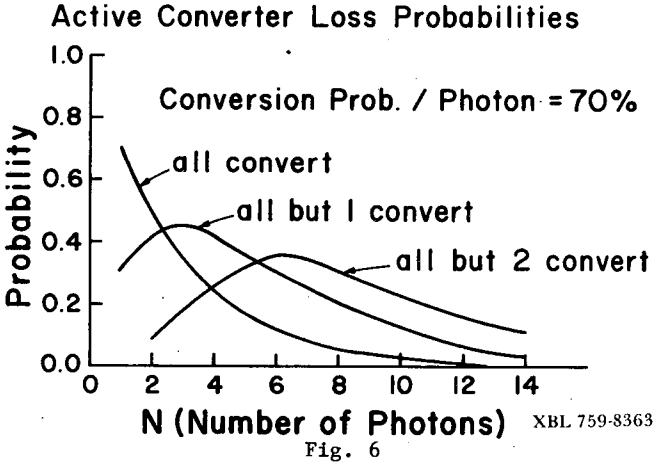

XBL 759-8363

Fig. 6

the active converter as a function of the total number of gammas incident. It is most relevant to consider N as the number of photons in an unresolved energy blob in the ball so that N in the 2-6 range is suggested by the jet model.

A possible geometry for the active converter is shown in figs 7 and 8. The changes from the SPEAR version of the ball are:

(a) reduction of the radial thickness of the ball by $2X_o$, this being replaced with the active converter. The inside radius then becomes 28 cm.

(b) beveling of the inner edges as shown to allow for the cylindrical geometry of the converter. Only 17% of the sphere is affected by this modification.

Table III. Active Converter Properties

	$1X_o$			
	(MeV)			
E_γ	100	200	400	1000
Conversion probability[7]	.46	.48	.50	.54
Energy loss in converter[7]	13	14	15	19
Overall resolution with Pb-glass	5.8%	3.3%	1.9%	1.2%
Angular resolution (mr) due to MCS only	35	18	8.9	3.5

	$2X_o$			
E_γ	100	200	400	1000
Conversion probability[7]	.70	.72	.74	.79
Energy loss in converter[7]	32	40	50	70
Overall resolution with Pb-glass	9.0%	5.1%	3.0%	1.6%
Angular resolution (mr) due to MCS only	77	38	19	7.7

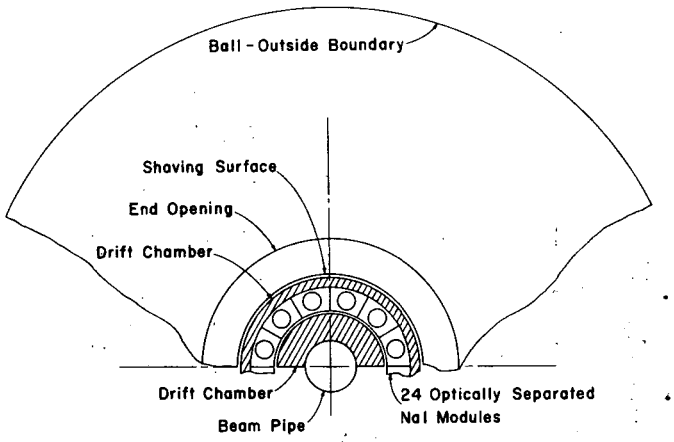

Fig. 7

The active converter is segmented into 24 parts, 12 modules around the circumference, split at the center of the interaction region. Drift chambers are used for position determination.

The dominant source of direction uncertainty for low energy γ's is the multiple scattering of the converted electrons in the active converter. The rms radial position uncertainty at the detector for a single electron of energy E passing through a thickness d_1 of scatterer of radiation length X_o followed by a drift space d_2 to the detector is

$$\frac{21}{E(\text{MeV})}\sqrt{\frac{(d_1+d_2)^3 - d_2^3}{3X_o}} .$$

Thus, this contribution to the angular resolution goes inversely as E. This has been used to estimate the average angular resolution as a function of γ energy of the configuration shown in fig. 7. The resolution has been averaged over conversion points, energy partition between the conversion pair, and photon production angle and ranges up to several times the average value shown. We assume that the event contains charged particles so that the vertex is known. For high energy photons, the

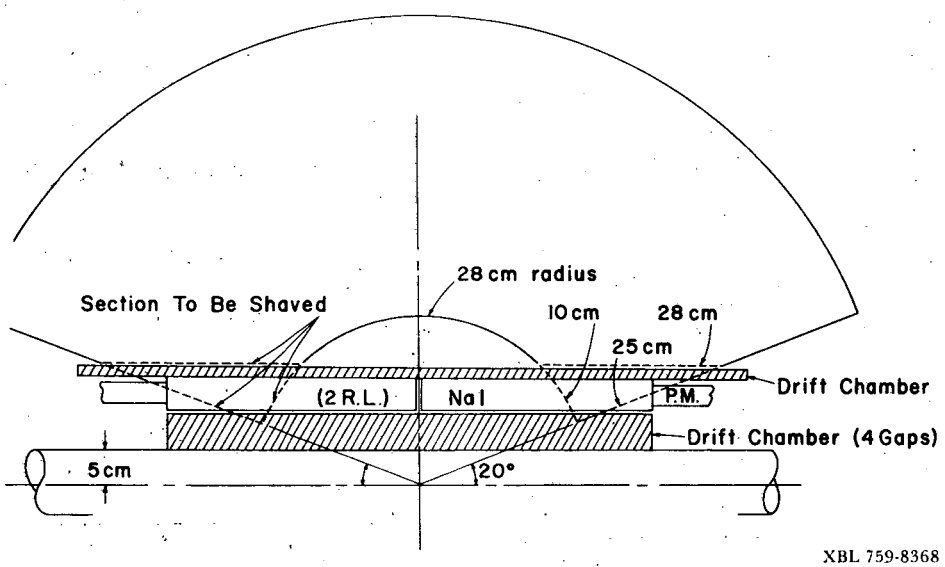

Fig. 8

0 0 0 0 4 5 0 1 6 0 0

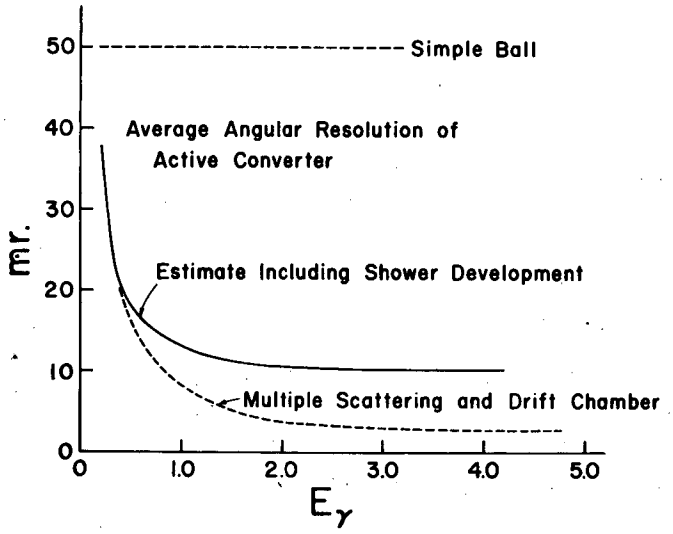

Fig. 9 XBL 759-8361

resolution is determined by the size of the showers after 2 r. l. This has not been evaluated, but experience with a similar arrangement at DESY suggests 10 mr as the limiting resolution. Figure 8 shows the expected average angular resolution, for photons.

There are several difficulties with this system which we can point out, but have not fully evaluated. First, the segmentation into only 24 parts implies serious overlap between uncorrelated photons, even if they are isotropically distributed. Figure 5 shows the probability that no two photons are in the same active converter segment as a function of the number of isotropically distributed photons in an event (curve with f = 4.2%). In the frequent case that two or more photons fall in the same active converter element, we will be unable to disentangle the part of their energies lost in the active converter. Thus, we anticipate that the overall energy resolution with this system will be seriously deteriorated. A second problem is that the size of the shower at the drift chamber will fluctuate strongly depending upon the conversion depth in the active converter. Thus, the expected average angular resolution of 10 mr is not a good measure of the ability to resolve two nearby photons. For example, the pair from a late converting photon can be easily lost in the shower of a nearby, early converting one. In conclusion, the desireability of an active converter depends upon a more precise definition of physics goals than given here, but we think we have identified the most important experimental trade-offs with such an addition.

Other Modifications

We considered two other possible modifications to the simple ball. One was the addition of a small magnetic field to the inner cavity to provide the sign of charged particles, and the other was a radial segmentation of each prism into two parts, separated at about $3X_0$, to allow some π-e separation. The first interacts with the active converter just described. Since it would be impractical to shield its phototubes from a several kG field, these two options could not be mixed. Since we felt that the arguments for photon angular resolution are stronger than those for a field, the matter was not pursued to a practical design.

Two methods of segmenting a prism were suggested, one based upon polarization of the light from the inner segment, and the other based upon a sharp cutoff filter, tuned to split the spectrum. Both require doubling the number of phototubes in the system but this is possible with 1" tubes. The polaroid idea would work nicely if only total internal reflection were used to propagate the light in the prism. This, however, leads to a ~4:1 ratio of light collection efficiency from one end to the other, and so is intolerable. Thus, diffuse reflectance is required, and this is expected to lead to some depolarization. Without experimental work, it is impossible to speculate on the achievable separation with this method.

The second method is to separate the two segments with a sharp cutoff filter, and put a similar filter in front of one phototube. Suitable filters for splitting the spectrum are available.

CONCLUSIONS

It appears practical and desirable to augment the SPEAR version of the Crystal ball with an external calorimeter for use at PEP. It is expected that the resulting system would give a calorimetric measurement of total energy, and so would yield a total hadronic cross section from one photon exchange with different biases than the magnetic spectrometer methods. We find that an active converter is geometrically feasible, but its desirability is not so clear. A definitive evaluation of these additions must await Monte Carlo studies, but the "back of envelope" designs seem promising enough to warrant more detailed work. Finally, the calorimeter clearly does not deteriorate the response of the system to low energy photons for which most other instruments are relatively blind; an active converter is much more problematic in this regard.

REFERENCES

1. Stanford Linear Accelerator Proposal SP-24.
2. "The Study of Neutral Particles at PEP" in this proceedings.
3. J. Engler, et al., Nuclear Instruments and Methods 106, 189 (1973).
4. F. J. Sciulli, California Institute of Technology Report No. CALT 68-502 (1975)
5. E. Bloom and M. Richardson, private communication.
6. R. L. Walker, California Institute of Technology Report No. CALT-68-330 and F. Bulos, "Resolving Overlapping Gammas in a Modular Neutrals Detector", in this proceedings.
7. H. Nagel, Ann. Physik 186, 313 (1965).

A LIQUID ARGON NEUTRALS DETECTOR (LAND) FOR PEP

A. Eisner, G. Hanson, D. Hitlin, U. Koetz, M. Marshak, T. Mast,
J. Matthews, C. Peck and D. Yount

Summary

We discuss the physical effects limiting the gamma energy resolution of a liquid argon calorimeter without passive converter plates. An example of such a detector based on the General User's Magnet designed at this Summer Study is given.

1. MOTIVATION AND GOALS

The general motivation for an apparatus sensitive to low energy photons at PEP has been discussed in "Neutrals Detection at PEP," a paper from this Summer Study. That paper describes our general ideas about neutrals detection, the physics available to a neutrals detector, and the multiplicity, energy, and angular distributions of gammas expected at PEP. Our emphasis on low energy photons is motivated by the realization that general detectors will provide adequate resolution and sensitivity in the GeV range.

One approach to observing the expected large number of low energy photons would be to use the Crystal Ball detector presently being built for SPEAR. This detector has some nice properties and some obvious disadvantages, both of which are described in the paper "The Crystal Ball at PEP" from this Summer Study. The major advantage is the excellent energy resolution and nearly 4π solid angle coverage. In addition the small size makes it very feasible to surround it with a hadron calorimeter. The major disadvantages are the lack of measurement of the charged particle sign and momenta, the relatively coarse angular resolution, and the lack of flexibility coming from the expense and fixed geometry of the crystals. An alternative which we have studied is a new detector using liquid argon ionization chambers.

We were motivated by the successful construction and operation of liquid argon calorimeters during the past year.[1] Our initial goal was to design a detector with energy resolution for low energy gammas (less than 500 MeV) that was comparable to that of NaI. In addition we wanted modest momentum resolution for charged particles, flexibility in terms of being able to match given geometries of other detectors and magnets, and hopefully low cost. Our initial vision was a small solenoidal magnet surrounded by a large pure liquid argon gamma detector (i.e., without plates of passive converters). In addition to the above features such a detector would have some nice capabilities coming from the longitudinal information available in a liquid argon counter. This information and the good energy and momentum resolutions would yield excellent electron-hadron discrimination. In addition the longitudinal information in the argon provides measurement of the ionization energy loss for charged particle identification.

The major effort of the group was not the design of a specific detector, but instead the study of the considerations that would go into such a design and the feasibility of achieving the goals described above. In Section 2 we describe the results of that study. In Section 3 we do describe very briefly one possible configuration for such

Table 1. Properties of shower counter materials (Ref. 3)

Material	dE/dx (MeV/cm)	X_0(cm) Radiation length	$\left(\frac{dE}{dx}\right)X_0$ (MeV) Critical Energy, E_c	Interactions on protons/X_0 (σ_p in mb)	Moliere radius 21.2 X_0/E_c (cm)	Density g/cc
Argon	2.11	14.1	29.8	$15.6\ 10^{-4}\ \sigma_p$	10.0	1.40
Lead Glass (F2)	5.38	3.22	17.3	$9.31\ 10^{-4}\ \sigma_p$	3.9	3.61
Aluminum	4.37	9.00	39.3	$23.5\ 10^{-4}\ \sigma_p$	4.9	2.70
Lead	12.8	0.56	7.17	$2.55\ 10^{-4}\ \sigma_p$	1.7	11.35
NaI	4.84	2.59	12.5	$5.5\ 10^{-4}\ \sigma_p$	4.4	3.67
Copper	12.9	1.45	18.7	$9.0\ 10^{-4}\ \sigma_p$	1.6	8.96
Iron	11.6	1.77	20.5	$10.2\ 10^{-4}\ \sigma_p$	1.8	7.87

0 0 0 0 4 5 0 1 6 0 1

a detector. Finally we summarize in Section 4 our conclusions on the feasibility of using liquid argon for a high resolution neutrals detector, and we outline the work that we think needs to be done before a detailed design can be made.

2. CHARACTERISTICS OF LIQUID ARGON DETECTORS

The use of liquid argon in high energy physics was originally studied with the view of achieving very high spatial resolution for charged particles.[2] More recently considerable success has been achieved in using it in hadronic and electromagnetic shower detectors.[1] This work of the past few years is well described in the literature and we will not review it here. We have summarized in Table 1 some of the characteristics of liquid argon and other materials used in shower counters.

The detectors used to date have contained plates of passive converters (lead or steel) in order to reduce the depths of the counters. Compared to a pure liquid argon counter these plates seriously degrade the energy resolution for low energy gammas. Thus our main emphasis was on a detector without such plates, and we simply accept the deep counters which this implies. However, we were concerned with the relatively large transverse spread of a shower when these plates are absent. Consequently some work was done on detectors with them.

In Section 2.1 we describe the contributions to the energy resolution of liquid argon electromagnetic shower detectors. One of the advantages of a liquid argon detector may be a low sensitivity to magnetic fields and we discuss this in Section 2.2. In Section 2.3 we describe the problems of spatial localization of gammas.

2.1 Energy Resolution

Electromagnetic showers create ionization in the liquid argon; the collection of electrons from this ionization then induces a signal in the detector; and finally this signal is processed by the electronics. We use this series of events to classify the various contributions to the energy resolution as follows:

A. Fluctuations in ionization coming from fluctuations in:
- (1) energy loss out the back end,
- (2) energy loss in a magnet coil and dewar,
- (3) energy loss in passive converter plates,
- (4) energy loss transversely out of a shower fiducial volume,
- (5) tracklength induced by electromagnetic hadron production.

B. Fluctuations in the pulse induced in the electronics coming from fluctuations in shower track positions.

C. Electronic Noise.

We discuss each of these below. In general, we adopt the attitude that fluctuations at the 1% level must be experimentally determined. Thus, our goal in the analysis is only to identify what must be done to reduce the effect of any given fluctuation source to this level (if possible).

(A) Fluctuations in Ionization

Energy loss out the back end of the detector. We have made Monte Carlo calculations of the fluctuations in energy loss out of the back end of pure

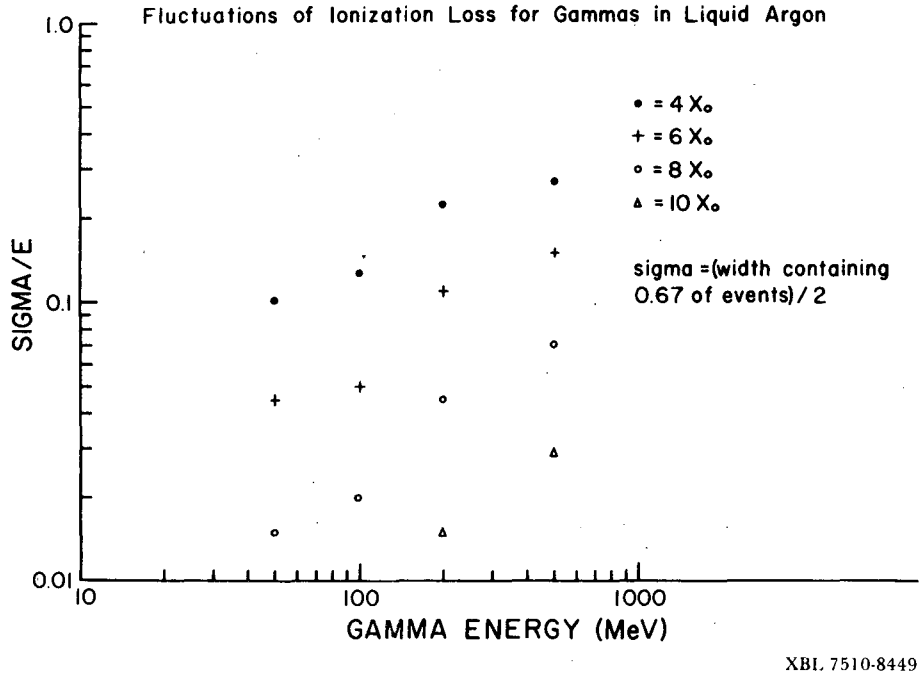

XBL 7510-8449

Fig. 1

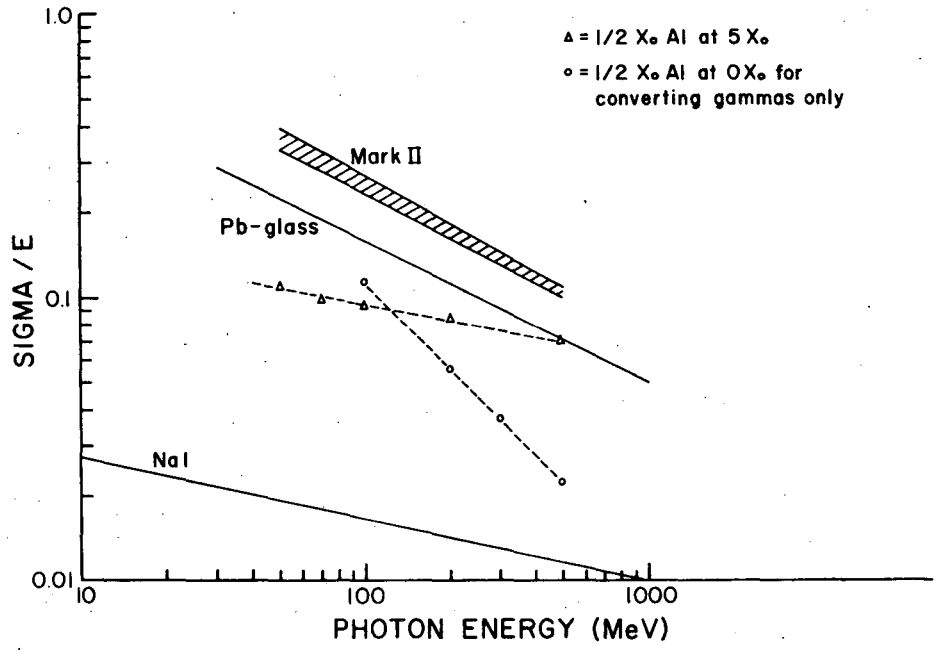

XBL 7510-8458

Fig. 2

liquid argon counters of various thickness. The results are shown in Fig. 1 as a function of gamma energy. For the low energy showers that we are emphasizing, about 10 radiation lengths are sufficient to maintain an energy resolution of $\leq 2\%$.

Energy loss in a magnet coil and dewars. During the past year considerable progress has been made in designing and testing thin superconducting magnets.[4] A solenoid coil presently being constructed will have a thickness of 0.33 radiation lengths. Considering the oblique angle of some gammas and the liquid argon dewar thickness we consider the effects of 0.5 radiation lengths of passive material (aluminum).

With the magnet coil in front of the shower detector[5] about 27% of the gammas convert in the coil, and the rms energy loss for these converting gammas is plotted in Fig. 2. Shown for comparison are the resolutions, for lead glass, sodium iodide, and that expected for the Mark II SPEAR Magnetic Detector.

Since we do not want to degrade the resolutions of low energy gammas, we have considered the case where the coil follows 5 radiation lengths of gamma detector. (The motivation was to make the length large enough to get most of the shower energy and small enough to minimize the wasted magnetic field.) The results are also shown in Fig. 2. These latter results are based on the fluctuations in energy loss at various depths in the shower shown in Fig. 3. From this calculation, we conclude that a lumped passive converter, such as a coil, embedded in the γ detector is unacceptable for our purposes.

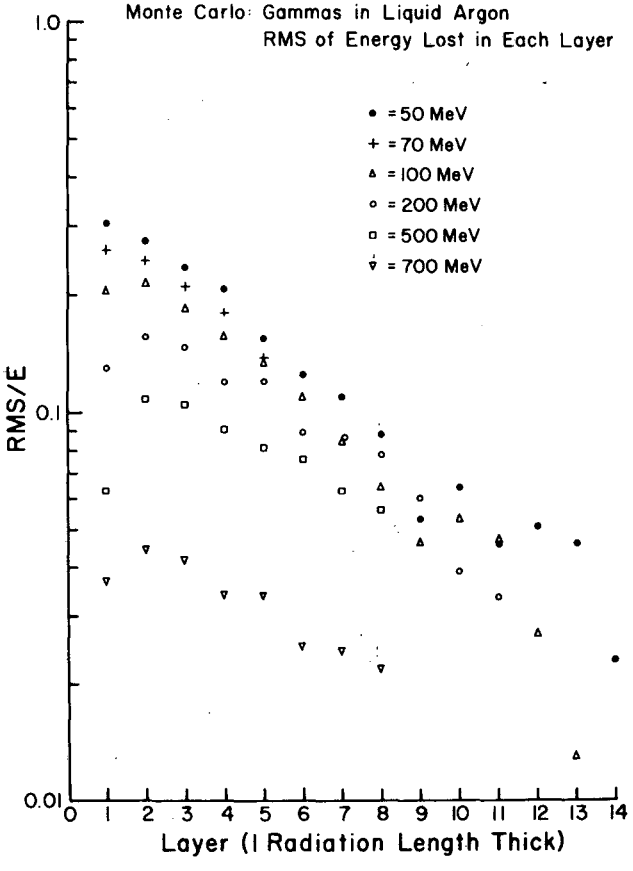

XBL 7510-8459

Fig. 3

0 0 0 0 4 5 0 1 6 0 2

Energy loss in passive converter plates. Although the addition of very thin lead plates to a pure liquid argon detector will add energy loss fluctuations, it may also decrease the electronic noise and reduce the transverse spread of the showers (See Sections 2.13 and 2.3 below). Thus it is important to calculate the size of these fluctuations as a function of the plate thickness. The usual rules of thumb for these fluctuations (see for example Ref. 1) are not valid for very thin plates. Unfortunately we have not found an analytic expression for these fluctuations which agrees with both intuition and existing data. Either an analytic or Monte Carlo solution of this problem is needed for an optimized design. However, on the basis of some rough estimates we feel that enough material to significantly reduce the shower spreading would probably significantly degrade the energy resolution.

Fluctuations in energy loss transversely out of a shower fiducial volume. In practice one will add together a large enough number of readout cells to contain the shower. As this number is increased the fraction of energy escaping and the fluctuations in this energy are reduced. However, the electronic noise increases as the square root of the number of cells added (to be discussed later). Thus there is some optimum number of cells to be added together, and this number depends on the particular configuration of the detector and the energy of the shower. In Section 2.1 of this paper we discuss the electronic noise for various configurations, and in Section 3 we discuss the transverse size of the shower. However, we have made no detailed optimization to determine the size of shower fiducial volumes and this would probably have to be determined by the experimental calibration of each particular detector.

Fluctuations in track length induced by electromagnetic hadron production. At some low level there will be fluctuations in the ionization due to the production of hadrons by electrons and photons in the shower. This sets a floor under the achievable resolution of any electromagnetic shower detector. For the low energy showers that we are emphasizing here, we expect this effect will be below the 1% level.

(B) Fluctuations in the Pulse Induced in the Electronics

The pulse induced by the collection of an electron in an ion chamber depends on the original position of the electron, i.e., the position of the original ionization.[6] Since the position of tracks will fluctuate, the above effect will give rise to fluctuations in the output. We have estimated the size of these effects for parallel plate and cylindrical-wire collection geometries.

Parallel plate geometry. For most showers the number of track-gaps will be very large and the fluctuations in the position of the ionization within the gaps will be reduced by the square root of this large number. So we consider an extreme case, a 50 MeV gamma in a pure liquid argon detector with 1 cm gaps. Since the critical energy is 30 MeV, we have about two tracks. In other words the original electron-positron pair will be formed and then come to rest through ionization loss. If the tracks are perpendicular to the collection plates, there will be about 25 track gaps. Fluctuations in the relative lengths of the tracks give rise to track-gap variations of 1/2 track gap. The rms over the mean is then $(1/2/\overline{12})/\ 25 = .006$. If the tracks are at 45° to the plates, this is increased to .008. We conclude that this effect will be small, and we relegate it to the general unresolved background of 1% effects.

Cylindrical-wire geometry. Wire collection electrodes are attractive for mechanical reasons in a practical counter. We have therefore considered some of the effects associated with this option.

In a cylindrical volume of radius b with a wire of radius a, the voltage pulse induced by the collection of an electron originating at radius r equals $(e/2\pi\epsilon)\ln(r/a) = k \ln(r/a)$.[6] For a uniform distribution of ion pairs the mean voltage equals $k(\ln(b/a)-1/2)$ and the (root mean square deviation about the mean)/mean $= 1/(2\ell n(b/a)-1)$ The latter varies from 0.18 at b/a = 25 to .07 at b/a = 2000. (A 10 mm radius volume with a 5 micron radius wire has b/a = 2000.) Thus if a shower consisted of only one ion pair the resolution would be poor. This resolution is improved by the square root of the number of randomly distributed ion pairs, and since this will be quite large for most showers, this contribution to the resolution will be negligible. For low energy showers (50 MeV or less) this effect will contribute significantly to the resolution in a geometry with the wires longitudinal along the gamma direction. Such a geometry was considered by A. Odian at last year's Summer Study[7] and rejected for this reason. We conclude that wire collection electrodes transverse to the shower axis, replacing the conventional parallel plate geometry, will not contribute significantly to the energy resolution for the reasons considered here. However, it must be pointed out that we have not considered the effect of inductance in the wire geometry and this bears on electronic noise. Indeed it may be that the characteristic impedance of a wire collection electrode (treated as a transmission line) is large enough that the lumped component analysis used here is not applicable and considerations such as given in Ref. 8 should be used. We have not done this.

(C) Electronic Noise

We have considered three possible collector geometries.

(1) Squares. These were suggested at last year's Summer Study by A. Odian.[7] The hope was to connect them in tower arrangements (Shish-kebob geometry) so each detector defines a unique solid angle and each has a low capacitance. We have not devised a convenient way to connect the high voltage and readout squares. In addition there would be an enormously large number of elements requiring electronics and so we considered this arrangement no farther.

(2) Strips. These will be easier to construct and have a relatively low capacitance, but they will

have the problem that more than one gamma will hit the same strip.

(3) Wires. These will be similar to strips and perhaps easier to construct.

The capacitance for the wires and strips are not very different, so we use strips as an example for the following discussion of electronic noise.

We follow the electronic noise analysis of Willis and Radeka[1] based on a system where the signal from the collectors passes through a transformer into an FET preamplifier. The results of the analysis are shown in Table 2. The first two columns define the geometries considered, d is the liquid argon gap length and w the strip width. Column 3 shows the capacitance (C_d) for strips 1 meter long and with enough strips connected in parallel to make 1 radiation length in depth (= 1 cell). Column 4 gives the collection time assuming a drift velocity of 200 nsec/mm. The optimum transformer ratio (column 5) is given by $n = (C_d/C_A)^{1/2}$ where C_A is the FET, transformer, and stray capacitance. We follow Ref. 1 and take C_A = 30 pF.

Column 6 gives the rms energy fluctuations from electronics noise for 1 cell. = (52.8 MeV lost/signal electron detected) $4\sqrt{2}\, e_{n_{1/2}}\, (C_d C_A)^{1/2}/\lambda^{1/2}$, where e_n is the FET noise, 1 nV/$H_z^{1/2}$, and λ is the resolving time, which we take as 1.5 × collection time. In order to contain the entire shower we add together the cells for a depth of 12 radiation lengths and for a transverse distance of 60 cm. The noise from these cells adds in quadrature and is given in column 7. Finally, column 8 gives the ratio of the noise without a transformer to that with a transformer = 0.5(n + 1/n). For the last geometry it may be possible to eliminate the transformer.

The energy resolution for each of the geometries is shown in Fig. 4, and the resolution of NaI is shown for comparison. In the low energy region liquid argon is comparable to NaI for configuration f. The resolution increases as the square root of the length of the strips, so for 3 meter strips these resolutions are increased by 1.7. The resolution also varies as $d^{-3/2}$ so considerable improvement can be achieved if d, the spacing between electrodes, is increased. One pays linearly in collection time and the required high voltage as d is increased.

Attempts have been made to reduce the collection time by increasing the drift velocity through the introduction of polyatomic organic compounds to cool the electrons. A group (Ref. 9) at LBL has increased the drift velocity in liquid argon (at 10 kV/cm) by 30% using 500 ppm methane. An experimental program to study this problem has been started in Berlin by Gerhard Knies.[10]

One way to reduce the capacitance of the detector, which was used by Knies and Neuffer (Ref.11), is to couple the plates within a cell in series instead of parallel. We have not made an analysis of the noise nor the constructional difficulties for this configuration.

Electronic Noise with Passive Converter Plates. As plates of passive converter are added to pure liquid argon, the number of gaps per radiation length decreases, and thus the capacitance and electronic noise per radiation length is reduced. However, since the amount of energy being deposited in the argon is also reduced, the size of the signal is reduced, and eventually the fractional electronic noise increases. For the electronic noise with lead plates we find that the expression used above for the electronic noise in pure argon must be multiplied by the factor $F = (1 + 6.07\ r)/(1 + 25.2\ r)^{1/2}$ where r is the

Table 2. Electronics noise for various configurations of a pure liquid argon detector

(1) Type	(2) Collector dimensions w (mm)	d (mm)	(3) Capacitance for 1 meter by 1 X_0 (pF) = 1 cell	(4) Collection time (μs)	(5) Optimum transformer ratio	(6) rms energy fluctuations per cell (MeV)	(7) rms energy fluctuations per shower (MeV)	(8) Ratio of noise without transformer to that with it
a	10	2	4956	0.4	12.9	0.93	26	6.5
b	10	5	793	1.0	5	0.24	6.6	2.6
c	10	10	198	2.0	2.6	0.083	2.3	1.5
d	20	5	1586	1.0	7.3	0.33	6.6	3.7
e	20	10	396	2.0	3.6	0.12	2.3	1.9
f	20	20	99	4.0	1.8	0.042	0.82	1.2

0 0 0 0 4 5 0 1 6 0 3

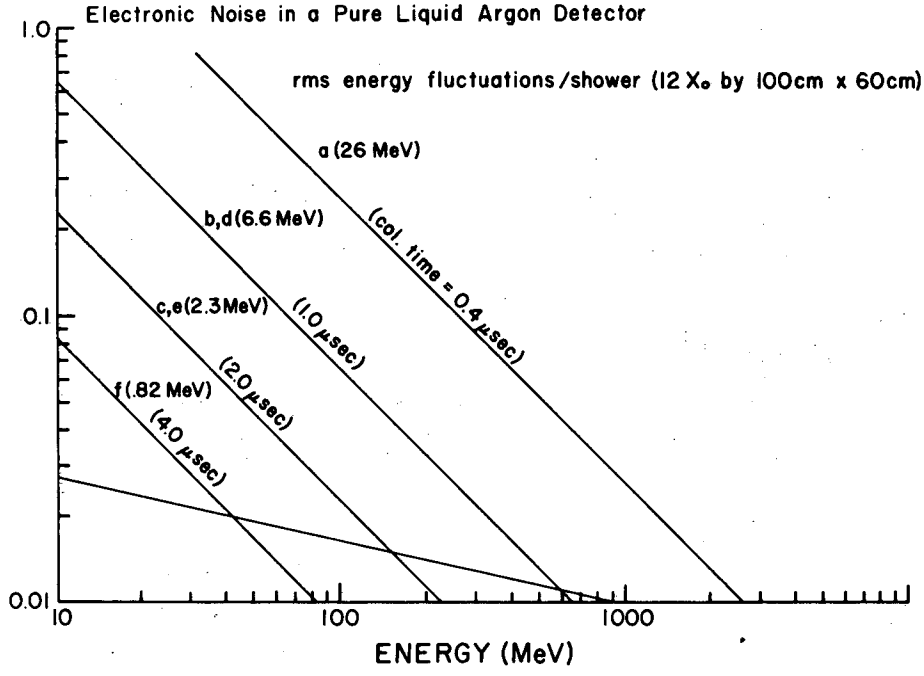

Fig. 4

XBL 7510-8457

ratio of the length of lead (cm) to the length of argon (cm) in each gap. The numerator in F comes from the reduced signal seen in argon and the denominator comes from the reduced capacitance per radiation length. This factor is plotted in Fig.5 and shows a shallow minimum at r = 0.085. For a gap of 2 cm in liquid argon, this implies a thickness of 1.7 mm of lead, which would introduce fairly large energy loss fluctuations in the lead. Our conclusion is that the noise reduction due to adding lead plates is small, and we expect that it would be more than offset by the energy loss fluctuations in the lead.

If no transformer is used, then the functional dependence of the noise on the capacitance changes from $(C_d C_A)^{1/2}$ to $(C_d + C_A)$, and the effect of adding plates is different. The factor relating the resolution in this case to that of pure liquid argon with transformer is given by

$$1/2 \left[(C_d/C_A)^{1/2}/(1 + 25.2\ r) + (C_A/C_d)^{1/2} \right] (1 + 6.07\ r).$$

This is plotted for two values of C_d/C_A in Fig.6, and again the electronic noise is not strongly reduced by the addition of lead plates.

In the above considerations we have not included the reduction in electronic noise that comes from the fact that the transverse shower spread may decrease as lead is added and thus fewer cells need be added to contain the shower.

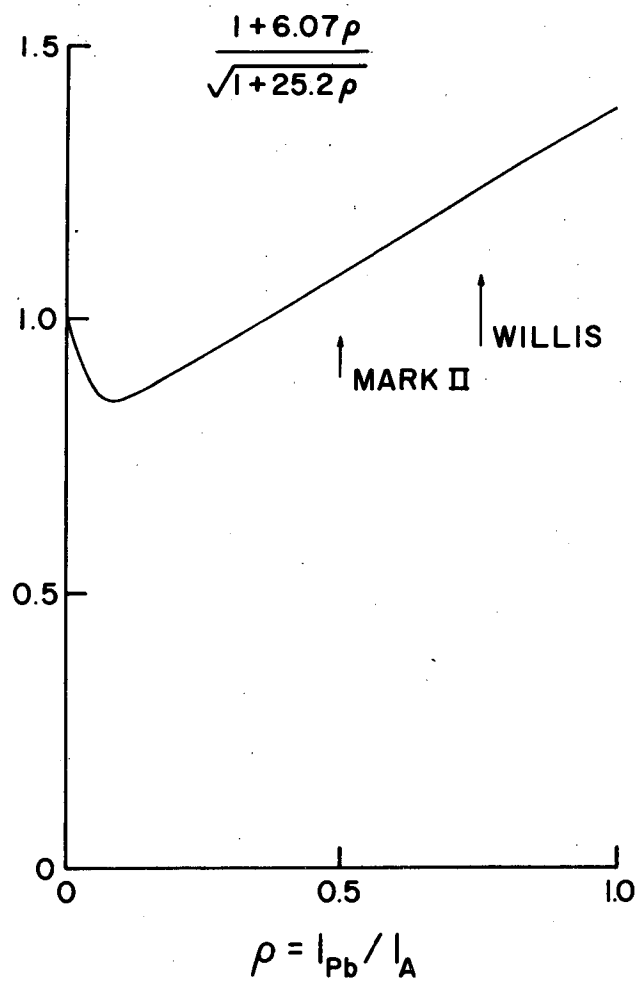

XBL 7510-8456

Fig. 5

2.2 MAGNETIC FIELD EFFECTS

The Electronic Effects

As noted earlier, signals from liquid argon are transmitted via ferrite core transformers ex-

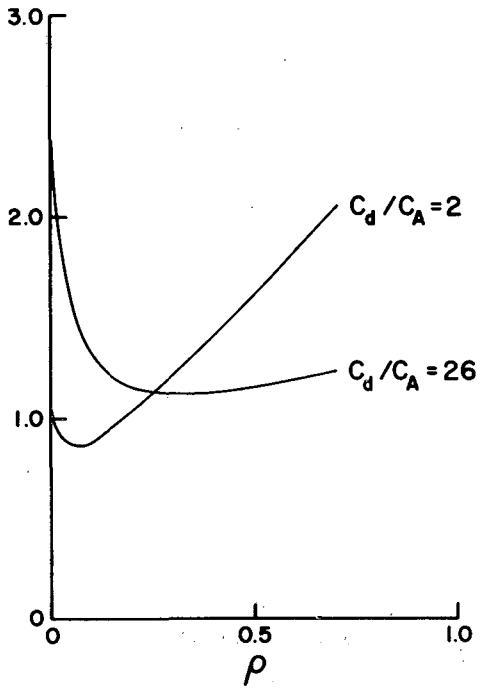

Fig. 6 XBL 7510-8448

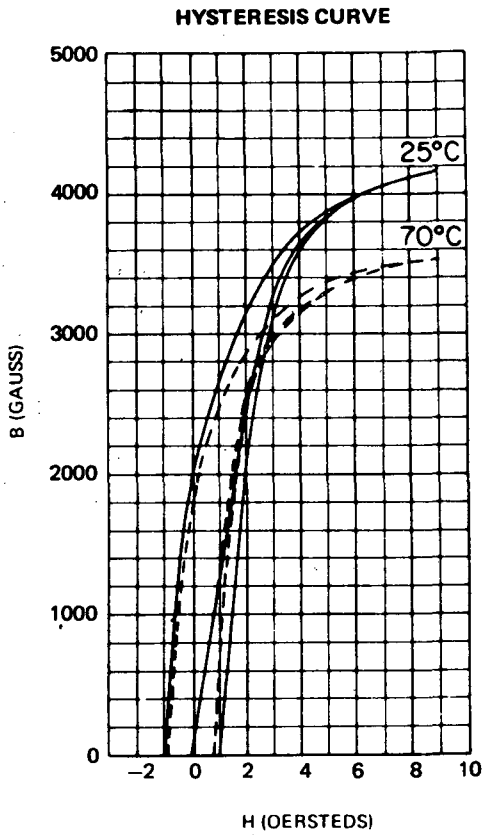

Fig. 7 XBL 7510-8486

cept in the unusual circumstance of very low ion chamber capacitance. The signals are small, and thus the excursions on the characteristic hystresis curves are also small. The response of the transformer then depends only on the slope of the hysteresis curve at the ambient excitation. The characteristic curve for the 3D3 ferrite, shown in Fig. 7, (Ref.12) appears to be linear for fields up to about 1600 gauss. Typically, a high-permeability material in air will gather flux from an area of order four times the cross section perpendicular to the field. Thus a 3D3 ferrite in an ambient field of 400 gauss would shunt a field of order 1600 gauss. We conclude that a 3D3 ferrite would have an output independent of ambient field up to about 400 gauss--providing that the core operates always on the same hysteresis curve. This implies that such cores could be used routinely in fringing fields, possibly with some magnetic shielding, but they would not operate in the high field region of typical magnetic detectors. A further point is that calibration pulses should be injected into the electronics in situ upstream of the transformers, rather than downstream, to incorporate any magnetic field effects into the calibration.

Shower-Track Sampling Effects

Pure Liquid Argon Detector. In a total absorption detector, such as liquid argon or sodium iodide, virtually all of the shower energy appears ultimately in the form of ions, photons, and free electrons. It makes no difference whether shower tracks are straight or curved due to a magnetic field. In particular, the number of ions, free electrons, or photons is independent of the field.

Sampling Detector. To be specific, we consider a sampling detector consisting of lead plates and liquid argon gaps. The gain is determined by the fraction of the ionization that occurs in the argon. This fraction is normally small so that, for example, doubling the gap doubles the signal. We then ask: To what extent does the presence of a magnetic field alter the fraction of the ionization that occurs in the liquid argon sensitive volume?

The pathological example shown in Fig. 8 illustrates that the fraction of the ionization sampled can be influenced by a magnetic field. Case 1 corresponds to a lead-liquid argon detector with no field, and Case 2 corresponds to the same device in a field so large that no charged shower particle reaches the next lead plate. Evidently,

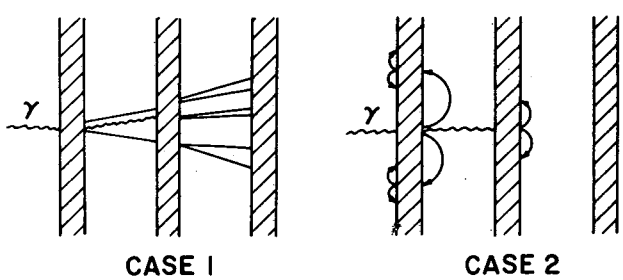

Fig. 8 XBL 7510-8452

0 0 0 0 4 5 0 1 6 0 4

the amount of detectable ionization is proportional to the width of the liquid gap for Case 1 and independent of it for Case 2. This shows that the presence of the field does change the response and that the magnitude of the effect can be large. For example, it can be larger than a factor of 10.

A rule of thumb for track sampling is that the magnetic deflection of shower tracks at the critical energy of the absorber plates should be small compared to the spacing between plates. For example, if the absorber plates are of lead (critical energy of 8 MeV) and if the plate spacing is 2 mm, then fields of a few thousand gauss would cause significant changes in gain.

If a large lead-liquid argon detector is operated in the fringing field of a magnet and if the field is high enough to cause sampling errors of the type just described, then variations in the field would lead to non-uniformity of the detector response as a function of position. Calibration and correction of such an effect would be tedious and difficult in a large device.

Electron Collection

To what extent does the collection of electrons depend upon the magnetic field?

In the case of integrating detectors, such as the ionization quantameter, the integration time is very long and fully covers the time interval during which induced current flows from both the primary ions and electrons. Any recombination of ions and electrons would be sensitive to the ambient magnetic field, but this is minimized by using an ionization medium, gas or liquid, of sufficiently high purity. Thus this type of device can be made to have no magnetic field dependence due to this source.

In a detector sensitive to individual tracks (or events) such as we have been considering, the electronic integrating time is long enough to include the induced current from the motion of the primary electrons, but so short that it includes almost none of the current from the much slower motion of the heavy positive ions. This is just the effect that gives rise to the dependence of output signal on position of ionization considered in Section 2.1.2. As is illustrated for an extreme case in Fig. 8, the equivalent location of ionization is at the center of the gap in Case 1, but displaced from the center in Case 2. Thus in addition to the effect on output signal due to the change in energy deposition in the liquid discussed above, the magnetic field will also give rise to a change in the output signal induced by this ionization.

Summary

It appears that liquid argon detectors will be sensitive to magnetic fields via: (1) saturation of ferrite cores in the readout, (2) change of track length of low energy shower tracks in the liquid (applicable when lead plates are used), (3) change of the equivalent location of the ionization between the plates (applicable whether or not lead plates are used). The first of these can be controlled by locating the cores in a low field region for which the price may be increased capacity and inductance in the coupling cable. Displacement of the shower tracks would occur throughout the large volume of the detector itself, and the results are harder to anticipate or correct. Clearly it is important to operate liquid argon and lead-liquid argon detectors in a magnetic field before large devices of either type are constructed.

2.3 Spatial Resolution

The spatial and angular resolution for individual gammas will be determined by taking the centroid of the shower on the strips, and we expect the spatial resolution will be equal to or less than a strip spacing of 1 or 2 cm. For the LAND detector described below this will give an angular resolution of about 10 milliradians or better.

However, a matter of some concern in a pure liquid argon shower detector is the transverse size of the showers since this leads to non-negligible overlap probabilities for the expected gamma multiplicities of 10 to 15. Analytic shower theory[13] gives the result that about 90% of the energy in a shower is contained in a cylinder, of diameter 3.6 R_M (36 cm), where R_M is the Moliere radius

$$R_M = \frac{21 \text{ MeV}}{E_c} X_0 = 10 \text{ cm for liquid argon,}$$

where E_c is the critical energy and X_0 the radiation length. This shower model assumes that electromagnetic processes lead to negligible angular displacements and only the effect of the multiple Coulomb scattering of the shower particles is considered.

Experimental work (Ref. 14,15), however, indicates that in low Z materials the transverse sizes are larger than those which analytic theory predicts. This is attributed to the annihilation radiation, but the experimental evidence is independent of this interpretation. In Figs. 9 and 10 we show the observations of transverse shower size in units of R_M. Extrapolating smoothly in Z to argon leads us to expect that 90% of the shower is contained in a cylinder of radius 3 R_M = 30 cm at 185 MeV and 2.25 R_M = 23 cm at 900 MeV.

In a shower detector of the kind we are considering, the radial distribution is not measured. Instead the transverse projection of this onto strips is detected. If we take the radial distributions implied by the data in Figs. 9 and 10 and project them transversely onto the strips, we see 90% of the energy in a transverse distance of $4R_M$ (2.8 R_M) for the 185 MeV (900 MeV) shower. Thus for the low energy showers, the transverse size is about 40 cm.

This relatively large transverse size has two consequences. First, there will be random overlaps of the showers from uncorrelated gammas and secondly, the two gammas from a high energy π^0 will be strongly mixed. Walker[16] has given a method based upon second moments which allows one to reconstruct the invariant mass of an overlapping gamma pair, and thus search for π^0's. The analysis

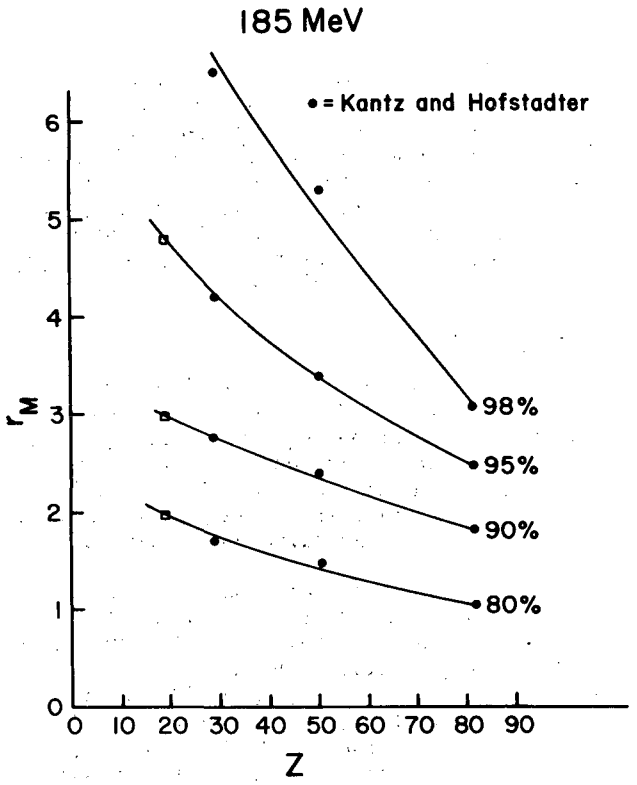

Fig. 9

XBL 7510-8454

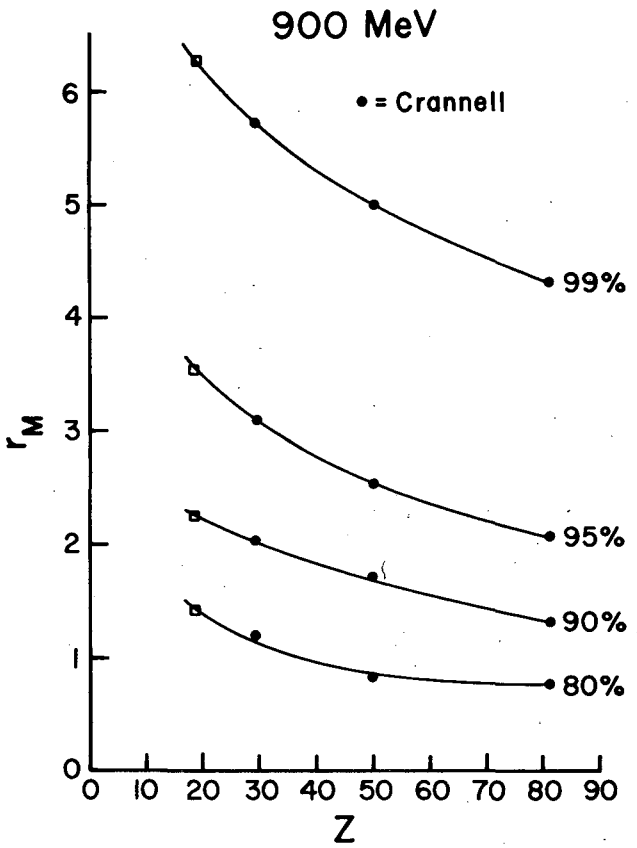

Fig. 10

XBL 7510-8453

he gives assumes that the photons strike the detector perpendicular to the readout planes and this will probably not be the case in a PEP detector. However, the longitudinal development of a shower is measured so that a correction can be applied for non-normal incidence. The general problem of overlapping showers is considered in detail by Bulos in "Resolving Overlapping Gammas in a Modular Neutral Detector," a paper from this Summer Study and it seems feasible to use an analysis similar to Walker's.

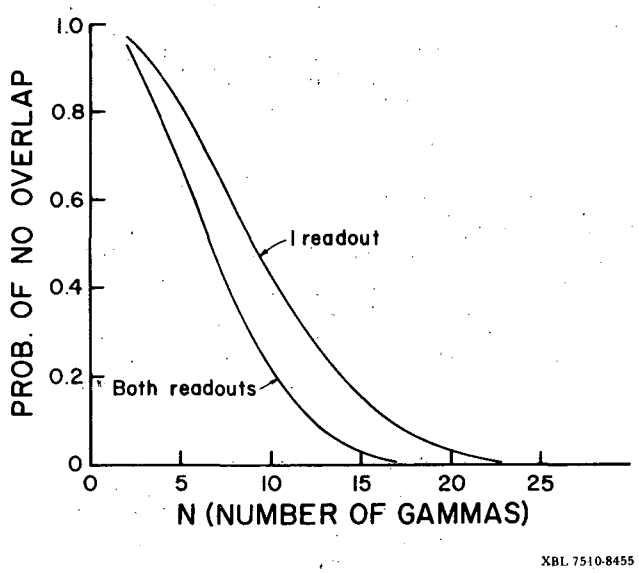

XBL 7510-8455

Fig. 11

The probability of no overlapping gammas in an event with N photons with isotropic distribution is

$$\prod_{n=2}^{N} (1 - nf),$$

where f is the fraction of the total space used by each photon. It is interesting to calculate the fraction of events in which there is no overlap in either of two orthogonal readouts for the liquid argon detector described in Section 3. The detector is broken into octants, split longitudinally along the beam into two 2-meter sections, and the shower maxima occur at a radius of about 2.2 m. The value of f for the strips parallel to the beam is $(0.40)/(2\times 2\pi \times 2.2) = 0.0145$ and for the transverse strips $(0.40)/(8\times 4.0) = 0.0125$. Figure 11 shows the probability per event of no overlap on a single longitudinal readout and on neither of the two readouts. It is seen that with the assumptions made here, essentially every event will have at least one pair of gammas overlapping for the expected photon multiplicities, even ignoring the correlations between them implied by the jet model. The energy resolution for these overlapping gammas will be degraded, and the importance of this needs to be studied further.

3. A NEUTRALS DETECTOR FOR THE GENERAL USER MAGNET

The General User Magnet (GUM) is described in detail in a paper from this Summer Study. It has a segmented coil to produce a solenoidal magnetic

0 0 0 0 4 5 0 1 6 0 5

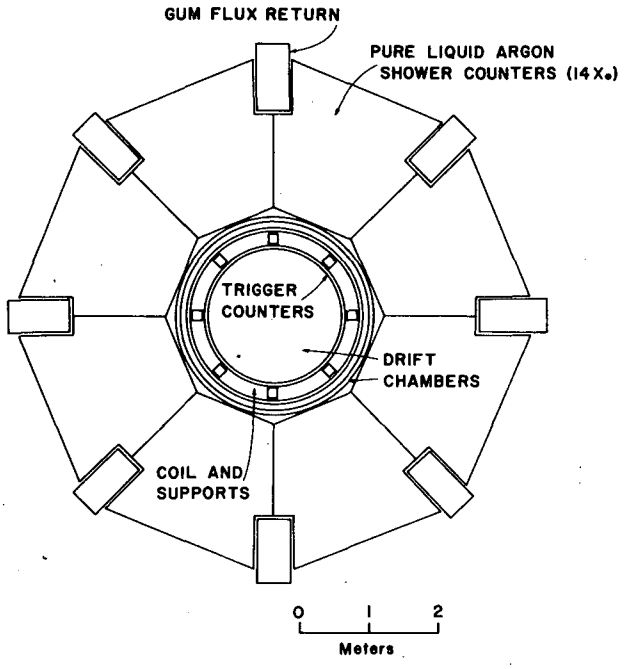

XBL 7510-8451

Fig. 12

field region of 1-meter radius, and this field region is instrumented with drift chambers. We describe here a possible design for instrumenting the region outside the coil with a pure liquid argon detector (see Fig. 12).

The GUM has a lumped coil which leaves 78% of the solid angle down to $\theta = 30°$ unobstructed in θ and 82% of the ϕ coverage unobstructed. Thus 56% of the total solid angle, or 71% of the coverage down to $\theta = 30°$ has a minimum of material. Of course in practice this region has some material; 0.05 radiation lengths for scintillation trigger counters, 0.05 radiation lengths for cryogenic insulation of the superconducting coils, 0.10 radiation lengths for the structure and insulation of the liquid argon tank. In the region covered by the coils and their support structure there is very poor or no gamma energy measurement. In contrast, for a uniform solenoidal coil 0.33 X_0 thick, the energy resolution is degraded throughout the entire region for those gammas which convert (about 27% of the gammas). This degradation is described in Section 2.1.1. A disadvantage of the GUM design is that the coil support and end cap flux return make it very difficult to achieve good neutrals coverage for $\theta < 30°$. It would be possible to put a more compact photon detector, such as lead glass/liquid argon sandwich, in front of the vanes, but we have not attempted this in our design.

We have divided the liquid argon detector into eight identical modules fitting between and suspended from the flux returns of the GUM. The modules are trapezoidal in cross section (see Fig. 13), 2 m (14 radiation lengths) in depth, 1.25 m in their transverse dimension inside and 3 m outside. Their volume is 17 m^3/module and

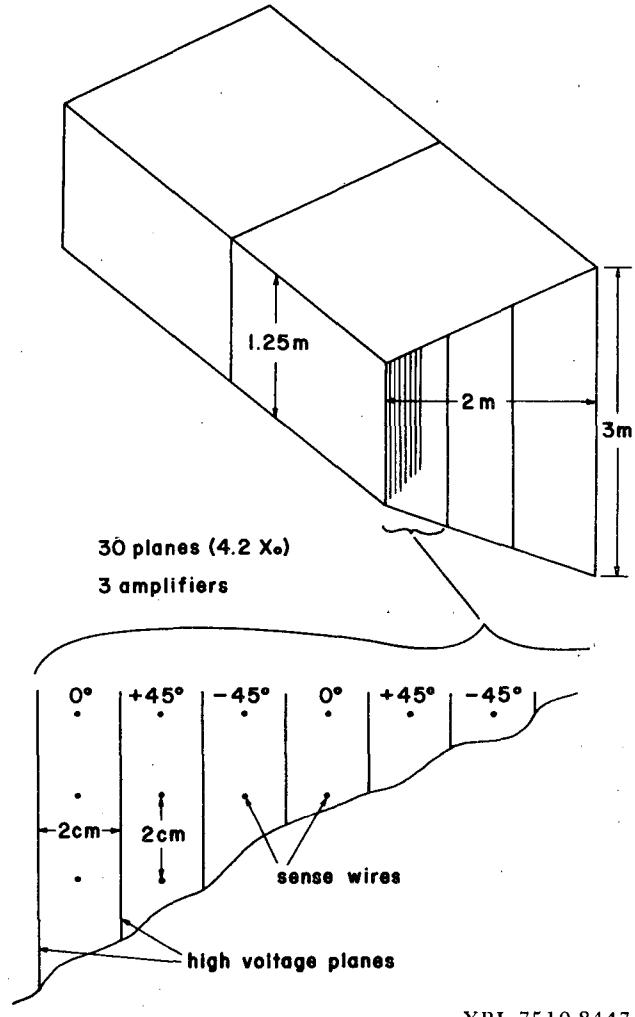

XBL 7510-8447

Fig. 13

they each weigh 24 metric tons when filled. This is quite heavy, but does not constitute an assembly problem, since the unfilled tanks will weigh only a few tons. We have not estimated the cost of the detector, but we note that the cost of the liquid argon at 50¢/liter is $8500 per module and so this part of the expense is negligible. With this large volume, a refrigerator is clearly preferred over a heat exchanger that boils LN.

The readout consists of 100 planes of cells. High voltage wires or planes spaced 2 cm in depth are stretched along the 4-m dimension in each module. Each longitudinal half of the module is read out separately. Readout wires are placed midway in each layer, 2 cm apart. These wires are alternately at 0°, +45°, and -45°. About 10 wires of a given orientation are grouped in depth and connected to a single amplifier. Thus there are six channels in depth (two for each of three orientations) and an average of 130 transversely. Thus, each module requires 2×6×130 = 1560 channels of readout; the eight modules then require 12,500 channels of electronics, which probably makes it economically necessary to multiplex the ADC's.

The energy resolution for this detector (coming solely from electronics noise) is shown in Fig. 14.

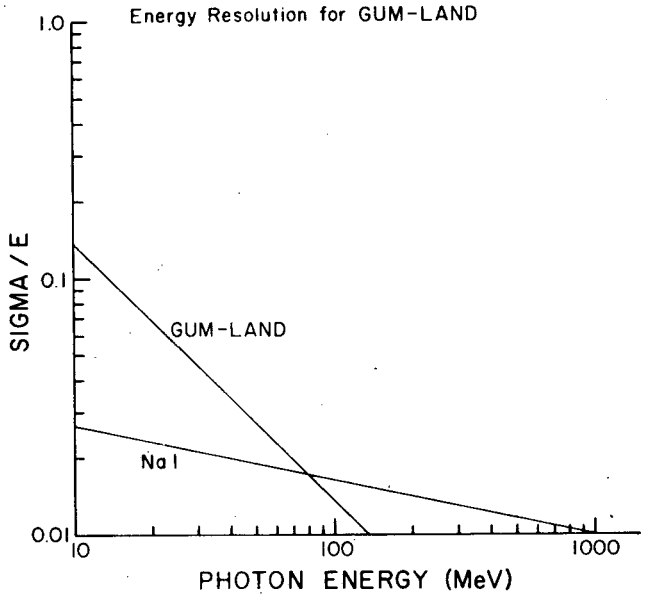

Fig. 14

4. CONCLUSIONS

We conclude that it is feasible to build a pure liquid argon detector for PEP that will have energy resolutions for electrons and gammas above about 100 MeV that are comparable to those achieved by NaI. In addition, such a detector can measure the longitudinal development of a shower which is useful for electron-hadron discrimination. The detector is flexible in the sense it can be designed to fit into a variety of geometries and is inexpensive enough to be built around a magnetic charged particle detector with good momentum resolution.

We have discussed in this report various aspects of the design of a pure liquid argon counter but have not presented a detailed design of a complete detector system for PEP. The following work needs to be done before a detailed design can be made.

(1) A better understanding of the effect of lead plates on the energy loss fluctuations and the transverse spreading of showers is needed to know whether such plates can be used to reduce the gamma overlap problem without destroying the good energy resolution.

(2) More experimental work needs to be done on increasing the electron drift velocity through the use of organic additives.

(3) Experimental measurements of the effect of magnetic fields on liquid argon chambers will establish constraints or freedoms in the design of a practical PEP detector.

(4) A more detailed study should be made of effects we found here which contributed to the resolution at about the 1% level.

References

1. W. J. Willis and V. Radeka, Nuclear Instruments and Methods 120, 221-236(1974).

2. S. E. Derenzo, et al. Nuclear Instruments and Methods 122, 319 (1974).

3. Particle Data Group. Physics Letters, 50B (April 1974).

4. M. A. Green. "The Large Superconducting Solenoid for the Minimag Experiment." Lawrence Berkeley Laboratory Report LBL-3677.

5. T. S. Mast and J. E. Nelson. 1974 PEP Summer Study, PEP-153.

6. H. H. Staub. Experimental Nuclear Physics. Volume 1, E. Segrè, editor John Wiley, New York (1953).

7. A. Odian. 1974 PEP Summer Study, PEP-156.

8. V. Radeka. IEEE Trans. Nucl. Sci. NS-21, 51 (Feb. 1974).

9. Private communication, S. Derenzo, A. Kirschbaun, T. Tometani, H. Zaklad.

10. G. Knies, private communication.

11. G. Knies and D. Neuffer. Nuclear Instruments and Methods 120, 1 (1974).

12. "Ferroxcube Linear Ferrite Materials and Components." Ferroxcube Corporation, Saugerties, New York, 2nd edition, pp. 1-11 (1974).

13. Grieson, Progress in Cosmic Ray Physics. vol.3 (1956).

14. C. J. Crannell, Phys. Rev. 161, 310 (1967).

15. Kantz and Hofstadter. Phys. Rev. 89, 607 (1953) and Nucleonics 12, 36 (1954).

16. R. L. Walker. California Institute of Technology Report CALT-68-330.

0 0 0 0 4 5 0 1 6 0 6

RESOLVING OVERLAPING GAMMAS IN A MODULAR NEUTRALS DETECTOR

F. Bulos

Abstract

It is shown here that in a segmented neutral detector the method of moments can be used to determine whether a connected region of energy deposit involving several modules contains one, two, or more γ's. Up to 2 γ's can be handled analytically to solve for their energy and position. Further it is shown that if the positions of the γ's are determined externally, then the method of moments can be used to solve the problem of more than 2 γ's analytically.

* * * * * * *

It was shown by Walker et al (Calt-68-330) that the method of moments can be used to determine the ratio M/E for a particle depositing energy (via its γ decay) in a connected region of a segmented neutral detector. Essentially, if all the overlapping γ's come from the same particle (e.g.) 2 γ's from π^0), the ratio M/E for the particle can be determined and hence one can identify the particle.

The method however cannot separate the γ's and hence is not suitable for recognizing individual (isolated) γ rays. The analysis described here (developed with the help of J. Friedman, SLAC computation Group) is an attempt at separating overlapping γ's analytically.

The principle involved has been verified experimentally and with Monte Carlo calculations namely:

Consider a γ (c) of energy E_0 incident on a slab of radiator of a depth along the γ direction sufficient for total absorption. The fractional energy E_r deposited in a cylinder with its axis along the γ direction of radius between r and r + dr and length equal to the depth of the total radiator (i.e., energy is integrated longitudenally) is independent of the γ energy E_0 and is a function of r only:

$$\frac{E_r}{E_0} = f(r).$$

If f(r) is projected on an axis z, one obtains f(z) which has the same property, i.e.,

$$\frac{E_z}{E_0} = f(z).$$

The two functions differ only in normalization. Instead of the fractional energy, the fractional energy density $(E_r/A_rE_0) = \rho(r)$ will be used here and its counter part $\rho(z)$ with:

$$\int_0^\infty \rho(r)\, 2\pi r\, dr = 1; \qquad \int_{-\infty}^{\infty} \rho(z)\, dz = 1$$

and

$\rho(z) = \rho(-z)$; i.e., $\rho(z)$ is an even function.

We will assume that the areas of the individual segments of the detector are equal or known, and so the areas will not appear explicitly.

Two cases will be dealt with here: Case I where no external determination of the γ position is made and Case II where γ positions are known.

CASE I

Let (x_i, y_i) be the centers of energy deposit E_i in module i with respect to co-ordinate system X,Y. parallel to the plane of detector (i.e., the Z axis is along the longitudinal direction of the modules).

E_i is known from the pulse height of the module and x_i, y_i can be taken to be the center of the module.

Then the following averages are known

$$\bar{X} = \Sigma x_i E_i/\Sigma E_i = \Sigma x_i E_i/E_{TOT}$$

$$\bar{Y} = \Sigma y_i E_i/E_{TOT}$$

$$\overline{XY} = \Sigma x_i y_i E_i/E_{TOT}$$

$$\overline{X^2} = \Sigma x_i^2 E_i/E_{TOT}$$

$$\overline{Y^2} = \Sigma y_i^2 E_i/E_{TOT}.$$

The equations of the major and minor axis of the energy deposit and its major and minor variances are given by the eigen vectors and eigen values obtained by diagonalizing the following matrix:

$$\begin{bmatrix} \overline{X^2}-\overline{(X)^2} & \overline{XY}-\bar{X}\,\bar{Y} \\ \overline{XY}-\bar{X}\,\bar{Y} & \overline{Y^2}-(\bar{Y})^2 \end{bmatrix}$$

Let the eigen axes and eigen variances be u,v and λ_s, λ_ℓ respectively. Figure 1 helps illustrate the method. Note that the eigen vectors pass through the center of gravity and for the case of two γ's their centers must fall on the major axis.

To differentiate one, two, or more γ's, one proceeds as follows

a) $\lambda_s = \lambda_\ell$ indicates one γ or a conspiracy.

b) For two γ's, $\lambda_s \neq \lambda_\ell$, and further more the distribution is skewed along the major axis un-

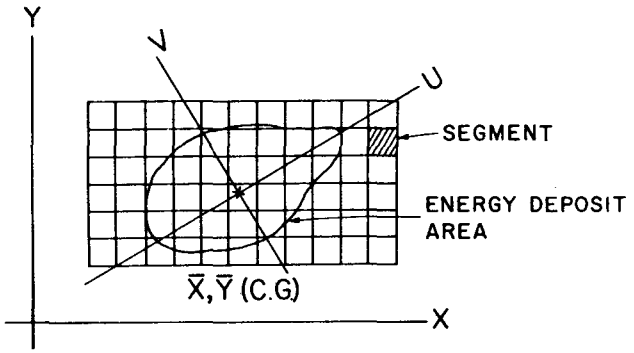

Fig. 1 XBL 7510-8384

less the two γ's are equal. The third moment M_3 with respect to the c.g. co-ordinate system where u is the major axis, can be used to measure skewness ($M_3(u) = \Sigma E_i u_1^3/E_{TOT}$). Hence

$$\lambda_s \neq \lambda_\ell,\ M_3(u) \neq 0,\ M_3(v) = 0$$

indicate two γ's of unequal energies

$$\lambda_s \neq \lambda_\ell,\ M_3(u) = 0,\quad M_3(v) = 0$$

indicate two γ's of equal energies or conspiracy.

c) $\lambda_s \neq \lambda_\ell,\ M_3(u) \neq 0,\ M_3(v) \neq 0$

indicate more than two γ's.

Complete Solution of Two γ's

With the help of Fig. 2 for two γ's one can write the following set of equations

$$E_1 + E_2 = E_{TOT} \quad (1)$$

$$E_1 v_1 + E_2 v_2 = 0 \quad (2)$$

$$(E_1 v_1^2 + E_2 v_2^2)/E_{TOT} = \lambda_\ell - \lambda_s \quad (3)$$

$$\lambda_s = \sigma^2 (E_1 + E_2)/E_{TOT} = \sigma^2 \quad (4)$$

where σ^2 is the (width)^2 of the single γ linear fractional density function $\rho(z)$ described above. Remember that σ is a constant for all γ's, known from $\rho(z)$ either experimentally or by Monte Carlo.

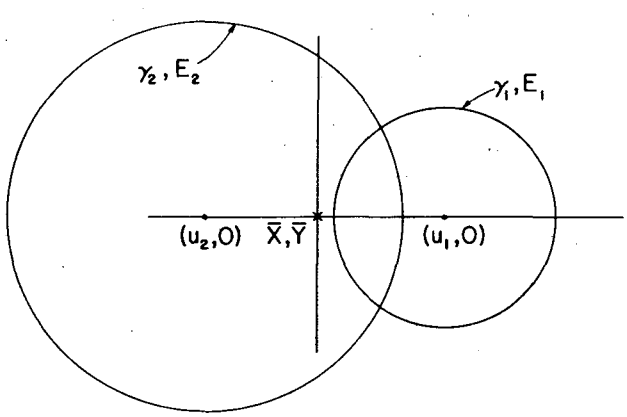

Fig. 2 XBL 7510-8386

Only one of the equations (Eq. (3)) is not immediately obvious. Its proof becomes clear in Case II below.

We thus have four equations with four unknowns E_1, E_2, v_1, v_2, i.e., the two energies and positions of the γ's. (Recall that $u_1 = u_2 = 0$, an additional equation which has been already used in Fig. 2). Hence the case of two γ's can be solved completely. For more than two γ's we do not have enough equations. This is discussed in Case II below.

CASE II. Effect of position measurement on the separation of individual γ's.

Let x_n, y_n, E_n be the co-ordinance and the energy deposit measured in the n-th module (these quantities are known). Then the first moments give

$$\bar{X} = \frac{\Sigma E_n x_n}{\Sigma E_n} = \frac{\Sigma E_n x_n}{E_{TOTAL}}$$

$$\bar{Y} = \frac{\Sigma E_n y_n}{\Sigma E_n} = \frac{\Sigma E_n y_n}{E_{TOTAL}}$$

The second moments give

$$\sigma_x^2 = \frac{\Sigma E_n x_n^2}{E_{TOT}}$$

$$\sigma_y^2 = \frac{\Sigma E_n y_n^2}{E_{TOT}}.$$

Thus we have the following known quantities:

$$(\bar{X},\bar{Y}) \text{ (center of gravity)},\ E_{TOT},\ \sigma_x^2,\ \sigma_y^2.$$

Consider i γ's whose positions are known (from an external converter - position identifier). Let the co-ordinates of γ's with respect to a co-ordinate system translated to $\bar{X},\bar{Y}$ as center be u_i, v_i. These are known.

We now use the properties of the linear fractional density function of a single γ which was described before.

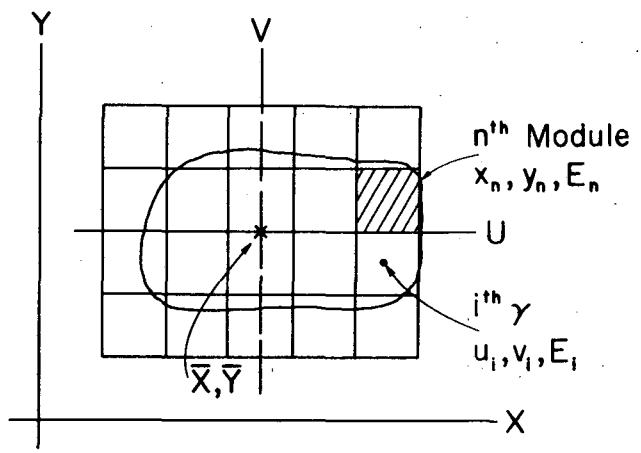

Fig. 3 XBL 7510-8385

0 0 0 0 4 5 0 1 6 0 7

Let E(u) be the continuous linear energy deposit in the cluster projected on the u axis; E(v) is projected on the v axis. It is easy to see (Fig. 3) that

$$E(u) = \Sigma E_i \, \rho(u_i - u)$$

$$E(v) = \Sigma E_i \, \rho(v_i - v)$$

$$\sigma_u^2 = \frac{1}{E_{TOT}} \int E(u) u^2 \, du$$

$$\sigma_v^2 = \frac{1}{E_{TOT}} \int E(v) v^2 \, dv$$

Thus we can write

$$\sigma_u^2 = \frac{1}{E_{TOT}} \int (\Sigma \, E_i \, \rho(u_i - u) u^2) du$$

$$\sigma_v^2 = \frac{1}{E_{TOT}} \int (\Sigma \, E_i \, \rho(v_i - v) v^2) dv$$

For each term in the integrand we write $u = (u-u_i)+u_i$ and similarly for v. Substituting in the integrands and recalling that $\rho(z)$ is an even function of z, we obtain

$$\sigma_u^2 = [\sigma^2 \, \Sigma E_i + \Sigma E_i u_i^2] / E_{TOT}$$

$$\sigma_v^2 = [\sigma^2 \, \Sigma E_i + \Sigma E_i v_i^2] / E_{TOT}$$

where σ is the known constant width of single distribution function.

We thus have the following general equations (compare with Case I)

$$\left.\begin{aligned} \Sigma E_i &= E_{TOT} \\ \Sigma E_i u_i &= 0 \\ \Sigma E_i v_i &= 0 \end{aligned}\right\} \quad \text{C.G.}$$

$$\sigma_u^2 = \frac{1}{E_{TOT}} [\sigma^2 \, \Sigma E_i + \Sigma E_i u_i^2]$$

$$\sigma_v^2 = \frac{1}{E_{TOT}} [\sigma^2 \, \Sigma E_i + \Sigma E_i v_i^2]$$

The only unknowns are the E_i. In principle then the case of up to five γ's whose positions are known can be handled analytically.

REPORT OF THE GENERAL PURPOSE DETECTOR GROUP

A. Barbaro-Galtieri, W. Bartel, F. Bulos,
R. Cool, G. Hanson, U. Koetz, R. Kotthaus
S. Loken, D. Luke, A. Rothenberg

Abstract

In this report we describe a general purpose detector for PEP. The main components of this detector are a 1 meter radius, 15 kilogauss superconducting solenoidal magnet with drift chambers to detect and measure the momentum of charged particles, a liquid argon neutral detector and hadron calorimeter, and a system of Čerenkov and time-of-flight counters for identification of charged hadrons. A major consideration in the design of this detector was that it be flexible: the magnet coil and drift chambers form a core around which various apparatus for specialized detection can be placed.

I. INTRODUCTION

A general purpose detector for PEP should have the following properties:

1. Large solid-angle coverage for detecting and measuring both charged and neutral particles;

2. Good momentum and angular resolution for charged and neutral particles over a large solid angle;

3. Good charged-particle identification over as large a solid angle as possible;

4. Good muon and electron identification over a large solid angle.

The problems involved in designing such a detector were considered separately by three subgroups of the General Purpose Detector Group: the Streamer Chamber Subgroup, the Time-Projection Chamber Subgroup, and the Wire-Chamber Subgroup. The first two subgroups have submitted separate reports to this Summer Study. We present here the conclusions of the Wire-Chamber Subgroup.

II. MAGNETIC FIELD CONFIGURATION

Three possible field configurations were considered in relation to their suitability for a general detection facility for PEP. A magnetic field transverse to the beam axes was rejected because a large field integral is required (~ 10 - 20 T-m) and the synchrotron radiation would produce a serious source of background. The possibility of using a toroidal field was also given some consideration. It was concluded that the toroidal field is not optimal for a general detection facility for the following reasons: (1) the forces on the conductors to produce the required field integral are very large, (2) as a result of (1), the material required to restrain the forces will obscure too large a fraction of the aperture, and (3) the fringing magnetic field for a relatively open configuration would place severe limitations on the choice of detection system. In particular, detectors using phototubes would be severely handicapped and central detectors requiring a uniform field, such as the time-projection device,[1] would be eliminated. Moreover, the strongly nonuniform field would place an unnecessarily heavy burden on a pattern recognition system for the expected high-multiplicity events at PEP energies.

For the reasons outlined above, we have chosen to study the use of a solenoidal field configuration with its axis parallel to the beam axes for use with a general detection facility. We recognize that the configurations which we have rejected for our purpose may in fact be required in other specific experimental situations.[2]

Finally, the solenoidal field may be generated either by a continuous, uniformly wound coil over the required length or by a set of "lumped" coils spaced along the axis, with no material between coils other than that required to restrain the magnetic forces. We consider here the continuous solenoid, while the "lumped" coil configuration is the subject of another report.[3]

Two possible designs for general detection facilities using continuous solenoid coils were presented in the PEP Summer Study Report of 1974.[4] This report should therefore be considered as an updating of the 1974 study based on the SPEAR physics results which have become available within the year, the decision by SLAC to build a new Mark II detector for SPEAR, and, of course, new techniques and new ideas which have been advanced.

Our starting point is the assumption that the Mark II SPEAR general detector system will be available as a facility at PEP. A general detector system specifically designed for PEP must therefore be complementary to Mark II and be designed taking into account the much higher energies which will become available.

During the past year, studies of new techniques for building superconducting coils requiring a small fraction of a radiation length of material have made considerable progress at CERN, LBL, and elsewhere. Descriptions of this work given during the Summer Study[5] lead us to conclude that, on the PEP time scale, we can foresee with considerable confidence its use for high-field (~ 15 kG) solenoids with radii of about one meter. Based upon the data available to us, we will therefore assume that a continuous solenoid coil of 1 m radius with 15 kG can be constructed, and that the total material of the conductors and cryostat can be held to about one-half radiation length in thickness. There is a distinct advantage if this assumption is correct.

0 0 0 0 4 5 0 1 6 0 8

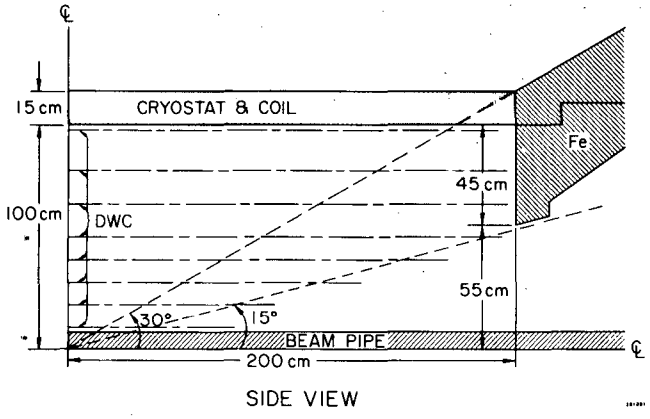

Fig. 1 Side view of the central region of a continuously wound, superconducting solenoid magnet.

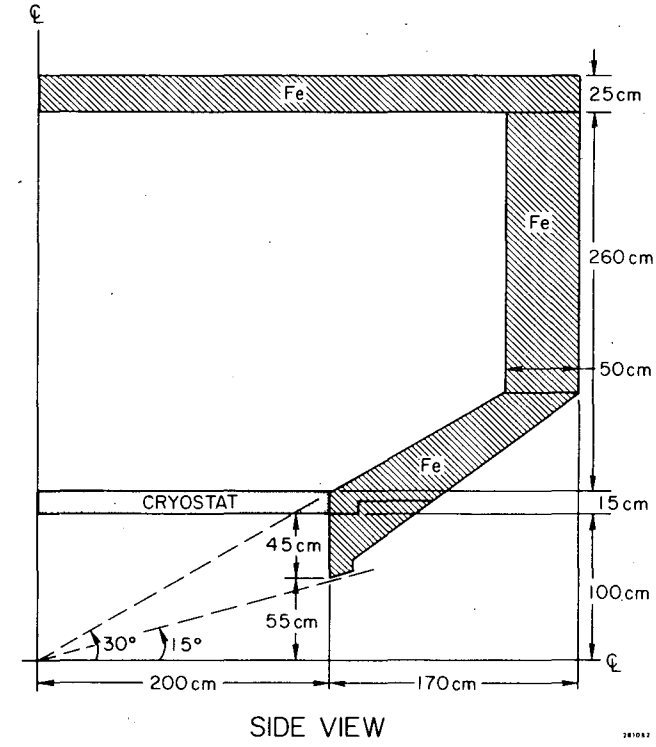

Fig. 2 Side view of a continuously wound, superconducting solenoid magnet showing the proposed Fe magnetic flux return.

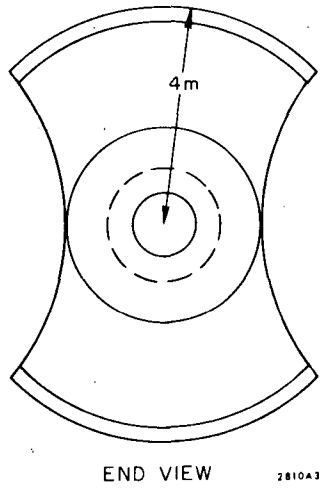

Fig. 3 End view of the proposed magnet configuration.

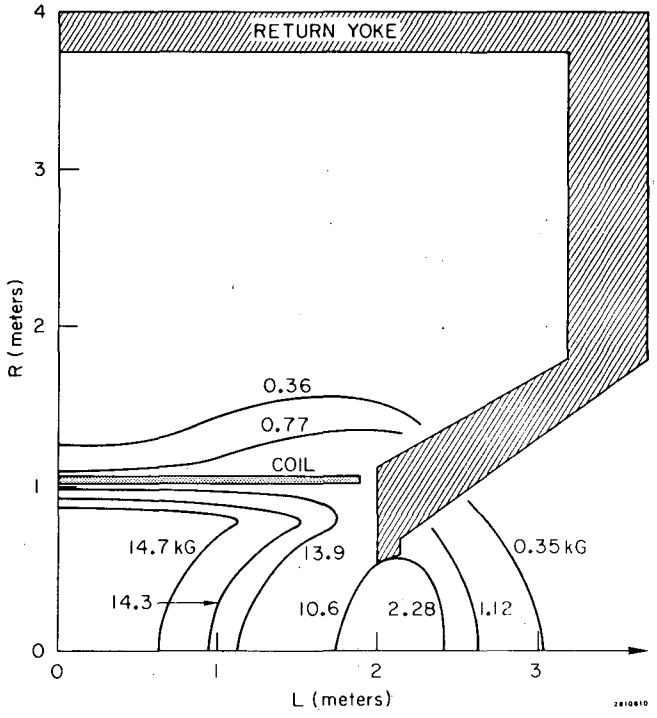

Fig. 4 Magnetic flux map for the proposed magnet configuration showing lines of constant magnetic field (kG).

Since PEP will produce higher momentum secondaries than SPEAR,[6] a larger field integral is desirable to minimize the error for high momentum particles. This larger field integral can be achieved on a smaller radius and, since the cost of detectors is typically proportional to the square of the radius, potential cost savings are considerable.

To supplement Mark II, it would be desirable for a new PEP device to cover a larger solid angle within which measurements of charged-particle momenta and γ-ray energies can be made with adequate accuracy. Considerations of 2-γ physics, which are discussed elsewhere in this report,[7] strongly suggest that a cone of $\sim 15^{\circ}$ opening angle be left open in the forward and backward directions and that the magnet design be compatible with upstream and downstream external detectors. We have adopted these suggestions as design criteria.

A possible design for a magnet which appears to meet the above criteria is shown in Figs. 1, 2 and 3. The cryostat and coil are assumed to represent a total of about one-half radiation length. The physical thickness of $\approx$ 15 cm is taken from the CERN ISR solenoid design. In Fig. 4, the magnetic flux map is displayed. The magnetic field is uniform to within 6% in the central region of the detector.

It should be noted that the iron magnetic flux return shown is, in a sense, quite artibrary.

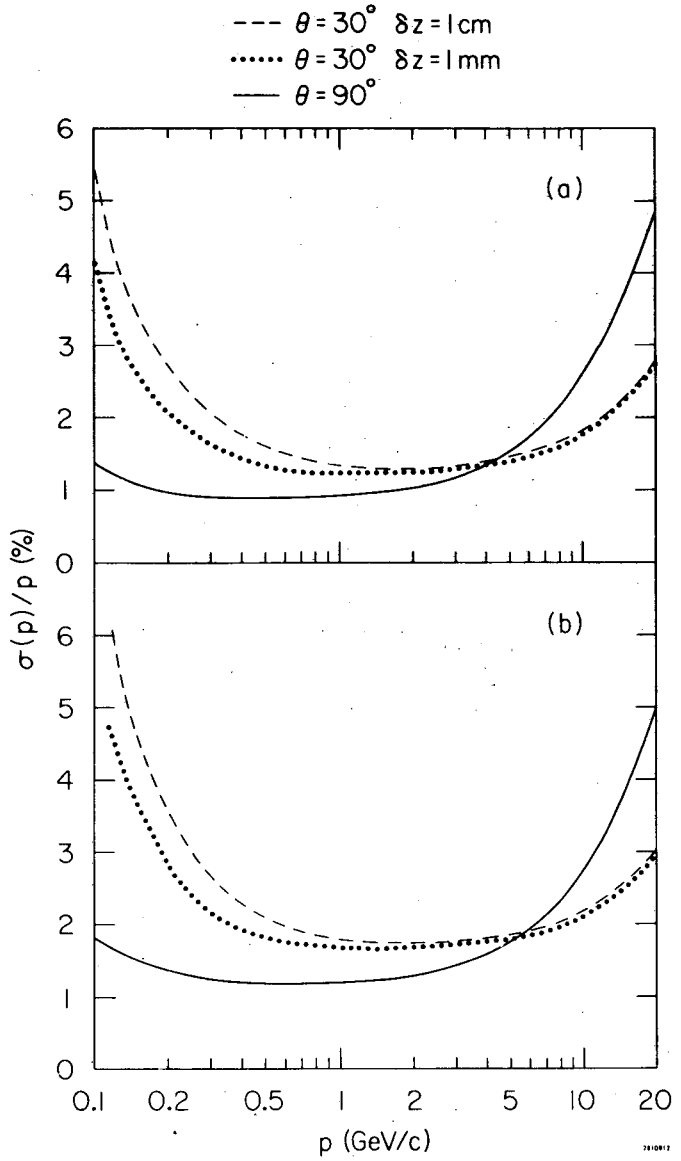

Fig. 5 Momentum resolution σ(p)/p for charged particles in a 1 meter radius solenoid with 15 kG field. The position resolution in the drift chambers is assumed to be 150 μm. Curves are shown for resolution along the beam direction of values δz = 1 mm and δz = 1 cm for two polar angles. The effect of multiple scattering in 8 double drift chambers is included. Calculations are shown for two different thicknesses of material per chamber: (a) X = 0.005 radiation length and (b) X = 0.01 radiation length.

The pole tips clearly must be removable for access to the internal central detector. They are therefore flexible and interchangeable. Those shown leave open a 15° cone for 2-γ physics and as a result produce the field nonuniformity of Fig. 4. A closed pole tip would produce an almost uniform field, while a small, vestigial pole tip would severely distort the internal field while leaving ≈ 30° open. In all cases, the fringing field from $30^\circ < \theta < 150^\circ$ is minimal. Apart from the pole tips, the iron return path is almost completely arbitrary and should have negligible effect on the internal field so long as the iron cross section is adequate to carry the flux. Both the end pieces and yoke can be rearranged to suit almost any external detector configuration. Cost would appear to be the only decisive consideration. The specific arrangement shown is compatible with the external detection systems we have considered.

TABLE I CENTRAL DETECTOR PARAMETERS

A. Magnet (continuous solenoid)

Radius of coil	1 m
Coil thickness	0.5 radiation length
Length of coil	4 m
Radius of return yoke	4 m
Magnetic field	15 kG

B. Drift Chambers

Number: 8 double gap chambers

Chamber Number	Radius of Chamber (cm)
1	10 cm
2	20
3	30
4	40
5	50
6	65
7	80
8	95

Material in each chamber X = 0.005 X_o or 0.01 X_o

Spatial resolution

azimuthal coordinate	150μm
longitudinal coordinate	δz = ± 1 mm or ± 1 cm

C. Momentum Resolution

σ(p)/p at p = 1 GeV/c:

	θ = 90°	θ = 30°	
		δz = 1 mm	δz = 1 cm
X = 0.005 X_o	0.90%	1.25%	1.35%
X = 0.01 X_o	1.20%	1.70%	1.80%

III. CENTRAL DETECTOR

For the purpose of measuring charged particle trajectories, we have chosen to consider cylindrical drift wire chambers (DWC). During the past year considerable progress has been achieved in this field and a number of new techniques are under test. Progress reports from CERN, LBL, and SLAC were presented during the study. The basic fact which permits designing a device around a small, high-field magnet is that an accuracy of about 150 μm in a direction perpendicular to the field lines appears to be achievable in large systems. We assume it in our calculations. It is less certain whether or not the optimal design of DWC will use a separately-shaped drift field. New designs at LBL and SLAC now under test eliminate this feature and minimize the total material of the detector. Our view is that it is highly probably that the total material can be kept in the range between 0.005 and 0.01 radiation length per chamber. Our calculations are made for both values to indicate the sensitivity of σ(p)/p to this quantity.

The method and accuracy of the longitudinal (z-coordinate) measurement is the most contro-

0 0 0 0 4 5 0 1 6 0 9

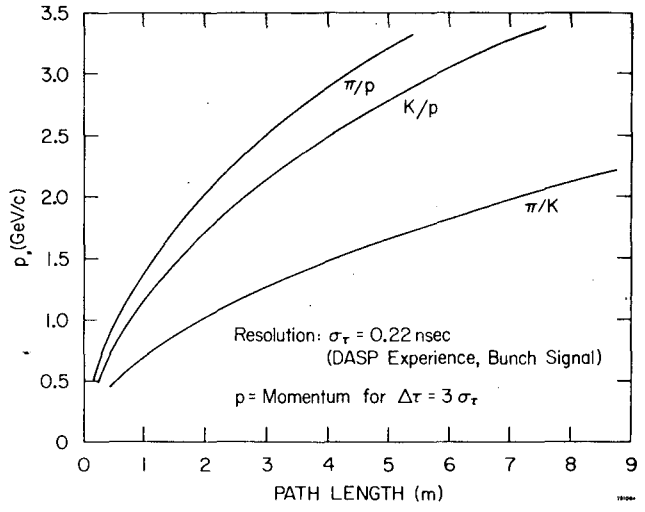

Fig. 6 Mass separation by time-of-flight as a function of path length.

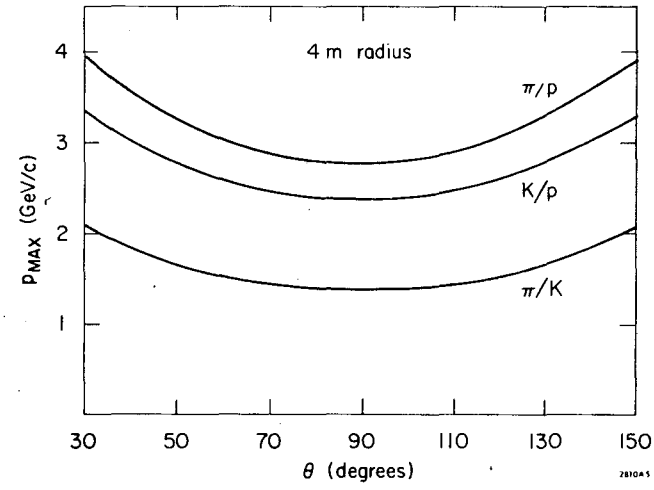

Fig. 7 Mass separation by time-of-flight as a function of polar angle θ for 4 m path length.

versial. Three methods were discussed, namely, delay lines, small angle stereo with wires, and large angle stereo with cathode strips. Each of these methods is now under development and test. Since no firm conclusion seems now possible, we have made our $\sigma(p)/p$ calculations for two extreme cases to show the sensitivity: (1) $\delta z = \pm 1$ cm which seems now achievable and (2) $\delta z = \pm 0.1$ cm which appears possible.

Calculations of the momentum resolution are given in Fig. 5 for the chamber configuration shown in Fig. 1. The characteristics of the central detector are summarized in Table I.

Our study concludes that EWU's are likely to be a leading candidate for the central detector. For the development now underway, we would emphasize the importance of two factors: (1) the minimization of material both for low momentum, charged particle and for low energy γ-ray measurements, and (2) the importance of the z-coordinate measurement technique in relation to pattern recognition for realistic PEP multiplicities. In particular, careful Monte Carlo studies should be carried out for the competing methods.

IV. CHARGED HADRON IDENTIFICATION

We propose to identify charged hadrons ($\pi^{\pm}$, $K^{\pm}$, $p^{\pm}$) with momenta up to 15 GeV/c using time-of-flight (TOF) measurement and Čerenkov tagging.

Complete hadron separation is possible in the solid angle range not covered by the flux return iron. i.e, $-45^{\circ} < \varphi < 45^{\circ}$ and $135^{\circ} < \varphi < 225^{\circ}$, $30^{\circ} < \theta < 150^{\circ}$, $\Delta\Omega/4\pi = 0.43$. Some particle identification can be done in the solid angle range of the return iron using the TOF information of a cylinder of scintillation counters surrounding the magnet coil.

A. TOF System

420 scintillation counters ($210 \times 20 \times 2$ cm^3) are arranged cylindrically at a distance of 400 cm from the interaction point. Each counter is viewed by 2 photomultipliers (2" photocathodes, e.g., RCA 8575).

With a similar system of TOF counters the DASP Collaboration at DESY achieved a TOF resolution of $\sigma_\tau = 0.26$ nsec.[8] The TOF measurement was started by the signal of a small scintillation counter close to the beam pipe. At PEP with the bunch crossing signal ($\Delta\tau \sim 0.13$ nsec) a more precise start signal for TOF measurement will be available. We therefore expect a TOF resolution of $\sigma_\tau = 0.22$ nsec. Figure 6 shows the momentum p_{max} at which hadrons of different masses are separated by $3\sigma_\tau$ as a function of the TOF path length. Figure 7 shows p_{max} vs. polar angle θ for the proposed TOF counter arrangement. At $\theta = 90^{\circ}$ π and K are separated up to 1.5 GeV/c, K and p up to 2.4 GeV/c, and π and p up to 2.8 GeV/c. In the range above these momenta particle masses will be determined by Čerenkov tagging.

B. Čerenkov Counter System

A system of three threshold Čerenkov counters C1, C2 and C3 will serve to identify hadrons in the momentum range not covered by the TOF measurement. Table II lists the detector parameters and Fig. 8 shows how the counters are used in identification. The combined Čerenkov counter and TOF information produce unambiguous particle signatures except for the momentum range of 2.4 to 4.9 GeV/c, where K and p cannot be separated. If desired, this gap can be narrowed by increasing the TOF path length or using a higher index of refraction Čerenkov counter instead of (or in addition to) C1. Silica aerogel radiators[9] could be used to separate K and p in the momentum range not covered by the proposed gas Čerenkov counters.

Each Čerenkov counter is subdivided into optical cells small enough to be viewed by one 5" photomultiplier tube. The light collection system has not been designed in detail, but the optical cell size and arrangement have been chosen in a way that the optics outlined in Ref. 6 can be

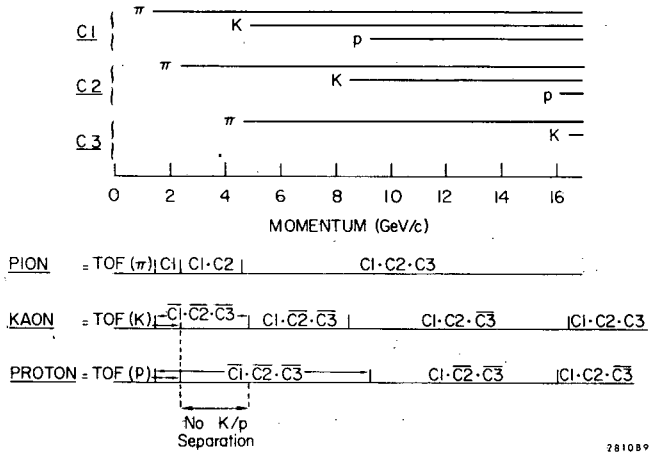

Fig. 8 π, K, and p identification as a function of momentum using time-of-flight over a 4 m path length and Čerenkov tagging with threshold Čerenkov counters C1, C2, and C3.

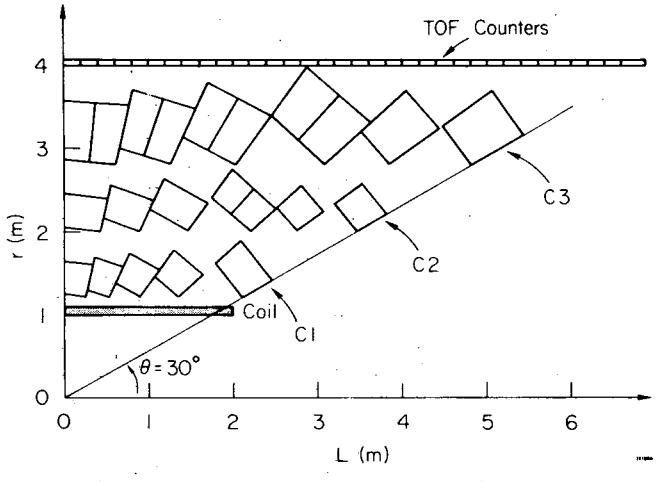

Fig. 9 Side view of the Čerenkov and time-of-flight counter arrangement.

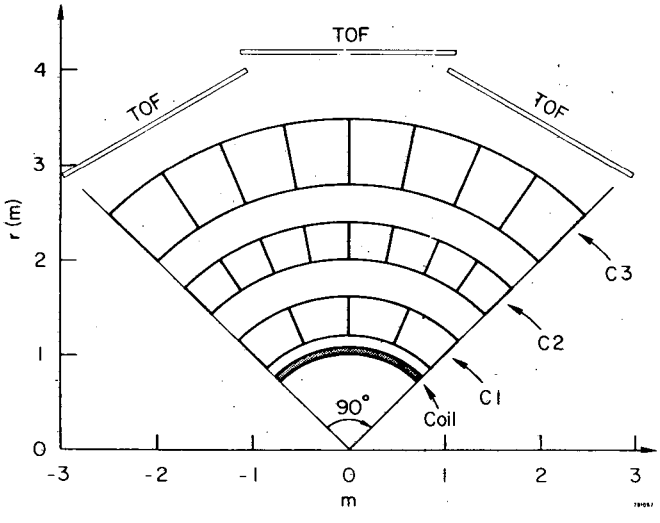

Fig. 10 End view of the Čerenkov and time-of-flight counter arrangement.

TABLE II

Parameter \ Counter	C1	C2	C3
Radiator	Freon 12	Pentane	CO_2
Radiator Length	40 cm	40 cm	70 cm
$(n-1)_{1\ atm}$	1.3×10^{-3}	1.7×10^{-3}	$.45 \times 10^{-3}$
Pressure	4.0 atm	1.0 atm	1.0 atm
Total amount of material (including pressure vessel) — collision length	8.3%	2.2%	2.4%
Total amount of material (including pressure vessel) — radiation length	19.8%	3.0%	3.4%
Number of optical cells = number of photomultipliers	80	224	320

adapted for the counter cells proposed here. Figures 9 and 10 show two different views of the Čerenkov and TOF counter arrangement.

Design Considerations

Freon 12 has been chosen as the radiator in the pressurized counter C1 in order to minimize the pressure (i.e., the amount of material) necessary for a given index of refraction.

The radiator lengths L given in Table II have been calculated according to:

$$n_e = N_o \cdot L \cdot \sin^2\theta,$$

where

n_e = number of photoelectrons

θ = Čerenkov angle

N_o = design number.

n_e was required to be at least four (> 98% efficiency). For C1 and C2 we assumed $N_o = 50\ cm^{-1}$ which is a conservative estimate for an ordinary 5" photomultiplier and the gases chosen.

$N_o = 100\ cm^{-1}$ is necessary for C3 in order not to make the counter prohibitively long. This can be achieved by making use of a high-sensitivity photomultiplier or wavelength shifters.

C1 was placed closest to the interaction region in order to minimize the area to be covered with pressurized cells.

A crude cost estimate, including scintillator material, photomultipliers, voltage dividers, mechanics, discriminators, ADC's, and TDC's (only for the TOF counters) gives:

\$1000 per TOF channel (2 channels/counter)
\$1800 per C1 cell
\$1100 per C2, C3 cell.

Total cost is:

TOF system:	840 × \$1000	=	\$ 840 k
C1 :	80 × 1800	=	144 k
C2 :	224 × 1100	=	246 k
C3 :	320 × 1100	=	352 k
Total cost of particle identification system		=	\$1582 k.

0 0 0 0 4 5 0 1 6 1 0

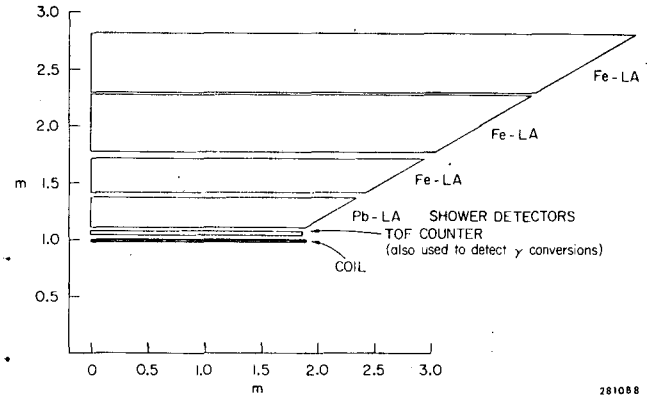

Fig. 11 Modular calorimeter.

V. SAMPLING CALORIMETER

A modular calorimeter is used to detect electrons, photons, and charged and neutral hadrons. The properties of the detector are shown in Table III. Each module is self-contained and covers 1/16 of the solid angle of the general detector ($0.054 \times 4\pi$ sr).

A. Electron-Photon Detector

The first block of the calorimeter (see Fig. 11) consists of a lead-liquid argon detector. Between each 1.4 mm sheet of lead is a 4 mm cell of liquid argon with a plane of wires for ion collection in the middle (see Fig. 12). The wires are bussed together to form channels of constant angle. The use of wire planes rather than strips simplifies construction of the variable-width channels used to keep constant angle acceptance.

To achieve good resolution in both polar and azimuthal angles, we use overlapping channels in θ and φ. Readout in θ is alternated with φ, as indicated in Fig. 12. The energy resolution of this system is expected to be $\sigma(E)/E = 7\%/\sqrt{E}$ (E in GeV). Of course, the photons which convert in the magnet coil (see Fig. 13a) will have worse energy resolution (see Fig. 13b). The resolution shown in Fig. 13b should be added in quadrature to the above resolution for those photons which convert.

In order to help separate π's and e's we segment the detector in depth. The first three radiation lengths are combined to obtain one pulse

48 plates total, each $\frac{1}{4}$ radiation length = 1.4 mm

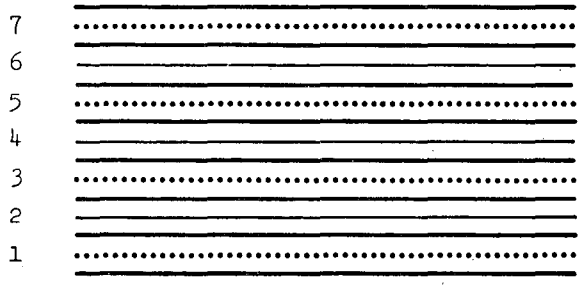

7 - θ identical to 3

6 - φ identical to 2

5 - θ channels identical to 1

4 - φ displaced by $\Delta\varphi/2$

3 - θ channels displaced by $\Delta\theta/2$

2 - φ channels of constant $\Delta\varphi$

1 - θ wires joined to form channels of constant $\Delta\theta$

5 cm at $\theta = 90^\circ$
10 cm at $\theta = 30^\circ$

To collect ionization, we sum all channels of the same angle in two parts: one up to 3 radiation lengths, and one from 4 to 12 radiation lengths.

For example, one sum is 1 + 5 + 9
another is 13 + 17 + 21 + 25 + 29 ... + 45

Total readout:
20×2 θ cells (50 mrad)
22×2 $\theta + \Delta\theta/2$
16×2 φ
18×2 $\varphi + \Delta\varphi/2$

Total = 152 channels

Cost at \$100/channel = \$15.2k

Fig. 12. Shower Detector - Schematic

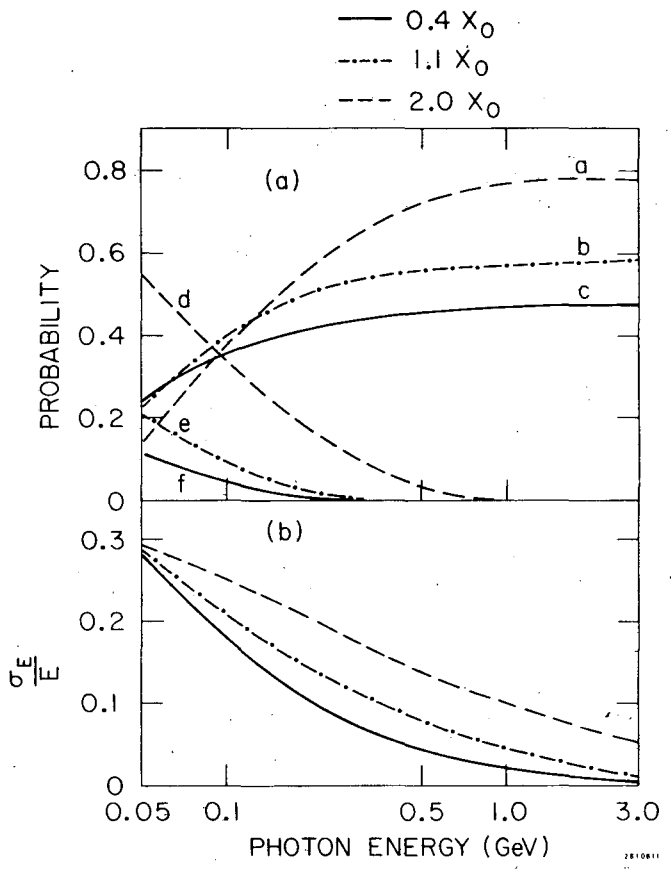

Fig. 13(a) a,b,c. Probability for photons to convert in an aluminum coil of indicated thickness in radiation lengths (X_0) with one or more electrons of energy $\geq$ 2 MeV coming out of the coil.

d,e,f. Probability for photons to convert in the coil with no electrons of energy $\geq$ 2 MeV coming out of the coil.

Fig. 13(b) Rms energy loss for photons traversing an aluminum coil of indicated thickness.

These results are based on Monte Carlo calculations.

height, and the next nine are combined to obtain a second pulse height.

It should be noted that 12 radiation lengths may not be adequate to contain all shower energy at high energy. However, since the detector is followed by the hadron calorimeter, no energy is lost.

B. Hadron Detector

The hadron calorimeter is similar to the electron-photon detector with lead replaced by iron (see Fig. 11). In order to contain all shower energy up to 15 GeV, we use a total of 1 meter of iron.[10] For ease of construction, this is divided into three sections.

The first section consists of 20 plates each 1 cm thick separated by liquid argon and wire

TABLE III

Properties of Modular Calorimeter

Acceptance:	Polar Angle	$30^\circ \leq \theta < 90^\circ$
	Azimuth	$\Delta\varphi = 45^\circ$
Resolution:	$\sigma(E) = \left[\sigma^2_{track}(E) + \sigma^2_{noise}\right]^{1/2}$	
	$\sigma_{track\ e,\gamma}(E)/E = 0.07/\sqrt{E}$	(E in GeV)
	$\sigma_{noise\ e,\gamma} = 5$ MeV	
	$\sigma_{track\ had}(E)/E = 0.50/\sqrt{E}$	(E in GeV)
	$\sigma_{noise\ had} = 10$ MeV	
	$\sigma(\theta) = 6.6$ mrad	
	$\sigma(\varphi) = 6.6$ mrad	
Weight/Module:	Pb	2 metric tons
	Fe	48 metric tons
Cost/Module:	Mechanical	\$40 k
	Readout	\$26.4 k
Number of Channels:	eγ	152
	hadron	112
	total	264
π/e Rejection[12] (including the effect of a 1 radiation length coil):	$< 10^{-2}$ for p ~ 500 MeV/c	
	$< 10^{-3}$ for p $\gtrsim$ 1500 MeV/c	

planes. The readout is again divided into cells of constant $\Delta\theta$ and $\Delta\varphi$ (in this case 100 mrad). Improved resolution in angle is achieved by using a second set of cells offset by $\Delta\theta/2$ and $\Delta\varphi/2$. By combining these channels weighted by the pulse height we can find the centroid of the shower in both the lead and iron detectors.

The second and third sections consist of 40 cm of iron each: 20 plates of 2 cm thickness in the second section and 10 plates of 4 cm thickness in the third. Wires are divided into 100 mrad cells in θ and φ, but no overlapping channels are used. A channel consists of a sum over 15 gaps in either θ or φ. Again, pulse height allows interpolation between channels.

In considering the design of the hadron calorimeter, we have chosen for simplicity and cost reasons to use iron. A significant improvement in resolution is possible using uranium since it is in effect possible to sample energy from nuclear fragments.[11] In a detailed design of a detector of this type, uranium should be given more consideration.

VI. SUMMARY AND CONCLUSIONS

We have presented a general purpose detector design for PEP. The core detector consists of a

0 0 0 0 4 5 0 1 6 1 1

15 kG, 1-meter-radius continuous-coil superconducting solenoidal magnet inside of which are eight drift wire chambers to measure the positions and momenta of charged particles. The core detector covers $0.9 \times 4\pi$ sr solid angle. The momentum resolution for charged particles is calculated to be $\sigma(p)/p = 0.9\%$ at $p = 1$ GeV/c, $\theta = 90^\circ$, and 0.005 radiation length of material per chamber. Identification of charged hadrons over $0.43 \times 4\pi$ sr is accomplished using time-of-flight and Cerenkov counters. π, K, and p are separated over the complete momentum range up to 15 GeV/c except for the range 2.4 to 4.9 GeV/c where K and p are not separated. A lead-iron, liquid-argon calorimeter covering $0.43 \times 4\pi$ sr (eight modules) is used to detect photons with energy resolution $\sigma(E_\gamma)/E_\gamma = 0.07/\sqrt{E_\gamma}$ and angular resolution $\sigma(\theta) = \sigma(\varphi) = 6.6$ mrad. Hadron calorimetry is provided with $\sigma(E_{had})/E_{had} = 0.50/\sqrt{E_{had}}$. π/e rejection of 10^{-2} to 10^{-3} for momenta from 0.5 to 1.5 GeV/c is obtained by segmenting the front part of the calorimeter radially. In addition, the large path of iron provides an excellent muon filter with negligible punch-through. The only ambiguity in muon identification will come from decays in flight. Cones of 15° opening angle forward and backward have been left open for two-photon physics. Photon-tagging apparatus as described in Ref. 7, or possibly a simpler version, can be placed in this region.

This general purpose detector can be used to study a wide range of e^+e^- physics. The feasibility of the superconducting solenoid and the drift-chamber and liquid-argon-calorimetry systems should be ascertained within the coming year through developmental work now being carried out at various laboratories.

REFERENCES

1. D. R. Nygren, PEP-144, Proceedings of the 1974 PEP Summer Study, p. 58; 1975 PEP Summer Study.
2. See for example the experiments of the Weak Interactions reports in this volume (1975 PEP Summer Study).
3. Report of the General User Magnet Group, 1975 PEP Summer Study.
4. A. Barbaro-Galtieri, et al., PEP-148, Proceedings of the 1974 PEP Summer Study, p. 118.
5. See for example M.A. Green, LBL-3677 (1975), and A General Users Magnet Design (PEP-189) in this volume (1975 PEP Summer Study).
6. See for example, G. Buschhorn, et al., PEP-146, Proceedings of the 1974 PEP Summer Study, p. 86.
7. Report of the Two-Photon Physics Group, 1975 PEP Summer Study.
8. DESY Report 75/14, May 1975, and submitted to Phys. Letters.
9. M. Cantin, et al., Nucl. Instr. and Meth. 118, 177 (1974).
10. F. Sciulli, rapporteur talk at the workshop on calorimetry held at Fermilab (1975).
11. W. J. Willis, talk presented at the workshop on calorimetry held at Fermilab (1975).
12. SP-26 SPEAR Proposal.

CONSIDERATIONS FOR A GENERAL FLEXIBLE DETECTOR

F. Bulos

ABSTRACT

Starting from a set of desirable features, a general shape of the detector is chosen. To decide on the size and magnetic field 4 cases are compared. A good compromise is chosen and illustrated here

General Features

The general features chosen were divided into two groups: Basics that should be present over as near 4π solid angle as possible, and others that would be costly and complicated such that they would be used in a fraction of the total solid angle. However the magnet flexibility should allow adding more coverage at will

A. ~ 4π Solid Angle Features - Basic
1. Good momentum measurement
2. Energy and position measurement for γ's
3. π-e separation
4. Real flexibility over 2π azimuth.
5. Provisions for fast trigger

B. Limited Solid Angle Features - Additive
1. Finer measurements for γ's
2. Particle identification extensions
3. Provisions for a forward tagger to help identify 2γ processes as recommended by the 2γ group study

With these features in mind a solenoidal magnetic field is chosen. The flux return is a set of 8 ribs capable of returning the flux without further additions. A rib must block as little space as possible azimuthally. In any case, enough space is provided between the coil and the

Table I

	CASE I	II	III	IV
Magnetic Field* (K.G)	5	12	15	15
Coil ID (Meters)	1.5	1.0	.85	.75
No. of removable flux return sections	8	8	8	8
Cross-sectional area of Mag Field (SQ. Meters)	7.07	3.14	2.27	1.77
Cap area required (SQ. Meters):				
1 Field in iron 18 k.g.	1.96	2.1	1.89	1.48
2 Field in iron 20 k.g.	1.77	1.9	1.70	1.33
Cap area available (SQ.Meters)	6.68	2.75	1.89	1.38
Width of flux return rib (Meters) (Thickness fixed at 20 cms.				
1 Field in iron 18 k.g.	1.25	1.32	1.2	.95
2 Field in iron 20 k.g.	1.10	1.2	1.05	.85
X-sectional area for radial coverage out from coil surface of 40 cms. and full azimuth:	4.5	3.3	2.9	2.6
Mom. Meas. capability (Mark II Units)+	1.0	1.0	.83	.57

*All $\geq$10 k.g. coils are superconducting.

+Mark II as presented by B. Richter during PEP Study is based on ~115 cms radial track measurement, 200 microns drift chs. resolution, and 5 k.g. field. Quoted momentum resolution

$$\left(\sigma_{p/p}\right)_{meas} = .75\ p\left(GeV/_c\right), \quad \left(\sigma_{p/p}\right)_{coulomb} = 1\%$$

0 0 0 0 4 5 0 1 6 1 2

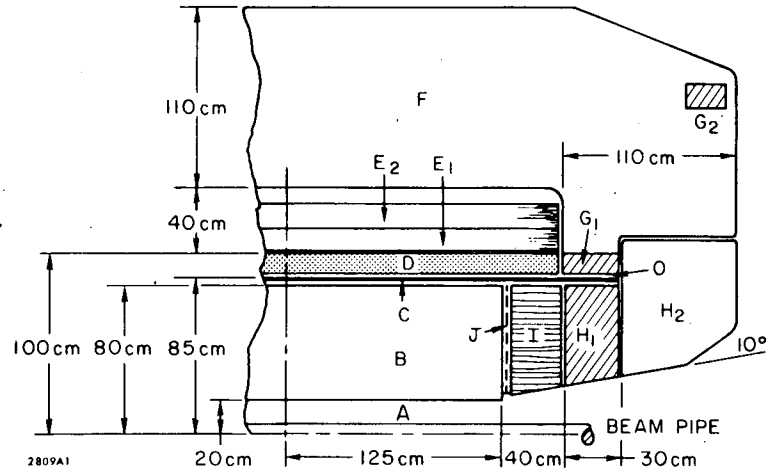

Fig. 1-- Cross section of basic detector - 1/4 shown only.

A Space available for pipe cntr and prop chs.

B Drift chs - momentum analysis.

C Trigger cntrs.

D Coil

E_1 1st part of shwr cntr lead-scint - prop chs sandwich.

E_2 2nd shwr cntr lead scint $E_1 + E_2$ give energy meas. Division helps π-e separation.

F Flux return rib.

G_1 and G_2 Struts for structure. G_1 is separated from end cap by space for light guides - opening O.

H_1 and H_2 End cap and end flux rib.

I Shower:* Either liquid argon or as in E_1, E_2.

J Prop chs - Coarse digitization - used as forward trig. cntr.

K Front tagger opening (10^o).

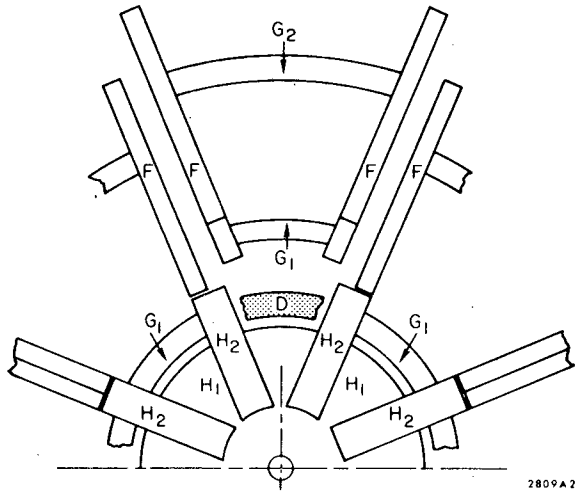

Fig. 2-- End cap and flux sections - 1/2 shown only. One section shown exploded.

*If light guides are used they can be taken out through K or O which can be increased for that purpose.

ribs to allow continuous coverage with most of the additive detectors invisaged. The thickness of the rib azimuthally was chosen to be 20 cms.

To decide on the radius of the coil and the value of the magnetic field 4 cases were considered all having the same features above. The results are shown in Table 1.

From the table one concludes that case IV, the smallest magnet, is not useful because of the loss in momentum measurement capability and the marginal cap area available.

Cases I-III are acceptable. However case I the largest magnet is costly from the point of view of additive features (1,2). Case II is also still costly for the same reasons and also requires a rather wide flux return rib. Case III needs careful consideration by magnet experts to determine the shape of end cap ribs.

Since the magnet shape is the same for all cases and case III seems like a good compromise, this case was chosen for illustrations. Figs. 1, 2 show the structure of the magnet including all the basic features listed in A. above.

Flexibility played a major part. It is easy to see that any experimentalist can build one or more flux return sections (iron is relatively cheap), equip it at will with additive features and test it without interfering at all with an on going experiment. When ready the new section/sections can replace the old ones in a very short time. The replaced sections can be used similarly by physicists next in line. Although not shown in Figures, it is trivial to give the physicist the option of removing the shower counters together with the flux section or leaving them in place (for example if he is interested in adding μ detection only).

THE STREAMER CHAMBER AS A GENERAL DETECTOR

G. Barbiellini, R. Kotthaus, S. Poucher
A. Seidl, F. Villa, and D. Yount

Abstract

A general purpose streamer chamber facility is described. The multiplicities and momenta of charged particles are determined in the central region of the chamber over a solid angle of about $0.85 \cdot 4\pi$. The remainder of the visible volume is devoted to $\pi^{\pm}/e^{\pm}$ separation and to π^{0} and gamma ray detection. The former is achieved by observing electromagnetic shower development and the latter by measuring both the conversion point of each primary interaction gamma ray and the momentum of each shower track produced in an array of coaxial lead-oxide plates. There are 9 such plates, spaced 8 cm apart, and the plate thickness is 0.6 radiation lengths. Separation of $\pi^{\pm}/e^{\pm}$ is effective above 250 MeV/c, and gamma ray detection is practical above 100 MeV by this method. The solid angle of the lead-oxide shower detector is about $0.5 \cdot 4\pi$. Muons above about 1 GeV are distinguished from charged hadrons by a single layer (which gives three track coordinates) of multiwire proportional chambers that determine whether a given particle has interacted strongly in the coils or flux return plates of the magnet. This "external muon identifier" also subtends a solid angle of about $0.85 \cdot 4\pi$. Good separation of π/K, K/p, and π/p is obtained by ionization below 0.7, 1.0, and 1.4 GeV/c, respectively, and useful separation (about 1.6 standard deviations for π/K, 0.7 standard deviations for K/p, and 2.2 standard deviations for π/p) is achieved in the region of the relativistic rise in ionization. The ionization measurements are supplemented by time-of-flight, which is effective for π/K, K/p, and π/p at momenta up to 1.0, 1.7, and 2.0 GeV/c, respectively.

INTRODUCTION

The streamer chamber has been discussed as a possible central track detector in a previous PEP Summer Study Report.[1] Advances in technology during the past year, particularly in spatial resolution,[2] in filmless readout,[2] and in particle separation in the region of the relativistic rise in ionization[3] have added significantly to the already impressive arguments[1] favoring this technique. We have therefore re-examined the streamer chamber approach with two basic questions in mind: (1) What auxiliary equipment can be added to the central detector already discussed to make it a general-purpose facility? (2) How can the recent advances in technology be implemented to optimize system performance?

ADVANTAGES

Among the advantages that we see for the system described below are:

(1) Superb spatial resolution, possibly better than $\sigma = 40\ \mu$ in the plane perpendicular to the magnetic field and $\sigma = 120\ \mu$ along the magnetic field.[2]

(2) Excellent multiple-track efficiency.

(3) High information density of about 2 streamers per cm (useful in pattern recognition, momentum, and dE/dx measurements).

(4) Large solid angle.

(5) Good gamma ray angle and energy measurement, allowing precise determination of the mass of particles that decay into two photons.

(6) Electron identification via electromagnetic shower development.

(7) Good separation of hadrons at low energies and also partially in the region of the relativistic rise in ionization, via dE/dx.

(8) Muon identification.

PHYSICS

The advantages listed above suggest that the streamer chamber would be particularly well suited to the following types of experiments:

(1) Any investigation requiring measurement of high momentum.

(2) Strange particle production (V's can be reconstructed).

(3) High multiplicity studies (pattern recognition).

(4) Search for new particles.

(5) General class of experiments in which one particle or more is identified (e.g., ψ inclusive).

(6) Inclusive spectra of particles (π^{0}, η, ...) that decay into two gamma rays.

(7) Inclusive spectra of charged particles.

(8) Total cross section.

(9) Multiplicity of charged hadrons.

(10) Two-gamma-ray experiments (gamma ray tagging must be added).

GEOMETRY

The streamer chamber facility is shown in top view in Fig. 1 and in beam view in Fig. 2. Two streamer chambers are placed back-to-back, and two coils in a Helmholtz configuration (coil separation equals coil radius) produce a rather uniform magnetic field of about 15 kG parallel to the beam pipe. The electrodes of the chambers are perpendicular to the beam pipe and yield electric fields parallel to the beam pipe and thus to the magnetic field. The chambers are driven by Blumleins and Marx generators on one side of the magnet, left open for this purpose.

The inner core of the detector, extending from 25 cm to 90 cm in radius, is devoted to dE/dx and momen-

0 0 y 0 4 5 0 1 6 1 3

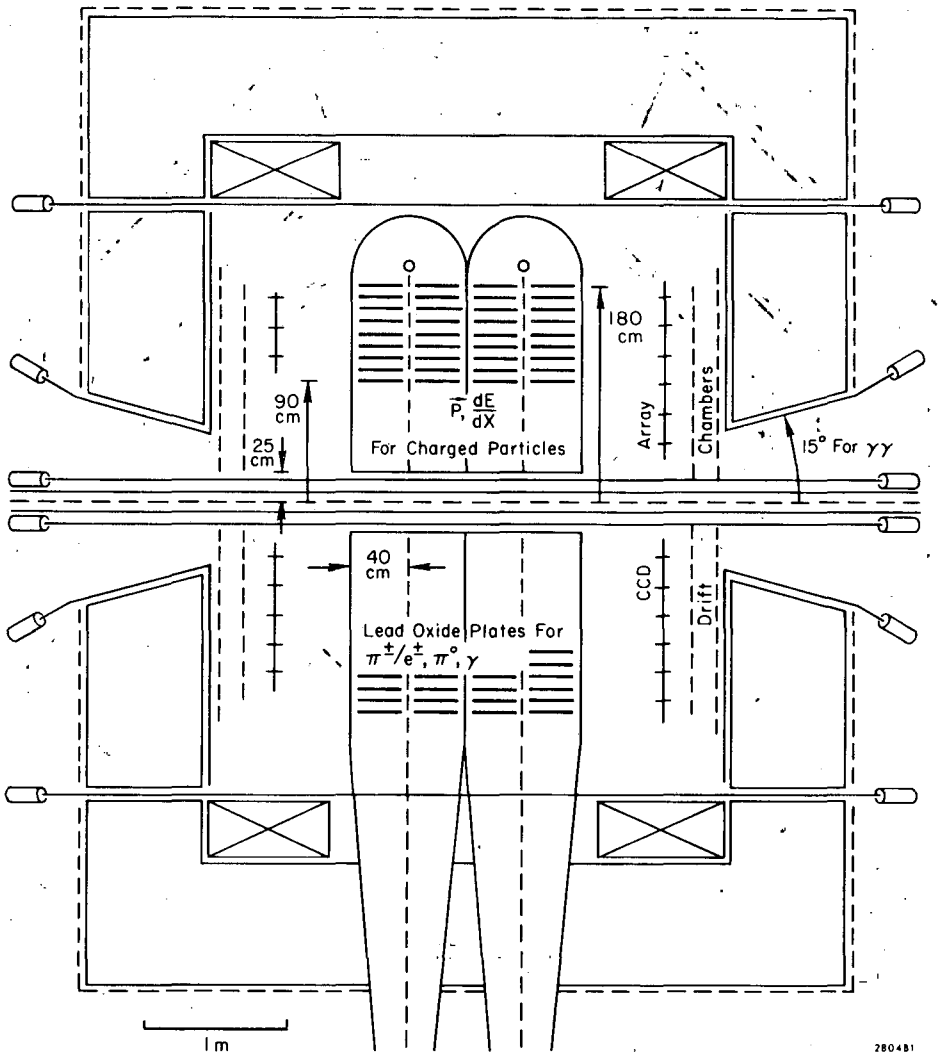

Fig. 1

tum analysis of charged particles. The region from 90 cm to 180 cm in radius is provided with lead-oxide plates that permit π^o/γ and $\pi^o/e^{\pm}$ separation, as well as measurement of electromagnetic shower energy. A single layer of multiwire proportional chambers (MWPC) with delay-line readout surrounds the iron flux return plates and is used to identify muons via their failure to interact strongly in the iron. Streamer track data (including brightness) are digitized octant-by-octant using arrays of self-scanning "charged coupled devices" (e.g., CCD-211 by Fairchild Solid State Division). Drift chambers just inside the magnet end plates provide some sensitivity to charged particles in the small-ϕ region not accessible to the streamer chamber. The trigger consists, for example, of a beam crossing signal, a two-particle signal from beam pipe scintillators, and a two-particle signal from an array of scintillators located outside the streamer chamber and covering as large a solid angle as is practical. The latter counters are used in identifying particles by time-of-flight, supplementing the ionization measurements.

OPTICS

It has been demonstrated experimentally in Ref. 2 that the residues of the streamer position measurements over a one-meter-long track can be as low as 40 μm in space. These results were obtained with a digitizing sensor (Nocticon tube, Thompson-CSF TH 9655) at a demagnification of about 100. In the present application, charged-coupled devices (CCD-211 by Fairchild Solid State Division) could be used. These devices have a dynamic range of about 1000 to 1 and a light sensitivity of about a factor of ten higher than that of the most sensitive film used to record streamer tracks. Equally important, they can be operated in high magnetic fields. Thus the charge-coupled devices can be installed with the remainder of the optical system within the high-field region at a distance of about 40 cm from the nearest electrode.

The number of CCD sensors required can be calculated from the sensor dimensions, the field of view, and the demagnification. A possible layout compatible

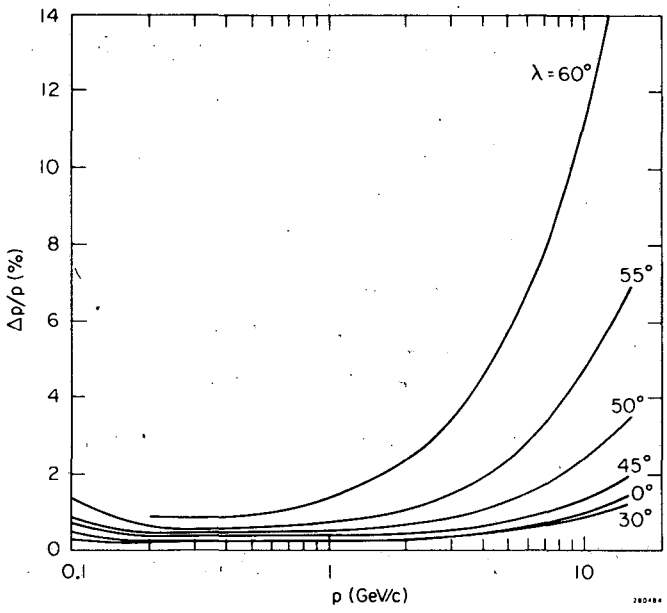

Fig. 4

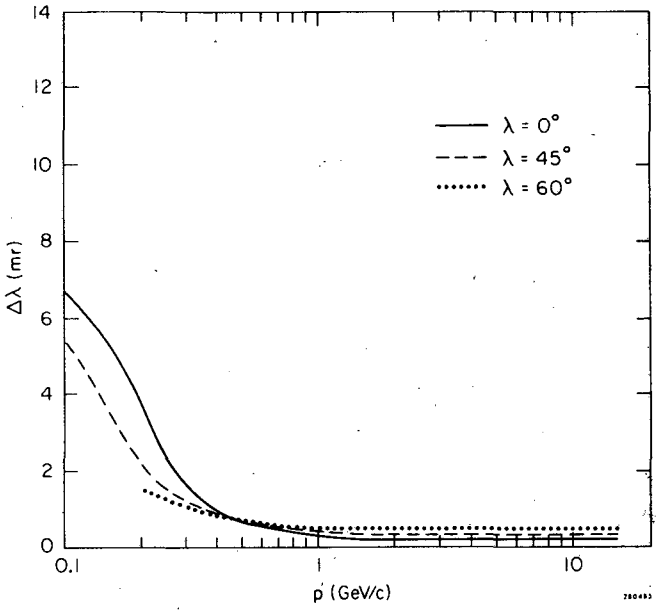

Fig. 5

where α is the angle between particles 1 and 2 and $\Delta\alpha$ is the corresponding error.

In Fig. 7, the mass resolutions calculated, respectively, for a phase-space model and for a jet model at $\sqrt{s}$ = 30 GeV/c are plotted. Figure 8 gives the mass resolution for the $\psi(3100)$ as a function of momentum for a dip angle of $\lambda_\psi = 30^o$. The streamer chamber yields excellent mass resolution, which is necessary in finding narrow states in the presence of a possibly large background.

NEUTRAL MASS RESOLUTION

Gamma ray energies are determined over a solid angle of about $0.5 \cdot 4\pi$ by measuring the momenta of positrons and electrons pair-produced in an array of lead-oxide plates. In effect, this region of the streamer chamber serves as a pair spectrometer consisting of 9 plates spaced 8 cm apart and having a total thickness of $9 \times 0.61 \approx 6$ radiation lengths.

The "visible" energy spectrum obtained by Monte Carlo calculation for 3-GeV incident gamma rays is shown in Fig. 9. A low-energy cut-off of 10 MeV has been assumed. The horizontal scale gives the fraction of the incident energy actually materialized, and the vertical scale indicates the number of gamma rays (out of 2000) in each bin. The half-width-at-half-maximum is ± 7% of the most probable visible energy.

In Fig. 10, the energy uncertainty (HWHM) in percent is plotted versus photon energy in GeV. The Monte Carlo results at 1, 3, and 6 GeV can be summarized by the expression

$$\Delta E_\gamma / E_\gamma = a + b E_\gamma , \qquad (5a)$$

where

$$a = 5 \times 10^{-2} , \qquad (5b)$$

$$b = 10^{-2}\ \mathrm{GeV}^{-1} . \qquad (5c)$$

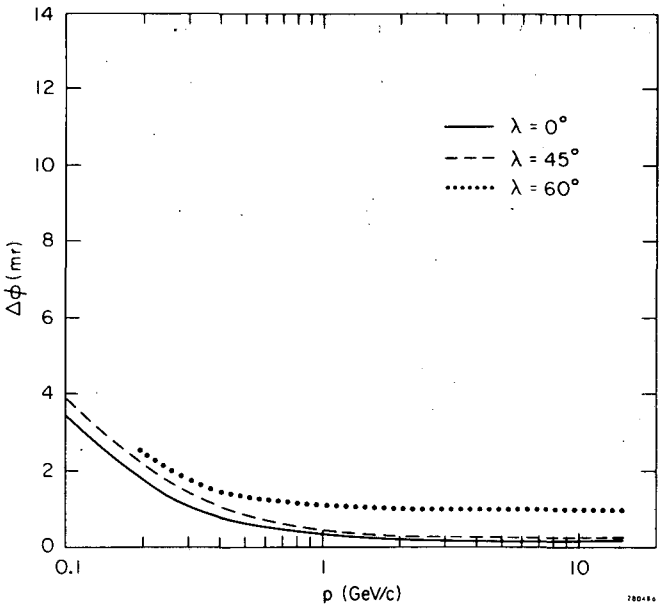

Fig. 6

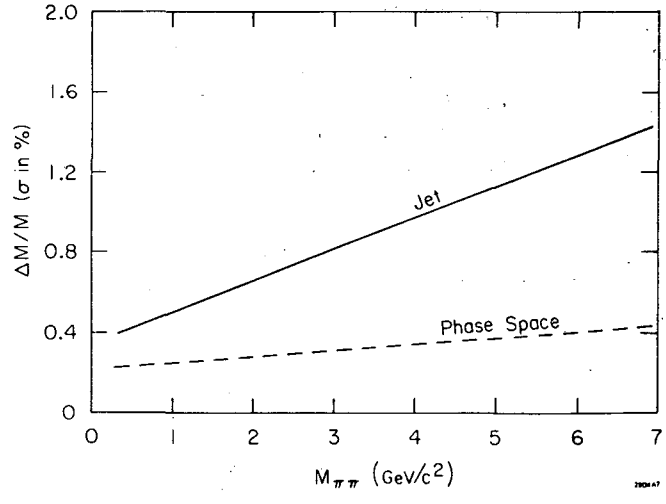

Fig. 7

0 0 0 0 4 5 0 1 6 1 5

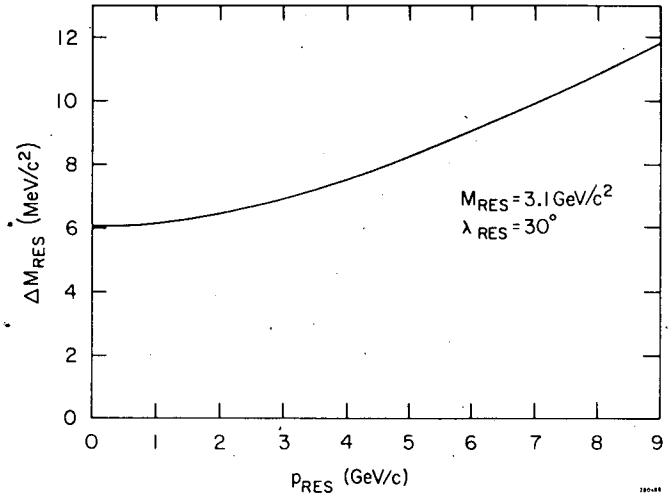

Fig. 8

In Fig. 11, the mass resolution $\Delta M/M$ in percent is plotted versus energy for a neutral particle decaying into two gamma rays. The mass resolution was obtained from the expression[6]

$$\frac{\Delta M}{M} = \frac{1}{2}\left[\left(\frac{4E_1E_2}{M_0^2} - 1\right)\Delta\theta_{\gamma\gamma}^2 + \left(\frac{\Delta E_1}{E_1}\right)^2 + \left(\frac{\Delta E_2}{E_2}\right)^2\right], \qquad (6)$$

where $\Delta\theta_{\gamma\gamma}$ is the uncertainty in gamma ray opening angle in radians, M_0 is the mass of the decaying neutral particle, and $\Delta E_1/E_1$ and $\Delta E_2/E_2$ are the uncertainties in the respective photon energies given by Eq. (5a, b, c). In this calculation, the uncertainty in opening angle (less than 1 milliradian) is negligible, and the result is therefore independent of neutral mass M_0. The mass resolution of the streamer chamber pair spectrometer is comparable with that of a crystal ball (sodium iodide sphere with parameters similar to those given in Ref. 6), although the solid angle of the latter is about a factor of two larger.

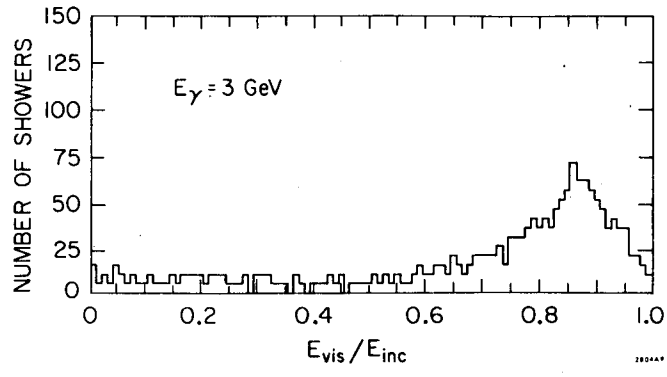

Fig. 9

PARTICLE IDENTIFICATION

The usual $\pi^\pm/e^\pm$ rejection factor for particles of known momentum incident on a total-absorption shower detector is of the order of 10^{-3}. This limit is set mainly by π^- charge exchange via the reaction $\pi^- + p \rightarrow \pi^0 + n$. The $\pi^\pm/e^\pm$ rejection for the streamer chamber pair spectrometer should be about one order of magnitude better since the high resolution permits one to distinguish a single gamma ray from two gamma rays by the small opening angle of the π^0 decay. In addition, some $\pi^\pm/e^\pm$ discrimination is provided by the dE/dx measurements made in the central region of the chamber.

Particle identification via streamer brightness or streamer density (dE/dx) was discussed in detail in last year's PEP Summer Study.[1] Good separation of π/K, K/p, and π/p can be obtained by ionization below 0.7, 1.0, and 1.4 GeV/c, respectively. In the region of the relativistic rise, the separations of π/K, K/p, and π/p are about 1.6, 0.7, and 2.2 standard deviations.

Recent unpublished streamer chamber data[3] comparing dE/dx for electrons and pions in the region of the relativistic rise are shown in Fig. 12. The data were obtained by measuring track brightness, rather than by counting streamers or gaps. The total amount

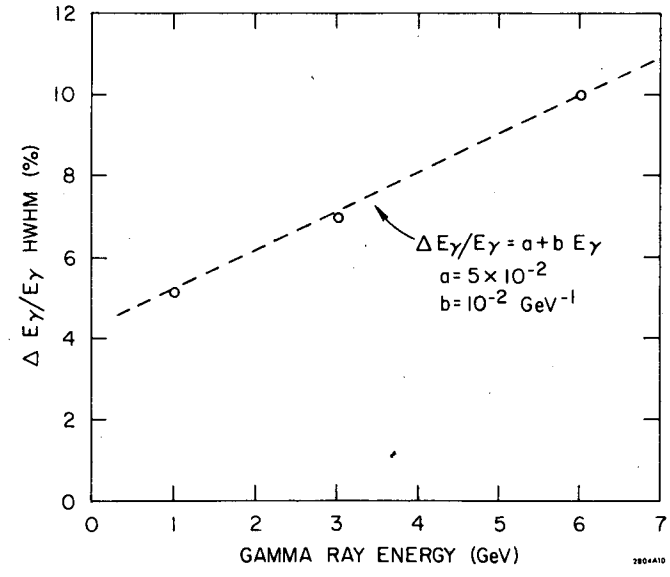

Fig. 10

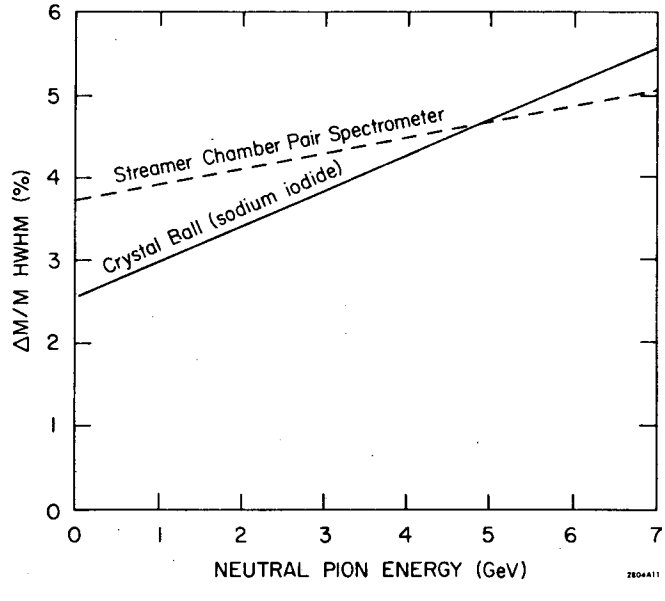

Fig. 11

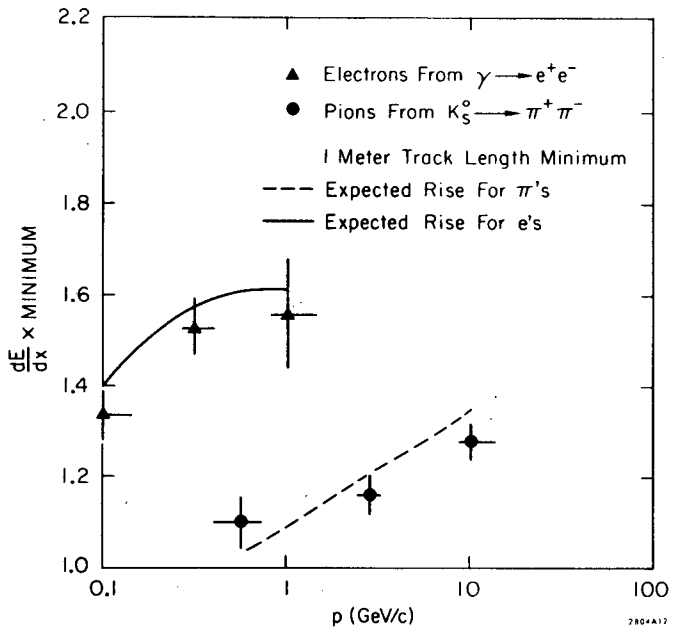

Fig. 12

of light was determined from the local transparency of the film, and a correction was made for the known film-response non-linearity. The $e^{\pm}$ tracks were obtained from pairs produced by gamma rays in the chamber, and the $\pi^{\pm}$ tracks were from reconstructed K^o decays. A total of 126 $e^{\pm}$ tracks and 98 K^o V's (98 π^+ and 98 π^- tracks) were measured. The errors in Fig. 12 indicate the boundaries of the (momentum) x (dE/dx) regions that contain all of the measured tracks of a given type.

The trigger counters surrounding the streamer chamber are also used for charged hadron separation via time-of-flight. This is illustrated in Fig. 13, where particle momentum for a three-standard-deviation separation is plotted versus time-of-flight path length in meters. A timing resolution of $\sigma_\tau = 0.22$ ns has been assumed on the basis of results obtained at DASP. For the two-meter flight path of Fig. 1, three standard deviation separation of π/K, K/p, and π/p can be obtained up to 1.0 GeV/c, 1.7 GeV/c, and 2.0 GeV/c, respectively.

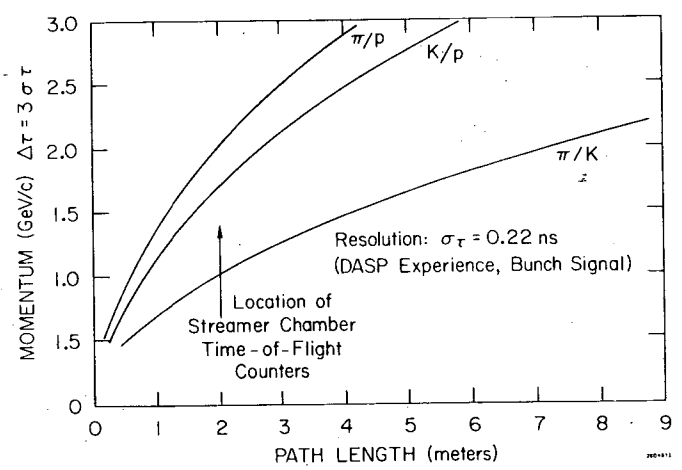

Fig. 13

With the combined information from ionization and time-of-flight, the following hadron separations can be achieved:

π/K/p below 1 GeV/c,

π/(Kp) below 1 GeV/c and above 5 GeV/c,

(π K)/p below 1.7 GeV/c .

Muons are distinguished from charged hadrons by determining whether a given particle has interacted strongly in the magnet coils or iron flux return plates. For any track observed in the streamer chamber or small-angle drift chambers, a multiple scattering circle can be calculated such that if the track is a muon, it will lie within that circle with high probability after emerging from the magnet iron. Hadrons, on the other hand, have a high probability of undergoing a strong interaction, which is signaled by the absence of a track within the muon multiple-scattering circle or by a multiplicity of tracks from a hadronic cascade. Since the hadronic cross sections vary slowly with energy in the accessible range, the hadron/μ rejection factor is essentially constant above the momentum threshold set by the magnetic field and by the muon range in iron, about 1 GeV/c in the present case.

In tests of this technique using pions and muons at 3 GeV/c,[7] it was found that a single multiwire proportional chamber, following only 50 cm of iron, can reject pions with 96% efficiency while accepting 96% of the incident muons. This should improve in the geometry of Fig. 1 since the iron flux-return plates are tentatively 80 cm thick. At low momenta near the detection threshold, the main limitation is pi-mu decay in flight. At 1 GeV/c, this process occurs with a probability of about 7% for a 4-meter path length.

It should be noted that the spatial resolution required for muon identification is low and that large areas can be covered at a modest cost by using delay-line readouts. A system of this type is presently in operation behind the 15-foot bubble chamber at the Fermi National Accelerator Laboratory. The cost, excluding the original development, is about $3500 per m^2, including electronics. The area covered in Fig. 1 is about 180 m^2, corresponding to a total cost for muon identification of about $630,000. This could be substantially reduced by using drift chambers.

SUMMARY

Beginning with the streamer chamber as a central track detector, we have added electromagnetic shower sensitivity, time-of-flight discrimination, and muon identification. The resulting facility appears to have better mass resolution for states decaying into charged particles than does the SPEAR Mark II magnetic spectrometer. This is combined with a mass resolution for states decaying into two photons that is comparable with that envisioned for the SPEAR Crystal Ball, although the solid angle of the latter is about a factor of two larger. In the realm of particle identification, the streamer chamber system is the most comprehensive yet proposed. It is, for example, ideally suited to studies of jet structure in which multiplicity is high, pattern recognition is difficult, and the range of particle momenta is large. Generally speaking, the streamer chamber extracts maximum information from each event. Thus it occupies an ecological niche, illustrated schematically in Fig. 14, that is unique and augurs well for its survival.

0 0 0 0 4 5 0 1 6 1 6

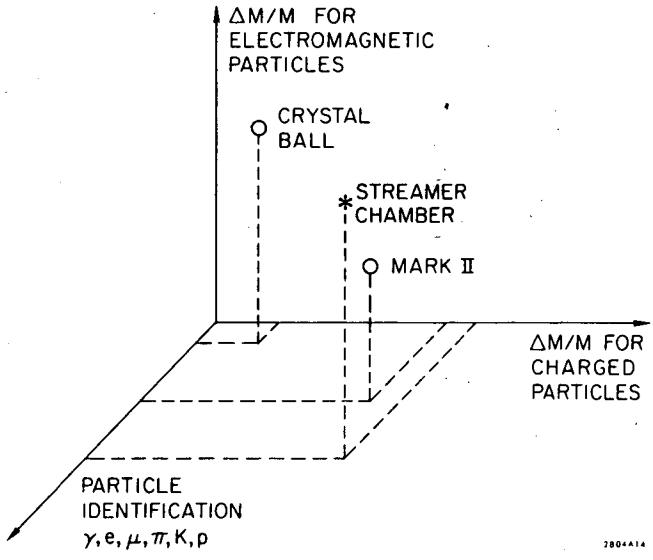

Fig. 14

REFERENCES

1. G. Buschhorn, H. Meyer, A. Odian, and D. Yount, "A Streamer Chamber Detector for PEP," PEP Summer Study Report: PEP-151 (1974).
2. J. Badier, E. Delacour, R. Marbot, J. Y. Parey, A. Romana, and R. Vanderhagen, "On-Line Digitization of Low Luminosity Streamer Tracks," LPNHE-Ecole Polytechnique preprint: LPNHE/X/75-05 (1975).
3. F. Villa (private communication).
4. F. Villa, "The Streamer Chamber," SLAC preprint: SLAC-PUB-1250 (presented at the International Conference on Instrumentation for High Energy Physics, Frascati, Italy, May 8-12, 1973).
5. C. M. Fisher, "Optimization of Bubble Chamber Design Parameters: Measuring Accuracy for Charged Particles," CERN Report: CERN 67-26, Vol. 1, page 25 (1967).
6. T. Mast and J. Nelson, "Some Design Considerations for a Large Solid Angle Charged Plus Neutrals Detector for e^+e^- Storage Rings," PEP Summer Study Report: PEP-153 (1974).
7. F. A. Harris, S. I. Parker, V. Z. Peterson, D. E. Yount, and M. L. Stevenson, "Muon Identification Using Multiwire Proportional Chambers," Nucl. Instr. and Meth. 103, 345 (1972).

THE TIME-PROJECTION CHAMBER-1975

Dave Nygren

Abstract

New experimental results relevant to the performance of the time-projection chamber (TPC) are presented. These include certain properties of the "ball-wire" readout scheme, the suppression of electron diffusion by magnetic fields, and the effects of E × B components. The challenging problem of particle identification is discussed in the framework of a TPC.

* * *

Last year in the 1974 PEP Summer Study Report[1] I discussed a new concept for the detection of charged particles, the time-projection chamber. The interested reader should refer to this report for a presentation of the basic ideas. Lacking at that time, however, were data on electron transport in various gases relevant to the PTC. Therefore, an experimental program has been carried out to determine those properties.

I. DIFFUSION SUPPRESSION

Central to the feasibility of the TPC is the existence of substantial suppression of the diffusion of electrons as they drift through a gas. This apparent conflict with basic motions of thermodynamics can in fact occur by the simple act of imposing a strong magnetic field parallel to the drift electric field. If the radius of curvature of the electrons in the magnetic field can be made small relative to the electron mean free path, then the diffusion suppression can be large. The ratio of the diffusion coefficients D for diffusion transverse to the fields is given quantitatively by the expression[2]

$$\frac{D(B)}{D(0)} = \frac{1}{1 + \omega^2\tau^2} . \qquad (1)$$

Here ω is the cyclotron frequency of the electron, eB/mc, τ is the mean collision time of the electrons in the gas, and D(B) is the diffusion coefficient as a function of magnetic field.

The spatial distribution of an ideal point swarm of electrons after a time T is described by a Gaussian form of width

$$\sigma = \sqrt{2DT} \qquad (2)$$

where σ is the rms normal distance to an arbitrary plane containing the origin of the swarm. In the presence of an electric field (2) can be rewritten approximately as

$$\sigma = \sqrt{2D\frac{L}{W}} . \qquad (3)$$

Here L is the drift length, and W is the drift velocity in the direction of the electric field. Since $D = V\ell/3$, where V is the speed of the electrons (not to be confused with the drift velocity), and ℓ is the mean free path, σ can be rewritten in more fundamental terms.

In the absence of a magnetic field, the transverse distribution is given by

$$\sigma = \sqrt{\frac{2L}{3W}} \times \sqrt{V\ell} , \qquad (4)$$

which can be compared with the strong magnetic field case ($\omega\tau >> 1$)

$$\sigma = \sqrt{\frac{2L}{3W}} \times \sqrt{\frac{V^3}{\ell\omega^2}} . \qquad (5)$$

In the strong magnetic field regime, the best resolution is obtained with a gas giving the longest mean free path, whereas just the opposite obtains without magnetic field. In addition, the resolution obtained with strong magnetic fields depends much more sensitively on the electron temperature. Equations (4) and (5) indicate that a minimum σ will exist for some value of the drift field E since low fields correspond to small W values, and high fields lead to increased V due to non-thermal agitation energies. These qualitative features are born out by the data presented in Figs. 3 and 4, which were obtained by the technique described below.

Figure 1 shows schematically a small drift chamber designed to measure directly the distribution of single electrons after a 15 cm drift interval. This is done by counting with a proportional counter those electrons which "fall through" a 70 micron wide slit in the bottom plane. The slit and counter are mounted on a micrometer-driven stage so that the relative counting range versus x can be mapped out. At the bottom plane, the distribution of electrons is expected to be of the form

$$\frac{d^2N}{dxdy} \propto e^{-(x^2 + y^2)/2\sigma^2} . \qquad (6)$$

The slit effectively integrates over y, so that the resulting dN/dx distribution directly determines σ. The point source of the electrons is a 25 micron diameter pin-hole in the top plane, in reality a gold foil of 50 micron thickness.

Electrons are generated by ionization in the space above the foil by a 140 μcurie (^{244}Cu) α particle source. In the source region, a separate, variable electric field can be imposed to regulate the maximum counting rate at the proportional counter below. Background rates are easily determined by reversing the source field, driving the electrons up and away from the pin-hole. In

0 0 0 0 4 5 0 1 6 1 7

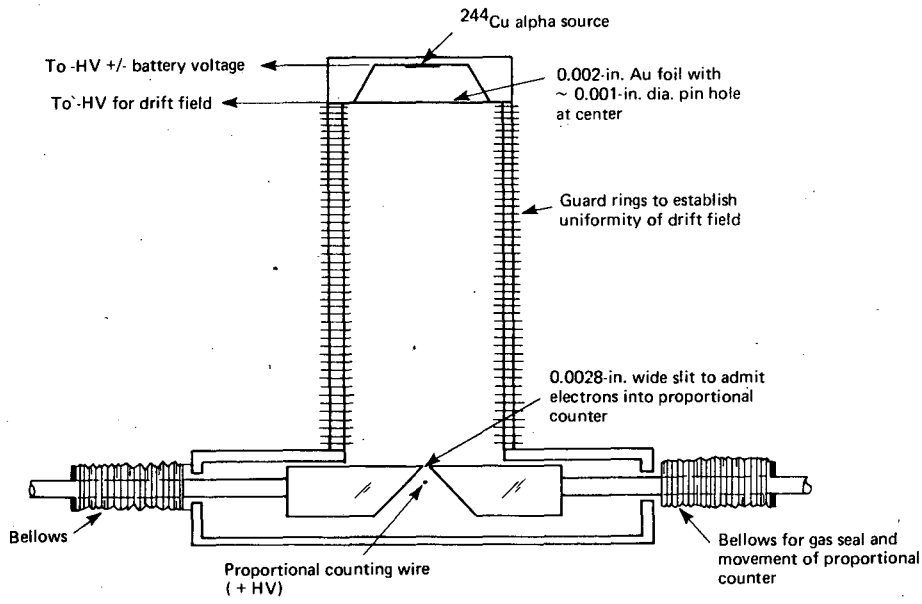

XBL 7512-9777

Fig. 1. Cross-section view of chamber for measurements of transverse diffusion of electrons in various proportional gas mixtures. Free electrons are continuously generated in the space above the gold foil by alpha particles born in the curium source. A weak electric field of either polarity can be created in this space by a battery which rides with the potential of the gold foil. Thus electrons can be driven either towards the pin hole or away from it to study signal/background ratios, typically 100 to 1000 to 1. Not shown in this figure is a micrometer which moves the proportional counter assembly remotely.

practice, signal-to-noise ratios of 100 to 1000 were typically obtained. The entire apparatus fits into the 8 inch-high aperture of a Bevatron 18×36 LPH magnet. Figure 2 shows a typical distribution, along with a Gaussian fit to the data. The systematic errors are typically 1 to 2 percent. A fitting program has been used to find the first and second moments of the data.

An intriguing possibility noted in the original paper[3] on the TPC is the beneficial impact of the Ramsauer-Townsend effect. This is the quantum mechanical phenomenon of a very deep minimum in the electron-atom collision probability at electron energies of about 1/3 eV. The effect is significant for noble gases and simple molecules like methane, which has an electron shell structure similar to neon. As Eq. (5) suggests, the very large mean free path due to the transparency of the noble gases may result in the best resolution being obtained from a mixture of methane plus a noble gas. The data in Figs. 3 and 4 bear this out, although the mixtures show a rapid deterioration at high E/p due to increased agitation energy.

At another extreme is carbon dioxide, which has a very small mean free path for electrons. A 20% CO_2-80% Argon mixture was evaluated for comparison with the methane mixtures. Predictably, it shows the smallest effect as the magnetic field is applied.

It is worth emphasizing that the diffusion along the direction of the fields is unaffected as the magnetic field is applied. However, it turns out not be safe to assume that the transverse diffusion obtained without magnetic field should be the same as the longitudinal diffusion.[4] For pure argon (without magnetic field) the ratio of D_L/D_T can be as large as 1/7. For all other molecules or atoms the ratio is close to unity, but no calculations or experimental comparisons appear in the literature for methane. Because methane is a good moderator, the ratio can be expected to be close to one in the quasi-linear or low E/p regime. The measurements of Cochran and Forester[5] predict a transverse diffusion of 950±100 microns after 15 cm drift for pure methane at an E/p of 1.1 and atmospheric pressure. Our own results, referred to atmospheric pressure yield a transverse diffusion of 860±30 microns. A Saclay group[6] (E/p = 1.1, atmospheric pressure, pure methane) obtain a longitudinal resolution of 295±60 microns for 15 cm drift. Their result, however, may not represent the single-electron

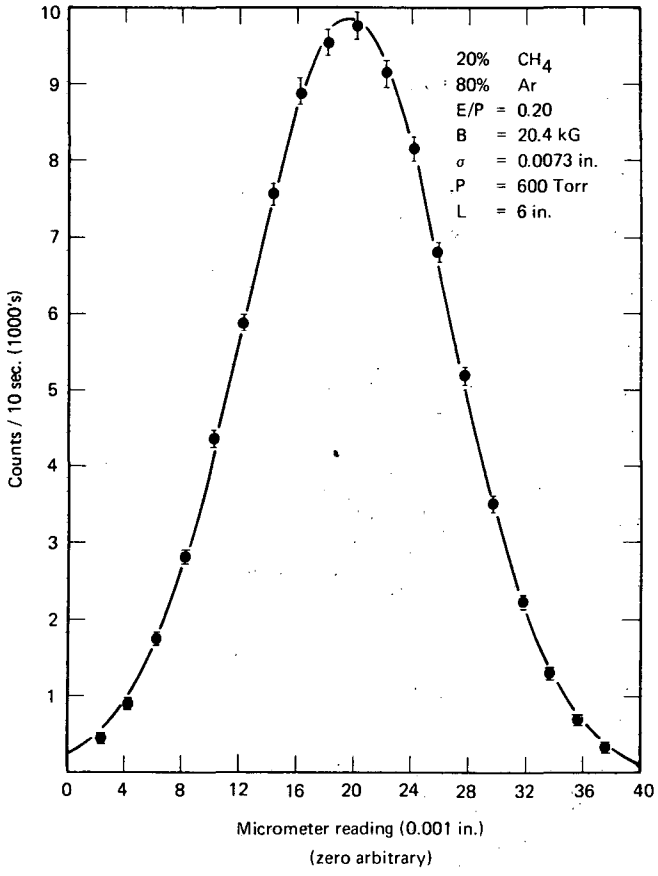

Fig. 2. Typical data and fit for a particular set of conditions. This data represent the probability distribution for single electrons to enter the slit as a function of slit position. Systematic errors are typically 1 to 2%. This set of conditions does not correspond to the best resolution obtained.

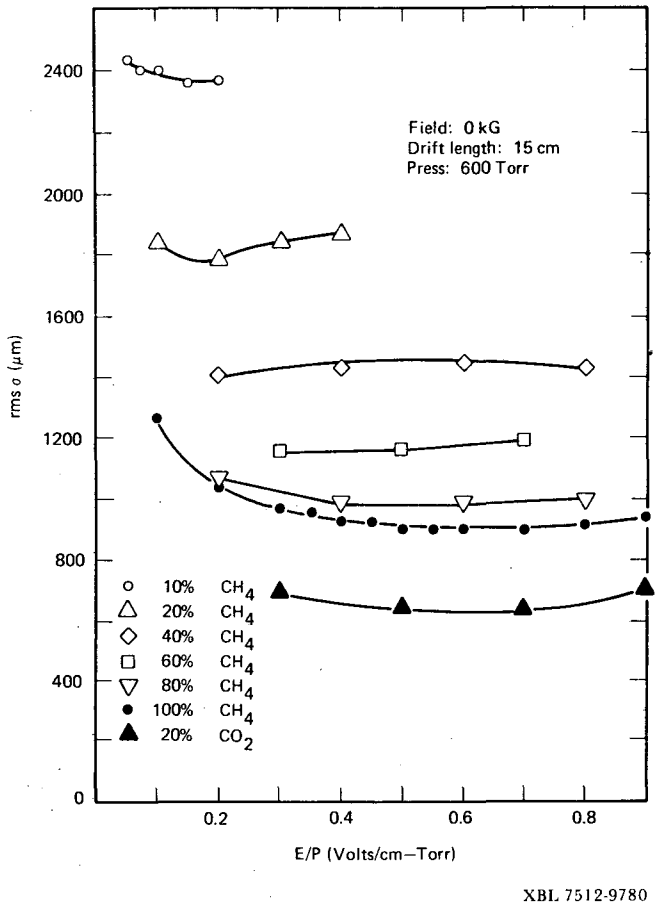

Fig. 3. Transverse diffusion results without magnetic field as a function of E/P. Without magnetic field, CO_2 mixtures give smallest diffusion. Lines are drawn to guide the eye. Addition of argon to methane increases the diffusion, as expected.

transport value because their electronics may have been integrating over the arrival of several electrons. In any case, the distinction between longitudinal and transverse should be maintained even in the absence of magnetic fields.

The diffusion suppression has been measured as a function of magnetic field for various argon-methane mixtures. The results are given in Fig. 7.

The data of Figs. 3 and 4 have been combined according to Eq. (1) to give values of $\omega\tau$ and τ shown in Fig. 5. For convenience, the experimentally observed[7] drift velocities in argon-methane mixtures are presented in Fig. 6. In general, the maximum $\omega\tau$ is reached at E/p values less than those corresponding to the maximum W values.

To give some specific numbers, a 1.8 meter (90 cm each direction) long TPC should give a resolution for single electrons of 500 microns at 20 kgauss using pure methane at an E/p of 0.5. If the Saclay groups' results can be a guide, the resolution for particle tracks may be substantially better than this figure.

To summarize this section, the existence of a substantial suppression of transverse diffusion has been experimentally demonstrated for methane and argon-methane mixtures under conditions suitable for high-energy physics. The accuracy of the data is estimated conservatively as ±5%, and can be safely extrapolated to larger or smaller drift intervals.

II. $\vec{E} \times \vec{B}$ EFFECTS

In practice, the attractiveness of a TPC will depend in part on the extent to which non-perfect alignment of the E and B fields distorts or degrades the track information. Since the fields are strong, one naively expects the effect to be potentially serious. This effect has been recently explored by mounting the diffusion chamber in a cradle which can rotate the chamber body (and hence E) relative to B. These measurements involve mapping the movement of the mean impact point in the direction perpendicular to the plane defined by E and B as the angle between the fields is varied. Some preliminary results are shown for selected conditions in Fig. 8. These data do not seem to be easily understandable in terms of simple models. Generally, the higher the $\omega\tau$ product, the smaller the $E \times B$ effect.

0 0 0 0 4 5 0 1 6 1 8

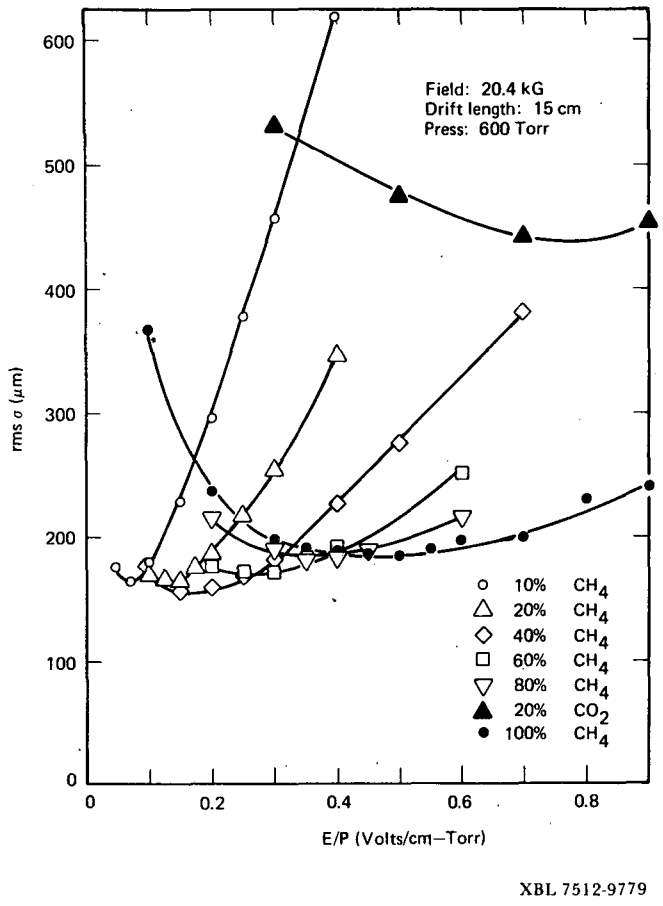

Fig. 4. Companion set of transverse diffusion results, with magnetic field. Here CO_2 is the poorest choice, and mixtures of argon-methane give best results.

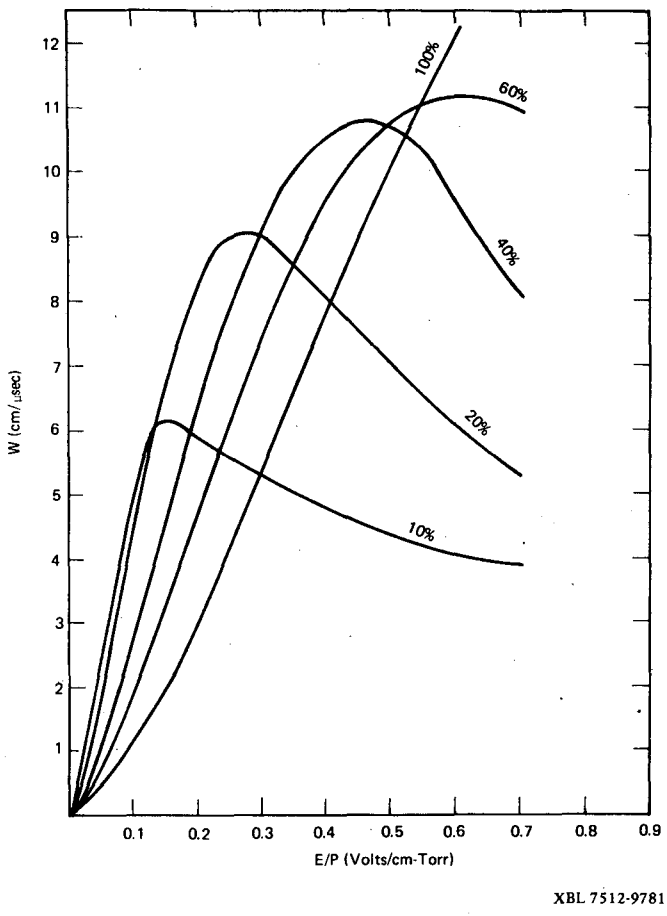

Fig. 6. Values of W, the drift velocity, for various argon-methane mixtures, as taken from English and Hanna, Can. J. Phys. 31, 768 (1953). The accuracy of these curves is probably not better than ± 15%; other measurements indicate that the maximum drift velocity is closer to 10 cm/μsec, shown here as a convenience in estimating TPC parameters.

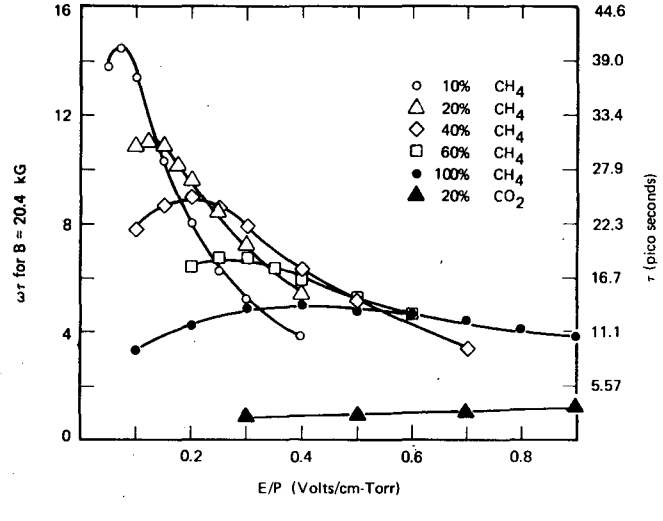

Fig. 5. Values of τ, the mean collision time in picoseconds and $\omega\tau$ (dimension less), as extracted from the data of Figures 3 and 4 using Eq. 1 (see text).

The most significant result implied by the data of Fig. 8 is that the $\vec{E} \times \vec{B}$ effects are small, much smaller than some simple models would predict. One way to view the problem is to compare the shift introduced by $E \times B$ to the resolution introduced by diffusion.

In the example given above, the diffusion is 500 microns in 90 cm, or 1 part in ~1800. To keep the shift introduced by $E \times B$ to the same level (in angle), the fields can be systematically misaligned by 1 part in 330 or $\approx$ 1/3%. This kind of accuracy is achievable without exorbitant effort and cost.[8] $E \times B$ shifts of a few times the resolution can be corrected for, so that even greater mixmatches can probably be tolerated.

Theoretical and experimental work on the $\vec{E} \times \vec{B}$ effects will continue. Curiously, the $\vec{E} \times \vec{B}$ effect increases as the magnetic field is reduced (still compatible with the inverse sensitivity to $\omega\tau$). The data, in spite of this paradoxical situation, are reproducible and regarded as reliable.

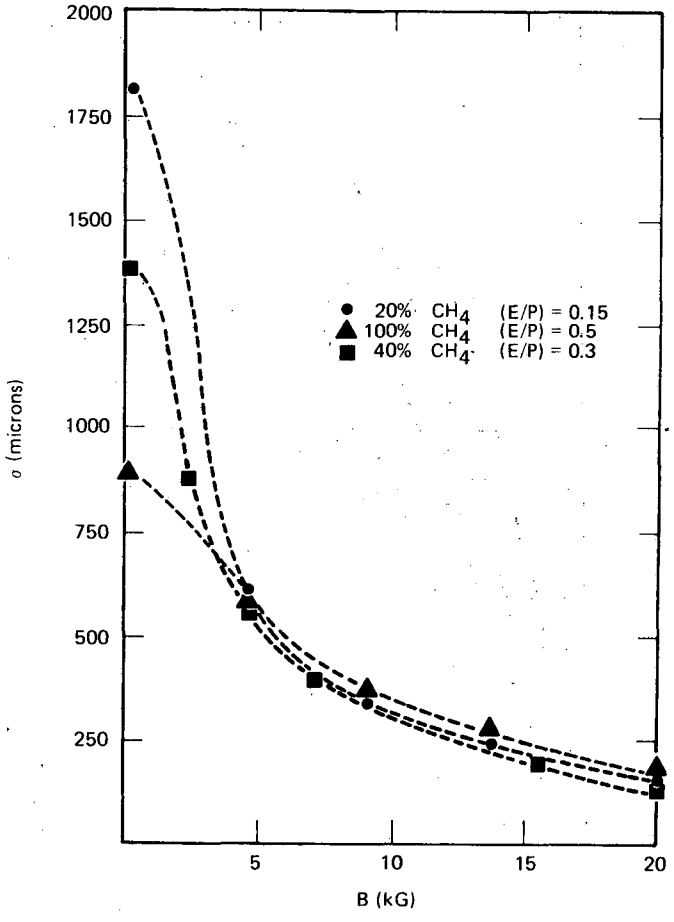

XBL 7512-9782

Fig. 7. The dependence of the transverse diffusion on magnetic field. The results follow Eq. 1 to an accuracy of about ± 5%.

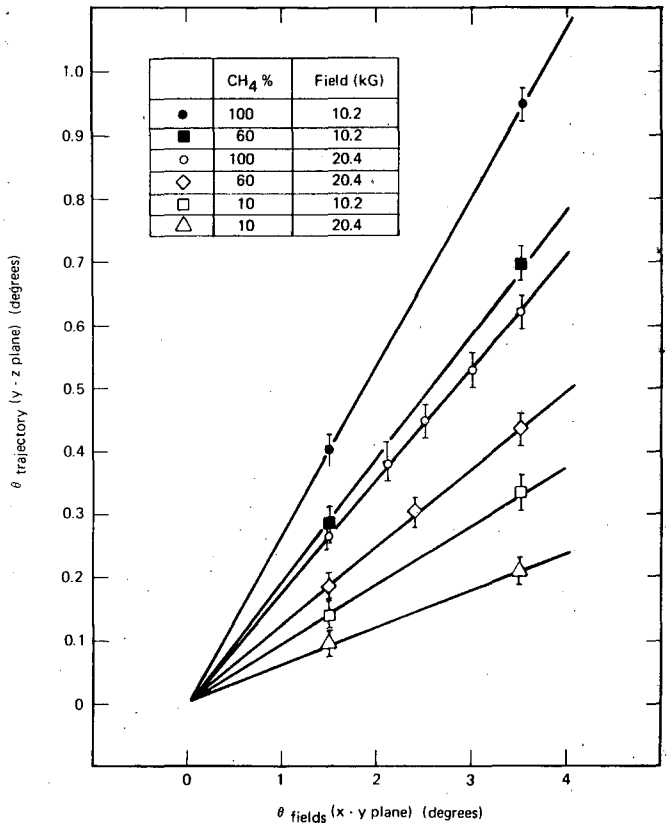

XBL 7512-9783

Fig. 8. The effect of nonvanishing $\vec{E} \times \vec{B}$ components for three mixtures at full and half field. These results are very surprising for two main reasons; 1) the effect on the electron trajectory is very small- note difference in scale between electron trajectory angle and field angle; 2) the magnitude of the effect increases as the field is reduced. At quite low fields, ≈ 1000 G, the sense of the effect changes to what one ordinarily expects.

To summarize this section, the impact of the $\vec{E} \times \vec{B}$ effect has been experimentally shown to be remarkably small, and should not place severe demands on the engineering specifications of the magnetic field design.

III. THE BALL-WIRE READOUT SCHEME

In last year's Summer Study Report I discussed one of several possibilities for readout at the end-caps,viz, the ball-wire detector. This geometry is attractive for several reasons: 1) very high gain can be obtained, with good stability; 2) ball-wire data is intrinsically 3-dimensional, eliminating the N^2 ambiguity problem of pattern recognition; 3) the readout plane has (in principle) a simple mechanical design.

Several, but not all, of the interesting aspects of the ball-wire readout have now been explored. A so-called magic mode has been discovered, in which extremely uniform pulse heights on the order of 10 millivolts can be obtained even across loads as small as 100 ohms. The recovery time has been studied. The dependence of the pulse height on the length of the wire above the plane of the dielectric has been determined. Remaining to be studied are the time response in a magnetic field as the electron impact parameter is varied, what diameter of ball gives optimum performance, and what geometry is mechanically convenient.

The magic mode occurs in argon-isobutane mixtures for isobutane concentrations less than about 8%, as indicated by flowmeters. It manifests itself at high gain and is most simply explained as a semi-Geiger type of response occurring over, but limited to, the surface of the ball. The pulse height spectrum in the magic mode is shown in Fig. 9. At higher rates, some broadening appears due to space charge effects. The purpose of mentioning this phenomenon here is that the magic mode provides a very convenient tool for exploring the properties of the detectors, and to point out that detectors using ball-wires can have simpler and cheaper electronics because high thresholds can be safely employed.

The recovery time has been studied in two ways, one, by observing the dependence of the pulse height of the second of two single-electron pulses on the time interval between them. This

0 0 0 0 4 5 0 1 6 1 9

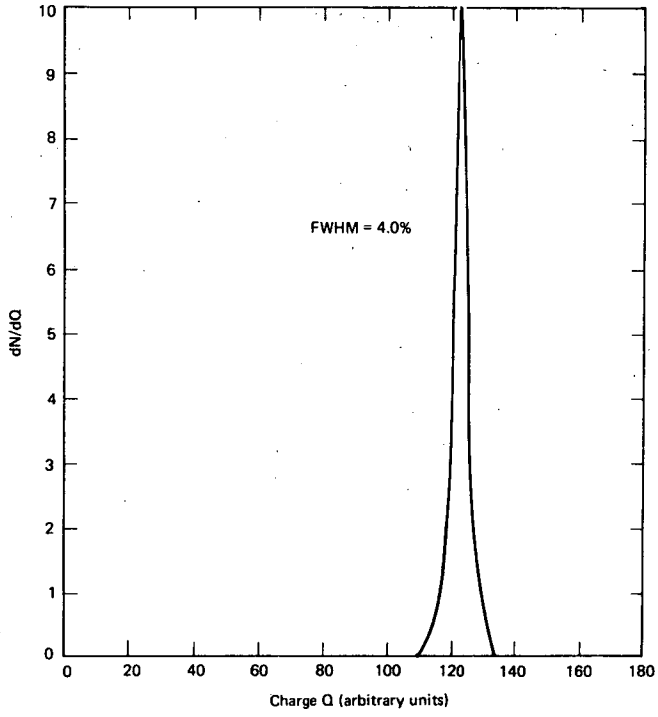

XBL 7512-9784

Fig. 9. The pulse-height spectrum observed from a ball-wire detector under "magic mode" conditions (see text). The counting rate here was approximately 500 H_Z.

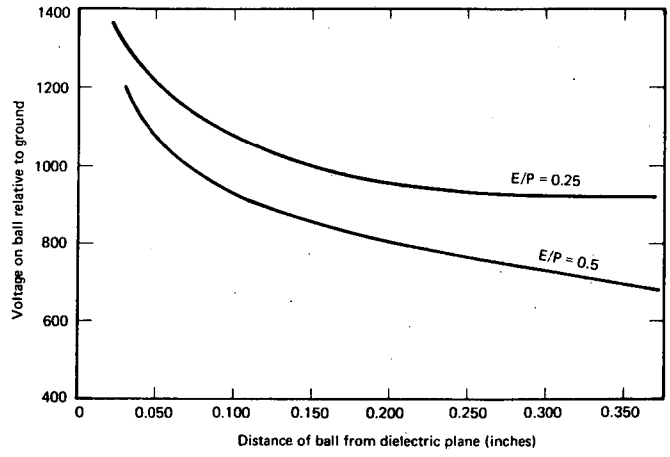

XBL 7512-9785

Fig. 10. The relationship between pulse-height and the distance of the ball-wire above the dielectric plane. This relationship is shown for a constant magic mode output, 10 MV into 125 ohms; the ordinate is the HV needed to maintain this output as the distance is changed. As these curves are for a single ball-wire, the corresponding curves for a cluster may be somewhat different.

recovery time depends on the mobility of the positive ions moving away from the ball, and is typically 200 micro seconds, using the high-gain magic mode. However, the recovery time in practice depends on the sensitivity of the electronics and to only a small extent, the gain at the ball. Using fast circuity with 250 micro volt threshold and 2K ohm input resistance, recovery times have been always less than 250 nano-seconds, for a variety of conditions. The explanation is that while high gain operation requires a very long time to fully recover, the low threshold doesn't require much gain in the first place. Low gain operation leads to correspondingly smaller space-charge effects, so that low-gain operation also recovers very quickly. The conclusion to be drawn from these remarks is that a ball-wire can resolve separate tracks which cross within its sensitive volume if they are separated by ~ 2 cm along the drift axis.

The voltage required to maintain a 10 mW pulse height/electron has been studied as the length of the wire beyond the dielectric plane has been varied. The results are shown in Fig. 10. It does not appear necessary to have the wire protrude more than ~ 4 mm to achieve good response.

Much more is known about ball-wire detectors than has been presented here. Interested parties should feel free to contact the author.

To summarize this section, the properties of the ball-wire detector show no particularly undesirable aspects and should be capable of providing superb pattern recognition. However their ability to provide momentum resolution competitive with drift chambers is not yet clear. Further studies are planned.

IV. THE SUPER TIME-PROJECTOR (PARTICLE IDENTIFICATION REVISITED)

Last year, I discussed a geometry of approximately one meter diameter, and noted that while dE/dx information is available, the ~ .5 meter path length is not long enough to provide clean particle identification in the region of the relativistic rise. Time-of-flight techniques are not useful above a GeV/c or two, and several layers of Čerenkovs may not turn out to be a very attractive solution either, for a variety of reasons. In principle, one can identify electrons, pions, kaons and protons using dE/dx alone except where the dE/dx curves cross (Fig. 11). In these regions, a time-of-flight measurement or a Čerenkov must be employed to resolve the ambiguity.

To utilize dE/dx with time-of-flight to identify these four types of particles, one is driven to substantially larger diameter detectors to obtain the requisite resolution. A four-meter diameter detector will give 5% rms dE/dx resolution using argon-methane.[9] π-K time-of-flight difference at the ambiguous point is about 0.7 nsec; K-p time-of-flight difference is only .3 nsec, a very difficult separation to achieve. The availability of micro-channel plate photomultipliers would alleviate this problem, but their evolution to the stage of off-the-shelf competitively-priced commercial stock is by no means guaranteed even within the PEP time-scale.

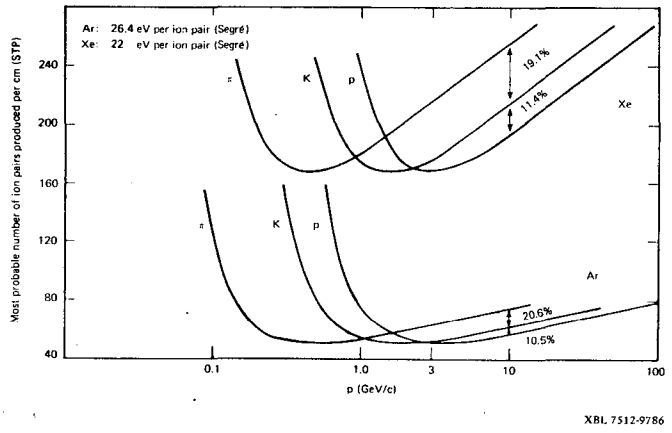

Fig. 11. The most probable number of ion pairs/cm for argon and xenon at STP, as a function of P(GeV/c) for pions, kaons, and protons. Not shown are the curves for electrons, which would be essentially flat at the asymptotic values goverened by the density effect.

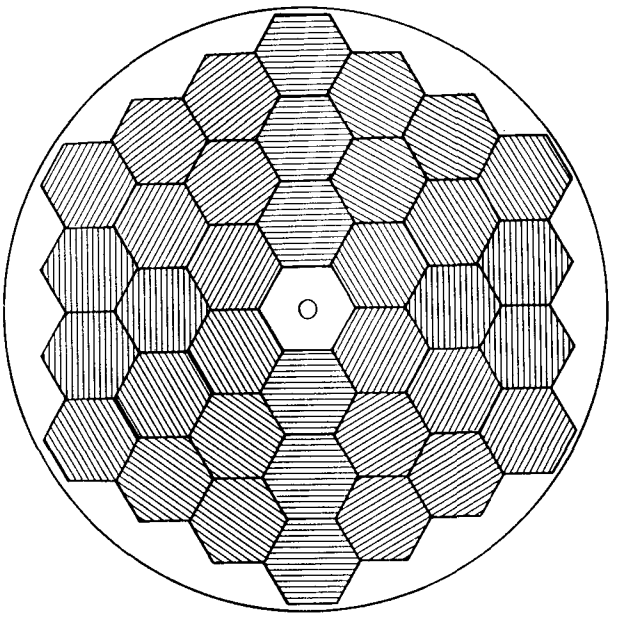

XBL 7512-9860

Fig. 12. A possible configuration of a super TPC end cap, 36 hexagonally shaped modules of wires fill an end cap 1.9 m in radius. Each module might contain $\approx$ 50 wires ($\approx$ 1 cm spacing) for a total of $\lesssim$ 2000 wires/end cap. Each wire will be capable of a pulseheight read-out for several tracks within the STPC drift-time. Every fifth wire can be equipped to provide read-out along the wire, so that tracking and momentum information can be obtained. In the central hexagonal region, through which the beam pipe passes, arrays of ball-wires can be placed to ensure 100% pattern recognition capability for any multiplicity.

The resolution obtainable in a 2 meter flight path through argon-methane still allows several percent misidentification due to overlap in π-K, and K-p separation. It is therefore worthwhile to consider xenon for two reasons: 1) it gives steeper slopes in the relativistic rise region,[10] and, 2) dE/dx is approximately 3 times larger than for argon, thereby giving much better resolution in a given path length. I assume that 2 m of xenon will give at least the resolution obtainable in 6 m of Argon: 2.5% rms using the optimum sampling thickness (3 cm Ar or 1 cm Xe). If this resolution can be achieved in practice, π-K separation should be > 99% efficient, K-p approximately 90% (in the relativistic rise region). In the low p region, either time-of-flight or dE/dx can provide close to 100% identification. Electron identification at all energies should be essentially 100%, due to their extreme relativistic nature.

A xenon + methane filled STPC of 4 m diameter and 4 m length (2 m drift length) can be readout again in several ways. The diffusion in xenon-methane is unknown, but is probably larger than in argon-methane. A rough estimate indicates that multiple scattering is still the dominant contribution at 8 Kgauss field for a 4 meter diameter STPC.

Readout at the end-caps in the STPC will probably be made of modules of wires, in the plane of the end-caps arranged so that the drift time to the wires, the pulse height on the wires, and the position along the wires (i.e., current division, induced signals, or delay lines) can be read out. Approximately 4000 wires will suffice to read out the entire end-caps. The mechanical advantages of this geometry compared with a drift chamber system of comparable volume are worth emphasizing. Fig. 12 shows a possible hexagonal module pattern for the end-caps; squares are also possible.

Cosmic ray fluxes will not contribute noticeably to the background in an STPC. However, the maximum drift times of 20-30 microseconds open the STPC to background from ~ 10-15 extra beam crossings. How severe a problem this would be in practice is not safely predictable without experience at PEP itself. However, background studies done at last year's PEP Summer Study have led to rather sanguine conclusions, especially that by suitable scraping and pumping, particle losses can be very suppressed near the intersection region.

As part of the program to evaluate the TPC concept, plans are being laid to study ionization loss in xenon mixtures, in order to measure the slope of the relativistic rise, the intrinsic resolution, and the optimum sampling thickness.

V. CONCLUSIONS

The TPC concept remains a potentially superior approach for the detection of charged particles at PEP. Much work remains to be done before a critical comparison with drift chambers or streamer chambers, etc. can be made with clarity. We conclude by noting that in recent times, the physics now accessible to study, made possible by great strides in accelerator technology, has been seriously hampered by inadequate and/or very costly detector technology. The pursuit and development of new ideas in this arena of physics deserves more attention than it regularly receives.

0 0 0 0 4 5 0 1 6 2 0

I wish to acknowledge the numerous contributions of Peter Robrish to this work. He has contributed not only his time, but many ideas as well.

REFERENCES

1. D. R. Nygren, "The time-projection chamber-a new 4π detector for charged particles." PEP Note 144, in 1974 PEP Summer Study, (PEP 137).
2. See Ref. 7 in above reference.
3. D. R. Nygren "Proposal to investigate the feasibility of a novel concept in particle detection." LBL internal report, Feb. 1974.
4. James H. Parker, Jr., and John J. Lowke, Phys. Rev. 181, 290,302 (1969).
5. L. W. Cochran and D. W. Forester, Phys. Rev. 126, 1785 (1962). The accuracy of these results are regarded with considerable reservation by Huxley and Crompton in "The Diffusion and Drift of Electrons in Gases", John Wiley and Sons, 1974, p. 405.
6. See Ref. 3 in Reference 1 of present work.
7. W. N. English and G. C. Hanna, Can. J. Phys. 31, 768 (1953). The reliability of these measurements is probably not better than 10%.
8. Private communication, Dr. Klaus Halbach, LBL.
9. M. Aderholz et al., N. I. M. 118, 419 (1974).
10. Somewhat contradictory evidence exists: see A Rousset et al. Nuovo Cimento 14, 365 (1959). See also R. M. Sternheimer and R. F. Peierls Phys. Rev. B3, 3681 (1971) for theory.

COMPARISON OF TIME-PROJECTION AND DRIFT CHAMBER DETECTORS

J.A.J. Matthews and A. Rothenberg

Abstract

Time-projection and drift chamber detectors are suggested for the central region of a small-radius, high-field solenoid spectrometer. A general comparison of these detectors is made, along with a quantitative study of their resolution. We find that at present time-projection chamber and drift chamber detectors give essentially equivalent performance.

1. INTRODUCTION

Time-projection chambers (TPC) have been proposed[1] as a substitute for drift chambers (DC) for use as the central detector in solenoid spectrometers at PEP. With experimental data now available on the suppression of diffusion transverse to the electric (and parallel magnetic) field[2] a quantitative comparison of TPC's and DC's is now possible.

A comparison of the TPC and DC resolution will be discussed first. In particular, we will consider the recognition of, and resolution for, tracks originating within the detector, such as from neutral V's. This will be followed by a general discussion of pattern recognition, dE/dx measurements, solid angle coverage, etc.

2. DESCRIPTION OF TPC AND DC DETECTORS

The operation of a TPC requires a uniform magnetic field of $\sim$20 kG. Such a magnetic field can be made using an aluminum stabilized superconductor with a continuous coil design, complemented by appropriate steel end plates and associated flux returns. The necessity of a high field, plus the desire to limit the total extent of the TPC along the beam, recommends the TPC for those experiments requiring a compact detector. Therefore, for our comparison we take: a) B = 20 kG, and b) a detector sensitive region of 70 cm radius (from the beam), and of length 2 m (see Fig. 1). The resulting detector has a solid angle of $\sim 0.8 \times 4\pi$ with full field. We will assume, arbitrarily, that the first 20 cm (radically) are not available for chambers, being occupied by the beam pipe, proportional wire chambers, trigger scintillators, voltage distribution for the TPC, etc.

The TPC is divided into two 1 m modules to reduce the maximum drift distance. The spatial resolution of the TPC has been estimated using the experimentally measured transverse and longitudinal diffusion for a 15 cm drift path.[2] These values are scaled[3] to the present geometry and added in quadrature with a 200 μ overall error (see Table 1). We assume a TPC measurement for every cm of radial distance such as could be realized by a ball-wire detector[1] at each end of the apparatus. Other envisioned schemes,[2] e.g. arrays of short tangential wires at various radii,

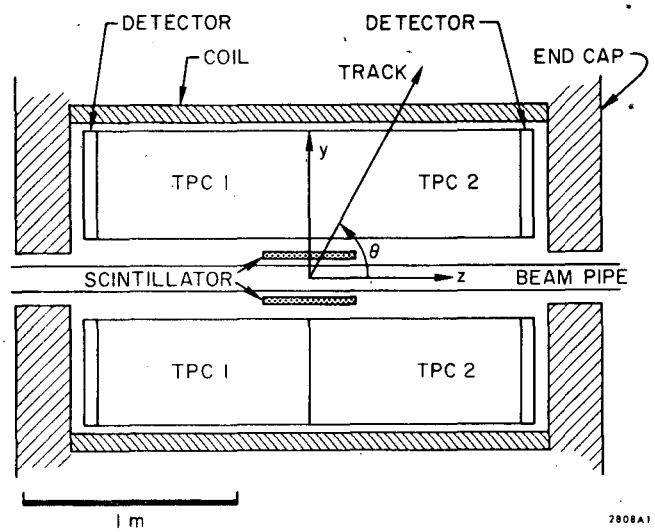

Fig. 1 Magnet with TPC's.

may substantially improve the resolution in the future.

For comparison to the TPC, several DC systems will be considered:

a) 10 chambers distributed uniformly in r, or

b) 5 groups of 2 chambers distributed uniformly in r, as shown, for example, in Fig. 2. Two levels of longitudinal resolution are also considered: delay lines parallel to sense wires,

TABLE 1: Chamber Parameters

		Drift Chambers	
	Time-Projection Chamber (TPC)	10 planes DC 10	5 double planes DC 5 × 2
Azimuthal resolution, ϵ (cm)	0.04	0.02	$\frac{0.02}{\sqrt{2}} \approx 0.014$
Longitudinal resolution, δz (cm)	0.15	0.3 [a)] 1.0 [b)]	$\frac{0.3}{\sqrt{2}} = 0.21$ $\frac{1.0}{\sqrt{2}} \approx 0.70$
No. of points on full track	50	10	5
Chamber Dimensions: Inner radius (cm) Outer radius (cm) Length (m)	20 70 2 - 1 m chambers	20|10 equally 70|spaced planes 2	20|5 equally 70|spaced chambers 2
No. of readouts	~ 32000 (ball wires) (1 cm spacing)	~ 1900 (wires) (1.5 cm spacing) ~ 4000 (strips) [a)] ~ 3800 (delay lines) [b)]	~ 1900 (wires) ~ 4000 (strips) ~ 3800 (delay lines)
Amount of material (r.l.)	~ 0	0.03 - 0.1	0.03 - 0.1
Maximum data collection time	~ 13 μs [c)]	~ 0.5 μs (delay lines)	~ 0.5 μs (delay lines)

a) Drift chambers with 1 cm cathode strips at 90° to sense wires.
b) Drift chambers with delay lines parallel to sense wires. These should have a better multihit/wire efficiency than the cathode strips.
c) For pure methane and E/p ~ 0.5 volts/cm-Torr minimizing the e diffusion[2]

0 0 0 0 4 5 0 1 6 2 1

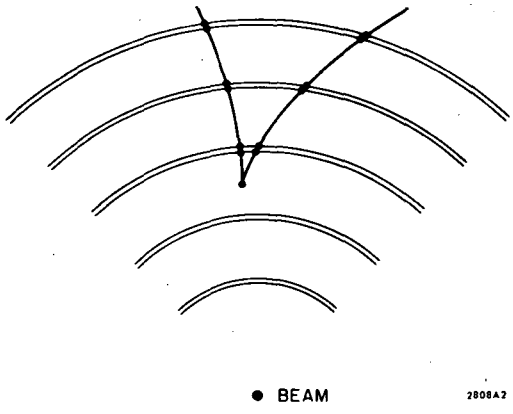

Fig. 2 DC 5 × 2 showing decaying particle.

with $\delta z \sim 1$ cm, or cathode strips orthogonal to the sense wires, with $\delta z \sim 0.3$ cm. The assumed final resolutions, wire spacings, and numbers of readouts are given in Table 1.

3. RESOLUTION

Momentum and angular resolutions for the TPC and DC systems are calculated following Glucksstern[4] (see Appendix 1). The predicted resolutions in azimuth, momentum, and polar angle are shown in Figs. 3a, 3b, and 3c, respectively, as a function of the radial starting point of the track. Tracks coming from the primary vertex start at a radius of zero, those from neutral decays start at a radius greater than zero.

With the measurement resolutions given in Table 1, we observe that the TPC and DC systems should measure momentum and azimuth equally well; the TPC provides a distinctly better determination of the polar angle. For general solenoid geometries, a direct quantitative comparison of the two systems is obtained by simply taking the ratio of the predicted resolutions in Appendix 1. For example, to obtain equal momentum resolution (see Appendix 1):

$$\frac{\delta p_{TPC}}{\delta p_{DC}} = \sqrt{\frac{\epsilon_{TPC}^2 A_{TPC}}{\epsilon_{DC}^2 A_{DC}}} = 1$$

or the spatial resolution:

$$\epsilon_{TPC} = \epsilon_{DC}\sqrt{\frac{A_{DC}}{A_{TPC}}} \sim \epsilon_{DC}\sqrt{\frac{\text{No. TPC Measurements}}{\text{No. DC Measurements}}}$$

$$= (0.014 \text{ cm})\sqrt{\frac{67.0}{13.1}} \approx 0.032 \text{ cm}$$

for 50 TPC measurements compared to the DC 5 × 2 detector.

One of the advantages of the TPC is the ease of detection of neutral V's due to the large number of points on each track. However, the resolution degrades rapidly with decreasing radial path length L,

$$\frac{\delta p_\perp}{p_\perp^2} \propto \frac{1}{L^{5/2}}$$

(see Appendix 1), with the result that the TPC has mainly a pattern recognition advantage over the DC. Thus, the principal advantage of the TPC, in our example, is that for radii $r \geq 44$ cm the DC 5 × 2 system has only two point-pairs left and a track[5] cannot be reconstructed.

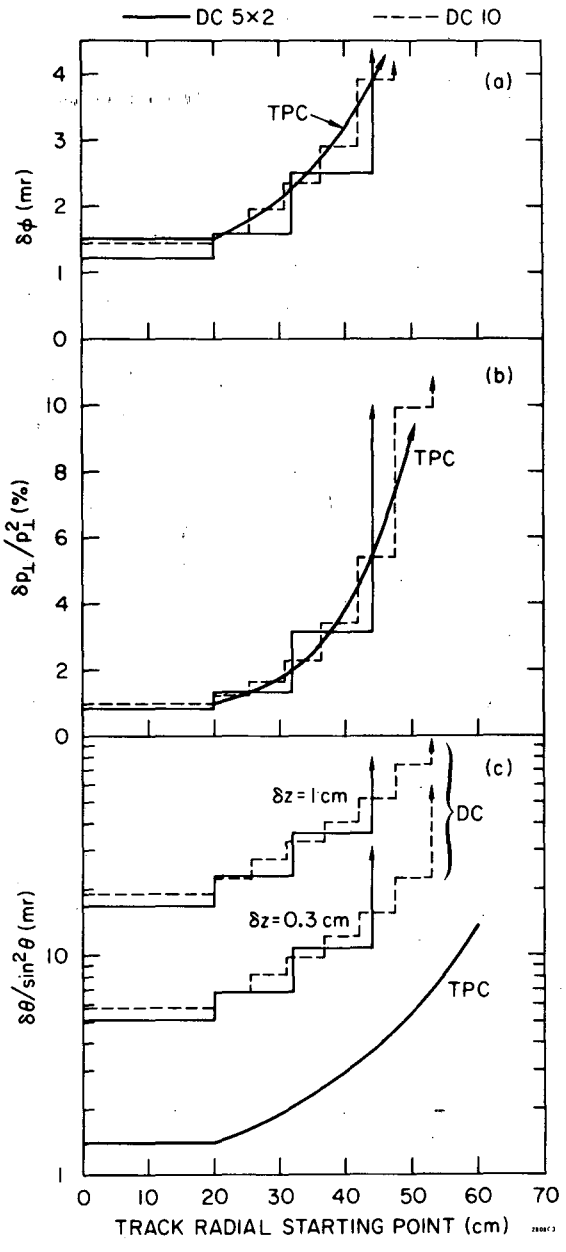

Fig. 3 Resolutions for TPC and DC systems as a function of track radial starting point for (a) azimuth, (b) momentum, and (c) polar angle.

The contributions of track momentum and polar angle uncertainties to two-body mass resolution (at a mass of 2 GeV) are shown in Fig. 4 and discussed in Appendix 1. Except for the DC's with delay lines ($\delta z \sim 1$ cm), the momentum uncertainty is predicted to dominate the angular uncertainty at $M_{12} \sim 2$ GeV, but only dominates the TPC angular uncertainty at $M_{12} = 1$ GeV (not shown). Thus the superior polar angular resolution of the TPC may yield somewhat better two-body mass resolution than the present DC detectors.

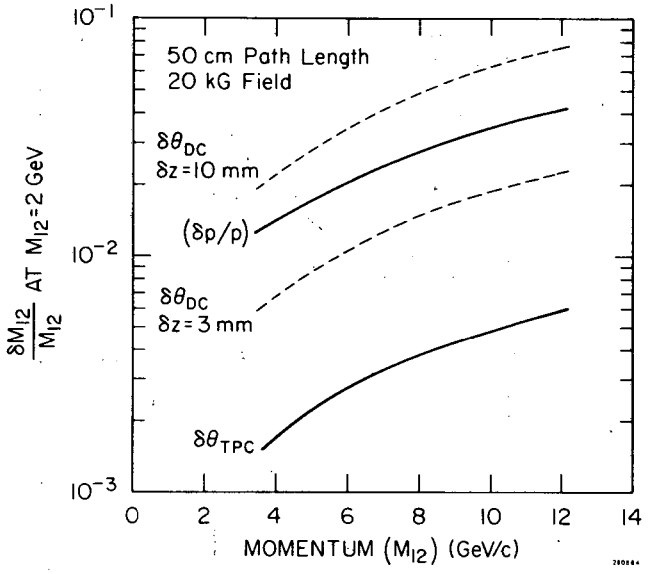

Fig. 4 Contributions to two-body mass resolution due to track-momentum and polar-angle uncertainties at a mass of 2 GeV.

TABLE 2: Maximum Solid Angle Acceptance

System	Minimum [a] radius (cm)	$\frac{d\Omega}{4\pi}$	$\left(\delta p_1/p_1^2\right)$ (%/GeV/c)
Time-Projection Chamber	28 (38)	96% (94%)	≤ 10%
Drift Chambers DC 10	26.5 (36.5)	96% (94%)	≤ 10%
DC 5 x 2	34 (44)	94% (91%)	≤ 3.1%

a) Includes 10 cm for beam pipe plus possible trigger counters, plus the requirement that $\delta p_1/p_1^2 \leq 10\%$/GeV/c. The numbers in parentheses correspond to the model used in this paper where the first 20 cm are not available for chambers.

4. QUALITATIVE DISCUSSION OF TPC AND DC

a) Pattern recognition: Space points will probably be essential for DC detectors and were assumed in estimating the number of readouts, etc., in Table 1. The large number of points/track for the TPC's should be an advantage in high multiplicity events, but may be degraded by the presence of old tracks due to the long chamber memory time (see Table 1).

b) dE/dx: Possible for the TPC in the low momentum region, $p \lesssim 1$ GeV/c (where TOF may provide adequate separation), but not in the region of relativistic rise.[6]

c) Solid angle coverage: DC's and TPC's appear equal when resolution is also considered (see Table 2 and examples of V resolution in Fig 3). We note, however, that increased spatial resolution for both TPC and DC systems only increases the solid angle coverage for the TPC's, since the DC's were geometrically limiting.

d) Low mass: The TPC will typically be less massive (and therefore have smaller multiple scattering) than a DC system. These differences can be made quite small, however.[7]

e) Gas, field monitoring: DC's with paired planes (offset by 1/2 cell) can be continuously monitored.[8] Alternatively, an additional monitor must be added to the TPC (e.g. source of electrons) for checks at regular intervals.

f) Special TPC problems: (i) Effect of old events and positive ions from the e avalanche onto ball-wire detectors. (ii) Very large number of channels to be read out. This suggests that the TPC is possibly better compared to a streamer chamber detector than to a DC system. (iii) Sensitivity to nonuniform magnetic fields. However, recent measurements indicate that for an angle θ between E and B fields, the resulting e drift trajectory deviates by only $\sim 0.07\,\theta$. (iv) High electric field, ~30 kV, is required to establish the drift gradient. (v) Large drift time implies clocks with large ranges. Typical parameters might be 10 ns minimum count and 13 μs maximum count. Such a readout requires a few more bits than a DC readout, but a much lower clock rate.

5. CONCLUSIONS

Taking reasonable values for the TPC and DC resolution, we find that both TPC and DC detectors give essentially equivalent performance. Drift chambers are therefore recommended for the near term on the basis of reduced amounts of electronics and volume of data to be handled. Continuing development of the TPC (in particular, tests to determine the spatial resolution for real tracks), of streamer chamber readouts, and of large cylindrical systems, leave unresolved the final choice of a PEP central detector.

REFERENCES

1. D. R. Nygren, PEP-144, Proceedings of the 1974 PEP Summer Study, p. 58.
2. D. R. Nygren, Communications to the 1975 PEP Summer Study.
3. Assuming tracks uniformly fill the detector $\langle\sigma\rangle = 2/3\ \sigma(100\text{ cm})$, and
$$\sigma(100\text{ cm}) = \sigma(15\text{ cm})\sqrt{\frac{100\text{ cm}}{15\text{ cm}}}\,.$$
4. R. L. Gluckstern, Nucl. Instr. and Meth. 24, 381 (1963).
5. We believe that three point-pairs are sufficient since there is a strong constraint in the longitudinal view (z vs. r) and, in fact, a constraint in the transverse plane due to the measurement of position and direction (local tangent) at each of the point-pairs. Similarly, for the DC 10 system four points are assumed to be sufficient.
6. W.W.M. Allison et al., Nucl. Instr. and Meth. 119, 499 (1974); M. Aderholz et al., Nucl. Instr. and Meth. 118, 419 (1974).
7. B. Richter et al., Proposal for the SPEAR Mark II Detector.
8. G. Charpak, Drift Chambers, Presented to Workshop on Research Goals for Cosmic-Ray Astrophysics in the 1980's ESRIN (Frascati) (1974).

0 0 0 0 4 5 0 1 6 2 2

APPENDIX 1: Collection of Resolution Formulae

For tracks that have a sagitta that is small in comparison to the track radius of curvature, we obtain the relations: [4]

(a) momentum: $$\frac{\delta p_\perp}{p_\perp} = \frac{(3.3 \times 10^3 \text{ cm})}{B(\text{kG})\, L^2}\, p_\perp \sqrt{\epsilon^2 A_N}$$

and $$\frac{\delta p}{p} = \sqrt{\left(\frac{\delta p_\perp}{p_\perp}\right)^2 + \left(\frac{\delta\theta}{\tan\theta}\right)^2}$$

(b) azimuth: $$\delta\varphi = \frac{\sqrt{\epsilon^2 B_N}}{L}$$

(c) polar angle: $$\delta\theta = \frac{\sin^2\theta}{L}\sqrt{\delta z^2 C_N}$$

where:

(i) $p_\perp = p \sin\theta$ (see Fig. 1 for coordinate system)

(ii) L is the "projected track length", viz., the radial separation of the first and last points on the track.

(iii) ϵ, δz are the measurement uncertainties in azimuth and along the beam.

(iv) B is the magnetic field in kG assumed along the z axis.

(v) A_N, B_N, C_N are parameters depending on the number of equally spaced points, N, on a track: [4]

$$A_N \approx \frac{720}{(N+5)} \quad \text{for } N \gtrsim 10,$$

$$B_N \approx \frac{192}{N+4.9} \quad \text{for } N \gtrsim 10,$$

and

$$C_N = \frac{12N}{(N+1)(N+2)}\,.$$

Note that for N large, the above parameters are all proportional to $\frac{1}{L^{1/2}}$. Thus, for example, $\frac{\delta p_\perp}{p_\perp^2} \propto \frac{1}{BL^{5/2}}$ in the solenoidal geometry.

For the inclusion of multiple scattering see Gluckstern. [4]

The resulting two body mass resolution for symmetric decays ($p_1 \approx p_2$, and $m_1 \sim m_2 \sim 0$) is approximately:

$$\frac{\delta M_{12}^2}{M_{12}^2} = \frac{2\delta M_{12}}{M_{12}} \approx \sqrt{\left(\frac{4p_1p_2 - M^2}{M^2}\right)\left(\delta\theta_{12}^2\right) + \left(\frac{\delta p_1}{p_1}\right)^2 + \left(\frac{\delta p_2}{p_2}\right)^2}\,,$$

where θ_{12} is the laboratory angle between $\vec{p}_1$ and $\vec{p}_2$.

THE MARK II MAGNETIC DETECTOR FOR SPEAR

Rudolf R. Larsen

The Mark II Detector, presently in the design stage, is a SLAC/LBL detector project to replace the Mark I[1,2] now in operation at SPEAR. While similar in concept to the Mark I it will have improved momentum resolution, shower detection, solid angle coverage for both triggering and tracking and a magnet design providing easier access to those particles transmitted through the aluminum coil.

MOMENTUM RESOLUTION

By using an array of 16 cylinders of drift chambers in the 5 kG field volume we expect to achieve a momentum resolution of $\sigma p/p$ (%)=p (GeV/c) at 90°. This resolution will deteriorate by about × 10 at small angles ($\sim$ 15).

SHOWER DETECTION

Design and prototyping of a system of liquid argon and Pb ionization chambers is proceeding. The goal is a special resolution of order 1 cm and energy resolution of order 10% at 0.5 GeV/c. Two arrays are contemplated: one array of modules surrounding the solenoid magnet coil ($\sim$ 1 r.l. of aluminum) and another assembly with planes normal to the beam direction located at each end of the coil. Angular coverage extends over 2π in azimuth and polar angles $\gtrsim 15°$.

TRIGGER AND TRACKING SOLID ANGLE

As in the Mark I, a cylindrical array of scintillators at a radius of $\sim$ 1.5 m will provide time-of-flight information and, in conjunction with the shower detectors and additional contemplated proportional chambers, will provide a triggering solid angle of $\sim 0.95 \times 4\pi$. The potential of triggering on tracks reconstructed on-line from the drift chambers is being studied. The tracking solid angle will be essentially the same as the triggering solid angle.

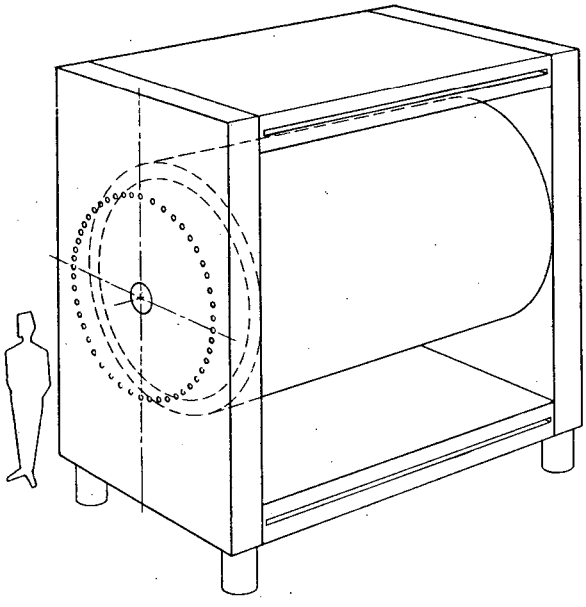

Fig. 1. Mark II Detector without shower counters.

THE MAGNET

The magnet is a "conventional" solenoid with field uniformity of a few percent at large polar angles and, unlike the Mark I, the flux return iron will be located only on the top and bottom of the coil. This provides greater external access (after removing some shower detectors) to those particles transmitted thru the coil, and it should be a valuable asset for "outrigger" experiments.

It is expected that the Mark II will be in operation at SPEAR by Fall 1977.

References

1. SLAC Proposal SP-1.
2. J.-E. Augustin, et al., Phys. Rev. Letters 34, 233 (1975).

0 0 0 0 4 5 0 1 6 2 3

DETECTION OF HIGH MOMENTUM PARTICLES WITH IDENTIFICATION OF THE FINAL STATE

U. Becker, R. Cashmore, E. Groves, L. Keller, S. Loken,
C. Morehouse, S. Poucher, and M. Strovink

Abstract

Two detectors for PEP are described which will measure and identify charged particles with good momentum resolution in the range 0.2-15 GeV/c. Complete identification is attempted for almost all charged hadrons as well as for a significant fraction of electrons, muons, and photons. In this way, events involving high momentum particles can be studied nearly completely. Whereas both detectors use solenoidal magnets with Cerenkov and time of flight counters and drift chambers, the more favorable design assumes light sensitive detectors operating within a magnetic field. A comparison to the detector designed by the 1974 group is made, and ideas suggesting substitutions for part of this apparatus are discussed.

INTRODUCTION

e^+e^- annihilation has offered many surprises in 1974-75. In particular, many states with heavy masses and thus highly energetic decay products have been observed, as well as indications of jet structure. Therefore, energetic secondaries deserve particular interest, as do the other particles which complete these final states. Apparatus for detection of high momentum particles and identification of the final state at PEP may aim to provide various levels of information:

1. Velocity and momentum analysis of charged particles within a relatively small solid angle adequate for measurement of inclusive single-particle yields. Part of the remaining solid angle may be devoted to tracking without magnetic field. Apparatus representative of these goals is in operation at the ISR, SPEAR, and DORIS.

2. Analysis of momenta and of highest velocities over a large fraction of the solid angle, with measurement of lower velocities ($\beta \lesssim 0.998$) over a smaller aperture adequate for inclusive yield measurements. Such an apparatus would determine inclusive particle spectra with additional charged particle correlation information, but would not identify all the charged particles in the final state. A detector of this type was studied in the 1974 analog[1] to this report. Appendix A of this paper describes the possibility of achieving some similar capability by adding Čerenkov counters to the Mark II SPEAR detector now under construction.

3. Full velocity and momentum analysis of charged particles over most of the solid angle. The present report is focussed upon this type of detector, which would completely analyze and identify many of the charged final states that include high-momentum particles. Capabilities such as detection of neutrals and lepton identification would be developed to the extent practical.

RATES AND PHYSICS

Reconsideration of event rates and physics goals in the light of developments since the 1974 PEP Summer Study has guided our approach to high-momentum particle and final state detection. New data from SPEAR and DORIS are in general agreement with the semi-empirical formula for inclusive rates given last year by Richter,[2] as is the limited $p_\perp$ model developed recently.[3] Figure 1 demonstrates agreement of inclusive rates vs. $x \equiv 2p/\sqrt{s}$ as predicted by the two models.[4] These rates are low. For example, particles of any type with momenta exceeding 10 GeV/c at PEP are as rare as $\approx$ 100/day. Particular types of particles such as antiprotons could comprise $\lesssim$ 10% of these events, while the range of extrapolation from present observations

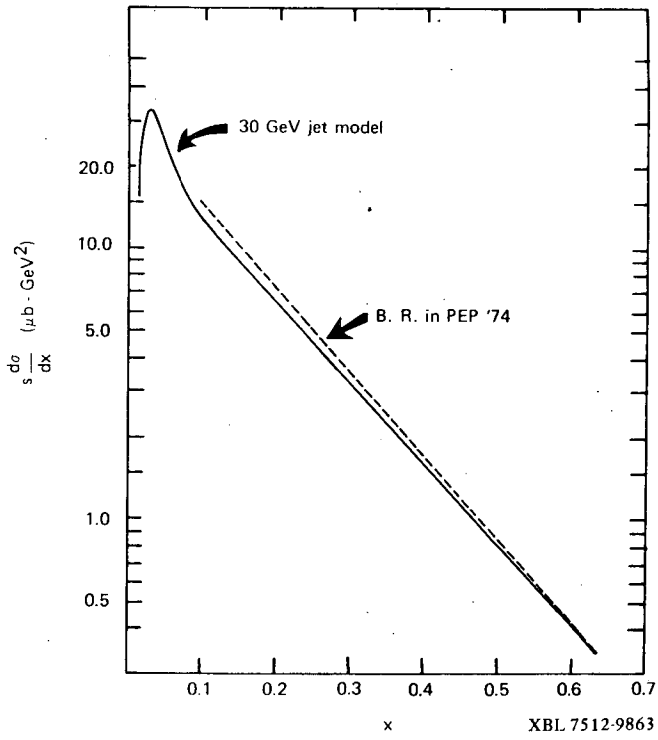

Fig. 1. $d\sigma/dx$ vs $x = 2p/\sqrt{s}$ at $\sqrt{s}$ = 30 GeV according to the limited-transverse-momentum jet model (Refs. 3,4). The dashed line is the semi-empirical formula used by the 1974 group (Ref. 2).

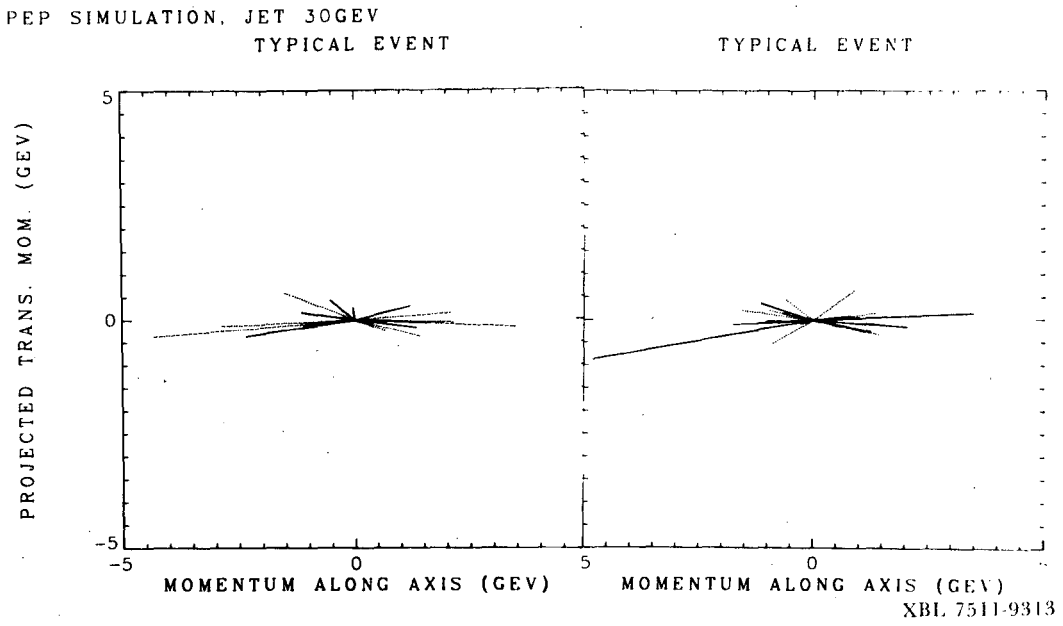

Fig. 2. Typical multihadron final states at $\sqrt{s}$ = 30 GeV generated according to the limited-transverse-momentum jet model (Refs. 3,4).

properly introduces overall rate uncertainty at the order-of-magnitude level. These event yields demand large solid angle for identification of charged particles over the full momentum range. As much as possible of the final state accompanying these rare high-momentum particles should be identified and momentum-analysed. The rates do not permit piecing together the needed information from fragmentary measurements of a large number of events, nor from measurements of correlation functions.

Logarithmic extrapolation of existing e^+e^- data suggests charged multiplicities of 7-8 at $\sqrt{s}$ = 30 GeV and neutral multiplicities of 4-7. The γ multiplicity is assumed to be nearly twice the latter figure. Concurrent detection of neutrals clearly is necessary for apparatus attempting full reconstruction of a significant fraction of final states.

Particular emphasis should be placed on precision in high-momentum resolution for these studies. With event rates decreasing approximately as exp(-8x), accurate measurement of large x is essential. Further, uncertainty in high-momentum measurement will dominate the error in momentum balance of the final state. With a relatively good resolution of $\Delta p/p^2 \approx 0.005/(\text{GeV/c})$, Δx would be ± 0.07 at $x = 0.9$, $\sqrt{s}$ = 30 GeV; the uncertainty in recoiling momentum would be ±910 MeV/c.

New evidence for jet structure[3] in e^+e^- annihilation at high s intensifies the interest in high-momentum secondaries, which in the "sphericity" analysis[3] largely determine the jet axis. If the jet structure and associated polarization phenomena exhibit further s-dependence at PEP energies, the composition of the jet particles will be studied intensively. Clearly, fine granularity of individual detector cells will be required to detect the nearly collinear parallel and antiparallel members of the jet. Examples of simulated jet structures[4] at PEP energies are found in Fig. 2; Fig. 3 is the simulated distribution of opening angles between particles. We shall return to the study of cell granularity in greater detail.

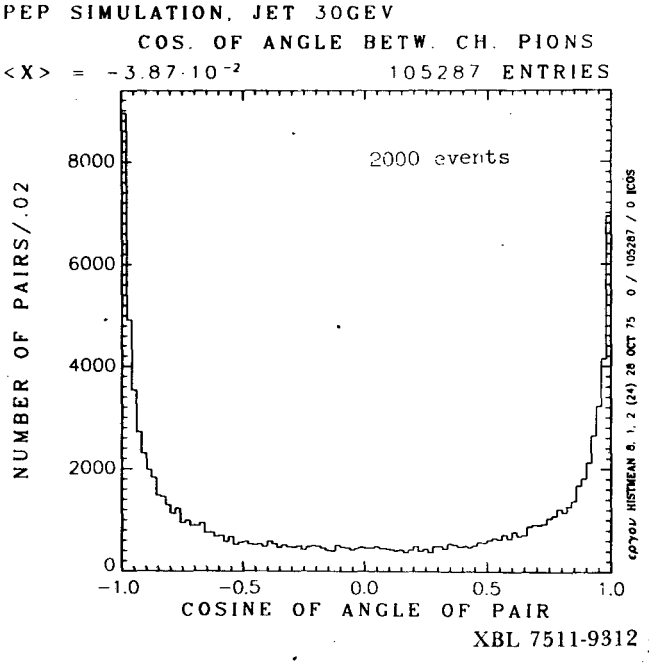

Fig. 3. Distribution of opening angle cosines bebetween final-state hadrons at $\sqrt{s}$ = 30 GeV generated according to the limited-transverse-momentum jet model (Refs. 3,4).

0 0 0 0 4 5 0 1 6 2 4

As further motivation for study of a detector with the capabilities underlined above, one might imagine the role its analog would have played in the exploration of properties of the new particles[5] at the existing e^+e^- storage rings. The best examples cannot be cited, since information from such a device to a large extent is not available now. Obviously, a much larger sample of

$$\psi'(3684) \rightarrow P_c + \gamma$$
$$\hookrightarrow J(3095) + \gamma$$
$$\hookrightarrow \mu^+\mu^-$$

would exist than has been detected[6] in the DASP aperture. This example stresses the importance of precise charged particle momentum and γ conversion point measurement over a large solid angle. The alternative decays

$$\psi'(3684) \rightarrow \chi(3410) + \gamma$$
$$\hookrightarrow (\pi^+ \text{ or } K^+?) + (\pi^- \text{ or } K^-?)$$

observed[6] at SPEAR would be identified properly and the parent mass determined independently. The observed[6] scale-breaking excess flux of charged prongs at $\sqrt{s} = 4.1$ GeV and $x \approx 0.4$ would be identified as to particle type and composition of the accompanying final state. Again, this is the more important at high s, where the rate will be so low that the fraction of recognizable events must be enhanced.

MAGNET STRUCTURE

Initially we attempted to use as a starting point the detection system studied by the high-momentum hadrons group[1] at the 1974 PEP Summer Study. Their detector, shown in Figs. 4 and 5, employed

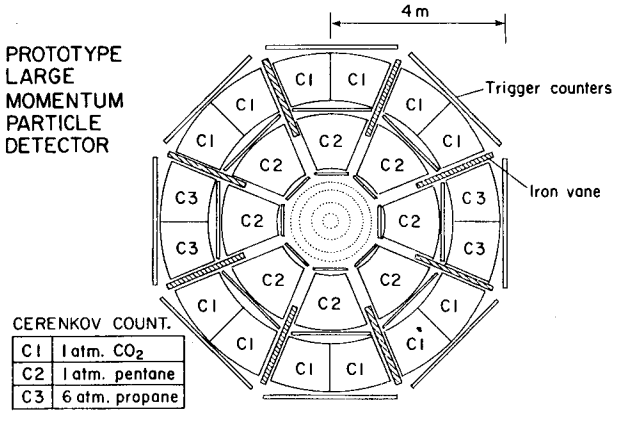

XBL 756-3200A

Fig. 4. End view of PEP'74 high-momentum hadron detector. The Cerenkov counters labelled C_1, C_2, C_3 have refractive indices similar to those described in Fig. 8.

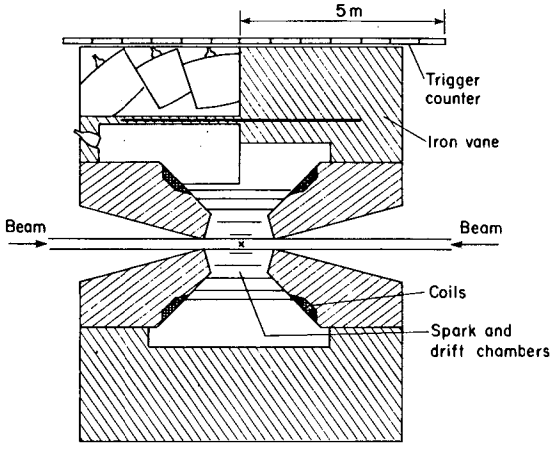

XBL 756-3200B

Fig. 5. Side view of PEP'74 high-momentum hadron detector. The right half is a section through one of the flux return legs.

an "open" cylindrical magnet with flux return vanes and a nonuniform field reaching 8 kGauss at the interaction point. Two layers of Cerenkov counters produced hadron separation over a fraction of the momentum range and 65% of 4π steradians. No muon or high-energy electron identification was attempted. Within its limits, the design represents a well-conceived approach to the experimental problem.

Our attempts to modify that magnet design were aimed toward increasing the polar angular aperture, improving the field uniformity in order to ease computation problems in reconstruction, and raising the magnetic field in order to improve momentum resolution. These efforts were frustrated by the fact that both the pole tips and flux return vanes were nearly saturated in the existing design. Other, quite different magnet systems were considered. High field superconducting toroids without iron were rejected because of excessive forces on the coils.[7] Two magnet designs were selected for further study:

Large volume low magnetic field. Because $\Delta p/p^2 \propto B\ell^2$, a solenoid of radius $\ell = 3$m can provide good momentum resolution with a modest central field of B = 3kGauss. A large (600 ton) magnet is implied, with very small forces on the coil. The photosensitive devices implied by a particle identification system would need to be located within the magnetic field. These could be the microchannel photomultipliers described in the following report.[8]

"Conventional" solenoid. The lumped[9] superconducting coil would provide 15 kGauss central field within a radius of 1 m. All phototubes would be located in low field regions outside the coil.

In addition, an aluminum-coil solenoid like the "existing" Mark II magnet could be equipped with Cerenkov counters over a small fraction of the solid angle. This possibility is explored in Appendix A.

Figure 6 contains sketches of the two magnet configurations with a comparison to the scale of the magnet proposed by the 1974 group. If the return yoke is included, their radii are similar. The 1975 magnets are longer along the beam direction, reflecting a desire to study for example beam polarization effects over a larger range of polar angle. Economics could force a retrenchment in this attitude.

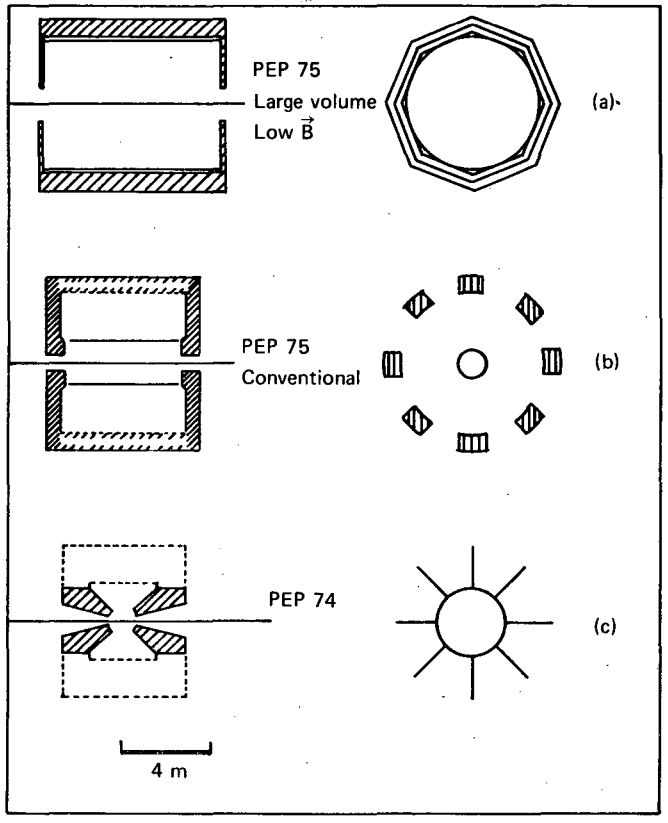

XBL 7512-9864

Fig. 6. Comparison of the sizes and shapes of the solenoidal magnets (a) and (b) studied in this report, and (c) the magnet envisaged by the 1974 group.

DETECTION SYSTEMS: GENERAL CONSIDERATIONS

Before considering details of the detectors associated with each magnet configuration, certain common features are more briefly described below.

Cell Granularity

The probability that no two charged particles of multiplicity N = 7 are counted in K = 100 uniformly illuminated cells is

$$\prod_{j=1}^{N-1} \left(1-\frac{j}{K}\right) = 0.81.$$

That is, even in systems with 100 elements, 19% of the events will suffer at least one ambiguity. Examples of such systems are Čerenkov and time-of-flight (TOF) counters, and wire chambers, which tend to have fewest elements close to the beam. The probability that the entire detector will unambiguously detect an event is the product of probabilities like the above for each independent subsystem of elements. For this reason it may be advantageous to arrange layers of for example Čerenkov cells to subtend the same elements of solid angle (ignoring curvature in the trajectories).

The problem is exacerbated by upward fluctuations in event multiplicity; additional tracks from γ conversions, δ rays and strong interactions in detector material; and correlations in particle directions introduced by energy-momentum conservation and by dynamics such as observed at SPEAR and described by the limited-$p_\perp$ jet model[3] mentioned earlier. For example, for 12 tracks the 100-element detector yields at least one ambiguity 50% of the time. Figure 7 displays these probabilities for various multiplicities and cell granularities. Earlier in Fig. 3 a jet-model simulation of the distribution of particle opening angles at $\sqrt{s}$ = 15 GeV was shown. It implies a concentration of particle density in the jet direction which is $\approx$ 4 times that expected without correlations between particles. Effectively, the number of detector cells is reduced by a similar factor!

Pending detailed Monte Carlo study, we have constrained layers of proposed detection system to possess $\geq$ 100 cells. Coarser systems surely will not work; finer systems probably will be necessary.

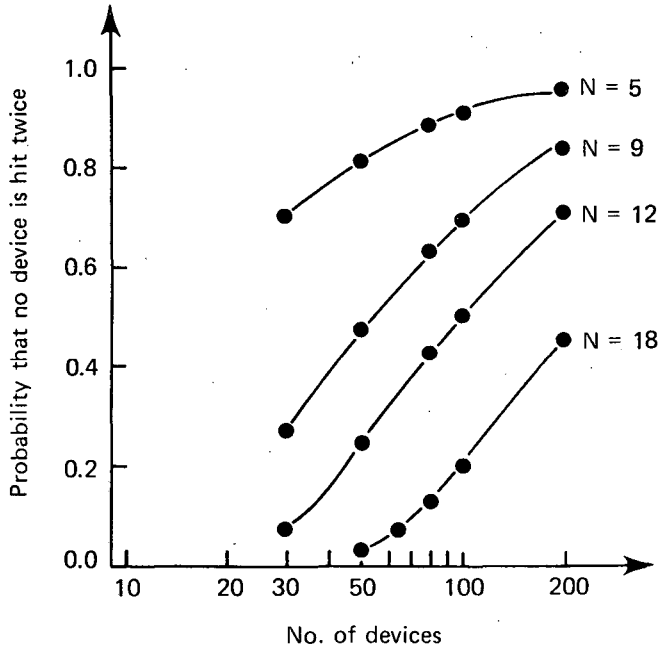

XBL 7512-9865

Fig. 7. The probability of no double hits, given N uncorrelated tracks and 30-200 devices (cells).

0 0 0 0 4 5 0 1 6 2 5

Velocity Measurement

For complete πKp separation in the range below 15 GeV/c, five types of velocity measurement are needed (Fig. 8):

a) Time-of-flight over 3-m flight path with σ = 0.22 nsec.[10] Maintaining this timing accuracy over huge hodoscopes at this radius would provide > 3σ πK separation below 1.3 GeV/c and Kp separation below 2.1 GeV/c.

b) Aerogel threshold Čerenkov counter with refractive index n $\leq$ 1.04. This material is in the development stage.[11] Aerogel with n = 1.06 has been produced and indices down to 1.025 are thought to be possible. The latter index would be ideal, providing πK separation between 0.6 and 2.2 GeV/c and Kp separation between 2.2 and 4.2 GeV/c. In the large volume low $\vec{B}$ detector, ~ 600 cells roughly 15 cm on a side would be needed--an enormous quantity by present standards. In the conventional solenoid at larger radius, at least five times more would be required! Even in the more favorable case, the use of aerogel on this scale is regarded only as a possibility.

c) Isobutane threshold Čerenkov counter, n = 1.006 at 4.1 atmospheres, providing πK(Kp) separation between 1.3 and 4.5 (4.5 and 8.5) GeV/c. Six atmospheres of propane could substitute for the isobutane, at the expense of thicker vessel walls. Freon is not an acceptable substitute in this case of wide angle optics, because it scintillates excessively (~ 1.7 photons/cm).[12]

d) Isobutane or pentane[13] threshold Čerenkov counter near atmospheric pressure with n = 1.0015 or 1.0017, providing πK (Kp) separation between 2.4 and 8.5 (8.5 and 16.1) GeV/c (for n = 1.0017).

e) CO_2 threshold Čerenkov counter at one atmosphere (n = 1.00045), providing πK separation above 4.7 GeV/c and eπ separation below 4.7 GeV/c.

The radiator lengths were chosen to give comfortable light levels except in the case of the CO_2 counters where a minimum of $N_e \approx 5$ photoelectrons would be produced if $N_e = 100\ L\theta^2$. Achievement of the latter figure requires use of special photocathode and phototube window material, or wavelength shifter,[14] or both. Phototube and collector sizes were chosen considering both the size of the Čerenkov ring and the track curvatures at lowest relevant $\pi^{\pm}$ momenta.[15] Most phototubes illustrated in the figures have a photocathode area roughly the same as that of a standard 5-inch tube. In these figures and in Fig. 8, counters (b), (c), (d), and (e) have been dubbed C_4, C_3, C_2, and C_1 respectively.

We would be happy to replace this array of apparatus with simpler means of velocity measurement. Appendix B is an initial attempt to explore the use of microchannel - plate phototubes to record Čerenkov ring radii. Unfortunately, in the example chosen, 25 m^2 of 1 cm^2 photosensitive elements are required. We did not seriously consider relativistic-rise dE/dx velocity measurement, as the necessary sampling lengths seem excessive. Pulse-height analysis on Čerenkov counters with large light levels conceivably could provide additional information sufficient to eliminate one layer of Čerenkov counters.

Triggering

We approach the intractable problem of designing a trigger with sufficiently low background rate by assuming that the PEP vacuum is as good as that at SPEAR and that beam-gas scattering continues to contribute 5-10% of the multi-hadronic event rate. In this case an adequate and flexible trigger scheme would make use of 2-3 coaxial cylindrical proportional counters (or other fast high-resolution devices) close to the beam pipe. Azimuthal coincidences of hits at different radii in these counters, in time with the beam crossing and TOF counters, would form a fast bias-free ~ 1 kHz pretrigger. Flexibility in setting majority requirements on the number of azimuthal coincidences would be retained. Some cosmic ray configurations would fail to satisfy the TOF coincidence.

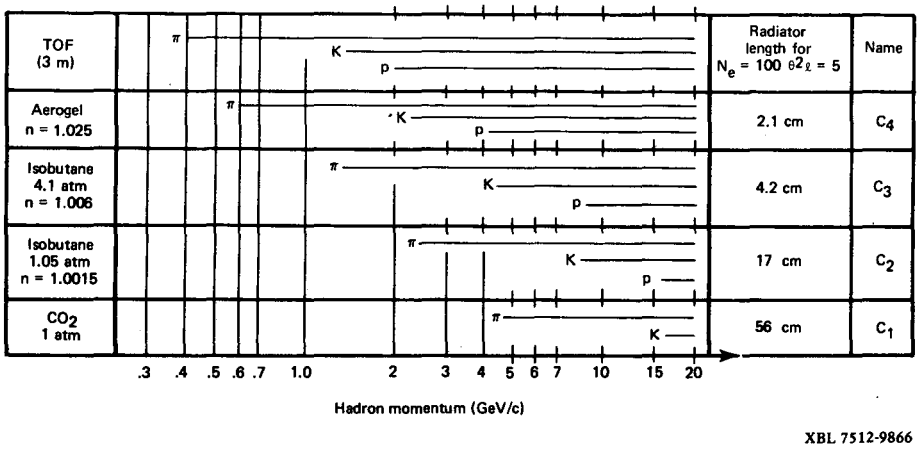

Fig. 8. System of 5 counters for particle identification (described in the text). The time-of-flight (TOF) solid lines labelled π,K, and p indicate the momentum ranges over which eπ, πK, and Kp respectively are separated by less than 3σ. The threshold Cerenkov (C_1,C_2,C_3,C_4) solid lines indicate the momenta above threshold.

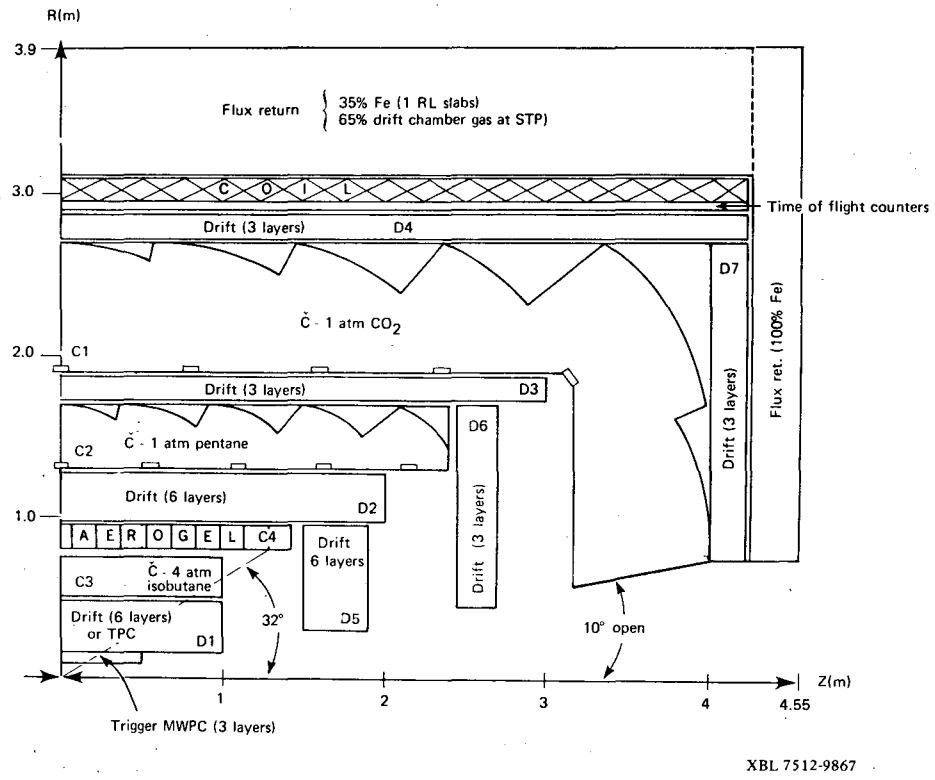

Fig. 9. Side view of one quadrant of the large volume low magnetic field detector.

After the pretrigger, a scheme similar to those in use at PLUTO and envisioned for the SPEAR Mark II detector would perform fast track reconstruction within ~100 μsec. Only drift chamber wire occupancies (rather than digitized coordinates) would be used. Control of momentum cutoffs, multiplicity, and topology would remain flexible. The two-level trigger is intended to provide a logging rate of ~ 1 Hz with < 10% dead time.

LARGE VOLUME LOW MAGNETIC FIELD DETECTOR

Magnet

The 3 kGauss solenoidal magnet, with a coil of radius 3 m and length 8 m, already has been mentioned and its outline shown in Fig. 6(a). Figures 9 and 10 depict portions of its side and end sections in greater detail, along with the detector array. The allocated coil space is sufficient either for a superconducting coil or for a simple aluminum winding. The superconducting approach is made attractive by the low field, minimal coil forces, and low stored energy (~ 7 MJ), but not by the large cryostat. A scaled-up "MINIMAG" design[16] seems too expensive. The coil area is 4.3 × that of the Mark II magnet and the field 58% as large. With half the Mark II current density a conventional Al coil would draw 3 MW and still present less than one radiation length.

The magnet flux is returned on eight sides of an octagon by laminations of 1 radiation length steel plate, with total steel thickness 30 cm and total lamination thickness 80 cm (Fig. 10). The remaining 50 cm are used for position and energy measurement of showers (discussed below). The 30 cm thick endcaps leave a 10° cone for electron tagging of the $\gamma\gamma$ process. A very homogeneous solenoidal field is expected. Total weight of the iron is 600 metric tons.

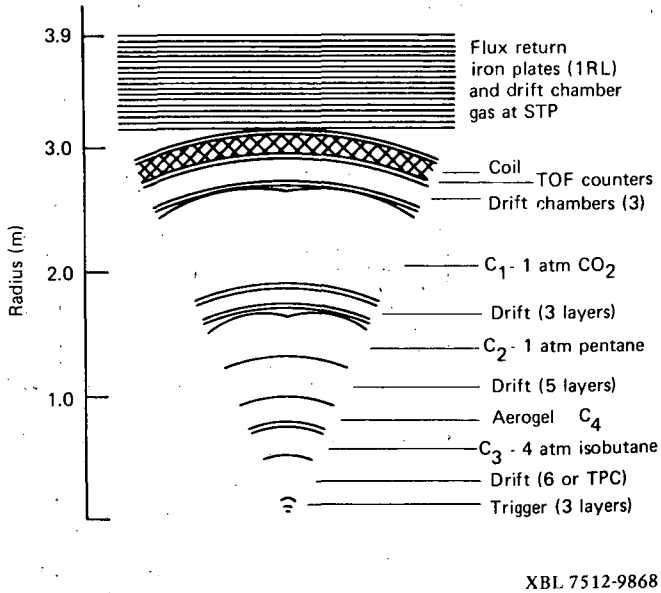

Fig. 10. End view of one octant of the large volume low magnetic field detector.

0 0 0 0 4 5 0 1 6 2 6

Particle Identification

The prime advantage of this detector is that the Čerenkov counters C_3 and C_4 (see Fig. 8), which have highest index and large cost per unit volume, may be kept manageable in size by placement near the beam crossing point. This choice combined with the low magnetic field minimizes the effect of track curvature on their optics. The counters lie in the region 50 cm < radius < 95 cm and subtend the range $32° < \theta < 148°$ (84% of 4π). Their location is shown in Fig. 9 (sideview of one quadrant) and Fig. 10 (endview of one octant), with optical details in Fig. 11. Using overpressure safety factors in excess of 3, their material(mainly Al) amounts to 0.24 radiation lengths. Despite the relative compactness of the aerogel counter, it still requires 608 elements roughly 15 cm on a side. This volume of aerogel may exceed projected production capabilities, leading to a large reduction of the solid angle of the counter. In this case a hole in Kp separation between 2.1 and 4.5 GeV/c may be created in the otherwise full momentum range for hadron identification.

The time-of-flight scintillation counters subtend 82% of 4π steradians just inside the coil. The length of this system (8.5 m) probably makes it necessary to split the coil about the plane z = 0 (not shown in Fig. 9) for phototube readout at z = 0 in addition to $z = \pm 4.25$ m. The number of TOF elements would exceed 100 and the number of phototubes (conventional or microchannel) would exceed 200. These counters are inaccessible to particles with $p_\perp < 135$ MeV/c. Possibly, additional Kp separation at lower momenta could be obtained with TOF information from drift chambers at smaller radius.

The atmospheric-pressure counters C_1 and C_2 are interleaved with drift chamber layers outside the aerogel (Figs. 9 and 10). The integral tracking and momentum analysis is intended to discriminate between original secondaries and daughters arising from knock-on and strong interactions in C_3 and C_4. C_2 subtends 84% of 4π, while C_1 is extended to 98% of 4π because of the interest in clean identification of single electrons with $x \leq 0.3$. More energetic electrons will be identified by the shower counters used for detection of neutrals (described below).

Muons are identified with 85% confidence over 73% of 4π by comparing the coordinates of charged tracks outside 30 cm of steel with extrapolations of their trajectories within the solenoid.[17] This confidence level is not badly matched to the levels of decay background; for example, the 5-GeV $K^+_{\mu 2}$ decay probability is 0.06 at $\theta = 90°$.

Sensing Čerenkov Light within the Magnetic Field

Each of the Čerenkov counters mentioned above employs single reflections from aluminized surfaces onto photomultipliers located within an ambient 3 kGauss magnetic field. The necessary photocathode area of each indicated light-sensitive device is roughly that of a 5-inch phototube. Obviously, magnetic shielding of conventional photomultipliers would be too unwieldy.

The assumption sustaining our interest in this detector is that, by 1980, microchannel-plate photomultipliers ("μCPM's") with sufficient insensitivity to magnetic fields will exist in adequate quantities (~ 400 excluding aerogel counters). A brief introduction to μCPM's is

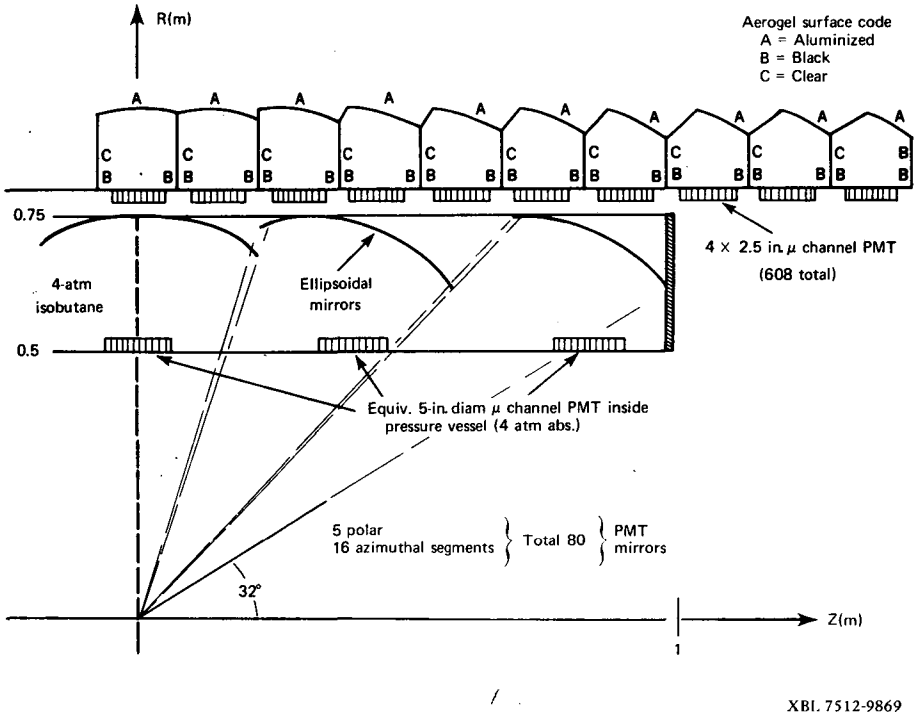

Fig. 11. Side view of high pressure and aerogel threshold Cerenkov counters used in large volume low magnetic field detector.

found in the following report.[8] Sufficiently compact μCPM's with adequate gain exist now at outrageous prices. The price seems more a matter of supply and demand than one of manufacturing cost. The unresolved technical questions concern quantum efficiency and magnetic field sensitivity. Quantum efficiency is determined by photocathode chemistry and primary photoelectron collection efficiency. We assume that bi- or tri-alkali photocathodes evaporated onto quartz or Vycor windows can be mated to the microchannel multipliers. The collection efficiency is thought to exceed the fraction (≈ 60%) of plate area which is channel-aperture rather than channel wall, due to local focussing effects at the beginning of the channel. With presently obtainable channel diameters as small as 9μm,[8] a photocathode might (we imagine) be placed as close as 25 μm to the channels, at a relative potential of ~ -10 V. Under these circumstances the $\vec{E} \times \vec{B}$ deflection would be $\leq 10\mu m$ – perhaps large enough to disrupt the local focusing effects mentioned above, but not large enough to cause the photoelectrons to be lost altogether. Once inside the channel, the photoelectron, if anything, would seem to suffer more wall collisions in the presence of a perpendicular magnetic field, resulting in greater multiplication. Obviously, these suppositions need to be tested soon.

Certain early photomultiplier designs used magnetic fields as a necessary part of the focusing structure. Although requiring specific orientation with respect to the field, such devices might be worth reincarnating for our purposes.

An alternative to light detection within the field is to pipe the light out. Systems of light pipes opening into the Cerenkov gas volumes can be engineered to require few bounces and obstruct a minor fraction of the drift chamber tracking area. Unfortunately, even quite an elaborate framework of light pipes would service only two layers of Cerenkov counter, which is not an advance over the 1974 detector.[1]

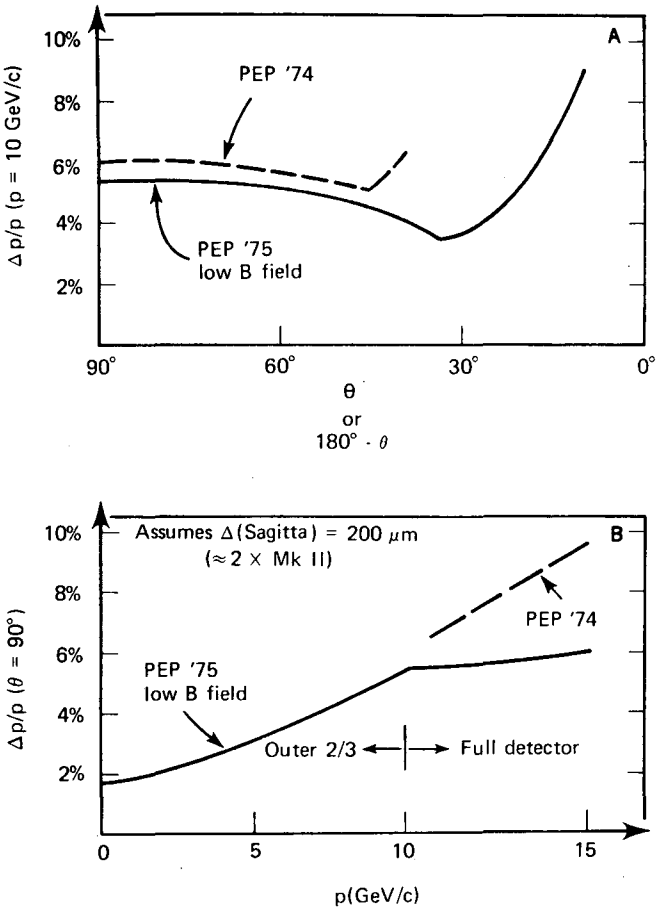

Fig. 12. Momentum resolution of large volume low magnetic field detector (a) vs. momentum p, (b) vs. polar angle θ, assuming sagitta resolution of 200 μm. Below 10 GeV/c only the outer 2/3 of the detector is used in order to minimize Coulomb scattering effects.

Tracking

Charged particle trajectories are detected by seven sets of drift chambers, detailed in Table 1(a) and Fig. 9. These are divided into two main groups. In the cone $32° < \theta < 148°$, cylindrical chamber sets D_1-D_4 with small-angle stereo in sequence +5°, -5°, 0° are planned. Cell sizes of 4 cm are used except in the innermost set of chambers, where 2 cm cells may give fine enough granularity. A particle passing through D_1-D_4 intersects a total of 18 layers of drift chamber. For momenta less than than 10 GeV/c, momentum measurement will use D_2, D_3, and D_4 only, in order to avoid the effects of Coulomb scattering in C_3 and C_4. The chamber set D_1 provides track direction information at radii inside C_3 and C_4 for interpretation of these counters, and for improved momentum resolution anchors the trajectories of particles with momenta exceeding 10 GeV/c. Assuming (conservatively) 200 μm resolution in sagitta of tracks projected upon the z = 0 plane, the momentum resolution, as shown in Fig. 12, is better than 6% at p = 15 GeV/c, θ = 90°, and improves further in the range $20° < \theta < 90°$.

Although we have described D_1 as a set of conventional drift chambers, the time-projection chamber described by Nygren[17] is a candidate for use in this region. The reason is that information of sufficient density for local track reconstruction is sought in an annular region only 30 cm thick. The location, centered on a point of high symmetry in the solenoid, would provide exceptional magnetic field uniformity[18] since the time-projection chamber would occupy only a tiny fraction of the (already uniform) field volume.

The regions $10° < \theta < 32°$ and $148° < \theta < 170°$ are serviced by D_1 and by drift chamber sets D_5,D_6 and D_7. Each of the latter sets is a -60°, 0°, 60° configuration for highest information content of each individual plane. The inner 10° cones are tentatively left open for access and to prevent beam-gas background at low θ from creating too many extra wire hits.

The total solid angle for charged particle track reconstruction is 98% of 4π.

0 0 0 0 4 5 0 1 6 2 7

Table 1. Drift Chamber Wires

(a) Large Volume Low $\vec{B}$ [a]

	r	Length (cm)	Layers	Cell size(cm)	Angles	Wires	Total
D_1	32.5±12.5	110	6	2	±5° ±3° 0°	102	612
D_2	120±10	505	6	4	±5° 0°	188	1128
D_3	180±10	650	3	4	±5° 0°	283	849
D_4	282±10	840	3	4	±5° 0°	442	1326
D_5		180	6	4	±30° 90°	45	270
D_6		350	4	4	±30° 90°	87	348
D_7		550	3	4	±30° 90°	136	408
							4.9 K

(b) Conventional

D_1	20±8 30±2	100 150	4 1	1 2	±5° Delay line	63 95×3	252 288
D_2	55±10	275	5	2	±5° 0°	141	707
D_3	95±5	410	4	3	±5° 0°	200	
D_4	125±4	510	3	3	±5° 0°	260	780
D_5	300±8	600 ×210	6	10	0° 60° 120°	240	1920
							4.8 K

[a] Does not include shower detector.

Detection of Neutrals

The one-radiation-length ("$1X_0$") steel flux return plates, subtending 73% of $4\pi^0$ steradians, ideally would be sampled by a liquid argon system (of enormous area). Since the choice of sampling device is governed by cost analyses which at this stage are not complete, we instead shall describe an example of what may represent a manageable system. It has the advantage of emphasizing precision in direction of the neutral particle, which to a certain extent has been neglected even by proposed detection systems that concentrate on neutrals. For this purpose the location of these counters at 3 meter radius is a distinct advantage, not only because of the large lever arm for direction measurement but also because those γ's which are tightly collimated have an opportunity to spread out and produce separate showers.

The chosen sampling medium is drift chamber gas (mainly argon) at STP. Thicknesses of 5 cm follow each of the first four $1X_0$ radiators (the coil counts as the first radiator). Thicknesses of 2.5 cm follow the next ten $1X_0$ slabs, and alternate $1X_0$ slabs in the final four radiation lengths. Each 2.5 cm of gas is contained within one drift chamber, with cell spacing designed to minimize cost, consistent with granularity requirements. Most drift wires run in the $\hat{z}$ direction, except for the outermost chamber and half of the eight chambers within the first four radiation lengths, which have wires in a rectilinear direction approximating $\hat{\phi}$. The innermost pair of chambers is azimuthally segmented to follow the coil shape. The innermost eight chambers have wires staggered and at slight stereo angles in order to resolve ambiguities, and are read out individually with electronics giving 1.5 mm spatial resolution, while preserving pulse height information. Corresponding wires of the next five and five chambers, respectively, are connected to common electronics channels. The outermost two chambers are read out individually in order to identify muons. The intention is that the first 4 X_0 portion of the counter detects conversion electrons with 1.5-mm resolution both in Z and $r\phi$; the first $14X_0$ portion measures electromagnetic shower energies with $1X_0$ sampling; and the entire $18X_0$ ($2L_{abs}$) counter observes hadron showers with $\leq 2X_0$ sampling and identifies muons.

Each of eight octants by this prescription would contain 20 drift chambers of a size exceeding 2×8 m, with electronics for the equivalent of 12 chambers. We imagine that the iron laminations themselves would supply most of the frame stiffness and gas enclosure for these chambers. Nevertheless, without considerable design innovation their construction cost would be staggering. Total drift chamber electronics channels would not exceed the $\approx$ 5000 allocated to the inner detectors. Their low level of required performance needs to be exploited fully in order to keep the cost within reason.

The conversion point resolution is limited by Coulomb scattering of the produced pair within the radiator at low energies. As a function of energy E(GeV), at $\theta = 90°$ the projected γ direction is known to

$$\pm 0.5(1 + (3/E)^2)^{\frac{1}{2}} \text{ mrad}$$

for typical conversions in the coil, and

$$\pm 0.5(1 + (0.5/E)^2)^{\frac{1}{2}} \text{ mrad}$$

for typical conversions in the iron.

Electromagnetic shower energy resolution suffers contributions both from the shower statistics and from delta rays in the gas.[20] For the case of $1X_0$ sampling in iron with 2.5 cm of argon at STP, these contributions to $\sigma(E)/E$ are estimated to be $0.22/\sqrt{E}$ and $0.39/\sqrt{E}$ rms, respectively. Thus the anticipated γ energy resolution is $\sigma(E)/E \approx 0.45/\sqrt{E}$, or $\approx$ 6 times worse than may be achievable with liquid argon and thin Pb plates.

Above 3 GeV, this γ energy resolution combined with the high angular precision will achieve $>3\sigma$ separation of π^0 from η^0. Once identified, the γ pair's energy resolution can improve dramatically if opening angle information is used. Let M and E be the π^0 or η^0 mass and energy, and k_1 and k_2 the γ energies. Then

$$E \cong (M/\theta)\ (1 + k_1/k_2)^{\frac{1}{2}}\ (1 + k_2/k_1)^{\frac{1}{2}};$$

$$\frac{\sigma^2(E)}{E} = \frac{\sigma^2(\theta)}{\theta^2} + \left(\frac{k_1^2}{E^2} - \frac{k_2^2}{E^2}\right)^2 \left(\frac{\sigma^2(k_1)}{k_1^2} + \frac{\sigma^2(k_2)}{k_2^2}\right).$$

A 3-GeV π^0 or η^0 with $k_1 = k_2$ has better than 2% energy resolution. If $k_2 \cong 2k_1$ the resolution rises to 18%.

Events with up to four γ's that cannot be identified as π^0 or η^0 may still be fully reconstructed, provided that the γ's fall within the 75% of 4π devoted to neutrals detection and the charged particles lie within the 98% of 4π which is instrumented for charged particle reconstruction. Since the γ energies are not used in the fit, the number of constraints drops from 4 to 0 as the number of γ's rises from 0 to 4. Even the OC events are subject to the condition that the fitted energies be consistent with their independently measured values. If π^0 or η^0 are presumed to be the γ-ray parents,[21] one may demand with good accuracy that two independent γ pairs each match one of these parent masses.

Separation of $e^{\pm}$ and $\pi^{\pm}$ is performed by the shower counter only above 4.6 GeV/c, because of the existence of the CO_2 Cerenkov counter C_1. For $\pi^{\pm}$ that feed $\leq 1/3$ of their energy into electromagnetic showers, the separation of $e^{\pm}$ from $\pi^{\pm}$ will exceed 4σ.

At energies below 15 GeV, the 30 cm of Fe will contain > 80% of the hadron shower energy.[22] Crudely taking into account containment effects and δ-ray confusion in the drift chamber gas, we compute an abysmal hadron energy resolution $\sigma(E)/E \approx 2/\sqrt{E(\text{GeV})}$. Neutron and K_L^0 directions are measured by the muon identifier chambers. This class of particles can be identified with low (~ 30%) efficiency and high confidence if they first interact in the outer half of the shower counter. We note that 30 cm of steel is not a bad $K_L^0 \rightarrow K_S^0$ regenerator.

0 0 0 0 4 5 0 1 6 2 8

DETECTOR USING "CONVENTIONAL" SOLENOID

The side view of one hemisphere of this detector is shown in Fig. 13 and its end view in Fig. 14. The right-hand quadrant in Fig. 13 shows a section between the laminated flux return legs, while the left-hand quadrant shows a section within the legs.

Magnet

The magnet was chosen to have 15 kGauss over 1m radius for sufficient momentum resolution. A superconducting coil was selected for power economy, and preference given to a lumped coil to keep γ conversion and hadron interactions localized to the relatively small coil obstruction of 10%. Also the cryostat is manageable. The field is returned through 8 legs of 3.4m inner radius which occupy 1/3 of the azimuth. By these demands, the magnet turned out to be similar to the General User Magnet. For details of a typical design, the reader is referred to their report.[23]

Particle Identification

The detector uses a time-of-flight system that is similar to that previously described, except that the counters at 3 m are inaccessible to particles with momenta $\leq$ 225 MeV/c. Because of the very large volume of radiator that would be

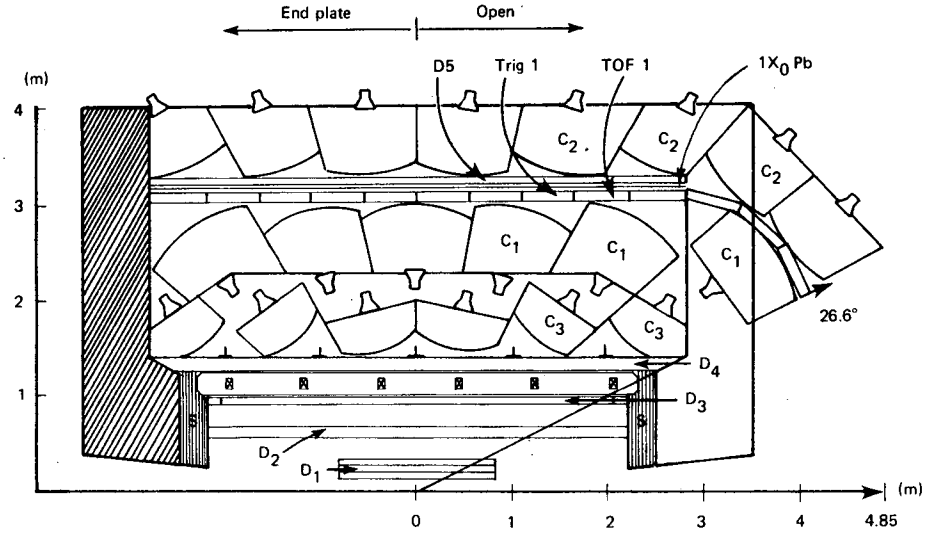

XBL 7512-9871

Fig. 13. Side view of "conventional" superconducting solenoid detector.

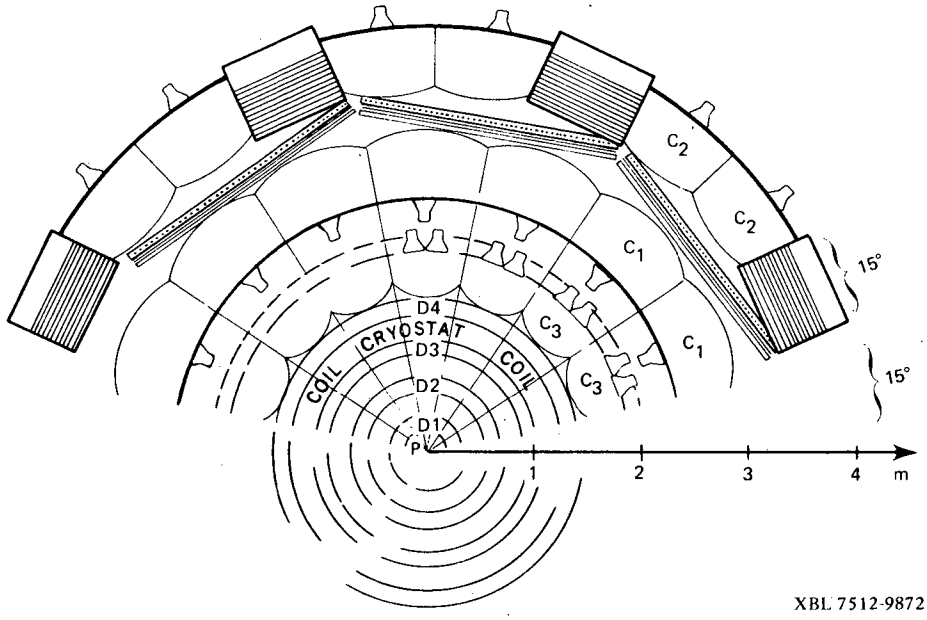

XBL 7512-9872

Fig. 14. End view of "conventional" superconducting solenoid detector.

required, an aerogel counter covering an appreciable fraction of the solid angle is not envisaged. The gas Čerenkov counters C_1, C_2, and C_3 (Fig. 8) perform the same particle separation functions with the same refractive indices described earlier. The high-pressure isobutane counter (C_3) lies innermost, beginning at a radius of 1.4 m. It and the surrounding atmospheric-pressure CO_2 counter (C_1) subtend 82% of 4π steradians. These counters perform πK separation above 1.3 GeV/c, and Kp separation between 4.5 and 8.5 GeV/c. Kp separation above 8.5 GeV/c is provided over 2/3 of the azimuth by the atmospheric-pressure counter C_2.

Technically, the counter C_3, which produces plenty of light, employs double-reflecting optics, consisting of outer and inner spherical mirrors with respective radii of curvature 1.8 and 0.6 m. The momentum dispersion created by the magnet field integral of 450 MeV/c makes it necessary to use two 5-in. tubes per cell in order to make the light collection efficiency momentum-independent. Inexpensive tubes like RCA4525 may be used,[24] since timing and rate are no problem. The phototubes and mirrors will be enclosed by a cylindrical pressure vessel of 0.7 cm Al wall thickness.[25]

Photons will not trigger the TOF scintillation counters and thereby can be distinguished from charged particles. The drift chamber outside the $1X_0$ Pb absorber will determine coordinates of a charged particle or the vertex of a γ conversion with 50% efficiency. The Pb absorber will produce new δ rays while absorbing those produced at smaller radii. By constraining charged particle trajectories, this chamber will recognize interactions in the walls of C_3 and especially in the lumped coils, which is a problem specific to this design.

Muons are identified with 97% confidence over 27% of 4π by drift chambers outside the flux return legs (not shown). Electrons below 4.7 GeV/c are identified by C_1 over 82% of 4π. Higher-energy electrons are identified over 31% of 4π by 5000 crossed proportional tubes interleaved with $1X_0$ iron laminations in the flux return legs and shower counters close to the pole faces, (Fig. 13). These laminated detectors identify neutrals in a manner similar to that discussed previously for the large volume low $\vec{B}$ detector.

Tracking

Five sets of drift chambers D_1-D_5 record the trajectories of charged particles. D_1-D_3 subtend 90% of 4π. Using the partial information in D_1-D_2 gives less precise momentum reconstruction over 96% of 4π. The momentum resolution using the sets D_1-D_4 (subtending 82% of 4π) has the high-energy asymptote

$$\Delta p/p^2 = 0.0055/\text{GeV}$$

at $\theta = 90°$, again with the assumption of 200 μm sagitta resolution.

The details of these drift chambers are found in Table 1(b). D_1-D_4 are sets of drift chamber layers in sequence +5°, -5°, 0°, except that D_1 possesses an extra layer of delay-line drift chamber cells for improved pattern recognition. The chambers in D_5 are almost square in shape and equipped with wires at +60°, 0°, -60°. These provide additional tracking precision as well as identifying γ conversions in the Pb. The total number of drift chamber wires is 4900.

COMPARISON OF DETECTORS

Size and Equipment

An immediate comparison of the size of the two magnets discussed above with their 1974 counterpart[1] has been displayed in Fig. 6. Greater detail is provided in Table 2. Although the magnets have grown by ~ 25% radially and up to 50% longitudinally since 1974, they still are accommodated by the 4-m pit floor clearances anticipated for five experimental areas. More than half of the interaction area length (20m) will be available for compensating coils, electron tagging, etc. Magnet tonnages also have grown by 50-150%. However, most of the ton weight of the largest magnet is composed of plates that also serve as media for shower development.

The 1975 detectors each substitute ≈ 3000 drift chamber channels for ≈ 3000 MWPC wires plus 42000 spark-chamber capacitive-readout channels used in the 1974 design. The large volume low $\vec{B}$ detector's shower counters would require up to 5000 additional low-resolution drift chamber channels with pulse height capability, while the "conventional" detector would add 5000 proportional tubes. Total scintillator area has dropped by 20%. The number of Čerenkov layers has risen from 2 to 3 (or 4 with the low $\vec{B}$ aerogel option), while the number of Čerenkov cells has trebled to ~ 400 (excluding aerogel). Most of the latter increase is needed to solve ambiguity problems, rather than to service the extra layer. One measure of difficulty in constructing the explosive 4.1-atmosphere Cerenkov counters is the total area of the innermost pressure windows. This is 24 m^2 for the 1974 detector, 48 m^2 for the 1975 "conventional" detector, and 6 m^2 for the 1975 low $\vec{B}$ apparatus.

Performance Summary

Table 3 summaries the relative performance of the 1974 and two 1975 detectors. Listed are solid angles for tracking, various ranges of πK and Kp separation, and electron, muon, and neutrals detection. The 1975 detectors have only 10-30% of the 1974 tracking inefficiency. The high-momentum πK separation (C_1) extend over 98% or 82% of 4π, as opposed to 48% in 1974. Intermediate momentum πK and Kp separation (C_2) subtends 82% for the low $\vec{B}$ detector and ≈ 60% for the others. Lower-momentum separation (C_3) has the largest gain: > 80% of 4π, as opposed to 16% in 1974. The low $\vec{B}$ detector retains the possibility of an aerogel Čerenkov layer (C_4, 82% of 4π) which overlaps the TOF separation region. The TOF systems in all three detectors cover similar solid angles.

Identification of muons and high-energy electrons, capabilities absent from the 1974 detector,

0 0 0 0 4 5 0 1 6 2 9

are performed over ~ 75 or ~ 30% of 4π . The confidence levels for muon identification range from 80% to 90%. Photons are detected with excellent accuracy in direction over 75% or 30% of 4π , and with modest energy resolution $\sigma(E)/E^{\frac{1}{2}} = 0.45$ $GeV^{\frac{1}{2}}$. Some K_L^0 and neutron identification is possible. Capability for neutrals detection again was absent from the 1975 detector.

Summary of New Design Features

Essential new features of the 1975 detectors are:

Homogeneous magnetic fields tremendously simplify the tracking software.

e,γ,μ, and neutral hadron detection capabilities are added with lamination of the iron return yoke in order to provide a medium for shower development.

Full use of drift chambers reduces chamber electronics requirements while make possible "slow" trigger decisions.

Simpler Čerenkov optics improve counter performance and reduce cost. The set of Čerenkov counters is more complete.

Location of high pressure counter at smaller radius decisively improves the design of the large volume low $\vec{B}$ detector. Its high pressure isobutane counter has a 6-m^2 inner-pressure window subtending 84% of 4π. The corresponding 1974 counter had a 24-m^2 inner window subtending 16% of 4π.

FULL IDENTIFICATION OF THE FINAL STATE ?

With the detectors specified, the report concludes with a brief estimate of their ability to achieve the original goal--full identification of a non-negligible fraction of the final states accompanying the high-momentum particles. We consider an event as $\sqrt{s}$ = 30 GeV with 6 charged particles and 4 π^0's. Loss or ambiguity in particle identification may occur because of:

Finite solid angle for charged particle tracking and Čerenkov aperture. For each momentum,

Table 2. Detector Comparisons: Scale

Detector	PEP'74	PEP'75 [Large volume low $\vec{B}$ field]	PEP'75 [Conventional]
Outside dia × length (m)	6.5×6.74	7.8×9.1	8.0×9.7
Magnet			
Peak field (kGauss)	8	3	15
Yoke weight (tons)	230	600	330
Coil weight (tons)	5	23	
Čerenkov detectors-no. of cells			
CO_2 (1 atm)	72	176[a]	96
Isobutane or pentane (1 atm)	32	144	112[a]
High pressure (n = 1.006)	24	80	96[b]
Total 5 in photomultipliers[d]	128	≥ 400[e]	≥ 400
Total pressure window area[f] (m^2)	24	6	48
Drift wires	1960	4900 + shower	4800
MWPC wires	3500	~500	~500
Spark chamber channels	42,000	—	—
Scintillator area (m^2)	210	170	160
Proportional tubes	—	—	5000
OPTION: Aerogel Č (n = 1.025)	—	$608\{^{\text{cells}}_{\text{PMT}}\}$	—

[a]Number of phototubes may be larger.
[b]192 phototubes.
[c]All phototubes approximately equivalent in area to 5 in dia.
[d]Excludes time-of-flight counter phototubes (approx. 200 in. each case).
[e]Microchannel-plate photomultipliers
[f]Inside window only.

Table 3. Detector Comparisons: Performance

Detector	PEP'74	PEP'75 [Large volume low B field]	PEP'75 [Conventional]
I. $\Delta\Omega/4\pi$ Full tracking (partial tracking)	0.64	0.98	0.90 (0.96)
II. $\Delta\Omega/4\pi$ for particle identification			
(a) C_1: πK separation (p>4.6 GeV/c)	0.48	0.98	0.82
(b) C_2: πK separation (2.4<p<8.5) Kp separation (p>8.5)	0.64	0.84	0.56
(c) C_3: πK separation (1.3<p<4.5) Kp separation (4.5<p<8.5)	0.16	0.84	0.82
(d) C_4: Kp separation (2.2<p<4.2)	–	(0.84)[a]	–
(e) TOF: πK separation (p<1.3) Kp separation (p<2.1)	0.64	0.82	0.56
(e) TOF: πK separation (p<2.1) Kp separation (p<3.6)	0.16	–	–
III. Electron identification - $\Delta\Omega/4\pi$			
(a) C_1 p<4.6 GeV/c	0.48	0.98	0.82
(b) Shower counter p>4.6 GeV/c	–	0.75	0.31
IV. Muon identification			
(a) $\Delta\Omega/4\pi$	–	0.73	0.28
(b) Punch-thru + $K^{\pm}_{\mu\nu}$ prob. @ 5 GeV/c	–	$\approx$0.15 +$\approx$ 0.06	$\approx$0.03 +$\approx$ 0.06
V. Photon measurement			
(a) $\Delta\Omega/4\pi$	–	0.75	0.31
(b) $\Delta E/E^{1/2}$(GeV$^{1/2}$)	–	0.5	0.5
(c) $(\Delta\theta$ or $\Delta\phi)_\gamma$	–	1 mrad[b]	1 mrad[b]
VI. K^0_L and neutron identification	–	$\Delta\Omega/4\pi \approx 0.75 \times \approx 0.25$ efficiency	
	–	$\Delta E/E^{1/2} \approx 2$ GeV$^{1/2}$	

[a] Aerogel costs may be unrealistic.
[b] Typical; see text.

0 0 0 0 4 5 0 1 6 3 0

two particular Čerenkov layers must be crossed. The tracking probability for the (a) low $\vec{B}$ or (b) conventional detector is 0.98 or (partial tracking) 0.96 respectively. The Čerenkov solid angles are near 0.83 of 4π steradians except for Kp separation in the conventional detector at $p > 8.5$ GeV/c. Jet structure which correlates the particles may lead to ~2X reduction in the effective number of independent isotropic track directions, except for fine-structure in the Čerenkov acceptance due to 10% coil lumps in the conventional detector. These effects give efficiencies

$$\varepsilon_a \tilde{=} (0.98)^3 \times (0.83)^3 = 0.54$$

$$\varepsilon_b \tilde{=} (0.96)^3 \times (0.83/0.90)^3 \times (0.90)^6 = 0.39.$$

Multiple hits in detector cells. We assume that drift chamber redundancy and staggered cell azimuth confine this problem to two Čerenkov counters whose cells occupy the same solid angle element. Six particles plus two converted gamma rays share only 50 cells due to jet effects. The efficiencies are

$$\varepsilon_a = \varepsilon_b = 0.55.$$

Disabling of Čerenkov cells by interactions. Delta-ray background is worst in the high pressure counter C_3 at the level of ≈ 2%. Its walls will create ≈ 1% δ-ray background in C_2. Inelastic strong interactions occur at the ≈3% level in these walls. We have already discounted the effects of coil lumps. The efficiencies are

$$\varepsilon_a \tilde{=} \varepsilon_b \tilde{=} (0.95)^6 = 0.74$$

Decays. K decay is dominant. Perhaps two of the particles are K's with $\langle p \rangle$ = 2 GeV/c and decay probability (out to 2m) ≈ 15%. Hence

$$\varepsilon_a = \varepsilon_b = 0.72.$$

Soft particles. Tracks with momenta smaller than 135 MeV/c or 225 MeV/c, respectively, fail to reach the TOF counters. A (model-dependent) guess is that 5% or 10% of events, respectively, have a particle in these ranges, yielding

$$\varepsilon_a = 0.95; \quad \varepsilon_b = 0.90.$$

Detection of neutrals. The detection efficiencies are 0.75 and $(0.31 + 0.56 \times 0.5) = 0.59$ respectively (0.5 is the detection efficiency of the $1X_0$ Pb). Assume that the effects of the jet model and $\pi^0 \to 2\gamma$ decay reduce the number of effectively isotropic tracks from 8 to 3. Then

$$\varepsilon_a = (0.75)^3 = 0.42$$

$$\varepsilon_b = (0.87)^3 \times \left[\frac{0.59}{0.87}\right]^8 = 0.007.$$

Reconstruction of neutrals. For the conventional detector, reconstruction of 8 γ's is virtually impossible since crude energy information is available only for ~ 3 of them. In the low $\vec{B}$ detector we speculate that 5-10% of 8 γ systems could be reconstructed unambiguously. In both detectors, (good OC + pseudoconstraint) fits can be made to ($\leq 4\gamma$ + charged) final states. The strong dependence of reconstruction efficiency on γ multiplicity means that most reconstructed events will be drawn from downward fluctuations in neutral multiplicity rather than fluctuations within a fixed multiplicity as in our example.

Results. The numbers quoted above are meant as guidlines rather than as estimates appropriate to all possible multiparticle configurations. The products of these crudely estimated efficiencies for reconstructing and identifying this 6-particle charged final state are 0.15 and 0.10, respectively, for the large volume low $\vec{B}$ and conventional detectors. Detection (not reconstruction) of 8 γ's plunges these efficiencies below 10% and 0.1%, respectively. It is probably safe to conclude that full reconstruction and identification of "typical" charged plus neutral final states at $\sqrt{s}$ = 30 GeV will not be made with more than ≈ 10% efficiency. Of course, the events containing one or two ambiguously identified particles are still rich in correlation information; many complicated multiparticle states of known baryon number, strangeness, and invariant mass will become available for study.

ACKNOWLEDGEMENTS

It is a pleasure to acknowledge the contributions of D. Coyne, R. C. Field, M. I. Green, G. Hanson, K. Halbach, P. LeComte, P. Oddone, D. Nygren, V. Perez-Mendez, and M. L. Stevenson to this report.

Appendix A

INSTRUMENTING THE MARK II DETECTOR WITH HIGH-MOMENTUM PARTICLE IDENTIFICATION

GENERAL

The Mark II, proposed for general purpose detection of multi-hadron events, has no provision for charged hadron identification above 0.6 - 1.0 GeV/c momentum. This note sketches a detection system over the available solid angle.

The Mark II detector as now envisioned consists of a 3 m diameter, 3 m long solenoid magnet filled with tracking chambers. This cylindrical magnet is enclosed in an iron flux return box open on two sides. Each open side allows $\pi/2$ in azimuthal angle and $\pi/2$ in polar angle free at the iron flux return, or 0.18 of 4π solid angle. If the open sides are oriented in the horizontal, both could be instrumented with particle identification; if the open sides are at the top and bottom, then only the top could be instrumented. As presently designed, the Mark II coil is surrounded by liquid argon shower detector modules. The modules occluding the solid angle subtended by the particle identification package would have to be removed. The major disadvantage to instrumenting the Mark II with particle identification modules is the fact that the modules can be brought no closer than 1.5 m to the source, requiring enormous volumes of detectors.

IDENTIFICATION SCHEME

Particles will be identified in a triple tandem array of Cerenkov counters. The counters are primarily threshold devices, but pulse height detection will increase the range of separation. The three counters, labeled I1, I2, I3, have refractive indices 1.0045, 1.008, 1.05 respectively. A chart of Fig. A-1 shows where particle separation is made.

With this scheme π-K-p separation is accomplished between 1.6 GeV/c and 10 GeV/c. Pulse height comparisons are required in the aerogel, I3, to separate K-p from 3.2 GeV/c to 4.2 GeV/c and in the propane, I2, to separate K-p from 8.5 GeV/c to 10 GeV/c. Separation of π from K and p is complete from 0.6 GeV/c to 15 GeV/c. K-p separation ends at about 10 GeV/c, and perhaps lower depending upon the ability to measure pulse heights in I2.

Assuming a conversion efficiency of Cerenkov photons produced to photoelectrons of 0.1 in each counter type, a β = 1 particle yields 8 photoelectrons in the 2 m I1, 40 photoelectrons in the 50 cm I2, and 100 photoelectrons in the 10 cm I3.

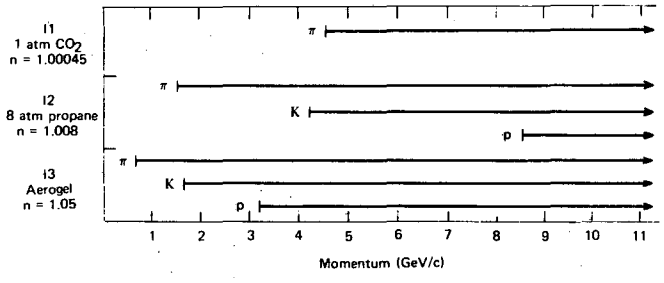

Fig. A-1

CONFIGURATION

The particle identification module is shown in Fig. A-2 (plane view) and Fig. A-3 (elevation view). It consists of four different elements. We describe a module for one of the open quadrants; numbers of elements refer to one module subtending 18% of 4π. There are two large tracking chambers with position resolution of ~ 1mm to flag hadrons interacting in the magnet coil and δ-rays produced in the coil. The chambers each have an area of 1.7 m ×3.5 m = 5.8 m^2. Next comes a 10 cm thick layer of aerogel at a distance of 2 m from the interaction region. The 12.6 m^2 area is composed of a 16 × 20 array of aerogel modules, each 20 cm × 20 cm on a face with a 30 cm light-collection assembly behind leading to a phototube. 320 of these 60 cm deep elements will be required. Following the aerogel layer comes a layer of 8 pressure vessels of diameter 1.3 m and length 3.5 m. Each vessel contains 8-atm propane and three optically separate Cerenkov systems with 50 cm active length. The mirror area in each cell is 4.5 m^2, divided into three 1.5 m^2 mirrors, one for each separate optical system. The 8 high pressure cells

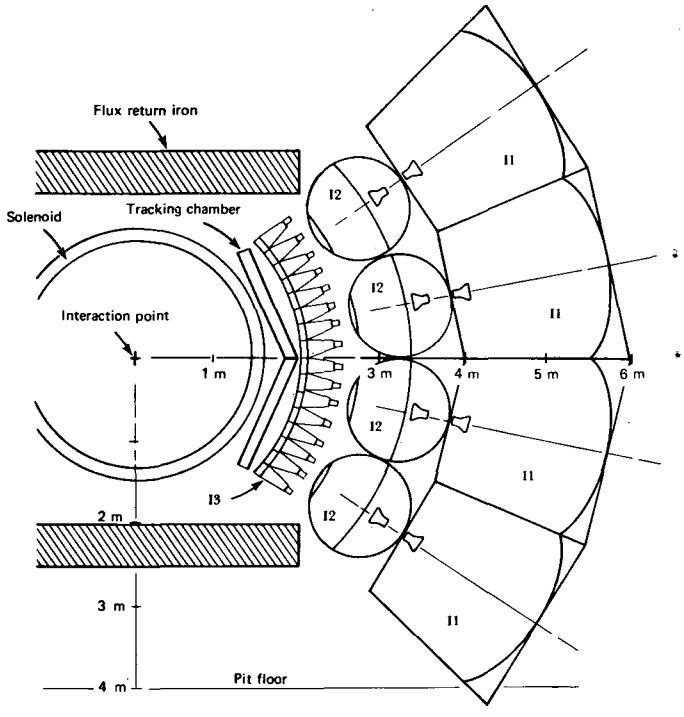

Fig. A-2. Plan view of particle-identification system which could be added to the SLAC-LBL Mark II detector.

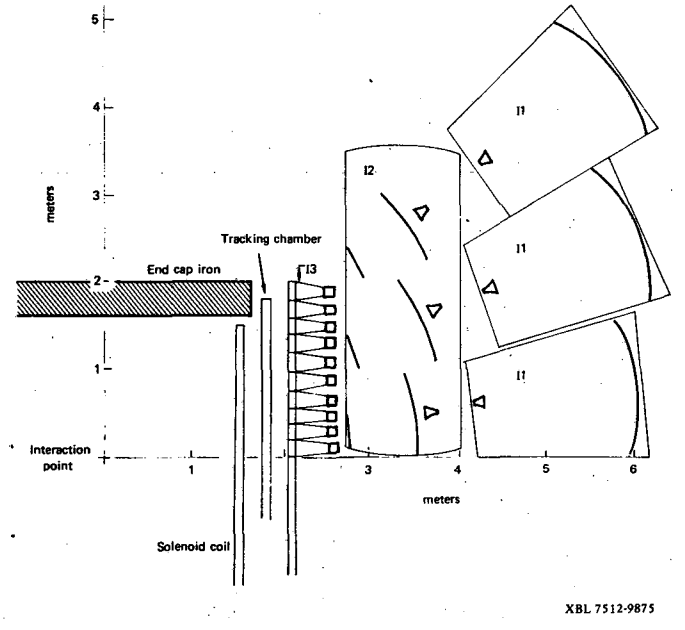

Fig. A-3. Elevation view of particle-identification system which could be added to the SLAC-LBL Mark II detector.

will contain a total of 24 separate Cerenkov counters. The final elements of the system are 24 atmospheric CO_2 Cerenkov boxes each 2 m long with a 2.4 m × 2m mirror on the back. The distance of the last Cerenkov mirror from interaction region

0 0 0 0 4 5 0 1 6 3 1

is 6 m and the area of the rear of the array is 12m ×9.4m = 113m^2. There are a total of ~ 1000 drift wires and 368 phototubes. Realistically the module probably covers only 15% of 4π taking into account support frames, etc.

DECAY AND MISIDENTIFICATION

Decay. In detectors of the size we are considering, a crude table helps to evaluate decay probabilities.

p_K	Prob.Decay
2	20%
5	10%
10	5%
15	3%

The kaons which decay will yield muons which will radiate Čerenkov photons. These rates can be reliably calculated once the spectrum of surviving kaons is known.

δ-Rays. In the counters we are proposing 0.2-1% of slow particles will count in the Čerenkov medium itself due to δ-ray production. The low index materials (atmospheric pressure gases) have the 0.2% confusion level; the high index materials (high pressure gas or aerogel) have the ~ 1% confusion. In addition, pressure vessels contribute 2-3% confusion in high pressure gas counters. Tracking chambers with ~ 1 mm resolution positioned 10 cm behind δ-ray producing materials (such as magnet coils) will reduce the 5-10% confusion so generated to ~ 0.5%.

Appendix B

LARGE SOLID-ANGLE DIFFERENTIAL ČERENKOV COUNTER USING MICROCHANNEL PHOTOMULTIPLIERS AND AEROGEL

This note explores the possibility of a large-solid-angle differential Čerenkov counter. Such a device is impossible with presently available photosensitive detectors which, because of their expense, require optical systems to collect photons produced. No optical system has been devised which focuses images directed over 4π solid angle. However, if a photosensitive device with a large and segmented area could be obtained, no optics would be necessary and a differential counter could be imagined. Microchannel photomultipliers (μCPM) could be the answer to the large-area device required. However, scaling up from existing 5-10 cm^2 areas to 25 m^2 and 1-cm position resolution required make this hypothetical for the near future.

Assume that the μCPM is available in large areas with a 1-cm square cell readout. Then a differential counter could be constructed by placing a Čerenkov radiator of refracting index n ~ 1.1 at small radius surrounded by a drift region to allow the Čerenkov cones to separate in space, followed by the μCPM to record the positions of the photons. A detector (Fig. 17) could consist of an inner proportional counter, a 2-cm layer of n = 1.1 aerogel, and a 1 m drift region containing tracking chambers inside the μCPM. Assuming the μCPM records positions only, a layer of scintillation counters follows for time of flight (TOF) measurements. The TOF and μCPM must be followed by an atmospheric gas Čerenkov counter to separate high momentum π and K.

The 2 cm thick aerogel with a 1 m drift region and 450 mrad Čerenkov angle gives a 9 mrad wide circle of Čerenkov light. The π-K Čerenkov cones are separated by 9 mrad at 5 GeV/c and the K-p Čerenkov cones are separated by 9 mrad at 9 GeV/c. Thus the identification is:

1. TOF π K to 0.6 GeV/c K-p to 1.2 GeV/c
2. Aerogel π-(Kp) 0.4-1.2 GeV/c
   π-K-p 1.2-5 GeV/c;
   K-p up to 9 GeV/c
3. 1 Atm CO_2 π-(Kp) above 5.5 GeV/c.

The tracking chambers give momentum and direction of the particle to be identified and a search is made of the three possible Čerenkov rings. Assuming photocathode efficiency of 0.2 and transmission efficiency in aerogel of 0.7, approximately 15 photoelectrons are produced with which to define the Čerenkov rings.

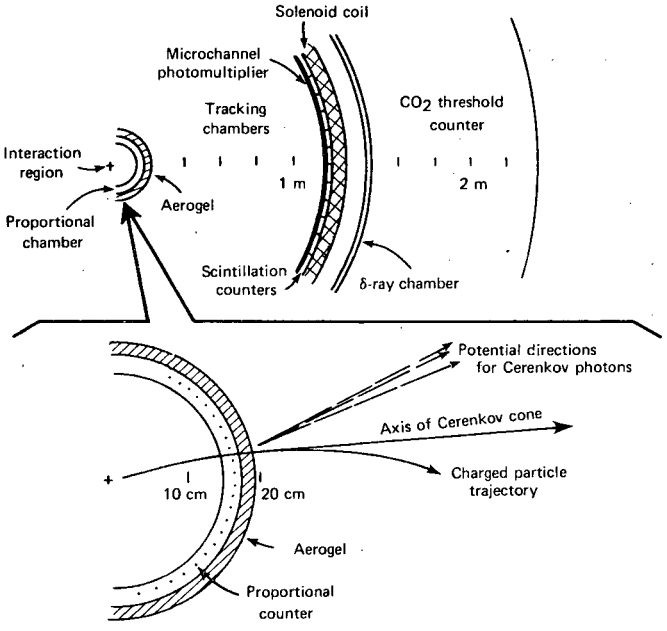

XBL 7512-9876

Fig. B-1. Schematic end view of possible future differential Čerenkov counter system using aerogel radiator and microchannel photomultiplier detectors with 1 cm^2 area covering 25 m^2.

REFERENCES

1. G. Buschhorn et al., PEP-146,86 (1974).

2. B. Richter, PEP-140,24 (1974).

3. G. Hanson, reported at 1975 SLAC Summer Institute in Particle Physics, and private communication.

4. G. Hanson and P. Oddone, private communication.

5. J. J. Aubert et al., Phys. Rev. Letters 33, 1404 (1974); J-M. Augustin et al., Phys. Rev. Letters 33, 1406 (1974).

6. SPEAR and DORIS contributions to 1975 Lepton/Photon Symposium at SLAC.

7. K. Halbach, private communication.

8. P.LeComte and V. Perez-Mendez, PEP-201, in this volume.

9. Similar to the "General User Magnet," PEP-188, in this volume.

10. The DASP TOF system achieved σ = 0.26 nsec resolution which, with a beam crossing time determined to 0.13 nsec rms as at PEP, would improve to 0.22 nsec.

11. M. Cantin et al., Nucl. Inst. and Meth. 118, 177 (1974).

12. CERN-Heidelberg $\Lambda\beta$ group, private communication.

13. The scintillation properties of pentane were not measured by the authors of Ref. 12.

14. We are indebted to R. C. Field for addressing our group on this subject.

15. These considerations imply larger light collectors than were used, for example, in the high pressure counters of Ref. 1.

16. M. A. Green, [LBL-3677 (1975)], and private communication.

17. Similar to the Fermilab External Muon Identifier. F. A. Harris et al., Nucl. Inst. and Meth. 103, 345 (1972).

18. D. Nygren, PEP-197, in this volume.

19. The 3 kGauss field would be too weak to provide significant transverse diffusion suppression of the type Nygren has measured. This may or may not be a problem depending on the information required from the chamber (tracking vs. momentum fitting) and the readout method used.

20. Katsura et al., Nucl. Inst. and Meth. 105, 245 (1972).

21. We are cautioned by discoveries of the radiative decays of $\psi'(3684)$ and $J(3095)$ against wholehearted embrace of this prejudice. It must be noted, however, that measurements of γ direction rather than energy were central to these discoveries.

22. F. Sciulli, rapporteur talk at Fermi Lab Calorimetry Workshop (1975).

23. PEP-188, in this volume.

24. These have all the properties of more expensive 5-in tubes with conventional photocathodes, except for a long risetime which is of no consequence here.

25. The inside window will be ribbed in order to minimize its unsupported length and thickness. Where possible, the ribs will be in the shadow of the coil lumps. The outside window is necessarily corrugated (Fig. 13), giving added strength.

0 0 0 0 4 5 0 1 6 3 2

USE OF MICROCHANNEL ELECTRON MULTIPLIERS IN HIGH ENERGY PHYSICS

P. Lecomte and V. Perez-Mendez

Lawrence Berkeley Laboratory

PROPERTIES OF THE MICROCHANNEL ELECTRON MULTIPLIERS

Microchannel plates were developed for military purposes, mainly for night vision applications, but some of their characteristics are of great interest in high energy physics. We will summarize briefly the properties of the available plates, bearing in mind that they are designed for image intensifiers and that they could be further optimized for our particular applications.

These plates can be presently obtained with useful diameter between 25 and 75 mm, channel diameters from 9 to 50 microns, and electron gain per plate around 10^3 to 10^4 (Fig. 1); the transit time of the electron is about one nanosecond, and the time spread is well below 100 ps. The plates are extremely compact and are not affected by magnetic fields, but are sensitive to heavy ions, low energy electrons, soft x-rays and UV light.

Gains in excess of 10^7, with noise of 3 counts/cm^2 sec are obtained when cascading two plates. A "chevron" arrangement is needed to reduce the positive ion feedback, which could damage the photocathode; spatial resolution is then divided by two. As an alternative, plates could be manufactured with twisted channels.

Photomultipliers incorporating these microchannel plates could be manufactured in various shapes; they should be extremely compact and, in the so-called Wafer design, where the photocathode is in close proximity to the microchannel plate, (extensively used in image intensifiers and in some microchannel photomultipliers, Fig. 2 and 3) they should exhibit good insensitivity to magnetic fields and extremely low time jitter for single electron response.

It should be noted that this type of tube is not well suited for energy measurements, the pulse height distribution of one plate being either exponential or saturated.

The imaging capabilities of these plates are also of great interest and several methods of electronic readout are presently developed, inspired by the techniques employed with proportional chambers.

SOME POSSIBLE APPLICATIONS

(a) To our knowledge, no other device can presently compete with microchannel photomultipliers for timing measurements at low light levels; this means in practice either improved momentum resolution or, and often more important, decrease of required flight distance, resulting in an increased solid angle.

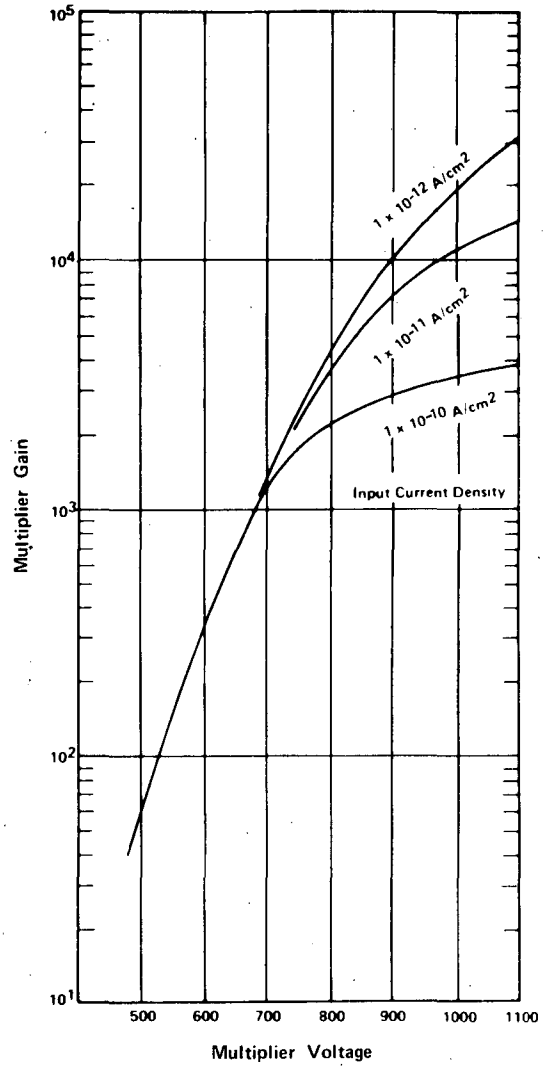

Typical Characteristics

L/d_c	=	42
d_c	=	14.5 μ
OAR	=	60 %
R	=	3 x 10^8 Ω

XBL 759-8332

Fig. 1

Scintillation counter hodoscopes using difference in transit time of light could be built with resolution of about one cm, even for low energy gamma rays; presently, this resolution can

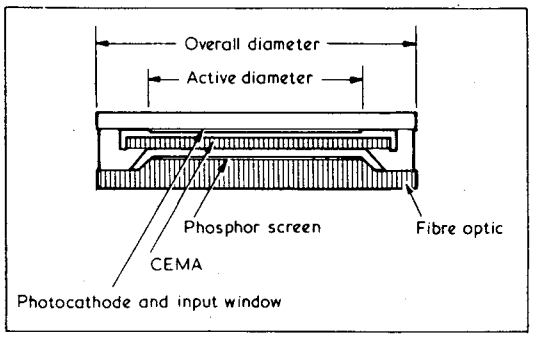

Cross-section of proximity-focused CEMA intensifier.

XBL 759-8333

Fig. 2

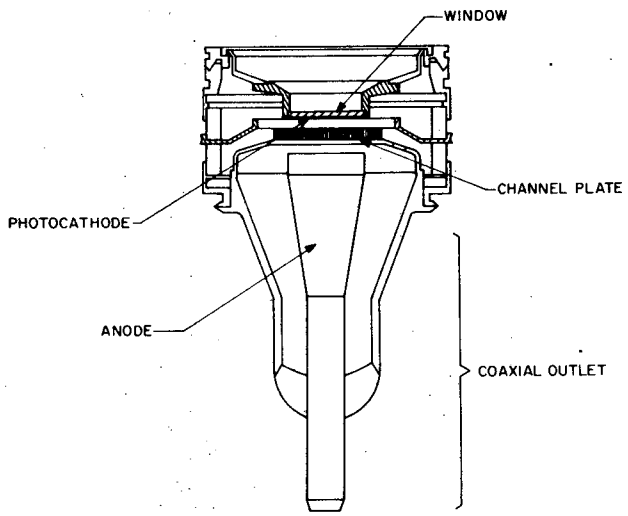

Channel photomultiplier with a coaxial output provides a short response time and a high output brightness.

XBL 759-8334

Fig. 3

be achieved only with energy losses of 10 to 30 MeV in the scintillator.

(b) Conventional photomultipliers could be replaced by microchannel plates as long as a good energy resolution is not required, where space is critical or where high magnetic fields are present.

(c) The imaging capabilities of the microchannel plates, even at ultra low light level and high speed, allow them to compete favorably with such devices as return beam Vidicon and image dissectors. They could be used for pattern recognition in Cerenkov counters, that is to record size and position of the ring of Cerenkov light for digitization of streamer chambers, for imaging of multicell liquid scintillators and, of course, without photocathode, for imaging with various types of particles and radiations.

CONCLUSIONS

From the preceding, it is apparent that microchannel photomultipliers and electronic imaging devices are of great interest in high energy physics.

Several manufacturers have the ability to produce such devices, but, in order to obtain products well adapted to our applications at a reasonable cost, we must define the exact specifications we require and convince the manufacturers that a satisfactory market exists.

Preliminary conversations show that, once this is done, prototypes could be obtained within some months.

REFERENCES

A good summary of the properties of microchannel plates can be found in "Microchannel Plate Imaging Detectors", by D.J. Ruggieri. IEEE transactions on Nuclear Science NS-19, No. 3 (1972).

Applications to image intensifiers are described in: "The Proximity Focused Image Intensifer", Bendix Technical Memorandum EOTH 7201 (1972).

Some other interesting papers are "High Gain Imaging Electron Multiplier", W.B. Colson, et al., Rev. Sci. Instr. 44, No. 12 (1973).

"Photomultipliers and the Transfer Technique", J. Nussli, Philips Technical Review 30, 236.

"The Channeltron Electron Multiplier Array and Its Applications to Low Level Detection Devices" First European Electro-Optics Markets and Technology Conference.

"Solving Intensifier Problems with Channel Plates", J. Adams, Electro-Optical Syst. Design, November 1969.

"Fast Timing Measurements using a Chevron Microchannel Plate Electron Multiplier", Mike I. Green et al. N.I.M. 126, 175 (1975).

0 0 0 0 4 5 0 1 6 3 3

PHOTON-PHOTON PHYSICS

G. Barbiellini, A. Benvenuti, K. Berkelman, A. Courau, F. Foster, K.-W. Lai, F. Lobkowicz, J. Matthews, N. Mistry, and T. Rhoades

". . . Further, when one considers the extreme speed with which light spreads on every side, and how, when it comes from different regions, even from those directly opposite, the rays transverse one another without hindrance, one may well understand that when we see a luminous object, it cannot be any transport of matter coming to us from this object . . ."

Christiaan Huygens[1]

I. INTRODUCTION

Experimental research with e^+e^- colliding beams has been centered on the study of the one-photon mechanism and

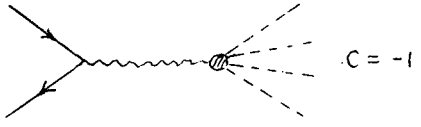

the production of C = -1 states. With the advent of high-energy high-luminosity facilities such as PEP it will also be possible to study the two-photon process and thereby

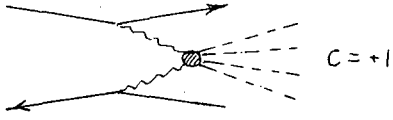

probe not only the realm of C = + 1 states[2], but also the inner structure of the photon itself.[3-5]

This is the report of a study which extends the work of the 1974 PEP study group[6] on two-photon processes, mainly by considering the experimental cuts in tagging measurements required to obtain high-quality data, the resulting effects on the tagging efficiency, the effects of transverse e^+ and e^- beam polarization, a possible design for a parasite tagging apparatus, and a suggestion for a prime photon-photon experiment. A systematic explanation of the kinematics and quantum electrodynamics of tagging, including polarization effects, is given in the appendix to this report.

In the two-photon process we are concerned with the reaction $e^+e^- \to e^+e^-$ + hadrons, which we view in terms of a head-on collision of two almost-real photons:

$$\left.\begin{aligned} e^+ &\to e^+\,\gamma \\ e^- &\to e^-\,\gamma \end{aligned}\right\} \gamma\gamma \to \text{hadrons}.$$

The process is identified by detecting in coincidence the outgoing e^+, e^-, and presumably at least one hadron. The e^+, e^- detection fixes the energies E'_1 and E'_2, polar angles θ_1 and θ_2, and azimuthal angles ϕ_1 and ϕ_2 of the outgoing

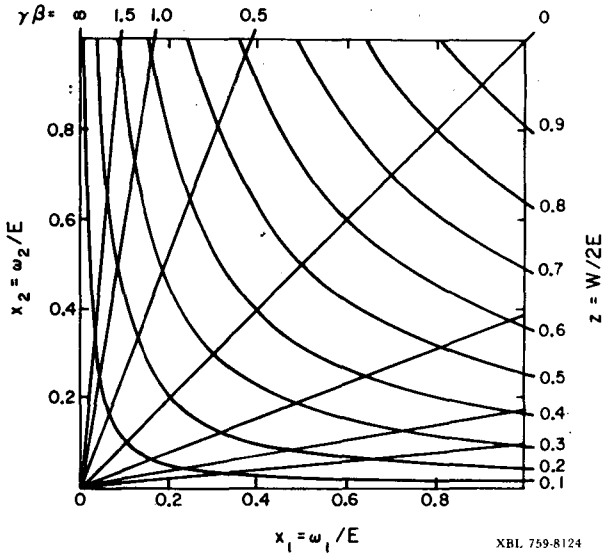

1. Tagging kinematics: the relations among the $\gamma\gamma$ center-of-mass energy, the center-of-mass motion, and the laboratory photon energies. Definitions and formulas are given in appendix I.

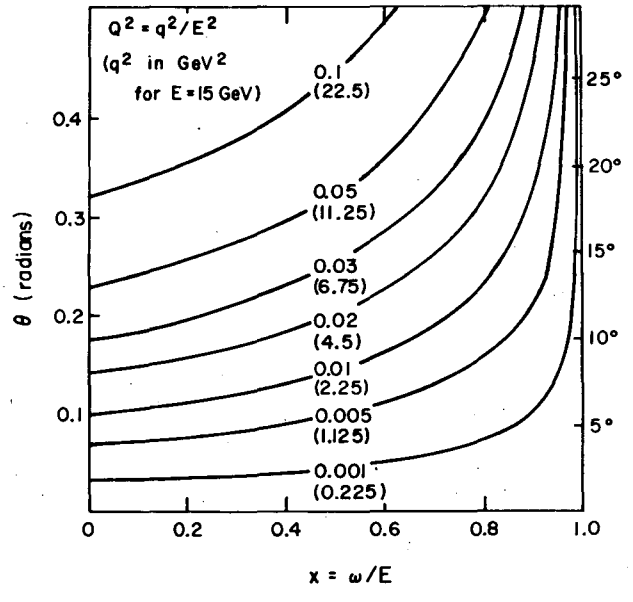

2. Deep inelastic kinematics: four momentum transfer as a function of tagging angle and photon energy. Definitions and formulas are given in appendix I.

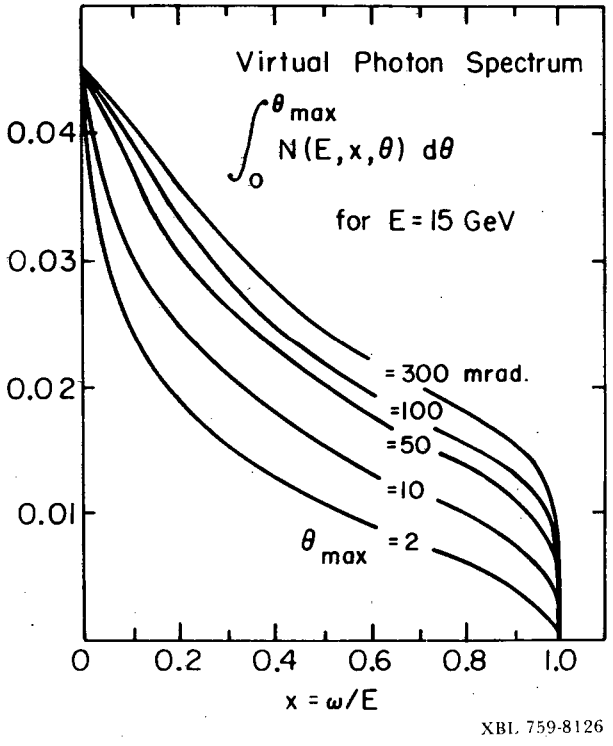

3. The virtual photon energy spectrum integrated over tagging angle from zero to θ_{max}, for various values of θ_{max}. Since the dependence on beam energy E is only logarithmic, these curves are approximately valid for a wide range of E. See appendix II for more details.

e^+e^-. These variables together with the incident e^+ or e^- energy E determine the energies ω_1 and ω_2, the four-momentum-squared q_1^2 and q_2^2, and the polarization of the tagged virtual photons. The laboratory photon energies ω_1 and ω_2 determine the $\gamma\gamma$ center-of-mass energy W and the lab velocity β of the center-of-mass. The relevant formulas are given in appendix I and plotted in Figs. 1 and 2.

II. TAGGING CUTS

A. Angles

The backgrounds expected to be important in the tagging system are discussed in detail in the 1974 PEP study report[7]. Any detector sensitive to electrons which have lost energy but are emitted at $\theta = 0^o$ will have 100% occupancy from beam-beam bremsstrahlung. Even at very low beam currents or at 100% beam duty cycle, the coincidence rate from the 0^o double bremsstrahlung[8] would completely dominate over the desired two-virtual-photon tagging rate. Fortunately, however, these and other backgrounds decrease much more rapidly with angle (typically θ^{-3}) than does the θ^{-1} distribution for virtual photon tagging (see appendix II).

Tagging at $\theta = 0^o$ is unnecessary. It is clear from Fig. 3 that as long as ω/E is not too small, the lost events with $\theta < 10$ mrad do not amount to a very large fraction of the total. This is about the minimum tagging angle that one can achieve without magnetic deflection, using detectors just outside the beam pipe (about 10 cm radius) 10 meters from the interaction point.

The counting rate for a tagging detector sensitive over the range $\theta_{min} < \theta < \theta_{max}$ is proportional to $\ln(\theta_{max}/\theta_{min})$ (appendix II). Since this decreases rather gradually with θ_{max}, it is difficult to decide on an upper limit. In practice, the decision will depend on the desire for deep inelastic data, economic considerations, and compatibility with other parts of the experiment. We will show (in section IV) that reasonable deep inelastic rates can be obtained out to about θ = 300 mrad.

B. Energies

There will be some minimum energy E'_{min} below which it will be impractical to tag the outgoing e^+ or e^-. It is difficult to distinguish electrons by shower detection below $E' \sim 100$ MeV; multiple scattering in the beam pipe can degrade the θ and E' resolution; and background electrons and photons from beam-gas collisions[7] will cause random coincidences if E'_{min} is too low. Since it is rather difficult to predict what E'_{min} will have to be, it is fortunate that the $\gamma\gamma$ luminosity is not very sensitive to ω_{max}. $d\mathcal{L}_{\gamma\gamma}/dW$ depends on ω_{max} only for the higher portion of the W range and then only through the $\ln(2\omega_{max}/E)$ factor (see A10, A12). For rate estimates we will therefore use $E'_{min} = 0$, $\omega_{max} = E$.

One will also have to set a maximum energy cut E'_{max}, either in the trigger electronics or in the data analysis. There are several reasons for this.

1) Elastic and radiative e^+e^- scattering gives a high rate at $E' \approx E$.[7] Although this reaction is distinguishable by having ω_1 and ω_2 both very small and collinear e^+e^- (or at least coplanar, if there is radiation before scattering), one may be able to exclude some accidental coincidences by rejecting high E' tags.

2) The effective photon spectrum $N(\omega/E, \theta_{min}, \theta_{max})$ goes to zero as $\omega/E \to 0$ (Fig. 4).

3) For the case $E'_1 \gg E'_2$ the resolution in W is given by

$$\frac{\delta W}{W} \approx \frac{1}{2}\frac{E'_1}{E - E'_1}\left(\frac{\delta E'_1}{E'_1}\right).$$

It diverges as $E'_1 \to E$.

4) For the case $E'_1 \gg E'_2$ the $\gamma\beta$ of the photon-photon center of mass relative to the lab is

$$\gamma\beta \approx \frac{E'_1}{2\sqrt{E(E - E'_1)}}$$

0 0 0 0 4 5 0 1 6 3 4

and diverges as $E'_1 \to E$. Note that $\gamma\beta = \cot\alpha$, where α is the laboratory angle of a relativistic particle emitted at 90^0 in the center of mass. If $\gamma\beta \gg 1$ the hadron angular distribution will be considerably distorted by the c.m. → lab transformation.

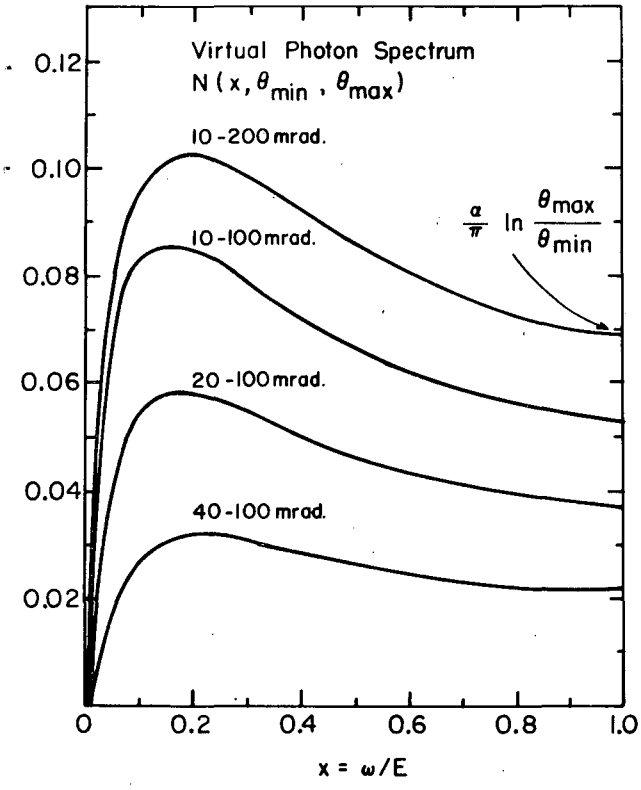

XBL 759-8127

4. The virtual photon energy spectrum integrated over tagging angle from θ_{min} to θ_{max}. See appendix II for details.

Taking all effects into account, it appears that E'_{max}/E = .80 to .95 is probably reasonable. For most of the rate estimates we will then use

$$\omega_{min}/E = .1.$$

C. Single Tagging

It is clear from Fig. 1 that if one could integrate over all angles θ_1 for one of the e^+ or e^- by not requiring its detection, one would gain in tagging efficiency, especially for low values of the corresponding photon energy ω_1. This would certainly increase $d\mathcal{L}_{\gamma\gamma}/dW$ at the lowest W. Such a tagging mode was recommended in the 1974 PEP study[6] for observing the one- and two-body final states in $\gamma\gamma$ collisions at W < 2 GeV. Another advantage of a single tagging system is that one has somewhat more freedom to place scrapers and shields in the unused end of the straight section to help in reducing backgrounds in the tagging.[9]

Although any double tagging system, such as we propose here, can in principle be used for single tagging, we doubt if this mode will be practicable. Without a two-fold tagging coincidence one will certainly be much more vulnerable to backgrounds from beam-gas processes, double bremsstrahlung, misidentified hadrons, and so on[7].

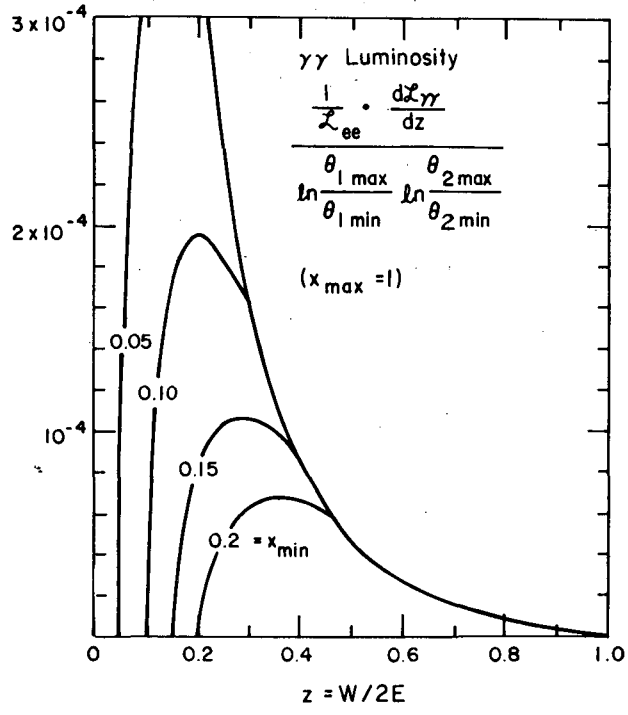

XBL 759-8128

5. The photon-photon luminosity (defined in appendix II) with the dependence on angle cuts divided out. The various curves correspond to different tagging energy cuts. The counting rate for ee → eeX in a bin of $\gamma\gamma$ energy from W to W + ΔW is obtained by multiplying the value from the curve by the ee luminosity (in $cm^{-2}sec^{-1}$), the angle cut factors $\ell n(\theta_{1max}/\theta_{1min})\ \ell n(\theta_{2max}/\theta_{2min})$, the normalized $\gamma\gamma$ energy bin width, $\Delta W/2E$, and the cross section $\sigma_{\gamma\gamma}$ for $\gamma\gamma \to X$.

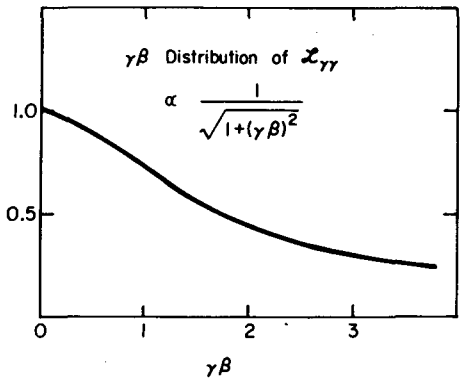

XBL 759-8129

6. The form of the distribution of $\gamma\gamma$ luminosity in the $\gamma\beta$ of the center-of-mass, at fixed c.m. energy W.

Furthermore, one photon has an unknown energy ω_1, and hence W and β are unknown except in rare cases where one can reconstruct the hadron final state and infer the mass and momentum of the missing virtual photon. The lower energy e^+e^- rings may be better suited to investigate the W < 2 GeV range.

III. PHOTON-PHOTON ENERGY RESOLUTION

A. Dependence on Tagging Resolution

Since the $\gamma\gamma$ center of mass energy is given by

$$W \approx 2\sqrt{(E-E_1')(E-E_2')},$$

the energy resolution δW is

$$\frac{\delta W}{W} = \sqrt{\left(\frac{1}{2}\frac{\delta E_1'}{E-E_1'}\right)^2 + \left(\frac{1}{2}\frac{\delta E_2'}{E-E_2'}\right)^2}.$$

Since any measurement at fixed W covers a range of ω_1 and ω_2 values (Fig. 1), the data will include events with a range of W resolution. It will be best for symmetric tags, $\omega_1 = \omega_2 = W/2$, and worst for the most asymmetric tags. In the latter case the contribution to δW from the highest E' will dominate.

$$\left(\frac{\delta W}{W}\right)_{best} = \frac{1}{\sqrt{2}}\frac{2E-W}{W}\frac{\delta E'}{E'}, \qquad (1)$$

$$\left(\frac{\delta W}{W}\right)_{worst} \approx \frac{1}{2}\frac{1-x_a}{x_a}\frac{\delta E'}{E'}, \qquad (2)$$

where $x_a = \max(\omega_{min}/E, W^2/4E\omega_{max})$ (see A10).

B. Intrinsic Limits on $\delta E'/E'$

The e^+ or e^- energy detected in any electromagnetic reaction will always be degraded somewhat because of radiation of an extra photon or photons in the reaction itself or later in the material through which the e^+ or e^- passes on its way to the detector. If P(k)dk is the probability of an energy loss between k and k+dk we have for the integral[10]

$$\int_0^{\Delta E'} P(k)dk \approx 1 - \left[\frac{2\alpha}{\pi}\left(\ln\frac{q^2}{m^2} - 1\right) + t\right]\ln\frac{E_o'}{\Delta E'},$$

where q^2 is the four-momentum-transfer-squared in the reaction and t is the number of radiation lengths (assumed << 1) of intervening material. E_0' is the e^+ or e^- final energy in the absence of extra radiation. P(k) itself has the typical k^{-1} behavior as shown in the sketch.

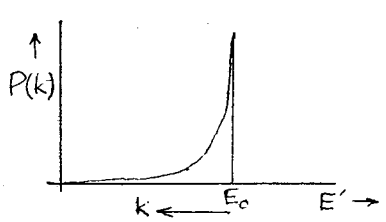

The $\Delta E'/E_0'$ within which we have 50% of the area under the peak is

$$\frac{\Delta E'}{E'} = \exp\left\{-\frac{1}{2}\left[\frac{2\alpha}{\pi}\left(\ln\frac{q^2}{m^2} - 1\right) + t\right]^{-1}\right\}.$$

The "equivalent radiation length" of the reaction,

$$\frac{2\alpha}{\pi}\left(\ln\frac{q^2}{m^2} - 1\right),$$

varies from .055 to .076 for q^2= .1 to 10 GeV^2. This would imply (for t=0) a $\Delta E'/E'$ between .01% and .14%, a completely negligible contribution to the experimental energy resolution.

The statement was made in the 1974 PEP Study[11] that "The inherent resolution of the tag is limited by . . . radiative effects (1-3%)". This we believe is misleading. The question is how one characterizes the resolution of such a pathological function (see sketch). Although the average $\Delta E'$ is several percent (because of the long tail), most of the energy losses are less than a small fraction of a percent. We believe that when looking for resonances and other structure in energy, the latter criterion is more relevant. The long tail contributes to the background but does not affect the "resolution". If this were not true, the masses of the ψ and ψ' would not have been measured so precisely. The important inherent limit is probably the spread in initial e^+e^- energy $\delta E/E$, just as in the case of the ψ and ψ'. This will be about .5% r.m.s.

It should be noted that radiation in the beam pipe, etc. will affect the resolution only if the energy is measured by magnetic deflection.

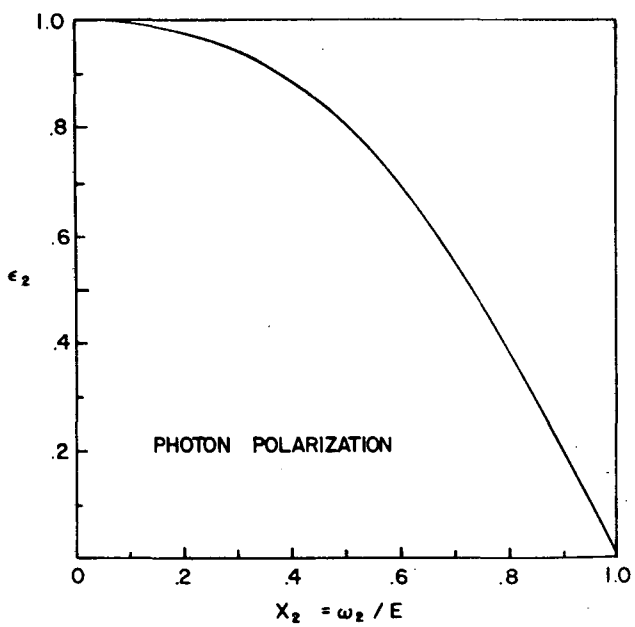

XBL 759-8130

7. Approximate dependence of the virtual photon polarization (see appendix IV) on photon energy.

0 0 0 0 4 5 0 1 6 3 5

Otherwise, the radiation will contribute to the electron shower and no energy will actually be lost. The energy scale of a shower detector will be self-calibrating because of the Bhabha scattering events.

IV. SOME POSSIBLE EXPERIMENTS

A. 3 to 20 GeV Survey

Suppose we assume the following conservative cuts in tagging angles and energies,

$$10 \text{ mrad} < \theta_1, \theta_2 < 300 \text{ mrad},$$

$$.1E < \omega_1, \omega_2 < E,$$

and take E = 15 GeV and $\sigma_{\gamma\gamma}$ = .3 μb (actually, it probably will decrease with energy[2] like $\sigma_{\gamma\gamma}(W)$= .24 μb + (.27 μb-GeV)/W.). We can then derive from (A1) and Fig. 5 the expected number of counts for an experiment in which $\int \mathcal{L}_{ee} dt = 10^{38} \text{cm}^{-2}$ (see Fig. 8). Assuming an average $\mathcal{L}_{ee} = \frac{1}{4} 10^{32} \text{cm}^{-2}\text{sec}^{-1}$, such an experiment would take 46 days. The integrated number of counts over the whole W range is 2 x 10^4. This should be compared with 5 x 10^4, the expected number of ee→hadrons events, assuming R = 6.

Fig. 8 also shows the maximum value of γβ for the motion of the two-photon center of mass (see also Fig. 1). The angular distribution of hadrons in the center of mass will presumably be similar to that observed in hadron-hadron collisions. We can probably expect the charged hadron multiplicity in the final state to increase logarithmically from $\bar{n} \approx 2.8$ at W= 4 GeV to $\bar{n} \approx 5.4$ at W= 15 GeV. Measurements of inclusive distributions rather than exclusive final states will be of increasing importance at the higher W. Such distributions may be characterized by the usual variables, $P_\perp$ and $X_F = P^*_{\parallel} / P^*_{max}$ (* denotes center of mass). Assuming that the two photons are almost real, the physics devides roughly into two regions:

1) Central region $|X_F| < .1$

2) Photon fragmentation region $|X_F| > .1$

If one of the photons has $q^2 >> 1$ GeV^2, there may be a third region, the so-called parton fragmentation region. Under the assumption that the X_F distribution is flat in rapidity, we would expect similar total rates in the two regions. Figs. 9 and 10 show the relation between laboratory angles and X_F, $P_\perp$ for two choices of W, γβ: a "worst" case in Fig. 9 and a more typical situation in Fig. 10. The central region of X_F corresponds to $\theta > 30^0$ except at the lowest $P_\perp$. Furthermore, the fragmentation region for the "slow" photon

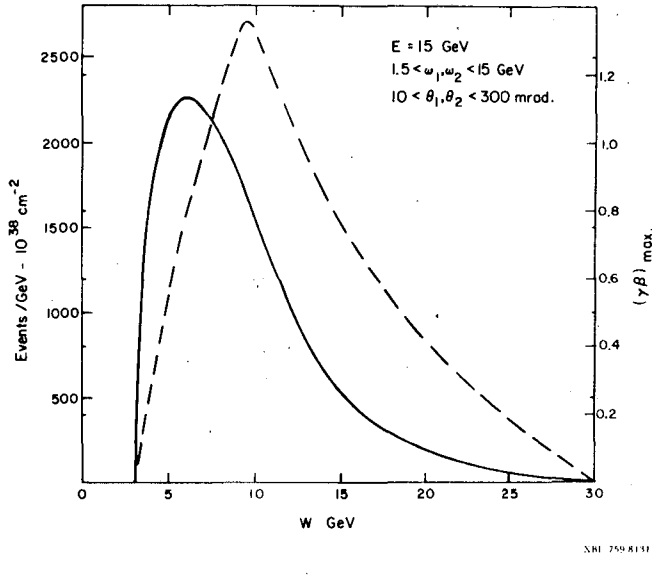

8. Estimated number of events per GeV interval in W for an experiment with E= 15 GeV, $.1E < \omega_1, \omega_2 < E$, $10 < \theta_1, \theta_2 < 300$ mrad, and $\int \mathcal{L}_{ee} dt = 10^{38} \text{cm}^{-2}\text{sec}^{-1}$. The dashed curve shows the maximum γβ of the center-of-mass motion for the same experiment. See section IV-A for details.

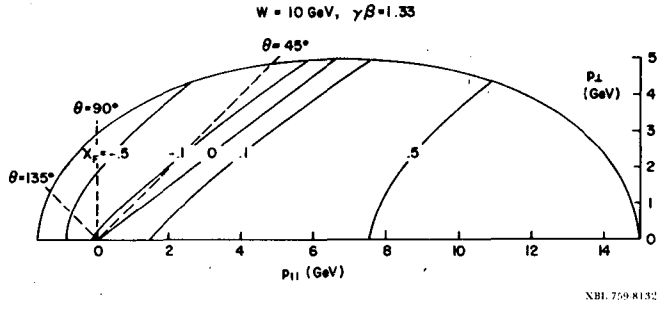

9. Laboratory-frame Peyrou plot for γγ collisions with W = 10 GeV, γβ = 1.33. Curves of fixed center-of-mass fractional longitudinal momentum $x_F = p_{\parallel}^*/p_{max}$ are indicated. This represents a worst case in terms of distortion of the angular distribution by center-of-mass motion, for the experiment described in section IV-A.

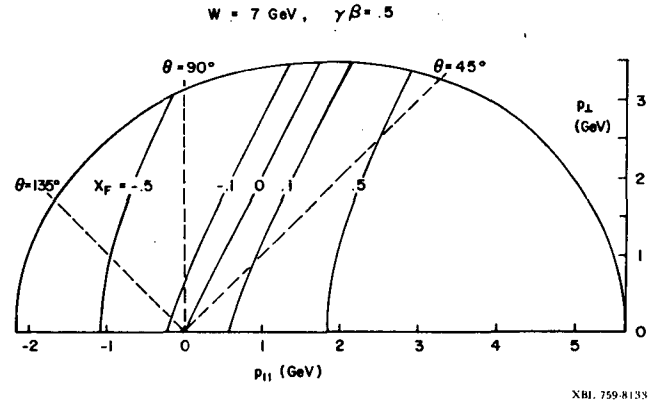

10. Laboratory-frame Peyrou plot for γγ collisions with W = 7 GeV, γβ= .5. Curves of fixed x_F are indicated. This is a rather typical situation in the experiment described in section IV-A.

(i.e., $X_F < 0$) also corresponds to large lab angles. By symmetry the inclusive distributions cannot depend on the sign of X_F, so that one would not lose any inclusive information by ignoring the more difficult to detect fast photon fragments. Note that the interesting high $P_\perp$ events, where kinematically allowed, always appear at large angles.

The resolution δW will be no worse than .4 GeV multiplied by the percent tagging resolution $\delta E'/E'$ (see Fig. 11). This is certainly appropriate for a survey experiment in which the data might be grouped in ΔW = 1 GeV bins.

The above facts imply that such an experiment is quite appropriate for running as a parasite with a single-photon experiment using a "conventional" detector with an added tagging system which is interrogated every time a hadron trigger occurs. Whatever the host experiment is doing (σ_{tot}, inclusive spectra, jets, correlations, high $P_\perp$, neutrals, etc.) the $\gamma\gamma$ experiment will also do -- with comparable statistics, but with a distribution of energies W. The parasite experiment also measures the $\gamma\gamma$ contamination in the host experiment, of course.

It is also clear from the $\gamma\beta$ curve in Fig. 6 and from Figs. 9 and 10 that for an experiment in which one wishes to see several or all of the final state hadrons one would prefer to have an angular acceptance for hadrons which extends to much smaller angles (say $\sim 5^0$) than is customary for a detector designed for single-γ experiments.

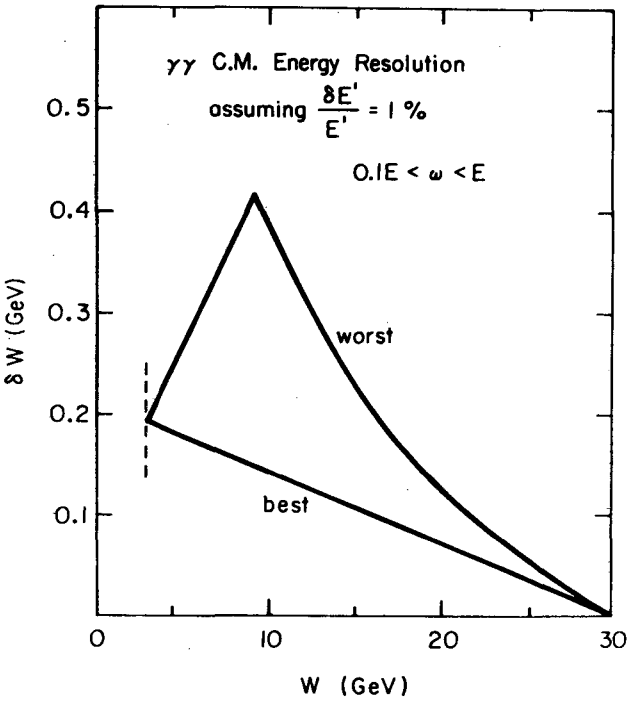

XBL 759-8134

11. The resolution in the $\gamma\gamma$ center-of-mass energy for the experiment described in section IV-A implied by 1% resolution in the tagged e^+ and e^- energies.

A simpler argument leading to the same conclusion is made by noting that a "typical" hadron is emitted at a center-of-mass angle given by

$$\begin{aligned}\langle\theta\rangle &= \sin^{-1}(\langle P_\perp\rangle / \langle P\rangle) \\ &= \sin^{-1}(\langle P_\perp\rangle \bar{n}/W) \\ &= \sin^{-1}(.3\ \text{GeV} \times 10/10\ \text{GeV}) \\ &= 17^0.\end{aligned}$$

B. Resonance Hunting

Since the 1974 PEP study we have come to suspect the existence of many resonances in the energy range 2 GeV < W = 5 GeV. Some should have C= +1, accessible only in $\gamma\gamma$ process. (or through decay of higher 1^- resonances). We list here a number of known and suggested C= +1 (and $J \neq 1$) particles and their properties.

NAME	M(GeV)	J^P	$\Gamma_{\gamma\gamma}$(keV)	Γ_{tot}(MeV)	decay
π^o	.135	0^-	.0078	$7.8\text{-}10^{-6}$	$\gamma\gamma$
η	.550	0^-	.30	.001	$\gamma\gamma$, $\pi\pi\pi$
ε	.7	0^+	1.3?[12]	600	$\pi\pi$
η'	.958	0^-	4.5? (SU3)	.023	$\gamma\pi\pi$,$\rho\gamma$
f^o	1.27	2^+	6?[12]	170	$\pi\pi$
A_2^o	1.31	2^+	?	100	$\rho\pi$, $\eta\pi$
A_3^o	1.64	2^-	?	300	$f\pi$
η_c	3?	0^-	13?[13]	6.5[14]	$\gamma\gamma$. . .

The energy-integrated production cross section for any such resonance is[12,15]

$$\int \sigma_{\gamma\gamma}\, dW = \frac{4\pi^2}{M^2}(2J+1)\,\Gamma_{\gamma\gamma}. \qquad (3)$$

The observable peak resonance cross section is

$$\sigma_{pk} = \begin{cases} \dfrac{8\pi}{M^2}(2J+1)\dfrac{\Gamma_{\gamma\gamma}}{\Gamma_{tot}} & (4) \\ \text{if } \Gamma_{tot} \gtrsim \delta W, & \\ \dfrac{(2\pi)^{3/2}}{M^2}(2J+1)\dfrac{\Gamma_{\gamma\gamma}}{\delta W} & (5) \end{cases}$$

where δW is the r.m.s. resolution in W.

Could we find the η_c resonance in a $\gamma\gamma$ experiment at PEP? With the conservative tagging cuts and ring energy E assumed in the previous section, the $\gamma\gamma$ luminosity (Figs. 5 and 8) goes to zero at W= 3. We consider three alternatives: (a) reducing the ω_{min} cut to .05E, (b) setting ω_{min}=.025E, (c) reducing the ring energy E to 7.5 GeV (leaving ω_{min} =.1E). The θ range is assumed to be 10 to 300 mrad.

Do we have enough rate? For an experiment of $\int \mathcal{L}_{ee}dt = 10^{38}\text{cm}^{-2}$ the total number of tag coincidences from η_c production will be

$$n = (10^{38}\text{cm}^{-2})\frac{1}{\mathcal{L}_{ee}}\left(\frac{d\mathcal{L}_{\gamma\gamma}}{dz}\right)_{z=M/2E}\frac{1}{2E}\int \sigma_{\gamma\gamma\to\eta_c}\, dW\,,$$

0 0 0 0 4 5 0 1 6 3 6

where $\int \sigma_{\gamma\gamma\to\eta_c} dW = 22$ nb-GeV from (3).

a) $\frac{1}{\mathcal{L}_{ee}} \frac{d\mathcal{L}_{\gamma\gamma}}{dz} \approx 23\times10^{-4}$ from (A9)

$\therefore n \approx 170$ counts.

b) $\frac{1}{\mathcal{L}_{ee}} \frac{d\mathcal{L}_{\gamma\gamma}}{dz} \approx 40\times10^{-4}$

$\therefore n \approx 300$ counts.

c) $\frac{1}{\mathcal{L}_{ee}} \frac{d\mathcal{L}_{\gamma\gamma}}{dz} \approx 23\times10^{-4}$

$\therefore n \approx 340$ counts.
(this should be reduced a factor of 4, since $\mathcal{L}_{ee}$ is proportional to E^2, in order to complete the experiment in the same time.)
$\therefore n \approx 85$ counts

These rates are rather low but not impossibly low.

What about resolution? Suppose we assume that the non-resonant background cross section $\sigma_{nr} = .3$ μb². In order to get $\sigma_{pk} = \sigma_{nr}$ for the η_c, we can compute the required resolution from (5):

$$\delta W_{req} = 30 \text{ MeV (r.m.s.)}.$$

The expected average tagging resolution can be estimated by averaging equations (1) and (2) and assuming optimistically that $\delta E'/E' = 1\%$:

a) $\delta W = 240$ MeV
b) $\delta W = 390$ MeV
c) $\delta W = 110$ MeV

In all of these examples the expected energy resolution is insufficient to see the η_c with the assumed properties at a signal/background of better than one. There are several ways out.

1) Run the experiment at a much lower energy E or at a lower energy machine. But although the resolution will improve, the expected number of counts will be lower, taking into account $\mathcal{L}_{ee} \propto E^2$ expected for PEP and the lower $\mathcal{L}_{ee}$ of other machines.

2) Reconstruct the resonance mass from the detected decay products instead of from the tagged e^+ and e^- energies. This will not be easy. Many events will have high γβ values (see Fig. 1), implying small lab angles; and 0^- resonances usually have large branching ratios into neutral modes. The requirement that the final state be reconstructable will certainly reduce the number of useful counts.

3) Use single tagging. This improves the rate but since the energy of one of the initial photons is unknown, one still has to reconstruct the resonance mass from the decay products. The backgrounds will be worse, since a single tag is not enough to guarantee that it is a two-gamma event.

4) Give up on low-energy resonances and make the search at higher masses where the resolution (Fig. 11) is much better. Here again, the rate will be lower unless $\Gamma_{\gamma\gamma}$ increases sufficiently to offset the M^{-2} in the cross-section (equation 3) and the W^{-1} in the luminosity (Fig. 5).

In conclusion, resonance hunting is difficult or even impossible unless the expected $\Gamma_{\gamma\gamma}$ is much larger than the 13 keV predicted for the η_c.

C. Deep Inelastic Electron-Photon Scattering

One can divide the γγ physics program into three areas according to the characteristics of the virtual photons: both photons almost real (already discussed), one almost real photon and one far off the mass shell, and both photons far off the mass shell. This division is in increasing order of experimental difficulty, since the γγ luminosity contains a factor q^{-2} for each photon (equation A14).

The second area of research may be the most exciting, since it allows us to probe the inner structure of the photon itself[3-5]. The idea is to use the flux of almost real photons emitted by one of the beams as a target for large-angle scattering by the other. The reaction studied is then

$$e^+ + \gamma \to e^\pm + \text{hadrons};$$

and the cross section is given in (A18) in terms of photon structure functions.

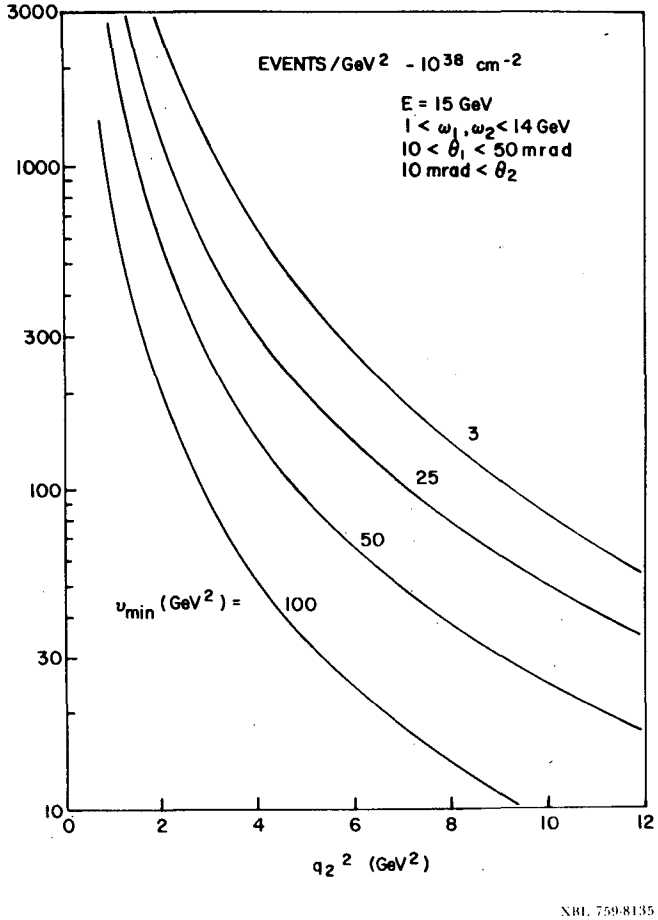

XBL 759-8135

12. The number of deep inelastic events per GeV² interval in q_2^2 for the experiment described in section IV-C, assuming various values for the minimum ν.

In order to estimate counting rates for a deep inelastic scattering experiment, we assume E= 15 GeV, we assume that the "target" photon is tagged with $1 < E_1' < 14$ GeV and $10 < \theta_1 < 50$ mrad, we assume that the "deep" spacelike photon is tagged with $1 < E_2' < 14$ GeV and with θ_2 fixed by q_2^2 (although always $\theta_2 > 10$ mrad), and we take a naive guess at the values of the structure functions (appendix V). The predictions are then plotted in Fig. 12 as a function of q_2^2 and ν_{min}. The event rate per GeV^2 shows several thousand events at reasonable q_2^2, ν values for a typical experiment of $\int \mathcal{L}_{ee} dt = 10^{38} cm^{-2}$. For $\nu_{min} = 3$ GeV^2 studies should be possible out to $q_2^2 = 10$ GeV^2. Fig. 13 shows the differential scattering cross section for various values of θ_2. The bulk of the events are predicted to occur for $70 < \theta_2 < 400$ mrad.

There are three structure functions that can be measured in an experiment in which the photons can be transversely and longitudinally polarized. In order to discuss the possibility of separately measuring the three functions, we use the equivalent form[5] of the cross section in terms of $\sigma_{\gamma\gamma}$ (A17):

$$\sigma_{\gamma\gamma} = \sigma_T + \varepsilon_2 \sigma_L + \varepsilon' \varepsilon_2' \sigma_A \cos 2\phi.$$

The σ_T, σ_L, σ_A, which are functions of q_2^2 and W (or ν), are given (A19) in terms of the structure functions W_1^γ, W_2^γ, W_3^γ. The transverse polarization asymmetry σ_A is separated by noting the dependence of the counting rate on the angle ϕ between the two photon polarization planes (appendix IV).

To separate the transverse σ_T and the longitudinal σ_L we must measure $\sigma_{\gamma\gamma}$ twice at the same q_2^2 and W but with different values of ε_2. This is actually nowhere near as difficult as it is in electron-nucleon scattering. The longitudinal polarization ε_2 is mainly a function of just ω_2/E (appendix IV), and counting rates are not overly sensitive to it. Consider the following pair of measurements at E= 15 GeV, W= 15 GeV, $q_2^2 = 6.6$ GeV^2, $q_1^2 \approx 0$, for example.

1) $\omega_1 = 14$, $\omega_2 = 4$ GeV, $\theta_2 = 200$ mrad
   $\varepsilon_2 = .916$
2) $\omega_1 = 5.6$, $\omega_2 = 10$ GeV, $\theta_2 = 300$ mrad
   $\varepsilon_2 = .394$

The counting rates are essentially in inverse ratio of the angles θ_2 and are therefore not very different. In this example, using the ϕ-averaged measurements $\sigma(1)$, $\sigma(2)$ we have

$$\sigma_L = \frac{\sigma(1) - \sigma(2)}{.916 - .394},$$

$$\sigma_T = \frac{.916\sigma(1) - .394\sigma(2)}{.916 - .394}.$$

In practice one will make the separation by fitting all the data at a fixed q_2^2 and W. Since the center-of-mass motion also changes when one varies ε_2 at fixed q_2^2 and W, it is important to insure that hadron detection biases do not distort the comparison of rates.

Finally, the $\gamma\gamma$ processes with both photons quite far off the mass-shell are of great theoretical interest[4] and can provide critical tests of the scaling and short distance behavior predicted by quark-parton and light-cone models. Although the $\gamma\gamma$ luminosity for such events is low, it should be possible to start studying them at PEP.

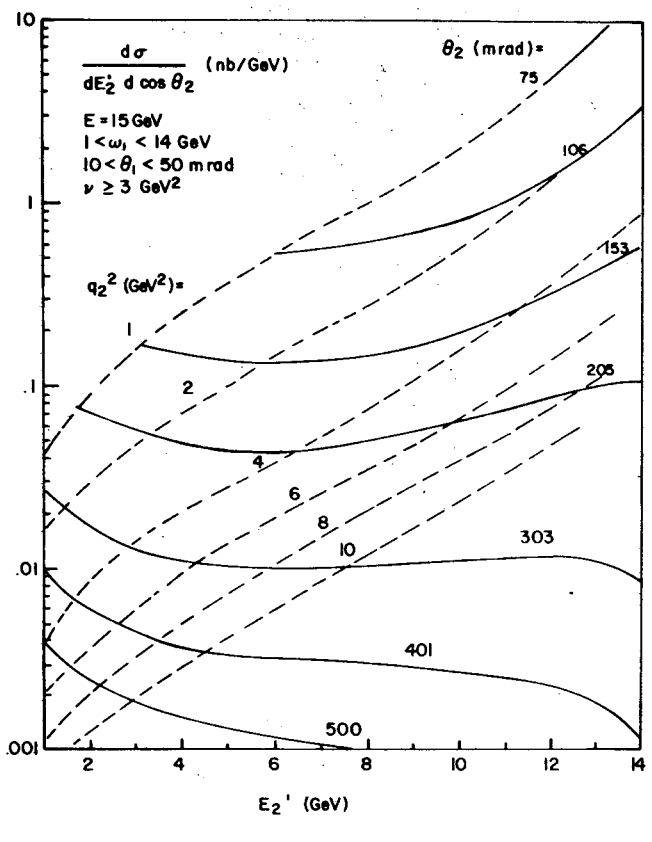

13. The deep inelastic cross section for e+γ→e+ anything as a function of the outgoing electron energy and angle. Lines of constant q^2 are also indicated.

V. PARASITE TAGGING SYSTEM

A. Requirements

Every PEP experiment should have a two-photon tagging system, such as the one we describe here. For the host experiment the tagging provides not only the obvious physics bonus -- a comparable number of events of a new and fascinating process -- but also serves to monitor the $\gamma\gamma$ background.

A general-purpose double tagging system should have the following characteristics:

1) detection of electrons with energies between about 1 and 14 GeV and at angles between about 10 and 300 mrad,
2) energy resolution of the order of .3 GeV r.m.s. or better (if one wishes to hunt for C= +1 resonances, the resolution should be as good as the ultimate machine

0 0 J 0 4 5 0 1 6 3 7

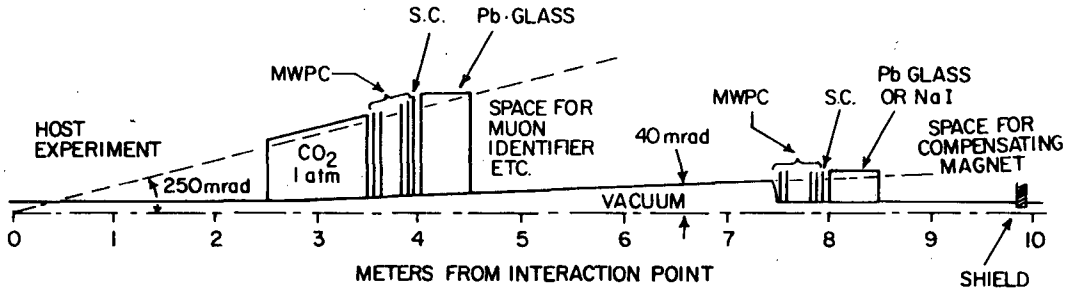

XBL 759-8137

14. One quadrant view of the proposed parasite tagging system described in section V. It is symmetrically arranged on both sides of the interaction point and around the beam line.

energy accuracy (∿.08 GeV), at least for tagging at small angles),

3) angular resolution of the order of 2% r.m.s. or better,
4) shields and scrapers to minimize backgrounds from beam-gas collisions and synchrotron radiation,
5) low cost, if possible.

An apparatus meeting these requirements is shown in Fig. 14. The detector on each side of the interaction region consists of two parts, dividing the angular range at 40 mrad.

B. Small-Angle Tagger (10-40 mrad)

The resolution requirements can be met by using lead-glass (or sodium iodide if one needs the ultimate resolution)[17]. A total frontal area of 1 m^2 and a thickness of 14 radiation lengths will be sufficient to cover the angular range on both sides of the interaction region. The angular resolution can be accomplished with multiwire proportional chambers with 2 mm wire spacing. It may be advisable to include a layer of scintillation counters to improve timing resolution to suppress backgrounds. Ideally the detector should be placed close to the first quadrupole magnet Q3, 9.5 m from the interaction point, however compensating magnets may have to be installed, so that 8 m may be more likely. The actual θ_{min} will be determined by this distance as well as by the minimum clearance between beam and counters that can be tolerated by the beam and by the counters. The double tagging rate varies as $\ln^2(\theta_{max}/\theta_{min})$.

Since these detectors will be located very close to the beam line, they will be especially vulnerable to backgrounds from beam-gas collisions and synchrotron radiation getting past the scrapers at the far end of the straight section and scattered from the scrapers at the near end. Some lead shielding will certainly have to be placed between the detectors and the beam pipe. As soon as possible, tests of these backgrounds should be made to optimize the placement of detectors, shields, scrapers, etc.

The small-angle tagging system is essentially the same as that proposed in the 1974 PEP study[16].

C. Large-Angle Tagger (40-300 mrad)

Here again we use lead-glass for energy resolution, proportional chambers for angular resolution, and scintillators for timing. To minimize the area, the distance to the interaction point is made as small as the detector of the host experiment will allow. This distance and the size of the open cone in the host experiment determine the actual upper limit of the acceptable angular range. The lead glass covers a total area of about 7 m^2, 14 radiation lengths deep, for both sides of the interaction point. Since that is a considerable amount of lead glass (and proportional chamber area), one may not wish to equip every interaction region with such a large detector. A smaller θ_{max} may be sufficient for many experiments. At the larger angles one can also group chamber wires and still have the required resolution.

An atmospheric pressure CO_2 Cerenkov counter is included to give pion rejection.

D. Constraints on the Host Experiment

1) The central detector must have an open cone of at least 10^o half angle in both beam directions, corresponding to the tagging aperture. A solenoidal field in this region does not significantly perturb the tagged e^+ and e^- trajectories; the effect can be taken into account in the analysis.

2) Compensating magnets, if required, must be placed beyond the tagging counters at the extreme ends of the 20 m straight section. The maximum field B in a solenoid compensator, and therefore the minimum length ℓ is limited by the following rule[17], which insures that $\Delta\nu$ remains less than .02 per compensator:

$$\frac{(B_{kG}\,\ell_m)\,B_{kG}\,\beta_m}{p^2_{kG\text{-}m}} \leq 1.2 \ ,$$

where $B\ell$ for the compensator is $\frac{1}{2}$ $B\ell$ for the central solenoid, say $\frac{1}{2}$ x 40 kG-m for the General User Magnet; β= 500 m; and $p_{kG\text{-}m} = p_{beam}/.03$ = 500 kG-m at 15 GeV. This implies $B \leq$ 30kG, which

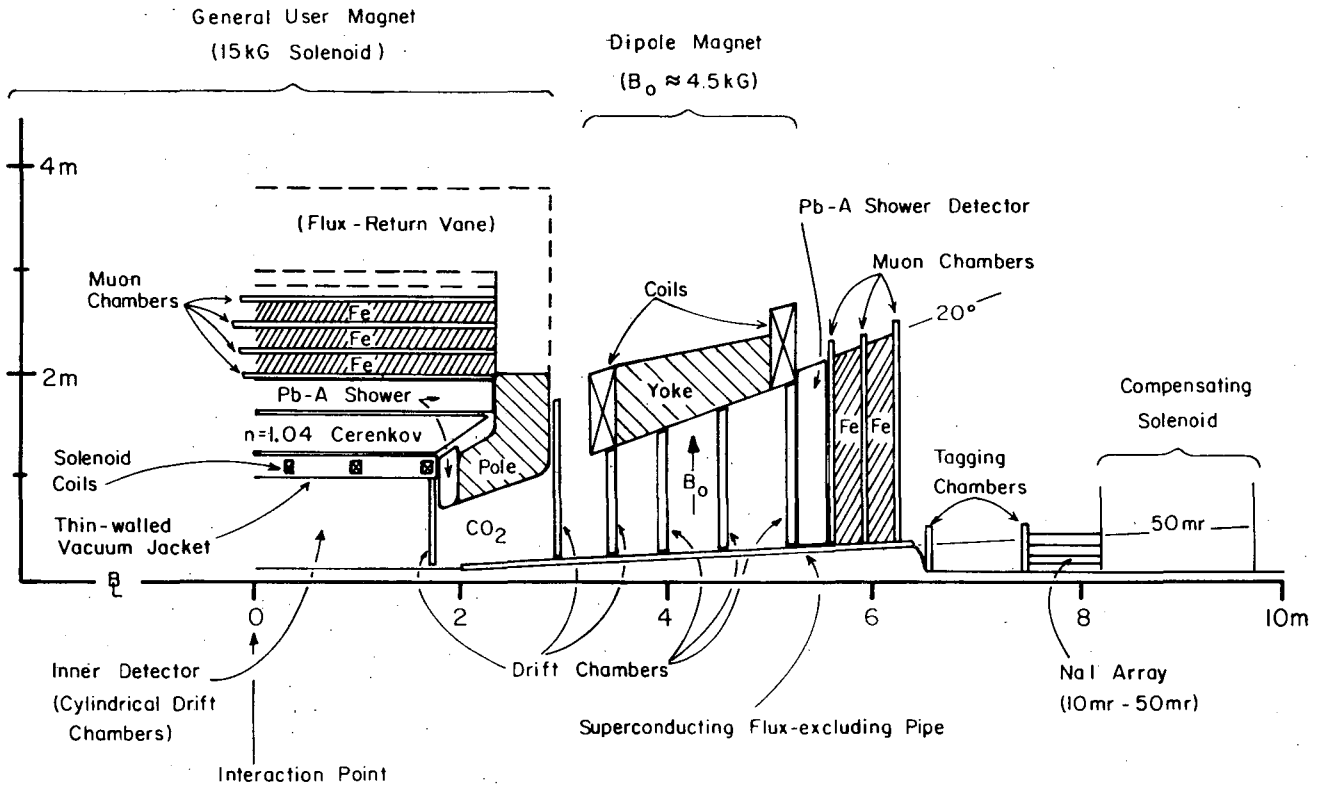

XBL 758-8123

15. One quadrant view of the prime photon-photon experiment described in section VI. It is symmetrically placed on both sides of the interaction point and around the beam line.

means that the field of the compensator can be 20 kG and its length one meter. The limitation becomes more serious at lower beam energies. If the compensator is only one meter long, one will have to lower all the solenoid fields for beam energies below 12.2 GeV.

VI. PRIME PHOTON EXPERIMENT

We describe here a detector system designed specifically for two-photon processes, to be run as an independent experiment. The system is identical in the electron and positron beam directions, and symmetric around the beam axis. Only one quadrant is shown in Fig. 15.

A. Tagging Systems

Two tagging systems are provided. A small-angle tagging system, in the angular range about 12mr to 50mr, utilizes an array of NaI crystals arranged around the beam pipe. The front face of the NaI array is 7.5m from the interaction point. It is assumed that 1.5m - long compensating solenoids will be installed at the ends of the interaction region as close to the quadrupoles (Q3) as possible. The beam pipe in this region has an outer radius of 8cm. with a sheet of lead around it to shield the NaI from soft X-rays. Two sets of drift chambers spaced one meter apart provide trajectory information for the scattered electrons. Scintillation counters with good timing resolution distinguish electrons from photons and suppress background due to scattered electrons travelling in the wrong direction. The energy resolution of the NaI detector is assumed to be $\delta E/E = 0.02/E'/4$ (FWHM).[17] The resulting resolution in W can be obtained from Section III.

The large-angle tagging system spans the range about 75mr to 350mr. This angular range is covered by the "forward" detectors consisting of large dipole magnets straddling the beam-pipe, with "flux-excluding" pipes to shield the circulating beams. The wall thickness of such a superconducting pipe, including coil, coolant, insulation, and vacuum vessel, is expected to be about 4 cm.[19] A 30W He-refrigerator would be required for the two sections. The large dipole magnets, of aperture 3m x 3m, are suitable for use at 90° with the General User Magnet as high momentum analyzers.

The forward detectors also serve to detect and identify hadrons produced at small angles to the beam direction. Sets of drift chambers (transverse to the beam axis) provide trajectory information with high resolution (0.2mm). The momentum resolution in this angular range is chosen to match the momentum resolution in the central solenoid detector for tracks at about 30° to the beam axis. With a dipole field integral of 10 k Gauss-meters, and trajectory information from a lever-arm equal to the length of the magnet (L=1.5m) as well as within the magnet, the resolution is expected to be $\delta p/p^2 \sim 0.3\%(\text{GeV/c})^{-1}$. The material in the inner detector before the forward trajectory chambers is restricted to about 0.02Xo. Note that a special beam-pipe with "saw-tooth"

0 0 0 0 4 5 0 1 6 3 8

corrugations should be installed for a length of about 1.4m to provide minimum material in the path of electrons of 75mr < θ < 350mr.

B. Central Detector

The proposed General User Magnet (PEP - 1975, elsewhere in this Report) is particularly suited for use as the central detector for a 2γ-experiment. Its large aspect ratio (L/R = 4m/1m) allows good acceptance and resolution for forward - going hadron states which are produced in asymmetric 2γ collisions. The iron end - plate is specifically designed with an open cone up to $\theta = 20^0$ (350mr) to allow tagging and detection of very forward - going hadrons. The solenoid is

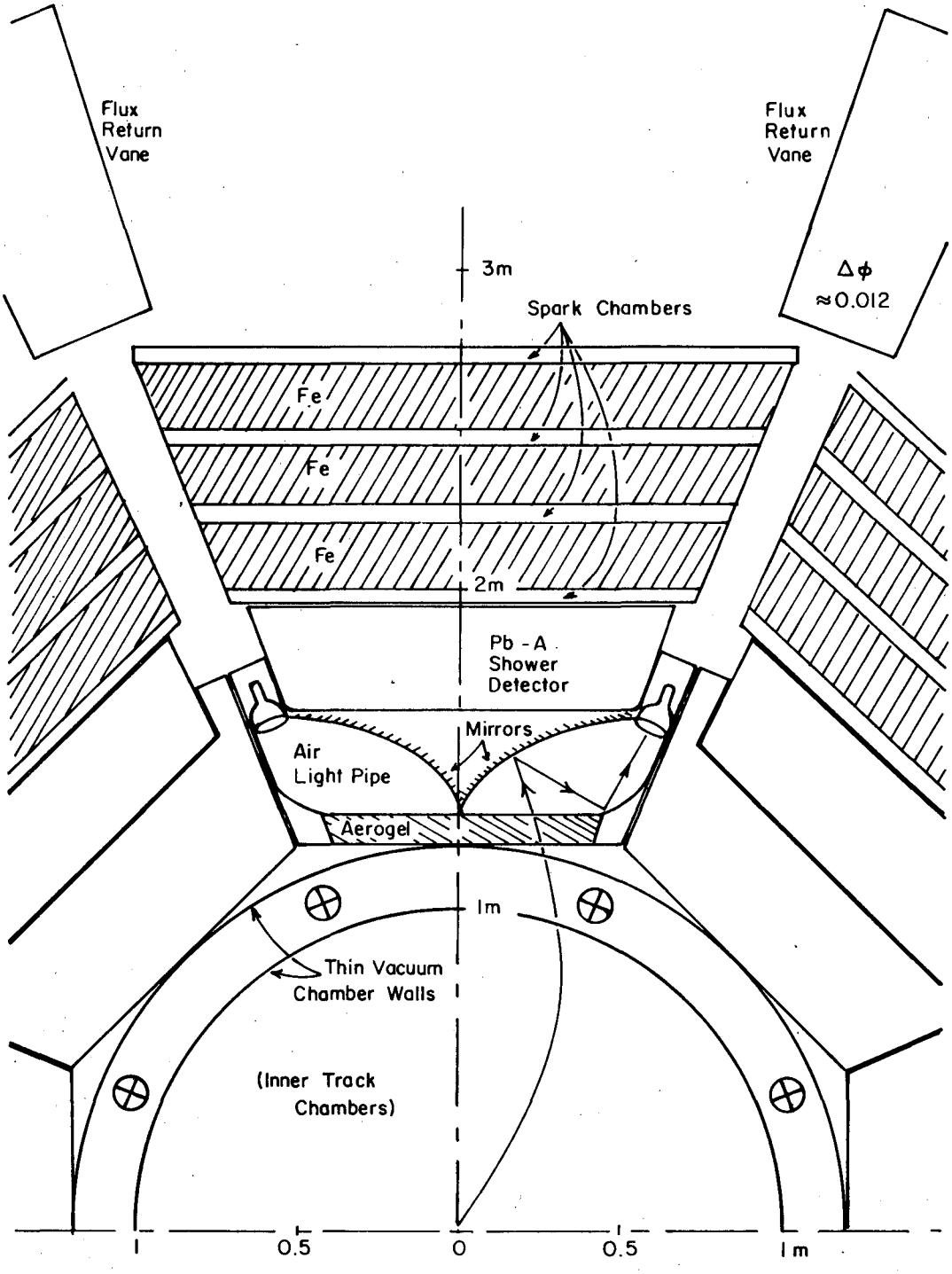

XBL 759-8122

16. Section view of a portion of the prime photon-photon experiment in a plane normal to the beam line.

expected to produce a reasonably uniform 15kGauss field, with momentum resolution $\delta p/p^2 \sim 0.56\%$ $(GeV/c)^{-1}$ at 90^o; this assumes a radial distance of 0.8m for trajectory measurement within the solenoid. The resolution improves as sin θ for forward tracks up to $\theta \sim 30^o$ and then deteriorates rapidly as the tracks leave the solenoid ends. However, the resolution is still about 0.6% (GeV/c) down to $\theta \sim 22^o$. Tracks at angles less than 20^o are analysed in the forward detectors.

The solenoid of the G.U.M. is provided with an inner detector system of cylindrical drift chambers, which provide at least five space - points along each track within the range $20^o < \theta < 160^o$. The resolution along the azimuth is expected to be $\sim$ 0.2mm, while the z-resolution may be a few mm. A drift chamber transverse to the beam - axis is placed at each end of the solenoid, as shown in Fig. 15, to provide precise information for the polar angle θ, for tracks with $\theta < 30^o$, where the precision in z is not adequate. Details of the cylindrical drift - chamber are presented in the G.U.M. report.

Immediately surrounding the cylindrical cryostat of the solenoid coil is a layer of Cerenkov counters. The Cerenkov medium is "Aerogel"[20] of refractive index n= 1.04. It is assumed that this material will be available in cells of at least 10cm x 10cm x 5cm thick. The Cerenkov counters are made up in azimuthal "strips", 20cm wide and 10cm thick (.075Xo), each strip covering about 1/8 of 2π azimuth. These strips cover the open sectors between the eight support struts of the solenoid. The two phototubes for each strip lie over the strut and do not occupy any useful solid - angle. Each aerogel counter is then about 80cm long, with an air light-pipe about 30 cm thick viewed from both ends by fast 5" phototubes. The stray field at a radius of 1.4m from the beam is expected to be appreciable, so that magnetic shielding will have to be provided for the phototubes. Threshold momenta for n=1.04, (density 0.2gm.cm) are: p_π=0.49 GeV/c, p_K= 1.72 GeV/c, p_p= 3.29 GeV/c. For β= 1, and 100% light collection, 80 photoelectrons is the expected yield from a bialkali photocathode. Using position information provided by the inner detector, it should be possible to obtain good time-of-flight information from a layer of scintillators behind the Cerenkov counters. Assuming a TOF resolution of 0.5ns FWHM and requiring a separation of 1ns over the 1.3m flight path, π-K separation is achieved up to p 0.64 GeV/c and π-p separation up to $p \approx 1.3$ GeV/c. Fig. 16 shows a section transverse to the beam axis of the upper half of the central detector. Note that between the lumped coils the 8 struts obscure a total of $0.5/2\pi$ of the azimuth. Material between struts is about $.05X_o$.

Surrounding the shell of Cerenkov counters is a layer of shower detectors in an octagonal array. The proposed detectors are Pb-liquid Argon proportional chambers, with a radial depth of $15X_o$. Each sector of the shower detector is an independent cryogenic unit with its own insulating jacket. Each sector is approximately 1.2m wide and 4.6m long. The depth of $15X_o$ is sampled in $\frac{1}{2}$ -cell units of 2mm of liquid Argon behind 1mm of Pb. There are 84 such $\frac{1}{2}$ -cells in depth, with 3 full cells making up approximately one radiation length ($1.07X_o$). These cells are grouped for readout. The first three cells are grouped together (about $1X_o$). The next two cells are read out in ϕ and θ strips respectively. The ϕ (azimuthal) strips running parallel to the beam are uniformly 2cms wide. The θ strips are 2cms wide at $\theta = 90^o$ and increase in width as $(2cm/\sin\theta)$ to provide uniform resolution in opening angle, $\Delta\theta$. The next three cells are again read out as one unit. The ϕ, θ pattern is repeated for the next two cells, the readout being paralleled with the first ϕ, θ set. These are followed by two more groups of three cells each. The last 29 cells are all read out together in one unit of $\sim 10.2X_o$. The ϕ, θ division is provided to allow identification of two separate photons from a high energy π^o. The resolution is adequate to allow separation of the photons from a π^o of 10 GeV/c decaying with minimum opening angle. A further coarse segmentation is provided as follows: the sectors are longitudinally divided in two, making a total of 16 sectors in azimuth; parallel to the beam axis, the readout is divided into 15 segments, of size $(20cm/\sin\theta)$, again to provide uniform resolution in $\Delta\theta$. Thus there are 30 segments capable of independent energy measurement in each octant of the shell. The resolution in energy is expected[17] to be $\delta E_\gamma/E_\gamma \sim 7\%/(E_\gamma(GeV))^{1/2}$ assuming a judicious choice of soft-ware pulse-summing to minimize noise for low energies. With this energy, and only coarse spatial resolution, one may expect a π^o mass-resolution $(\delta m/m)_{\pi^o} \sim 40\%$ at 1 GeV/c. Fine resolution gives $(\delta m/m)_{\pi^o} \sim 12\%$ at 1 GeV/c. For the process $2\gamma \to \eta_c$ (3 GeV) with the worst case $\gamma\beta \sim 1.4$, the mass resolution would give $\delta m = \pm$ 100 MeV, as in this case the fine resolution in ϕ, θ could be used. The coarse segmentation into a total of 240 segments in the range $30^o < \theta < 150^o$ appears adequate to handle the multiplicity of particles at 2E = 30 GeV. The fine sampling in radiation depth should provide very good π/e rejection ($\sim 5 \times 10^{-3}$). Note that the total material between the last drift-chamber and the shower detector is $\sim 0.15X_o$.

For more forward angles, the region $20^o < \theta < 30^o$ (in each beam direction) is covered by similar Pb-Argon shower detectors placed between the coil-cryostat and the iron "pole" of the flux-return. These are separated into octants by the 8 coil-supporting struts. Coarse segmentation is into two θ regions (20^o-25^o and 25^o-30^o) and two ϕ wedges in each octant. Within each coarse segment, ϕ and θ fine resolution is provided with 2cm wide strips. Sampling in depth is exactly as in the shell counters, except that due to limited space, 1.5mm Pb plates have to be used in order to make up $15X_o$. The resolution is expected[17] to be $\delta E_\gamma/E_\gamma \sim 9\%/(E\ (GeV))^{1/2}$.

In order to distinguish final states with muons, a muon-hadron discriminator is needed. Muons from two-body decays of the hadronic states produced in $\gamma\gamma$ collisions will be mostly contained within $35^o < \theta < 145^o$ if we assume that the maximum $\gamma\beta$ of the produced mass W is limited to 1.4. (See Section II). Thus a muon detector must be provided for the central region, due to the limit

0 0 0 0 4 5 0 1 6 3 9

on the velocity β imposed by the tagging cuts described in Section II. Since the central detector is essentially without interaction material up to $\sim$ 1.7m radius, the contribution due to $\pi \to \mu$ and $K \to \mu$ decays is appreciable. It is estimated that the contamination due to pion and kaon decays is $\sim 2\times10^{-2}$ σ(Hadronic) for muons with momentum above 3 GeV/c (see New Particles Report, PEP-1975) for a decay path of 2m. A muon detector at a radius R > 2m thus need have hadron rejection at the most equal to the contamination due to decays of pions and kaons. Assuming that the inclusive momentum spectra of hadrons in 2γ-reactions is similar to that observed in annihilation at $S = W^2$, we will require a rejection ratio of about 2×10^{-2}. This is obtained with 4 absorption lengths or 70cms of Fe.. Since the Pb-Argon shower detectors also serve as a muon-hadron discriminator of 0.8λ absorption, we need only add 60cms of Fe. Fig. 16 shows the iron divided into three slabs of 20cms. each. In the slots, magnetostrictive wire spark chambers are installed; the last three sets of chambers are all required to have a clean track with no accompanying extra sparks within a radius of say, 20cms, in order to signal a muon. The overall hadron rejection will then be about 3%, including contamination due to decays.

In the region $20^0 < \theta < 30^0$, the transverse drift chamber behind the iron pole (85cm thick) will serve as a hadron discriminator, with similar rejection efficiency.

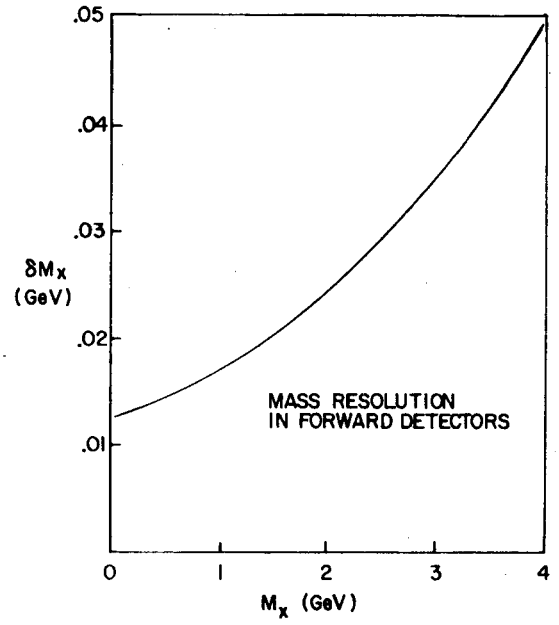

XBL 759-8121

17. Mass resolution predicted for reconstruction of two-body decays of a mass M_x moving along the beam with momentum p_x = 10 GeV/c, assuming the detection apparatus described in section VI.

C. Small Angle Detectors

At $\theta < 20^0$, particles will pass through the holes in the solenoid end-caps and will be analysed in the dipole magnets. Trajectories are determined by a set of transverse drift chambers as shown in Fig. 15. Each chamber provides an unambiguous space point, with 0.2mm resolution in the bending plane and a few mm in the other dimension. With a chamber at 5m from the interaction point, the angular resolution in the non-bend plane should be < 2mr. The momentum resolution, with a central field of 4.5k Gauss, ($BL^2 \sim$ 10k Gauss - meter^2), is $\delta p/p^2 \sim 0.3\%$ (GeV/c)$^{-1}$, with these errors in momentum and angle, the mass resolution obtained from reconstructing two-body decays of a mass M_x moving along the beam with high momentum p_x = 10 GeV/c is shown in Fig. 17. Thus a ρ^0-meson at $p \sim$ 10 GeV/c would be reconstructed with an error $\delta M_x \sim \pm$16 MeV. Note that particles at 50mr < θ < 75mr are absorbed in the material of the flux-excluding beam-pipe. Those at θ < 50mr travel in a field-free region once they are beyond the solenoid, and are detected in the NaI tagging counters, where they deposit about 250 MeV in $20X_0$. This represents a lower limit on the acceptance of tagged energy. We emphasize that $\gamma\gamma$ collisions at $q^2 \approx 0$ may resemble pp collisions at the ISR, with typical small transverse momenta $p_\perp$ = 300 MeV/c, requiring good resolution and identification at small angles.

Following the drift-chambers in the dipole is an array of shower detectors. These consist of segmented Pb-Argon cells as in the central detector, with a total depth of $15X_0$. The fine resolution is provided by 6cm wide strips in x and y, while coarse segments divide the counter in ϕ and θ segments: $\Delta\phi \sim 2\pi/16$, $\Delta\theta \sim$ 100mr. The fine resolution is sufficient to identify the two photons of a 10 GeV/c π^0 decaying with minimum opening angle.

The hole in the solenoid end-cap can be filled with a gas-cerenkov counter, 1.2m long, preferably at atmospheric pressure with thin windows, the total material being restricted to about $.02X_0$. CO_2 at atmospheric pressure will separate electrons from pions up to about 4.6 GeV/c, and pions from kaons up to about 16 GeV/c. The yield at β= 1 is about 10 photoelectrons for 100% light collection.

The detection of forward muons suffers from the background from decays of pions and kaons, because of the 6m flight path. This rejection limit is now 6×10^{-2} σ(Hadronic), for muons above 3 GeV/c, so that an optimum of $3\lambda_{abs.}$ should suffice to keep the hadron rejection at the level of 6%. Thus 50cms of Fe in two slabs, with two sets of spark chambers is sufficient.

D. Trigger

The trigger for 2γ events is a double-tag, in any combination, of one small-angle NaI counter or one large angle shower-counter segment. In each range of θ, a thin scintillator is included in the trigger to demand a charged particle. As shown in Section II, the cuts in ω require that the scattered electron energies lie between E' = 0.1E and 0.9E. The trigger hardware should demand limits slightly outside these, so as to allow clean cuts in the analysis.

VII. RECOMMENDATIONS

1. Every PEP experiment should have a two-photon tagging system, such as the parasite apparatus we have described. This requires that every experiment be open at each end (at least 10^0) to accomodate the tagging aperture, and that any compensating magnets be placed at the ends of the 20m experimental straight section.

2. A two-photon experiment optimized for hadron detection at angles down to about 4^0 should be done. We suggest a possible setup using the proposed General User Magnet supplemented by transverse field magnets at the ends.

3. As early as possible, tests of the background rates with various tagging arrangements, shields, scrapers, etc., should be tried to optimize the details of the tagging system before the final design.

APPENDIX I. KINEMATICS AND NOTATION

Measured quantities

E = initial e^+ or e^- energy

E_1', E_2' = final e^+ or e^- energy

θ_1, θ_2 = final e^+e^- polar angle (we will usually take θ_2 to be the larger one)

ϕ_1, ϕ_2 = final e^+ or e^- azimuthal angle

Derived quantities

$\omega_1 = E - E_1'$ = virtual photon energy (similarly ω_2)

$q_1^2 = 2E\,E'_1\,(1-\cos\theta_1) + m^2\,\frac{\omega_1^2}{E_1'}$ = photon spacelike four-momentum-squared (similarly q_2^2)

$W = \sqrt{4\omega_1\omega_2 - q_2^2 E'_1/E}$ (assuming $q_1^2 \ll q_2^2$, $m \ll E$)

= total $\gamma\gamma$ c.m. energy

$2\sqrt{\omega_1\omega_2}$ if $q_1^2,\ q_2^2 \ll 4\omega_1\omega_2$

$\beta = \frac{\omega_2-\omega_1}{\omega_2+\omega_1}$ = velocity of $\gamma\gamma$ c.m.s. relative to lab

Dimensionless normalized quantities

$x_1 = \omega_1/E$ (similarly x_2)

$z = W/2E = \sqrt{x_1 x_2}$

$Q_1^2 = q_1^2/E^2 \approx (1-x)\ \theta_1^2$ (similarly Q_2^2)

The relations between z, β and x_1, x_2 are plotted in Fig. 1, and the relation between Q_1^2 and x_1, θ_1 in Fig. 2.

Photon-photon luminosity

Let y = any variable or variables (such as x_1, z, Q_2^2, . . .).

The counting rate per unit y can be expressed as

$$\frac{dn}{dy} = \mathcal{L}_{ee}\ \frac{d\sigma}{dy}(ee \to ee X) = \frac{d\mathcal{L}_{\gamma\gamma}}{dy}\,\sigma(\gamma\gamma \to X). \qquad (A1)$$

$\frac{d\mathcal{L}_{\gamma\gamma}}{dy}$ contains the QED factors for the fluxes of the two virtual photons.

APPENDIX II. W DISTRIBUTION OF $\gamma\gamma$ LUMINOSITY

In the Weizsäcker-Williams approximation we have[21]

$$\frac{1}{\mathcal{L}_{ee}}\,\frac{d\mathcal{L}_{\gamma\gamma}}{dx_1 d\theta_1 dx_2 d\theta_2} = \frac{N(E,x_1,\theta_1)}{x_1}\,\frac{N(E,x_2,\theta_2)}{x_2}, \qquad (A2)$$

where

$$N(E,x,\theta) = \frac{\alpha}{\pi}\sin\theta\, x^2(1-x)\,\frac{1}{Q^4}\left[Q^2 + \frac{(1-x)^2}{x^2+Q^2}\sin^2\theta\right]. \qquad (A3)$$

We have already integrated over ϕ_1 and ϕ_2 (see appendix IV). The small-angle dependence of $N(E, x, \theta)$ is approximately

$$\frac{\theta_\gamma}{\theta_\gamma^2 + \left(\frac{m}{E}\right)^2} \propto \frac{\theta}{\theta^2 + \left(\frac{m}{E}\,\frac{x}{1-x}\right)^2}. \qquad (A4)$$

Note that since $\theta(1-x) \approx \theta_\gamma x$, one should avoid using approximate formulas where θ is large and x is small; the implied θ_γ is unphysically large. In the limit of small x the θ distribution is very strongly peaked at $\theta = 0$, although not actually divergent, as the approximate expression implies. As $x \to 1$ the forward peaking becomes gentler.

If only the distribution of $\mathcal{L}_{\gamma\gamma}$ in W and/or β is desired and not the distribution in Q_1^2 or Q_2^2, we need the integral of $N(E, x, \theta)$ over θ:[21]

$$\int_{\theta_0}^{\theta_c} N(E,x,\theta)\,d\theta = \frac{\alpha}{\pi}\left[\left(1+(1-x)^2\right)\left(\ln\frac{E\theta_c}{2m} - \frac{1}{2}\right) + \frac{x^2}{2}\left(\ln\frac{2(1-x)}{x} + 1\right) + \frac{(2-x)^2}{2}\ln\frac{2(1-x)}{\sqrt{x^2+(1-x)\theta_0^2}}\right]. \qquad (A5)$$

Fig. 3 shows plots of this integral for E=15 GeV (the corresponding plot in the 1974 PEP study[6] is in error by about 10%).

To integrate the photon spectrum $N(E, x, \theta)$ given in (A3) over θ between θ_{min} and θ_{max}, the most accurate procedure is to take the difference between two evaluations of the integral (A5) taken for $\theta_0 = \theta_{max}$ and $\theta_0 = \theta_{min}$. Thus,

0 0 0 0 4 5 0 1 6 4 0

$$N(x,\theta_{min},\theta_{max}) = \frac{\alpha}{\pi}\left[(1+(1-x)^2)\ln\frac{\theta_{max}}{\theta_{min}} - \frac{(2-x)^2}{4}\ln\frac{x^2+(1-x)\theta_{max}^2}{x^2+(1-x)\theta_{min}^2}\right]. \quad (A6)$$

This is plotted as a function of x for several choices of θ_{min}, θ_{max} in Fig. 4. Note that $N(x, \theta_{min}, \theta_{max})$ is independent of z; $N(x=0)= 0$; and

$$N(x,\theta_{min},\theta_{max}) \approx \frac{\alpha}{\pi}\left[1+(1-x)^2\right]\ln\frac{\theta_{max}}{\theta_{min}} \quad \text{for } x >> \theta_{max}. \quad (A7)$$

We now have

$$\frac{1}{\mathcal{L}_{ee}}\frac{d\mathcal{L}_{\gamma\gamma}}{dx_1 dx_2} = \frac{N(x_1,\theta_{1min},\theta_{1max})}{x_1}\,\frac{N(x_2,\theta_{2min},\theta_{2max})}{x_2} \quad (A8)$$

or

$$\frac{1}{\mathcal{L}_{ee}}\frac{d\mathcal{L}_{\gamma\gamma}}{dx_1 dz} = \frac{2\,N(x_1,\theta_{1min},\theta_{1max})\,N\left(\frac{z^2}{x_1},\theta_{2min},\theta_{2max}\right)}{x_1 z}$$

An accurate integration over x_1 can only be done numerically, but a rather good approximation, exact in the limit $x_{min} >> \theta_{max}$, can be obtained by using (A7):

$$\frac{1}{\mathcal{L}_{ee}}\frac{d\mathcal{L}_{\gamma\gamma}}{dz} \approx \frac{16\alpha^2}{\pi^2}\ln\frac{\theta_{1max}}{\theta_{1min}}\ln\frac{\theta_{2max}}{\theta_{2min}}\,\frac{1}{z}\cdot \int_{x_a}^{z}\left(1-x_1+\frac{x_1^2}{2}\right)\left(1-\frac{z^2}{x_1^2}+\frac{z^4}{2x_1^2}\right)dx_1$$

$$\approx \frac{16\alpha^2}{\pi^2}\ln\frac{\theta_{1max}}{\theta_{1min}}\ln\frac{\theta_{2max}}{\theta_{2min}}\,\frac{1}{z}\left[\left(\frac{z^2}{x_a}-x_a\right)\cdot\left(\frac{\frac{z^2}{x_a}-x_a}{4}-1-\frac{z^2}{2}\right)+\left(1+\frac{z^2}{2}\right)\ln\frac{z}{x_a}\right] \quad (A9)$$

The limit of integration x_a can be seen in the sketch. We integrate along a curve of constant z within the upper left triangle bounded by dashed lines (there is a factor of 2 to account for the other triangle).

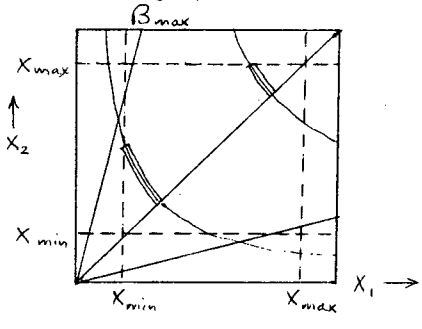

Thus $x_a = \begin{cases} x_{min} & \text{if } z \gtrless \sqrt{x_{min}x_{max}} \\ z^2/x_{max} \end{cases}$

If one also imposes a cut on β (see sketch), the limit becomes

$$x_a = \max\left(x_{min}, \frac{z^2}{x_{max}}, z\sqrt{\frac{1-\beta_{max}}{1+\beta_{max}}}\right). \quad (A10)$$

Equation (A9) is plotted in Fig. 5, with the dependence on θ_{min} and θ_{max} divided out.

A simpler but cruder approximation to $d\mathcal{L}_{\gamma\gamma}/dz$, accurate within about 20%, is obtained by taking (cf. A7)

$$N(x,\theta_{min},\theta_{max}) \sim \frac{5\alpha}{4\pi}\ln\frac{\theta_{max}}{\theta_{min}} \quad (A11)$$

This gives

$$\frac{1}{\mathcal{L}_{ee}}\frac{d\mathcal{L}_{\gamma\gamma}}{dz} \sim \frac{6\alpha^2}{\pi^2}\ln\frac{\theta_{1max}}{\theta_{1min}}\ln\frac{\theta_{2max}}{\theta_{2min}}\cdot\frac{1}{z}\ln\frac{z}{x_a}. \quad (A12)$$

APPENDIX III. γβ AND Q_2^2 DISTRIBUTIONS OF $\mathcal{L}_{\gamma\gamma}$

The γβ factor of the motion of the photon-photon center of mass is a convenient measure of the distortion of the hadron angular distribution. For any choice of x_{min}, x_{max}, and z one can read off the maximum γβ from Fig. 1. We rewrite (A8) in terms of z and γβ, using the approximation (A11):

$$\frac{1}{\mathcal{L}_{ee}}\frac{d\mathcal{L}_{\gamma\gamma}}{dz\,d(\gamma\beta)} \sim \frac{3\alpha^2}{\pi^2}\ln\frac{\theta_{1max}}{\theta_{1min}}\ln\frac{\theta_{2max}}{\theta_{2min}}\cdot\frac{1}{z}\frac{1}{\sqrt{1+(\gamma\beta)^2}} \quad (A13)$$

That is, at all z the liminosity is distributed in γβ almost uniformly (see Fig. 6) up to the maximum value.

If one of the tagged e^+ or e^- is defected at a moderately large angle (say θ_2), the corresponding photon will be off the mass shell, with a spacelike four-momentum-squared Q_2^2. The γγ luminosity for such collisions is obtained from (A2) and A(3). We reexpress $N(E, x_2, \theta_2)$ in terms of E, x_2, and Q_2^2 and integrate $N(E, x_1, \theta_1)$ over θ_1 as in (A6). The resulting function of x_1, x_2, Q_2^2 is integrated over x_1, x_2 at fixed z (with some simplifying approximations) to get

$$\frac{1}{\mathcal{L}_{ee}}\frac{d\mathcal{L}_{\gamma\gamma}}{dz\,dQ_2^2} \sim \frac{5\alpha^2}{2\pi^2}\ln\frac{\theta_{1max}}{\theta_{1min}}\,\frac{1}{z}\ln\frac{z}{x_a}\,\frac{1}{Q_2^2}. \quad (A14)$$

Note that in contrast to the situation in ep scattering, the effective virtual photon flux drops of rather gradually, as Q_2^{-2}.

APPENDIX IV. POLARIZATION EFFECTS

A systematic theoretical treatment of the two-photon process with transversely polarized e^+ and e^- beams has apparently not yet been done. Some generalizations can be made however.

1) The rate of tagging counts will be uniform in azimuth ϕ_1 and ϕ_2 even when the e^+ and e^- beams are transversely polarized.[22]

2) If the e^+ and e^- beams are unpolarized, there will be a polarization of the virtual photon with $\vec{\varepsilon}$ in the plane of tagging. The degree of polarization will be[5,23,24]

$$\varepsilon_1 = \frac{1-y_1}{1-y_1+\frac{y_1^2}{2}} \qquad \text{(similarly for } \varepsilon_2\text{)} \qquad (A16)$$

where $y_1 = (q_1 q_2)/(p_1 q_2) = \dfrac{W^2+q_1^2}{4E\omega_2}$

$\approx x_1$ if $q_1^2 \ll 4E^2$

q_1, q_2 = photon four-momenta

p_1, p_2 = initial e^+ or e^- four-momenta

The dependence of ε_1 on x_1 is shown in Fig. 7. At low x_1 this polarization is almost 100%, and must therefore be independent of the transverse polarization of the initial e^+ or e^-.

3) In the limit $x_1 \to 1$ the photon polarization ($\vec{\varepsilon}$) is 100% in the plane of the e^+ or e^- spin[23,24]. For intermediate x_1 values the situation is presumably some mixture of the two limiting cases.

On general grounds the $\gamma\gamma$ cross section can be decomposed as follows:[5]

$$\sigma_{\gamma\gamma}(W, q_2^2, \phi) = \sigma_T(W, q_2^2) + \varepsilon_2\sigma_L(W, q_2^2) + \varepsilon_1'\varepsilon_2'\,\sigma_A(W, q_2^2)\cos 2\phi, \qquad (A17)$$

where $q_1^2 \ll q_2^2$

ϕ = angle between photon polarization planes

ε_1' ε_2' = transverse polarization of the photons = ε_1, ε_2, if e^+ and e^- are initially unpolarized (A16)

$\sigma_T = \frac{1}{2}(\sigma_{\parallel} + \sigma_{\perp})$

$\sigma_A = \frac{1}{2}(\sigma_{\parallel} - \sigma_{\perp})$

$\sigma_{\parallel} = \sigma_{\gamma\gamma}$ for two photons with parallel transverse polarization

$\sigma_{\perp} = \sigma_{\gamma\gamma}$ for two photons with perpendicular transverse polarization

$\sigma_L = \sigma_{\gamma\gamma}$ for the collision of a longitudinal (scalar) photon and an almost real unpolarized transverse photon: $\sigma_L = 0$ at $q_2^2 = 0$.

APPENDIX V. DEEP INELASTIC

If the final e^+ or e^- is detected at a large angle θ_2, the process can be described as the deep inelastic scattering of an electron from an almost real photon target. The cross section, which has the form given in (A17), can also be written in terms of photon structure functions analogous to the W_1 and W_2 defined for the proton:

$$\frac{d\sigma}{dE_2' d\cos\theta_2} = \frac{8\pi\alpha^2 E E_2' \omega_1}{q_2^4 \nu}\int_{x_{min}}^{x_{max}} N(x_1, \theta_{1\,min}, \theta_{1\,max})\frac{dx_1}{x_1} \cdot \left[\frac{y_2^2 q_2^2}{2\nu} W_1^{\gamma} + (1-y_2)\nu W_2^{\gamma} + \varepsilon_1 \frac{q_2^2}{\nu}(1-y_2) W_3^{\gamma}\cos 2\phi\right], \qquad (A18)$$

where $q_1^2 \ll q_2^2$

$\nu = q_1 \cdot q_2 = \frac{1}{2}(W^2 + q_2^2)$.

The structure functions are related to the σ_T, σ_A, and σ_L defined in (A17) as follows:

$$\sigma_T = \frac{\pi\alpha}{\nu} W_1^{\gamma},$$

$$\sigma_L = \frac{\pi\alpha}{\nu}\left(\frac{\nu^2}{q_2^2} W_2^{\gamma} - W_1^{\gamma}\right), \qquad (A19)$$

$$\sigma_A = \frac{\pi\alpha}{\nu} W_3^{\gamma}.$$

The parton model predicts[5]

$$W_1^{\gamma} = 2\alpha \sum e_i^4 \left[1 - 2x(1-x)\right] \ln\frac{W^2}{m^2},$$

$$\frac{1}{2x}\nu W_2^{\gamma} - W_1^{\gamma} = 2\alpha \sum e_i^4 \cdot 4x(1-x),$$

$$W_3^{\gamma} = 2\alpha \sum e_i^4 (-x^2),$$

where $x = q_2^2/2\nu$ $\qquad (0 < x < 1)$

$\sum e_i^4$ = sum of fourth powers of parton charges.

In order to estimate rates we assume (without justification) that $W_1^{\gamma} = \frac{1}{2x}\nu W_2^{\gamma}$ (i.e., $\sigma_L = 0$), and $\nu W_2^{\gamma} \sim (\sigma_{\gamma p}/\sigma_{pp})\,\nu W_2^{p} \sim (1/300)\,(.3)$.

REFERENCES

1. C. Huygens, Treatise on Light (The Hague, 1690).
2. S. J. Brodsky, Journal de Physique 35, C2-69 (1974).
3. S. J. Brodsky, T. Kinoshita, H. Terazawa, Phys. Rev. Letters 27, 280 (1971).
4. T. F. Walsh, Journal de Physique 35, C2-77 (1974).
5. R. P. Worden, Rutherford Lab. preprint RL-74-065.
6. G. Barbiellini, G. Ringland, B. Shen, W. Toner, W. Vernon, 1974 PEP Summer Study, PEP- B7, p. 525.
7. Ref. 6, p. 534.
8. P. DiVecchia, M. Greco, Nuovo Cimento 50A, 319 (1967).
9. Ref. 6, p. 530.
10. L. W. Mo, Y. S. Tsai, Rev. Mod. Phys.
11. Ref. 6, p. 529.
12. T. F. Walsh, Lecture notes, Maria Laach, 13 Sep. 73.

0 0 0 0 4 5 0 1 6 4 1

13. E. Eichten, K. Gottfried, T. Kinoshita, J. Kogut, K. D. Lane, and T. M. Yan, Phys. Rev. Letters 34, 369 (1975).
14. T. Appelquist, A. deRujula, H. D. Politzer, and S. L. Glashow, Phys. Rev. Letters 34, 365 (1975).
15. H. Terazawa, Rev. Mod. Phys. 45, 615 (1973).
16. Ref. 6, p. 531.
17. E. Bloom et al., 1974 PEP Summer Study PEP-137, p. 276.
18. J. M. Paterson (priv. comm.)
19. S. St.-Laurant (priv. comm.)
20. Cantin et al., Nucl. Instr. 112, 177 (1974).
21. S. J. Brodsky, T. Kinoshita, H. Terazawa, Phys. Rev. D4, 1532 (1971).
22. S. J. Brodsky, G. Grammar (priv. comm.)
23. N. Dombey, Rev. Mod. Phys. 41, 236 (1969).
24. J. D. Bjorken, Phys. Rev. D1, 1376 (1970).

REPORT OF THE NEW PARTICLE GROUP

A. Carroll, B. Cox, A. Eisner, K. W. Lai, F. Lobkowicz,
M. Marshak, J. Marx, J. Matthews, N. Mistry, C. Morehouse,
J. Poucher, A. Rothenberg, A. Seidl, and D. Yount

Abstract

We review the properties of possible new particles, and conclude that there are some general features that a New Particle Detector can exploit. We investigate backgrounds in the most likely signatures and propose a New Particle Detector Facility. Several more specialized detectors are also described.

Table of Contents

I. Introduction

II. Summaries of New Particle Properties (from 1974 PEP Summer Study)

III. Signatures and Experimental Parameters

1. Quarks
2. Magnetic Monopoles
3. Tachyons
4. Heavy Leptons
5. Stable Charged Particles
6. Stable Neutral Particles
7. Charmed Particles
8. Scalars
9. Vectors
10. 2-γ Production
11. Compton Production

IV. Hadronic Background to Lepton Signals

1. Introduction
2. Misidentification of Hadrons as Electrons
3. Misidentification of Hadrons as Muons
4. Conclusions

V. New Particle Detector Facility

1. Detector - General
2. Magnet
3. Inner Detector
4. Outer Detector
5. Summary

VI. Specialized New Particle Detectors

1. General User Magnet (GUM)
2. Split Chamber
3. Liquid Argon Neutrals Detector (LAND)
4. Off-Axis Solenoid
5. Streamer Chamber

Appendix: PEP Cross-Sections Estimates from Hadron Machines

I. INTRODUCTION

It is desirable in searching for new particles to have some general signatures which would reveal the existence of more than one type of new particle. It is apparent from the excellent tabulation of "conventional new particles" in the 1974 PEP Summer Study (included here in Section II) that the presence of leptons is the most general signature for a search. We analyze background contributions to these signatures and methods for decreasing the backgrounds relative to the signature signals. A New Particle Detector Facility is proposed which compromises the new particle signatures as little as possible relative to a more general multiparticle detector. Finally, a few specialized detectors are described.

II. SUMMARY OF NEW PARTICLE INFORMATION

(1) Heavy leptons - excited, sequential, gauge theory, and quasi-stable heavy leptons

(2) Charged Intermediate Vector Bosons

(3) Charmed Hadrons

(4) Resonances

(5) Quarks

(6) Gluons

(7) Monopoles

(8) Higgs Scalers

(9) Neutral Intermediate Bosons

(10) Lee-Wick Particles

(11) Tachyons

The following abbreviations are used in the tables:

ℓ = either e or μ
h = hadron
MM = missing mass
M = new particle mass
m^* = invariant mass
COP = coplanar
ACP = acoplanar
COL = colinear
β = velocity of new particle in center-of-mass system
R = $\sigma(e^+e^- \rightarrow \text{hadrons})/\sigma(e^+e^- \rightarrow \mu^+\mu^-)$
FF = form factor

III. SIGNATURES AND EXPERIMENTAL PARAMETERS

1. Quarks

We consider the detection of stable quarks of fractional charge and unstable quarks. Stable integer charge quarks are considered elsewhere. Quarks are assumed to be produced in pairs so that they carry the beam energy, E_0.

Fractionally Charged Stable Quarks

Detection requires charge and/or mass measurement. Since $dE/dx \sim Z^2/\beta^2$ anomalous ionization can be measured if the quark velocity is high enough. Landau fluctuations in a given ionization measurement introduce fluctuations in dE/dx of $\sim$ 20%, so that one should independently sample ionization at least 3 times with each sampling required to be

Particle	Production Mechanism	Rate per $\begin{cases} 10^{38}\ cm^2 \\ 10^{4}\ \mu^+\mu^- \end{cases}$	Decay Modes/ Branching Ratios	Experimental Signatures	Present Limits	PEP Limit
(1) HEAVY LEPTONS [1]						
(A) Excited leptons $\ell^-, \ell^{*-} \ldots$, $\nu_\ell, \nu_\ell^* \ldots$	$e^+e^- \to \ell^{*+}\ell^{*-}$ $\ell^{*+}\ell^{*-}$ $\ell^{*+}\ell^-$ $\ell^+\ell^{*-}$ 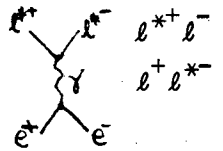	$10^{+4} \times (\frac{3\beta-\beta^3}{2})$	$\ell^* \to \ell\,\gamma$	1) acp pair $\ell^+\ell^-$ + 1 or 2 hard γ's 2) bump in $m^*_{\ell\gamma}$	$m_{\ell^*} \lesssim 2$ GeV [4] $\lambda^2 < 10^{-3}$	$m_{\ell^*} \lesssim 25$ GeV
	$e^+e^- \to \nu_\ell^*\overline{\nu_\ell^*}$ 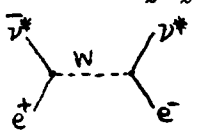	$250 \times (\frac{3\beta+\beta^3}{4})$ [3]	If ν_ℓ^* massive, $\nu_\ell^* \to \ell^-(\ell^+\nu_\ell)$ $\to \ell$ + h's $\Gamma(\text{h's})/\Gamma(\ell) \sim R$	1) acp $\ell\ell$ pairs 2) ℓ + h's 3) > 2 charged ℓ's 4) missing $p_\perp$ and E	$m < 1.2$-2.2 GeV	$m \lesssim 14$ GeV
(B) Sequential Leptons $\begin{pmatrix}\ell\\ \nu_\ell\end{pmatrix}, \begin{pmatrix}\ell'\\ \nu'_\ell\end{pmatrix}, \ldots$	$e^+e^- \to \ell'^+\ell'^-$ 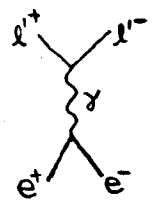	$10^{4} \times (\frac{3\beta-\beta^3}{2})$	$\ell'^- \to \nu'_\ell(\ell\nu_\ell)$ $\to \nu'_\ell$ + h's $\Gamma(\text{h's})/\Gamma(\ell) \sim R$	1) acp $\ell\ell$ pair 2) ℓ + h's 3) missing $p_\perp$, E	$m_\ell < 1.2$-2.2 GeV [9] [10]	$m_\ell \lesssim 14$ GeV

[1] General searches: M. L. Perl, SLAC-PUB-1062 (1972); Decays and Production: Y. S. Tsai, Phys. Rev. D4, 2821 (1971); K. J. Kim and Y. S. Tsai, Phys. Lett. 40B, 665 (1972).

[2] S. V. Golovkin et al., paper No. 848, XVI Intl. Conf. on HEP, Chicago (1972).

[3] A. M. Litke, Thesis, Harvard University, p. III-8 (1970).

[4] C. Bacci et al., Phys. Lett. 44B, 530 (1973); Super-Adone Proposal; DESY Seminar.

000045016422

Particle	Production Mechanism	Rate $\frac{10^{38}\ cm^2}{10^4\ \mu^+\mu^-}$	Decay Modes/ Branching Ratios	Experimental Signatures	Present Limits	PEP Limits
HEAVY LEPTONS (contd.)						
(C) Gauge Theory Leptons [5]	$e^+e^- \to L^+L^-$ 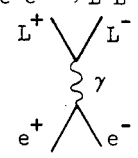	$10^4 \times (\frac{3\beta - \beta^3}{2})$	$L^+ \to \nu_\ell(\ell\nu_\ell)$ $\to L^o(\ell\nu_\ell)$ $(M_{L^+} > M_{L^o})$	Same as Sequential Leptons -- see (B)	$m_{M^+} \gtrsim$ 7-8 GeV [7] $m_{M^+} \lesssim 8$ GeV [9]	$m_{E^+} < 14$ GeV
$\begin{pmatrix}\nu_e\\ e^-\\ E^o\\ E^+\end{pmatrix}$	$e^+e^- \to L^o\bar{L}^o$ 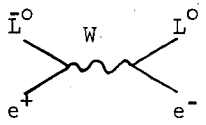	> 450 [6]	$\to \nu_\ell$ + h's $\to L^o$ + h's		$m_{E^o} \gtrsim$ 1.2 - 2.2 GeV [9] $m_{M^o} < 4$ GeV	$m_{E^o} \lesssim 20$ GeV
$\begin{pmatrix}\nu_\mu\\ \mu^-\\ M^o\\ M^+\end{pmatrix}$ L = E or M	$e^+e^- \to L^o\bar{\nu}_\ell$ 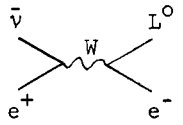	> 200 [6]	$L^o \to \ell^-(\ell\nu_\ell)$ $\to \ell^-$ + h's $\to \nu_\ell$ + h's $\Gamma(h's)/\Gamma(\ell) \sim R$			
(D) Quasi-stable leptons	$e^+e^- \to L^+L^-$ 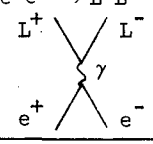	$10^4 \times (\frac{3\beta - \beta^3}{2})$	Decay not seen in typical size detector $\tau \gtrsim 10^{-8}$ sec	Massive ($p_L < p_{BEAM}$), weakly interacting, collinear pairs	$m_L < 1$ - 5 GeV [2]	$m_L \lesssim 15$ GeV

[5] Bjorken and Llewellyn Smith, Phys. Rev. D7, 887 (1973), Georgi and Glashow, Phys. Rev. Lett. 28, 1494.
[6] For Georgi-Glashow model with sin $\theta_G = 1$ and M_{L^o} as indicated above, see Ahmed Ali, Stevens Institute of Technology preprint, 1974.
[7] B.C. Barish et al.
[8] Based on $(g-2)_\mu$ experiments, see Primack and Quinn, Phys. Rev. D6, 3171 (1972).
[9] Washington Meeting APS SPEAR Report (April 1974), Drito et al., Phys. Lett. 48B, 165 (1974), Bernardini et al., Bonn Conference (August 1973).
[10] Possibly a signal for 1.8 GeV/c^2 sequential leptons has been observed at SPEAR, M. Perl, et al.

Particle	Production Mechanism	Rate 10^{38} cm^2 / 10^4 $\mu^+\mu^-$	Decay Modes/ Branching Ratios	Experimental Signatures	Present Limits	PEP Limits
(2) CHARGED VECTOR BOSONS	(a) $e^+e^- \to W^+W^-$	1000 for M_W = 13.8 GeV assuming: (i) charge form factor = 1, (ii) no magnetic moment, (iii) no quadrupole moment.	$W^\pm \to \ell^\pm \nu$ $e^\pm \nu / \mu^\pm \nu \approx 1$ $W^\pm \to$ hadrons $W^\pm \to \varphi\gamma$ if $M_W > M_\varphi$ [φ = Higgs-scalar meson] $\Gamma(h's)/\Gamma(\ell) \approx R$	(a) Final states $\ell^+\ell^-\nu\bar{\nu}$ $\ell^\pm \nu$ + h's Look for acp μe, ee, and $\mu\mu$ pairs in ratio 2:1:1; missing $p_\perp$ and E	Present: $M_W \gtrsim 13$ GeV νN-NAL [2] $M_W > 18$-24 GeV $pp \to \mu^\pm X$ ISR [3]	< 14 GeV
	(b) $e^+e^- \to e^\pm \nu W^\mp$	5 for [4,5] M_W = 13.8 GeV 50 for M_W = 6 GeV		(b) $e^+e^-\nu\bar{\nu}$ $e^\pm\mu^\mp\nu\bar{\nu}$ $e^\pm\nu$ + h's with acp ee, eμ pairs; missing $p_\perp$ and E		< 30 GeV
	[7] (c) $e^+e^- \to V^+V^-$ (vector partons)	$\frac{\sigma_{VV}}{\sigma_{\mu\mu}} \approx \frac{S}{M_V^2}$	Probably totally into hadrons	(c) Constant hadronic cross section with S		< 15 GeV

[1] See for example N. Cabibbo and R. Gatto, Phys. Rev. 124, 1577 (1961).
[2] B. Aubert et al. "Test of Scaling in High Energy Neutrino Interactions" 6th Int. Symp. on Electron and Photon Interactions, Bonn Aug. 1973, 2nd Aix-en-Provence Int. Conf. on El. Particles, September 1973.
[3] G. Manning, Private Communication.
[4] F.A. Berends and G.B. West, Phys. Rev. D1, 122 (1970), Phys. Rev. D2, 1354 (1970).
[5] Mikalian and J. Smith Phys. Rev. D4, 785 (1971).
[6] We have rewritten equation (19) of Berends and West (reference 4)to demonstrate explicitly that, neglecting the electron mass terms, σ is only a function of M_W/E.
[7] J. Clemans, G. Kornen, Nucl. Phys. B78, 396 (1974).

0 0 0 4 5 0 1 6 4 3

Particle	Production Mechanism	Rate per $\begin{cases} 10^{38}\ cm^2 \\ 10^4\ \mu^+\mu^- \end{cases}$	Decay Modes/ Branching Ratios	Experimental Signatures	Present Limits
(3) CHARM [1,2,3]	1) $e^+e^- \to C\bar{C}$	~ 1 - 100, $= \Lambda\bar{\Lambda}$	$C \to S$ + h's (S = strange hadron) $\Gamma \sim \cos\theta_{Cabibbo}$ $C \to$ h's (non-strange) $\Gamma \sim \sin\theta_C$	1) Apparent violation of strangeness if $C \to$ h's (non-strange), $\bar{C} \to$ h's + strange hadron $\Gamma \sim \sin\theta_C \cos\theta_C$	2 GeV < M < 10 GeV
	2) $e^+e^- \to C\bar{C}'X$ electromagnetic	~35 for M_C = 10GeV ~ 1000 [4] above threshold ≈ inclusive baryon production	$C \to S + (\ell\nu)$ $\Gamma(\ell\nu)/\Gamma(h's) \sim$ 10% - 50%	2) Anomalous change in production of strange particles as E_o passes through Charm threshold $\Gamma \sim \cos^2\theta_C$	
	3) $e^+e^- \to CX$ weak	~ 20 for M_{Z^o} = 100 GeV	$\tau \sim 10^{-12}$ sec	3) Signature 2) with an associated charged lepton	

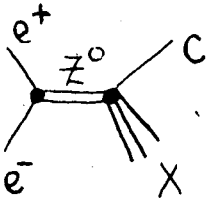

[1] G. A. Snow, Nucl. Physics B55, 445-454 (1973).

[2] M. K. Gaillard, NAL Conf. 74/43-THY (April 1974).

[3] S. L. Glashow, IV Intl. Conf. on Meson Spectroscopy.

[4] J. Marx, private communication.

Particle	Production Mechanism	Rate per $\left\{ \begin{matrix} 10^{38}\,cm^2 \\ 10^4\,\mu^+\mu^- \end{matrix} \right.$	Decay Modes/ Branching Ratios	Experimental Signatures	PEP Limits
(4) RESONANCES	(a) Formation $e^+e^- \to X$ 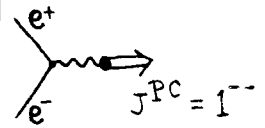 E.g., high-mass vector meson daughters (v') of ρ, ω, and ϕ [1]	In principle, v' formation could account for a large fraction of $\sigma(e^+e^- \to \text{hadrons})$ [1]	For vector mesons, $v' \to$ hadrons, ~100%; $v' \to \ell^+\ell^-$, $\lesssim$ few %.	Peaks in σ vs E_0 for particular final states.	30 GeV
	(b) Two-photon exchange $e^+e^- \to e^+e^-X$ 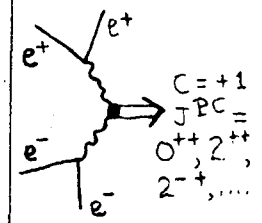 	5×10^5 with $2 < M_X < 6$ GeV [2,3]	Depends on specific resonance	For fixed E_0, peaks in M_X for specific states X, or, inclusively, for any X.	30 GeV
	(c) Production 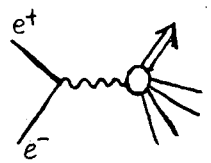 	Depends on specific resonance	Depends on specific resonance	(v') Invariant mass peaks in multi-h, γ-h, ℓ-h, γ-ℓ, ℓ-ℓ, etc., combinations. E.g., see e* in $M(e\gamma)$ for $e^+e^- \to e^*e$ $(e^* \to e\gamma)$ (ii) Missing mass peaks.	30 GeV

[1] F. M. Renard, Montpelier (France) Univ. Report No. PM/74/3 (Feb. 1974)
[2] David W. G. S. Leith, SLAC-PUB-1440 (June 1974)
[3] J. Rosner, SLAC-PUB-1391 (1974)

0 0 0 4 5 0 1 6 4 4

Particle	Production Mechanism	Rate per $\begin{cases} 10^{38}\ cm^2 \\ 10^4\ \mu^+\mu^- \end{cases}$	Decay Mode	Experimental Signatures	Present Limits	PEP Limit
(5) QUARKS [1]	$e^+e^- \rightarrow q\bar{q}$	$z^2\sigma_{\mu\mu}\left(\frac{3\beta-\beta^3}{2}\right)$ × FF	Low mass: may be quasi-stable High mass: may decay into hadron jets	(a) Anomalous dE/dx (for fractionally charged quarks) (b) Massive COL particle pair at low velocity (c) COL hadron jets	$\sigma < 10^{-35}\ cm^2$ for $M_q < 12$ GeV (for $p\bar{w} \rightarrow q\bar{q}X$ at $p_{inc} = 300$ GeV/c, $Z = e/3$ or $2e/3$) [2]	15 GeV
					$\sigma < 3 \times 10^{-34}\ cm^2$, $Z = e/3$, $M_q < 22$ GeV; $\sigma < 6 \times 10^{-34}\ cm^2$, $Z = 2e/3$, $M_q < 13$ GeV (for $pp \rightarrow q\bar{q}X$ at $s \approx 2500\ GeV^2$) [3]	
					$\sigma < 10^{-39}\ cm^2$, $Z = e/3$, $M_q < 4.7$ GeV; $\sigma < 2 \times 10^{-37}\ cm^2$, $Z = 2e/3$, $M_q < 4.7$ GeV (for $p + A\ell \rightarrow q\bar{q}X$ at $p_{inc} = 70$ GeV/c) [4]	

[1] For quark search review see L. W. Jones, Phys. Today 26, 30 (1973), No. 5.

[2] L. B. Leipuner et al., Phys. Rev. Letters 31, 1226 (1973).

[3] M. Bott-Bodenhausen et al., Phys. Letters 40B, 693 (1972).

[4] Yu. M. Antipov et al., Phys. Letters 30B, 576 (1969).

Particle	Production Mechanism	Rate per $\begin{cases} 10^{38}\ cm^2 \\ 10^4\ \mu^+\mu^- \end{cases}$	Decay Modes/ Branching Ratios	Experimental Signatures	Present Limits	PEP Limits
(6) GLUONS [1]						
(A) Neutral $J^{PC} = 1^{--}$ Color singlet SU_3 singlet (B) Vector [2] Color SU_3 Multiplet	Possibly 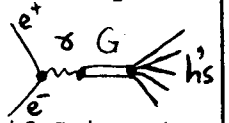 if G is not a SU_3 singlet, or if symmetry breaking [3]	Not known [1],	G → h's (like ρ,ω,φ → h's)	s dependent [4] structure in $\sigma_T(e^+e^- \to h's)$, $\sigma(e^+e^- \to \pi^+\pi^-)$, $\sigma(e^+e^- \to K\bar{K})$, etc.	none	30 GeV

[1] S. Weinberg, Phys. Rev. D8, 605, 4482 (1973). [2] Fritsch, Gell Mann, Leutwyler, Phys. Lett. 47B, 365 (1973).
[3] Chanowitz, Drell, Phys. Rev. Lett. 30, 807 (1973), Phys. Rev. D9, 2078 (1974).
[4] Dalitz, Talk given at PEP Summer Study, 1974.

0004501645

Particle	Production Mechanism	Rate per $\begin{cases} 10^{38}\ cm^2 \\ 10^4\ \mu^+\mu^- \end{cases}$	Decay Modes/ Branching Ratios	Experimental Signatures	Present Limits	PEP Limits
(7) MONOPOLES [1,2] /DYONS	$e^+e^- \rightarrow D^+D^-$ 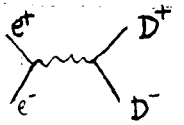	No method to calculate rate because of the strong magnetic charge ($g^2/\hbar c \approx 137$) [2], [4]	[4] (A) Free monopoles--stable (rather unlikely) (B) Monopoles annihilate and γ's are emitted. Or, for Dyons, hadrons may be emitted. 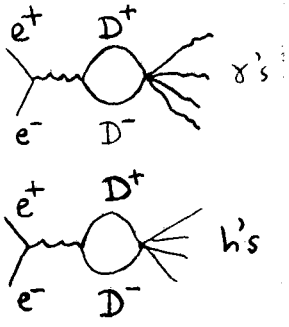	(A) Magnetic charge--accelerated in magnetic field. (B) Heavy ionization (C) Cerenkov radiation with electric vector field direction rotation of 90° from charged particles [8] (D) No reliable estimates on M_D, but large masses (~ 6 GeV to $137 \times M_W$) have been suggested [2,3] (E) Large number of γ's from D^+D^- annihilation [4]	$\sigma(pN \rightarrow p'N'D\bar{D}) < 1.4 \times 10^{-43} cm^2$ for $M_D < 5$ GeV [7]	$M_D < 15$ GeV

[1] Dirac, Phys. Rev. 74, 817 (1948).

[2] Schwinger, Science 165, 757 (1969).

[3] t'Hooft, CERN PREPRINT TH-1876 (1974).

[4] Newmeyer and Trefil, Phys. Rev. Lett. 26, 1509 (1971); Nuovo Cimento 89, 703 (1972); and Trefil, private communication.

[5] Alvarez, Eberhard, Ross and Watt, Science 167, 701 (1970).

[6] Fleischer, Price and Woods, Phys. Rev. 184, 1398 (1969).

[7] Adair, Proceedings of the 16th International Conference on High Energy Physics, Batavia, 4, 307 (1972).

[8] Shcherbakov, Proceedings of the 16th International Conference on High Energy Physics, Batavia, 2, 340 (1972).

Particle	Production Mechanism	Rate $\begin{cases} 10^{38}\ cm^2 \\ 10^4\ \mu^+\mu^- \end{cases}$	Decay Modes/ Branching Ratios	Experimental Signatures	Present Limits	PEP Limits
(8) HIGGS SCALAR PARTICLE [2]	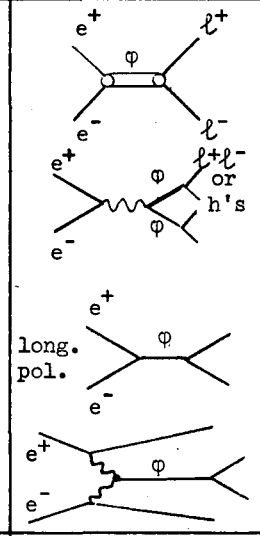	~ 10^2 ~ 10^2	$\varphi \to \ell^+\ell^-$ $\to$ h's	Sharp peak in [3] $\sigma_{\ell\ell}$ vs s($\Gamma_\varphi \sim M_\varphi^3 \sim 1$ MeV for $M_\varphi = 1$ GeV) Peak in σ vs S Peak in missing mass of e^+e^-	M > 0.5 GeV (from K_L^o decay) [4] M > 0.5 GeV [4] or very small [6]	30 GeV
(9) NEUTRAL INTERMEDIATE BOSON [1]	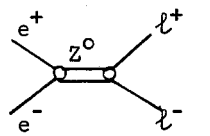	~ 10^2	$Z^o \to \ell^+\ell^-$ $\to$ h's	[3] 1) Peak in $\sigma_{\ell\ell}$ vs s. 2) Interference between weak and EM production of $\mu\mu$, ee.		30 GeV
(10) LEE-WICK PARTICLE [5] (Heavy Photon)	$e^+e^- \to \varphi \to e^+e^-$ $\to \mu^+\mu^-$ 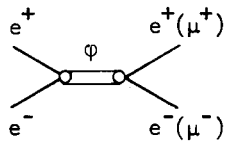	$\frac{\Delta\sigma}{\sigma} = \pm \frac{8E^2}{\Lambda^2}$ in $e^+e^- \to \mu^+\mu^-$ (+) for Lee-Wick (-) for Heavy Photon	$\varphi \to e^+e^-$ $\to \mu^+\mu^-$ $\to$ hadrons(?)	1) Deviation from QED cross section and angular distribution in $e^+e^- = e^+e^-$ 2) Deviation from QED total cross section in $e^+e^- \to \mu^+\mu^-$	25 GeV	200 GeV Virtual exchanges produce effects in QED reactions well below the threshold for production.

[1] Weinberg, Phys. Rev. 19, 1265 (1967), Salam, Elementary Particle Physics, ed. Svartholm (Stockholm 1968), p. 367.
[2] Higgs, Phys. Rev. Letters 13, 508 (1964).
[3] J. Kirkby, talk given at PEP Summer Study (1974).
[4] From K_L^o decay, see [3].
[5] Lee and Wick, Nucl. Physics B9, 209 (1969), A. Litke, Ph.D. Thesis, Harvard University (1970).
[6] Barshay, S., Phys. Rev. D10, 2313 (1974).

0 0 0 4 5 0 1 6 4 6

Particle	Production Mechanism	Rate per $\begin{cases} 10^{38}\ cm^2 \\ 10^4\ \mu^+\mu^- \end{cases}$	Decay Modes/ Branching Ratios	Experimental Signatures	Present Limits
(11) TACHYON [1]	$e^+e^- \rightarrow T^+T^-$ $\rightarrow T^oT^o$	?	?	(a) $T^{\pm}$ emit Cerenkov light at $\approx 90^o$ in electric field (b) $v > c$ (c) $M_T^2 < 0$ (d) COL particle pair	Photoproduction (E_γ = 1.2 MeV) $\sigma < 1.7 \times 10^{-33}\ cm^2$ for 0.5 e < tachyon charge < 1.9 e [2]

[1] O. M. P. Bilomink et al., Am. J. Phys. 30, 718 (1962); G. Feinberg, Phys. Rev. 159, 1089 (1967).

[2] T. Alväger and M. N. Kreisler, Phys. Rev. 171, 1357 (1968); M. B. Davis, M. N. Kreisler, T. Alväger, Phys. Rev. 183, 1132 (1969).

0 0 0 0 4 5 0 1 6 4 7

several (probably 3) standard deviations from minimum ionizing. Thus we require

$$\Delta dE/dx \leq N|dE/dx(Z=1,\ \beta=1) - dE/dx(\text{quark})|$$

or

$$\frac{\Delta dE/dx}{dE/dx}\Big|_{\text{quark}} \leq N\left|\frac{\beta^2}{Z^2} - 1\right|$$

where β is the quark velocity, Z its charge, and N the number of standard deviations required in the effect. Using $\Delta dE/dx = 0.20\ dE/dx$ and $N = 3$ we obtain

$$\beta^2 \geq (1.07)Z^2$$

$$\beta^2 = 1 - \frac{M^2}{E_0^2}$$

$$M \leq (1 - 1.07Z^2)^{1/2}E_0 \quad .$$

If $Z = 2/3$ we have $M \leq 0.72E_0$. Of course, above this value of $M/E_0(\beta < 0.67)$ the velocity can be determined to an error of .02 with 100 ps of timing resolution over 50 cm flight path. Thus by combining TOF and dE/dx the full kinematic range in quark masses can be covered.

A second method for identifying fractional charge is to use magnetic analysis to search for particles with an apparent momentum greater than E_0/c (due to their fractional charge reducing the bend angle in the magnetic field). If the quarks produced in pairs have the energy of the beam, this method is sensitive for masses such that

$$M \leq E_0\sqrt{1-Z^2} \quad .$$

The requirement that both members of the pair have "supermomentum" would eliminate most background due to errors in momentum measurement (due to inefficiency + accidental in a chamber).

The identification of colinear pairs with low velocity is useful as a signature for any massive stable particle (including quarks of any charge). The relevant velocity measurements can be performed by TOF or using Čerenkov counters. The uncertainty in the mass using TOF is

$$\Delta M = \frac{c}{d}\frac{E^2}{M}\left(1 - \frac{M^2}{E^2}\right)^{3/2}\Delta t$$

where d is the flight path, E the energy and Δt the time resolution. The mass is determined for colinear pairs by $M = E\sqrt{1-\beta^2}$. Values of $\Delta t \sim$ 100 ps can, in principle, be obtained by using segmented solid Čerenkov radiators coupled to photosensitive multichannel electron multiplier plates. Such plates are positioned $\sim$1 mm behind a photo cathode in order to achieve this excellent time resolution. In Fig. III-1 we depict ΔM versus M for Δt = 100 ps and d = 50 cm for E = 5 GeV, 10 GeV and 15 GeV. Since we consider colinear pairs, this energy is the beam energy. If we require $\Delta M \leq 2$ M so that we can tell a massive object of mass greater than 2 GeV from a proton, we find that at 15 GeV the method works for M > 4.8 GeV, at 10 GeV and at 5 GeV for M > 2 GeV. Thus to search for relatively low mass objects by TOF one reduces the machine energy.

Čerenkov identification of low velocity colinear pairs can be accomplished by setting the Čerenkov threshold well below that for protons of energy E_0. This method is limited by the inefficiency of the Č counters and by the necessity to eliminate almost colinear events with enough missing energy so that a pair of conventional particles is slow. Considering these difficulties and the cost of large solid angle coverage with Čerenkov counters, the TOF method is preferable.

In the case of inclusive quark production both searches for anomalous ionization and for apparent momenta greater than E_0/c would be effective. Time-of-flight would also be effective in searching for high mass particles if combined with calorimetry to determine their energy.

Unstable Quarks

Unstable quarks would be difficult, if not impossible, to identify. One would look for colinear hadron jets each of which carries the full beam energy. The distribution of $P_\perp$ within each jet would have to be quite limited ($\langle P_\perp \rangle \leq 350$ MeV/c or so). To identify such a complete jet requires 4π detection of charged and neutral hadrons. Such a detector borders on being prohibitively complicated and expensive, and even if such a complete jet structure were seen it would be difficult to prove that they were due to unstable quarks rather than some dynamics.

In all quark searches it is important to realize that one should observe a threshold in the signal with S. Such a threshold would confirm the quark mass and give an indication that the signal is not the result of a class of background which itself doesn't have a threshold.

Conclusion

Fractionally charged stable quarks can be detected by anomalous dE/dx (possibly combined

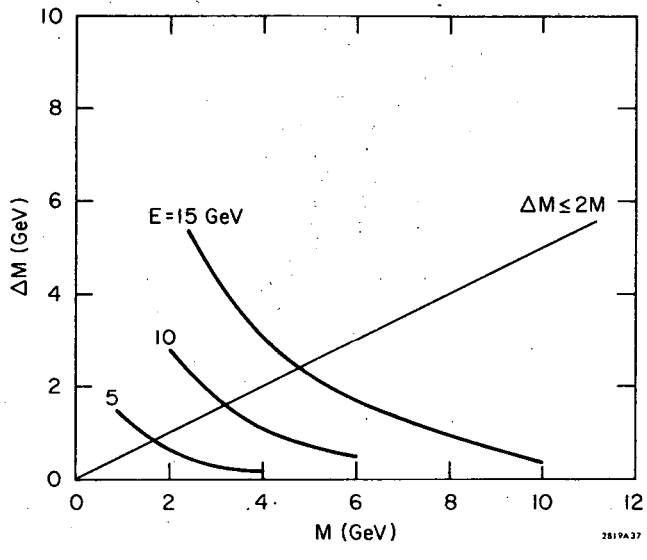

Fig. III-1 Error in Calculated Mass vs. Mass for Collinear Pairs (Δt = 100 ps, d = 50 cm)

with velocity measurement), anomalous momentum (greater than the beam energy) or by the observation of slow massive colinear pairs using TOF or Čerenkov counters. Unstable quarks would be quite difficult to identify in a model-independent manner.

2. Magnetic Monopoles

The theoretical basis for the predicted existance of magnetic monopoles is discussed in PEP-174. In the unlikely situation that monopoles can be produced as free particles, they can be detected from the Emf which results when they pass through a superconducting coil (a la Alvarez and Eberhard). A second handle on their detection is to search for extremely heavy ionization (≥ 40 GeV/gm). Unfortunately, a free monopole will be so heavily ionizing that it will never penetrate very far into a detector. The following table gives the range in matter for monopoles produced at the full PEP energy.

Table III-1

Monopole Mass (GeV)	Monopole Range In Aluminum	Scintillation	Steel
2	1.2 mm	2.3 mm	0.4 mm
5	0.9 mm	2.5 mm	0.3 mm
10	0.5 mm	1.3 mm	0.15 mm
15	0	0	0

In addition to this massive energy loss, monopoles suffer acceleration to energies of 4 GeV/Kg-m of magnetic field. Thus monopoles emitted at low kinetic energies will be accelerated along the beams if solenoid magnets are used. The appropriate detector for free monopoles is then an Alvarez coil wrapped around the beam pipe several meters downstream from a solenoid magnet. The magnet acceleration gives the coil a large effective solid angle.

The best limit on the monopole production cross section in accelerator experiments is 1.4×10^{-41} in 70 GeV proton collisions. At 70 GeV the cross section for the production of virtual photons can be calculated as a function of the photon mass (see Appendix). Photons of mass greater than 4 GeV are needed to produce 2 GeV monopoles. This cross section is $\sim 4 \times 10^{-35}$ cm^2. For 5 GeV monopoles the corresponding cross section is $\sim 2 \times 10^{-38}$ cm^2. When this is compared to the limit of 10^{-41} cm^2 we can say that the probability of a massive virtual photon making monopole pairs is less than $1/4 \times 10^{-6}$ for 2 GeV monopoles and less than 2×10^{-3} for 5 GeV monopoles. If a typical PEP experiment represents an integrated luminosity of 10^{38} cm^{-2} sec^{-1} and if $\sigma_m = 20$ nb at PEP, then an experiment consists of the production of 2×10^6 massive virtual photons. Thus we conclude from the proton experiment that at most, ~ 1 event will be seen if the monopole mass is 2 GeV while the upper limit for 5 GeV monopoles is 4000 events.

In any case, it is rather unlikely that free monopoles will be produced because of the strong attractive force between monopole pairs. This results in the emission of many photons from the radiative damping of the monopole pair. This damping can be thought of phenomenologically as the reason for the low coupling of virtual photons to monopoles discussed above (if the monopole mass is below 5 GeV). Thus, one should search for monopoles indirectly by detection events where the full center-of-mass energy appears in a large number of uncorrelated photons.

Such a detector requires 4π detection of γ's with adequate energy resolution and spacial resolution to reconstruct $\pi^0, \eta, \ldots$ so that each hadronic event can be eliminated from the sample of monopole candidates. The question of π^0 and η reconstruction is discussed in PEP-153 where formulas are given for the π^0 mass resolution in terms of the position and energy resolution of a γ detector. The resulting identification efficiency for NaI and Pb-glass is given in PEP-154, Figs. 9 and 10. If a monopole multigamma signal were seen it would be important to study its S-dependance in order to map the threshold behavior. The energy-dependance of a multigamma signal would help to enhance its credibility and would allow an estimate of the monopole mass.

We conclude that the best monopole detector in the unlikely possibility that free monopoles are produced is a superconducting coil around the beam pipes at a distance from an intersection region containing a solenoid magnet. A useful lower limit on free monopole production at PEP from proton experiments is 2 GeV. Indirect evidence of monopole production could come from events observed in a 4π photon detector where all of the center-of-mass energy appears as uncorrelated photons.

3. Tachyons

We describe briefly the properties of particles with velocity >c, called "Tachyons"[1], from the Greek work ταχυς, meaning swift. If we assume that the normal relativistic expressions for E and p hold for tachyons, then we must require that the mass m be an imaginary quantity in order that E and p, which are measurable quantities, be real. This is logically consistent, since the particles cannot be brought to rest, thus m is not a measurable quantity. We only require that if $\beta > 1$, it always remain so. Thus

$$m = i\mu \qquad (\mu \text{ real})$$

and $$E = \frac{\mu c^2}{(\beta^2-1)^{1/2}} \quad ; \quad |p| = \frac{\mu v}{(\beta^2-1)^{1/2}}$$

where $$\beta = \frac{v}{c} = \frac{|p|}{E} \quad \text{as usual.}$$

We see that $$E^2 - p^2c^2 = -\mu^2 c^4 \ ,$$

so that the four-momenta are always space-like. Further, when $\beta = \infty$, $E = 0$, $p = \mu c$, so that as tachyons lose energy, they speed up to infinite velocity. Both energy and momentum vary smoothly with β, and at $\beta = 1$, $E = \infty$, $|p| = \mu c$. Since the four-momentum is space-like, the sign of the energy component can be changed by an ordinary Lorentz transformation. States with positive energy turn into states of negative energy. However, the same transformation changes the sign of a time-interval so that a tachyon traveling in one direction may appear in another system X, moving such that

0 0 0 0 4 5 0 1 6 4 8

$\beta_T\beta_X > 1$, to be an antitachyon traveling in the opposite direction.[2]

Tachyons are assumed to be spinless, however, Feinberg[1] finds that scalar tachyons fields are quantized using anticommunication relations, and are therefore fermions and not bosons.

Finally, since $\beta > 1$, tachyons can emit Čerenkov radiation in **vacuum. The energy loss** per unit length is

$$\frac{dE}{dx} = -\frac{4\pi^2 Z^2 e^2}{c^2}\int_0^{E/h}\left(1 - \frac{1}{\beta^2 n^2}\right)\nu\, d\nu$$

$$= -\frac{Z^2 e^2}{2\hbar^2}\mu^2\frac{E^2}{p^2}\text{, where } n = 1 \text{ in vacuum and}$$

Ze = tachyon charge.

The rate of energy loss in vacuum is enormous, and within a distance less than 10^{-2} cm, even high energy tachyons (i.e., 15 GeV) are "accelerated" to < 1 eV! Thus as tachyons emerge from the production point, the energy is close to zero, but $\beta \backsim \infty$. Cerenkov light emitted at this stage is produced at $\backsim 90^\circ$ to the direction of motion.

Tachyons cannot be produced singly by normal particles[1] but can be produced in pairs. In particular, they can be produced through one-photon annihilation at PEP, as long as the total four-momentum-squared of this pair is positive. There is no threshold, since the pair can be produced at any energy, even $E_{pair} = 0$. However, since $|p_T| > E_T$, if tachyons are produced with beam energy E_0 each, their momentum will be $|p_T| > E_0$. In fact, since their energy is reduced to zero rapidly, the momentum of an emerging tachyon will be the minimum value $|p| = \mu c$.

If tachyons interact normally with an electromagnetic field (as they must, if they are produced by photons), then they can be made to reach a steady state energy E_1 by an electric field such that the energy lost through Čerenkov radiation is balanced by that gained in this field ϵ.

$$E_1^2 = 2\frac{\hbar^2 c^2}{Ze}\epsilon$$

The Čerenkov radiation emitted in a field of 3kV/cm is sufficient to be observable in an ordinary photomultiplier (spectral response 2.5 eV - 3.5 eV). This effect has been used to search for tachyons produced by γ-rays from radioactive decays.[3] The same method may be used at PEP. However, the intense flux of very soft X-rays near the beam pipes precludes placing a small detector immediately surrounding the interaction point. A large detector some meters away from the beam pipe would be impracticable because of poor light collection ($\theta_c = 90^\circ$).

It may be possible to time the flight of a tachyon through limited-aperture Čerenkov detectors. However, Feinberg[1] states that a tachyon wave-function cannot be localized, and doubts that the concept of a measurable "velocity" can be applied.

It is not obvious whether tachyons can ionize atoms when $\beta \backsim \infty$, since the time spent in the vicinity of any atom approaches zero. Thus zero energy tachyons ($\beta \sim \infty$) may not show tracks in scintillators or track chambers.

It may be that only neutral tachyons exist.[2] In that case the only evidence would be through tachyon exchange processes, for example in Bhabha scattering, where a narrow sharp resonance would be observed at fixed $q^2 = \mu^2 < 0$, independent of beam energy.

REFERENCES

1. G. Feinberg, Phys. Rev. 159, 1089 (1967).
2. J. Dhar and E. C. G. Sudarshan, Phys. Rev. 174, 1808 (1968).
3. Alväger et al., Phys. Rev. 171, 1357 (1968), and M. Davis et al., Phys. Rev. 185, 1132 (1969).

4. Heavy Leptons

Heavy Lepton Signatures and Detection Requirements

The characteristic signature of relatively short-lived heavy leptons is the presence of one or more $e^\pm$ or $\mu^\pm$ in the final state. (Long-lived heavy leptons are treated elsewhere.) While hadronic decays may dominate for some heavy leptons, final states in which all of those produced decay to hadrons plus neutrinos are detectable only via thresholds. Other particles with substantial purely-leptonic decays (such as $W^\pm$ if by some chance they can be produced at PEP) may also be considered here.

The following subsections detail the requirements on acceptance, resolution, and particle identification, using specific assumptions for the production and decay of various particles. Ironically, the most serious background to the decay of any one heavy lepton (aside from excited heavy leptons, for which mass plots may be formed) could well be the decay of another new particle. Scans versus machine energy - to search for thresholds - may be the only feasible way to handle such a problem if it exists.

a) Excited Heavy Leptons. These may be produced in pairs, $L^*\bar{L}^*$, resulting in a final state $e^-\gamma\, e^+\gamma$ or $\mu^-\gamma\,\mu^+\gamma$. For a particle coupling to the photon, there will be $\simeq 10^4$ of these for an integrated luminosity $\mathcal{L}$ of 10^{38} cm^{-2} sec^{-1}, with a rapid turnon (slightly faster than β) above threshold. If the decay width is sufficient, production of pairs like $L^*\ell^+$ (resulting in one fewer final state γ) may also occur.

If these occur at the rate indicated, they should be obvious as threshold effects in their final states, and from $\ell\gamma$ mass peaks. (If one γ goes undetected in an $\ell\,\ell^+\gamma\gamma$ final state, there is still enough information to reconstruct the event.) We require good μ, e, and γ identification, with γ's over as close to 4π as possible. The presence or absence of hadrons and extra γ's should also be known over 4π, but determinations of hadron momentum, type and charge are not necessary. Energy resolutions of $\sim$10 - 15% are probably adequate; angular resolutions of 3 - 4° will then give comparable or smaller contributions to mass resolutions above 5 GeV. (If these L*'s exist at much lower masses, they should almost certainly be seen at SPEAR and DORIS.)

Requirements on hadron misidentification as μ's or e's are less stringent than for other types of heavy leptons. Even if all 2-prong hadronic

events ($< 10\%$ of total, according to Monte Carlo predictions[1]) were candidates for misidentification, one could have misidentification probabilities of $.1\sqrt{\sigma/\sigma_{\mu\mu}}$ ($\approx .1$ for pointlike production) and still have $< 1\%$ backgrounds without even using the mass-peak or γ-counting information. Ordinary QED backgrounds can be made negligible by requiring acoplanar leptons and staying away from 0°.

b) Charged Heavy Leptons (and $W^\pm$) in Purely Leptonic Decay Modes. We consider pair-produced charged heavy leptons which both decay by $L \to \nu_L(\ell\nu)$. If both e's and μ's are detected (this gives us four times as many events as if only one type were detected), point-like production implies ≥ 500 events (for integrated $L = 10^{38}$) in which the only detected particles are acoplanar $\mu^+\mu^-$, $\mu^\pm e^\mp$, or e^+e^-. Backgrounds arise from misidentifying two hadrons as leptons, and (for like leptons) from electromagnetic processes with undetected γ's. A 4π acceptance for γ's will suppress the latter background. Photon position and energy resolution are not important, but a good e-π discriminating detector will provide these anyway.

The presence of hadrons in an event needs to be detected over close to 4π. We will assume that the γ and hadron detection are sufficient that $\lesssim 20\%$ of 2-prong events can simulate the real signature if two hadrons are misidentified. (This estimate should allow for any escaping neutral hadrons.) Counting hadrons ≥ 3 GeV and using $R \leq 10$, then for misidentification probability λ, the background cross-section is $\leq .2\ \lambda^2\ \sigma_{\mu\mu}$, as compared to a signal of $.05\ \sigma_{\mu\mu}$ for pointlike production. Thus $\lambda < .15$ should allow clean identification of such processes. However, in order to study the nature of the process (and allowing an extra factor of 10 in case of suppressed production), one should aim for $\lambda \lesssim .01$. These limits should really be momentum-dependent; this will be discussed in the section on backgrounds. However, the numbers given are probably very conservative (Perl[2] picked out a signal with $\lambda \approx .2$ and far from 4π coverage on γ's).

With 500 events, we can begin to measure some of the properties of the new particles, such as type, mass, whether there is more than one, etc. Three handles on such properties are s-dependence, lepton momentum spectra, and lepton-lepton angular correlations. These methods are complementary, and all should be used.

Consider the lepton momentum spectrum. Figure III-2 shows a rest frame decay distribution for $L \to \nu_L(\ell\nu)$, assuming massless neutrinos. The two curves represent the standard (μ-like) V-A $L\nu_L$ coupling and a V+A coupling suggested as a possibility in certain gauge theory models.[3] The V+A case corresponds to a Michel parameter $\rho = 0$,[4] as opposed to the usual $\rho = 3/4$. A 2-body $\ell\nu$ decay of a $W^\pm$ or some other weakly-decaying boson of mass M would show as a δ function at M/2 on this plot.

In an arbitrary frame, normalized decay distributions for the 3-body decays are

$$dN = \frac{2}{\pi M^6}\frac{d^3p}{E}\, P \cdot p(M^2 + 2(P - p)^2) \qquad \text{V-A}$$

$$dN = \frac{12}{\pi M^6}\frac{d^3p}{E}\, P \cdot p(P - p)^2 \qquad \text{V+A}$$

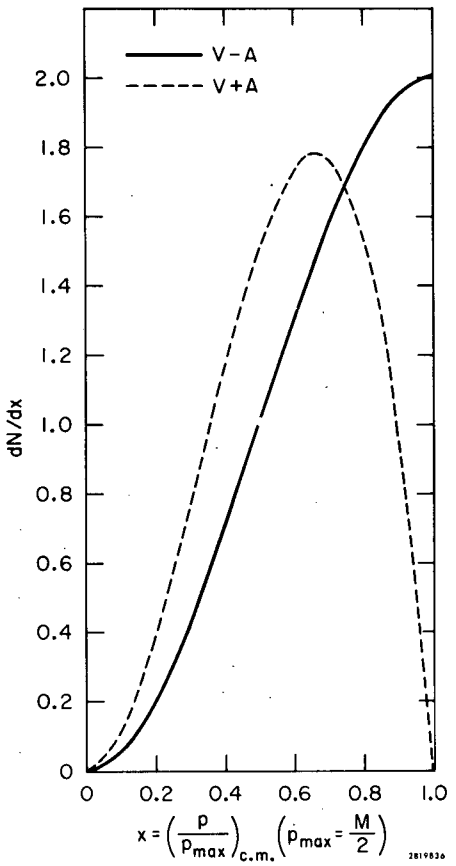

Fig. III-2 Lepton Distribution from Heavy Lepton Decay (M Rest Frame)

where P and p are the L and ℓ 4-momenta, and E is the ℓ's energy. For 15 GeV beams and three different values of M, the lab momentum spectra (assuming pair production) are shown in Fig. III-3/5. The 2-body decay of a pair-produced object gives rise

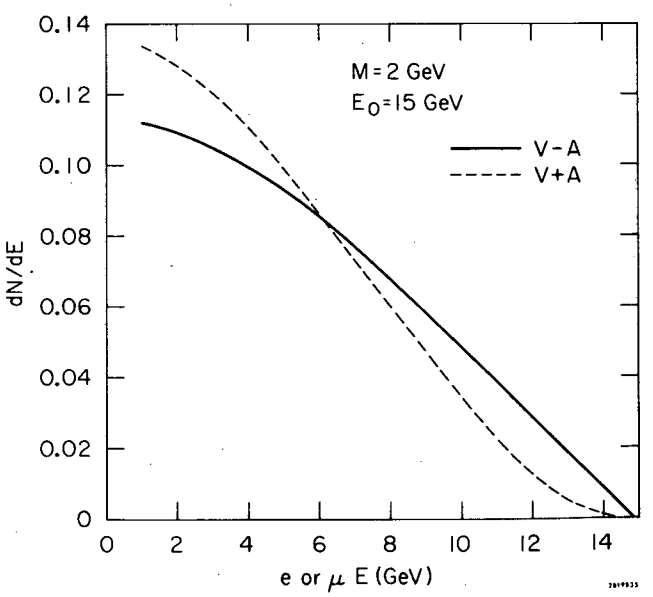

Fig. III-3 Lepton Distribution from Heavy Lepton Decay (Lab Frame) - $M_{HL} = 2\ \text{GeV}/c^2$, $E_{beam} = 15$ GeV

0 0 0 0 4 5 0 1 6 4 9

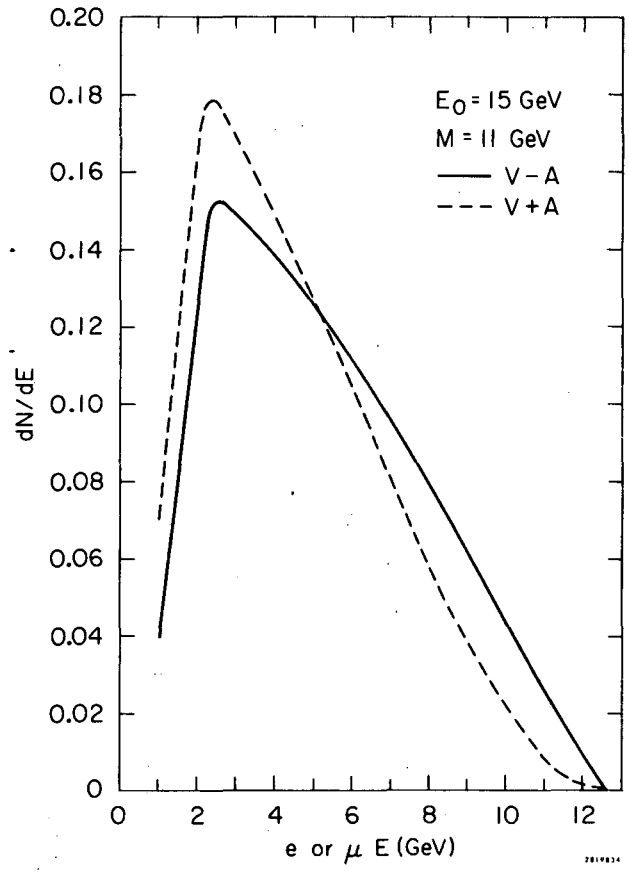

Fig. III-4 Lepton Distribution from Heavy Lepton Decay (Lab Frame), M_{HL} = 11 GeV/c^2, E_{beam} = 15 GeV

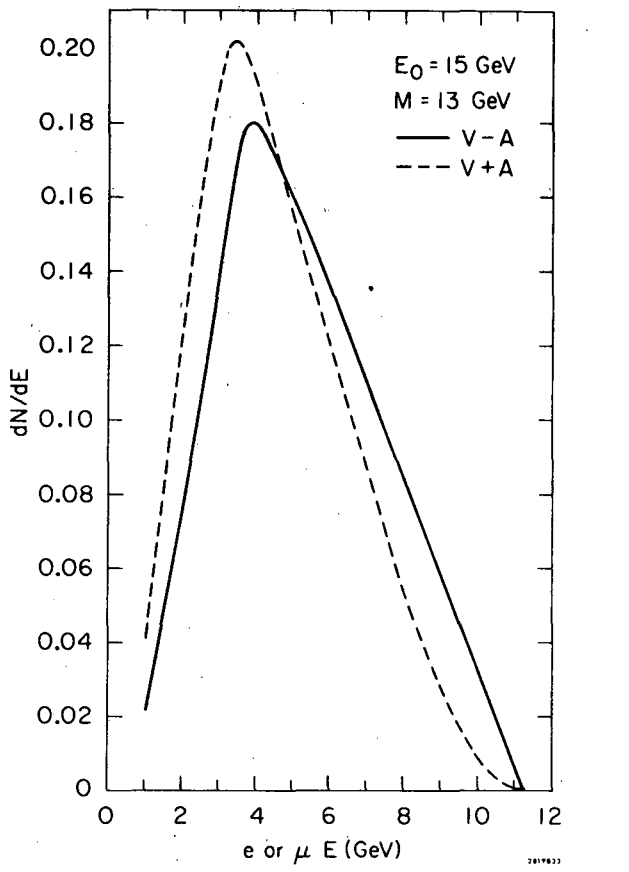

Fig. III-5 Lepton Distribution from Heavy Lepton Decay (Lab Frame) - M_{HL} = 13 GeV/c^2, E_{beam} = 15 GeV

to a flat spectrum between M-dependent kinematic limits. The distributions plotted were obtained by assuming 4π angular acceptance, and are thus independent of the L^+L^- production distribution. (The latter depends on the specific nature of the new particles - it is μ-like for "ordinary" L's - and also on transverse beam polarizations.) These spectra should be taken only as indications of the types of things a detector should be expected to sort out, and not as detailed predictions. For example, with M = 11 GeV, the V-A and V+A cases lead to ≈80 - 100 and 40 - 50 events above 8 GeV. With these statistics, momentum resolution $\Delta p/p^2 \approx$ .0075 can probably distinguish them adequately. However, it is clearly advantageous to have as good momentum resolution on e's and μ's as possible, especially at high momenta. For e's, a shower detector can provide an excellent 3% rms at 10 GeV (but a magnet must still give the sign).

Angular correlations between the decay leptons can probably provide even more information than momentum spectra, if biases are avoided. (Dependence on beam polarizations can also be used here, but not in distributions of single-L decays, since the average polarization of each L is zero.

To summarize the requirements:

(i) e and μ detection over as large a $\Delta\Omega$ as possible, for rate and to avoid biases.

(ii) γ and hadron detection over virtually 4π.

(iii) e and μ momentum resolution ($\Delta p/p^2$) rms ≤ .75% (and preferably $\Delta p/p$ < .05 at 10 GeV, at least for electrons); charges.

(iv) γ position and energy resolution not important.

(v) Hadron type and kinematic measurements necessary only crudely (or from other expts.?)in order to help understand backgrounds.

(vi) Hadron misidentification probabilities as μ's or e's of ≲.01 especially at high momenta.

(vii) Machine energy scans (if a signal exists at high S).

c) Charged Heavy Leptons with Hadron Decays. For pair production of pointlike heavy leptons, we can detect ≳2000 events (per 10^4 μμ) if we require only one purely leptonic decay (plus one decay to ν + hadrons). If leptonic branching ratios are much smaller than assumed this might be the only feasible detection method. (Certain types of gauge-theory heavy leptons may decay to states containing a μ or e (rather than a ν) + hadrons. These would be somewhat easier to detect inasmuch as final states would often contain two ℓ's.)

The requirements are similar to those in Section (b), with the following additions:

(i) Information on the identities and properties of hadrons may be useful; if we see the single-lepton signal, we will want to know what else is in the final state.

(ii) All hadronic events are now potential backgrounds. If we restrict our attention to momenta >20% of the beam energy, one expects[1] ~1 charged hadron/event, so that we need a hadron misidentification probability

$$\lambda \leq \frac{1}{10} \frac{.2\sigma_{\mu\mu}}{R\sigma_{\mu\mu}} \approx .002$$

for 10:1 signal noise. These backgrounds must really be considered vs. momentum. For convenience in background comparisons, Fig. III-6 shows the conventional (V-A) decay spectra of Figs. III-3/5 for all energies ≥E vs. E, normalized to $.2\sigma_{\mu\mu}$ times an appropriate threshold factor. (For heavy leptons decaying to e or μ + hadrons, a $\lambda \approx .004$ would allow us to study final state properties of a final state produced at the $.02\sigma_{\mu\mu}$ level.)

(iii) The signature of missing energy and momentum has been suggested, but the level of calorimetry needed to utilize this may not be feasible.

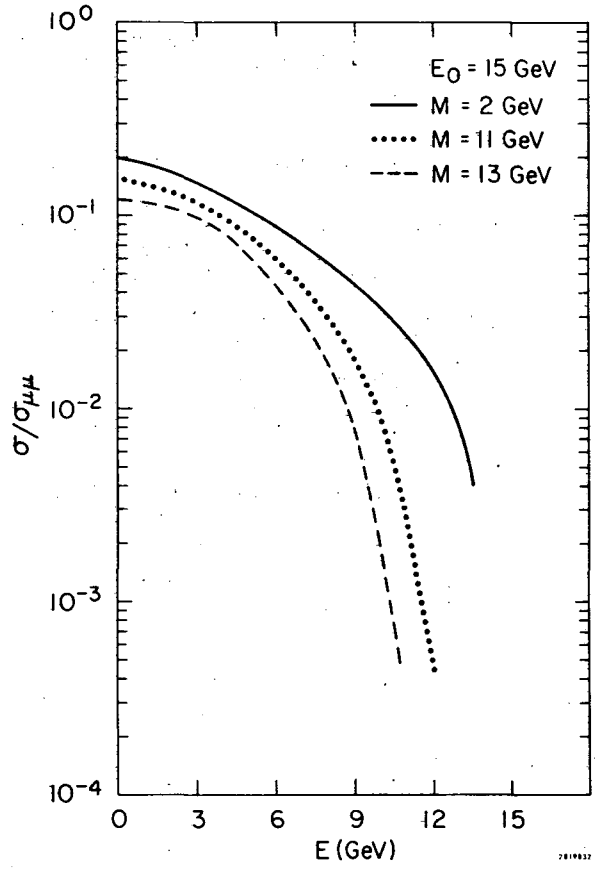

Fig. III-6 Cumulative Muons or Electrons at $p \geq E$ from $L_H \to \ell \upsilon \bar{\upsilon}$

d) Neutral Heavy Leptons (and Heavy Neutrinos)

Using the 1974 Summer Study's weak production estimates for single $L^o\bar{\nu}$) and pair production modes and decay branching ratios similar to those assumed for charged leptons, one can expect ≳50 and ≳20 purely leptonic events in these two modes, if these L^o's are of a type which couple to e's or μ's. The signatures are then 2 (acoplanar) or 4 charged ordinary ℓ's, respectively, with no other visible particles. The requirements including those on hadron misidentification needed to study charged heavy leptons (see subsection b) should be adequate to detect these decays. Because of the low rates, backgrounds from decays of other new particles are potentially a major difficulty.

For L^oL^o production, one can increase the sample considerably by measuring events in which either or both L^o's decay to μ or e + hadrons (if we can adequately handle the likely low-energy particles), and events in which one L^o decays leptonically and the other to ν + hadrons. All of these lead to final states with 2 ℓ's.

Certain other gauge-theory neutral leptons[3] will either decay to charged heavy leptons, or, if they're too light, may decay undetectably or not at all.

REFERENCES

1. G. Hanson, private communication.
2. M. L. Perl et al., to be published; M. L. Perl, SLAC-PUB 1592 (1975).
3. A. de Rujula, H. Georgi, and S. L. Glashow, to be published.
4. J. D. Jackson, in Elementary Particle Physics and Field Theory, Brandeis Summer Institute, 1962, W. A. Benjamin (1963).

5. Stable Charged Particles

We defined heavy stable changed particles as having the following characteristics:

1) $\tau > 10^{-8}$ sec, i.e., decay outside apparatus
2) M > 5 GeV. If they are lighter, assume they would have been discovered elsewhere
3) Charge of ±e, fractional charge will be discussed under the quarks section.

Without the additional signature of the fractional charge, the cross-section limits at proton accelerator and storage rings in $\sigma \lesssim 10^{-33}$ cm^2.[1] Hence though FNAL and the ISR have energies comparable to PEP, the proper combination of low production cross sections and hadronic backgrounds might mean that it is still possible that new heavy stable particles would be discovered at PEP.

The most sensitive region for searching for heavy stable particles is where their velocity is less than 0.5. In this region one can use a combination of TOF, range and simple lucite Čerenkov counters for identification. Particles with TOF differences greater than 1 nsec should be almost completely free of random background due to ~5 cm bunch length at PEP.

The mass resolution that one can obtain with separate momentum and TOF measurements assuming

0 0 0 0 4 5 0 1 6 5 0

negligible error in the momentum is

$$\Delta M = \frac{pc}{d} \frac{\Delta t}{\sqrt{1-\beta^2}}$$

where d is the flight path and c the velocity of light. If with micro-channel detectors one can achieve time resolution of 0.1 nsec, then over a flight path of 0.5 m for a 10 GeV particle with $p = 5$ GeV/c, $\Delta M = .34$ GeV/c^2.

More discrimination can be made by range measurements. For particles with $\beta = 0.5$, the range is $\sim(MH/Mp)25 gm/cm^2$, where M_h is the mass of the new heavy particle relative to the proton mass, Mp. If the new particle has no strong interactions or has an interaction length more than three times as long as the proton then there should be distinct range which can be seen in a segmented hadron calorimeter. Such a range measurement would also be a good cross check on the mass determination made by TOF.

A simple lucite Čerenkov counter with a threshold $\beta = 0.7$ would serve to reduce backgrounds from ordinary hadrons.

If the new particles have a lifetime in the range of 10^{-8} to 10^{-6} seconds, the observation of of a delayed coincidence due to a decay would be another extremely powerful means of identification of a new state.

It is most probable that these new heavy particles have quantum numbers such that they must be produced in pairs. Then in order to find these particles if their production cross-section yields a few events in an experiment with an integrated luminosity of 10^{38} cm^2, one must have a rejection probability of $\sim 3 \times 10^3$ on each particle which seems reasonable with the above techniques. To achieve 10^7 rejection on single particles in a nearly 4π geometry is not nearly so certain because the possibility of an unlikely combination of mismeasurement of the momentum and TOF. However, the presence of 5 to 10 events in a single 1 GeV mass bin would probably be identifiable above background.

REFERENCES

1. L. B. Leysuner et al., Phys. Rev. Lett. 31, 1226 (1973).
M. G. Albrow et al., submitted to Nucl. Phys. B, and A. Sessoms, private communications.
G. Giacomelli et al., Phys. Repts. 19C, 223 (1975).

6. Stable Neutral Particles

Long-lived neutral particles are very difficult to identify. If they only interact weakly (heavy leptons), their presence can only be deduced by the presence of missing transverse momentum. If calorimeters could be placed within ~10 mr of the beam as for the 2γ tagging detector, then missing transverse momentum of ≥ 1 to 2 GeV could be seen. The absence of electrons or muons accompanying the event would indicate that the missing transverse momentum was unlikely to be the result of ordinary neutrinos. In all probability such particles are more likely to be seen in neutrino experiments.

If the long-lived neutral particle had an anomalously low hadronic cross-section then its presence could be discovered by looking at the conversion depth distribution in a hadron calorimeter. An excess converting at larger than 5 neutron interaction lengths in time with the beam crossing would be an indication of such a new neutral particle. More refined calorimetry combined with TOF would in principle yield a mass determination.

7. Charmed Particles

Inclusive pair productions is the most likely source of charmed particles at PEP. Present estimates of charmed particle masses are 2 GeV $\lesssim M_c \lesssim$ 10 GeV with the lower limit in some trouble due to the nonobservance of charmed particles at SPEAR. Assuming the conventional decays into strange particles, the clearest signature involves strange particles associated with a single charged lepton (one charmed particle decaying semi-leptonically, the other decaying into hadrons). However, it is possible to construct models in which the strange particle decay is supressed. If this is indeed the case one is forced to look for peaks in invariant mass spectra associated with the other peaks or single leptons.

Taking cross-sections and multiplicities from PEP-140 we expect $\sim 7 \times 10^5$ hadronic events ($R \approx 6$) for an integrated luminosity of 10^{38} cm^{-2} with a mean charged multiplicity of ~7.5 charged particles/event. This gives $\sim 7.4 \times 10^6$ neutral 2-body mass combinations. Monte Carlo calculations give a combinatorial background of .7% (phase space model) and .5% (jet model) of the total combinations in a 50 MeV bin at M = 3 GeV. Thus we expect $\sim 5 \times 10^4$ background events/50 MeV at a mass of 3 GeV. This large background makes it unlikely that bumps in raw mass plots will be observed.

If we look at invariant masses associated with single charged leptons it is possible to supress the background by $\sim 10^3$ over a large solid angle ($10^{-4}\pi$/e rejections seem to be possible). Estimates of $\Gamma(c \to \ell\upsilon + \text{hadrons})/\Gamma(c \to \text{hadrons})$ range from ~10% to ~50%. For a semi-leptonic branching ratio of 25% we expect ~20% of the events containing charmed particles to have single $e^{\pm}$ signatures. If we assume inclusive charm production $\approx$ inclusive baryon production ($\sim$1000 events/10^{38} cm^{-2}) we can get a signal-to-noise ratio of ~1/1 at a mass of 3 GeV with a mass resolution of $\Delta M = \pm 50$ MeV.

Thus we need good mass resolution $\Delta M \sim .01M$ and good hadron/lepton rejection $\sim 10^{-4}$ if charmed particles are to be found at PEP with 1/1 signal noise ratios in 2-body mass distributions. Similar conclusions hold for decays to higher multiplicity final states.

8. Scalars

The Higgs scalar meson[1] is suggested in gauge theories. It may be found in e^+e^- collisions, in pairs via one-photon electromagnetic interactions, or singly via 2γ or weak interactions. In either case, the rates are expected to be low, of the order of $.01\sigma_{\mu\mu}$. The decay will be electromagnetic, so the width ought to be small. Experimentally the signatures would be: (1) a sharp peak in the total cross-section as a function of center-of-mass energy, but on top of a substantial background (expect for the longitudinally-polarized

beams case, where the ordinary electromagnetic processes are supressed); and (2) a peak in the missing-mass spectrum for the 2γ events $e^+e^- \rightarrow e^+e^- + X$.

REFERENCE

1. P. Higgs, Phys. Rev. Lett. 13, 508 (1964).

9. Neutral Vector States

We classify neutral $J^{PC} = 1^{--}$ states with the following notation:[1]

a) high mass vector mesons (ρ''',ψ''',) which have small coupling to $e^+e^-(\mu^+\mu^-)$;
b) heavy photons (B^o), having a large coupling to e^+e^-;
c) neutral currents, Z^o [2]; and
d) vector gluons.[3]

The states (exclusive of SU(3) singlet gluons) couple directly to $e^+e^-/\mu^+\mu^-/qq^-$, and can potentially appear as an enhancement in σ_{ee}^{tot} or $\sigma_{ee \rightarrow \mu\mu}$ at the resonance mass, $S = M^2$. Local variations in the charged/neutral ratio, baryonic or strange particle yields, average momentum $\langle p \rangle$, and jet structure in the hadronic decays provide signatures for those states with significant hadron widths.

The heavy photons, coupling strongly to e^+e^-, $\mu^+\mu^-$, produce deviations from QED in $e^+e^- \rightarrow e^+e^-$ and $e^+e^- \rightarrow \mu^+\mu^-$ reactions. Neutral current effects are probably best studied looking for $\gamma - Z^o$ interference with or without longitudinally polarized beams.[4] Possible particle signatures and cross-sections are summarized in Table III-2.

Many of the above states may also be produced with other particles, for example

a) gluons 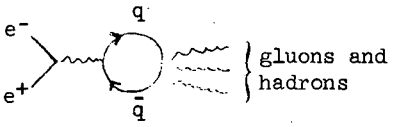

and b) heavy photons, vector mesons (in 2γ geometry):

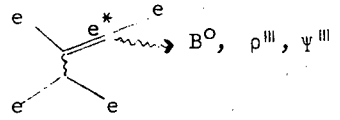

where e^* is an excited electron. In these cases the resolution of the detector may well be the limiting factor in observing these states.

REFERENCES

1. For a general description see D. Berley et al., 1974 PEP Summer Study, p. 450 (1974).
2. S. Weinberg, Phys. Rev. Lett. 19, 1264 (1967); A. Salam, in Elementary Particle Theory, edited by N. Svarthohm (1968); J. D. Bjorken, C. H. Llewellyn Smith, Phys. Rev. D7, 887 (1973).
3. C. H. Llewellyn Smith, Phys. Rev. D4, 2392 (1971); H. Fritzsch, M. Gell-Mann, H. Leutweyler, Phys. Lett. 47B, 365 (1973); M. S. Chanowitz, S. D. Drell, Phys. Rev. Lett. 30, 807 (1973).

TABLE III-2

POSSIBLE SIGNATURES OF NEUTRAL VECTOR STATES

CHARACTERISTIC PROPERTY	ρ''',ψ''''	B^o	Z^o	VECTOR GLUONS
LEPTONIC DECAYS	Γ_{ee},$\Gamma_{\mu\mu}$ small	Γ_{ee},$\Gamma_{\mu\mu}$ large	Γ_{ee},$\Gamma_{\mu\mu}$ significant	small if SU(3) singlet
HADRONIC DECAYS (LOCAL CHANGES IN σ^{TOT}, R, CHARGED/NEUTRAL RATIO, $\langle p \rangle$, etc.	$\Gamma_{HADRONS}$ large	small	$\frac{\Gamma_{had}}{\Gamma_{ee}} \approx R \times \frac{\sigma^{NC}}{\sigma_{CC}}$	$\Gamma_{HADRONS}$ large
JET STRUCTURE OF HADRONIC DECAYS	Prob. different from off resonance	------	------	Prob. different from off resonance
EFFECTS QED TESTS	no	yes	no	no
LONGITUDINAL POLARIZATION EFFECTS	no	no	yes	no
ESTIMATED $\left(\frac{\sigma_{ee \rightarrow x}}{\sigma_{ee \rightarrow \mu\mu}}\right)$	~ 1 (depends on total width)	~ 1	~ α	?

0 0 0 0 4 5 0 1 6 5 1

4. C. H. Llewellyn Smith, D. V. Nanopoulus, Nucl. Phys. B78, 205 (1974); Report of Longitudinal Polarization Group, PEP 1975 Summer Study.

10. 2γ Production

In the search for pseudoscalar and scalar $c = \pm 1$ objects which can be generated by the 2-photon production process one important signature is a state consisting only of a tagged e^+e^- and a neutral boson decaying into γ's, π^o's, or η's:

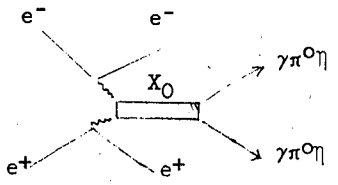

The mass range accessible at PEP for observing a significant effect in 2γ final states with the proposed 2γ tagging systems (see γ-γ group report) is

$$.62 \text{ GeV} < M < 5.0 \text{ GeV} \qquad \text{at } E_e = 15 \text{ GeV}$$

In setting this limit a significant effect was defined to be at least 25 events signal in a $\mathcal{L} e^+e^- = 10^{+38}$ cm^{-2} run and a signal-to-noise ratio greater-than or equal-to 1. These resonances are likely to be of the order of 10 KeV in width. In the calculation of the observable cross sections it is estimated that the measuring apparatus discussed at the Summer Study would be capable of better than 1 GeV resolution in invariant mass of the photon pair over this mass range.

The backgrounds for such resonance production would arise from the 300 mb 2-photon cross-section (as opposed to the much smaller single photon cross-section) from two sources:

1. Events in which the 2-photon process gave rise to a number of π^o's, two of which were identified.
2. Events in which one photon from each of two π^o's is lost, giving rise to a false 2-photon signature.

It has been assumed that the mass spectra arising from such false signatures would be uniform and that the dominant process would be 2 because of the expected momentum spectrum of the π^o's and the angular resolution for resolving separated showers in the liquid-argon type detector.

With these assumptions the ratio of signal-to-background behaves as shown in the following table:

Table III-3

Mass (GeV/c²)	Signal	Background	Ratio
.7	775	33	23.5
1.0	905	78	11.6
2.0	267	92	2.9
4.0	52	72	.72
5.0	25	53	.47
6.0	13	40	.33

where for pseudoscalar or scalar resonances

$$\sigma_{\gamma\gamma} dw = \frac{4\pi^2}{M^2} (2J+1)\Gamma_{\gamma\gamma} \qquad (\Gamma_{\gamma\gamma} \sim 10 \text{ keV}, J=0)$$

and the approximation

$$\text{signal} = \frac{4\alpha^2 E}{\pi^2 \sqrt{(E-E_1)(E-E_2)}} \left(\ln \frac{\theta max}{\theta min} \right)^2 \cdot \frac{1}{2} \ln \left(\frac{E-E_1}{E-E_2} \right) \cdot$$

$$\cdot 10^{38} \text{ cm}^2 \cdot \int \sigma_{\gamma\gamma} dw$$

has been used to calculate the signal

$$\left(w = 2\sqrt{(E-E_1)(E-E_2)} \right) .$$

11. Search for New Particle States at a Single Beam Energy (Compton Production)

The radiation of a hard photon by an electron or positron before annhilation into hadrons provide a method for searching for $J^{pc} = 1^{--}$ resonances over a large mass range at a single beam energy.

The process considered is shown kinematically below:

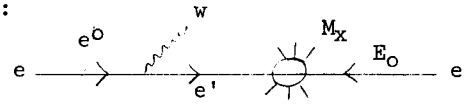

The corresponding Feynman diagram is:

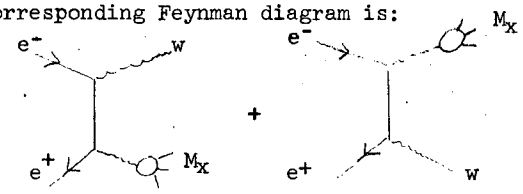

This process is clearly reduced by a factor α relative to the normal single-photon annihilation.[1] However, the annihilation cross-section to be considered is at the reduced value of $S' = M_X^2$ and hence considerably larger than at $S_o = 900$ GeV^2.

The spectrum of hard photons recoiling against the mass M_X should show corresponding structure. The kinematics are shown below:

$$S_o = 4E_o^2 \; ; \quad E' \equiv \chi E_o$$

$$S' = M_X^2 = 4 E_o E'$$

$$= 4\chi E_o^2$$

$$= \chi S_o \; .$$

Thus $$\chi = M_X^2 / S_o' \; .$$

The photon energy spectrum is

$$E_\gamma = w = E_o - E' \; .$$

$$= (1-\chi)E_o = \left(1 - \frac{m_X^2}{S_o}\right) E_o \; .$$

The limits are:

$$E_\gamma = 0 \qquad \text{when } M_X = 2E_o$$

and $$E_\gamma = E_o \qquad \text{when } M_X = 0 \text{ , i.e., a photon.}$$

Unfortunately, the range $0 < M_x < 9.5$ GeV is all compressed into the region 15 GeV $< E_\gamma <$ 13.5 GeV, for $E_o = 15$ GeV. However, even though the resolution is mass for any realistic photon energy-resolution is likely to be terrible, the advantages of a crude mass-search at a single beam energy are considerable.

The cross-section is expected to be of the form[2]

$$\frac{d\sigma}{dx} = E_o \frac{d\sigma}{dw} = G(x)\sigma(S')$$

where $G(x)$ is the probability of finding an electron or positron of fractional energy x, and $\sigma(S')$ is the normal hadronic cross-section at $S = S' = xS_o$.

$$G(x) = 2\frac{\alpha}{\pi}\left[\ell n\left(\frac{E_o}{Me}\right) - \frac{1}{2}\right]\frac{(1+x^2)}{(1-x)} \quad .$$

Thus

$$E_o \frac{d\sigma}{dw} = \frac{\alpha}{\pi}\left[\ell n\left(\frac{S_o}{Me^2}\right) - 1\right]\frac{(1+x^2)}{(1-x)}\,\sigma_{ee\to hadrons}(S')$$

The $\ell n(S_o/Me^2)$ term comes from the integration over very small angles of emission of the photon. Assuming for the moment that these photons can be detected down to $\theta_\gamma \sim 0$, we can evaluate the logarithim at $S_o = 900$ GeV^2.

$$\frac{\alpha}{\pi}\left[\ell n\,\frac{900}{Me^2} - 1\right] \sim 0.051$$

and expressing

$$\sigma_{hadronic}(S') = R(S')\sigma_{\mu\mu} = R(S')\,\frac{88\text{nb}}{S'(\text{GeV}^2)}$$

we get

$$\frac{d\sigma}{dw} = \frac{0.051}{E_o}\frac{(1+x^2)}{1-x}R(M_x^2)\cdot\frac{88}{M_x^2}\ \text{nb GeV}^{-1}$$

$$= 0.3\,\frac{(1+x^2)}{1-x}\,\frac{R(M_x^2)}{M_x^2}\ \text{nb GeV}^{-1}$$

If we take the example of the $\Psi(3100)$, where $R \gtrsim 100$,

$$\frac{d\sigma}{dw} = 0.3 \cdot 1 \cdot \frac{100}{9.6}\ \text{nb GeV}^{-1}$$

$$\cong 3\ \text{nb/GeV} \qquad \text{at the peak.}$$

This, of course, assumes a good mass resolution as in the original Ψ experiment. With a resolution of about 500 MeV/c^2 the effective value of R is reduced to about 2 and thus the Ψ would be lost in the background. The mass resolution is given by

$$\frac{\Delta M_x}{M_x} = \frac{2E_o w}{M_x^2}\,\frac{\Delta w}{w}$$

and improves rapidly with M_x so that prominent high mass resonances around 10 GeV/c^2 will stand out. The only background giving high energy tagging photons is $e^+e^- \to \pi^o X$, since Bhabha scattering is eliminated by requiring a neutral "tag" and a hadron signature in an apparatus like the 2γ system.[3] If we consider the π^o inclusive spectrum scaled from SPEAR, we expect 60 events/10^{38} cm^{-2} at $p_{\pi o} > 13.5$ GeV/c.[4] This corresponds to an average cross-section in the range 13.5 GeV - 15.0 GeV of $\sim 0.4 \times 10^{-36}$ cm^2/GeV, and is presumably isotropic.

The problem remains of tagging at 0°. If the smallest angle possible is 10 mr, as the 2γ case, the gain due to $\ell n\,(S_o/M_e^2)$ is lost. However, enough sensitivity is probably retained in looking for prominent resonances such as the Ψ, Ψ', etc. Integrals over photon angular acceptances need to be evaluated before the sensitivity can be established.

REFERENCES

1. The reduction is not α^2 as in PEP-174, p. 17.
2. Stan Brodsky, private communication.
3. 2γ Process Report, PEP-175.
4. See PEP-146 in 1974 PEP Summer Study.

IV. HADRONIC BACKGROUND TO LEPTON SIGNALS

1. Introduction

The rejection needed for lepton experiments at PEP depends on exactly which type of new particle one is hunting. For pair production in which both leptons are observed, signals $\gtrsim .01\ \sigma_{\mu\mu}$ might be expected. For single lepton experiments the level might be $\gtrsim .1\ \sigma_{\mu\mu}$. In both cases one is dealing with lepton momentum spectra that fall rapidly with momentum. Furthermore to determine the mass of such leptons one wants to run near threshold where the signal is supressed by an additional factor. Also signals from the leptonic decays of new hadrons could be at a lower production cross-section with momentum spectra that peak at lower momenta due to the multi-hadron final state in a semileptonic decay. Reduction of backgrounds to $\sim 10^{-2}\ \sigma_{\mu\mu}$ seems to be a reasonable goal for the single lepton experiments. This implies that a background rejection against pions and kaons $\sim 10^3$ is required. Figure IV-3 shows this background level at s = 900 and the integrated lepton yield from the decay of either of a pair of m = 11 GeV heavy leptons. For the two-lepton + unobserved ν's signature a considerably lower rejection $\sim 10^2/\pi$ should be sufficient.

2. Misidentification of Hadrons as Electrons

Rejection against charged pions can be achieved using the following techniques:

a) p = E (Momentum of particle = Energy of particle deposited into a total absorption electromagnetic shower counter.)
b) Shower growth - pion showers (hadronic cascades) in shower counters have different radial and longitudinal distributions than electron showers.
c) Cerenkov - pions below threshold (~5 GeV) do not give Cerenkov light in atmospheric

0 0 0 0 4 5 0 1 6 5 2

pressure N_2 counters $(n - 1) = 3 \times 10^{-4}$.

d) Transition radiation - pions give much less transition X-ray yield than electrons.

The last technique has been developed to the point where a rejection of 10 can be achieved in a 50 cm long module.[1] These modules are independent and can be stocked but the length required is excessive for use in or around a solenoid.

Čerenkov counters are very cheap and easy to operate. A 50 cm thick atmospheric pressure counter could give a sufficient yield. The principal problems are:

a) The low pion threshold $(n - 1) = 3 \times 10^{-4}$ means that if $p_\pi > 5.6$ GeV they will be a background. Below this momentum, π/e rejections of $\sim 2 \times 10^3$ have been achieved in experiments.[2]

b) Showers and δ rays (made in a solenoid coil) allow below-threshold π's and K's to be counted as e's. A highly-segmented counter can significantly reduce the shower problem.

These are sufficiently annoying for us to not consider them any further.

A combination of p = E and shower growth criteria appears to be the best way to achieve the necessary background rejection. Neither technique is sufficient in itself. A simple p = E requirement can only give a rejection of 10^2 against charged pions. Shower growth criteria can have a rejection of 10^3 against π's having p = E. This rejection power diminishes for pions of p > E. There is an additional background coming from a charged particle entering the shower counter in the same region as an energetic gamma ray. Requiring p = E and dividing the counter into small solid angle segments can eliminate this background. Several different combinations of counters can be used to give this rejection. For example, see Fig. IV-1.

a) A system consisting of 3 radiation lengths of lead glass in one block followed by 15 radiation lengths in a second block achieved a rejection of $\gtrsim 10^3$ on p = E plus shower growth criteria.[3] This was done without a passive converter (solenoid coil) in front. (The division of material into the two block was not ideal, more tests could improve the rejection power).

b) A system consisting of a simulated solenoid coil (~ 0.7 radiation length) a 1/4" scintillator, a 1-radiation length lead sheet, a second 1/4" scintillator, and then a lead-glass block has been tested to give a pion rejection $\sim 10^3$ for 2 and 4 GeV/c pions using p = E and shower growth criteria. This test indicates that system (a) is probably viable when a solenoid coil is present. The $\Delta E/E$ is not severely degraded by the presence of the coil and additional counters. At 2 GeV/c the lead-glass resolution after a simulated coil was measured to be $\sigma = 5.3\%$.

c) A system consisting of segmented lead-liquid argon shower counter is potentially the most promising. It seems reasonable that appropriate shower growth criteria would give rejections better or equal to those in the systems studied above. However, there doesn't seem to be any available data yet. Furthermore, the cost of lead-liquid argon shower counters has been estimated to be 1/3 - 1/2 and the overall thickness 1/2 - 3/4 of lead-glass systems.

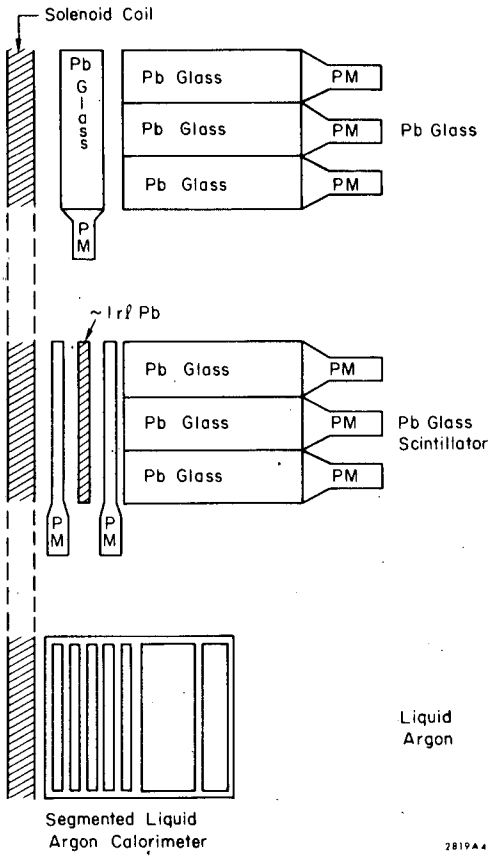

Fig. IV-1 Three Types of Electron Identification

Therefore for the function of electron identification the best system appears to be (if proponents are right) a lead-liquid argon calorimeter. To completely contain the shower a length of 15 - 18 radiation lengths would be required (~ 35 cm). It should be segmented into a least two but preferably more longitudinal segments. The criteria for segmentation in the transverse direction are normally dictated by the spatial resolution required for γ rays. (This is discussed elsewhere.) For the purposes of electron identification one wants a low probability of having another charged track or photon in the same region. Assuming a charged multiplicity of 7 and a π^0 multiplicity of 4 gives ~ 15 particles/event. A requirement of $< 5\%$ overlap in an isotropic model suggests that the solid angle be subdivided into ~ 300 pieces.

π^0 Dalitz decays and the conversion of γ's from π^0's are an additional contribution to the electron background. A typical apparatus will be interested in electrons of momentum $p > p_e$ and sensitive to electrons of $p > p_L$. The background comes from these cases where $\gamma \rightarrow e_1 + e_2$ and $p_{e1} > p_e$ and $p_{e2} < p_L$. Pe will typically be several GeV/c. P_L would pessimistically be ~ 2 X maximum transverse momentum of a trapped particle ($\sim .3$ GeV/c). (Trapped particles are those whose radius of curvature is less than 1/2 the solenoid radius.) For $p_{e2} > p_L$ we observe two oppositely charged electrons with 0° opening angle. If they come from a conversion they will verticize away from the interaction region.

To estimate this background we can do a calculation at 90° to the axis of the solenoid. The

probability of a π^o of energy p_o giving a background pair after assuming a conversion or Dalitz decay is:

$$\text{Prob.}_{p_L,p_e} \sim \int_{\min(p_e,p_o)}^{p_o} \frac{dp_\gamma}{p_o} \min\left(\frac{p_L}{p_\gamma}, 1 - \frac{p_e}{p_\gamma}\right)$$

$$\text{for } p_e < p_o \sim \frac{1}{p_o}\left[\min(p_L, p_o - p_e) - p_e \ln \frac{\min(p_L+p_e, p_o)}{p_e} + p_L \ln \frac{p_o}{\min(p_L+p_e, p_o)}\right]$$

This function is shown in the Fig. IV-2. The fact that p_L has a low value results in a strong suppression of this background. The value of p_L = .5 is equivalent to p_L = .3 at an angle of 37°. As one goes to decays that are further forward the background becomes worse for a fixed minimum detectable transverse momentum. This suggests the use of additional electron detectors in the solenoid to cover small angles. It also says that the background is liable to be lowest near 90°.

If we assume that π^o production is given by

$$S\frac{d\sigma}{dx} = 1.5 \times 10^4 \, e^{-7.4x} \text{ nb - GeV}^2 \qquad (x < .5)$$

and

$$S\frac{d\sigma}{dx} = 2.1 \times 10^3 \, (1 - x)^{2.5} \text{ nb - GeV}^2 \qquad (x < .5)$$

If $\sigma_{\pi^o} = \sigma_{\pi^\pm} = 0.5\sigma$ charged (a pessimistic assumption), and we compare the ratio of the Dalitz background cross-section to $\sigma_{\mu\mu}$ at s = 900 GeV^2,

$$\text{then} \quad \frac{\sigma_{p_L=3,p_e}}{\sigma_{\mu\mu}} = .012 \cdot \int_{p_o}^{\infty} \frac{1}{\sigma_{\mu\mu}} \frac{d\sigma}{dp_o} \text{Prob.}_{p_L,p_e} \, dp_o \cdot$$

The amount of background from conversions depends on the thickness of the vacuum pipe. A 200μ stainless pipe is .011 radiation lengths. In this case the conversion background from the pipe is roughly equal to the Dalitz background.

The above conversion background can be almost entirely eliminated if the following configuration is used:[2]

1. Place a MPWC or drift chamber immediately after the beam pipe.
2. Follow it with a highly segmented scintillation counter which is used to measure dE/dx.

Then we require the presence of a signal in the chamber and that the pulse height in the scintillator be < 1.5 minimum ionizing. Thus a

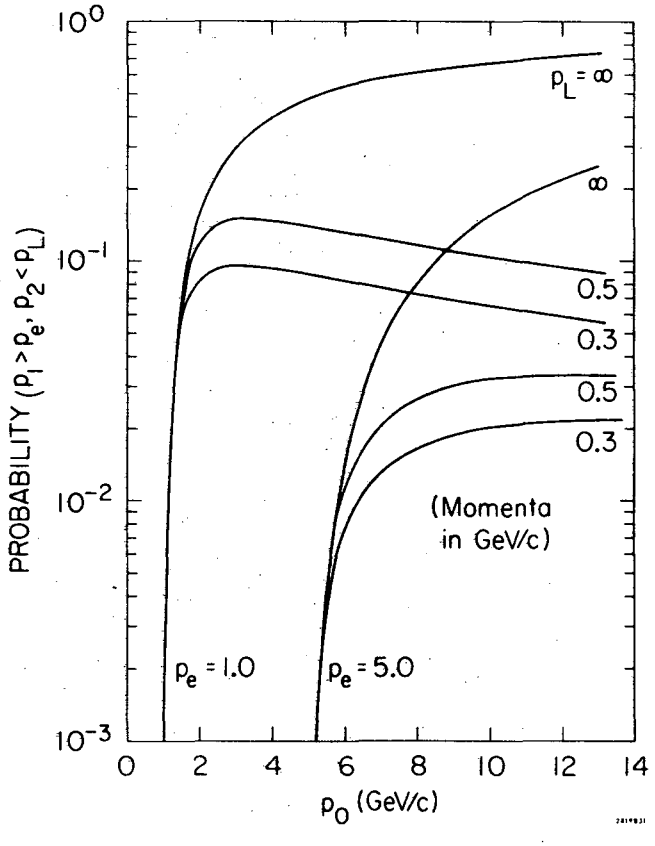

Fig. IV-2 Probability of Neutral Pion Giving Background Electron (Conversion and Dalitz Decay)

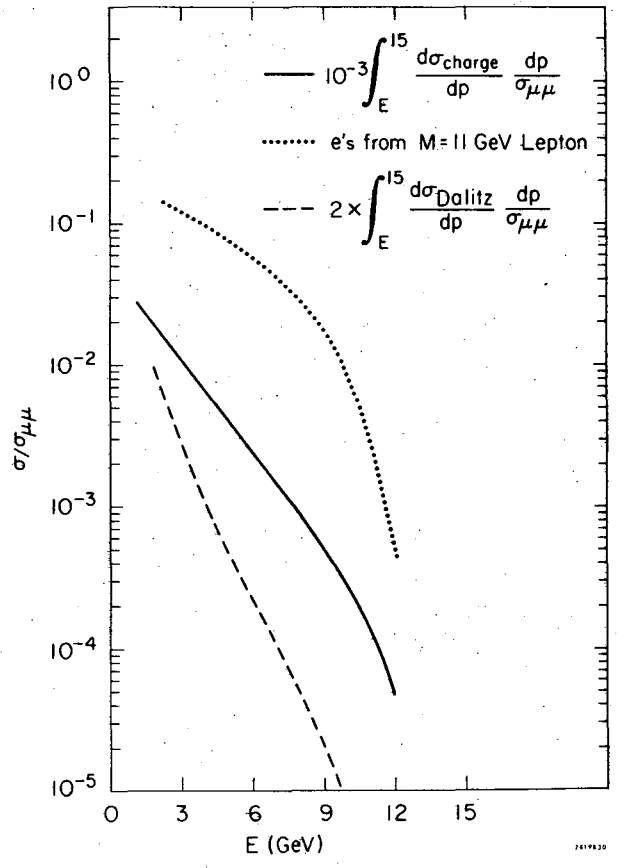

Fig. IV-3 Electron Backgrounds and Typical Signal for $E_e \geq E$

0 0 0 0 4 5 0 1 6 5 3

conversion in the pipe or chamber is rejected for pulse height and the conversion in the scintillator is rejected because there is no track. Real single electrons pass both cuts except for the $\lesssim 1\%$ that start to shower or give a δ ray in the pipe or chamber. Even if the finely divided counter is too much of a luxury for a given experiment the chamber should be retained for rejection of conversions after the beam pipe.

Thus the Dalitz and conversion background can be kept below the level of the pion background assuming a rejection of 10^3.

This is shown in Fig. IV-3 where we assume that the conversion background is equal to the Dalitz decay background and that the kaon background rejection (charged K's simulating e's) is no greater than the pion background rejection. Other backgrounds such as leptonic K decays are also well below this level if scaling holds.

3. Misidentification of Hadrons as Muons

A hadron can be misidentified as a muon by two mechanisms: Hadron decay (primarily the two-body decay modes of charged π's and K's), and hadron simulation of a muon signature. We will consider only energies ≥ 3 GeV, and assume that muon-hadron discrimination is to be done in a layered absorber + detector arrangement. For example, a muon signature might be a minimum-ionizing signal in each of a number of scintillator planes. Muons of $\gtrsim 2$ GeV should remain minimum-ionizing through a typical absorber of 1 meter of iron. Crudely, the signature misidentification (punch-through) probability is e^{-n}, where n is the number of inelastic interaction lengths for a typical hadron (i.e., a pion). We should choose n so that this contribution to false μ's is a bit smaller than that from decays. Another possible detector would use mean scattering angles in the iron (measured by chambers); n still would mean the number of 1/e rejection lengths. In any case, one requires adequate sampling to catch hadron interactions; and adequate angular segmentation, to avoid excessive μ detection inefficiency caused by occurrence of a hadron and a μ in the same segment. (Detailed design will be discussed elsewhere.)

Decay misidentifications will almost entirely be due to $\pi^{\pm} \to \mu^{\pm}\nu$ and $K^{\pm} \to \mu^{\pm}\nu$. Ignoring lab frame momentum-energy differences (even at 3 GeV, $p_K \simeq E_K$ to $< 1.5\%$), for a hadron energy E_h, the lab muon spectrum is uniform from $.574\ E_h$ to E_h for π decays and from $.044\ E_h$ to E_h for K decays. We will consider the two extreme cases of decays before and after momentum analysis. It seems unlikely that most decays occurring midway in the momentum analyzing device would be spotted as decays, so that case is intermediate.

If the decay occurs before or early in momentum analysis, then the background at E_μ GeV is due to hadron decays to E_μ from $E_h \geq E_\mu$. If the decay occurs effectively after momentum analysis, then the background is due to hadrons of $E_h = E_\mu$. Because the latter background would be larger than the other, even a 15 - 20% remeasurement of the muon's momentum (using magnetized iron) could be helpful, especially for K decays.

In order to estimate decay backgrounds we will use the naive thermodynamic expectation that high-energy π and K spectra are the same; and assume that both are obtained by scaling the inclusive charged hadron distributions from SPEAR energies. A parametrization good to $\simeq 10\%$ for $X = E/E_o$ up to $\simeq .8$ (E_o = beam energy) is then

$$S\,\frac{d\sigma}{dx} = 15\ e^{-7.4x}\ \mu b \text{ - } GeV^2$$

for π's and K's separately (but summing both charges)*. Most models do not predict as high a fraction of K's, so the thermodynamic assumption probably represents a worst case.

If momentum measurements are made only before decays, K's contribute 4.7 times as many μ's as do π's at given apparent E_μ (including factors for decay rates at the same $E_h = E_\mu$, and the $K \to \mu\upsilon$ branching ratio). Actually, the K contribution at low energies is somewhat reduced because muons of $\lesssim 1$ GeV or so will range out. At $E_o = 15$ GeV, one obtains (per meter of decay path):

$$\left(\frac{d\sigma\mu}{dx}\right)_{1\text{ meter}} = \frac{.103}{E_o x}\,\frac{d\sigma_\pi}{dx} = .114\,\frac{e^{-7.4x}}{x}\ nb \qquad (x \lesssim .8)$$

The fraction of misidentified hadrons (π's + K's) is thus $.0034/x$ at $E_o = 15$ GeV. This is a rather large 1.7% at 3 GeV (but more like 1.2% if we exclude ranged-out μ's), .7% at 7.5 GeV, and .4% at 12 GeV.

On the other hand, if the μ momenta are measured, the K contribution at a given $E_\mu > 8.6$ GeV is 2.1 times the π contribution (since K's spread their μ's over a wider energy range than do π's); at lower E_μ, the ratio becomes somewhat larger, because the highest-energy π's can no longer contribute. Under the same assumptions for the π and K spectra, the muon momentum distributions for a 1 meter decay path are as shown in Fig. IV-4. The total background is for this case only .6% of the hadronic yield at 3 GeV, .16% at 7.5 GeV, and .06% at 12 GeV.

In order to better illustrate the results, Fig. IV-5 shows the cumulative background spectra for $E_\mu > E$ for both cases, normalized to $\sigma_{\mu\mu}$, the QED μ-pair cross-section ($\simeq .096$ nb at 15 GeV). The low-E gains due to muon ranges in the first case are not included. Also shown is an expected spectrum for the $\mu\nu\nu$ decay of either of a pair of 11 GeV point-like heavy leptons. (A branching ratio of 10% is assumed, so that, including a threshold factor, these muons are produced with a total cross-section of $.13\ \sigma_{\mu\mu}$.) The signal-to-background ratio looks adequate above 3 GeV. However, a higher-mass heavy lepton will lead to fewer high-momentum μ's, and another type of new particle might have an appreciably smaller total signal.

Realistically, the actual background curve for a solenoid with external μ identification will lie somewhat below the upper curve in Fig. IV-5, perhaps 1/3 of the way toward the solid curve. (It will lie lower still if our conservative K production assumption proves to be too high.) Nevertheless, it seems desirable to do better for the detection of certain types of new particles via a

* The more correct parameterization given in the previous section has been used at $x \geq .8$, the only region in which it matters.

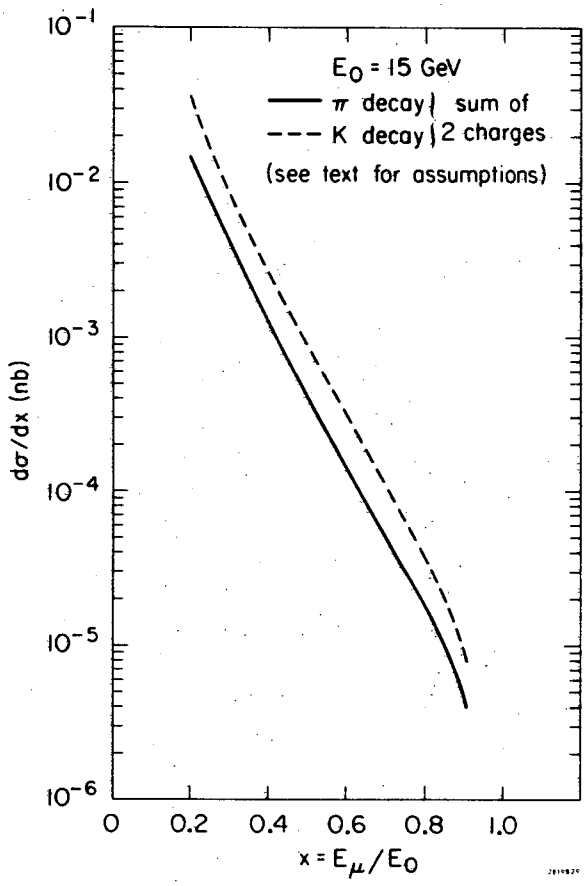

Fig. IV-4 Muon Momentum Spectra from Meson Decays (1 Meter Distance - See text for assumptions)

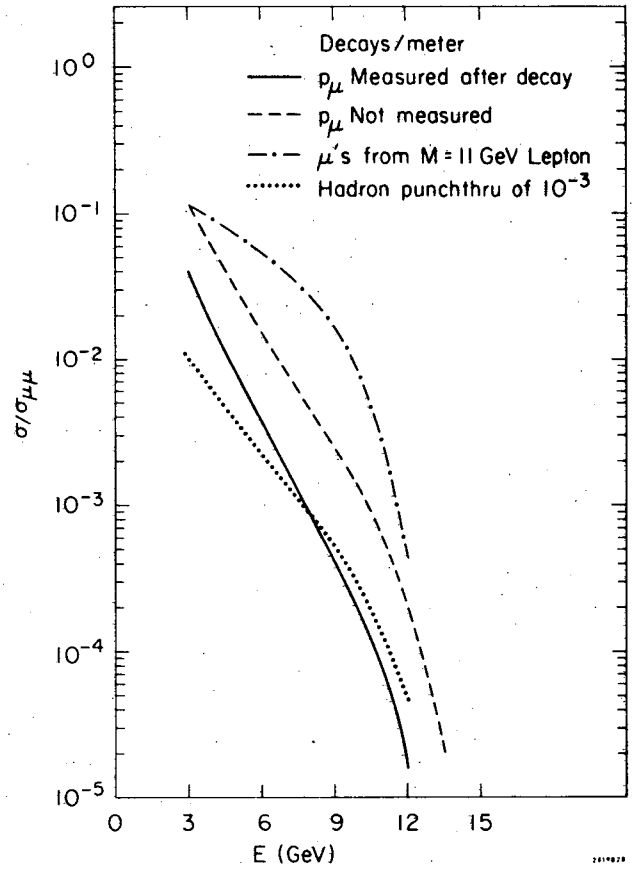

Fig. IV-5 Muon Backgrounds and Typical Signal for $E_\mu \geq E$

single-muon (+ hadrons) signature. One way to do better is to roughly remeasure the μ momentum using magnetized iron. Another way is to shorten the decay path by beginning μ-hadron discrimination as close to the interaction region as possible. (See the section on detectors for suggested methods. This has the disadvantage that the resolution needed for studying less difficult signatures may not be achievable.)

In order that the punch-through background be no greater than the decay background up to about 11 - 12 GeV, this requires $e^{-n} \lesssim .002$, or $n \approx 6$. If this is the number of pion inelastic interaction lengths, ~ 1.35 meters of iron is needed. Punch-through of 10^{-3} has been indicated in Fig. IV-5. (If one believes that for any of the reasons given above, the decay background will in fact be lower, then one should probably design n = 7.)

Finally it should be noted that for beam energies $E_0 < 15$ GeV the decay backgrounds relative to $\sigma_{\mu\mu}$ will be larger by a factor $15/E_0$ at any fixed X. (However, the lower momenta will make an approach to the analog of the solid curve in Fig. IV-5 somewhat easier.) This may be significant if it is necessary to search for the threshold of a low-mass state.

4. Conclusions

One clearly wants to design a new particles experiment to detect both μ's and e's. We cannot be sure that every particle which decays to one will decay to the other; and we also substantially increase the number of events this way.

We cannot conclude that for processes leading to two charged leptons, it should not be difficult to obtain the necessary rejection against misidentified hadrons for either e's or μ's (above $\approx$ 2 - 2-1/2 GeV). For the detection of single leptons (especially those resulting from decays of new hadrons), the higher rejection obtainable from electrons may prove important, and can be crucial if the region below 3 GeV is critical. It should be emphasized that the muon background curves are based on pessimistic K to π ratios, and that the electron curves may be technologically pessimistic. (The latter provides a cushion against hadronic yields much higher than anticipated.)

REFERENCES

1. J. Fisher et al., BNL 20063 (submitted to NIM).
2. F. Busser et al., PL 53B (1974), PL 56B, 212 (1975).
3. B. Blumfeld et al., NIM 97, 427 (1971).
F. Busser et al., PL 48B, 371, 377 (1974).
4. L. DiLella, private communication.

V. THE NEW PARTICLE DETECTOR FACILITY

1. New Particles Philosophy

The prediction of properties of undiscovered particles is a risky business. However, there are

0 0 0 0 4 5 0 1 6 5 4

features of most of the commonly discussed new particles on which a search for new particles can concentrate. The most common in the decay of new particles is the presence of leptons. Neutrinos can be detected only by kinematical effects caused by their absence in the measurement of the final state - acoplanarity of lepton pairs, large momentum-momentum loss transverse to the beam in multi-hadron events. Charged lepton detection is of course straight-forward but complicated at PEP because of feed-down from the normal hadronic final states. A less universal signature of new particles is an increase in strange particle production. This signature is most easily exploited in neutral strange particles where only momentum and angle measurements are required to reconstruct the unstable parent. Observation of threshold behavior in the total hadronic annihilation cross-section can signal the presence of new particles possessing no distinctive decay products. Of course stable new particles must be detected by effects of their mass and charge (ionization, dE/dx, TOF, deflection in magnetic field).

It is possible to construct a detector which sacrifices most features to emphasize one particular new particle signature. This type of detector might contribute to the discovery of a new particle but would probably not reveal much about the properties of the new particle. Since any search experiment will be time-consuming and even specialized detectors will be complicated and expensive, it is felt that the best detector would be reasonably general-purpose but with emphasis on good lepton detection. It is felt that other general-purpose detectors should include as good lepton detection as is possible. The detection triggers should be as loose as possible allowing an ex-post-facto search for anomalous effects rather than presupposing those effects.

2. Detector - General

The general features of new particle signatures and decays described above indicate the feasibility of a new particle facility which emphasizes lepton identification and momentum measurement, photon energy and direction measurement (for $\ell + \gamma$ mass reconstruction), vee reconstruction and identification, dE/dx (for anomalous ionization determination), time-of-flight (to identify slow massive particles), a superconducting coil surrounding the beam pipe (for monopole detection) and 2γ tagging (for 0^- production). In this section we describe in detail the design and characteristics of such a facility. The design has not been fully optimized in that detailed Monte Carlo studies are required to optimally configure the various calorimeters, drift chambers and magnetic field volumn. The detector consists of a high-field solenoid magnet whose radius is kept as small as possible consistent with adequate lever arms for momentum resolution and especially enought sensitive volume to be able to reconstruct most lambdas (vee's). The small radius is desirable if one is to obtain good muon identification over most of 4π by placing a hadron absorber as close as is feasible to the intersection point (consistent with other requirements). The magnetic field volume is essentially surrounded by liquid argon electron identifiers (which also serve as position-sensitive photon calorimeters), and by active hadron absorbers except for part of the endcaps which serve as return yokes and as passive hadron absorbers. High resolution time-of-flight detectors based on proximity-focused multichannel plate phototubes and dE/dx counters surround the beam pipe and magnetic field volume. A superconducting coil of the type used by Alvarez for monopole searches is located around the beam pipe at a position ~ 8 m away from the intersection point. In addition, the New Particle Facility should be equipped with a sophisticated 2γ tagging system to cover polar angles up to 12° to give tagging in search for scalar particles produced by $\gamma\gamma$ collisions and to increase the solid angle coverage for lepton identification to include small polar angles. Of necessity, certain design compromises have had to be made in order to achieve the versatility in detector characteristics and emphasis on lepton identification which is so desirable in searching for unpredictable phenomena. We have for example, foresaken the possibility of π-K-P separation above the momenta where TOF is useful. Such separation would be quite desireable if detailed studies of hadronic final states of new particles are to be made. Perhaps the further evolution of this detector would include compact Čerenkov detectors (e.g., aerogels) for such particle identification. In any case, we feel that the Solenoid New Particle Facility offers a conceptual solution to the problem of new particle searches at PEP.

In reading the following, reference should be made to Figs. V-1/3 which give detailed schematics of the proposed facility. Figure V-5 depicts further details of the modular blocks for electron and muon identification shown in Figs. V-1/3.

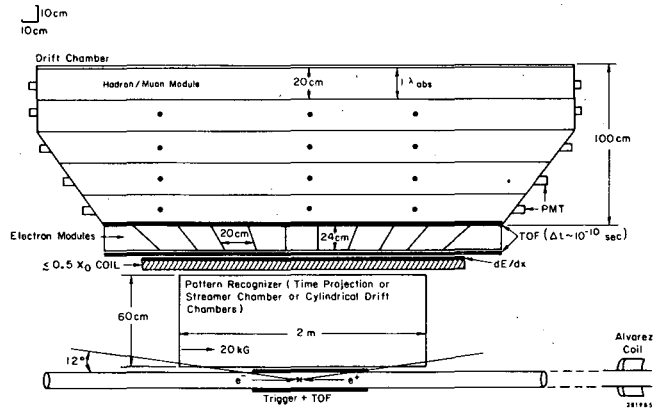

Fig. V-1 New Particle Solenoid Detector - One Octant General View

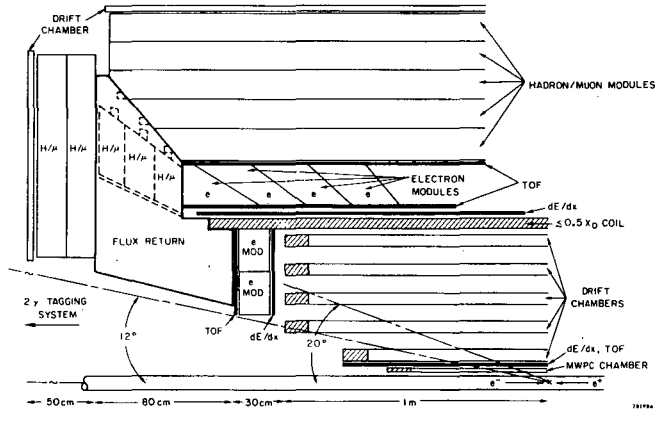

Fig. V-2 New Particle Solenoid Detector - End Cap and Pattern Recognizer Detail

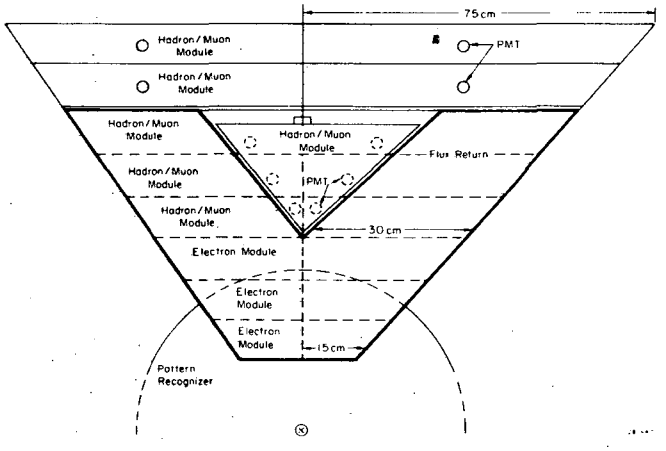

Fig. V-3 New Particle Solenoid Detector - End Cap End View

3. Magnet

The detector consists of an inner core which is a superconducting solenoid magnet with minimum useful length of uniform field of 2 m and a diameter of 1.3 m. The beam pipe is centered in the magnet and is ≤ 200 microns of stainless steel or its equivalent. This thickness was chosen to reduce the level of gamma conversion in the pipe to that of direct Dalitz decays of π^0's. The beam pipe diameter is to be a minimal value consistent with the beam stay-clear region so as to maximize the number of vee's decaying in the visible region of the magnetic core. The beam pipe is surrounded by a multiwire PWC and scintillator for γ conversion suppression, dE/dx and time-of-flight measurements. These elements are described in detail below.

The magnet is essentially a copy of that designed by M. Morpurgo for the CCRO experiment at the CERN ISR. The coil is constructed of ~1000 turns of aluminum-stabilized niobium-titanium conductor carrying 3300 A and generating a field of up to 20 kG and uniform to 1% in the fiducial volume. The coil designed for the CCRO experiment is ~1 radiation length thick but we

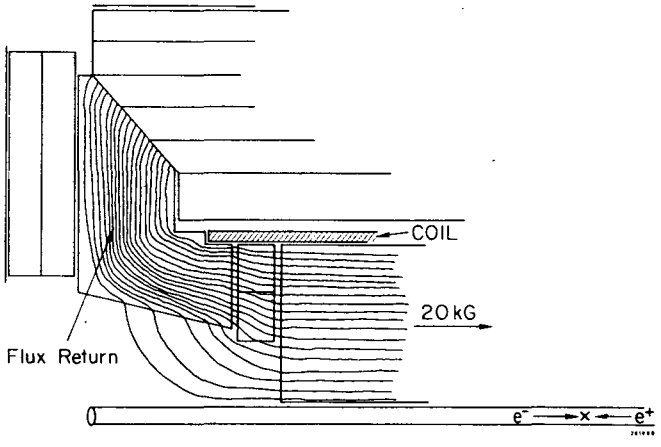

Fig. V-4 New Particle Solenoid Detector - Magnetic Field Configuration

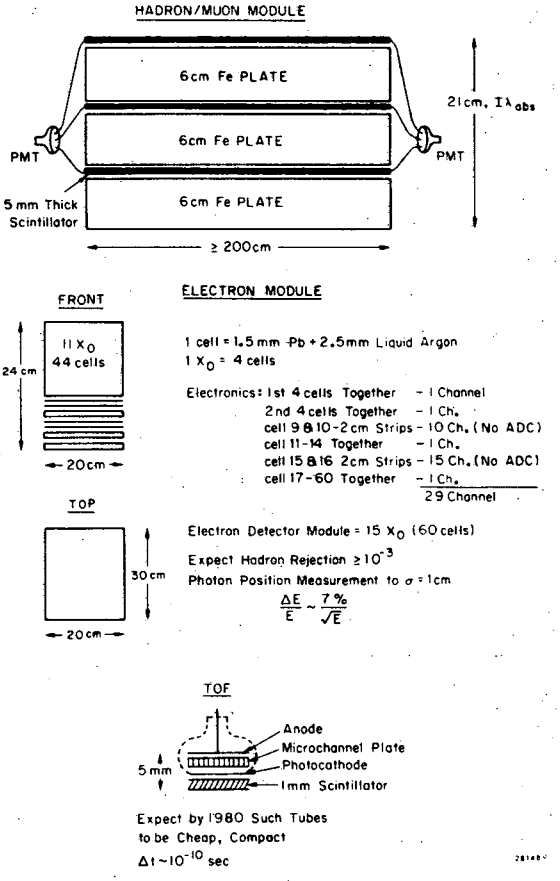

Fig. V-5 Hadron/Muon, Electron, and TOF Modules

hope that with increased experience the coil thickness for such a magnet can be reduced to 0.5 radiation length (minimag has a 0.33 Xo coil). The system stores ~3 M joules of magnetic energy and would consume ~20 liters/hour of liquid helium.

The magnetic flux return (see Figs. V-2 and V-3) is through eight vee-shaped iron end plugs at each end of the solenoid which butt up against the hadron/muon calorimeters to complete the return path. The calorimeters, which are described below, contain sufficient iron to serve as return yokes. This magnetic field does not hinder their function as calorimeters. Further study may indicate that fewer than eight vee end plates are required so that a larger fraction of the end caps can be devoted to active (hadron/muon modules) rather than passive hadron absorber. The vee-shaped end plugs are used to facilitate placement of photomultipliers and to maximize the amount of end cap devoted to active absorber. A crude mapping of the magnetic field configuration is given in Fig. V-4.

The cost estimate for the CCRP magnet is appropriate to our design. In 1974 this estimate, including iron, superconducting coil, cryogenics, power supply, mechanical supports, liquid helium dewers and transfer lines came to 1.62 M Swiss francs or ~ $0.5 M. We estimate a cost for the New Particle Facility solenoid of $0.8 M to account for inflation, further R and D on thin coils, contingency, and other unforeseen cost increases. Table V-1 summarizes the properties of the magnet and the CCRO cost estimate.

0 0 0 0 4 5 0 1 6 5 5

TABLE V-1

Design Parameters of Superconducting Solenoid Magnet

Useful Field Diameter	130cm
Useful Field Length	200cm
Volume	$3.0m^3$
Magnetic	20KG
Magnetic Energy	~ 3MJ
Coil Material	Al-stabilized Ni-Ti
Number of Turns	1000
Current	3000A
Total Weight	~ 80 Tons
Liquid He Consumption	~ 20 litres/hour

CCRO Cost Estimate (1974 in 10^3 Swiss Francs)

Iron (72 Tons)	kSF	400
Al-stablilized Ni-Ti conductor		350
Cryogenics		200
Power Supply		60
Supports		200
Transfer Line (15m long)		50
Two 1000 litre dewars		120
Helium Expansion Ballon		25
Recovery Line for Helium Gas (estimated)		10
Miscellaneous		200
TOTAL kSF		1615

4. Inner Detector

The problem of the optimum geometry for Λ^0 identification was studied by Hitlin, Marx and Yamin (PEP-164) who concluded that a solenoid geometry maximizes the yield (assuming an angular distribution of Λ's given by $1 + \cos^2\theta$ and momentum spectrum as given by Bjorken and Kogut for $\bar{p}$'s at PEP). Figure V-6 indicates the solid angle accepted by a solenoid of various aspects ratios and Fig. V-7 depicts the vee detection efficiency calculated by Hitlin et al. Their conclusions, which were applied to solenoids of 3 m length and 1.5 m diameter with a 5 kG field are almost directly applicable to this detector because of the high field and shorter visible track length required for reconstruction. It is the vee reconstruction

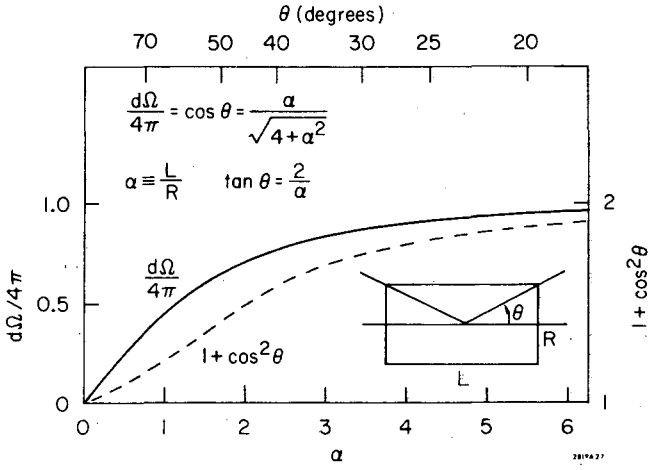

Fig. V-6 Solenoid Geometry Characteristics

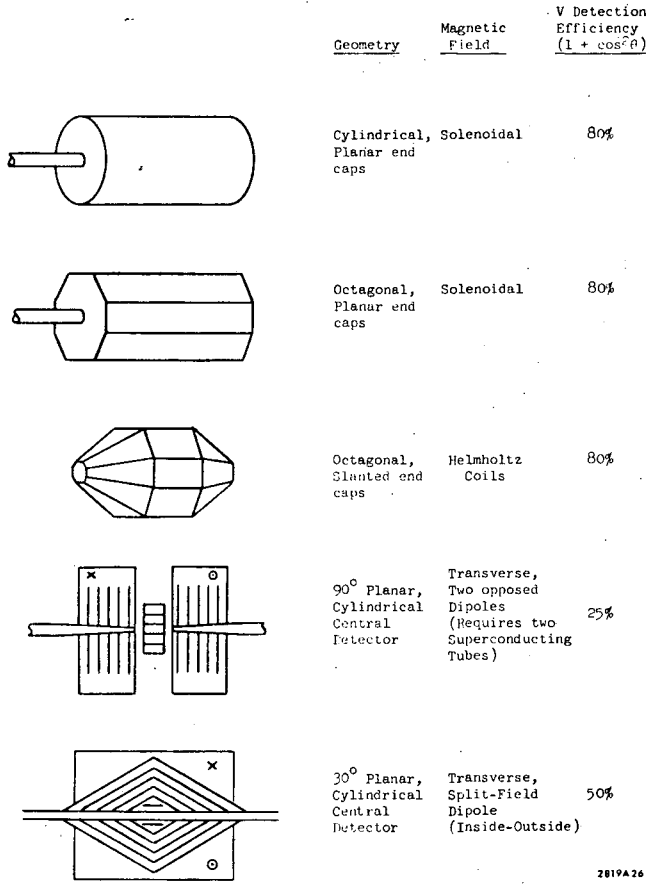

Fig. V-7 Vee Detection Efficiency in Various Geometries

efficiency which determines the shape and volume of the magnetic field required.

The volume inside the solenoid magnet is filled with position-sensitive detectors to form a "pattern recognizer". Two configurations were considered - - an array of cylindrical drift chambers and the time projector detector. In principle a streamer chamber would serve as such an inner detector. For track recognition and momentum measurement we will propose the canonical drift

TABLE V-2

MWPC and DC Parameters

Chamber	Radius	Length	Planes	Z-Readout	Sectors	Wire Spacing (mm)	# of Wires	# of Cathode Readouts	Cost
MWPC	8,42		1	none	2	2	250	----	$5 K
DC 1	14,80		2	54-90° delay line	2	15	120	108	Construction
2	26,180		2	120-90° strips	4	15	220	240	@ $6K/m^2
3	38,180		2	120-90° strips	6	15	320	240	~ $300 K
4	50,180		2	120-90° strips	8	15	420	240	Electronics @ $100/readout
5	62,180		2	120-90° strips	10	15	520	240	~ $260 K
						TOTAL	1600	1068	$560 K

chamber system.[1] There are several different schemes for large solid angle solenoid systems that are currently entering development or final construction. In a few years a more realistic choice will be possible. At this time there is more speculation than anything else.

For a new particle detector the momentum resolution does not have to be pushed to its limits. $\Delta p/p \sim .01$ should be sufficient. Furthermore, we do not have to worry very much about multiple scattering errors. A contribution of $\sigma \sim 1 - 2\%$ should be tolerable. It is also true that the polar angle θ does not have to be measured extremely well or the mass resolution would be dominated by momentum measurement errors (see section on $e\gamma$ or Λ). Therefore $\sigma(\Delta z) \sim$ 1 cm will be sufficient. The important points are high efficiency for reconstruction, including the recognition of vee's coming from the decays of neutral particles and the rejection of the conversion background to a single electron signal.

The first detector that a particle sees after passing through the beam pipe is a small MWPC. This chamber is not used for momentum measurement and could have its wires distributed azimuthally every 2 mm. This is followed by a scintillation counter that is divided into several azimuthal segments which are viewed at each end. The principle function of these two devices is the rejection of π^0 conversion background (see lepton background section).

The region from r = 11 cm to r = 65 cm is occupied by a system of 5 double gap drift chambers modules with induced cathode signal readout for the z-direction. (See Table V-2). At each of these modules the full position and the local tangent angle in the (r,ϕ) plane will be measured. Three such measurements are necessary for a fit of a track's momentum. Two are probably sufficient to recognize the existence of a track. Thus, recognition of the vee's will extend to vertices at r = 50 cm and mass reconstruction to r = 38 cm. In a similar sense track recognition and reconstruction will extend down to $\sim 20^\circ$ ($.94(4\pi)$) for tracks originating at the interaction point. The transverse momentum resolution[2] for fully measured tracks would be $\sigma = .009$ p for an assumed drift chamber resolution of 200 μ. Similarly, $\sigma(\Delta\phi) \sim$ 1.3 mr and $\sigma(\Delta\theta) \sim 17 \sin^2\theta$ mr for $\sigma(\Delta z) = 1$ cm. Somewhat better resolutions can be obtained by fitting observed tracks to the reconstructed event vertex.

The basic drift chamber design consists of $\sim$200 cm long chambers (180 cm active) with drift wires every 1.5 cm along the circumference. The drift wires would, of course, be staggered in each pair of gaps in the usual manner (see Fig. V-8). The individual gaps could be 1 cm although the practicality of such a geometry in 20 kG fields still needs some testing. There would be no azimuthal field shaping and the time measured should correspond to the distance of closest approach of the track to a wire. The maximum drift time would be $\sim$ 150 ns and, to maintain the full potential resolution, would have to be measured to $\sim$2 ns.

For the z-readout we could have 90°-stereo strips. 3 cm-wide strips are sufficient to give 1 cm resolution in each plane. The pairing between sense wires and cathodes can be done by demanding that the time on the cathode strip agree with the time on the sense-wire. For the outer four modules it is sufficient to have a simple cathode strip. In the innermost module the probability of a given sense wire or cathode strip being struck twice ie quite high. If there are two hits on a wire (or strip) there is a large probability that one will be lost due to the effective 50 - 100 ns minimum detectable separation between two pulses on the same wire. To minimize this effect we can make the cathod strip into a delay line of velocity $\sim$ 2 ns/cm. This 44 cm line is very easy to do with a simple zig-zag trace on a printed circuit. For this short length the usual dispersion problems are negligible. Thus under normal circumstances we measure 3 times for each hit t_s, t_{z1}, t_{z2}. From this we have to determine which sense wire was hit, at what time, and at what distance along it. Any two of these times is sufficient. For example, if we have lost t_s due to a multiple hit on the sense wire there is a high probability of still having the two z readouts. In this case, $t_{z2}-t_{z1}$ tells us which sense wire was hit and $t_{z2}+t_{z1}-t_L$ (where t_L is the full propagation time for the line) tells us when it was hit. The number of the z-readout gives us the zee position.

0 0 0 0 4 5 0 1 6 5 6

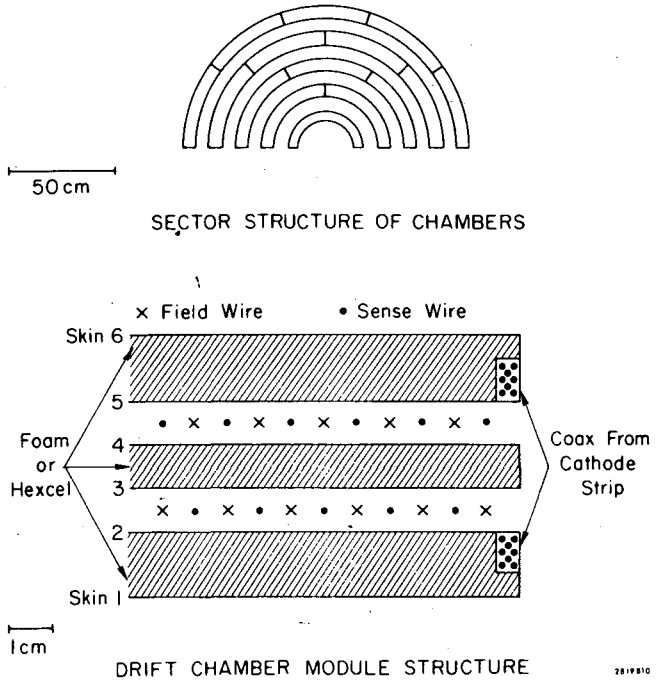

Fig. V-8 Drift Chamber Structures

The modules could be constructed as shown in Fig. V-8. Each module is divided into sectors of arc length ≈40 cm. The fabrication of several identical sectors for each radius and the more manageable size of the individual sectors should simplify the construction and lower the cost of these chambers. The sectors for each 1/2 cylinder can be held together at the ends by semi-sircular support rings. The ten half-chambers can be hung on vertical supports at each end of the solenoid.

We employ a sandwich construction using either foam or Hexcel as a low density matrix which is given rigidity by skins glued along the two faces. This assembly can be made into a cylindrical shell in an appropriately designed press. The skins (mylar, Kapton, or fiberglass) will be the cathode strip printed circuit in two cases (skins 2, 5 in Fig. V-8). This circuit is identical for the outer four modules. The other four skins will be covered with a plain copper or aluminum layer. The outer two (1, 6) can then serve as part of a Faraday cage for the entire chamber.

The signals from the cathode strips of each sector can be taken out on minature co-ax (~1 mm OD) at the edge of each sector. For all but the smallest radius the outputs of the cathode strips at a given zee can be OR'ed for each half-cylinder before being amplified and digitized. For the first module we want to look at both ends of each delay line. Those lines have to be terminated at their ends and the signals can be taken out after an emitter follower. All signals can be taken out of the solenoid on co-ax cables to external amplifiers. There is no need to have any power dissipation in the solenoid. This is important because temperature gradients can effect the alignment of the chambers and, therefore the wire positions.

Particles which have lifetimes in the range 10^{-11} to 10^{-8} sec can be observed as visible "kinks" or "vees" within the detector. These could either be the known kaons and hyperons, or new

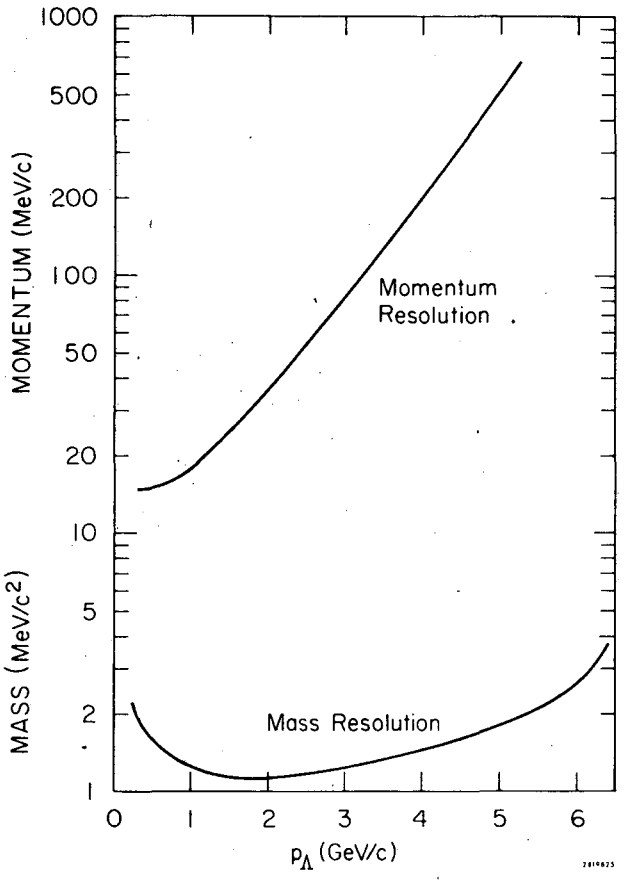

Fig. V-9 Lambda Resolution in New Particle Detector

unstable particles which are produced at PEP. The minimum decay distance which can be observed is limited by the finite beam size of σ_x = 1.2 mm. With a vacuum pipe of = .01 radiation length at 10 cm radius, and 0.2 mm resolution in the tracking device, the displacement at the beam is smaller than the beam size.

In order to obtain a feeling for the mass and momentum resolution possible inside a 70 cm radium pattern recognizer we consider the case of Λ decays. We assume that the Λ's decay in a plane perpendicular to the beam axis, at their mean decay distance. We use curves for the momentum and angular resolution given in Fig. V-9. In the region of Λ momentum from 0.2 to 5.0 GeV/c, the mass is determined to ~ ± 2 MeV, but above 5 GeV/c the resolution rapidly becomes worse due to the long decay distance and reduced momentum resolution. Most of the momentum resolution of the Λ comes from the Λ measurement of the proton momentum, so the Λ momentum, resolution follows the curve of $\Delta p = 0.0075p^2$, up to the point where the decay distance becomes important at 5 GeV/c. We have not included the fact that for Λ's with long decay paths, we have the additional constraints from the Λ direction.

For massive particles produced nearly at rest, the mass resolution is approximately equal to the momentum resolution of the two outgoing particles. Hence a 5 GeV particle produced at rest will have a mean resolution of ± 40 MeV, and a 10 GeV particle will have a resolution of ± 160 MeV.

The complicated experimental question of understanding the origin of a new particle signal is discussed elsewhere in this report. This discussion leads to a possible criteria for momentum resolution in the pattern recognizer in that one can use the momentum distribution of leptons from heavy lepton decay in order to learn about the structure of the currents responsible for the decay. Since some models now prefer heavy leptons coupled to V + A currents we require sufficient momentum resolution to resolve V - A and V + A heavy lepton decays from the measured momentum distribution of the final state charged lepton. As indicated in Section III.4 a value of $\Delta P/P^2 \sim 0.75\%$ is sufficient to separate the V + A from the V - A hypothesis adequately. This criteria may not be the most sensitive physics choice since angular distributions may contain more information, but it has been useful as a solvable quantitative problem for evaluating whether the resolution of the pattern recognizer is of any value other than for mass reconstruction (Λ, $\ell\gamma$, ...). Further studies of the new particles facility should include Monte Carlo simulations of particles decays and attempts to analyse these simulated events with resolution effects included. Unfortunately this is too time-consuming a chore to be attempted during the Summer Study. Perhaps if such calculations are done by the designers of Mark II, they can be adapted to the new particle Facility in order to answer questions of the extraction of detailed physics, rather than just a signal, in light of the resolutions we hope to achieve.

5. Outer Detector

Possible configurations for TOF counters are depicted in Fig. V-5 and their placement in the detector is shown in Figs. V-1 and V-2. The TOF is based on the availability of proximity-focused multichannel phototubes. These tubes contain flat multichannel plates ~1 mm from a flat photo cathode so as to give a jitter in response time of less than 100 ps (as experimentally determined from phototypes). The multichannel plates have gains of $\sim 10^6$ and thus produce signal levels similar to those produced by proportional wire chambers. The tubes would be read out by an anode (possibly segmented) at the back of the plate and PWC-type readout electronics. If such tubes become extremely cheap by ~1980 (an unlikely possibility) one can envision flat "tubes" with large areas (~ 0.5 cm thick) which can be placed in arrays behind plastic scintillator to give high-resolution ($\Delta_T \sim 10^{-10}$ sec) segmented TOF hodoscopes. If these tubes are too expensive to cover 10 - 15 m^2 of area, the scintillator can be viewed edge-on so that slabs of scintillator placed parallel to the cylinder axis as shown in Figs. V-1 and V-2 can be read out from both ends by such tubes. By correlating the time of signal arrival at each end the impact point along the axis can be determined so that the TOF from the interaction point can be calculated. If single photoelectron threshold levels are used one would be sensitive to Cerenkov light from the scintillator from particles with $\beta > .7$. For scintillator several mm thick this should allow time resolutions matched to those achievable with multichannel phototubes. Figure V-10 depicts the mass resolution achievable if $\Delta_T = 10^{-10}$ sec over a distance of 1 m for particles of various momentum and mass. The figure shows the range of mass and momentum where stable new particles can be recognized by such TOF resolution ($M > 2$ GeV, $\Delta M \leq 2$ M so that the new objects can be separated from the proton). K-π separation to 2 is achieved up to 1.7 GeV/c and K-P separation to 2σ is achieved up to 3 GeV/c. For time resolutions other than $\Delta_T = 10^{-10}$ sec or distance differing from d = 1 m the vertical scale in Fig. V-10 can be scaled by Δ_T/d.

Scintillators and conventional phototubes for dE/dx measurements (to search for anomalously ionizing particles) are located as depicted in Figs. V-1 and V-2. If we assume that each TOF counter and dE/dx cost \$1K /channel of PMT and digitizer and scintillator is \$1 K/m^2 the cost of TOF, dE/dx and trigger counters is \$280 K.

The importance of lepton identification and the background levels associated with single lepton identification have been discussed earlier in the report. The New Particle Facility uses lead plates and liquid argon for electron identification and γ-position measurement and calorimetry. Figures V-1 and V-2 depict the placement of these electron modules and Fig. V-5 depicts the configuration of one such module.

We have chosen liquid argon ion chambers with lead plates as an electron-photon detector because of its compact size and its good π-e separation capabilities. Each cell in the detector will have 1.5 mm of lead and 2.5 mm of liquid argon, so 22% of the shower energy will be deposited in the argon. This relatively small percentage of energy into the active converted implies less than optimal energy resolution, but we have traded resolution for compactness, since the detector is only 24 cm deep, not including the cryostat. The π-e separation is enhanced by our ability, with a liquid argon detector, to segment the detector longitudinally.

Physically, the detector consists of 60 cells, with each cell comprised of a 2.5 mm liquid argon gap and collection plates embedded with 1.5 mm of lead. The electron collection time for pure argon is 450 nsec.[3] The total detector depth is 17.1

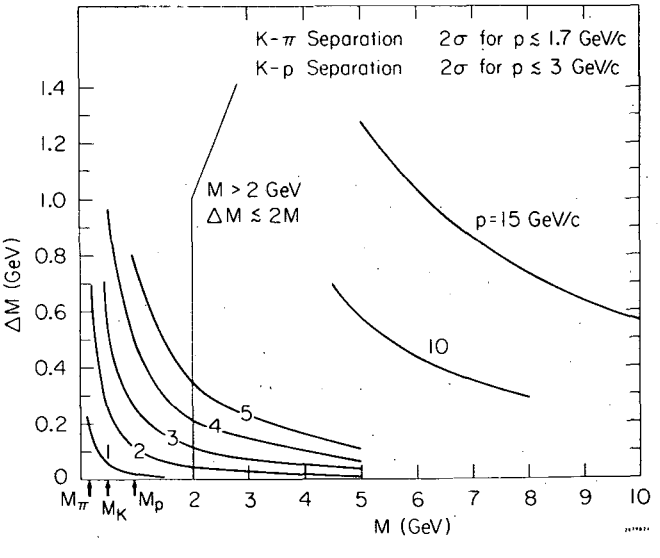

Fig. V-10 Time-of-Flight Resolution for d = 100 cm, Δt = 0.1 nsec

0 0 0 0 4 5 0 1 6 5 7

radiation lengths with 94% of the radiation lengths in the lead. In the transverse cross-section, each module is 60 cm by 20 cm, so that the capacitance of each module is 41 nF. The longitudinal develoepmtn of the shower will be monitored by electrically dividing the module into 5 regions with different depths. Each of the first four radiation lengths will constitute an individual region and the remaining 13 radiation lengths will be the final region. Since the momentum of an electron going into the detector will be known, this longitudinal segmentation should reject hadrons better than 1 in 10.[3] The transverse position of the shower will be determined by segmenting the electrodes in the third radiation length in depth into 2 cm strips. The first two cells will have x-strips and the next two cells y-strips to give 90° stereo. With this segmentation, 44 amplifier channels will be required for each module. As part of the total hadron calorimeter, the electron-photon detector represents 0.67 nuclear absorption lengths.

About 92% of the photons will convert before reaching the transversely-segmented region of the detector. The radial size of the photon shower can be estimated from the Moliere radius,[4] which is about 2 cm for this ratio of lead to argon. Typically, 70 to 80% of the shower energy is deposited within this radius, which we have chosen as the width of our transverse strips. With interpolation, location of the gamma with $\sigma \leq 1$ cm should be possible.

The energy resolution for gammas is the result of three sources of error added in quadrature. They are electronic noise from the FET in the charge amplifier, sampling fluctuations due to the presence of a passive radiator and sampling fluctuations from the escape of energy out the back and side of the detector. Willis and Radeka,[3] using a similar detector, have shown that the unavoidable FET noise is related to the square-root of the detector capacitance by the equation

$$\sigma_{noise} = (2.4 \text{ MeV})\sqrt{C}$$

where C is the detector capacitance in nF. Because of the small shower size, most showers will involve only one detector module, which gives $\sigma_{noise} = 15$ MeV. The sampling fluctuations due to the passive converter are proportional to $\sqrt{E}$, where E is the photon energy. The normalization of this error can be done several ways, but, probably the most reliable method is the fact that experiments with a similar configuration show a resolution of $.07/\sqrt{E}$ which mostly results from these fluctuations. With 17 radiation lengths of material in this detector, the energy losses out the back will be negligible except for the highest energy showers. Similarly, the small transverse extent of the shower makes the problem of radial energy loss relative small. Figure V-11 shows the estimated resolution for this detector for gammas. Each liquid argon module has 40 strip readouts (no ADC, ~$30/channel) and 4 ganged plate readouts into an ADC (~$100/channel). The electronics for each module costs ~$1600 and the system contains 144 modules giving an estimated electronics cost of $230 K. The electron modules cover an area of ~15 m^2 which gives a net cost of $225 K when Hitlin's figure of $15 K/$m^2$ (including electronics)

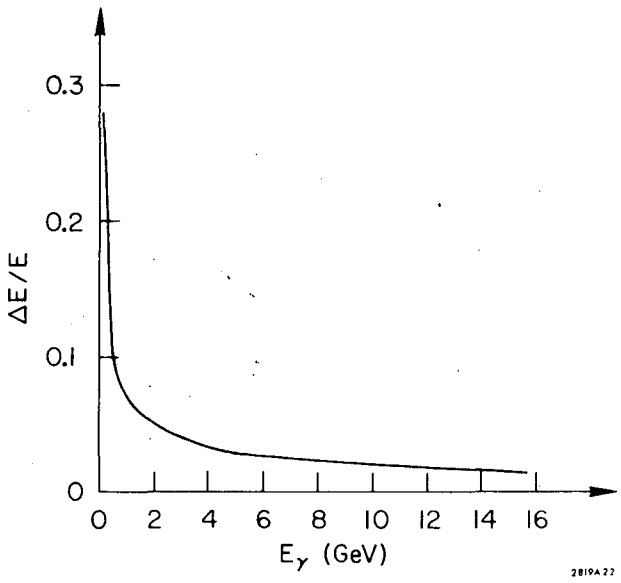

Fig. V-11 Photon Energy Resolution in New Particle Detector

is used. A reasonable cost is then something above $250 K - - we guess $300 K.

Judging from the experience of the CCR group with lead glass and segmenting of the first few radiation lengths, we expect a hadron rejection level of better than 10^{-3}. In the next year or so the experience of the Mark II group and Willis at CERN will hopefully provide confirmation of this expectation and also better data on the optimal configuration for liquid argon detectors. Lacking this information we have designed the system with the goals of achieving the values of σ_x, $\Delta E/E$ and hadron rejection given above.

The strip readout, which dominates the cost of the electron modules, was included to measure γ directions os that excited leptons which decay to $\ell\gamma$ can be investigated through reconstructing the $\ell\gamma$ mass spectrum and so that massive pseudoscalara with decays into $\gamma\gamma$, $\rho\gamma$, $\omega\gamma$,.... can be reconstructed. Using the parameters given here, Fig. V-12 depicts the $\ell\gamma$ mass resolution for various values of the mass and energy of an excited lepton. Mass resolutions of ~0.5 GeV are achieved for masses up to 7 GeV/c^2. For heavier masses in the 1 to 4 GeV region the mass error is due almost entirely to the error in the energy measurement since the opening angles are so large for the range of PEP energies.

The hadron rejection to 10^{-3} predicted for the electron modules, the 200 μ beam pipe thickness and the predicted π^0 spectrum can be used to predict the single electron background on this facility. The calculation and criteria are described in detail earlier in this report; the result is summarized in Fig. V-13. The single electron background for electrons of momentum greater than P_0, normalized to a hypothetical signal of single electrons of cross-section $\sigma_{\mu\mu}/5$ is shown for all sources of background (Dalitz decay, γ conversion, hadrons fooling electron modules). The background is less than 10% for $P_0 > 2.5$ GeV/c and is less than 2% for $P_0 > 5.5$ GeV.

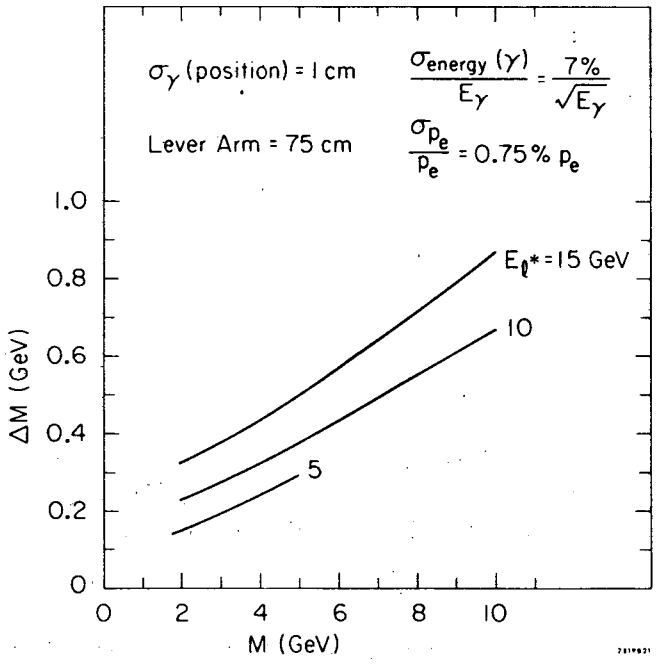

Fig. V-12 Resolution in Mass Reconstruction for $\ell^* \to \ell + \gamma$

Muons are identified by the hadron/muon modules whose placement is shown in Figs. V-1, -2, -3 and whose configuration is depicted in Fig. V-5. A single module is 1.10 interaction lengths deep, made of three iron plates, each 6 cm thick with scintillator between the plates. The scintillator is read out by phototubes at each end (into ADC's and TDC's) so that pulse height information and timing to determine position along the counter is extracted. The counters in the azimuthal detector are segmented into 16 azimuthal segments (two per octant) and segmented along the solenoid axis into two segments. This segmentation reduces the probability of a muon being vetoed by a hadron into the same segment. The hadron/muon modules in the end caps are of similar design with the segmentation indicated in Figs. V-2 and V-3. Five and one-half interaction lengths of depth of such modules (in addition to ~.7 interaction length in the liquid argon) cover the full solid angle of the detector except in the end caps where for part of the area the magnet end plates replace the first three interaction lengths of hadron/muon modules. These active hadron absorbers have fine-enough sampling to essentially give complete muon identification to the level of hadron punch-through. A traversing muon gives uniform pulse height (except for Landau fluctuations) while any hadron interaction produces large energy deposition and very non-uniform pulse heights. Except for punch-through the hadron rejection should be $\sim 10^{-3}$ or better. For six interaction lengths (a hadron sees 6.2 λ_{int} in this facility) the punch-through probability is 2.4×10^{-3}. As indicated in the section of this report describing backgrounds to muon identification, a hadron absorber need only be so thick as to give punch-through probabilities matching the backgrounds due to meson decays in the central free space. In the detector, meson decays dominate for muon momenta less than 6 GeV/c and the two backgrounds are approximately equal above 6 GeV/c muon momentum. Figure V-13 depicts the backgrounds to single muons as was done for electrons. The electron signal is seen to be lower in background than the muon signal by a factor of 10 at 2 GeV/c and 3 at 5 GeV/c muon momentum. We note that much of the iron in the hadron/muon modules is magnetized in its role as return yoke for the solenoid magnet. The presence of drift chambers as the most outside element of the detector will thus provide a crude (~20%) measurement of muon momenta outside of the pattern recognized so that the meson decay background appears at the muon momentum rather than the larger parent meson momentum. This a postiori measurement of the muon momentum thus has the effect of decreasing the effective single muon background at higher muon momenta. The ability of the hadron/muon modules to give crude hadron calorimetry helps to suppress beam-gas background in total cross-section bump hunting.

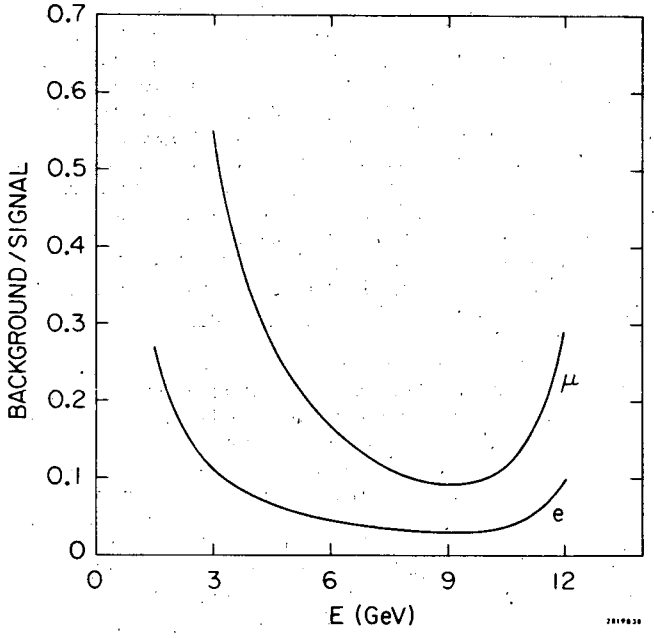

Fig. V-13 Background/Signal for $E_{lepton} > E$ in Leptonic Decay of One of 11 GeV Heavy Lepton Pair (E_{beam} = 15 GeV)

The outer drift chambers have been chosen to contain 5 cm cells in order to match the multiple scattering of muons in the absorber and to limit the sensitive time $\tau \sim 1$ μS. At $100/drift wire these chambers would cost ~ $100 K.

The hadron/muon modules contain ~300 tons of iron plates, 400 m^2 of scintillator, and 160 channels of 5" PMT, TDC, and ADC. If we assume the iron plates cost $1 K/ton, the scintillator #1 K/m^2 (liquid scintillator would be substantially cheaper), and $750/channel for PMT, base and electronics, the hadron/muon modules cost ~$820 K.

The Solenoid New Particle Facility requires two types of auxilliary detectors. First, a superconducting coil of the sort used by Eberhard and Alvarez in their monopole searches. Such a coil would circle the beam pipe at a distance of ~8 m from the interaction region and would detect stable monopoles which are accelerated in the beam directions by the solenoid magnetic field. Such a technique is detailed in the literature and elsewhere in this report. The second auxiliary detector is a 2γ tagging facility which would serve

0 0 0 0 4 5 0 1 6 5 8

TABLE V-3

Solid Angle for Lepton Identification		95% × 4m
Hadron/Electron Rejection		$\leq 10^{-3}$
Hadron/Muon Rejection		$\leq 2.4 \times 10^{-3}$
Λ Reconstruction Efficiency		> 80%
$\Delta P/P^2$		.75%
$\Delta E/E$ (γ)		$7\%/\sqrt{E}$
σ position (γ)		1 cm
Λ Mass Resolution		See Fig. V-9
$\ell\gamma$ Mass Resolution		See Fig. V-12
$\gamma\gamma$ Mass Resolution		See Fig. V-15
TOF Resolution 10^{-10} sec,		See Fig. V-10
Background to Single Leptons		See Fig. V-13
Weight		~ 430 Tons
Size		Cylinder: radius = 2m, Length = 5.2m
No. PWC Wires		250
No. Drift Chamber Wires		1600
Cost:	Magnet	$ 800 K
	TOF + dE/dX + Trigger	280
	Electron Modules	300
	Hadron/Muon Modules	820
	Outer Drift Chambers	300
	Pattern Recognizer	560
	SUBTOTAL	$ 3060 K
	ENGINEERING, SUPPORT STRUCTURE CONTINGENCY	1530 K
	TOTAL	4590 K

several purposes. It is necessary for total cross-section measurements (and bump hunting for $J^{PC} = 1^{--}$ states like ψ's) and for tagging 2γ production of pseudoscalar states. In addition it provides lepton identification at polar angles below 12^{o}. The use of 2γ processes to search for new particles is described elsewhere in the report.

If we use the formula of the $\gamma\gamma$ study group for the missing mass resolution derived from measurements of the tagged electron and positron and assume 1% measurement of the electron and positron energies for a particular event in which the scalar or pseudoscalar is made in the absence of other particles, we can calculate the resolution in the mass of a $\gamma\gamma$ system of mass W. Figure V-14 depicts this resolution as a function of W. The shaded area spans the space of possible $\gamma\gamma$ decay configurations. For values of W below 4 GeV the resolution is rather discouraging, independent of decay configuration.

6. Summary

Although the Solenoid New Particle Facility described here is optimized for the observation of new phenomena at PEP, it can be used to study other, expected, physical processes whose characteristics are matched to the detector's capabilities. Much of this physics is described in detail in other PEP reports. These include Λ and K_s inclusive studies, total hadronic cross-section measurements and especially weak interaction experiments using lambda longitudinal polarization as a polarimeter to search for parity violating effects. Such effects and their measurement were described by Hitlin, Marx and Yamin (PEP-164) and are of

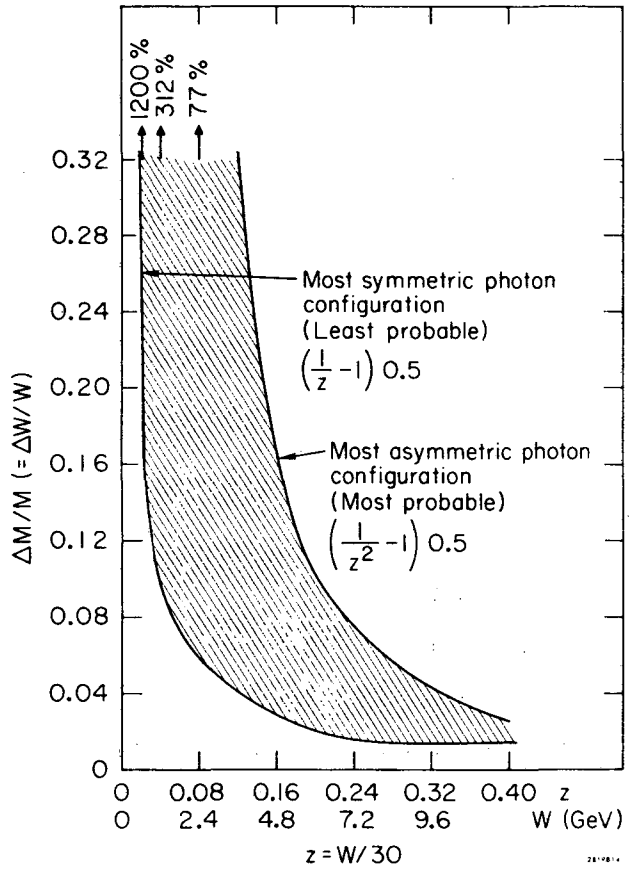

Fig. V-14 Resolution in $\gamma\gamma$ Mass from Tagging Apparatus

obvious interest in their own right. They are also relevent for new particle search in that, quasi-stable hadrons and heavy leptons can be expected to decay into strange particles through parity violating transitions. For this reason, this detector was scaled to observe Λ^{o}'s - not only to observe anomalous strangeness production from charmed particle decay, but also to use the Λ^{o} polarization to spot thresholds due to weak decays of new particles. The obvious utility of total hadronic cross-sections and lepton pair cross-sections to new particle searches has been demonstrated at SPEAR.

In Table V-3 we summarize the particle characteristics of the Solenoid New Particle Facility. It is a large solid angle detector with a multitude of characteristics of special relevence to new particle searches. As such we feel it is the kind of system best suited for studies of the "expected" new phenomena at PEP, and, more importantly, it is a system which may optimize the chances of being at the right place and time to observe the entirely unexpected phenomena which accompany all new accelerators.

REFERENCES

1. The ideas for the system described here are heavily influenced by:
   a. CCRO Solenoid Detector - high p leptons and hadrons at the ISR
   b. LBL MINIMAG Detector
   c. CERN-Scandinavian-Harvard-LBL-Rutherford-high p hadrons at the ISR
2. Using formulae from Gluckstern, NIM 24, 381 (1963)
3. W. Willis and V. Radeka, NIM 120, 221 (1974)
4. C. J. Crannell, Phys. Rev. 161, 310 (1967)

VI. SPECIALIZED NEW PARTICLE DETECTORS

1. General User Magnet

The ideal charmed particle detector shown in Fig. V-1 could in principle be adapted to the proposed General User Magnet. The main differences between the two magnets are the larger sizes of GUM.

GUM	New Particle Detector
R = 1.2 m	against 1 m
L = 4 m	against 2 m
B = 15 kg	against 20 kg .

The momentum resolution of the GUM is slightly better than that of our ideal detector (Bq^2 = 9.6 kgm^2 against 7.20 kgm^2). Its larger size implies that the external detection equipment (argon counters and γ-h identifiers) would be 20-30% more expensive. Also the larger distance transversed by any π before it can be identified as such implies that the π/μ rejection will be slightly (20%) worse. A possible arrangement using GUM as the central detector is shown in Fig. VI-1. If a continuous coil design is chosen for GUM, the radiation length presented by the coil would be the same. The end cap of GUM can be can be adapted to act as μ/h identifier. Should light detectors using micro channels become commercially available, it may well be advantageous to put the TOF inside the coil, thus making the two outer detectors even more comparable in size. (These devices presumably would work equally well in a magnetic field.)

There is a point to be made about the use of a general purpose detector as a new particle discoverer. That is, most attempts at identifying new hadronic quantum numbers at PEP involve studies of statistical distributions: e.g., K/π ratios, thresholds in scaling violations at small x, mass bumps, etc. It is also possible to discover a new quantum number, like charm, with one fortuitous event. One need only find a violation of strangeness conservation. Consider an event where a charm-anticharm pair are produced (with or without other particles). If both members of the pair decay hadronically, one to a strangeness zero final state and the other to a state with non-zero strangeness, then a detector which can detect all secondaries in the event and identify all strange particles would tell us that strangeness violation (and perhaps the existence of charm) has been found. One would see an event which is a 4-C fit with non-zero strangeness. The General Purpose Detector proposed at the 1975 PEP Summer Study (4π charged detection and hadron identification by Cerenkov techniques) could be such a detector.

2. "Split Chamber"

It is very well possible that excited states of the muon exist. Such states, apart from having the decay $\mu^* \rightarrow \mu + \gamma$, would also show the electromagnetic decays $\mu^* \rightarrow \mu + 2\pi$, $\mu + 3\pi$, etc. In order

0 0 0 0 4 5 0 1 6 5 9

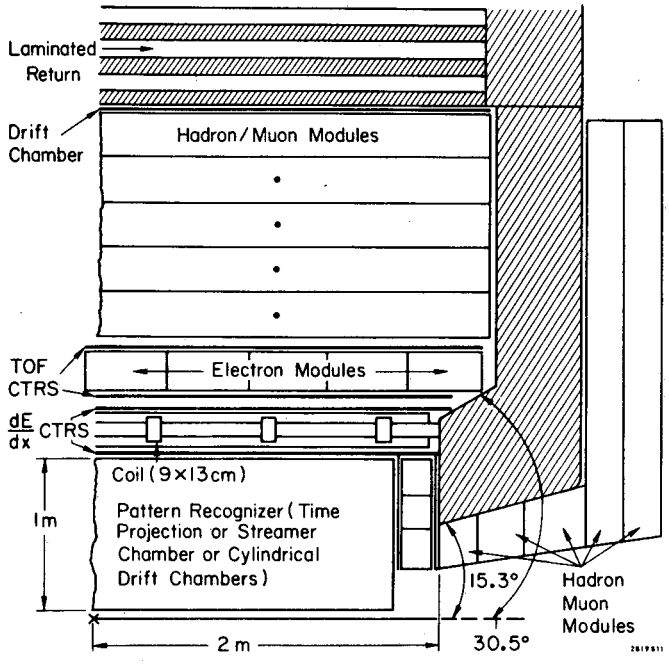

Fig. VI-1 New Particle Facility in General User Magnet (GUM)

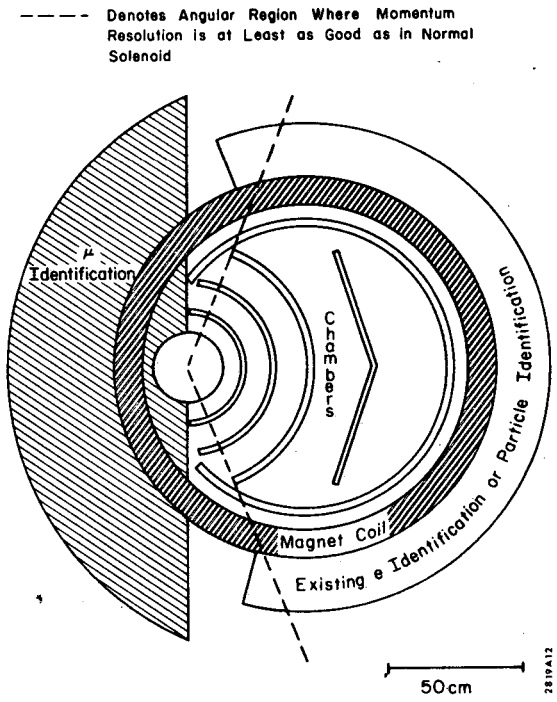

Fig. VI-2 OFF-AXIS Solenoid Detector

to study such decays, the π/μ rejection in the present detectors may not be adequate. If we assume that the μ^* are produced without a form factor, and the branching ratio into hadrons is B = 1%, then

$$\frac{\sigma(e^+e^- \to \mu^*\mu \to \mu\mu n\pi)}{\sigma(e^+e^- \to h)} \leq \frac{B}{R} \approx 10^{-3}$$

Threshold effects would further depress this ratio and since one of the two muons from the reaction would typically have low momentum ($< p > \simeq 15$ GeV/No. π's + 1) the π/μ rejection of the detector may not be sufficient. However, it would in such a case be possible to remove part of the inside tracking device and replace it over an azimuthal range $\Delta\phi \sim \pi/2 - \pi/3$ by a π/μ identifier similar to those used outside. The material of the now rather small internal π/μ identifier would have to be non-magnetic. Its purpose would be to yield for single fast muons a π/μ rejection of $1\text{-}2 \times 10^{-3}$. This rejection factor, when multiplied by the rejection factor $\pi/\mu \sim 2\%$ of the slower muon, would enable one to study such processes with only a small background.

3. Liquid Argon Neutrals Detector

LAND (Liquid Argon Neutrals Detector) emphasizes the high energy-and-position-resolution detection of neutrals without some of the disadvantages of other 4π neutral detectors such as the NaI (Tℓ) Crystal Ball. The major advantage over the Crystal Ball is the presence of a magnetic field and high resolution drift chambers immediately surrounding the interaction regions, which permits tracking and momentum resolution on charged particles. This momentum measurement and the longitudinal segmentation possible with liquid argon also improves the π - e discrimination capability. The trade-off for the best energy resolution is a large percentage of liquid argon compared to any passive heavy radiator which makes the LAND detector quite large. External muon identification is, therefore, not possible.

The group investigating LAND[1] did not reach an absolute conclusion about the inclusion of passive radiators within the liquid argon. These radiators degrade the energy resolution by introducing a fluctuation resulting from the variable amount of energy deposited in the liquid argon. The pure argon detector, on the other hand, permits the shower to spread radially over large distances. From the Moliere radius of 8.5 cm, one can estimate that a region 0.5 m in diameter will be required to capture 90% of the shower energy.[2] If a new particle is produced in a complicated state with many photons, the pure liquid argon detector may have hopeless ambiguities. Pure argon does have the advantage of short absorption length compared to radiation length. A 15-radiation length detector, for example, represents 2.6 absorption lengths. Even without external calorimetry, this detector would give about 200 to 1 rejection of π pairs as μ pairs.

The energy resolution of a pure liquid argon detector is somewhat speculative. In principle, it is limited only by the capacitance of the detector, the amount of radial spreading of the shower and the energy which leaks out the back. Since there is no passive radiator, in a pure liquid argon detector there is no error due to sampling. Liquid argon also does not have the low photon statistics problem of lead glass nor the light collection and crystal homogeneity problem of NaI(Tℓ). Of course, "gremlins" may appear but an energy resolution of $3\%/E$ should be possible. The resolution depends on E rather than $\sqrt{E}$ because it is dominated by electronic noise. (This resolution requires a detector to insure that the gamma has

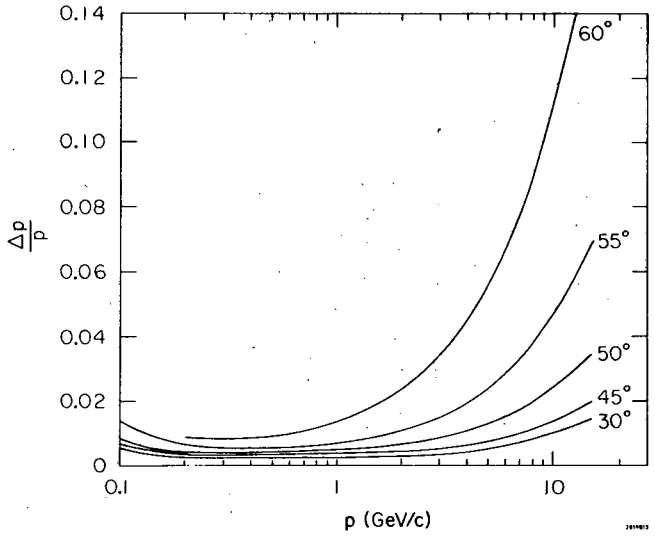

Fig. VI-3 Momentum Resolution in Streamer Chamber

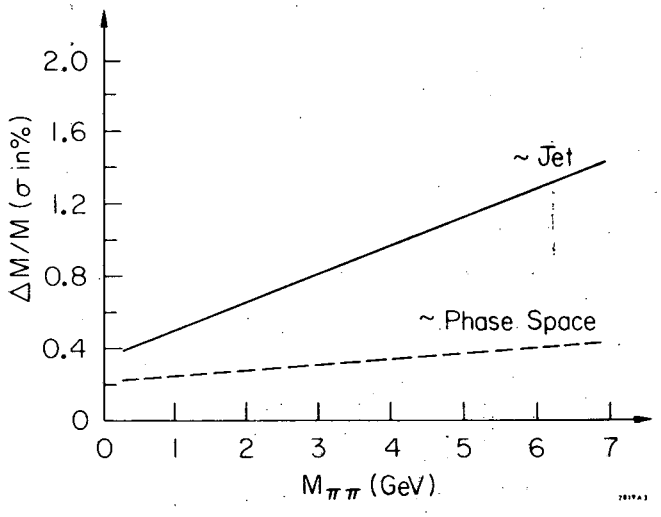

Fig. VI-4 Multiparticle Mass Resolution in Streamer Chamber

not converted in the solenoid coil.) Adding passive heavy radiators worsens this resolution and changes the energy dependence of the resolution to $\sqrt{E}$ except at the lowest energies. For example, if only 20% of the shower energy is deposited in the liquid argon, as is the case for the electron-photon module in the general new-particle detector, then the energy resolution above 500 MeV is about $7\%/\sqrt{E}$.[1]

Because the general new-particle detector involves the use of lead-liquid argon modules and a magnetic field surrounding the interaction region, it is instructive to compare a pure argon LAND with the new particles detector. The two are quite similar, but the LAND has better energy resolution for the gammas traded for poorer muon-hadron identification. The transverse position resolution for the gammas is also somewhat better for the LAND as is the π-e separation, both because of the greater segmentation of the detector. A detailed study would be required, however, to quantitatively estimate these differences.

In summary, for the new particle quest, LAND is superior to the general detector only for the study of heavy electrons which decay $e^* \to e\gamma$. The muon-hadron separation and the inability of LAND to measure total energy by calorimetry are severe disadvantages in new particle searches. Indeed, unless the e^* has a pathological decay scheme, it is likely that the γ will have sufficient energy for the general detector to do an acceptable energy measurement. We conclude that LAND has only limited use for a new particle search.

REFERENCES

1. See the report on LAND elsewhere in this Summary Study Volume.
2. Carol Jo Crannel, Phys. Rev. 161, 310 (1967).

4. Off-Axis Solenoid

One of the problems of single μ search at PEP is the background from meson decay. The effect of the ∼ 1m decay path typical of most solenoid detectors is to make a single μ search for $p_\mu \lesssim$ 3 GeV/c very difficult. The easiest way to reduce this problem is to reduce the decay path.

One way to reduce the decay path is to partially fill the interior of the solenoid with a dense non-magnetic material. This essentially wastes the magnetic field in that region. An equivalent effect can be achieved by moving the beam pipe OFF the axis of the solenoid without the loss of the magnetic field region. This allows an improved momentum resolution for particles in the opposite hemisphere. It also should be possible to use the same detectors as the normal solenoid configuration if they are designed in advance for this option. The problem of compensating for the effect of the magnetic field is probably equivalent to that for the normal solenoid. The radial field that occurs in the beam pipe near the end caps is small if the iron is not saturated and can be further reduced by surrounding the beam pipe with a μ-metal jacket in that region.

5. Streamer Chamber as a Core Detector for New Particle Searches

The principal report done on the streamer chamber during the study is included in the General Detector Group report. Here we review the properties of such a system and note its characteristics as a new particle detector.

Due to the high information densities possible with current electronic readout techniques, the streamer chamber can be used for very precise charged particle momentum measurement. With a chamber of length 1.5 m, outer radius .9 m and inner radius .25 m in a magnetic field of 15 kG, a measurement with $\Delta p/p < 1\%$ up to p = 10 GeV/c appears feasible over $.75 \times 4\pi$ solid angle (see Fig. VI-3). Angular measurements of comparable precision can be made, with resulting excellent multibody mass resolution (see Fig. VI-4).

Particle identification by ionization is possible over approximately the same range as usually done by time-of-flight. In addition, e/π, e/K and e/p separation can be done for $.2 < p < 10$, $p > .8$ and $p > 1.5$ GeV, respectively, due to the relativistic rise in particle ionization. Some π/K and π/p separation is also possible for $p \sim 2$ and $p > 3$ GeV/c, respectively, by the same technique. Excellent e/hadron separation and good

0 0 0 0 4 5 0 1 6 6 0

γ detection and energy measurement over a somewhat reduced solid angle can be obtained by insertion of PbO_2 plates in the outer region of the streamer chamber, which, however, requires either more radial space or reduced momentum measurement accuracy, as well as substantially increased data handling capacity. (It is already bad.)

Two access problems require solution. First, the chamber charger line must be brought through the coil, probably requiring a hold of 20 cm diameter through the coil. Second, the solid state readouts require perhaps 1 m (less with some lenses) of transparent spatial separation from both ends of the streamer chamber, although apparently they need not be outside the magnet pole caps.

A further requirement is that the trigger must be relatively low rate, with 5/sec or less probably being acceptable. The Marx charging time is of the order of 100 msec and readout time should be less than that. A two-particle trigger with inner MWPC, outer trigger counters and beam crossing should be satisfactory.

An apparatus built around a streamer chamber clearly has great advantages for searching for new particles whose decay modes must be studied considering: (a) high momentum particles; (b) Missing neutral p and E; (c) high multiplicity, particularly in jets; (d) mass reconstruction of multi-body states; (e) dE/dx; (f) electron identification. Many of the classes of particles sought have signatures detectable and studyable with such information.

APPENDIX 1

PEP Cross-Sections Estimates from Hadron Machines

New particle searches at proton machines have established limits on their production cross-sections. These limits have relevance to such searches at PEP if a model can be derived to relate hadron collisions to e^+e^- annihilation.

If we assume that all new particle production at hadron machines is due to pair production from virtual time-like photons we can use measurements of the cross section for

$$p + p \rightarrow l^+ l^- + \text{anything}$$

as a measure of the virtual photon flux in hadronic collisions. If this flux is then integrated over the appropriate kinematic range for new particles of a given charge, mass, etc., the cross section of vertical photons capable of producing a given particle in an experiment can be estimated and compared to the experimental limit. In this way one can estimate an upper limit to the number of new particles which can be produced at PEP for a given integrated luminosity by extracting mass limits from the hadronic experiments.

From scaling arguments (dimensional analysis) the cross section for $p + p \rightarrow l^+ l^- +$ anything can be written

$$\frac{d\sigma}{dq^2} = \frac{4\pi\alpha^2}{3q^4} F(q^2, S) \qquad (1)$$

where q^2 is the invariant mass^2 of the lepton pair (i.e., the virtual photon) and $F(q^2,S)$ is a dimensionless form factor; S is total center-of-mass energy in the P-P collision. If scaling holds then F is a function of the variable q^2/S.

Figure 1 depicts F(x) as a function of $x = q^2S$ for all existing data for P-nucleon experiments (Lederman and Ting at BNL and W. Lee at FNAL). The solid curve is the prediction derived from the parton distribution functions extracted from deeply-inelastic lepton scattering.

The production cross-section for pairs compared to u^+u^- from time-like virtual photons is

$$\frac{d\sigma}{dq^2}\ \text{pairs} \doteq \left(\frac{d\sigma}{dq^2}\right)_{\mu\mu} \left(\frac{Q}{e}\right)^2 \left[1 - \frac{4M^2}{q^2}\right]^{1/2} A\left(\frac{M^2}{q^2}\right) \qquad (2)$$

where M is the mass of a new particle and q^2 is the virtual photon mass

$$A\left(\frac{M^2}{q^2}\right) = \begin{cases} 1 + \dfrac{2M^2}{q^2} & \text{for fermions} \\ \left(\dfrac{E}{M}\right)^2 \left(1 + \dfrac{3M^2}{q^2}\right) & \text{for bosons} \end{cases}$$

Thus, the total pair cross section is a function of the mass of the new particles

$$\sigma_{pair}(M,S) = \left(\frac{Q}{e}\right)^2 \int_{4M^2}^{S} \left(\frac{d\sigma}{dq^2}\right)_{\mu\mu} \left(1 - \frac{4M^2}{q^2}\right)^{1/2} A\left(\frac{M^2}{q^2}\right) dq^2 \qquad (3)$$

If we let $x = q^2/S$ then

$$\sigma_{pair}(M,S) = \left(\frac{Q}{e}\right)^2 \frac{4\pi\alpha^2}{3S} \int_{4M^2}^{1} \frac{dx}{x^2} F(x) \left(1 - \frac{4M^2}{xS}\right)^{1/2} A\left(\frac{M^2}{xS}\right) \qquad (4)$$

This integral can be evaluated numerically for a given value of M using Fig. A-1 and the value of S appropriate for a given hadronic experiment. In this way one can translate an experimental upper limit for new particle production in hadronic collisions into a lower limit on the new particle mass which pair is produced. This mass limit can then be used with Eq. 2 to predict an upper limit on new particle production at PEP ($q^2 = 900\ GeV^2$).

A quick method of estimating whether it is reasonable to search at PEP for particles of given mass in light of hadron beam cross-section limits can be useful. In terms of the variable $x = q^2/S$ σ_{pair} is given by Eq. 3.

The quantity $F(x)/\ ^2$ is plotted in Fig. 2 so that the pair cross section in a hadronic experiment with center-of-mass energy S can be simply calculated from folding the kinetic factors with Fig. 2 for $x = 1$ to $x = 4M^2/S$. The ratio of the experimental limit to this predicted cross section gives the effective suppression factor for vertical photons to produce pairs of particle mass = M.

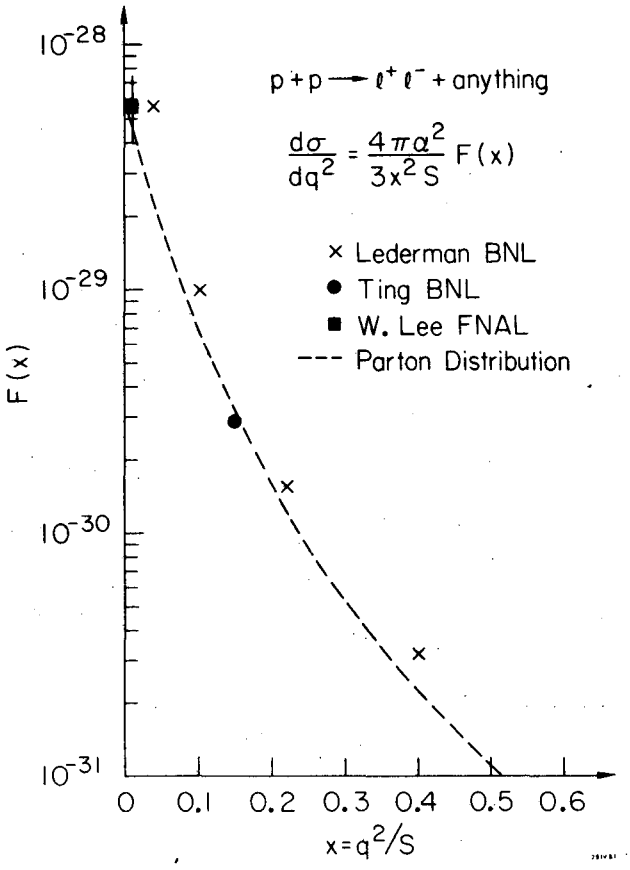

A-1 F(x) from Hadron Beams (see text for use)

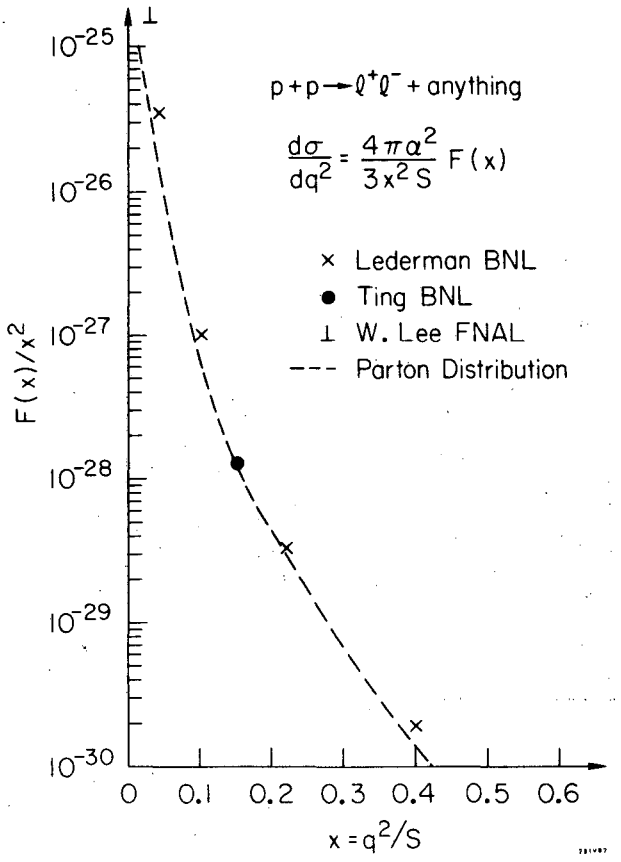

A-2 $F(x)/x^2$ from Hadron Beams (see text for use)

This suppression factor, whether viewed as a form factor, or as due to some dynamic suppression of the coupling, can be used trivially to estimate an upper limit on the number of events possible at PEP.

For example, if the predicted σ pair = 10^{-35} cm^2 for a mass of 2 GeV and an S appropriate to an experiment which gives a cross-section limit of 10^{-41} cm^2 for the production of a particular particle, then the suppression factor in cross-section is 10^{-6}. Since a typical PEP experiment with an integrated luminosity of 10^{38} cm^{-2} produces 2×10^6 virtual photons (if σ_T = 20 mb), the hadronic limit predicts only few events at PEP. One should, however, be very careful in neglecting the kinematic factors in the integral. It is better to include them and to calculate numerically the integral.

It should also be noted that the higher the mass the lower σ pair so that the suppression factor for a given experimental limit decreases with increasing mass. Another aspect of this procedure is that the hadron-hadron estimation of the virtual photon flux actually measures the product of flux and the partial width of the virtual photons to lepton pairs. It may be as in the case of the ψ and ψ' that the branching fraction to lepton pairs of a resonance state is small. This results in a relative insensitivity to the state in a lepton pair experiment in hadron beams while storage ring experiments could still observe large effects.

 0 0 0 0 4 5 0 1 6 6 1

REPORT OF EXPERIMENTAL AREAS GROUP

A. Carrol, B. Case, D. Coyne, F. Foster, F. Lobkowicz, F. Martin,
C. Morehouse, P. Oddone, C. Prescott, L. Keller, and G. Manning

1. INTRODUCTION

The 1974 PEP Summer Study made recommendations concerning the experimental areas. The majority of these have been incorporated into the updated PEP design. The description of the proposed experimental areas presented to the Summer Study is appended to this report. In the appended drawings the elevations are shown relative to the tunnel midplane. At the time of the Summer Study the proposal was to construct the e^+e^- ring 80 cm above the tunned midplane. The proton ring, located in the tunnel midplane, would be added later and the interaction point would then be lowered by 80 cm.

It will be seen that Area 6 is an open concrete pad of 40 × 40 m, 4.8 m below the proposed e^+e^- interaction point. The equipment is housed in a light flexible building that can be modified to satisfy experimental demands. Area 4 is deep below the surface and access is only through a tunnel of 3 × 3 m cross section that ends at the machine tunnel height, which is ~ 2 m above the pit floor.

Areas 2, 8 and 12 have access from the side 4 m above the pit floor level. Area 10 is very limited and is not intended for experimental physics.

All interaction points have 20 m between the high β quadrupoles giving ± 9.7 m free for experimental equipment. Areas 2, 4, 6 and 12 have the e^+e^- interaction point 4.8 m above the pit floor and Area 8 has 6.8 m. As proposed the ep interaction point for ep would be 80 cm below the e^+e^- interaction point.[1]

2. RECOMMENDATIONS FROM 1974 PEP SUMMER STUDY NOT INCORPORATED INTO UPDATED DESIGN

There are only two significant recommendations made by the 1974 Summer Study that are not included in the updated design. The first of these was the recommendation that three of the six interaction regions should have 10 m between the high β quadrupoles rather than 20 m -- the object being to get a higher luminosity in these regions. This recommendation was not included because of the cost. It is intended to consider this modification as a possible improvement program.

The second recommendation not adopted was that the e^+e^- and ep interaction heights should be the same. To achieve this it would be necessary to either install the electron ring magnets for phase I at the planned height of the proton ring for phase II or to deflect the e^+ and e^- beam down by 80 cm in the long straight sections. The former method is simpler.

The arguments for having the same interaction height for phase I and phase II is that experimental equipment will in practice grow to occupy the full 4.8 m available below the beam and it will then be very difficult to lower the equipment by the required 80 cm when the proton ring is added. Many detectors will be reused in phase II either to continue with e^+e^- physics or because they are suitable for ep physics.

The arguments for not having the same interaction height are the extra cost and inconvenience of longer supports for the electron magnets and the fact that the whole of the electron ring has to be moved when the proton ring is added rather than only half if the electron ring is placed 80 cm above the proton ring height in phase I.

From the experimental viewpoint the same height for e^+e^- and ep interaction points is still strongly recommended.[1]

3. SUMMARY OF DETECTORS PROPOSED DURING 1975 SUMMER STUDY

Table 1 gives a summary of relevant parameters of the detectors considered during the 1975 PEP Summer Study.

The following explanatory points need to be made:

a) Item 1 (the parastic 2γ tagging system) is not a full detector, but a possible 2γ tagging system that can be added to any other detector that leaves adequate room. Those experiments listed as using it need the equipment they specify plus that given in row 1 of the table.
b) Item 2 (general user magnet) is not a full experiment but is a magnet system plus a central drift chamber assembly for measuring momentum of charged particles. Space is left for the addition of other detectors required for specific experiments. Experiments using it need the equipment they specify plus that listed in row 2 of the table.

The following comments can be made on the information gathered.

3.1 The 1974 study included twenty experimental systems, the 1975 study includes ten. A possible extrapolation to 1976 could be five detectors which matches the five interaction regions--this may not be so unreasonable because the ten systems from this study include considerable duplication; the number could easily be reduced by a factor of two in removing this duplication.

Table 1. Requirements of the detectors designed by the 1975 PEP Summer Study. The symbol ⊕ means that the requirements of the device following the ⊕ symbol need to be added to the basic detector.

	Detector	Refs.	Electronics: Phototubes	MWPC wires	Drift chamber channels	Cables Sig.	Cables HV	Size of equip. ±L (m)	±W (m)	±H (m)	Size: Total wt. (tons)	Size: piece wt. (tons)	Size of largest piece L	W	H	Power MW	Magnet Field Kg.	Magnet Vol. m^3	Services: Special Gas	Gasses Vol (m^3)	Gasses P (atm.)	Refrigeration T (°K)	Refrigeration Power (wt.)	Refrigeration Mass (tons)	Counting rooms Close (m^2)	Counting rooms Far (m^2)	Monitors L	Monitors p^2 OL	Monitors YY tag
1	Parasitic 2γ tag.		1000	14000	–	1000	1000	9.7	1	1	< 1	< 1	1	1	1	–	–	–	1	--				–		10	10	X	✓	X
2	General user magnet GUM		20	–	5200	50	50	5.6	4	4	400	30	4	2	2	s/c	15	25	2	–			4	50	2	20	200	✓	X	✓
3	Two photon expt. ⊕ GUM		300	4000	5000	500	500	9.7	4	4	700	30	4.6	2	0.2	1.7	4.5	15	3	–			4 Flux Excluder	30	0.1	10	50	X	✓	X
4	Neutral detector ⊕ GUM ⊕[2γ tag.]		20	–	600	50	50	5.6	4	4	200	2	4	3	2	–	–	–	4	–			78	?	200	10	100	✓	✓	✓
5	Crystal ball + calorimeter ⊕[2 γ tag]		1000	–	1500	1000	1000	3.5 (9.7)	3.5	3.5	630	30	2.5	4	0.3	–	–	–	5	–			78	?	100	10	100	✓	✓	✓
6	High momentum (using magnet similar to GUM)		400	1000	3000	800	400	6	4	4	750	30	4	1	0.3	s/c	20	25	6	pentane propane	11 75	6 1	4	?	?	10	100	X	X	X
7	High momentum (using large magnet with low field)		600	500	5000	600	600	6	3.6	3.6	350	30	4.5	6	6	s/c	3	240	7	isobutane pentane	2 19	4 1	4	?	24	10	100	X	✓	X
8	General detector ⊕[2 γ tag]		300	–	1000 -5000	300	300	4.7 (9.7)	4	4	300	10	4	2.3	2.3	s/c	15	12	8	freon 12	8	4	4	200	?	10	100	✓	✓	✓
9	Streamer chamber ⊕[2 γ tag]		200	50 m^2 delay line	2000	200	200	4.5 (9.7)	3.5	3.5	1500	30	1	5	5	s/c	15	55	9	–			4	?	?	10	100	✓	X	✓
10	New particle search ⊕[2 γ tag]		340	250	2800	400	400	5.5 (9.7)	2	2	430	20	0.6	1	1	s/c	20	3	10	–			4 78	100 ?	2.5 24	10	100	X	X	✓
11	Iron ball ⊕ longitudinal pol'zer		150	–	1000	500	200	9.7	2.2	2.2	150	80 (15)	3.8	4.4	2.2	0.15	18	30	11	–				–		20	80	✓	✓	X
12	Split iron ball including polarizer		200	–	6000	400	200	9.7	3	3	630	30	9.4	3	0.5	0.2	18	80	12	–				–		15	100	X	✓	X

0 0 0 0 4 5 0 1 6 6 2

3.2 A "typical" experiment has 300 phototubes, 3000 cells of drift chamber and weights 400 tons. Adding the parastic 2γ tagging system increases the requirements by about 1000 phototubes and 14,000 wires of MWPC. A simplified and cheaper parasitic 2γ system is surely possible and should be designed.

3.3 Figure 1 is a scatter plot of the total length and total width of the twenty detectors from the 1974 study shown as dots. The detectors from the 1975 study are shown as crosses. The lengths shown are 2L given in Table 1, where the figures are those outside the brackets. This is the length required by the detector alone. The figures in brackets are the length required including addition of 2γ tagging.

Including these requirements it is clear that most experiments have expanded to fill the available interaction length and the height available.

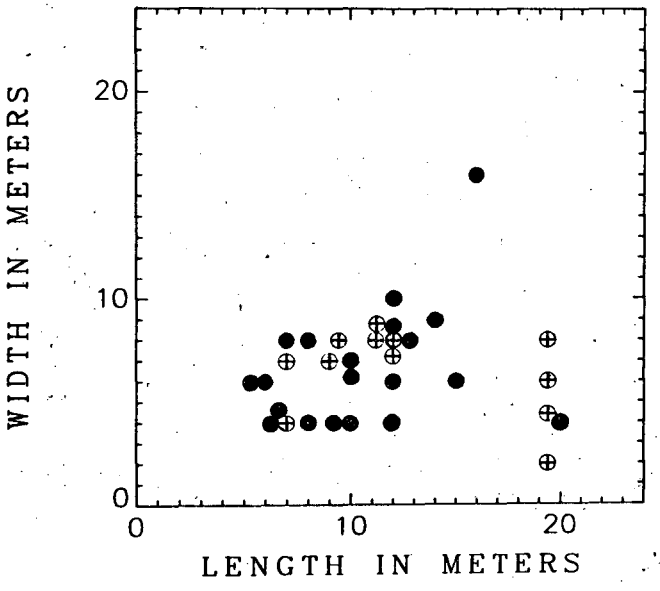

Fig. 1. Plot of length vs. width of detectors from 1974 (filled circles) and 1975 (crossed circles) PEP Summer Studies.

All experiments fit within a 4 m pit. Were experiments able to obtain higher luminosity by decreasing the interaction length, it is probable that some of them would accept either no 2γ tagging or a lower 2γ tagging efficiency.

3.4 All detectors have been persuaded to manage with a crane capacity of 30 tons, but several would benefit if a higher capacity were available.

3.5 Groups were asked to estimate the size of the largest single piece to be taken into the experimental area. These values are given in the table and show that access is required for large objects. Several experiments will not fit into region 4 for this reason.

3.6 Eight of the ten experiments use superconducting magnets. Hence, in general, the power requirements are low, even though large volumes of magnetic field are used.

3.7 There will be considerable requirements for refrigeration. For superconducting magnets there are up to 24 tons of coil at 4°K. For liquid argon calorimeters there are up to 200 tons at 78°K. Not all groups have estimated the refrigeration requirements and further work is needed in this area.

3.8 Most groups require areas for fast trigger electronics close to the detector (within 10 m) and an area of 10 m^2 seems adequate. Groups will also require about 100 m^2 of counting room which can be more remote--within 50 m. General facilities will require rather more room because more than one electronics system may be present at the same time.

3.9 All groups require gasses used for MWPC or drift chambers. Several groups require additional gasses for Čerenkov counters. These requirements are shown in the table.

4. RECOMMENDATIONS

4.1 The e^+e^- and ep interaction points should be at the same height above the experimental area floor.[1]

4.2 Counting rooms should be provided allowing 10 m^2 within 10 m of the detector plus 100 m^2 within 50 m. The former will have to be in the experimental areas, but the larger areas should be in separate counting houses as the experimental areas are expensive real estate. General purpose detectors used by more than one experiment will require more counting room area. All groups will require access to light workshop space.

4.3 The lower energy range of PEP should be decreased to ~ 4 GeV to provide an overlap with SPEAR.[1]

4.4 Survey should be made of the cryogenic requirements of detectors and how they can be most economically met.

4.5 A survey should be made of the computing requirements for PEP for both on-line and off-line use. There are obvious advantages in standardization of on-line computers.

4.6 Provision should be made for access to the experimental areas not only for large heavy loads but also for easy access for light loads--say of less than 2 tons and area less than 2 × 2 m.

These requirements are adequately met in region 6. Region 4 is special and it is recommended that the tunnel access should finish at the level of the pit floor.

Regions 2, 8 and 12 are similar in that access is from the side and is 4 m above the pit floor. Four methods were considered for access for light loads:

(a) A cage picked up by the overhead bridge crane.
(b) A cage picked up by a light capacity crane supported from the side wall.
(c) An elevator.
(d) A ramp.

Item (d) is not recommended. Item (a) is easily provided but will be inconvenient because a crane driver will be required for each minor load and often the bridge crane will be in use for other work.

Item (c) is preferred to item (b) but is probably more expensive.

Three methods were considered for access for large and heavy loads:

1. A hole in the roof with a lightweight cover.
2. Proposed doors and a removable platform under the bridge cranes.
3. A removable side wall to the building with the bridge crane extending beyond the pit.

Item 1 is not recommended as it is expensive, is not compatible with the 4 m of earth shielding required for the ep system, and is not essential. Item 3 is more expensive than item 2 and will make it very difficult to provide adequate shielding for the ep option. Item 2, which is the proposed system, is recommended providing sufficiently large doors are provided--doors about 6 m wide and 5 m tall seem desirable.

4.7 Most experiments will require a 2γ tagging system and it is recommended that suitable vacuum chambers and synchrotron shields be designed so that all interaction regions can have this option.

FOOTNOTES

1. Following the 1975 Summer Study recommendations a tentative decision has been reached to build the electron-position ring in the midplane of the tunnel. Similarly the lower energy capability of PEP will extend to 4 GeV. See Appendix 2 of this report.

Appendix 1

DESCRIPTION OF THE EXPERIMENTAL AREAS AS OF JULY 1975.

By convention, we number the areas according to the hours, with 12 o'clock to the north. Figure A-1 shows the contour lines of the site and Fig. A-2 an elevation cut along the ring. The topographical variation is an advantage for the varied experimental program that we are considering. Each area has strengths and limitations, and together they fit both the land and the varied needs of the program. The basic parameters of the experimental areas are shown in Table A-1.

The land pattern favors the clockwise (CW) direction for the future proton beam. Alcoves in the CW direction have been included in Areas 12, 2 and 8. The alcoves are 20 m long, 7 m wide and 5 m high. Some e^+-e^- experiments will almost certainly need some alcoves, and the implementation of Phase II with 200-GeV protons would require them. The cost of adding them later would be many times larger than that of providing them initially. Areas 4 and 6 are extended naturally in the CW proton direction, as described below.

Some of the special features of each area follow:

Area 12 (Figs. A-3a and A-3b)

This area is located in moderate terrain with the interaction point 5 m below natural ground elevation. Access to the experimental hall is from a yard located on the outside of the ring. The experimental hall is offset laterally from the beam line. This allows set-up of very large apparatuses in the 17×20 m area adjacent to the beam. A typical device, and how it may be arranged in the area, is shown in Fig. A-4. The most utilitarian mode of bringing materials into the experimental hall is through portable loading platforms placed under crance coverage, as also shown in Fig. A-4. The area has an alcove in the CW direction.

Area 2 (Figs. A-5a and A-5b)

This area is also located in moderate terrain with the interaction point 6 m below the natural land elevation. The experimental hall and yard are similar in dimensions to Area 12, except that the hall will be placed symmetrically with 12 m on each side of the beam line. This would allow operation of two experiments alternating in a push-pull configuration. The area would also be very useful for two experiments not requiring full solid angle coverage or a single experiment needing large transverse dimensions on both sides of the beam line. The area is extended by an alcove in the CW direction.

Area 4 (Figs. A-6a and A-6b)

Area 4 is on the side of a steep hill with the interaction point 12 m below natural ground elevation. The hall will be positioned asymmetrically along the beam line, favoring experiments needing length in the CW direction. The experimental hall is narrow (12 m) and long (40 m). Access is via a tunnel from an adjacent clear area near grade level. Because the CW direction is favored, no alcove is included.

Area 6 (Figs. A-7a and A-7b)

This area is in the lowest terrain, with the interaction point nearly at natural ground level. Taking advantage of the low terrain and a good sandstone base, the proposed area consists of a very large pad (40×40m) providing great flexibility. Portable cranes, light buildings, portable shielding and ad-hoc arrangements will be used to rig and service experiments. The area is offset in the CW direction, and access is possible from both sides of the beam line. The flexibility of this area is especially advantageous for future development.

0 0 0 0 4 5 0 1 6 6 3

Area 8 (Figs. A-8a and A-8b)

The interaction point in Area 8 is 5 m below natural ground level. The area is similar to Area 12, offset laterally relative to the beam and having an alcove in the CW direction. The special feature of this area is the extra depth below the beam (6 m) and the crane height above the beam line (8 m). Some large experimental devices will have particular need for this feature.

Area 10

This area is deep underground, with the interaction point 20 m below ground level. The development of this area will be very modest. The tunnel will be widened to about 7 m for a length of 20 m. The area will be devoted primarily to machine physics experiments. Anyone who has observed the prograss of operating effectiveness in modern accelerators, particularly the ISR and SPEAR, will appreciate the excellent benefit to all experiments that accrues from the investment of machine time in storage ring improvement studies. Several experiments designed by the 1974 Summer Study would fit in this area, but the apparatus would have to be carried in small pieces.

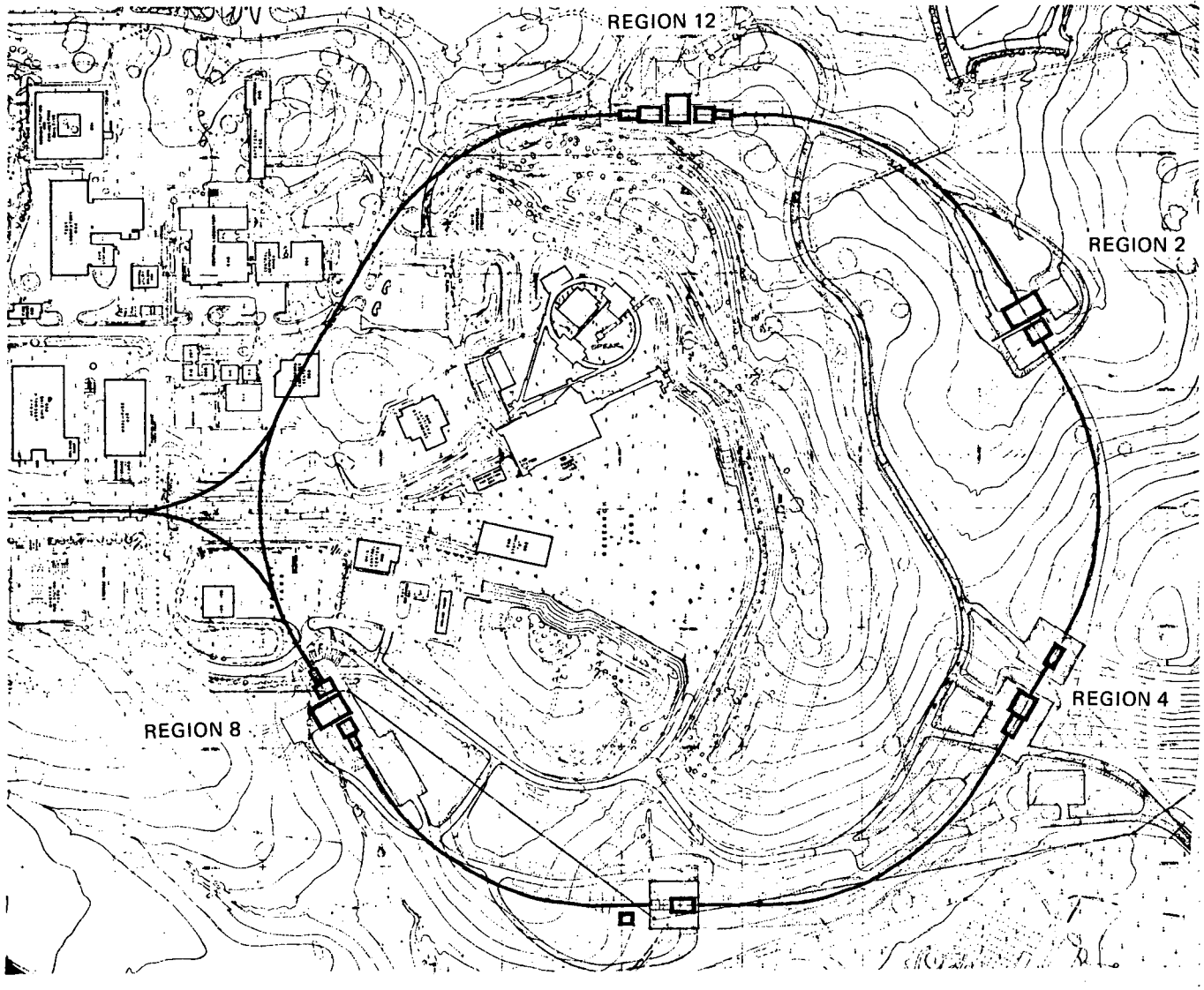

Fig. A-1. Topography of the PEP Site at SLAC .

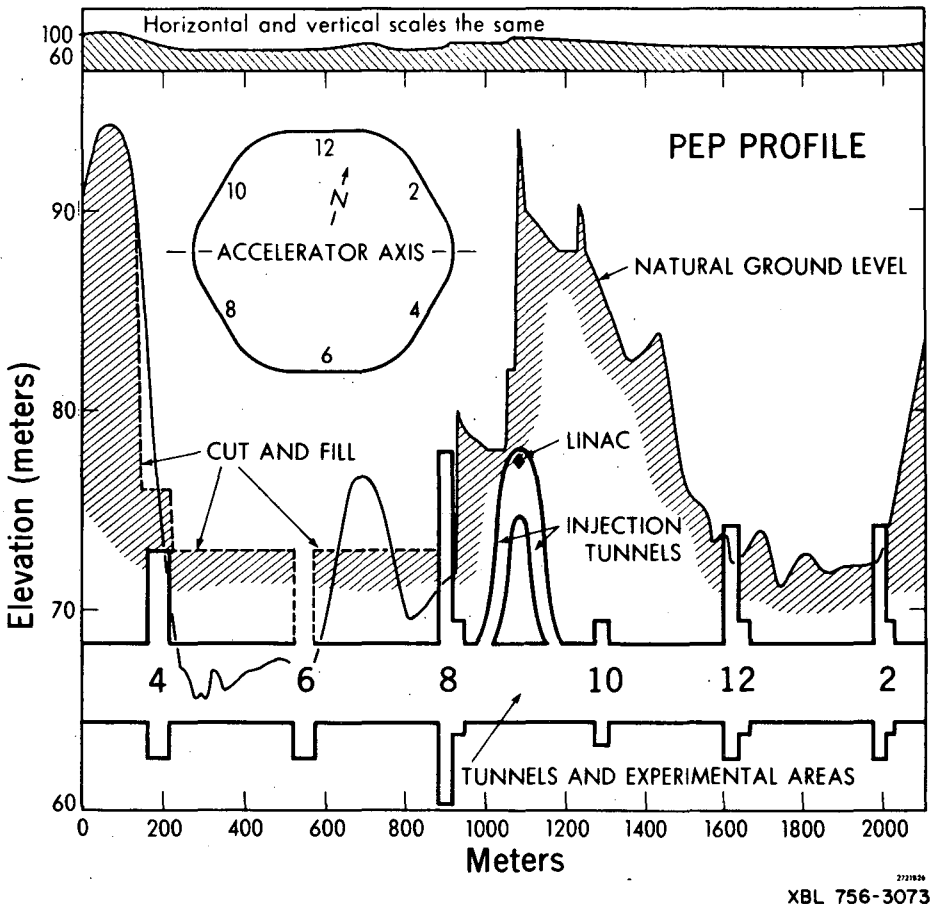

Fig. A-2. Topographical profile of the PEP Site.

0 0 0 0 4 5 0 1 6 6 4

Table A-1. Specifications for Experimental Areas.

	Area					
Specification	12	2	4	6	8	10
Length (m)						
Clockwise (CW)	10	10	30	25	10	10
Counter Clockwise (CCW)	10	10	10	15	10	10
Width (m)						
Inside	7	12	5	20	10	3.5
Outside	17	12	7	20	20	3.5
Height (m)						
Up (Crane Clearance)	5	5	4	∞	8	3
Down [a]	4.8	4.8	4.8	4.8	6.8	2.8
Crane (tons)	30	30	30	No	30	No
Nearby Space for Counting House	Yes	Yes	Yes	Yes	Yes	No
Alcove	Yes	Yes	No	No	Yes	No
Length (CW) (m)	20	20			20	
Width ± (m)	3.5	3.5			3.5	
Height {+ (m)	3	3			3	
- (m)	2	2			2	
Power (MW)						
Installed Capacity [b]	3	3	3	3	3	0
Distributed	1	1	1	1	1	0
Loading access	Outside (yard)	Outside (yard)	Outside (tunnel)	Both sides	Outside (yard)	Beam tunnel

[a] Drops by .8 m when the proton ring is added.

[b] Available at pad. The total for all areas is 10 MW.

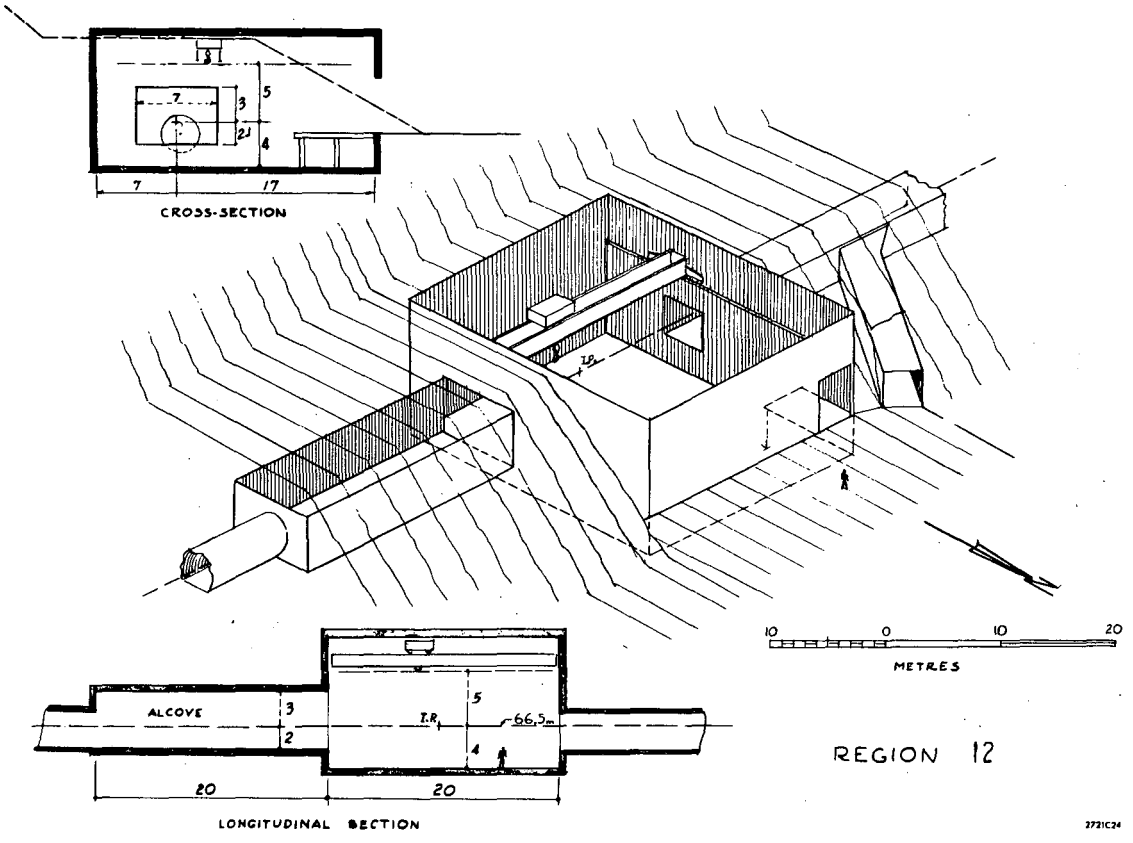

Fig. A-3a. Isometric view of Area 12.

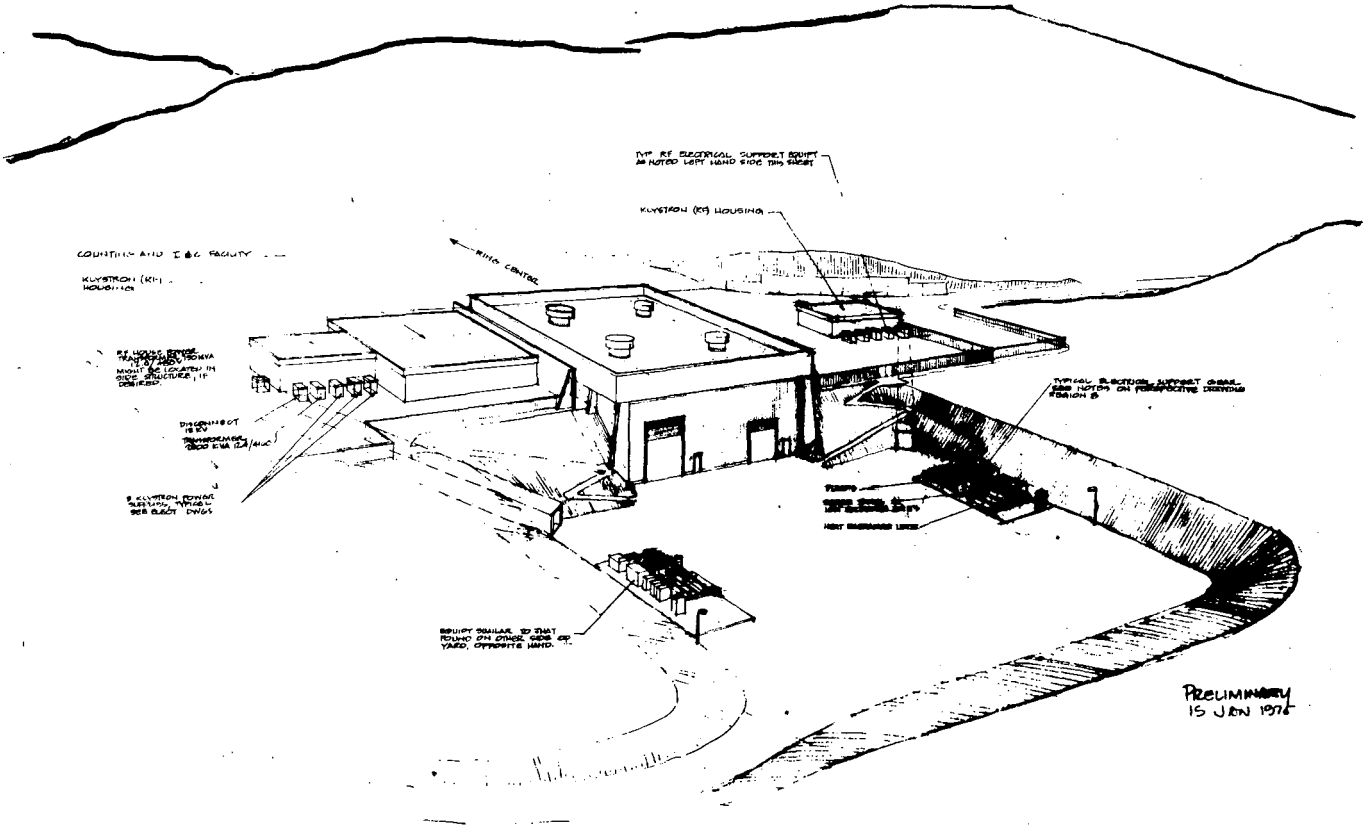

Fig. A-3b. Architectural view of Area 12.

0 0 0 0 4 5 0 1 6 6 5

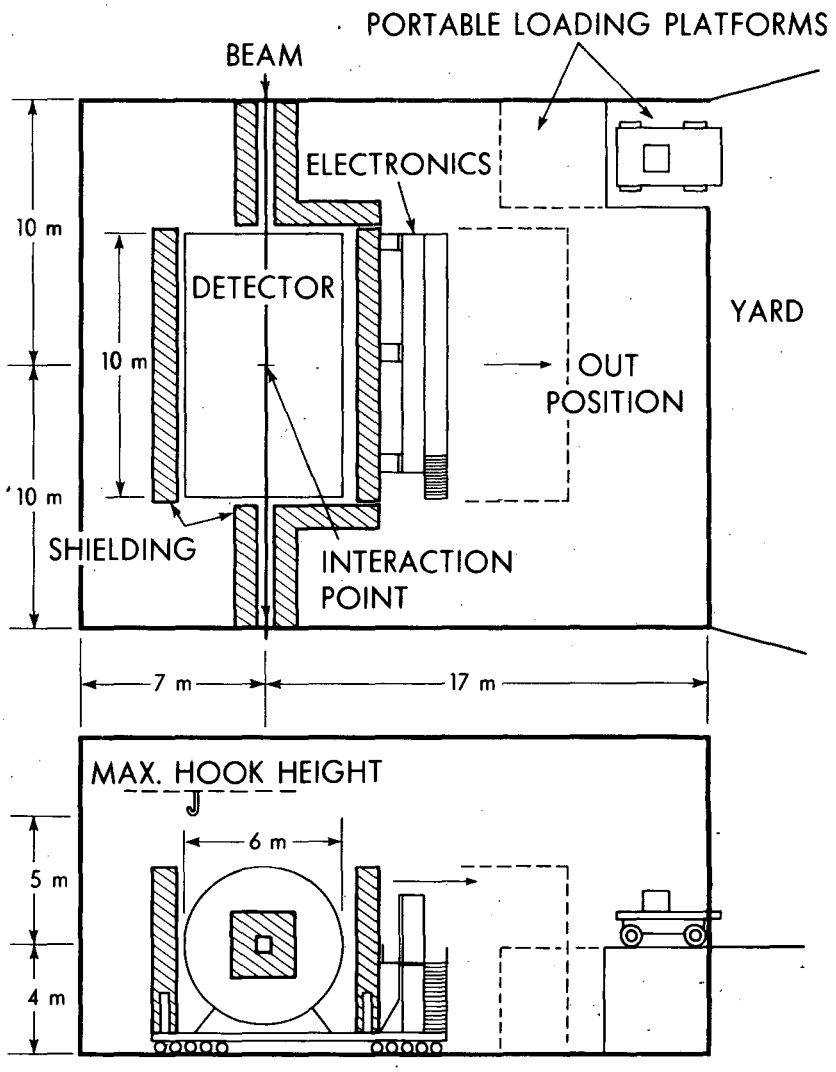

AREA 12: POSSIBLE EXPERIMENTAL SET-UP

2721825
XBL 756-3103

Fig. A-4. Possible experimental set-up for Area 12.

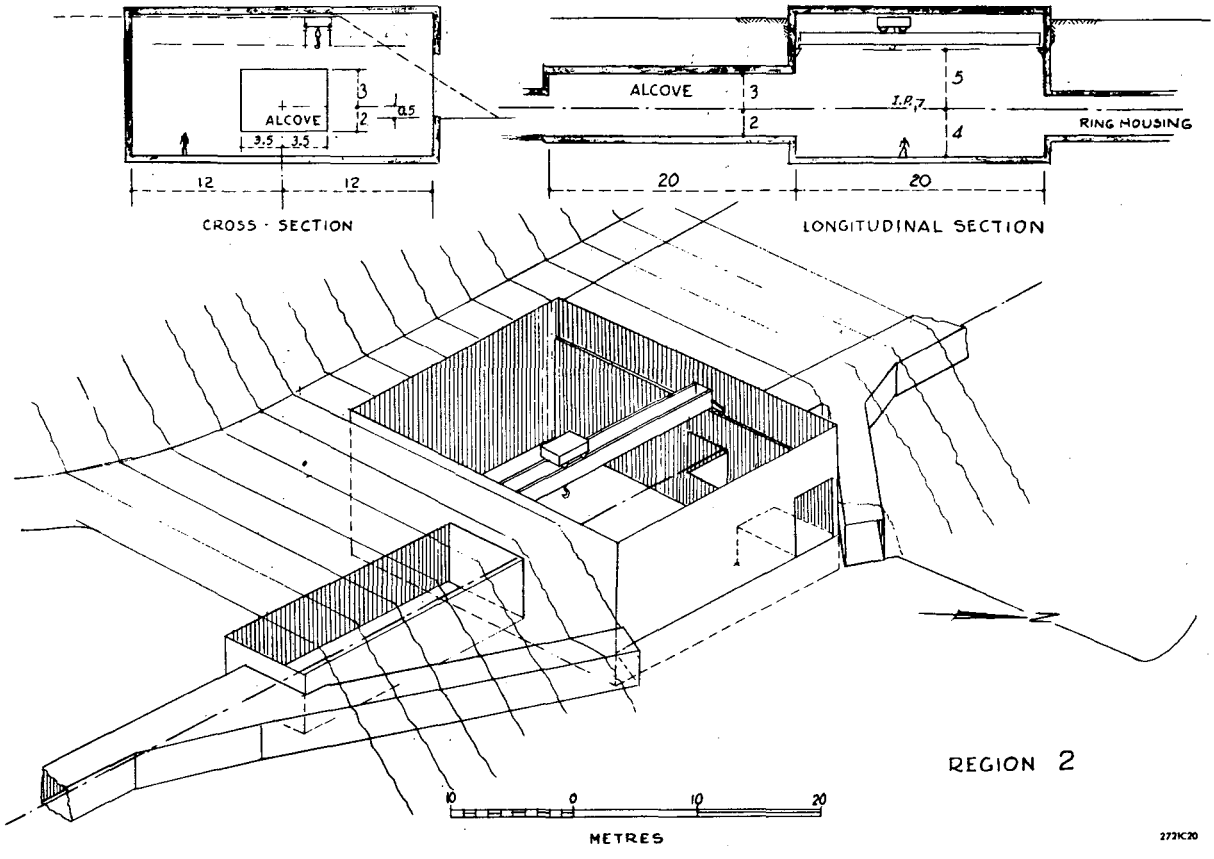

Fig. A-5a. Isometric view of Area 2.

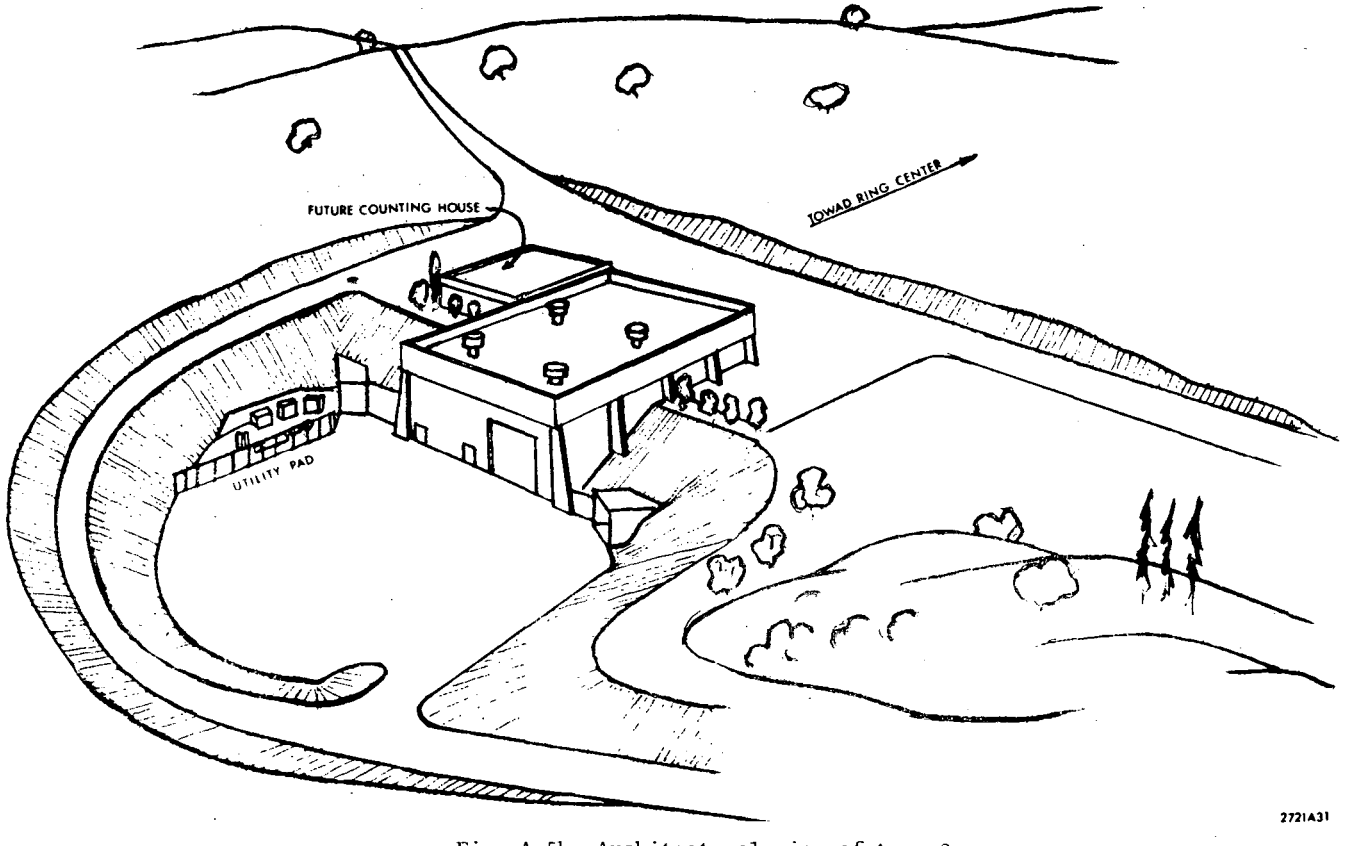

Fig. A-5b. Architectural view of Area 2.

0 0 0 0 4 5 0 1 6 6 6

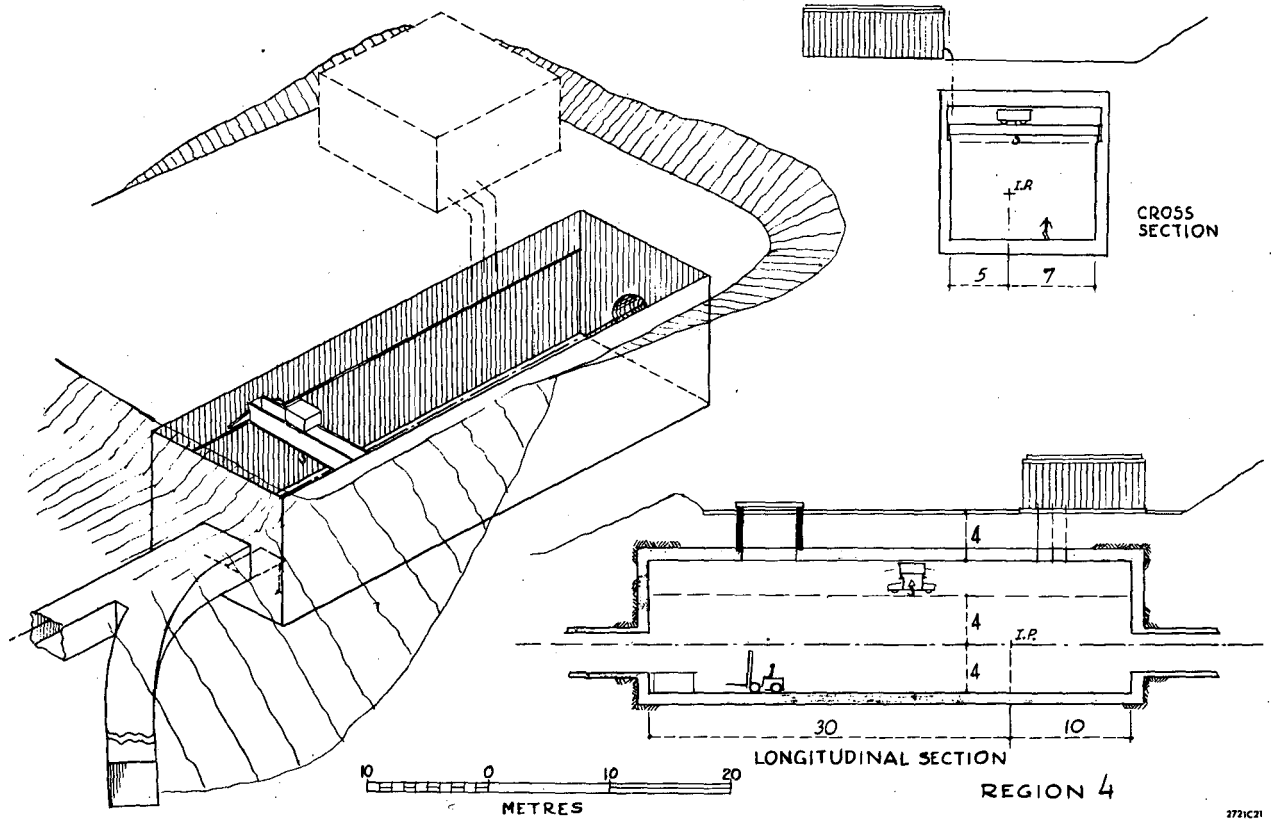

Fig. A-6a. Isometric view of Area 4.

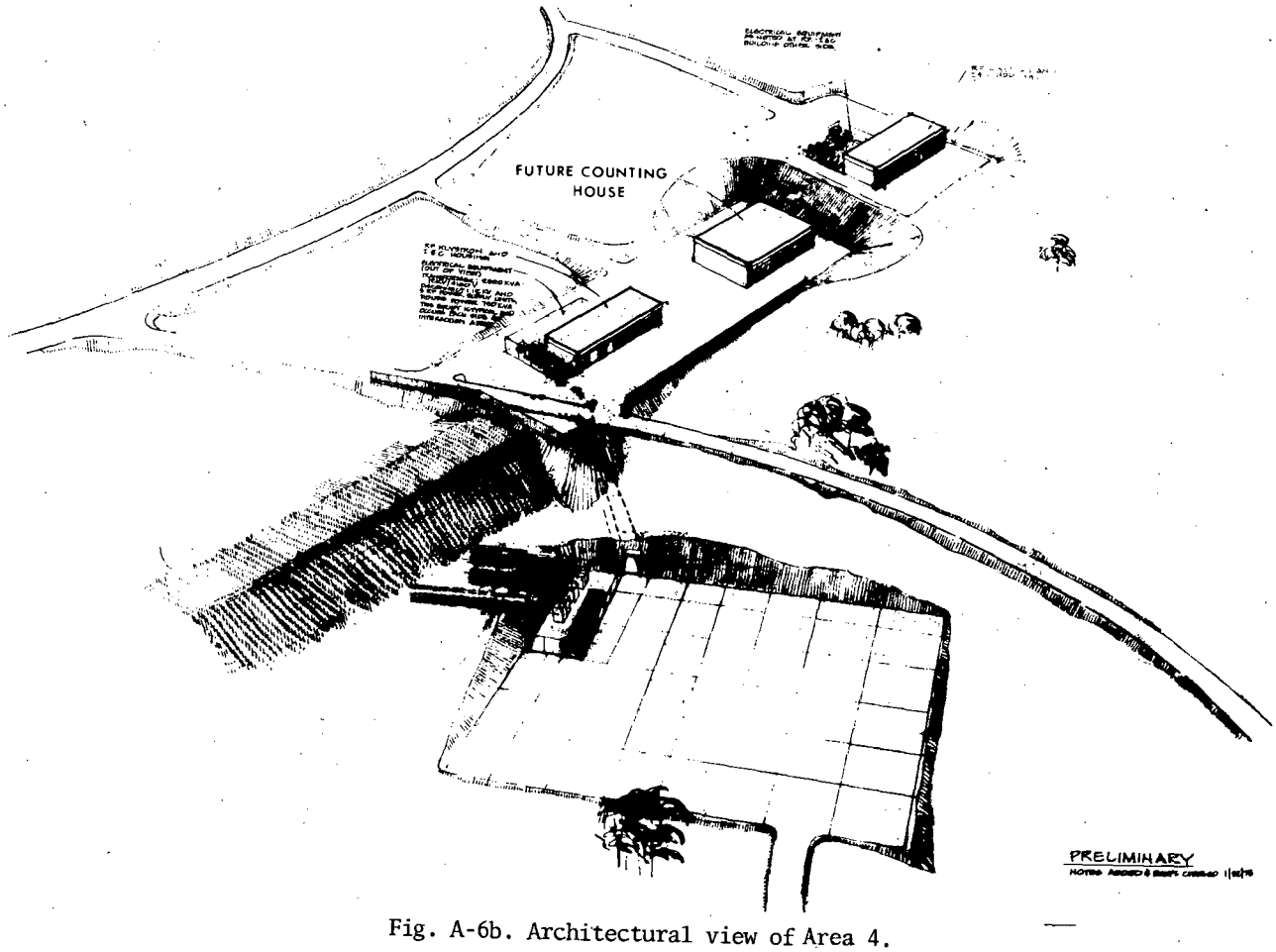

Fig. A-6b. Architectural view of Area 4.

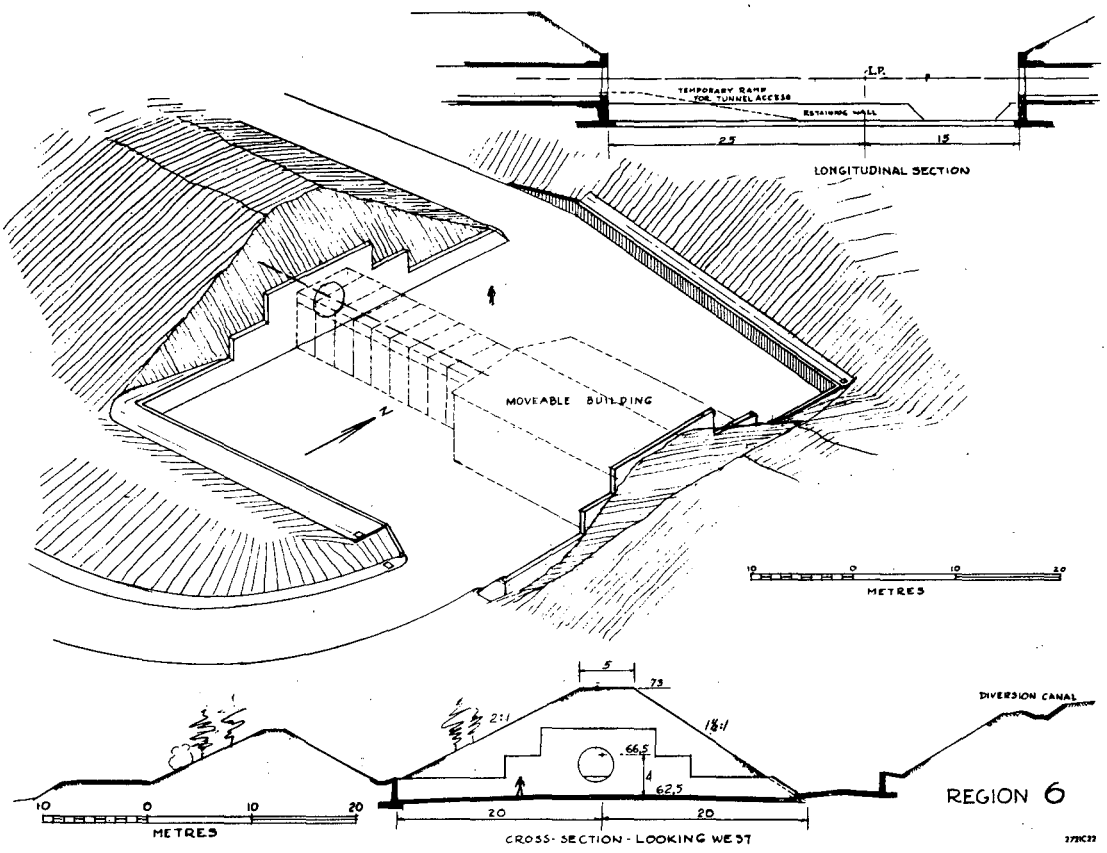

Fig. A-7a. Isometric view of Area 6.

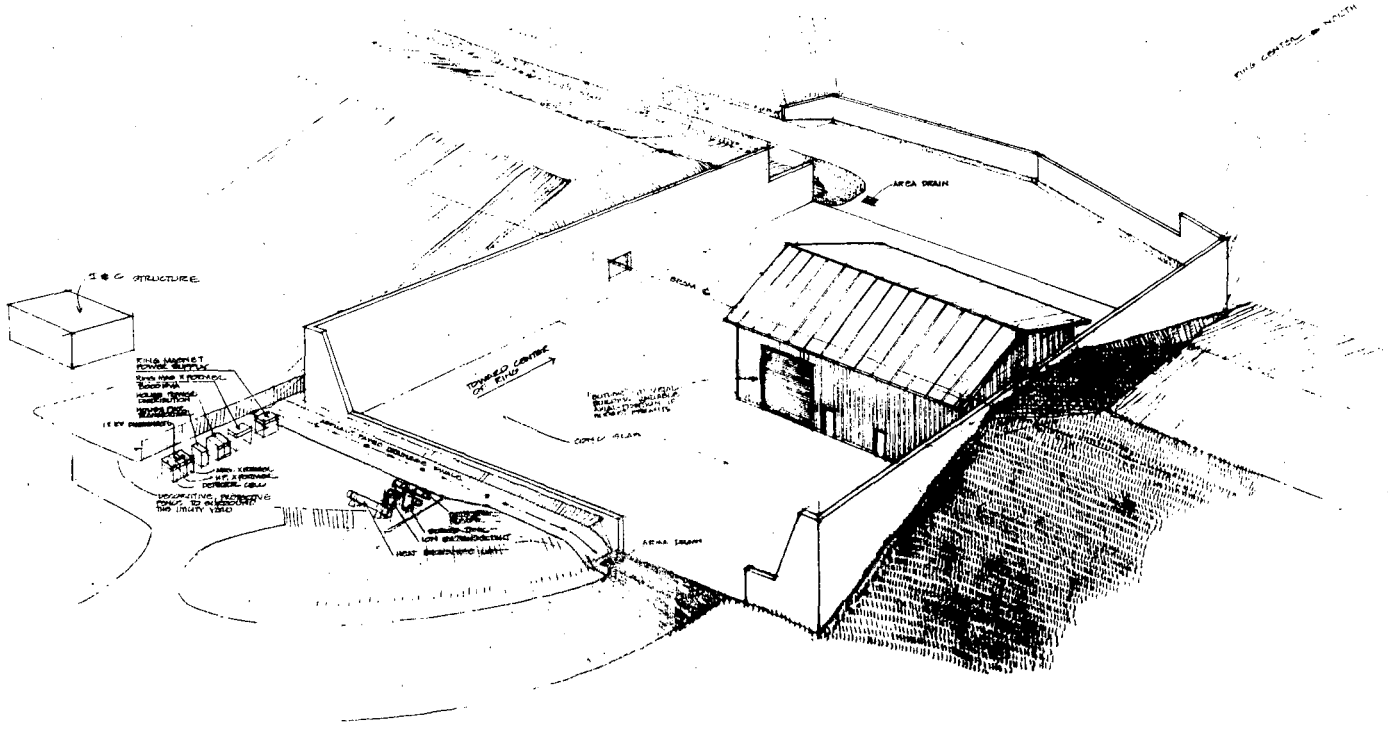

Fig. A-7b. Architectural view of Area 6.

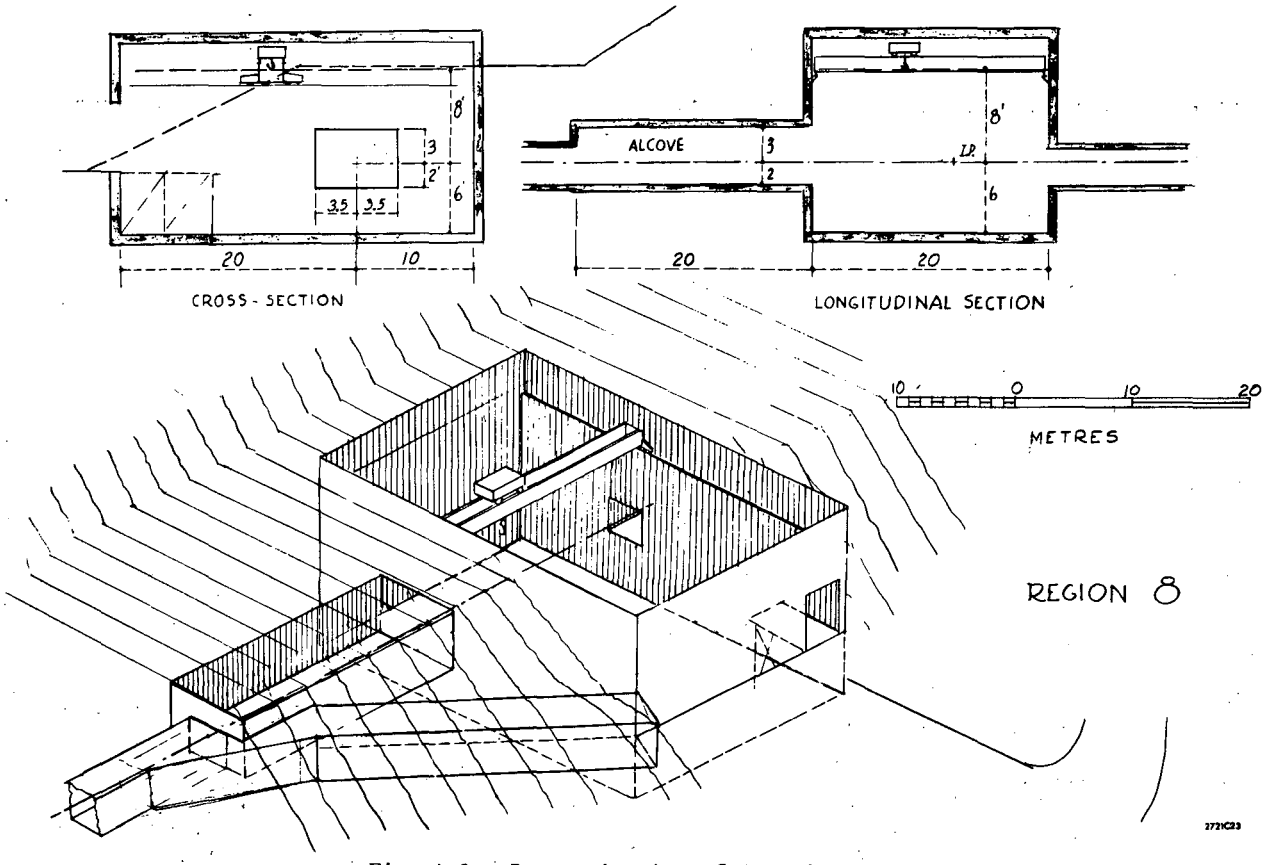

Fig. A-8a. Isometric view of Area 8.

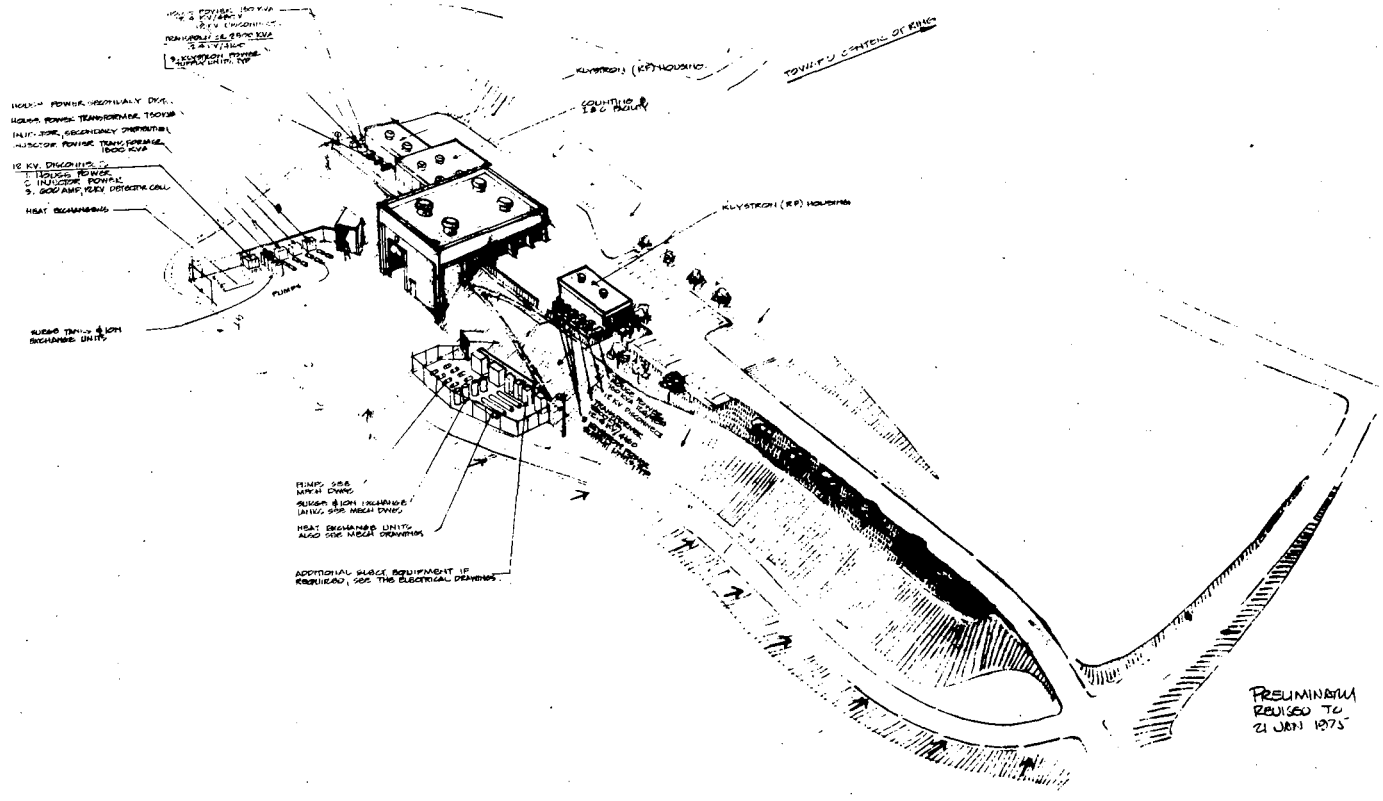

Fig. A-8b. Architectural view of Area 8.

Appendix 2

OFFICE MEMORANDUM • STANFORD UNIVERSITY • OFFICE MEMORANDUM • STANFORD UNIVERSITY • OFFICE MEMORANDUM

DATE: October 8, 1975

TO : PEP Distribution

FROM : J. R. Rees

SUBJECT: Working Decisions on Operating Energy Range and Beam Elevation

One of the recommendations of the 1975 PEP Summer Study was that the storage ring should operate down to a beam energy of 4 GeV in order to overlap the SPEAR operating range. This appears to be a reasonable and inexpensive criterion which we should adopt. It is therefore adopted as a working decision pending any outcries from the PEP group.

Another recommendation was that the beam height of the e^+-e^- ring should be the same as that planned for the proton ring. In our proposal, we were inconsistant in that the magnets in the tunnel were depicted as hanging just below the roof, 80 cm above the elevation planned for the eventual proton ring, while the beam line in the interaction regions was shown at the elevation of the proton beam. Whether to accept this recommendation has been the subject of many spirited discussions regarding cost, crane-hook clearance, shielding problems, the puerile irrepressibility of the average user and the passionately-held intestinal feelings of the storage ring builders. The working decision reached was that the beam height shall be that planned for the eventual proton beam.

These working decisions should be reflected in the Conceptual Design Report.

JRR:c

cc: G. Manning, Rutherford Laboratory
K. Strauch, Harvard University

• STANFORD UNIVERSITY • OFFICE MEMORANDUM • STANFORD UNIVERSITY • OFFICE MEMORANDUM • STANFORD UNIVERSITY • OFFICE MEMORANDUM
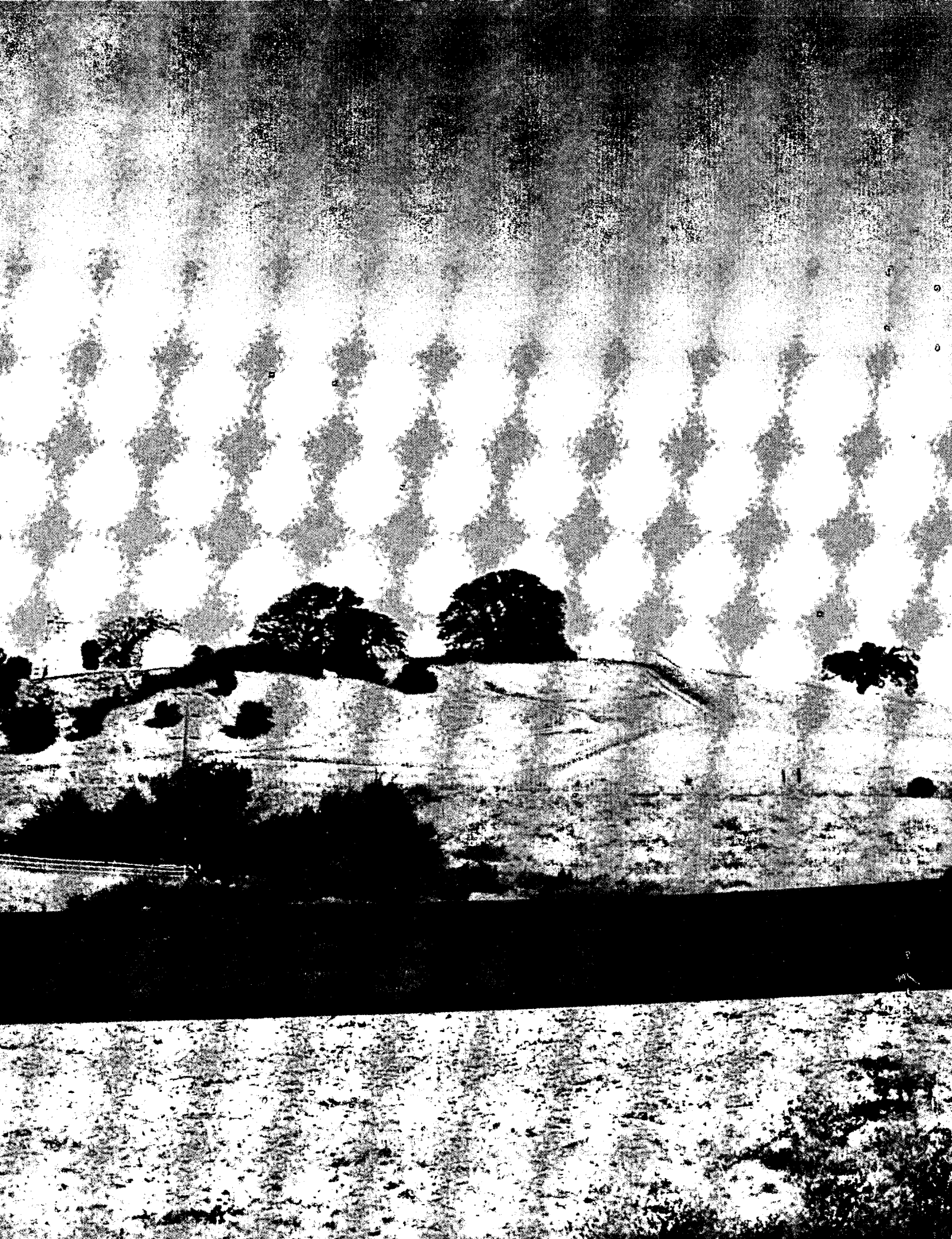
0 0 0 0 4 5 0 1 6 6 8